PilotSTRATEGY

# WP3 - Deliverable 3.5

## Report on near wellbore, caprock and faults/fractures integrity

**Release Status: Public**
**Date: April 2026**
**Filename and Version: V1.0**
**Project ID Number: 101022664**

PilotSTRATEGY (H2020- Topic LC-SC3-NZE-6-2020 - RIA)

**Editor:** Sarah Bouquet

**Contributing authors:**

France: Alayoine Axelle, Bouquet Sarah, Estublier Audrey, Frey Jeremy, Meiller Clémentine (IFPEN team)

Portugal: Pedro Pereira, Dounya Behnous, Augusto Mazezo, Júlio Carneiro, Karwan Khudhur, Theophile Guillon, Arnold Blaisonneau, Mário Santos and Maria Helena Caeiro.

Spain: Marta Mañas, Manuel Ron & Antonio Martín-Monge (Repsol team).

# 1. Document History

## 1.1 Location

This document is stored in the following location:

| | |
|---|---|
| **Filename** | PilotSTRATEGY_D3-5_NearWellbore_Caprock_Faults-fracturesIntegrity |
| **Location** | https://pilotstrategy.eu/about-the-project/work-packages/simulation |

## 1.2 Revision History

This document has been through the following revisions:

| Version No. | Revision Date | Filename/Location stored: | Brief Summary of Changes |
|---|---|---|---|
| V1.0 | | | |
| | | | |
| | | | |

## 1.3 Authorisation

This document requires the following approvals:

| AUTHORISATION | Name | Signature | Date |
|---|---|---|---|
| WP Leader | Sarah Bouquet | SB | 16/04/26 |
| Project Coordinator | Isaline Gravaud | IG | 16/04/26 |

## 1.4 Distribution

This document has been distributed to:

| Name | Title | Version Issued | Date of Issue |
|---|---|---|---|
| | | Public | 16/04/2026 |
| | | | |
| | | | |

The PilotSTRATEGY project has received funding from the European Union's Horizon 2020 research and innovation programme under grant agreement No. 101022664

Bouquet, S. 2026. Report on near wellbore, caprock and faults/fractures integrity. Deliverable D3.5. EU H2020, PilotSTRATEGY project 101022664, report pp 286.

**Disclaimer**

The information and views set out in this report are those of the author(s) and do not necessarily reflect the official opinion of the European Union. Neither the European Union institutions and bodies nor any person acting on their behalf may be held responsible for the use which may be made of the information contained therein.

The PilotSTRATEGY project has received funding from the European Union's Horizon 2020 research and innovation programme under grant agreement No. 101022664

## 2. Executive summary

This report summarizes the work that has been performed in Work Package 3 of PilotSTRATEGY, "WP3, Static and Dynamic modelling", task 3.4, "Quantification of phenomenological impacts".

The main objective of this task was to quantify the integrity of the near wellbore, the caprock and fault/fractures by simulation while injecting $CO_2$ and post-injection at the different targeted pilot project locations (French region, Portuguese region and Spanish region). Its secondary objective was to consider uncertainties from operational configurations or geological properties in this quantitative integrity assessment.

In that purpose, models adapted to the studied impacts (0D-3D, several physics coupling, local or large scale) were built to simulate the main physical and chemical mechanisms. Models' complexity also depends on available data and on functionalities of the considered simulation tool. Models are based on previous results from the PilotSTRATEGY project, in particular geo-characterization data from WP2[1], geological & static model from task 3.1[2] and well location definition and related flow simulations from task 3.2[3].

Regarding the large scope of the integrity study, it has been divided in three subtasks for clarity:

1. Subtask 3.4.1: The integrity of the wellbore is quantified through the calculation of the potential injectivity loss. Salt precipitation may occur around a $CO_2$ injection well due to evaporative drying, increasing brine salinity beyond saturation. This process can lead to the formation of solid salt deposits in the near wellbore pore space, reducing effective permeability and causing injectivity loss. On the other hand, $CO_2$-fluid rich can interact with in-place minerals leading to a change in petrophysical properties (with potentially both dissolution and precipitation) and thus changing the injectivity. This analysis was performed with a local model and/or radial wellbore model, modelling the fluid rock interactions and focusing on the injection period. Geochemical impacts of the $CO_2$ injection, leading to potential salt and mineral precipitation, are quantified through the mineral composition changes and its effects on the petrophysical properties (porosity, permeability, capillary pressure) and the injection rate (injectivity evolution).

2. Subtask 3.4.2: The caprock integrity related to the geochemical impacts of the $CO_2$ injection, i.e. potential impacts of $CO_2$-fluid rich in contact with caprock minerals, that could jeopardize the sealing quality of the caprock, is assessed through a reactive transport model applied to the caprock domain (local model). This model simulates the dissolved $CO_2$ migration by

[1] See Wilkinson, M. (Ed.), 2023. Report on petrophysics of all regions. *Deliverable WP2/D2.6, EU H2020 PilotSTRATEGY project 101022664 report;* Wilkinson, M. (Ed.), 2023. Report on Conceptual Geological Models. *Deliverable WP2/D2.7, EU H2020 PilotSTRATEGY project 101022664 report;* Fleury et al., 2023. Report on Geomechanical results for the 3 areas. *Deliverable WP2/D2.8, EU H2020 PilotSTRATEGY project 101022664 report.* Wilkinson, M. (Ed), 2025. Report of geochemical results for 3 areas. *Deliverable WP2/D2.9, EU H2020 PilotSTRATEGY project 101022664 report.*

[2] See Bouquet, S. (Ed.), 2024.3D static geological model. *Deliverable WP3/D3.1, EU H2020 PilotSTRATEGY project 101022664 report;* Bouquet, S. (Ed.), 2024. Report on static modelling with uncertainties. *Deliverable WP3/D3.2, EU H2020 PilotSTRATEGY project 101022664 report.*

[3] See Chassagne, R. (Ed.) 2024. Report on optimization – Injection strategy and storage capacity. *Deliverable WP3/D3.3. EU H2020 PilotSTRATEGY project 101022664 report.*

The PilotSTRATEGY project has received funding from the European Union's Horizon 2020 research and innovation programme under grant agreement No. 101022664

diffusion, the mineral composition change and its effects on the petrophysical property change (porosity, permeability, capillary pressure).

3. Subtask 3.4.3: Storage complex integrity is assessed with studies on its mechanical stability. A coupled fluid-flow geomechanics model is used to study the storage complex integrity. It is based on a geological model of the storage complex including overburden and underburden. The potential damage of the caprock induced by $CO_2$ injection is analysed by comparison of the stress state evolution with a failure criterion. When faults or fractures were characterized, further analyses are conducted to evaluate the potential impact of $CO_2$ injection on these pre-existing elements. Models include the main structures identified in the geological model of Task 3.1. The potential and preferential zone of reactivation are analysed through a Mohr-Coulomb criterion. Two aspects are considered: the potential reactivation of structures because of their pressurization related to $CO_2$ injection and the potential effect of reactivation on $CO_2$ flow (leakage risk).

Each region had its own specificities in terms of geology and thus its own focus for the integrity study:

- French region: As no faults were characterized in the studied area in the geo-characterization step (WP2), no such structures impact is evaluated in the geomechanical study. Storage complex integrity study focuses here on the risk of failure in storage and caprock formations through hydromechanical simulations and failure criterion analyses. On the other hand, the carbonate sedimentary context for the storage formation requires a comprehensive geochemical study to define if the potential fluid-rock interactions have a significant impact on storage behaviour and integrity at pilot-scale.

- Portuguese region: As geochemical reactivity in the reservoir is already assessed in deliverable D3.4 and with no major impacts, the geochemical assessment in the reservoir for the injectivity integrity only accounted for salt precipitation reactivity phenomena. However, for the caprock geochemical integrity, the full mineral composition of the caprock was considered in the reactive transport models. Also, main concerns for the storage would be, a priori, on mechanical stability, in particular at the existing faults. Thus, a comprehensive mechanical study was conducted on the storage complex.

- Spanish region: Following previous studies performed in this project (WP2 and Deliverables D3.3 & D3.4), the targeted Lopin structure is likely to have a constrained maximum capacity related to poor reservoir properties and the existing natural overpressure, which constrains the maximum injection rate through the fracture pressure limit. In addition, the injection area exhibits a high fault density, with susceptibility to fault reactivation and the potential for induced seismicity. Therefore, this deliverable emphasizes these geomechanical constraints, which ultimately govern the feasibility of Lopín as a geological $CO_2$ storage site. Regional stresses in the area of interest, pore pressure, and fracture gradient were quantified using wells located within a 70 km radius and with a sufficient dataset to perform the analysis. The modelling strategy follows a model adapted to the availability of geomechanical data. Only one well is located within the static/dynamic model area, which represents a primary limitation for the reliable spatial extrapolation of geomechanical properties. With single-well control, lateral and vertical variations of mechanical parameters cannot be constrained by data, and any three-dimensional property distribution would be largely assumption-driven. For this reason, a 2D fault-plane

The PilotSTRATEGY project has received funding from the European Union's Horizon 2020 research and innovation programme under grant agreement No. 101022664

geomechanical model was selected as a fit-for-purpose solution. By focusing on the fault plane, where the geomechanical response is most critical, and by implementing a one-way coupling with dynamic simulation results, the selected approach maximizes the use of the available data while avoiding unnecessary model complexity. Regarding wellbore integrity, given the high formation water salinity, a dedicated study was undertaken to assess the potential injectivity impairment at the Lopin site resulting from salt precipitation during continuous $CO_2$ injection. Geochemical and mineralogical analyses of the reservoir (Buntsandstein; Deliverable D2.7) indicate a silica dominated formation. Quartz ($SiO_2$) is expected to exhibit minimal dissolution/reactivity under $CO_2$–brine conditions[4]; therefore, reactive transport geochemical simulations within the reservoir are not considered necessary for this deliverable. With respect to the caprock, some $CO_2$ interaction with seal minerals may occur, but the expected effects are considered negligible in comparison to the geomechanical aspects and a simple PHREEQC 0D modelling was performed on this regard.

Following tables summarized the main modelling hypotheses and tools that were specifically used for each subtask and each region.

| **Well Integrity (geochemical)** | **Paris basin, France** (pilot-scale, injection of 300kt/yr for 4 months) | **Lusitanian basin, Portugal** (commercial scale, 30 years of injection) | **Ebro basin, Spain** (commercial scale, 30 years of injection) |
|---|---|---|---|
| Model type (geometry) | 2D radial wellbore model with reservoir + caprock, 11 km of lateral extent | 2D radial wellbore model with the reservoir only (bottom section of 50m), 50 km of lateral extent to reproduce the pressure buildup behavior during the injection period | 3D Reservoir model described and reported in Deliverables 3.2, 3.3 & 3.4. |
| Model type (problem solved) | Thermo-Hydro-Chemical (THC) models with one Salt THC model (including water evaporation but no rock reactivity) and one complex THC model (including rock reactivity, no water evaporation) | Thermo-Hydro-Chemical models with Salt (Halite) THC model (including water vaporization but no rock reactivity – geochemical reactivity of the reservoir already assessed in deliverable D3.4 and with no major impacts) | Near-wellbore halite precipitation model embedded within a multiphase flow simulator |

[4] as supporting background on quartz dissolution kinetics across acidic-to-neutral pH conditions, see Knauss & Wolery, 1987/1988.

The PilotSTRATEGY project has received funding from the European Union's Horizon 2020 research and innovation programme under grant agreement No. 101022664

| | | | |
|---|---|---|---|
| Timescale | Short-term (one year, including 4 months of injection) | Short-term (30 years of injection) | Injection period (30 years) |
| Uncertainties | Heterogeneities with P10, P50, P90 models from static (pore volume) analysis + petrophysical uncertainties and operational uncertainties | Vertical heterogeneities and simplified lateral homogeneities per vertical layer from each P50 models from static (pore volume) analysis as the base case scenario + uncertainties in the injection rate, reservoir salinity and injection temperature | P10, P50, P90 reservoir model realisations plus different permeability impairment scenarios simulated using a bracketing approach for the functional form of the $k_{rc}(S_a)$ mobility degradation curve |
| Numerical Tools | Geoxim and Coupling between Arxim and Geoxim | CMG GEM numerical simulator | SLB's Eclipse 300 (CO2STORE option) reservoir simulator, version 2025.1 |

| **Caprock integrity (geochemical)** | **Paris basin, France** (pilot-scale, injection of 300kt/yr for 4 months) | **Lusitanian basin, Portugal** (commercial scale, 30 years of injection) | **Ebro basin, Spain** (commercial scale, 30 years of injection) |
|---|---|---|---|
| Model type (geometry) | 1D (simplified with only two elements: reservoir and caprock) and 2D (radial wellbore model, same as the one in wellbore integrity study) | 3D model (simplified with only two elements: reservoir and caprock). Note: although the base simulation scenario is at the bottom of the reservoir for the injection, and only a small portion of the $CO_2$ reaches the caprock in the P90 model, in this task only the top layers of the reservoir was considered to evaluate chemical integrity of the caprock in the top reservoir/ caprock interface | 0D model (batch reaction modelling) |

The PilotSTRATEGY project has received funding from the European Union's Horizon 2020 research and innovation programme under grant agreement No. 101022664

| | | | |
|---|---|---|---|
| Model type (problem solved) | Complex geochemical model with simplified transport and Complex THC model for the radial one | Complex THC modelling for the 3D models of the top reservoir + caprock | Geochemical modelling |
| Timescale | Long-term (500 years) | Long-term (1000 years) | N/A |
| Uncertainties | Heterogeneities with only P90 model | Homogeneous properties of the reservoir (based on the P90 model to ensure the $CO_2$ will be in contact with the caprock) + heterogeneous caprock model (with 4 lithofacies based on the lithological information from a nearby legacy well) as the base case scenario + uncertainties in the mineral volume fractions and petrophysical properties of the caprock internal layers | N/A |
| Numerical Tools | Coupling between Arxim and Geoxim | CMG GEM numerical simulator | PHREEQC |

| **Storage complex integrity (geomechanical)** | **Paris basin, France** (pilot-scale, injection of 300kt/yr for 4 months) | **Lusitanian basin, Portugal** (commercial scale, 30 years of injection) | **Ebro basin, Spain** (commercial scale, 30 years of injection) |
|---|---|---|---|
| Model type (geometry) | 3D model (surface to underburden) 20 x 20 km with LGRs | Two 3D models: the first one for the caprock mechanical integrity subtask (reservoir + caprock + potential secondary caprock), the second one for the fault reactivation potential subtask (full 3D model with 7 regions packed from property | For caprock: Well-centric 1D assessment at CCS-1; no 3D geomechanical volume.<br>For faults: 2D fault-plane geomechanical model. One-way coupling with dynamic simulation results. |

The PilotSTRATEGY project has received funding from the European Union's Horizon 2020 research and innovation programme under grant agreement No. 101022664

| | | | |
|---|---|---|---|
| | | similarities into 4 layers from surface to underburden layers, covering the full extent in depth of the existing faults) | |
| Model type (problem solved) | Iterative and one-way hydro-mechanical coupling (flow; 2-phases) and mechanical calculators (poro-elastic; with the calculations of stress, displacements, overpressure and post-processing failure analyses with the Drucker-Prager failure criterion) | Thermo-Hydro-Mechanical (THM) models for the caprock integrity, and Hydro to Mechanical (H->M) models for the faults. Two-way coupling of the 3D models between fluid flow and mechanical module for the caprock and one-way coupling of the 3D models from fluid to mechanical simulation for the faults (stress, displacements, overpressure, porosity evolution, and post-processing failure analyses with the Mohr-Coulomb failure criterion, and safety factor for the caprock integrity subtask only) | For caprock: comparing stress and pore-pressure curves locally at the caprock base (~1,722 m TVD). Mechanical threshold only: comparing a Fracture Gradient (FG) = $S_{hmin}$ with 10% safety factor (FG×0.9) against a static $CO_2$ column (~0.007 MPa·m$^{-1}$); Biot ≈ 1; no fracture propagation, capillary, geochemical, or fully coupled poroelastic modeling.<br><br>For faults: One-way hydro-mechanical coupling. Integrates 1D geomechanics data, with oriented decomposition of stresses into normal and shear components. Fault stability is assessed using the Mohr–Coulomb criterion. |
| Timescale | Short-term (one year, including 4 months of injection) | Short-term (30 years during the injection period) for the fault reactivation assessment + short-mid-term (100 years, including 30 years of the injection period) for the caprock integrity assessment | For caprock: Two quasi-static states: Pre-injection and End-of-Injection (30 years)<br><br>For faults: Short-term (30 years of injection). |

The PilotSTRATEGY project has received funding from the European Union's Horizon 2020 research and innovation programme under grant agreement No. 101022664

| | | | |
|---|---|---|---|
| Faults | No (none were characterized in the area of study) | Yes, 6 existing faults were identified and characterized in the study area, and assessed mechanically and simultaneously in the respective subtask | Yes (13 faults) |
| Uncertainties | Heterogeneities with P10, P50, P90 models from static (pore volume) analysis + HydroMecha properties uncertainties (3 extreme cases + one intensive study with 175 simulations) | Heterogeneous with P50 models from static (pore volume analysis) as the base case for the 3 model regions considered for the caprock integrity assessment + heterogeneous with P50 models from static (pore volume analysis) as the base case for the reservoir and homogeneous petrophysical properties for the other 6 model's regions for the fault reactivation assessment. Uncertainty analyses of injection rate, perforation interval for $CO_2$ injection, and mechanical parameters (friction angle, Poisson ratio, Young modulus and cohesion) for the caprock integrity assessment + uncertainty analysis of mechanical parameters (friction angle) for the fault reactivation assessment | Caprock: sensitivity to stress heterogeneity and $S_{Hmax}$<br>Faults: 27 cases based on variability in reservoir permeability (P90–P50–P10), injection configuration (CCS-1, LOCD-1, and combined), and fault friction angle (30°, 25°, and 20°). |
| Numerical Tools | Coupling between Code_Aster and Geoxim | CMG GEM numerical simulator (caprock integrity task) + CMG GEM and FLAC 3D | Caprock: GeoSmart® (1D stresses, wellbore stability, FG); |

The PilotSTRATEGY project has received funding from the European Union's Horizon 2020 research and innovation programme under grant agreement No. 101022664

| | | | |
|---|---|---|---|
| | | numerical simulators to retrieve several time steps of the pressure evolution during the injection period, and for the mechanical analysis of the reactivation potential of the fault, respectively | Faults: Petrel™ subsurface software (SLB) and MOVE™ structural geology modelling software (Petroleum Experts Ltd.) |

## Paris basin (France) – Results Summary

To evaluate the integrity of the storage complex, comprehensive numerical geochemical and geomechanical studies were implemented with short- and long-term analyses, coupling flow with geomechanical and geochemical processes. Those studies were achieved for a pilot-scale $CO_2$ injection in the Oolithe Blanche formation (Dogger, deep saline aquifer), Grandpuits area, Paris basin, France, based on previous results from Task 3.1 (static modelling), Task 3.2 (well location definition and flow simulation) and WP2 (geological and geochemical characterization).

1. The near wellbore integrity has been quantified in terms of risk of injectivity loss due to salt precipitation and fluid-rock interactions. This numerical study is based on radial wellbore models within a short-term framework. Considering uncertainties in the static model, injection temperature, capillary pressure, injection rate variability, fluid flow parameters, and salinity, the simplified geochemical model (no rock reactivity but salt precipitation) has estimated an injectivity loss of the well perforations ranging between 0% and 4%. Additional losses arise from the uncertainties in capillary pressure (+0.6%) and salinity (+0.7%). However, a 4-month injection stop could significantly reduce the well injectivity (up to 23% for the P90 Max case) in contexts of high permeability (100 – 1000 mD). In this case, the injectivity remains still sufficient to continue to allow the targeted injection rate (300kt/yr) but this higher risk must be considered in cases of long stops for maintenance or for pilot upscaling for commercial exploitation. The complex geochemical model with fluid-rock interactions (but no modelling of dry-out effect and related salt precipitation) simulates a minor 0.09% increase in permeability due to calcite dissolution. This allows to conclude that no significant increase in injectivity loss is anticipated related to rock reactivity.

2. The caprock integrity has been assessed with a comprehensive 2D radial reactive transport simulation, that incorporates complex geochemistry and a realistic system configuration. In a long-term framework, the spatial and temporal evolution of the $CO_2$ plume has been assessed, as well as the chemical interactions between the injected $CO_2$, water, and the minerals. After 500 years of simulation, (dissolved and gas) $CO_2$ only reaches the first layer of Massingy marls without further penetration, demonstrating a degree of geochemical and structural stability in the studied system. The dissolution of minerals such as calcite and chlorite occurred, accompanied by the precipitation of dolomite, indicating pH buffering mechanisms and a slight reduction in porosity. Overall, this demonstrates a very limited geochemical impact on the caprock of the $CO_2$ injection at pilot-scale in the Dogger aquifer. Therefore, geochemical

The PilotSTRATEGY project has received funding from the European Union's Horizon 2020 research and innovation programme under grant agreement No. 101022664

impact on the caprock is not a major concern for the caprock in the studied case.

3. The risk of failure of storage formation and caprock has been quantified in terms of distance to failure criterion. This risk is related to geomechanical effects of the $CO_2$ injection on the storage complex, in particular in the injection phase. A coupled 3D hydromechanical model, under the assumption of linear poroelasticity, was used to evaluate the potential damage induced by $CO_2$ injection, analysing the evolution with time of the overpressure and of the distance to the Drucker-Prager failure criterion. A first analysis was performed considering uncertainties in static models and relevant subsurface properties with nine models covering the uncertainties ranges. Within a prior hypothesis on the initial stress state, all results from these models remain far away from the failure criterion in the storage formation and the caprock, with the prescribed limit of bottom-hole pressure. Except for few cases that were discarded accounting from new information on dynamic behaviour of the area, the pilot capacity is verified without jeopardizing the system integrity in the studied context. Another comforting result of these simulations is that the overpressure dissipates in all cases, in a short-term after the injection and no more significant impact on pressure system is expected 8 months after the end of injection. Further uncertainty study, with a systematic exploration of uncertain parameters space, leads to similar results in term of overpressure with a maximum expected overpressure around 3 MPa close to the injection well. Regarding the risk of failure, caprock integrity is also safe in all configurations. However, in some specific cases (1% over a resampling of 20,000) regarding the initial stress state, risk of failure may occur in storage formations in a critical area. This was obtained with the most conservative failure criterion (inner Drucker-Prager failure criterion) while the less conservative one (outer Drucker-Prager failure criterion) is never reached for any simulations from the considered design of experiments. This means that those cases are at risk but may not necessarily reach the failure. Additional analyses were performed on the deformation of the storage complex up to the surface. These analyses indicate that the dynamic of surface displacement would be sufficient to be monitored in the injection well area during the injection phase and shortly after the injection ceases. The total surface displacement due to the pilot-injection remains low (< 1 mm) and will not impact the surface installation. As no faults were characterized in the studied area, the study of fault stability was out-of-scope for this case.

Overall, those studies are positive regarding the storage complex integrity in a pilot-scale context for the studied area. No major concerns were raised either for the geochemical or geomechanical part. Only some cautions need to be addressed in case of long-term injection stops (> 3 month, even when scaling-up from pilot to industrial) and regarding the initial stress state combined with rock properties characterization that may lead to integrity issues in some specific and minor cases.

## Lusitanian Basin (Portugal) – Results Summary

The quantification of the phenomenological impacts was conducted for the pilot site of the Q4-TV1 prospect, located in the offshore setting of the Lusitanian Basin (Portugal). The $CO_2$ storage complex comprises several geological units, including the Torres Vedras Group reservoir and its overlying sealing system with regionally continuous argillaceous carbonates and mixed lithologies – the Cacém Formation caprock and the Aveiro Group (a potential secondary seal). This geological setting is representative of a saline aquifer storage complex, characterized by a laterally extensive clastic reservoir with adequate characteristics to accommodate industrial-scale $CO_2$ injection. The modelling

The PilotSTRATEGY project has received funding from the European Union's Horizon 2020 research and innovation programme under grant agreement No. 101022664

domains adopted in the different studies results from previous geological characterization (WP2) and reservoir modelling and simulation studies (Tasks 3.1, 3.2 and 3.3 of WP3).

1. The injectivity integrity assessment evaluated whether the Torres Vedras Group reservoir can sustain the planned $CO_2$ injection rates without operational impairment. High-resolution coupled thermal-hydraulic-chemical (THC) simulations demonstrate that injection-induced effects, primarily brine drying and halite precipitation, remain confined to the near-wellbore region, typically within approximately 20-30 m of the injection well and extending up to about 40-50 m under high salinity or high injection rate scenarios. These effects result in minor and localized porosity reductions, typically below 1% in the reference case and up to approximately 3-4% locally under worst-case conditions, which translate into moderate but localized permeability reductions due to the strong porosity-permeability relationship, while remaining restricted to the near-wellbore region and not affecting reservoir-scale flow performance. Under the reference injection scenario (0.5 Mt/y, reservoir salinity of 56 g/L, and injection bottom-hole temperature of 26°C), injection performance remains stable over 30 years, achieving approximately 14.5-15 Mt of stored $CO_2$, with reservoir pressures stabilizing at approximately 126-127 bar, well below the fracture pressure limit of 165 bar. Even under worst-case conditions involving higher salinity and injection rates, injectivity reductions remain moderate (approximately 10-15%), and injection performance stabilizes without progressive degradation. These results indicate that injectivity impacts are localized and self-limiting, and do not compromise long-term injection feasibility, although they remain dependent on the assumptions and operational conditions considered.

2. The geochemical integrity assessment of the Cacém Formation caprock, based on fully coupled 3D THC simulations over injection and post-injection periods extending up to 1000 years, demonstrates that free-phase $CO_2$ remains entirely confined to the reservoir, with gas saturation in the caprock remaining effectively zero ($\leq 10^{-5}$) throughout the simulation period. Dissolved $CO_2$ penetration into the caprock remains minimal and spatially restricted to the basal contact zone, while pH changes and geochemical reactions are strongly buffered by the caprock mineral assemblage. Although localized dissolution of carbonate minerals such as calcite and dolomite occurs at the reservoir-caprock interface, these reactions do not induce measurable porosity or permeability changes, and the caprock sealing capacity remains fully preserved. Uncertainty analyses exploring mineralogical variability and pessimistic petrophysical conditions confirm that even under degraded shale properties, $CO_2$ migration remains confined within this bottom caprock unit and does not propagate into overlying formations, demonstrating the long-term robustness of the caprock as an effective hydraulic and geochemical barrier.

3. From a geomechanical perspective, both caprock fracturing risk and fault reactivation potential remain consistently low across all investigated scenarios. Injection-induced pressure changes do not approach failure conditions, and mechanical responses remain elastic and reversible. Uncertainty analyses confirm a high margin of stability even under intensified injection rates and unfavourable mechanical parameter assumptions. Faults remain stable and no permeability enhancement or leakage pathways are generated. However, it is important to mention that these results are obtained under the specific modelling assumptions, parameter ranges, and boundary conditions adopted in this study, and should

The PilotSTRATEGY project has received funding from the European Union's Horizon 2020 research and innovation programme under grant agreement No. 101022664

therefore be interpreted within this context. A broader exploration of parameter variability and alternative boundary conditions would further strengthen the robustness of these conclusions. The geomechanical risk is therefore assessed as low. Mitigation is essentially preventive, consisting of pressure-controlled injection, avoidance of abrupt rate increases, and periodic updating of geomechanical models as additional field data become available.

Overall, the combined injectivity, caprock, and fault integrity assessments indicate that the storage complex at the pilot site in the Lusitanian Basin is suitable for $CO_2$ injection and storage. Injectivity remains stable with impacts confined to the near-wellbore region, the caprock preserves its geochemical and geomechanical sealing capacity without approaching failure, and faults remain far from reactivation under the tested scenarios. Together, these results increase confidence in the storage integrity and performance, suggesting a low risk of leakage or operational impairment under the proposed injection conditions.

## Ebro basin (Spain) – Results Summary

The geological structure at Lopín (Ebro Basin) was initially selected within the opportunity portfolio because preliminary static estimates suggested a storage size potentially exceeding 100 Mt. However, as the project progressed and new data were acquired, dynamic reservoir simulation results (Deliverables D3.3 & D3.4) indicate that this structure is likely to reach a much lower maximum capacity due to poor reservoir properties and the existing natural overpressure (≈ 43 bar above hydrostatic pressure at 1750 m depth). In addition, the injection area exhibits a high fault density, with susceptibility to fault reactivation. This section synthesizes the main dynamic and integrity-related findings for the Lopín $CO_2$ storage concept, with a focus on injectivity and geomechanical and fault-stability constraints. The analysis is based on the dynamic modelling case described in Deliverable D3.4 (Ben Rhouma et al., 2026), considering $CO_2$ injection from a single well at two alternative locations (CCS-1 or LOC-D), as well as from two wells operated simultaneously.

- Salt precipitation during $CO_2$ injection can reduce near-wellbore permeability and therefore impair injectivity. In this work, the effect is captured using mobility multiplier functions that decrease fluid mobility as solid (salt) saturation increases; the curve shape (often non-linear) strongly controls when impairment begins and how severe it becomes. Model results suggest that NaCl precipitation can occur under certain thermodynamic and flow conditions, causing localized injectivity decline, but the affected zone remains limited and can be mitigated operationally (e.g., periodic water flushing/brine injection or $CO_2$ humidification). Overall, the study provides a practical basis to assess salt-related injectivity risk for Lopín and recommends field-scale validation and extension to multi-salt systems.

- Regarding the caprock geochemistry model performed in PHREEQC:
  - Under a purposely conservative, dilute-baseline scenario that maximizes reaction affinity, the B2 seal remains geochemically resilient; destabilizing thermodynamic pathways are not observed. 96Seal mineral stability: Ca-montmorillonite, mica, and chlorite are thermodynamically stable (SI ≈ 0) across 25–100% $pCO_2$ exposure; kaolinite (SI ≈ 2.52–2.57) and dolomite (SI ≈ 2.46–2.89) are consistently oversaturated, indicating a robust tendency toward pore-filling precipitation (self-sealing behavior).

The PilotSTRATEGY project has received funding from the European Union's Horizon 2020 research and innovation programme under grant agreement No. 101022664

- ❖ Because high ionic strength suppresses mineral reactivity (common-ion effects, activity coefficients), in-situ high-salinity brines will be less reactive than the model baseline. Thus, the already favorable outcomes are conservative with respect to field conditions.
- ❖ Risk hierarchy: Geochemical processes pose a very low risk to containment and may enhance sealing passively. Geomechanics, driven by injection-induced pressure, is the primary constraint to be managed.
- ❖ Scope and next steps: Given the negligible geochemical risk within the bounding assumptions, no further geochemical modelling is required. Additional reactive-transport/kinetic or spatially resolved simulations are not warranted for screening, though they could be revisited if future design changes create materially different exposure conditions.
- ❖ Methodological note (for traceability): Batch equilibrium modelling (PHREEQC v3; 69 °C) using meteoric water as baseline and the B2 mineral mix (Quartz 34%, Mica 18%, Ca-Montmorillonite 15%, Calcite 13%, K-feldspar 10%, Chlorite 10%) was applied; $pCO_2$ sensitivity from 25% to 100% of reservoir value was evaluated to bracket plausible leakage/diffusion exposure.

- A four-well, multi-1D model (Ebro-1/2, Mayals-1, Lopín-1) indicates a normal-faulting regime at depth and strike-slip in the shallow section. The reservoir interval is naturally overpressured, narrowing operational pressure windows and elevating sensitivity to injection-induced stress changes. At the seal base (~1,722 m TVD, CCS-1), mechanical safety margins shrink from 9.8 MPa and 13.4 MPa ($Sh_{min}$) initially to 1.8 MPa and 5.4 MPa at the end of injection (30 years). The seal remains mechanically intact, but late-life injection operates close to thresholds, requiring conservative limits, careful rate management, and strengthened monitoring.

- The fault reactivation assessment was conducted integrating the results of the multi 1D analysis ($S_v$, $Sh_{max}$, $Sh_{min}$, Pore pressure, Fracture Pressure) and using a 2D fault-plane geomechanical modelling approach, one-way coupled with dynamic flow simulation outputs. The analysis is based on the Mohr–Coulomb failure criterion and the Critical Pore Pressure Change (CPPC) concept, evaluated at peak pore pressure conditions reached at the end of the 30-year $CO_2$ injection period. CPPC is used as a screening-level indicator of mechanical susceptibility, quantifying the remaining pressure margin to fault reactivation at the fault plane. Uncertainty was systematically explored through 27 scenarios, combining three fault friction angles (30°, 25° and 20°), three permeability realizations (P90, P50 and P10), and three injection configurations (CCS-1, LOCD-1 and dual injection). Negative CPPC values indicate mechanical instability in fault segments, with increasingly negative values reflecting a higher degree of instability. While this implies an elevated potential for fault reactivation and the possible occurrence of induced seismicity, no deterministic relationship is assumed between CPPC-based instability and the timing, magnitude or spatial distribution of seismic events. CPPC therefore provides a conservative, decision-oriented screening metric, rather than a predictor of seismic activity. Results indicate that fault stability is primarily controlled by fault friction angle and the magnitude of pore pressure transmitted to the fault plane. Lower friction angles systematically lead to more negative CPPC values and a wider spatial extent of instability. The fault friction angle emerges as both a dominant control and one of the largest

The PilotSTRATEGY project has received funding from the European Union's Horizon 2020 research and innovation programme under grant agreement No. 101022664

sources of uncertainty, as it cannot be reliably constrained using laboratory tests due to the difficulty of sampling representative fault-plane material. In addition, fault zones commonly contain gouge-rich materials with lower friction than intact host rock, supporting the use of conservative friction assumptions. The presence of an initially overpressured reservoir further reduces the pre-injection mechanical safety margin and increases sensitivity to injection-induced pressure buildup. Injection configuration exerts a strong secondary control on fault stability. Simultaneous dual-well injection (CCS-1 + LOCD-1) consistently produces the most negative CPPC values and the largest number of unstable fault segments across the evaluated uncertainty range, representing the least favorable operational configuration from a fault stability perspective. Single-injector operation yields more robust stability margins, with CCS-1 systematically less destabilizing than LOCD-1, highlighting injector-specific effects related to location, connectivity and proximity to critically oriented faults. Reservoir permeability shows a consistent but secondary influence, with low-permeability cases promoting pore-pressure accumulation at the fault plane. Several faults are identified as persistently unstable and highly sensitive to pressure changes, notably Falla014, Falla011 and Falla017, which exhibit mechanical instability across multiple friction angles and injection strategies. A second group becomes unstable mainly under low friction angles and high-pressure scenarios, while a smaller subset is only affected under extreme conditions. This classification enables clear prioritization of critical faults and high-risk operational combinations. Overall, the CPPC-based assessment provides a conservative and decision-oriented framework for discriminating between injection strategies and identifying conditions that require additional risk management measures. Configurations combining low fault friction, low permeability and simultaneous multi-well injection consistently represent the highest geomechanical risk and should not be implemented without mitigation. Preferred operational strategies include single-injector operation (particularly CCS-1), avoidance of simultaneous multi-well injection, application of injector-specific operational constraints, and adoption of phased or staggered injection strategies to limit peak pore-pressure buildup near sensitive faults. Within current data constraints, the adopted 2D fault-plane geomechanical modelling approach is considered fit-for-purpose, capturing the governing fault mechanics while providing a practical basis for monitoring prioritization and risk-informed decision making in $CO_2$ storage projects.

The PilotSTRATEGY project has received funding from the European Union's Horizon 2020 research and innovation programme under grant agreement No. 101022664

# Table of Contents



The PilotSTRATEGY project has received funding from the European Union's Horizon 2020 research and innovation programme under grant agreement No. 101022664

The PilotSTRATEGY project has received funding from the European Union's Horizon 2020 research and innovation programme under grant agreement No. 101022664

The PilotSTRATEGY project has received funding from the European Union's Horizon 2020 research and innovation programme under grant agreement No. 101022664

# 3. Introduction

The PilotSTRATEGY project is investigating geological $CO_2$ storage sites in industrial regions of Southern and Eastern Europe to support development of large-scale carbon capture and storage (CCS). Research is focused on deep saline aquifers (DSA), which promise a large capacity for storing $CO_2$ captured from clusters of industry. Detailed studies are being carried out on DSAs in the Paris Basin in France, the Lusitanian Basin in Portugal and the Ebro Basin in Spain. This report summarizes the work that has been performed in Work Package 3 of PilotSTRATEGY, "WP3, Static and Dynamic modelling", task 3.4, "Quantification of phenomenological impacts".

The main objective of this task was to quantify the integrity of the near wellbore, the caprock and fault/fractures by simulation while injecting CO2 and post-injection at the different targeted pilot project locations (French region, Portuguese region and Spanish region). Its secondary objective was to consider uncertainties from operational configurations or geological properties in this quantitative integrity assessment.

In that purpose, models adapted to the studied impacts (0D-3D, several physics coupling, local or large scale) were built to simulate the main physical and chemical mechanisms. Models' complexity also depends on available data and on functionalities of the considered simulation tool. Models are based on previous results from the PilotSTRATEGY project, in particular geo-characterization data from WP2, geological & static model from task 3.1 and well location definition and related flow simulations from task 3.2.

This report is divided into 3 parts, one for each storage site studied: Paris Basin – France, Lusitanian Basin – Portugal, Ebro Basin – Spain. For each site, the integrity assessment encompasses: 1/ the integrity of the wellbore and the potential injectivity loss; 2/ the caprock integrity related to the geochemical impacts of the $CO_2$ injection; and 3/ the storage complex integrity is and its mechanical stability. However, each region has its own specificities in terms of geology and thus its own focus for the integrity study.

# 4. Paris Basin Region (France)

This section focuses on a comprehensive geochemical and geomechanical study with short- and long-term analyses, coupling flow with geomechanical and geochemical processes, for a pilot-scale $CO_2$ injection in the Oolithe Blanche formation (Dogger, deep saline aquifer), Grandpuits area, Paris basin, France. The main objective is to evaluate the integrity of the storage complex at different levels and for different physical processes by simulation:

1. The integrity of the near wellbore is quantified in terms of risk of injectivity loss within a short-term analysis. The salt and mineral precipitation risk is evaluated based on a radial wellbore model to quantify their impact on well injectivity.
2. The caprock integrity in terms of mineral and petrophysical properties integrity is assessed through a reactive transport model. Both 0D and radial model are used to simulate the supercritical and dissolved $CO_2$ migration from the storage formation up and through the caprock. The mineral composition changes and their retroaction on petrophysical properties are quantified.
3. The storage formation and caprock integrity in terms of risk of failure that could be induced by the geomechanical effect of the $CO_2$ injection on the storage complex (short-term analysis: injection and short-term post injection periods). A coupled 3D hydromechanical model is used

The PilotSTRATEGY project has received funding from the European Union's Horizon 2020 research and innovation programme under grant agreement No. 101022664

to evaluate the potential damage induced by $CO_2$ injection, analysing the evolution with time of the overpressure and of the distance to the Drucker-Prager failure criterion. Additional analysis is performed on the deformation of the storage complex up to the surface. As no faults have been characterized in the studied area, the study of fault stability is out-of-scope for this case.

The flow and reactive transport simulations are carried out using CooresFlow (Ahusborde et al., 2024; Gassara et al., 2021), a thermal-hydro-mechanical-chemical simulator developed by IFP Energies nouvelles. This code is based on a fully implicit multiphase flow model coupled in an iterative way to chemical and mechanical models. It is based on mass conservation equations for fluid species and Darcy laws for flow modelling coupled with thermodynamic equilibrium equations. These equations are discretized in space with a finite volume scheme and solved with a Newton-type iterative method. The geomechanical calculations are carried out using Code_Aster (EDF, 2024). The coupling between hydro and mechanical calculations are briefly presented in section 4.4.1.

The risk analysis is also to be performed in regard with the inherent uncertainties of the geological media. For this, the integrity of the near wellbore and geomechanical integrity are studied for different cases, considering uncertain parameters. In particular, for the last one, an extensive uncertainties study has been performed on one of the geological models.

## 4.1 Problem Definition

**Case description**

The studied case is a potential pilot-scale $CO_2$ injection in a deep saline aquifer (Dogger, the Oolithe Blanche formation) in the Paris basin (Grandpuits area). Dynamic simulations focused on the injection period and short-term period post-injection to assess flow & geomechanical responses to the $CO_2$ injection. Additional dynamic simulations involved reactive transport modelling for long-term behaviour analysis, focusing on potential caprock reactivity.

Models are based on results from previous work from PilotSTRATEGY project, in particular task 3.1 (3D geological modelling, D3.1 & D3.2 (Christ, A.B., Mattioni, L., 2024), task 3.2 (Well location optimization, D3.3 (Alavoine et al., 2024)) and collected data on geological context and dynamic parameters from WorkPackage 2 "WP2, Geo-characterization"(see for example Bordenave and Issautier, 2023). The domain contains the storage complex zone (here the Dogger aquifer including Dalle Nacrée, Comblanchien, Oolithe Blanche and Lower Bathonian formations and caprock: Callovo-Oxfordian formation, including Massingy marls), and the underburden and overburden (up to the surface). Based on a 3D seismic analysis, no faults were observed in the area and thus no faults are modelled in this study. Consequently, no faults integrity study was performed here.

The Jurassic Oolithe Blanche Formation is the primary storage formation for the pilot $CO_2$ injection. This formation consists of a Jurassic oolithic carbonate ramp with an average porosity of around 10%, locally reaching up to 30% porosity. The Oolithe Blanche formation is capped by the Dalle Nacrée and the Comblanchien formations, also carbonates formation, but with less favourable petrophysical properties. The storage complex is capped by a continuous 120 m thick marly seal, the Marnes de Massingy. According to the existing literature, the Oolithe Blanche Formation is laterally and vertically heterogeneous in lithology and petrophysical properties. The complexity in geometry and spatial distribution of reservoir properties has been taken into account while modelling the area.

The PilotSTRATEGY project has received funding from the European Union's Horizon 2020 research and innovation programme under grant agreement No. 101022664

The injection site is onshore, and the top of storage formation is around 1734 m depth. The storage formation thickness is around 150 m. Initial pressure and temperature at the top of storage formation are 184 bar and 70.9°C, respectively. The aquifer salinity is 19 g/L.

The Oolithe Blanche formation thickness is partly perforated by the injection well (40 m over around 150 m thick). The injection rate is constrained by a maximum BHP limit (see the preliminary uncertainties definition). The maximum injection rate is 300 kt/yr, with an injection duration of 4 months. Thus, the total amount of $CO_2$ to be injected is 100 kt, targeting the objective of a CCS pilot-scale project.

### Model description

The model extent is 20 by 20 km to capture the lateral pressure build-up extent due to $CO_2$ injection (Figure 4-1). The suggested well location was defined in the previous task and is located around 3 km from the model's center [X = 695642.6; Y = 6836032.].

The inherited model geometry, 20 x 20 x 2.5 km mesh, has 2 embedded LGRs:

- 500 × 500 m – 40 × 40 cells (51 cells in X-Y direction) [Coarse]
- 125 × 125 m - 80 × 80 cells (34 cells in X-Y direction) [LGR1]
- 62.5 × 62.5 m – 128 × 128 cells (27 cells in X-Y direction) [LGR2] with a maximum vertical discretization of 5 m. The well is located at I = 44 and J =100 on this fine grid mesh.

With the vertical discretisation, this represents around 600 000 active cells. Notice that the model geometry has been adapted for the time-consuming process of reactive transport, as described in the two next sections (1D and radial models).

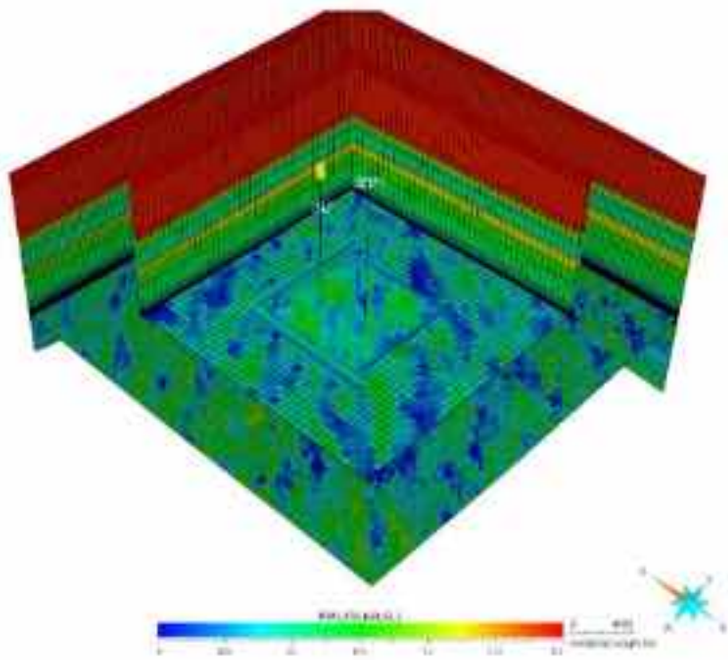

*Figure 4-1. 3D model of the studied area (Grandpuits area) for the $CO_2$ pilot injection site from D3.2 (Christ, A.B., Mattioni, L., 2024). SEIF-1 is a waste-water injection well, near-by a potential $CO_2$ source. INJ is the suggested well location in D3.3 (Alouaine et al., 2024).*

### Preliminary uncertainties definition

The PilotSTRATEGY project has received funding from the European Union's Horizon 2020 research and innovation programme under grant agreement No. 101022664

This previous static modelling task resulted in three static models. They all shared the same geometry, the same petrophysical properties but for the Oolithe Blanche Formation, the target storage formation, with different porosity and permeability fields resulting from the uncertainty studies on porous volume (porosity field simulated with SGS, sequential gaussian simulation). These three models are referred to as P10, P50, and P90, representing the pessimistic, base case, and optimistic scenarios, respectively, in terms of pore volume in the target formation (a net porous volume of 1123, 1246 and 1369 $m^3$, respectively, for the restricted area of 10 by 10 km). Permeability values are correlated to porosity values (see Figure 4-2 and details in D3.2 (Christ & Mattioni, 2024)).

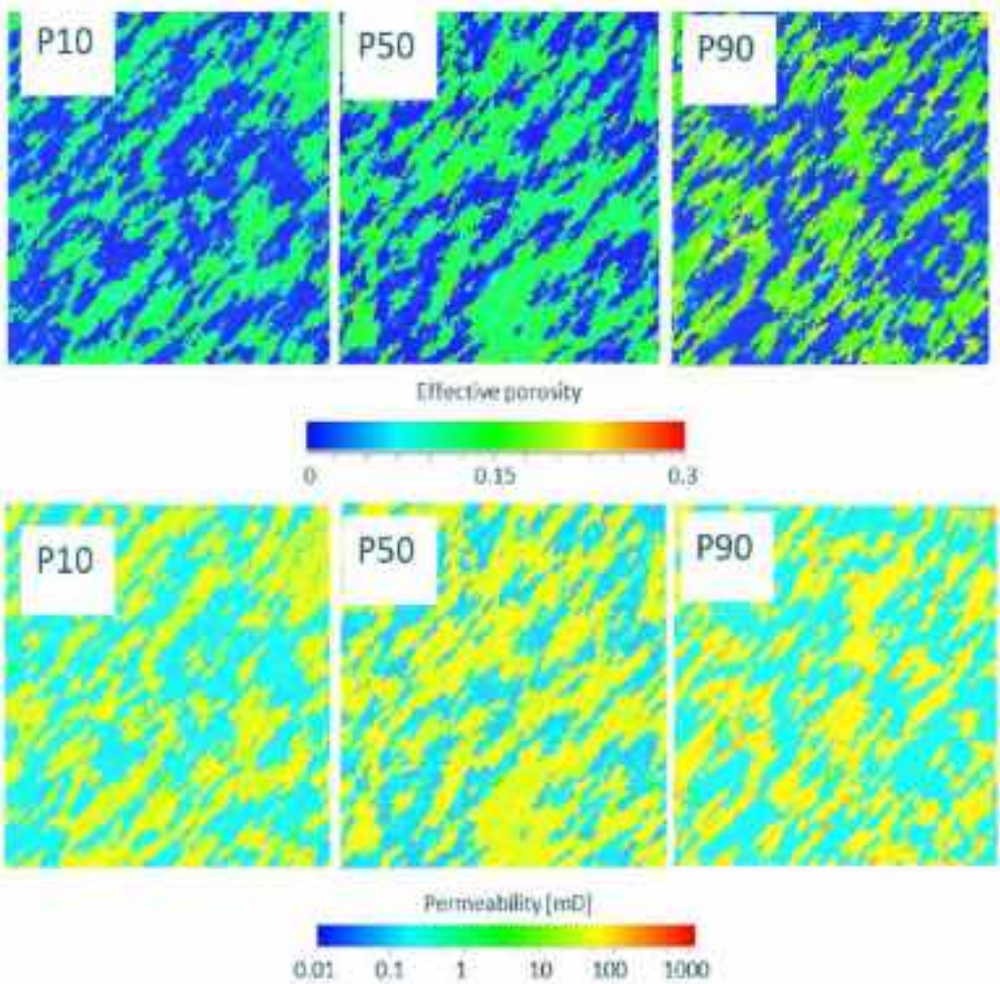


*Figure 4-2: 2D maps of porosity (top) and permeability (bottom) fields in the Oolithe Blanche formation for the three models P10, P50, P90 from D3.2 (Christ, A.B., Mattioni, L., 2024)*

To assess the impact of uncertainties, in addition to uncertainty on porosity represented by P10, P50 and P90 models, we also considered uncertainties related to poorly characterized parameters in three cases: two extreme cases that could be described as the best and worst scenarios (in term of overpressure) and one base case scenario. Uncertain parameters' values for those three cases are described in Table 4-1. Those three scenarios are applied to the three porosity/permeability fields models (P10, P50, P90 models) leading to nine cases.

The additional uncertain parameters are the following (see the detail in D3.3 (Alavoine et al., 2024) and Table 4-1 below):

The PilotSTRATEGY project has received funding from the European Union's Horizon 2020 research and innovation programme under grant agreement No. 101022664

- Oolithe Blanche (high porosity facies) formation 's permeability with an uncertainty in the K-Phi correlation parameter *[KPhi]*,
- Permeability anisotropy in Comblanchien formation [*AnisoComb*],
- Caprock permeability (Callovo-Oxfordian formation) (multiplier of permeability) [*multiKCOX*],
- Relative Permeability curves' parameters for the Oolithe Blanche, high porosity facies (residual gas saturation [*Sgr*] and exponent factor [*LambdaVG*]). A Van-Genuchten Mualem model is used for relative permeabilities and capillary pressure. Notice that entry capillary pressure and residual water saturation are scaled according to the porosity and permeability values (Timur et al., 1968; Leverett, 1941),
- Rock elastic properties for carbonates (elastic properties parameters [*Kc*], [*Gc*]) Bulk and shear moduli parameters for carbonates are used according to the correlation expressed in Bemer et al., 2004.

| | KPhi [-] | AnisoComb [-] | multiKCOX [-] | Sgr [-] | LambdaVG [-] | Kc [Pa] | Gc [Pa] |
|---|---|---|---|---|---|---|---|
| Base Case | 1 | 1. | 1. | 0.05 | 0.6 | 5.08E+09 | 3.79E+09 |
| 'Min' Worst case | 0.25 | 0.3 | 0.005 | 0.3 | 0.4 | 7.50E+09 | 5.00E+09 |
| 'Max' Best case | 4. | 3. | 1. | 0.05 | 0.7 | 3.80E+09 | 2.90E+09 |

*Table 4-1: Uncertain parameters' values for the three studied cases, applied to the three models P10, P50, P90, leading to nine studied models.*

Petrophysical and thermodynamic models are described in detail in deliverable D3.3 (Alavoine et al., 2024). In relation with petrophysical and elastic properties, the increase in BHP is limited to 70 bars, 60 bars and 27 bars for the P10, P50 an P90 models, respectively (see also deliverable D3.3).

The PilotSTRATEGY project has received funding from the European Union's Horizon 2020 research and innovation programme under grant agreement No. 101022664

## 4.2 Injectivity integrity

The loss of injectivity of a $CO_2$ injection well represents a significant challenge for $CO_2$ geological storage systems. During $CO_2$ injection into an underground reservoir, two primary processes can contribute to this issue. First, $CO_2$ dissolves in water, lowering the pH, which may disturb the fluid-rock equilibrium, resulting in mineral precipitation. Second, $CO_2$ injection can cause water evaporation within the rock pores near the well, leading to salt precipitation (e.g., sodium chloride). Both phenomena reduce permeability and, consequently, the injectivity of the well.

Section 3.1 presents the results of a numerical study that quantifies the loss of injectivity caused by salt precipitation and fluid-rock interactions in the potential pilot-scale $CO_2$ injection well of a deep saline aquifer (Dogger, the Oolithe Blanche formation) within the Paris Basin. This study uses reactive transport models applied to a radial mesh. These models evaluate the geochemical effects and their impact on the petrophysical properties and the injectivity index of the well perforations. Additionally, the study evaluates the risk of injectivity loss with uncertainties in the geological static model, injection temperature, capillary pressure, injection rate variability, fluid flow parameters, and initial salinity.

### 4.2.1 2D radial THC models

The THC models employed in this study integrate a thermal model (T), a fluid flow model (H), and a geochemical model (C). To uncouple the damage processes of the near wellbore due to salt and mineral precipitation, two THC models are used in this study. The first, referred to as the Salt THC model in this report, considers water evaporation and simplified geochemical modelling of salt precipitation but excludes rock reactivity. The second, named the Complex THC model, does not account for water evaporation but includes fluid-rock interactions using a complex geochemical model that considers the primary minerals. Detailed descriptions of these geochemical models are provided below.

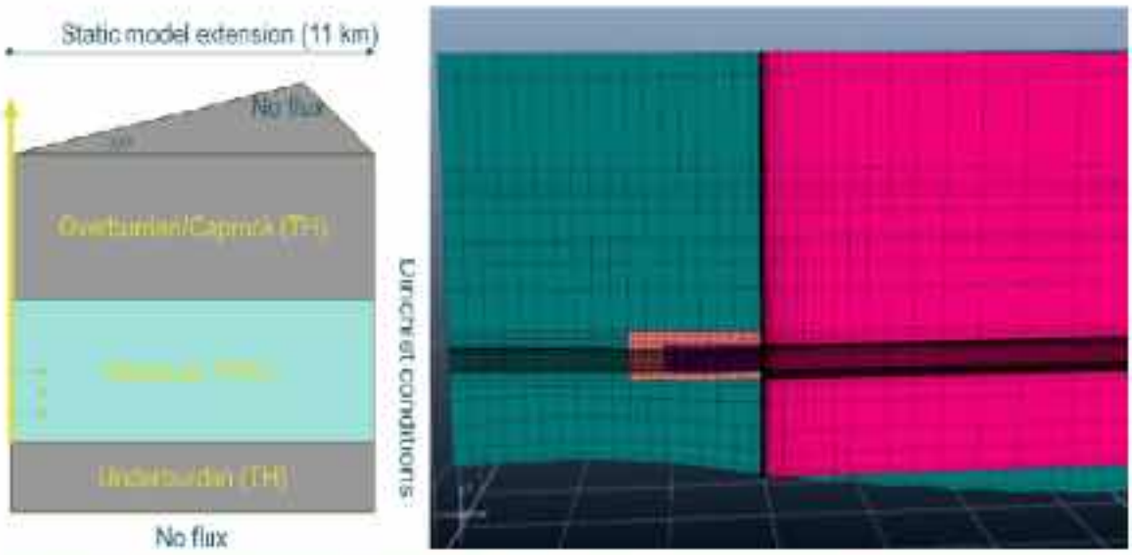


*Figure 4-3: (Left) Studied radial domain and boundary conditions and (Right) comparison between 3D static model and radial grid (pink)*

A radial mesh (Figure 4-3) is employed in this study, as radial grids are better suited for capturing radial flow and geochemical effects occurring near the wellbore. The THC models are applied to a 2D vertical

The PilotSTRATEGY project has received funding from the European Union's Horizon 2020 research and innovation programme under grant agreement No. 101022664

radial grid centred on the injection well. To reduce computational costs, only a 3.6° sector extending over 11 km is considered. This approach is acceptable, as heterogeneity near the wellbore is little influenced by orientation. This grid incorporates the Dogger reservoir, a transition zone consisting of Massingy marls, and the Callovo-Oxfordian caprock. To improve precision near the well, a geometric progression is employed, reducing the minimum horizontal cell size from 60 m (as used in the 3D static geological model of the target area) to 0.1 m (results of the grid sensitivity study in Section 3.1.2.2). Vertically, the same discretization size (minimum of approximately 5 m) as in the 3D static model (D3.1) is applied. Horizons are modelled as flat surfaces, with negligible impact expected, as the horizons are predominantly flat in the 3D static model and reactivity is anticipated to occur within a 500 m radius of the well. The final grid comprises 8,320 cells (130 cells in the x-direction, 1 in the y-direction, and 64 in the z-direction).

The diphasic compositional fluid flow model is based on the 3D fluid flow model built in WP3.2 (D3.3). The facies, porosity, and permeability are derived from the 3D static geological models developed in WP3.1. Three geological scenarios (characterized by porosity and permeability uncertainties corresponding to the percentiles "P10," "P50," and "P90") are used, along with upscaled relative permeability and capillary pressure curves for each facies and rock compressibility (Alavoine et al., 2024). Similar uncertainties as defined in D3.3 (Table 4-1) related to dynamic parameters—such as permeability for the Oolithe Blanche, Comblanchien, and caprock formations, as well as the shape of gas relative permeability for the Oolithe Blanche—are categorized into "Min", "Base", and "Max" cases. Additionally, if water evaporation is modelled, the capillary pressure curve of Oolithe Blanche is extended from the irreducible water saturation to 0. Given the uncertainty of the maximum capillary pressure within this saturation range, a multiplier parameter ranging from 1 to 5 is applied to assess its impact.

In this study, the fluid flow model considers an additional dependency on salinity and temperature for component transfer between phases using an equilibrium constant. This enables the simulation of $CO_2$ dissolution in brine, as well as $H_2O$ evaporation in the gaseous phase for the salt THC model. The equilibrium constant is represented by the Søreide & Whitson model, validated by experimental data from the literature (Figure 4-4) for the dissolved $CO_2$ molar fraction under injection conditions (temperature of 40°C and 60°C, pressure range of [50 - 400] bar, and salinity range of [0 - 300] g/L). Mineral and salt precipitation, which reduces porosity and consequently permeability, is modelled dynamically using the Kozeny–Carman equation (Equation 1) with critical porosity (Oolithe Blanche: 0% for Low porosity (<11%) – 5% for High porosity (>=11%)).

*Equation 1: Kozeny-Carman equation with permeability $K$, initial permeability $K_0$, porosity $\varphi$, initial porosity $\varphi_0$, critical porosity $\varphi_c$, $a(=3)$ and $b(=2)$ exponent parameters*

$$K = K_0 \left(\frac{\varphi - \varphi_c}{\varphi_0 - \varphi_c}\right)^a \left(\frac{1 - \varphi_0 + \varphi_c}{1 - \varphi + \varphi_c}\right)^b$$

The PilotSTRATEGY project has received funding from the European Union's Horizon 2020 research and innovation programme under grant agreement No. 101022664

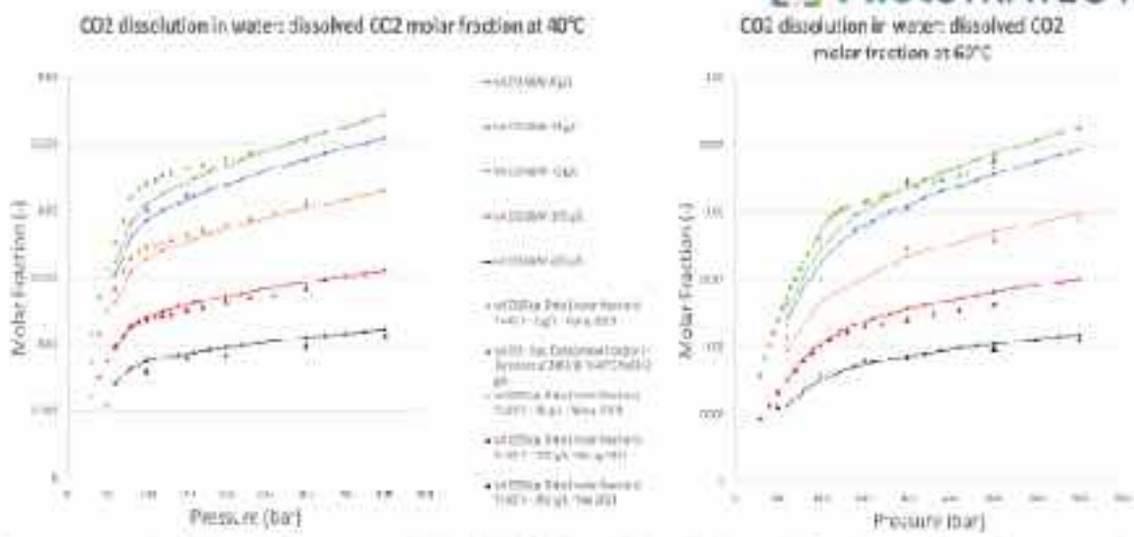


*Figure 4-4: Dissolved $CO_2$ molar fraction at 40°C and 60°C (values calculated by Soreide & Witson model and experimental data from literature)*

To simulate the impact of colder fluid injection on $CO_2$ migration and dissolution, salt precipitation and mineral reactivity, a thermal model is fully coupled to fluid flow models considering thermal conduction in the rock, parametrised by constant conductivity and thermal capacity values specific to facies (reservoir and caprock) and precipitated salt (Table 4-2).

*Table 4-2: Thermal parameters: Conductivity and thermal capacity for reservoir, caprock and precipitated salt. Data source: [a] BRGM RP-59591 report, [b] Bonte PhD*

| Thermal parameters | Reservoir | Caprock | Solid Salt |
|---|---|---|---|
| Conductivity (W/m/K) | 2.5[a] | 1.9[b] | 5.5[b] |
| Thermal capacity (J/kg/K) | 797[a] | 797[a] | 900 |

Finally, this study is based on two geochemical models. The simplified geochemical model of the Salt THC model considers a single salt species (sodium chloride). Salt precipitation and dissolution are modelled without kinetics using an equilibrium constant that accounts for thermal effects (Figure 4-5). The resulting THC model is fully implicit. On the other hand, the complex geochemical model described in 3.3.1.1 considers two mineral compositions (reservoir and caprock) and initial water compositions equilibrated with in-situ mineralogy, temperature and pressure and a salinity of 19 g/L. It also simulates kinetics of mineral reactions. It is coupled to the TH model with a sequential approach.

The PilotSTRATEGY project has received funding from the European Union's Horizon 2020 research and innovation programme under grant agreement No. 101022664

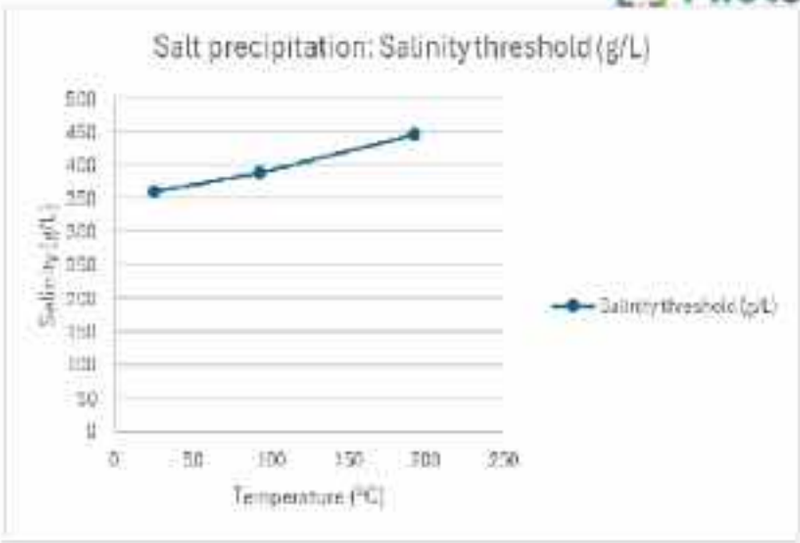


*Figure 4-5: Salt solubility threshold (g/L)*

As for WP3.2, the initial state of the fluid flow model is hydrostatic and saturated with brine at a salinity of 19 g/L (uncertainty range [17.5 - 23] g/L from D2.11 (Mathurin, 2023)). The $CO_2$ injection well is modelled as a vertical well with a radius of 0.069 m and a perforation length of 40 m, optimized for the target injection rate of 300 kt/year (9.5 kg/s, i.e. 0.095 kg/s for a 3.6° sector) on a commercial scale. A maximum injection of 100 kt of $CO_2$ is considered, restricting the injection duration to 4 months at the target rate. This rate, considered as the maximum allowable injection rate, will be constrained by the estimated fracture pressure (D3.2) and potential stops ranging from 10 days to 4 months simulating maintenance period or technical event. The temperature of the injected $CO_2$ stream at well bottom is constant over the injection period assuming an uncertainty range of [40 - 62]°C corresponding to the minimum temperature to prevent gas hydrates and to the expected temperature for $CO_2$ transported by pipeline. Regarding boundary conditions, no hydraulic and thermal flux is assumed at the top and bottom of the studied domain. The outer lateral boundary is modelled as open to hydraulic and thermal exchanges with the Dogger aquifer (Figure 4-3).

### 4.2.2 Simulation results of the Salt THC model

#### *4.2.2.1 P50 Base case results*

This section presents the simulation results of the Salt THC model applied to the P50 geological scenario and the fluid flow parameters of the Base case.

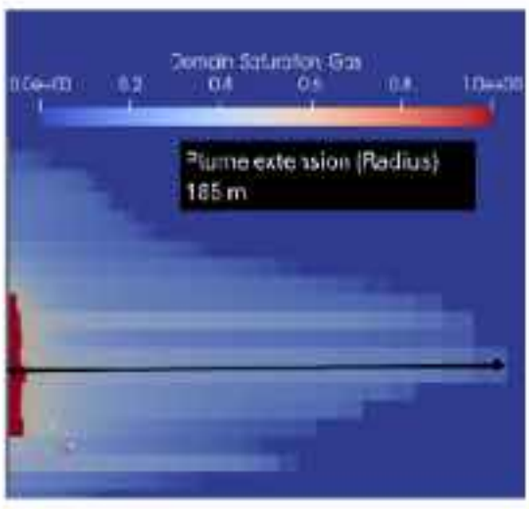


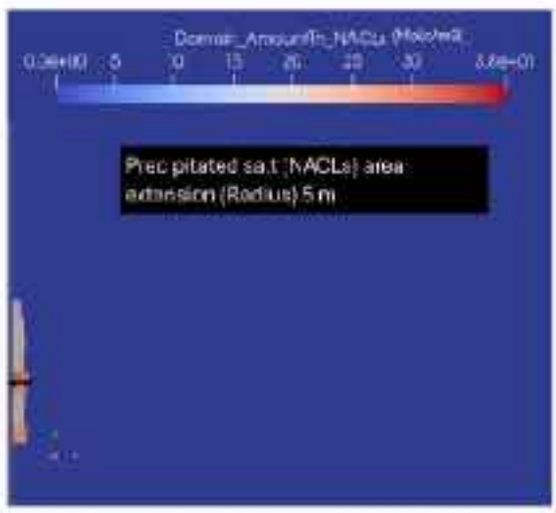


The PilotSTRATEGY project has received funding from the European Union's Horizon 2020 research and innovation programme under grant agreement No. 101022664

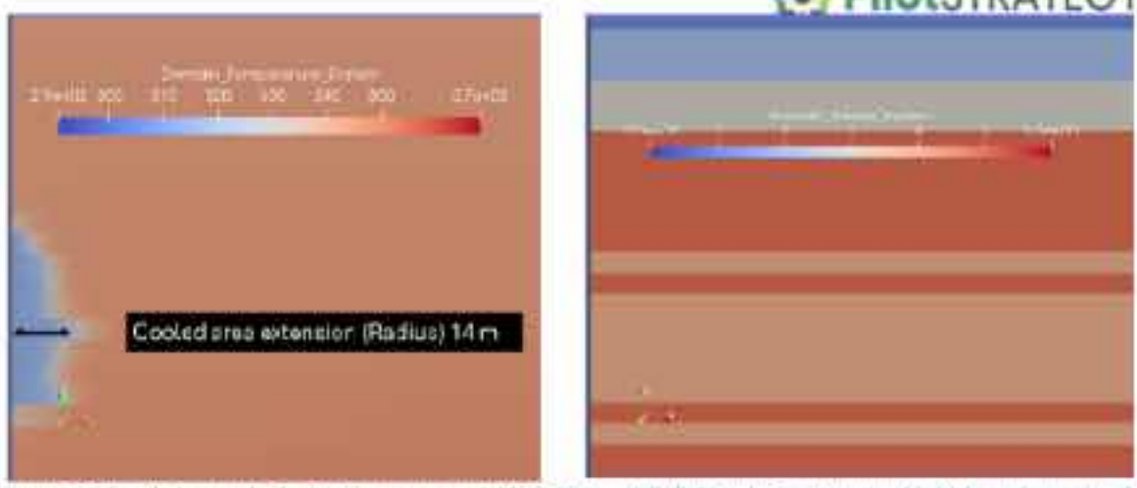


*Figure 4-6: Simulation results for P50 Base case model (Salt THC model): (left top) Gas saturation (-), (right top) amount of precipitated salt (mole/m3) and (left bottom) temperature (K) at the end of the injection period (4 months) and facies distribution*

Figure 4-6 illustrates the distribution of gas saturation, temperature and precipitated salt at the end of the $CO_2$ injection period (4 months). The extent of the $CO_2$ plume, which is primarily controlled by the vertical heterogeneity of petrophysical parameters, reaches 185 m around the well, with a cooled 14 m-thick zone and a dried 5 m-thick zone near the well. Compared to the results of WP3.2 obtained with the 3D static model, the gas plume is more extended vertically (+42m) and less laterally (-115 m of radius) mainly due to mesh refinement and water evaporation that lead to higher gas concentration close to the well (100% against 53%).

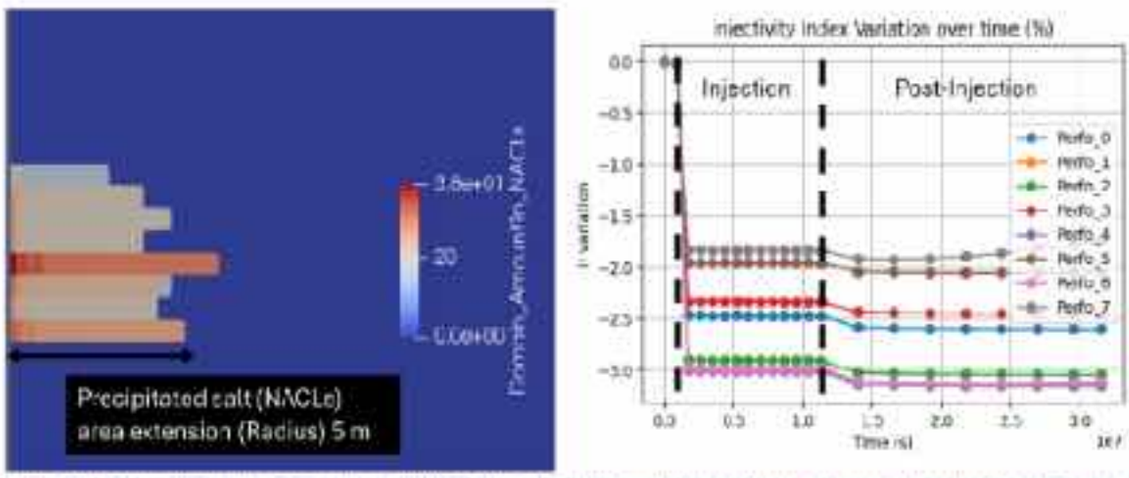


*Figure 4-7: (left) Lateral zoom of amount of solid salt (mole/m³) at 4 months and (right) injectivity index variation (%) over time for well perforations (the deepest perforation is labelled as '0'). Primarily governed by salt precipitation and dissolution, the variation in well injectivity is also influenced by rock compressibility, which is linked to pressure variation. This second-order injectivity loss is observable for instance after the end of the injection period on the right figure.*

Within the dried zone, a heterogeneous distribution of precipitated salt is observed (Figure 4-6 and zoom in Figure 4-7). This heterogeneity arises from variations in residual brine amounts caused by differences in pore volumes and horizontal in-situ salt migration toward the well due to brine imbibition. Thus, the highest accumulations of solid salt are found in cells adjacent to perforations. The maximum value of salt precipitation (due to the initial porosity) is located in front of the perforation '3' (the deepest perforation is labelled as '0'). At this location, the salt precipitation reduces the initial porosity of 17.3% by only 0.1%, corresponding to a decline in permeability of 2 mD from the initial value of 73 mD. The curves in Figure 4-7 (right), representing the variation of the injectivity index over time for each well perforation, show that this minor damage results in an

The PilotSTRATEGY project has received funding from the European Union's Horizon 2020 research and innovation programme under grant agreement No. 101022664

injectivity loss of 2.4% for perforation '3' during the injection period. Across all perforations, losses in injectivity range from 1.8% to 3% and remain generally constant over the 8 months following the injection end. This stability is attributed to the return of brine towards the well which is sufficiently slow to prevent solid salt dissolution.

#### 4.2.2.2 *Sensitivity to mesh refinement*

A concentrated accumulation of solid salt can significantly reduce the porosity and permeability of the rock. To accurately model this effect, it is crucial to apply a refined grid in the near wellbore, where fluid velocities are highest, to avoid artificial dilution and underestimation of the solid salt amount. For that purpose, the geometric progression of the horizontal cell size applied for the radial mesh is optimized to improve accuracy of the injectivity loss while preventing numerical issues. The tested minimum sizes of the cells in contact with the wellbore are 0.01 m (leads too many numerical issues), 0.1 m and 4 m. Figure 4-8 presents the solid salt distribution at the end of the injection period for the 4 m cell size. While the maximum solid salt amount (38 mole/m$^3$) and the three main deposit areas are similar due to initial salt amount, the distribution for the 0.1 m-dx grid is more laterally and vertically heterogeneous. According to Figure 4-8, this leads to a 2% injectivity loss to all the perforations with a 0.1 m-cell size and to only three perforations for a 4 m-cell size. Reduced to a single cell width, the salt deposit for the 4 m cell size takes longer time to form and becomes less stable over time following the injection period. As a conclusion, despite a large refinement compared to the 3D static model, a grid with a minimum 4 m-cell size still underestimates the injectivity loss. The grid with the minimum 0.1 m-cell size is applied for all the simulations done in this study.

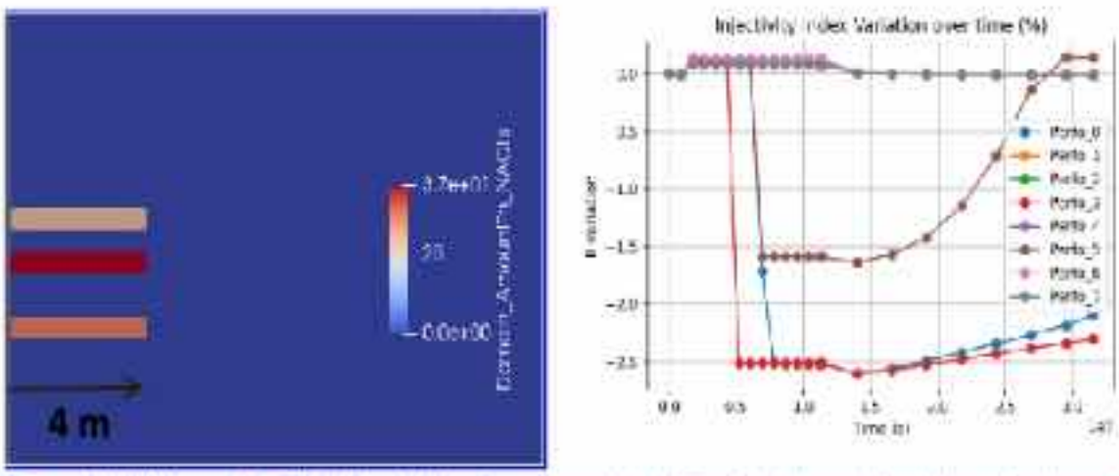


*Figure 4-8: (Left) Amount of solid salt (mole/m$^3$) at 4 months and (right) injectivity index variation (%) over time for well perforations for 4 m-cell size*

#### 4.2.2.3 *Impact of uncertain parameters*

This section presents the evaluation of the risk of injectivity loss due to salt precipitation with uncertainties in the geological static model (P10, P50 and P90), injection temperature, capillary pressure, injection rate variability, fluid flow parameters (Min, Base and Max cases), and initial salinity.

Regarding uncertainties in the geological static model and fluid flow parameters, Figure 4-9 illustrates the distribution of solid salt amount at the end of the injection period. Variations in porosity distribution across the P10, P50, and P90 scenarios (with the same irreducible water saturation of approximately 40% in the Oolithe Blanche) result in differences in the location of solid salt deposits. The maximum solid salt amount ranges

The PilotSTRATEGY project has received funding from the European Union's Horizon 2020 research and innovation programme under grant agreement No. 101022664

from 35 to 45 mole/m³, influenced by the petrophysical models and the corresponding fluid velocities, which are notably higher in the Min/Base/Max P90 and P10/P50/P90 Max models. This increase in fluid circulation creates a dried, salted area that is more laterally extended and less vertically spread compared to other models, particularly the Min cases. In the latter, the effective injection rate is lower than the target value (0.095 kg/s) because the fracture pressure threshold has been reached. Thus the [1.8% - 3%] range of injectivity loss for P50 Base case model previously described in section 3.1.2.1 slightly changes to [0% - 4%] with the scenarios P10, P50 and P90 associated with the Min, Base and Max cases (Figure 4-10, Table 4-3). Less variation in injectivity loss for Max cases should be noted. It results from homogenization of the salt distribution due to enhanced salt transport. These injection loss values remain constant after the injection end excepted for Max cases for which some or all perforations gain in injectivity one to four months after the stop due to salt dissolution induced by faster brine return. These results quantify the small impact of the geological scenarios and fluid flow properties uncertainty on the risk of injectivity loss due to salt precipitation.

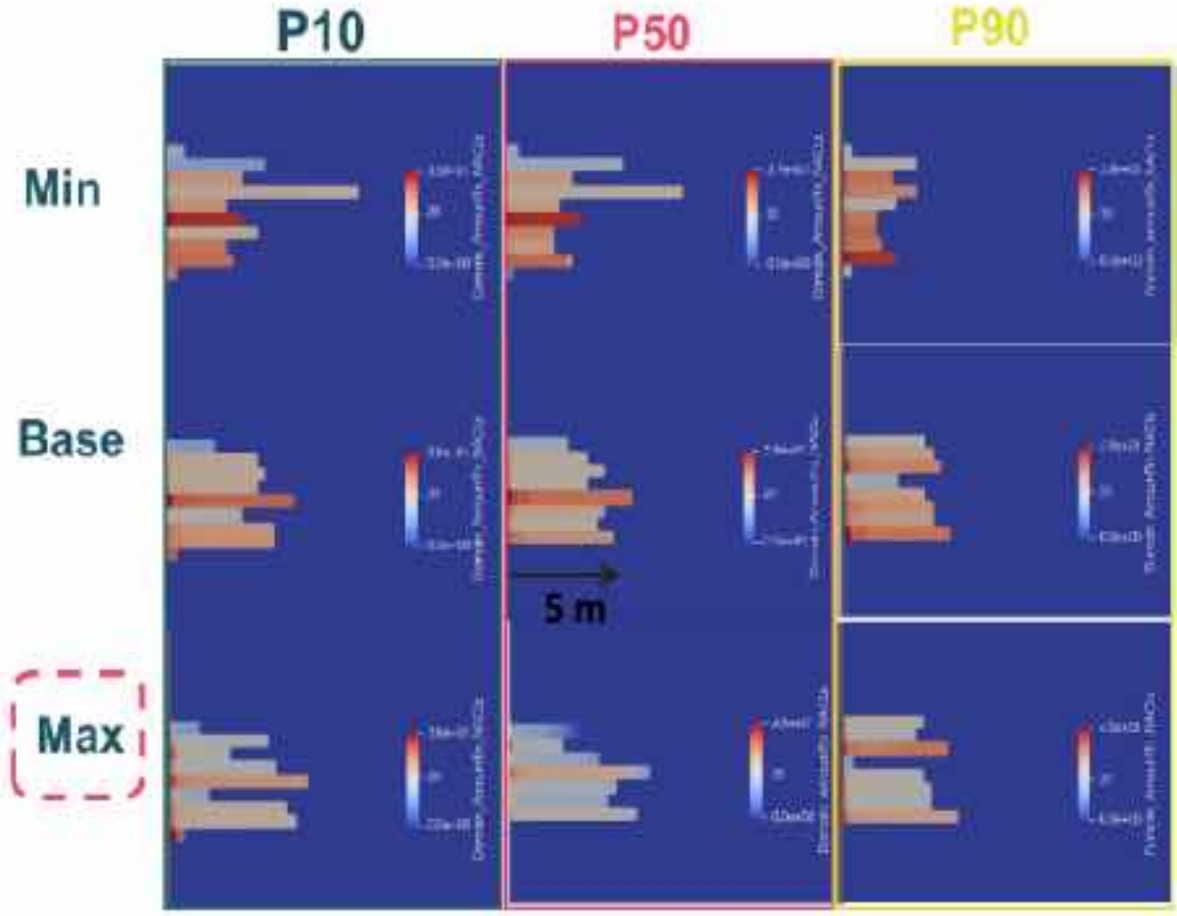


*Figure 4-9: Amount of solid salt (mole/m³) at 4 months for P10, P50 and P90 geological scenarios and Min, Base and Max cases*

The PilotSTRATEGY project has received funding from the European Union's Horizon 2020 research and innovation programme under grant agreement No. 101022664

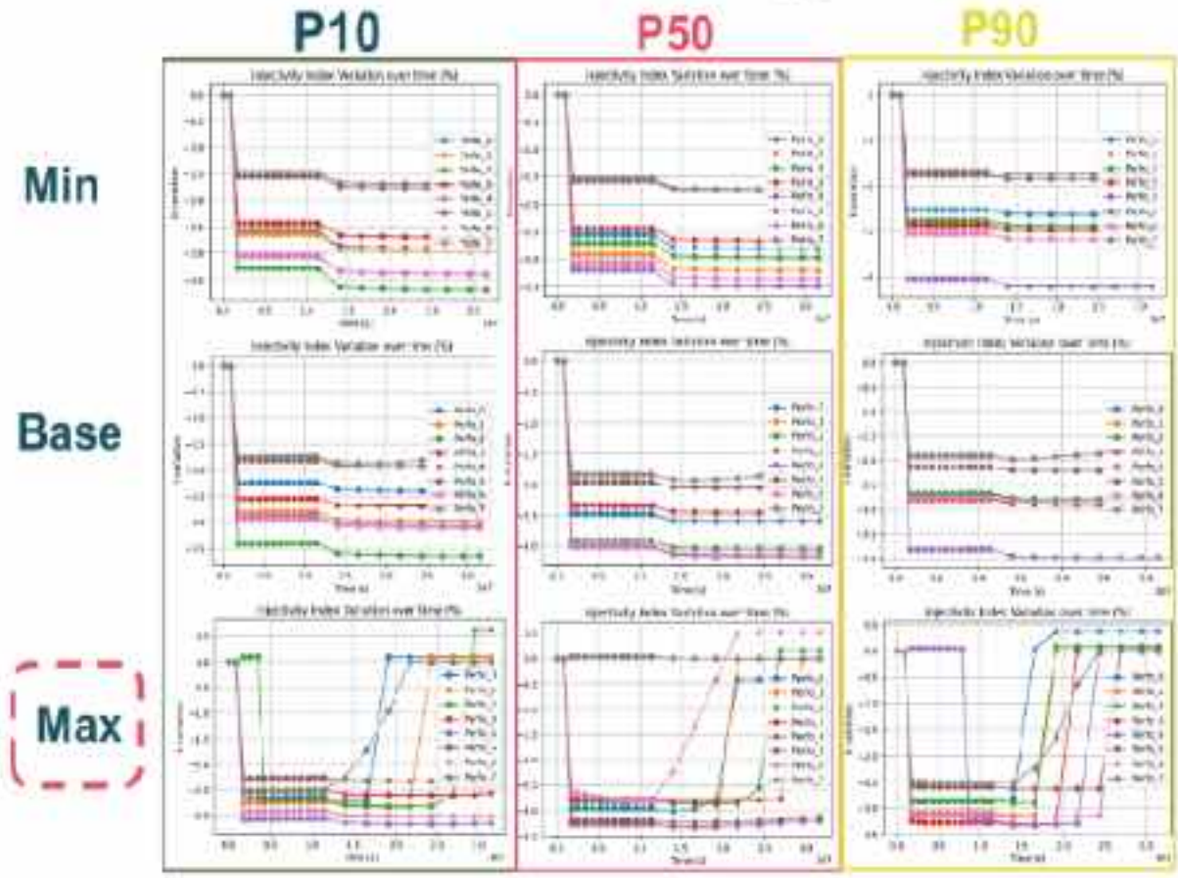


*Figure 4-10: Injectivity index variation (%) over time for well perforations for P10, P50 and P90 geological scenarios and Min, Base and Max cases*

*Table 4-3: Minimum and maximum injectivity index variation (%) during the injection period (4 months) for all well perforations for P10, P50 and P90 geological scenarios and Min, Base and Max cases*

| Injectivity loss (%) | P10 | P50 | P90 |
|---|---|---|---|
| Min | 1.5 - **3.25** | 1.5 - **3.25** | 1.7 - **4** |
| Base | 1.8 - **3.5** | 1.8 - 3 | **2** - **3.75** |
| Max | **2.25** - 3 | 0 - **3.25** | 0 - **3.25** |

Similarly (Figure 4-11), an uncertainty in the initial salinity [19 - 23] g/L only adds a 0.7% loss to the injectivity loss range according to P50 Base case results and a maximum capillary pressure multiplied by five adds 0.6% loss. In contrast, uncertainty in the injection temperature, between 40 and 62°C, and a stop ranging from 10 days (Figure 4-11) to 4 months (Figure 4-12) during the injection period do not have observable impact on the injectivity loss for the P50 model.

The strongest impact is simulated with a 4 months-stop, with the P90 Max model (Figure 4-13) that maximizes the fluid circulation related to higher permeability values. During the first phase of injection, the salt precipitation phenomenon causes a maximum injectivity loss of 3.3%. When the $CO_2$

The PilotSTRATEGY project has received funding from the European Union's Horizon 2020 research and innovation programme under grant agreement No. 101022664

injection stops, the fluid circulation, which is controlled by the upwards migration of supercritical $CO_2$ associated with the lateral brine flow towards the well, induces salt dissolution and its transport, i.e. salt accumulation multiplied by seven in cells adjacent to the four deepest perforations. When the $CO_2$ injection starts again, the precipitation of this bigger amount of salt induces greater damage to porosity (-0.7%) and permeability (-34 mD). Thus, by comparison with the P90 Base case (with an injection stop), the fluid circulation intensification increased drastically the injectivity loss from around 4% to [12% - 23%] for the four deepest perforations '0-3'. The overpressure increases from 6 to 7 bar resulting from the near-wellbore alteration, staying below the maximum threshold of 27 bar for preventing rock fracturing. Thus, despite a significant loss in injectivity, the effective injection rate is not impacted by salt precipitation, maintaining the target injection rate of 300 kt/year.

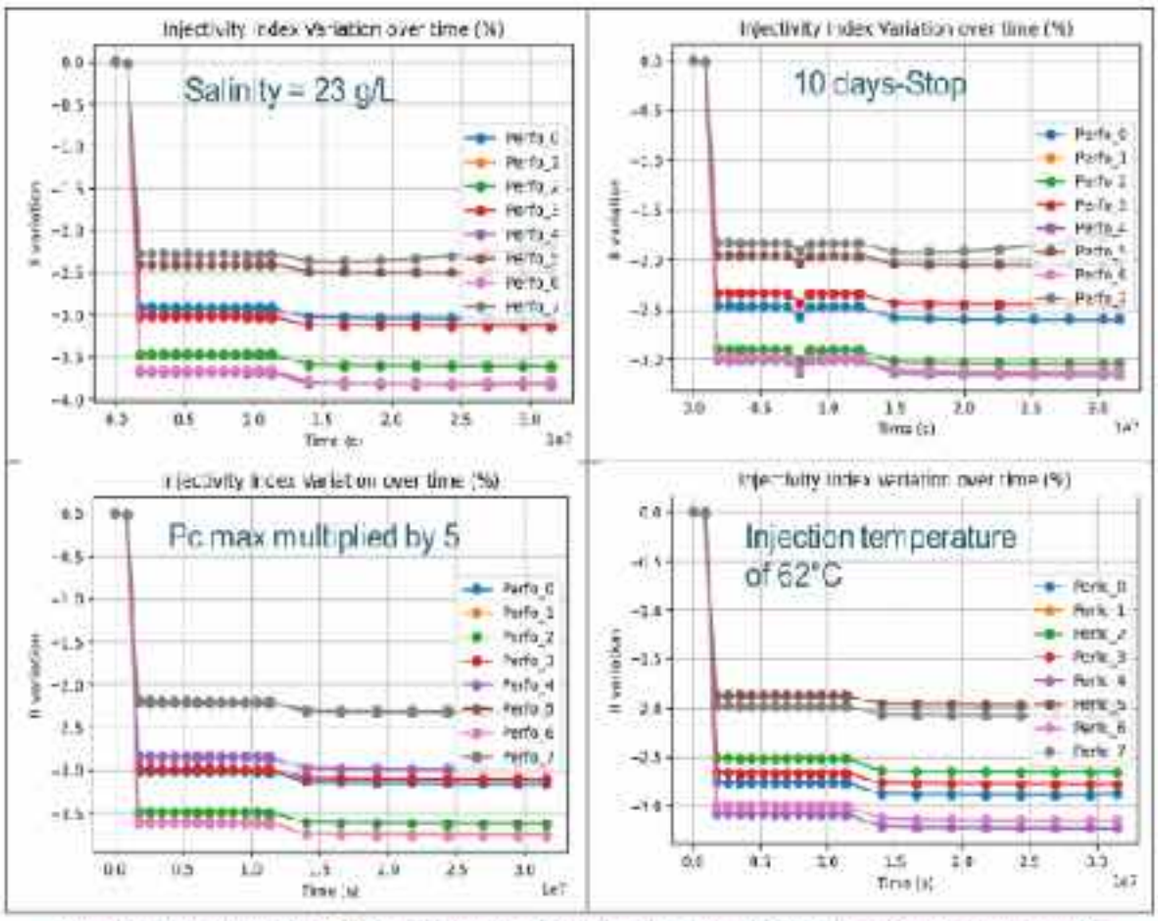


*Figure 4-11: Injectivity index variation (%) over time for well perforations with P50 Base case model and uncertain parameters (Salinity=23 g/L, 10 days-stop, maximum capillary pressure Pc multiplied by 5 and injection temperature = 62°C)*

The PilotSTRATEGY project has received funding from the European Union's Horizon 2020 research and innovation programme under grant agreement No. 101022664

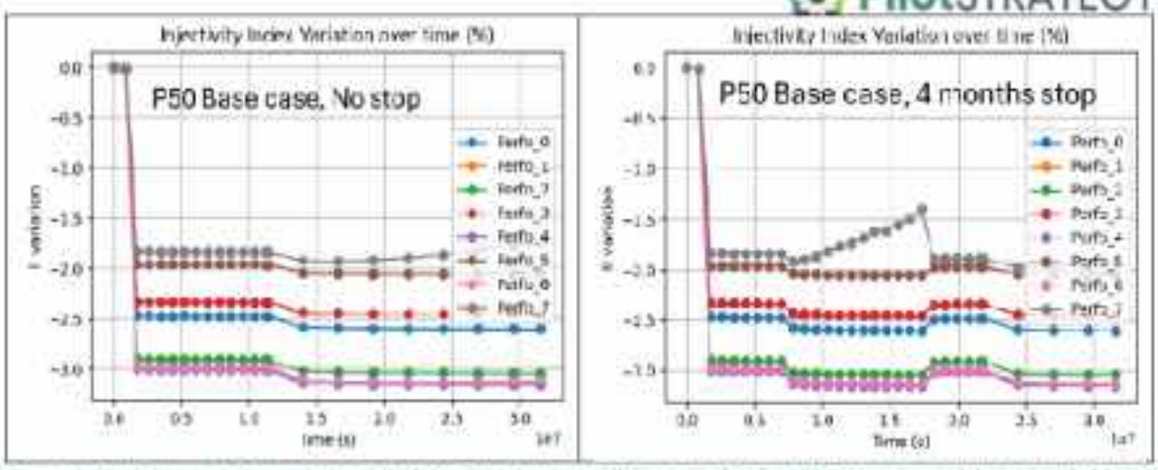


*Figure 4-12: injectivity index variation (%) of the $CO_2$ injection well over time for the P50 Base case model: no stop (left) and with a 4-months stop (right) during the injection period*

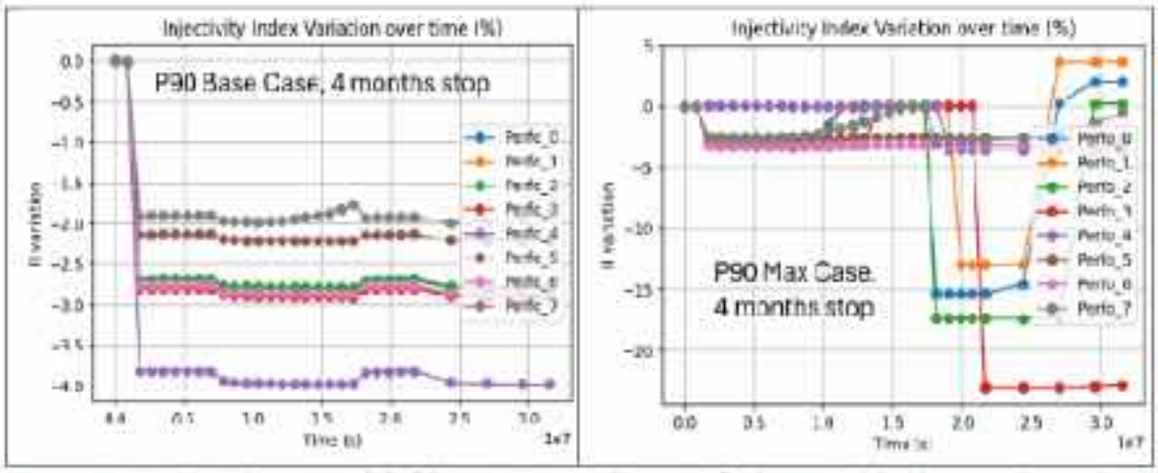


*Figure 4-13: injectivity index variation (%) of the $CO_2$ injection well over time for the P90 model with a 4-months stop during the injection period: Base case (left) and Max case (right)*

### 4.2.3 Simulation results of the Complex THC model

The targeted Oolithe Blanche formation is a carbonated rock mainly composed of calcite, whose dissolution could locally accelerate brine return in dried regions during $CO_2$ injection stops and worsen injectivity loss due to salt precipitation. This section presents the results of the Complex THC model applied to the P90 scenario (maximizing fluid flow) and Base case for fluid flow parameters. Their analysis is based on Figure 4-14 and Figure 4-15 displaying the gas saturation map at the end of the injection period and the change of the following parameters with time at different distance from the well (P1, P2 and P3 cells): gas saturation, temperature, dissolved $CO_2$ molar fraction, salinity, pH, mineral volume fraction, porosity and permeability. To complete the analysis, Figure 4-16 shows a 2D view of dissolved $CO_2$ molar fraction, temperature, pH and salinity.

The P1, P2 and P3 cells have different physical conditions that may impact the rock reactivity. For P1 located in the cooled area, the gas saturation quickly reaches the maximum value, i.e. in-situ brine is residual. Far from the well, P2 and P3 are little impacted by the cooling and the in-situ brine equilibrated with $CO_2$ (the minimum gas saturation is the residual value) is always mobile. Influenced by the low temperature, the dissolved $CO_2$ concentration is higher at P1 than at P2 and P3. In these conditions, pH decreases from 7 to 5.1 at P1 and to 5 at P2 and P3. Over time, this induces minor rock reactivity with a maximum at P1: salinity increase (+9 g/L), quick dolomite dissolution (-0.0004 of volume fraction (-)) and quick calcite precipitation (+0.00014 of volume fraction (-)) inducing an increase of porosity of 0.00027, i.e. relative increase of 0.2%, that leads to an increase of $4.10^{-16}$ $m^2$ (+0.4 mD) for permeability. With this

The PilotSTRATEGY project has received funding from the European Union's Horizon 2020 research and innovation programme under grant agreement No. 101022664

minor reactivity, resulting in a 0.09% gain in injectivity, no major impact on salt precipitation is expected if water evaporation is modelled.

This very low reactivity in carbonates has also been simulated by André et al.,2007 with a 1D radial reactive transport model. In their study, 300 kt of supercritical $CO_2$ are injected in 10 years in a 20-m thick reservoir modelling the Dogger saline aquifer. The petrophysical properties (0.12 as porosity and $10^{-13}$ $m^2$ (100 mD) as permeability) and the initial state (75°C for temperature and 180. $10^5$ Pa (bar)) are similar to our study parameters. Compared to this study, three times higher $CO_2$ amount is injected at ten times lower rate with twice lower horizontal transmissivity. At these conditions and with a Dogger mineralogy modelled by 0.7 of Calcite, 0.1 of Dolomite-Dis and 0.05 of Siderite, Illite, Albite and K-Feldspar, the $CO_2$ injection mainly induces dissolution (-0.007 of volume fraction (-)) of Calcite. André et al.,2007 also show that when injecting directly dissolved $CO_2$ in water (rather than supercritical gas) with an injection of 21 kg/s of water saturated with $CO_2$ induces higher reactivity with a dissolution (-0.7 of volume fraction (-)) of Calcite. This is due to a higher acidified water amount in contact with the rock. Overall, results from the current study and the one from André et al., 2007 are consistent with an expected low reactivity for a moderate injection of $CO_2$ at supercritical state.

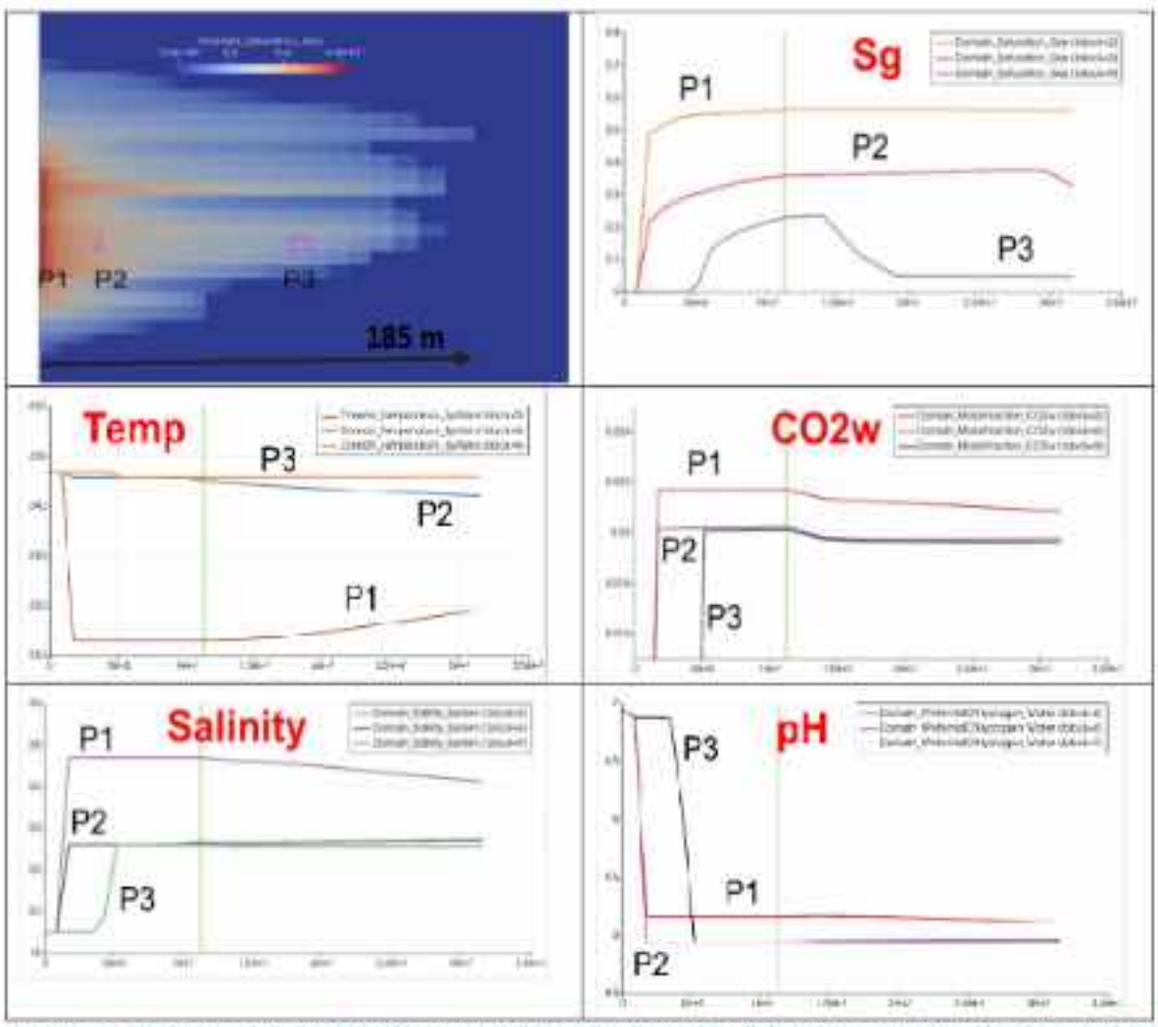


*Figure 4-14: Simulation results for P90 Base case model (Complex THC model) - (left top) Gas saturation (-) at the end of the injection period and parameter versus time in P1, P2 and P3 cells: Sg (gas saturation (-)), Temp (temperature (°C)), CO2w (dissolved $CO_2$ molar fraction (-)), salinity (g/L) and pH (-)*

The PilotSTRATEGY project has received funding from the European Union's Horizon 2020 research and innovation programme under grant agreement No. 101022664

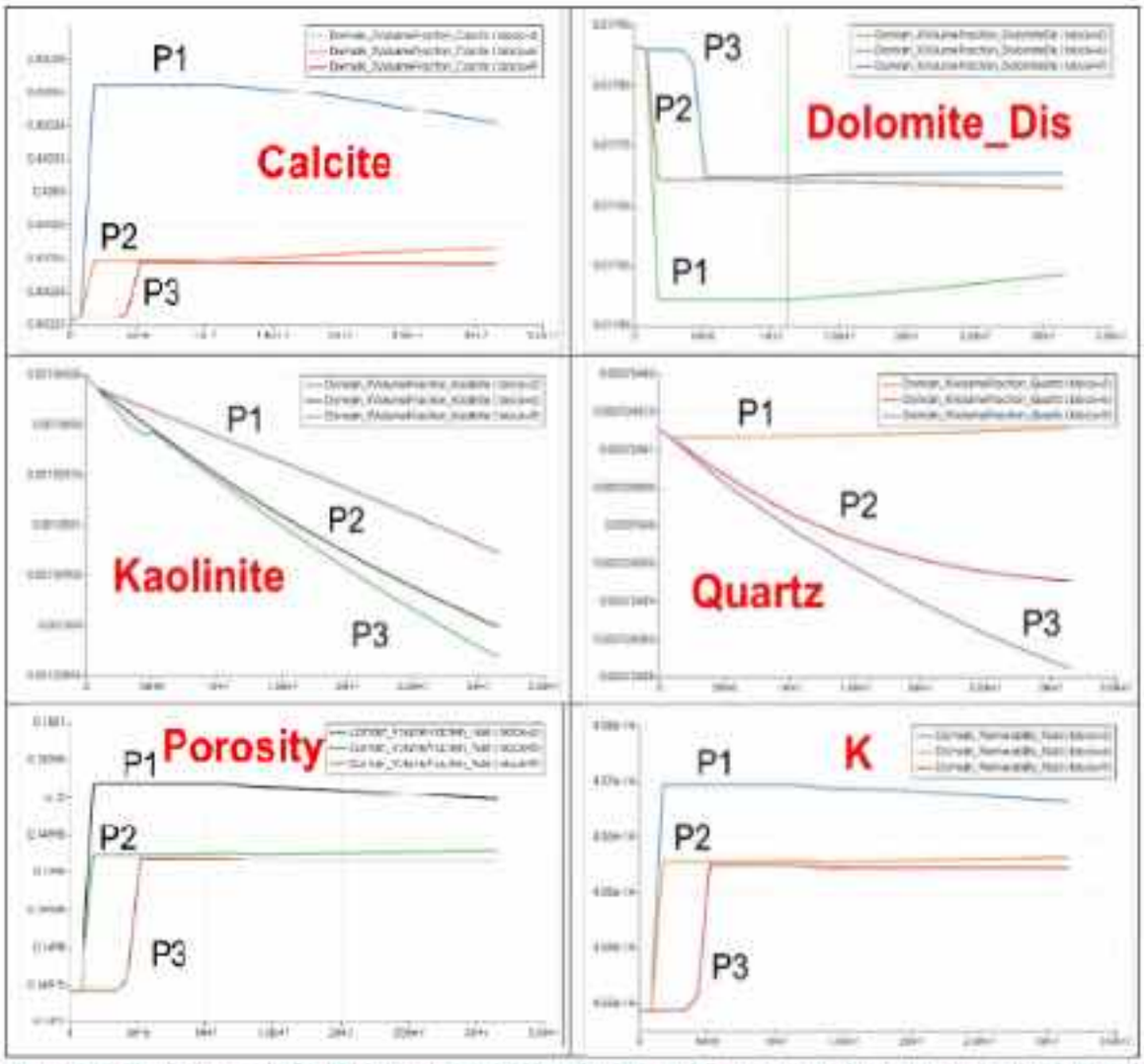


*Figure 4-15: Simulation results for P90 Base case model (Complex THC model) - parameter change versus time in P1, P2 and P3 cells: mineral volume fraction (Calcite, Dolomite-Dis, Kaolinite, Quartz) (-), porosity (-) and permeability K ($m^2$)*

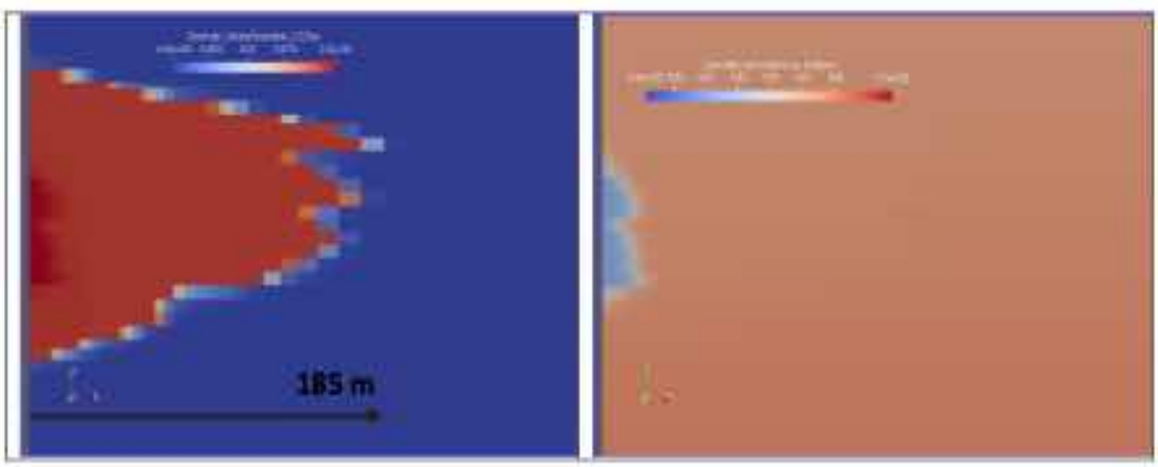


The PilotSTRATEGY project has received funding from the European Union's Horizon 2020 research and innovation programme under grant agreement No. 101022664

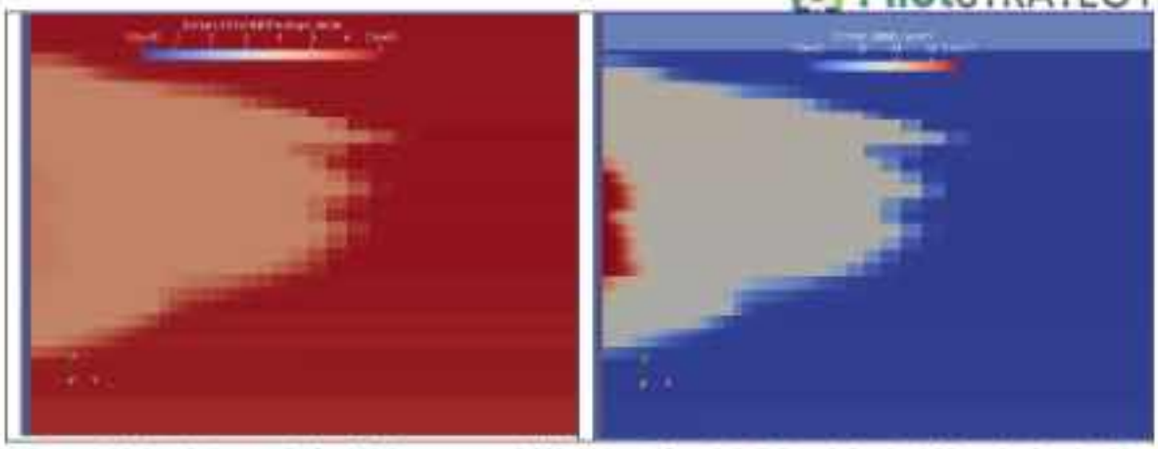

*Figure 4-16: Simulation results for P90 Base case model (Complex THC model): (left top) dissolved $CO_2$ molar fraction (-), (right top) temperature (°C), (left bottom) pH (-) and (right bottom) salinity (g/L) at the end of the injection period (4 months)*

### 4.2.4 Conclusion

This numerical study has quantified the loss of injectivity in a $CO_2$ injection well due to salt precipitation and fluid-rock interactions. The study has focused on a potential pilot-scale $CO_2$ injection into a deep saline aquifer (Dogger, Oolithe Blanche formation) within the Paris Basin, France. Two reactive transport models applied to a radial mesh have evaluated the geochemical effects and their impact on the petrophysical properties and the injectivity index of the well perforations. The first has considered water evaporation and simplified geochemical modelling of salt precipitation while excluding rock reactivity. The second has not accounted for water evaporation but has included fluid-rock interactions using a complex geochemical model that considers the primary minerals.

Considering uncertainties in the static model, injection temperature, capillary pressure, injection rate variability, fluid flow parameters, and salinity, the simplified geochemical model has estimated an injectivity loss of the well perforations ranging between 0% and 4%. Additional losses arise from the uncertainties in capillary pressure (+0.6%) and salinity (+0.7%).

However, the study has also revealed that a 4-month injection stop could significantly reduce the well injectivity (up to 23% for the P90 Max case) in contexts of high permeability (100 – 1000 mD). Still, in this case, the injectivity remains sufficient to continue to allow the targeted injection rate (300kt/yr) but this higher risk must be considered in cases of long stops for maintenance or for pilot upscaling for commercial exploitation. The results of the complex geochemical model, which simulates a minor 0.09% increase in permeability due to Calcite dissolution, allow to conclude that no significant increase in injectivity loss is anticipated related to rock reactivity.

The PilotSTRATEGY project has received funding from the European Union's Horizon 2020 research and innovation programme under grant agreement No. 101022664

## 4.3 Caprock integrity – Geochemical aspects

This section addresses aspects related to caprock integrity from the perspective of mineral reactivity. To this end, two types of calculation will be performed. Firstly, 1D calculations will be carried out, in which the transport component is resolved in a simplified way, but the geochemical model is complex. Secondly, coupled reactive transport 2D radial calculations will be performed, in which both transport and geochemistry are resolved in a complex way. The geochemical model is based on data from the SEIF1 well which is located in the studied area.

### 4.3.1 1D simplified reactive transport calculations with complex geochemistry

#### *4.3.1.1 Data and workflow*

To model the interface between the reservoir and the caprock, 1D simplified reactive transport modelling was performed. This type of calculations involves monophasic isothermal calculations but resolves complex geochemistry.

These calculations are carried out in two steps (Figure 4-17):

- Firstly, the water saturated with gaseous $CO_2$ is injected into a reactor representing the reservoir.
- At each time step, the composition of the fluid leaving the first reactor is injected into a second reactor representing the caprock.

Therefore, the calculations performed here model the venue in the caprock of a fluid that has already reacted with the reservoir rather than modelling the $CO_2$-saturated fluid directly, because $CO_2$ would be injected into the reservoir meaning that the fluid reaching the caprock would have passed through the reservoir.

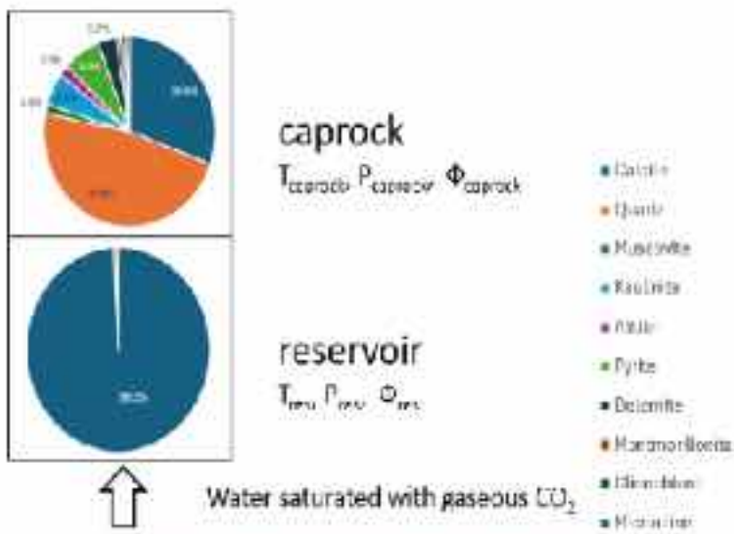


*Figure 4-17: Presentation of the workflow*

In order to mimic the real system, water saturated with gaseous $CO_2$ is injected into the reservoir for 4 months after which the simulation runs for 500 years. The reservoir and caprock volumes and the $CO_2$ flow have been calculated to be representative of the real case, based on a long-term transport simulation of the 3D model as well as porosities for each facies, pressure and temperature (Table 4-4). As a reminder: the studied system is representative of a pilot-scale injection: 100kt of supercritical $CO_2$ are injected into the Oolithe Blanche formation.

The PilotSTRATEGY project has received funding from the European Union's Horizon 2020 research and innovation programme under grant agreement No. 101022664

*Table 4-4: Parameters for each facies, based on the P90 3D model*

| | Reservoir | Caprock |
|---|---|---|
| Temperature (°C) | 72.85 | 69.85 |
| Pressure (bar) | 190 | 182 |
| Initial porosity (%) | 10 | 5 |

The initial volumes of the reactors are set to 1 $m^3$ and 0.5 $m^3$ for the reservoir and caprock respectively. The fluid flow is 0.007754 $m^3$/year, corresponding to the flow rate injected into the 3D model relative to the reservoir volume.

The mineral compositions of the reservoir and caprock are based on average composition values for well SEIF 1 (Table 4-5 and Table 4-6) located in the studied area (see Deliverable D2.9, Kilpatrick *et al.* 2025).

*Table 4-5: Average mineral composition of the reservoir based on SEIF1 well data (mol%)*

| Calcite | Quartz | Dolomite | Kaolinite |
|---|---|---|---|
| 98.6% | 0.1% | 1.2% | 0.1% |

*Table 4-6: Average mineral composition of the caprock based on SEIF1 well data (mol%)*

| Calcite | Quartz | Muscovite | Kaolinite | Albite | Pyrite | Dolomite | Montmorillonite | Clinochlore | Microcline |
|---|---|---|---|---|---|---|---|---|---|
| 30.6% | 47.5% | 5.5% | 6.9% | 1.0% | 2.0% | 1.5% | 3.5% | 1.0% | 0.5% |

The initial waters compositions are calculated to be equilibrated with in-situ mineralogy and a salinity of 19 g/L, and the injected water is calculated as the reservoir water equilibrated with a gaseous $CO_2$ sky (Table 4-7).

*Table 4-7: Waters composition (mol/kg$H_2O$)*

| | Reservoir water | Caprock water | Injected water |
|---|---|---|---|
| Na | 3.25E-01 | 3.62E-01 | 3.25E-01 |
| K | 1.00E-12 | 6.60E-06 | 1.00E-12 |
| Ca | 3.34E-04 | 5.53E-04 | 3.34E-04 |
| Al | 7.87E-06 | 6.88E-08 | 7.87E-06 |
| Si | 1.00E-03 | 5.99E-04 | 1.00E-03 |
| C | 7.70E-04 | 4.66E-02 | 1.77E+00 |
| Cl | 3.25E-01 | 3.24E-01 | 3.25E-01 |
| Fe | 2.72E-12 | 2.32E-09 | 2.72E-12 |
| S | 1.00E-12 | 1.09E-14 | 1.00E-12 |
| Mg | 4.36E-04 | 7.82E-04 | 4.36E-04 |

The PilotSTRATEGY project has received funding from the European Union's Horizon 2020 research and innovation programme under grant agreement No. 101022664

#### 4.3.1.2 Results

Figure 4-18 presents the evolution of geochemical parameters in the first reactor (reservoir) over a 500-year period. The system displays very low reactivity: the pH drops rapidly from approximately 9 to 6 immediately after $CO_2$ injection, then remains stable throughout the simulation. The saturation indices of the main minerals remain close to zero, indicating that all minerals are at or near thermodynamic equilibrium. Consequently, no significant mineralogical transformations occur, the mineral composition remains unchanged, and the porosity stays essentially constant at around 10%.

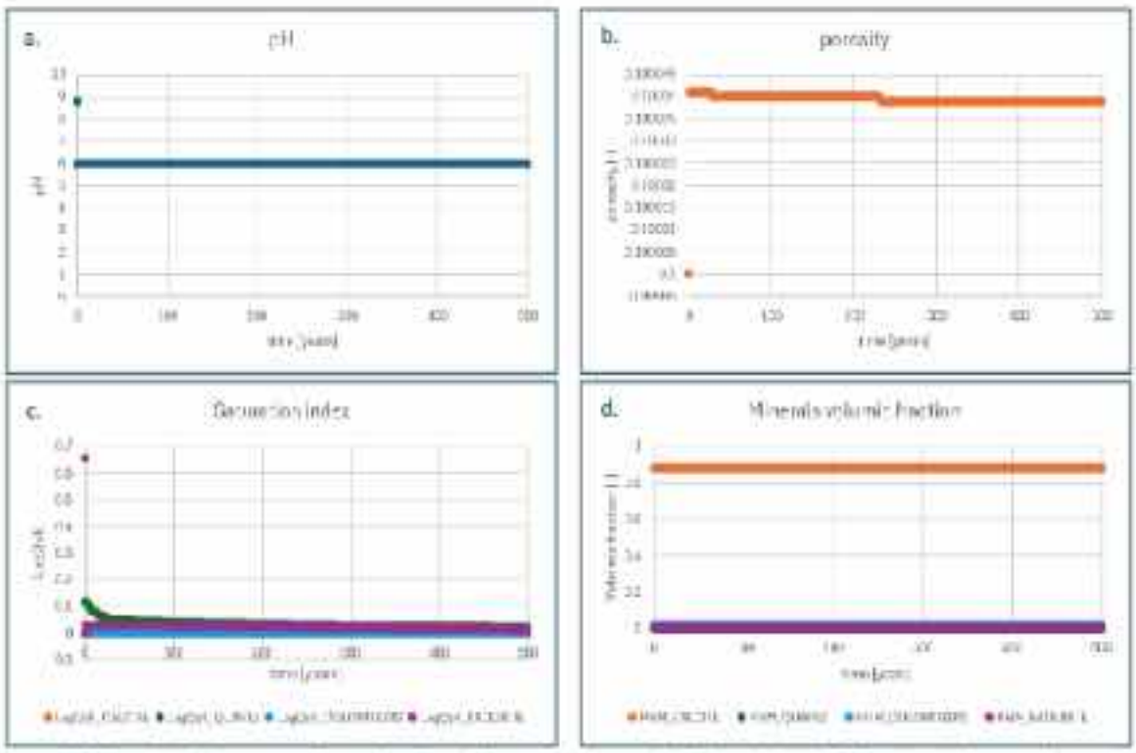


*Figure 4-18: Results for the reservoir as a function of time: a. decrease of pH when injecting $CO_2$ saturated wate ; b. porosity remains quite constant aroud 10%; c. saturation indexes stay close to 0: all the minerals are at equilibrium; d. mineral volumic fractions remains constant*

Figure 4-19 confirms this observation, showing that the overall mineralogical composition of the reservoir remains stable, with no significant variation in the proportions of calcite, quartz, dolomite, and kaolinite over time.

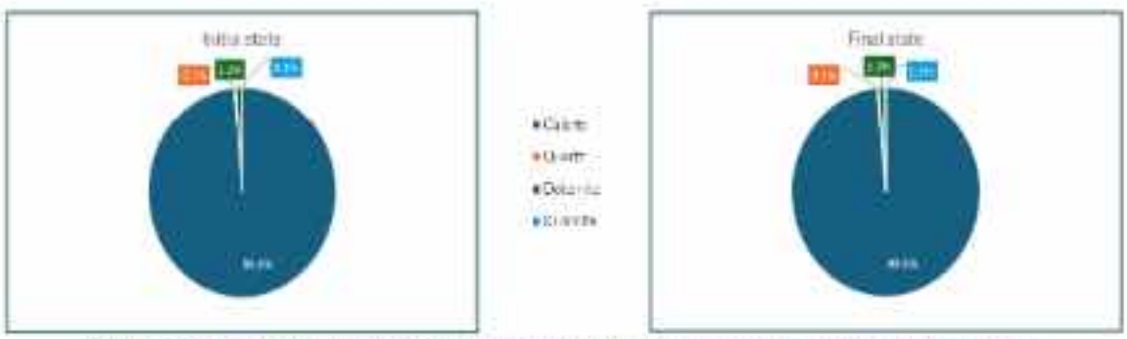


*Figure 4-19: Mineralogy at initial (left) and final state (right) (mol%) in the reservoir: there is no change*

In contrast, Figure 4-20 illustrates the evolution of geochemical parameters in the caprock, where reactivity is higher than in the reservoir. A sharp initial drop in pH is observed upon contact with the

The PilotSTRATEGY project has received funding from the European Union's Horizon 2020 research and innovation programme under grant agreement No. 101022664

$CO_2$-rich fluid, followed by a more gradual decrease from 6.85 to 6.45. In panels c and d, only the minerals exhibiting notable changes are represented. Quartz and montmorillonite show positive saturation indices, indicating a tendency to precipitate, whereas albite and clinochlore exhibit negative indices, suggesting a tendency to dissolve. The other minerals remain close to equilibrium, with saturation indices near zero. The evolution of volumetric fractions further confirms these trends: quartz, montmorillonite, and dolomite precipitate, while albite, clinochlore, and calcite dissolve. These mineralogical changes lead to a decrease of porosity from 5% to 4.76%.

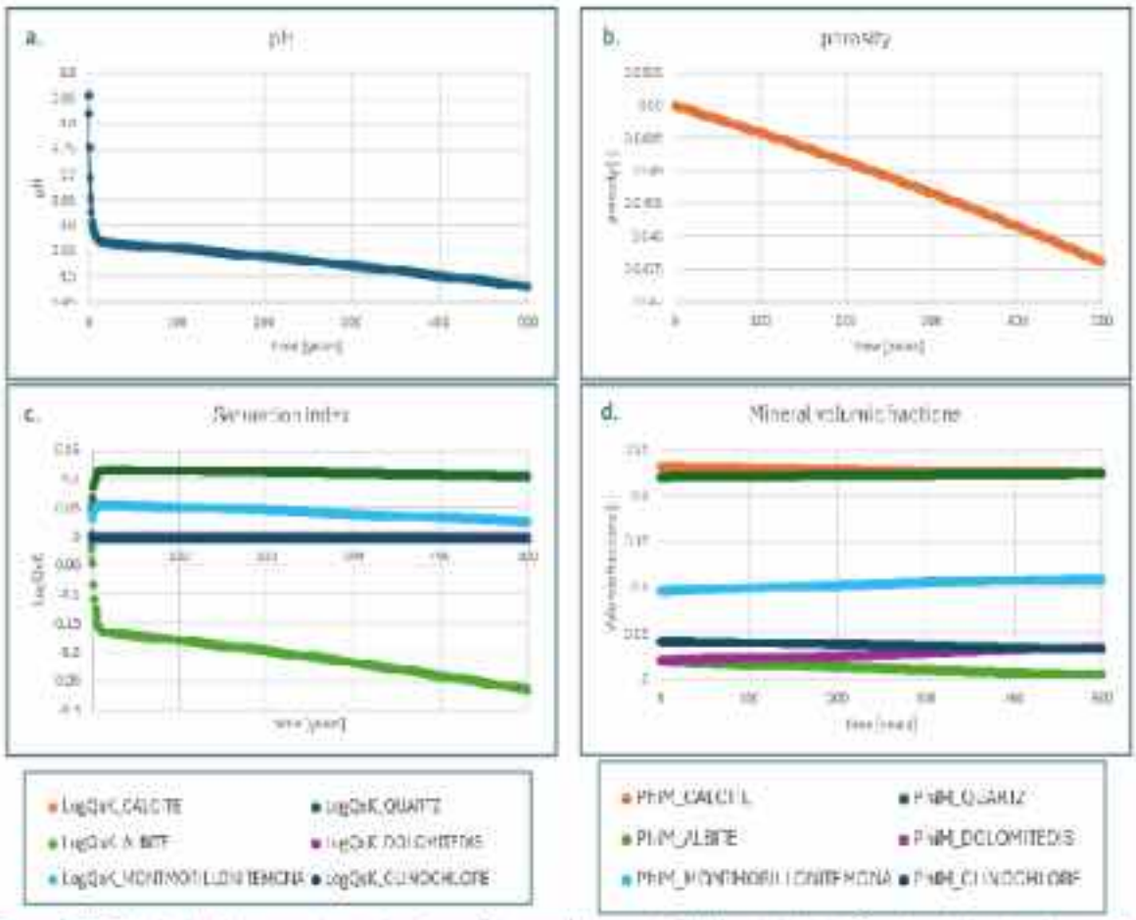


*Figure 4-20 : Results for the reservoir as a function of time: a. decrease of pH when injecting $CO_2$ saturated wate ; b. porosity decreases from 5% to 4.76%; c. saturation indexes stay close to 0: all the minerals are at equilibrium; d. mineral volumic fractions remains constant*

Finally, Figure 4-21 shows the evolution of the global mineral composition in the caprock. An increase in quartz, kaolinite, montmorillonite, and dolomite is observed, along with a decrease in calcite, albite, and clinochlore. These changes are consistent with the precipitation and dissolution processes highlighted in Figure 4-20.


The PilotSTRATEGY project has received funding from the European Union's Horizon 2020 research and innovation programme under grant agreement No. 101022664

*Figure 4-21: Mineralogy at initial (left) and final state (right) (mol%) in the caprock. The changes are minor: calcite, albite and chlinochlore are dissolved whereas quartz, montmorillonite and dolomite precipitate*

In conclusion, the 1D simplified reactive transport modelling, combining basic transport processes with complex geochemical interactions, reveals limited reactivity within the reservoir, and a higher degree of reactivity in the caprock. In the latter, a slight decrease in porosity is observed, from 5% to 4.76%, accompanied by the precipitation of quartz, kaolinite, montmorillonite, and dolomite, as well as the dissolution of calcite, albite, and clinochlore.

### 4.3.2 2D radial coupled reactive transport simulation on a long term

To complete the work performed on the simplified 1D simplified reactive transport calculations with complex geochemistry, a 2D radial coupled reactive transport calculation is performed.

The 2D radial model has been presented in the previous section (P90 model). It is composed by 6 facies: Lower Bathonien, Oolithes high and low (porosity), Comblanchien, Dalle nacrée and Massingy marls (Figure 4-22).

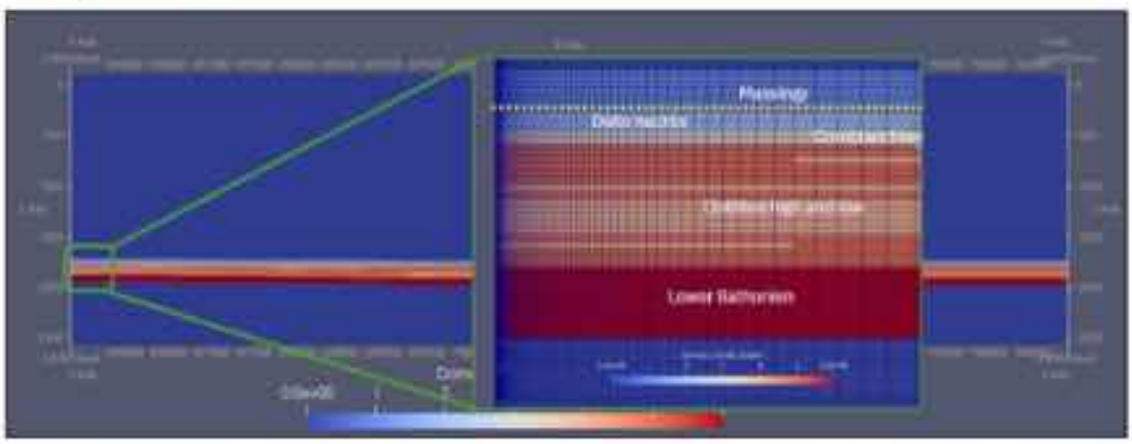


*Figure 4-22: 2D radial model and facies distribution. The dashed yellow line indicates the boundary between the Dalle Nacrée and the Massingy marls*

The geochemical model is the same as for the 1D simplified model: the mineral compositions for the reservoir and caprock are based on the data from SEIF1 (Table 4-5 and Table 4-6) and the initial waters compositions are set to be at equilibrium with the in-situ minerals (Table 4-7).

As for the near wellbore study, gaseous $CO_2$ is injected over a period of 4 months. However, in this study, the post-injection period is extended for the long-term behaviour study with a simulation carried out over a period of 500 years.

The Figure 4-23 shows the state of the system at the end of the injection period. The drop of pH is associated with the extent of the $CO_2$ plume. The first layer of Massingy marls is not reached by the $CO_2$ fluid (gas phase and $CO_2$-rich brine).

The PilotSTRATEGY project has received funding from the European Union's Horizon 2020 research and innovation programme under grant agreement No. 101022664

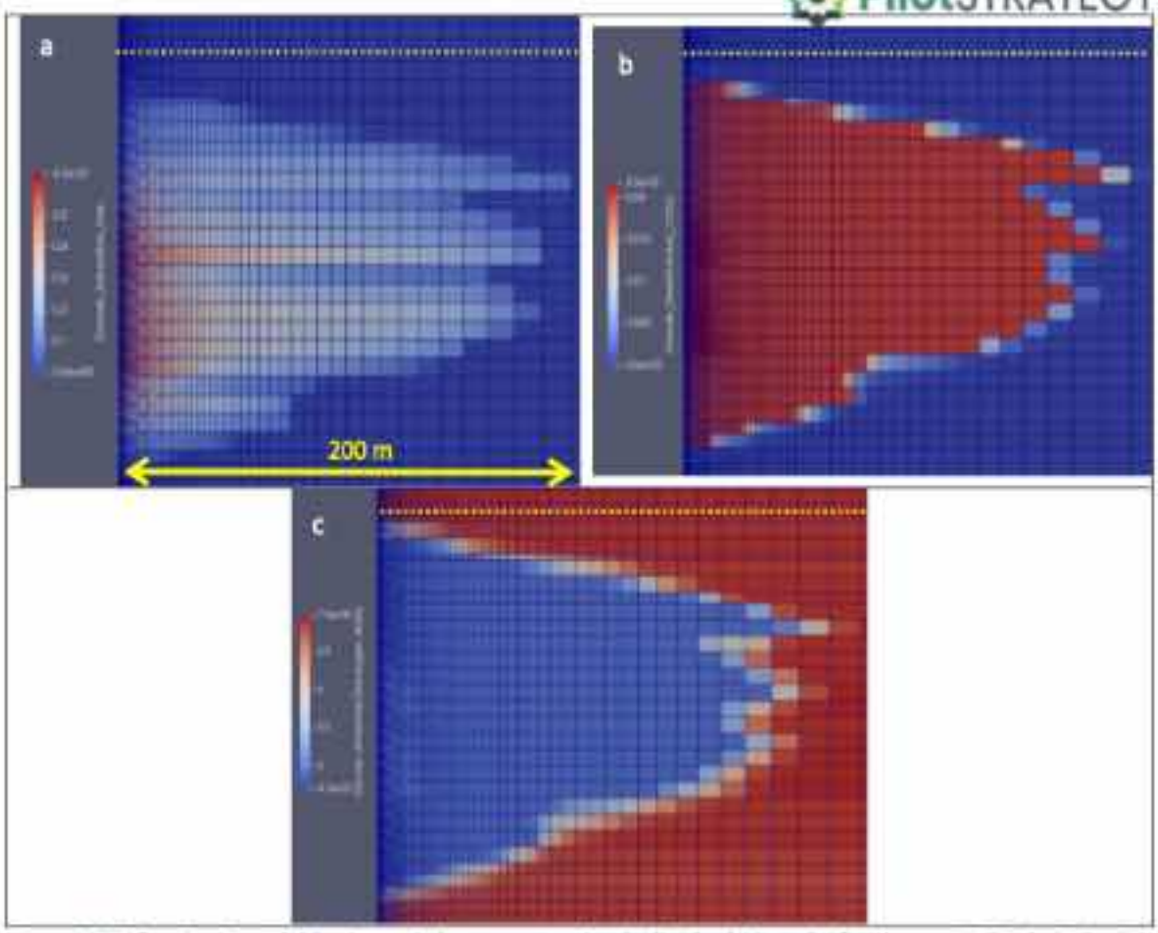


*Figure 4-23: After the 4-month injection period: a. gas saturation; b. dissolved $CO_2$ molar fraction; c. pH. The dashed yellow line indicates the boundary between the Dalle Nacrée and the Massingy marls*

Figure 4-24 illustrates the system's evolution after 11 years of simulation: the $CO_2$ plume spreads and the dissolved $CO_2$ reaches the first layer of Massingy marls.

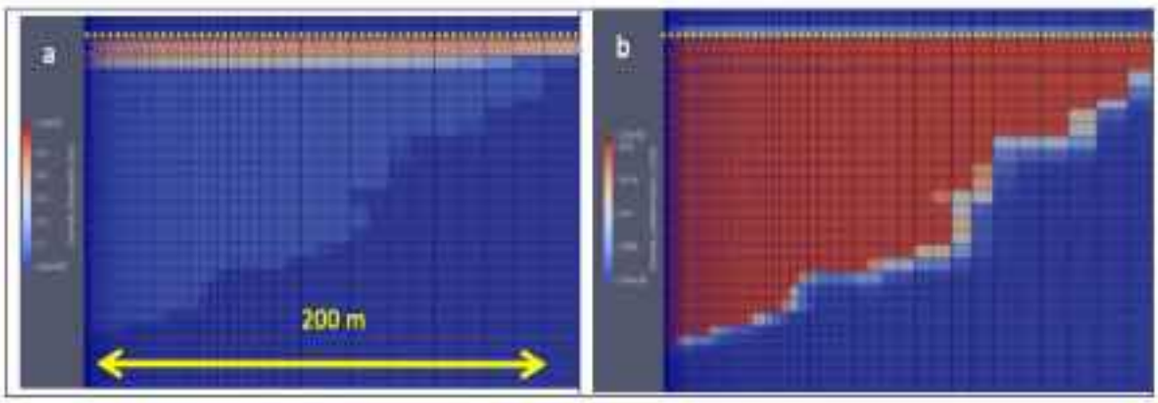


The PilotSTRATEGY project has received funding from the European Union's Horizon 2020 research and innovation programme under grant agreement No. 101022664

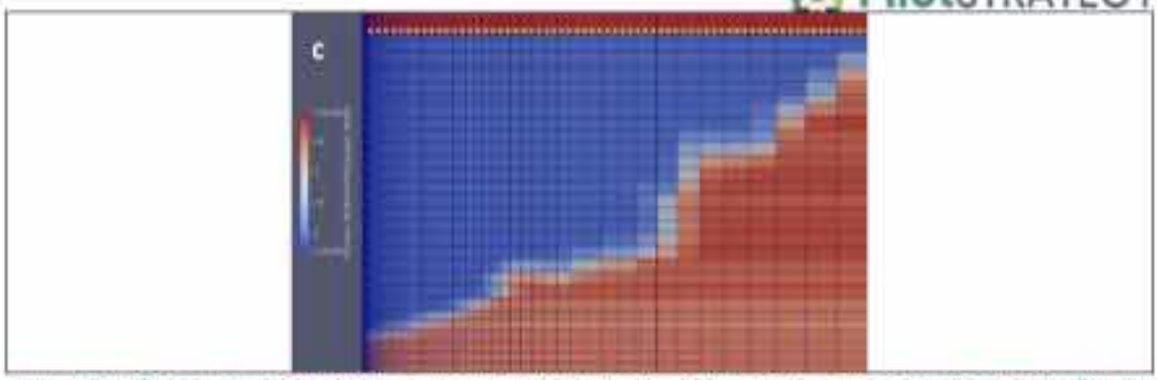


*Figure 4-24: After 11 years of simulation: a. gas saturation; b. dissolved $CO_2$ molar fraction; c. pH. The dashed yellow line indicates the boundary between the Dalle Nacrée and the Massingy marls*

After 500 years, at the end of the simulation, the $CO_2$, whether in gas form or dissolved in water, is present in the first layer of Massingy marls, but does not penetrate any further (Figure 4-25).

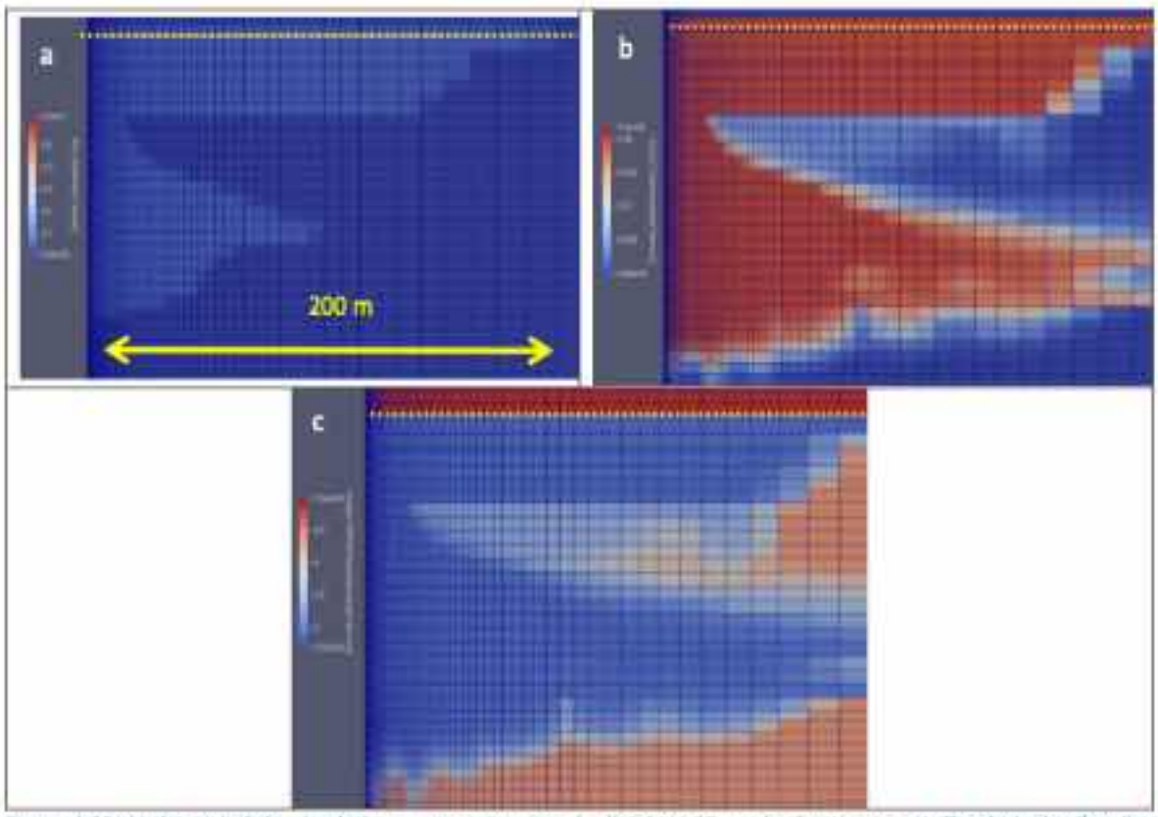


*Figure 4-25: At the end of the simulation: a. gas saturation; b. dissolved $CO_2$ molar fraction; c. pH. The dashed yellow line indicates the boundary between the Dalle Nacrée and the Massingy marls*

Regarding the geochemical reactivity of the caprock, Figure 4-26 displays a selected cell in the first layer of Massingy marls. This cell will be analysed in more detail later in the report.

The PilotSTRATEGY project has received funding from the European Union's Horizon 2020 research and innovation programme under grant agreement No. 101022664

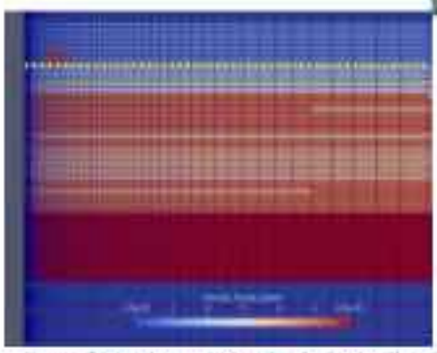

*Figure 4-26: Selected cell into the first layer of Massingy marls. The dashed yellow line indicates the boundary between the Dalle Nacrée and the Massingy marls*

The evolution of key parameters is shown on Figure 4-27. Dissolved $CO_2$ molar fraction starts increasing after 11 years and reaches the limit of solubility of $CO_2$ under these conditions, consequently, gaseous $CO_2$ appears. pH decreases from 6.85 to 6.67 when the dissolved $CO_2$ amount increases but when gaseous $CO_2$ appears, pH increases back to 6.85. Porosity decreases from 4.63% to 4.5%.

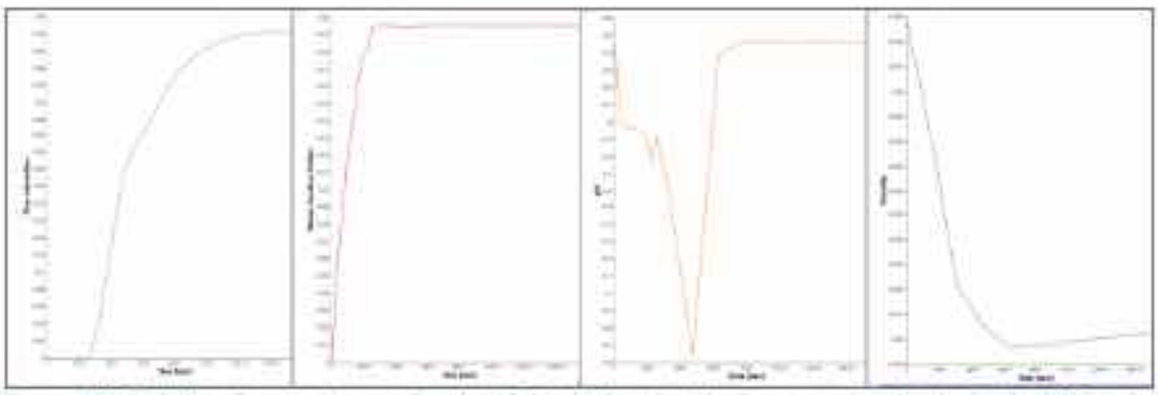

*Figure 4-27: Evolution of parameters as a function of time in the selected cell: a. gas saturation; b. dissolved $CO_2$ molar fraction; c. pH; d. porosity*

Figure 4-28 displays how the molar fractions of minerals in the selected cell change over time. Only minerals that exhibit notable changes are represented. Calcite ($CaCO_3$) and chlorite (clinochlore: $Mg_5Al(AlSi_3)O_{10}(OH)_8$) can be seen to dissolve, releasing $Ca^{2+}$, $Mg^{2+}$, $Al^{3+}$, $Si^{4+}$ and $CO_3^{2-}$ ions into the water. Consequently, the main mineral that precipitate is dolomite ($CaMg(CO_3)_2$). Montmorillonite ($Na_{0.34}Mg_{0.34}Al_{1.66}Si_4O_{10}(OH)_2$) and quartz ($SiO_2$) also precipitate, but only in small quantities.

The PilotSTRATEGY project has received funding from the European Union's Horizon 2020 research and innovation programme under grant agreement No. 101022664

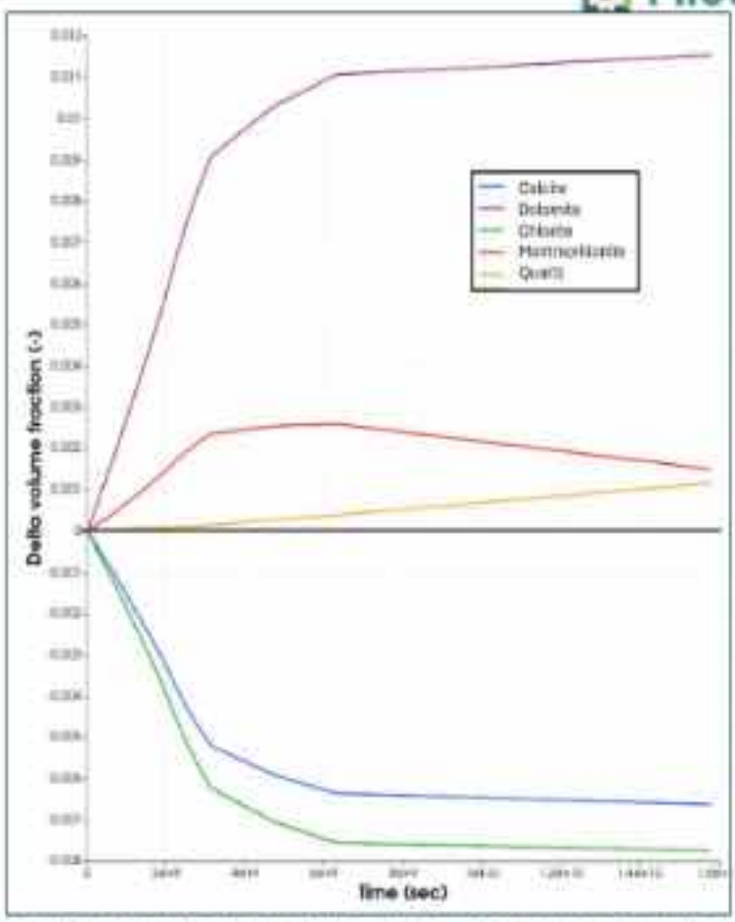


*Figure 4-28 : Variation of volume fraction of minerals that exhibit notable changes as a function of time in the selected cell. The black line depicts the 0-variation line.*

In conclusion, this study successfully developed a comprehensive 2D radial reactive transport simulation, that incorporates complex geochemistry and a realistic system configuration. The results highlight the spatial and temporal evolution of the $CO_2$ plume, as well as the chemical interactions between the injected $CO_2$, water, and the minerals present in the reservoir and caprock.

After 500 years of simulation, $CO_2$, in both dissolved and gaseous forms, reaches the first layer of Massingy marls without further penetration, demonstrating a degree of geochemical and structural stability in the studied system. Geochemical observations reveal the dissolution of minerals such as calcite and chlorite, accompanied by the precipitation of dolomite, indicating pH buffering mechanisms and a slight reduction in porosity. Overall, this geochemistry study demonstrates a very limited geochemical impact on the caprock of the $CO_2$ injection at pilot-scale in the Dogger aquifer. Therefore, geochemical impact on the caprock is not a major concern for the caprock in the studied case.

## 4.4 Storage complex integrity – Geomechanical aspects

### 4.4.1 Coupled flow-geomechanics model

The coupled simulations were carried out through a sequential coupling between CooresFlow and Code_Aster. Code_Aster is an open-source finite element-based simulator for solid mechanics and structural analysis (https://code-aster.org/). Simulations are subdivided into fixed coupling periods, and two algorithms are used: a simple one-way coupling in which the mechanical problem is solved independently without retroaction on

The PilotSTRATEGY project has received funding from the European Union's Horizon 2020 research and innovation programme under grant agreement No. 101022664

fluid-flow, and an iterative coupling which relies on a fixed-stress coupling algorithm (Kim et al., 2011). For the iterative approach, all exchanges and communications between simulators are managed by preCICE (https://precice.org/) an open-source co-simulation library (Chourdakis et al., 2021).

For each period, the quasi-static mechanical equilibrium equation is solved under the assumption of linear poroelasticity (Coussy 2004). Poroelastic properties are estimated from the porosity field using analytical models based on the effective medium theory. Two models were used depending on the facies: Bemer's model (Bemer et al., 2004) tailored to carbonate-rich formations present in the reservoir (the Dalle Nacrée, Comblanchien, Oolithe Blanche and Lower Bathonien), and a more general Mori-Tanaka model (Mori, Tanaka 1973) for caprock, overburden, and underburden formations. Parameters of these laws were deduced from available data (core samples from Charmottes-4 (CHM4), Vulaines-1 (VUS1) and DT log from VUS1). During one-way simulation, the pore compressibility moduli are calculated based on the poroelastic properties of each formation and porosity values, so that the variations in pore volumes estimated during fluid-flow simulations are consistent with calculated mechanical deformation. Several assumptions are possible to express this pore compressibility:

- Isotropic deformation with an incompressible solid skeleton (*iso b1*)

$$C_p = \frac{1}{\Phi_0 K}$$

- Isotropic deformation with compressible skeleton (*iso*)

$$C_p = \frac{1}{\Phi_0}\left(\frac{b^2}{K} + \frac{1}{M}\right)$$

- Oedometric deformation with incompressible skeleton (oedo b1)

$$C_p = \frac{1}{\Phi_0}\left(\frac{3}{3K + 4G}\right)$$

- Oedometric deformation with compressible skeleton (oedo)

$$C_p = \frac{1}{\Phi_0}\left(\frac{3b^2}{3K + 4G} + \frac{1}{M}\right)$$

With b, M, K, G respectively Biot's coefficient, Biot's modulus, bulk and shear elastic moduli. A comparison between one-way models based on these assumptions and an iterative calculation is available in the appendix (Figure 7-1).

To evaluate formation integrity, a Drucker-Prager criterion is used (Drucker, Prager 1952). The coefficients of Drucker-Prager criterion can be expressed in terms of the cohesion c' and friction angle ϕ' parameters of a classical Mohr-Coulomb. These parameters are estimated from the porosity field through empirical laws. For reservoir formation, these laws and their associated parameters were identified from triaxial tests on carbonates (Bemer et al., 2004). For caprock (callovo-oxfordian formation), parameters were taken from literature data (Menaceur et al., 2015). The distance expressed in the p', q invariants plane, between the local stress state and the failure criterion, is used as a risk indicator and calculated for each cell in the formations of interest.

The PilotSTRATEGY project has received funding from the European Union's Horizon 2020 research and innovation programme under grant agreement No. 101022664

- For reservoir formations, an "oedo-distance" is used, which corresponds to the distance to the criterion when the stress path follows a trajectory under oedometric conditions. This simple physical assumption is suitable for a cell primarily subjected to pore pressure variations.
- For the caprock, an orthogonal projection of the stress state onto the yield surface is used. This is the most conservative distance, as the cap-rock is subjected to more complex loading (pressure, bending, etc).

No in situ test results allowing to estimate the initial stress state (LOT, hydraulic fracturing tests, FIT, etc) for the area of interest were provided. The initial stress state is then estimated based on literature data and equilibrium calculations. The principal horizontal stress (SH) is oriented N150°E, and the stress ratio SH/Sv is close to 1 at the depths of interest, while the ratio Sh/Sv varies between 0.55 and 0.85 depending on the clay content of the formations (Gunzburger, Magnenet, 2014), (Vidal-Gilbert et al., 2009).

All reference parameters for elastic and plastic properties, as well as the initial stress state, are provided in Appendix 7.1. The complete description of the mechanical model and the identification of the chosen parameters is detailed in D3.3, appendix 7.1 (Alavoine et al., 2024).

The following analyses focus solely on the injection period (4 months) and short-term post-injection period (up to 8 months). Beyond this last period, the overpressure becomes negligible and therefore geomechanical effects become also negligible.

### 4.4.2 Geomechanical study on P10, P50, P90 models

The nine cases, described in section 4.1 (Table 4-1) and in deliverable D3.3 (Alavoine et al., 2024) have been simulated with an iterative hydromechanical coupling to improve the estimates of the overpressure induced by the injection and its related consequences to the subsurface deformation and surface displacement, and to assess the risk of failure through the calculation of the distance to the Drucker-Prager failure criterion. In these simulations, $CO_2$ was injected from day 10 to day 131 and the simulations continued for up to one year (365 days).

For the initial stress state here, the stress ratio SH/Sv is 1 for all cases and the stress ratio Sh/Sv is taken as follows for all 9 cases: 0.8 for the over/under-burden, 0.74 for the caprock, 0.6 for the Dogger, and 0.68 for the lower Bathonian (see Appendix 7.1 Table 7-3).

The resulting variables of these numerical simulations that are relevant to the study are:

- The pressure and overpressure in the reservoir and at the bottom of the caprock formation.
- The vertical displacement at the surface of the model and at the interface between the caprock and the reservoir.
- The distances to the failure criterion:
  - for the caprock: ortho-distance to the criterion,
  - for the storage formations: oedo-distance to the criterion.

The distances used to assess the storage integrity (caprock and storage formations) are distances to the inner Drücker-Prager criterion, they are described in the deliverable 3.3 (section 7.1.3.4).

The PilotSTRATEGY project has received funding from the European Union's Horizon 2020 research and innovation programme under grant agreement No. 101022664

For the sake of clarity, in the models, rock formations with the same mechanical properties are grouped together and treated as a single rock zone. It may vary from the layers defined in terms of flow properties. The formations of interest are defined as follows in terms of mechanical properties:

- Caprock: Callovo-Oxfordian (COX) and Massingy marls.
- Storage formations (also called 'reservoir'): Dalle Nacrée, Comblanchien, and Oolithe Blanche.
- Lower Bathonian : Lower Bathonian.

In this section, in all figures the system of coordinates is centred on the injection well location.

*Injection well results*

For most of the cases, the expected amount of $CO_2$ (100 kt) can be injected in 4 months while respecting the maximum Bottom-Hole Pressure (Figure 4-29), pre-calculated for mechanical integrity of the injection site (in D3.3, recalled in 4.1 section of this report). Only P10-Min and P90-Min cases reached the maximum BHP and have a limited amount of injected $CO_2$ after 4 months (around 10kt for P10-Min and 40kt for P90-Min). This is related to low values of permeability, with the considered K-Phi relationship leading to a low connectivity near the injection well (Table 4-8, see also Figure 4-30 and Figure 4-32). However, all three 'Min' cases are super-pessimistic in regards with Oolithe Blanche permeability values: indeed, these values are related to the lowest permeability values from core/plug measurements. Yet the matching of the wasted water injection well's history (SEIF-1 well) in the area, performed by the BRGM's partners (see D3.4, Ben Rhouma et al., 2026) required to increase three times the permeability field of the P50 model (base case). Thus, 'Min' cases are probably to be discarded with this new information about the dynamic behavior in this area, leading to an expected maximum overpressure around 20 bars for the remaining cases. In conclusion, on this basis, we do not expect any injectivity problem regarding the geomechanical aspect for the $CO_2$ pilot-scale injection in this area. This will be confirmed in the next section with the study of the failure distance criterion for each case.

The PilotSTRATEGY project has received funding from the European Union's Horizon 2020 research and innovation programme under grant agreement No. 101022664

*Table 4-8: Median permeability (mD) in the Dolithe Blanche formation (high porosity) in each cases.*

| | Median K (OB) P10 | Median K (OB) P50 | Median K (OB) P90 |
|---|---|---|---|
| Min/Pessimistic | 9.8 mD | 12 mD | 20 mD |
| Base Case / Most Probable | 39 mD | 48 mD | 80 mD |
| Max/Optimistic | 156 mD | 192 mD | 320 mD |

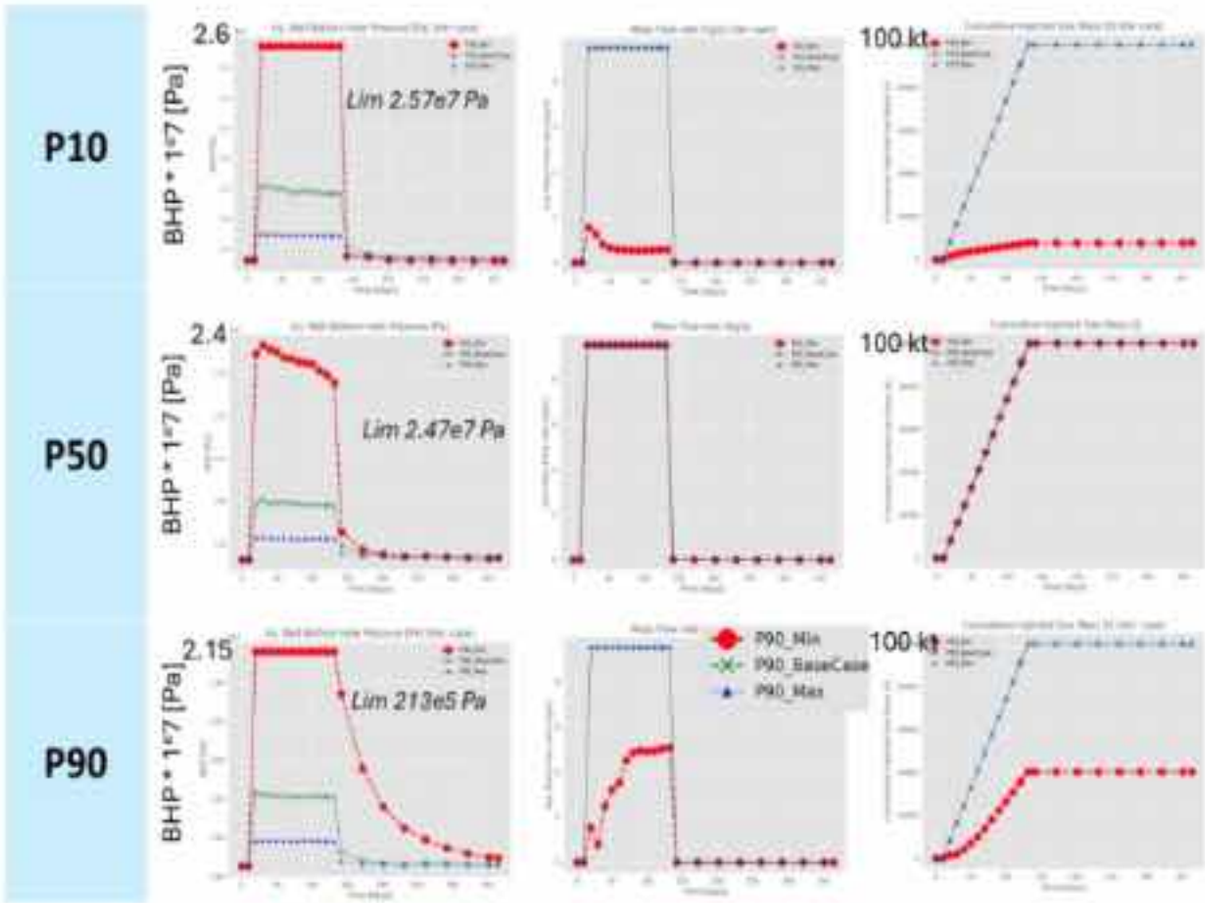


*Figure 4-29: $CO_2$ injection well results for the nine cases: Bottom-Hole Pressure (left), Injection flow rate (middle) and Cumulative injected mass (right)*

### *$CO_2$ migration results*

Compared to previous results in D3.3, the extent of $CO_2$ migration is slightly larger (laterally and vertically) but could also be related to the change in in-situ temperature (dissolution and density effects) compared to the previous models. Updated tables of $CO_2$ plume extent and snapshot of the cross-section of the $CO_2$ plume at the end of the simulation (1 year) are presented below for the sake of completeness (Figure 4-30, Figure 4-31, Figure 4-32).

Overall, the extent of the plume remains in the same order as previously, with a maximum extent about 350 m around the well. The $CO_2$ plumes never reach the caprock during the injection period and 8 months post-injection period (as described, in 4.3.2, the $CO_2$ plume only reaches the caprock interface about 11 years post-injection for the P90 model (radial)).

| P10_PSC – $CO_2$ plume Extent [m] | X | Y | Z |
|---|---|---|---|

The PilotSTRATEGY project has received funding from the European Union's Horizon 2020 research and innovation programme under grant agreement No. 101022664

| | | | |
|---|---|---|---|
| 'Min' Worst case @1year | 187 (187) | 187 (187) | 80 (74) |
| Base Case @1 year | 561 (499) | 561 (561) | **92 (86)** |
| 'Max' Best case @1 year | 561 (561) | **623 (623)** | 67 (67) |

*Table 4-9: P10 model – $CO_2$ plume extent [m], 8 months post-injection for the three studied cases from the iterative hydromechanical coupling. Values in brackets are values from the previous models in D3.3 (Alavoine et al., 2024). Notice that 'Min' Worst case injects only 10 kt of $CO_2$ (100kt for both other cases). In bold, maximum values in horizontal and vertical directions.*

| P50_BC – $CO_2$ plume Extent [m] | X | Y | Z |
|---|---|---|---|
| 'Min' Worst case @1year | 686 (624) | **686 (686)** | 84 (80) |
| Base Case @1 year | 561 (561) | 623 (623) | **86 (80)** |
| 'Max' Best case @1 year | 686 (561) | 686 (623) | 74 (68) |

*Table 4-10: P50 model – $CO_2$ plume extent [m], 8 months post-injection for the three studied cases from the iterative hydromechanical coupling. Values in brackets are values from the previous models in D3.3 (Alavoine et al., 2024). In bold, maximum values in horizontal and vertical directions.*

| P90_OPT – $CO_2$ plume Extent [m] | X | Y | Z |
|---|---|---|---|
| 'Min' Worst case @1 year | **624 (561)** | 561 (436) | 67 (67) |
| Base Case @1 year | 531 (561) | 499 (499) | **74 (74)** |
| 'Max' Best case @1 year | 561 (561) | 561 (499) | 68 (67) |

*Table 4-11: P90 model – $CO_2$ plume extent [m], 8 months post-injection for the three studied cases. Values in brackets are values from the previous models in D3.3 (Alavoine et al., 2024). Notice that 'Min' Worst case injects only 40. kt of $CO_2$ (100kt for both other cases). In bold, maximum values in horizontal and vertical directions.*

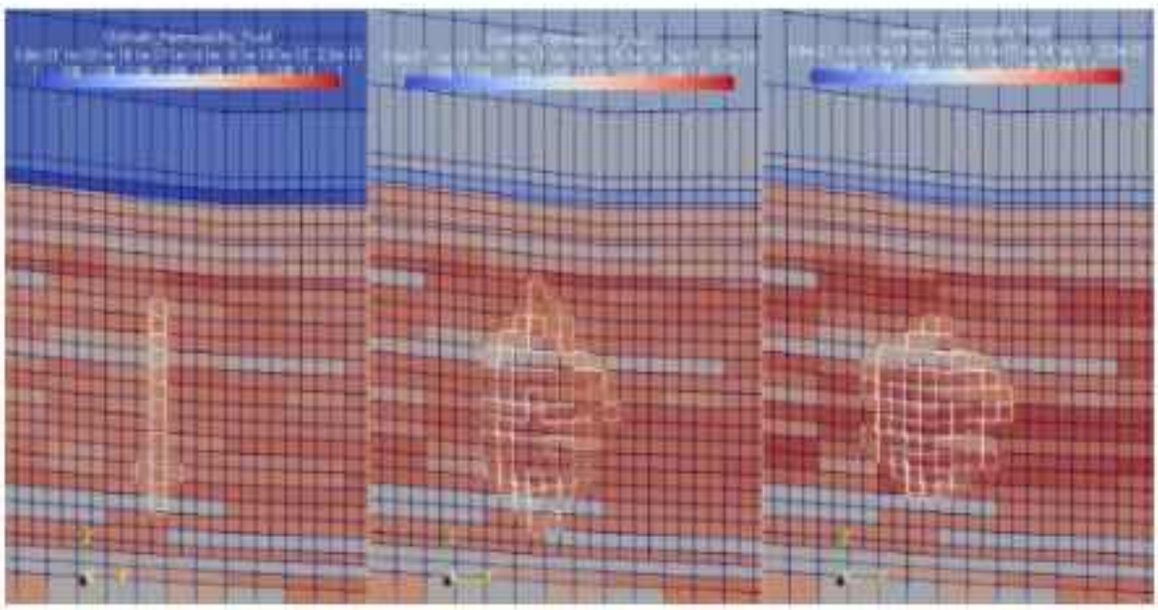

*Figure 4-30: 2D/Cross-section of the permeability fields (P10 model) with the $CO_2$ plume in wireframe, 8-months post-injection, for Min case (left), Base case (middle) and Max case (right). For scale reference: a lateral cell size is 62.5m in the storage formation.*

The PilotSTRATEGY project has received funding from the European Union's Horizon 2020 research and innovation programme under grant agreement No. 101022664

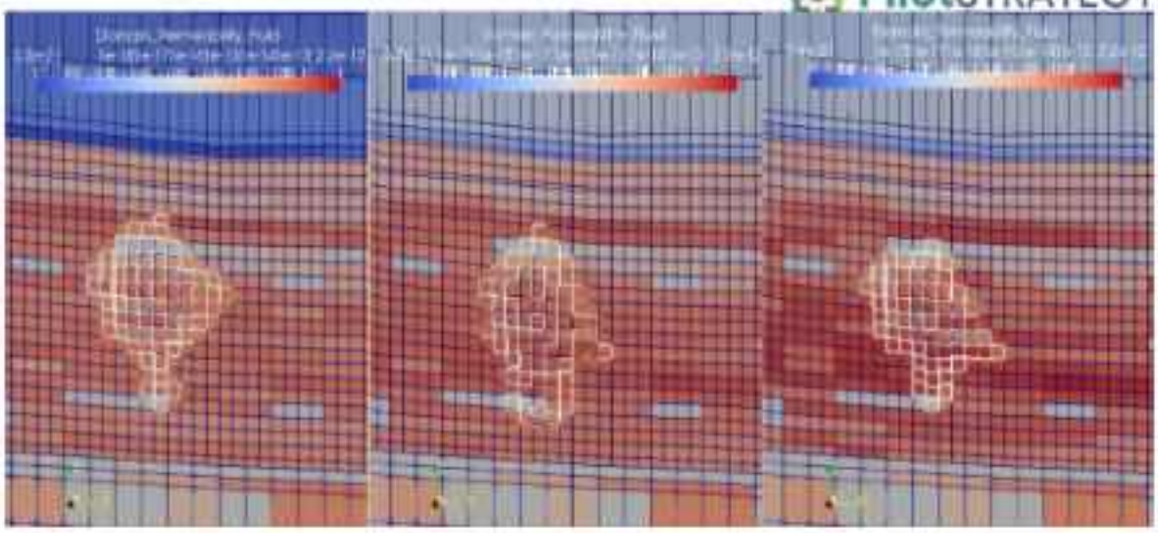

*Figure 4-31: 2D/Cross-section of the permeability fields (P50 model) with the $CO_2$ plume in wireframe, 8-months post-injection, for Min case (left), Base case (middle) and Max case (right). For scale reference: a lateral cell size is 62.5m in the storage formation.*

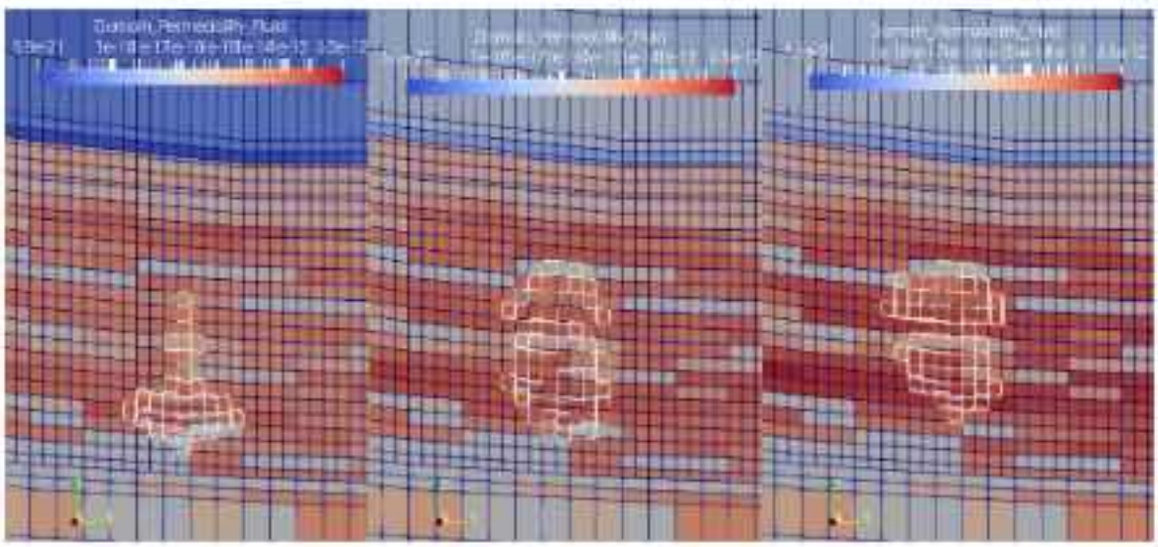

*Figure 4-32: 2D/Cross-section of the permeability fields (P90 model) with the $CO_2$ plume in wireframe, 8-months post-injection, for Min case (left), Base case (middle) and Max case (right). For scale reference: a lateral cell size is 62.5m in the storage formation.*

### *Overpressure results*

Figure 4-33 illustrates the spatial distribution and magnitude of the maximum overpressure (or pressure difference with the initial state) at the end of $CO_2$ injection into the storage formations (i.e. Oolithe Blanche, Comblanchien and Dalle Nacrée). The maximum overpressure was evaluated vertically for each column of the 3D grid and represented in 2D for clarity. The rows represent the P10, P50 and P90 models, while columns correspond to the additional three case scenarios (Min, Base case, Max). The initial maximum pressure in the reservoir ranges between 19 and 20 MPa.

The simulations showed that the maximum overpressure reached at the end of injection, upon closing the well, over the whole reservoir formation and over the 9 models, was 7.06 MPa (70.6 bar) in the P10_Min case (injection well results, see previous Figure 4-29). Looking more closely, the peak values

The PilotSTRATEGY project has received funding from the European Union's Horizon 2020 research and innovation programme under grant agreement No. 101022664

of overpressure in all cases are concentrated in a few cells above and below the injection point (see Figure 4-34 with the P10_Min case as an example). In 3D models, most of the maximum excess pressures appearing in Figure 4-33 are in a range closer to 1.5-2 MPa.

This overpressure was completely released in the reservoir at the end of simulation (after 1 year of simulation, 8 months post-injection) where the maximum value observed over the 9 cases was around 0.08 MPa (0.8 bar). This is clearly shown in Figure 4-35, which provides sections of the 2D maps of maximum overpressures in the reservoir from Figure 4-33, for all models and at different times. Sections are positioned just above the well location, to capture its peak value.

The overpressure in the storage formations therefore extend with relatively low values during injection, in comparison to the well pressures. If we look only at the top of Dalle Nacrée, at the end of injection, overpressure results have the same distribution but with even lower values (Figure 4-36). The maximum pressure value is 1.1 MPa, which is far from the 7 MPa at the injection point, and quite low compared to the maximum values distributed over the entire reservoir in Figure 4-33. This means that upon reaching the caprock layer, overpressures are significantly reduced, lowering the risk for caprock integrity.

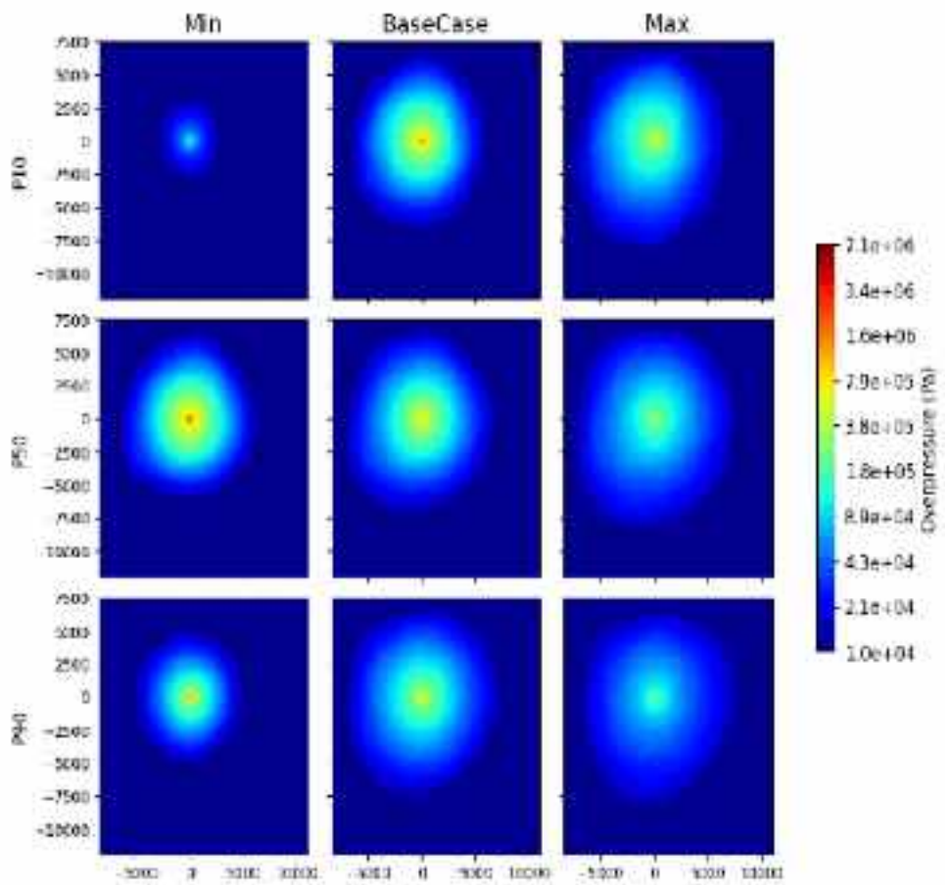


*Figure 4-33: Maximum vertical overpressure distribution at the end of the $CO_2$ injection in the reservoir, in all 9 models*

The PilotSTRATEGY project has received funding from the European Union's Horizon 2020 research and innovation programme under grant agreement No. 101022664

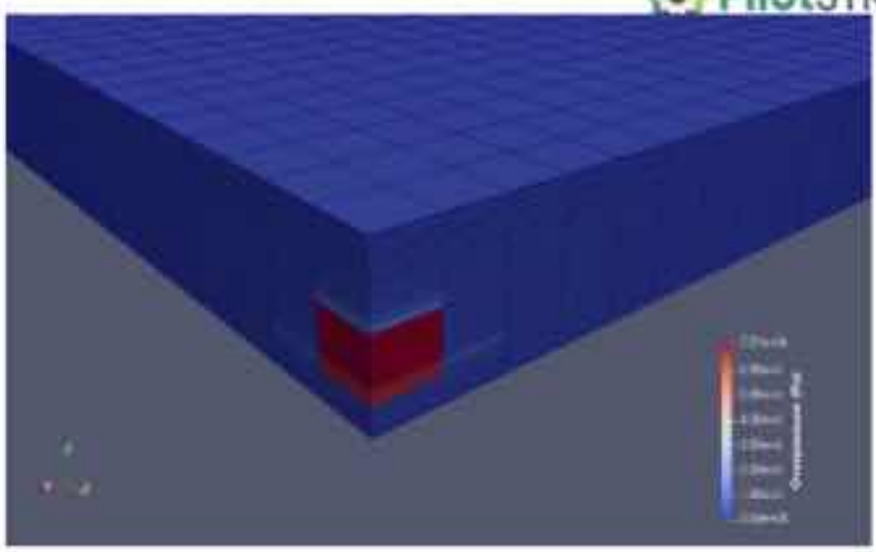

*Figure 4-34: Close-up of a section of the P10_Min model and its overpressure field at the injection point (only reservoir layers are displayed) at the end of injection (131 days)*

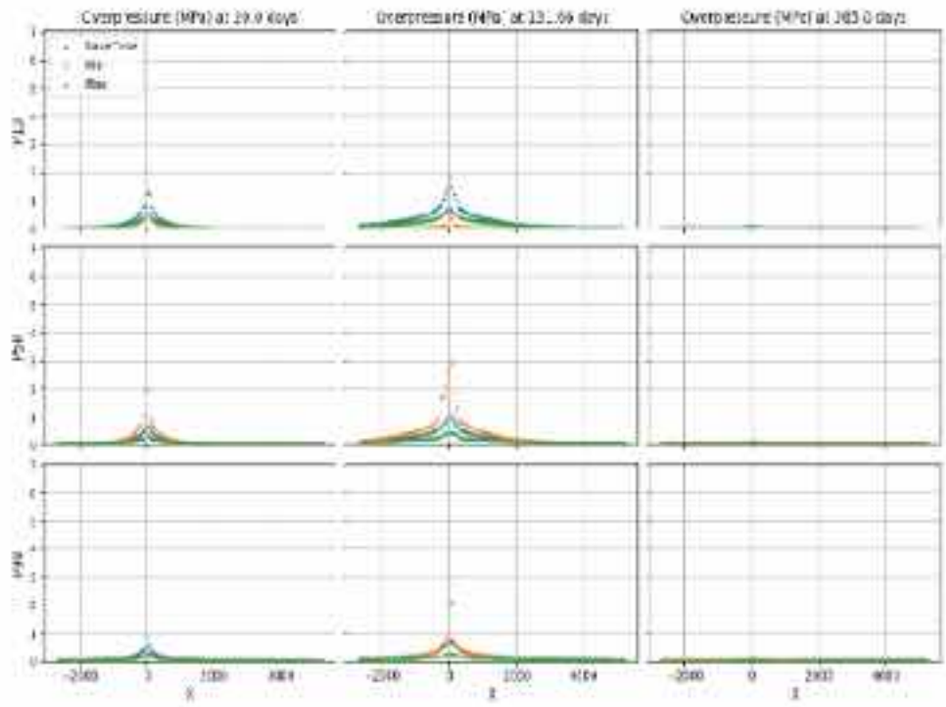

*Figure 4-35: Vertical maximum overpressure (MPa) profiles along a cross-section of all models, above well location, over the reservoir and at different times (start/end of injection, and after a year of simulation)*

Figure 4-38 completes these observations by showing the overpressure profiles on a cross-section of the models, still at the top of the reservoir and at different times. Unsurprisingly, the maximum value is around 1 MPa at the end of injection in the P50_BaseCase model, and all excess pressures disappear at the end of simulation (8 months after ending $CO_2$ injection).

In the caprock zone, maximum excess pressures occur at the bottom of the grid, and they do not exceed 0.6 MPa (or 6 bars) at the end of injection, as shown in Figure 4-39. All excess pressures of the nine cases drop down below 0.1 MPa at the end of simulation in the caprock. This level of overpressures remains very low, which means that the integrity of the caprock should not be greatly affected. This affirmation is reinforced by the analysis of the distances to the failure criterion in the

The PilotSTRATEGY project has received funding from the European Union's Horizon 2020 research and innovation programme under grant agreement No. 101022664

related section (following the displacement results). It should be noted that the peculiar aspect of the pressure distribution in Figure 4-39, is due to the heterogeneity of flow properties at the bottom of the caprock zone, in particular in the 'Min' cases with the lowest values of caprock permeability, and consequently with the highest permeability contrast between storage formation and caprock (see Figure 4-37).

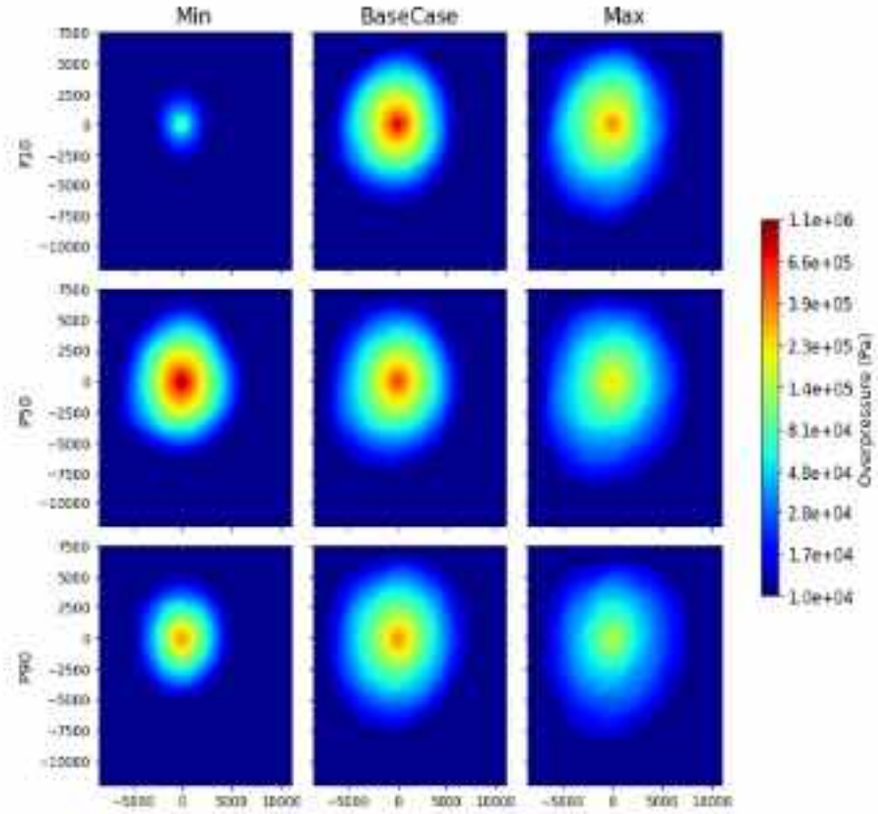


*Figure 4-36: Overpressure distribution at the end of the $CO_2$ injection at the top of reservoir, in all 9 models*

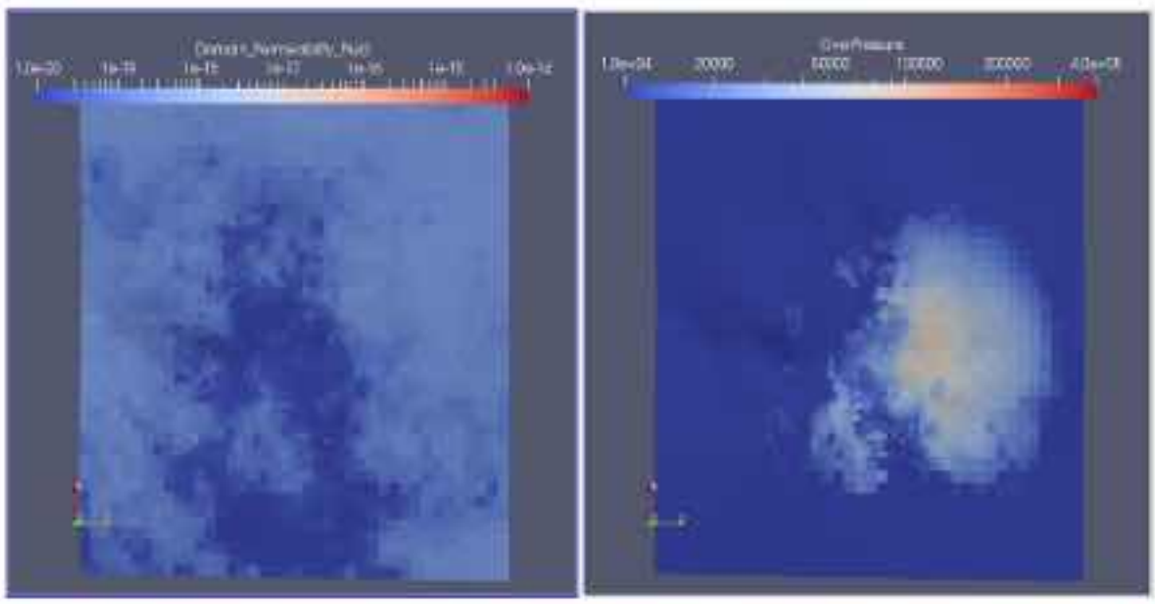

*Figure 4-37: Bottom caprock permeability field (left) and overpressure (Pa) in bottom caprock at the end of injection for the P50 'Min' model (View from the bottom). The overpressure propagates preferentially in the highest permeability zone of the caprock. Total model's size: 20 x 20 km.*

The PilotSTRATEGY project has received funding from the European Union's Horizon 2020 research and innovation programme under grant agreement No. 101022664

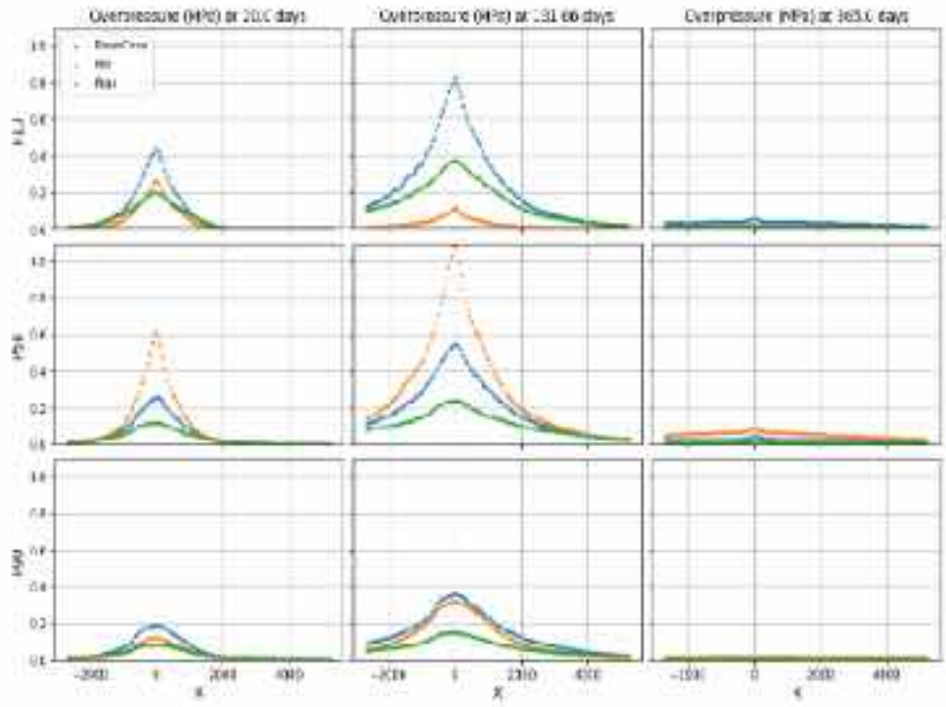


*Figure 4-38: Excess pressure (MPa) profiles along a cross-section of all models, above well location, at the top of reservoir and at different times (start/end of injection, and after a year of simulation)*

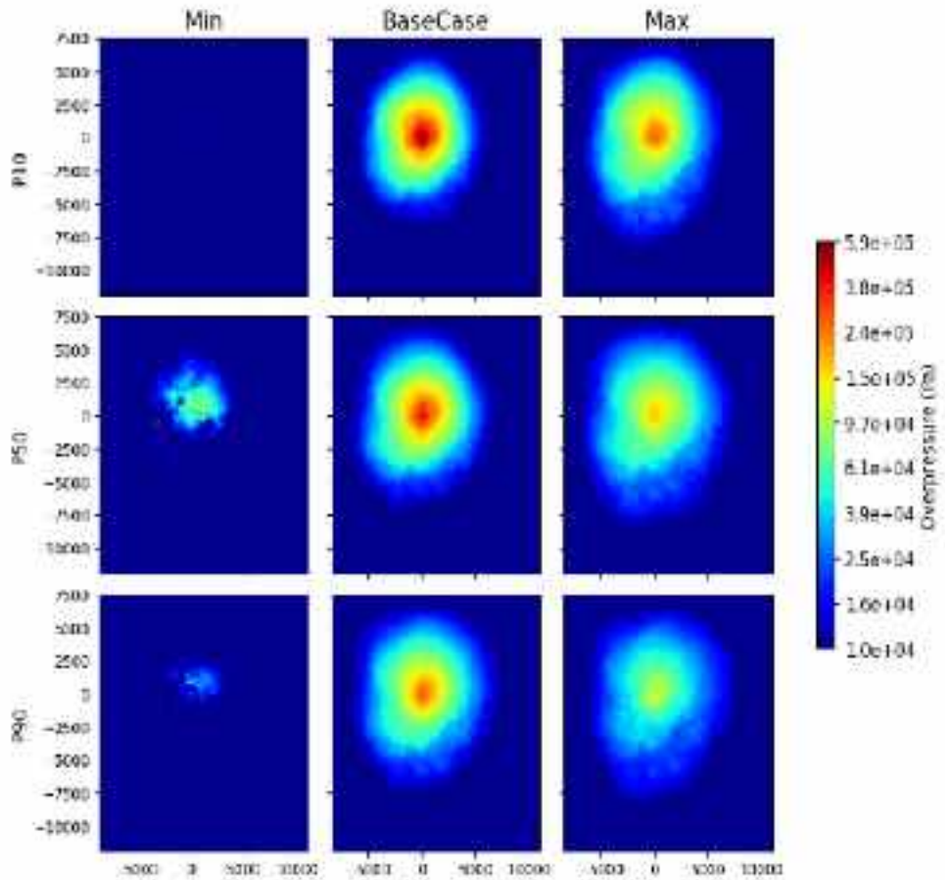


*Figure 4-39: Overpressure distribution at the end of the $CO_2$ injection at the bottom of caprock, in all 9 models*

The PilotSTRATEGY project has received funding from the European Union's Horizon 2020 research and innovation programme under grant agreement No. 101022664

*Displacement results*

In addition to the evolution of the resulting pressure field, the displacement field was also studied in the 9 simulated cases, especially the vertical displacements at the surface of the models and at the caprock-reservoir interface. Surface displacements provide insights into ground deformation, which can serve as an early warning for subsurface pressure buildup and associated risks to infrastructure. Displacements at the caprock-reservoir interface can give information about caprock integrity, highlighting potential damages.

What can be seen from the simulations in Figure 4-40 is that the vertical displacement at the surface remains very low, with a maximum value in the P50_Min and P10_Base cases of 0.8 mm, at the end of injection (131 days). The displacement in these cases drops down to 0.4 mm, 8 months after the end of injection. This figure shows the displacements of the surface nodes on a cross section along the X axis at a given Y position (12 475 m). This position is right above the well location to capture the maximum magnitudes of the displacements.

The nearly symmetrical shape of the curves indicates an almost radial distribution of the vertical displacements, centred on the well location. The propagation of overpressures shown before suggests that the distribution of the displacements follows the same trend, and that profile of the curves in Figure 4-40 and Figure 4-41 is quite the same in all cutting directions.

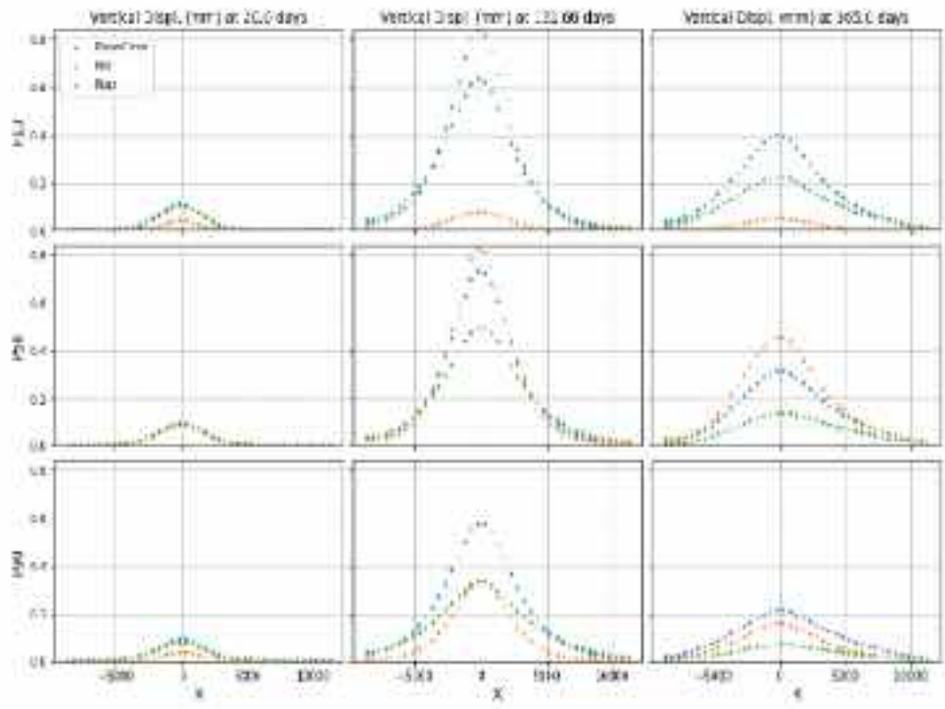

*Figure 4-40: Vertical displacement (in mm) at the surface of the models P10, P50, P90 for every cases (Min, Base, Max) along the X direction and above the well location, at different times*

The PilotSTRATEGY project has received funding from the European Union's Horizon 2020 research and innovation programme under grant agreement No. 101022664

The same observations can be made for the vertical displacements at the caprock-reservoir interface in Figure 4-41[5], where the magnitude of vertical displacements remains relatively low, with a maximum value of 1.75 mm for the P50_Min case at the end of injection. The maximum value then drops under 0.75 mm at the end of the simulation.

Tracking displacement velocities is one of the few possible monitoring methods, from the surface of the $CO_2$ injection site. Looking at the displacement velocity, averaged over 10 days at different times of injection, and for all models, it can be observed that the velocities are all within a range of -3 to 3 mm/year (Figure 4-42). The represented times in Figure 4-42 correspond to (from left to right): the first 10 days of injection ($t_f$ = 20 days), the last 10 days of injection ($t_f$ = 131 days), and the first 10 days after closing the well and ending the injection. Based on surface monitoring techniques such as InSAR (resolution ~1mm/year), all cases can be monitored at the beginning of the injection, and some until the well is closed. The post-injection phase is partially detectable over a short period of time but completely invisible in all 'Min' cases.

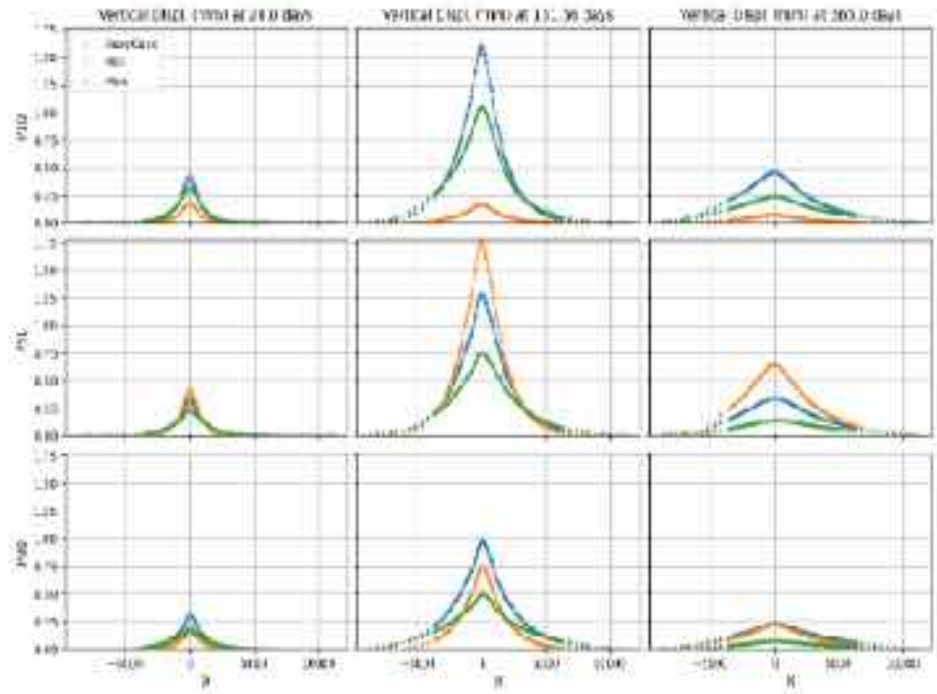

*Figure 4-41: Vertical displacement (in mm) at the caprock-reservoir interface of the models P10, P50, P90 for every cases (Min, Base, Max) along the X direction (above well location) at different times*

[5] The number of nodes plotted at the caprock-reservoir interface is higher than the number of nodes at the surface due to the mesh refinement. That explains also the finer representation of displacements at the caprock-reservoir interface for points with X positions between 5000 and 15000.

The PilotSTRATEGY project has received funding from the European Union's Horizon 2020 research and innovation programme under grant agreement No. 101022664

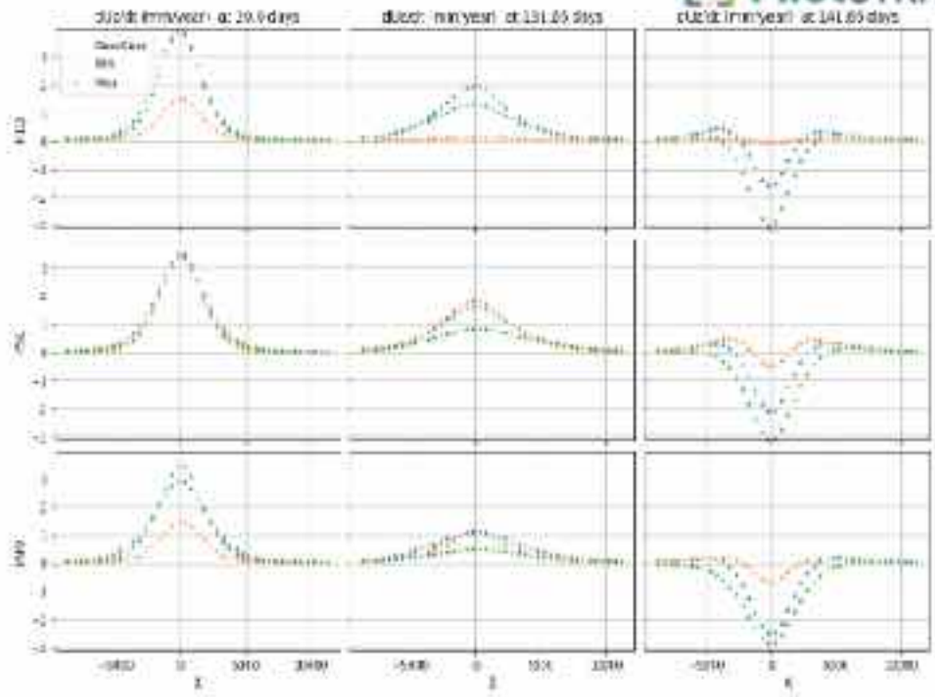

*Figure 4-42: Vertical velocity (evaluated over 10 days in mm/year) of the surface nodes of the models of a section in the X direction (above well location) and at different times (from 10 to 20 days, from 121 to 131 days, and from 131 to 141 days)*

### *Failure risk analysis*

Another important element in the analysis of caprock and reservoir integrity is the distance to the mechanical failure criterion. As described in deliverable 3.3 (section 7.1.3.4), a failure criterion (inner Drücker-Prager) was chosen, with parameters (cohesion, friction) varying as a function of porosity and formation type. The parameter that is looked at in this integrity study is the distance of the stress state of each grid cell from its own Drücker-Prager failure criterion. The methodology used to assess the distance to the criterion is described in deliverable 3.3.

A first look at the distances evaluated over the reservoir shows that, prior to injection, the initial stress states of each cell are far from the failure criterion. Just like the overpressure distribution in Figure 4-33, Figure 4-43 represents the minimum ortho-distance that was evaluated vertically for each column of the 3D grid, over the entire reservoir formation. The minimum values obtained are in majority close to 30 MPa, and the lower limit is 25 MPa, which is still a high value and a large distance to the failure criterion. In the caprock formation, all cells have an ortho-distance between 12 and 19 MPa, the lower values being in the upper layers of the concerned rock zone, subjected to lesser values of excess pressures driven by the injection. This range of values is still quite high, meaning that the caprock cells are quite far from the failure point.

The PilotSTRATEGY project has received funding from the European Union's Horizon 2020 research and innovation programme under grant agreement No. 101022664

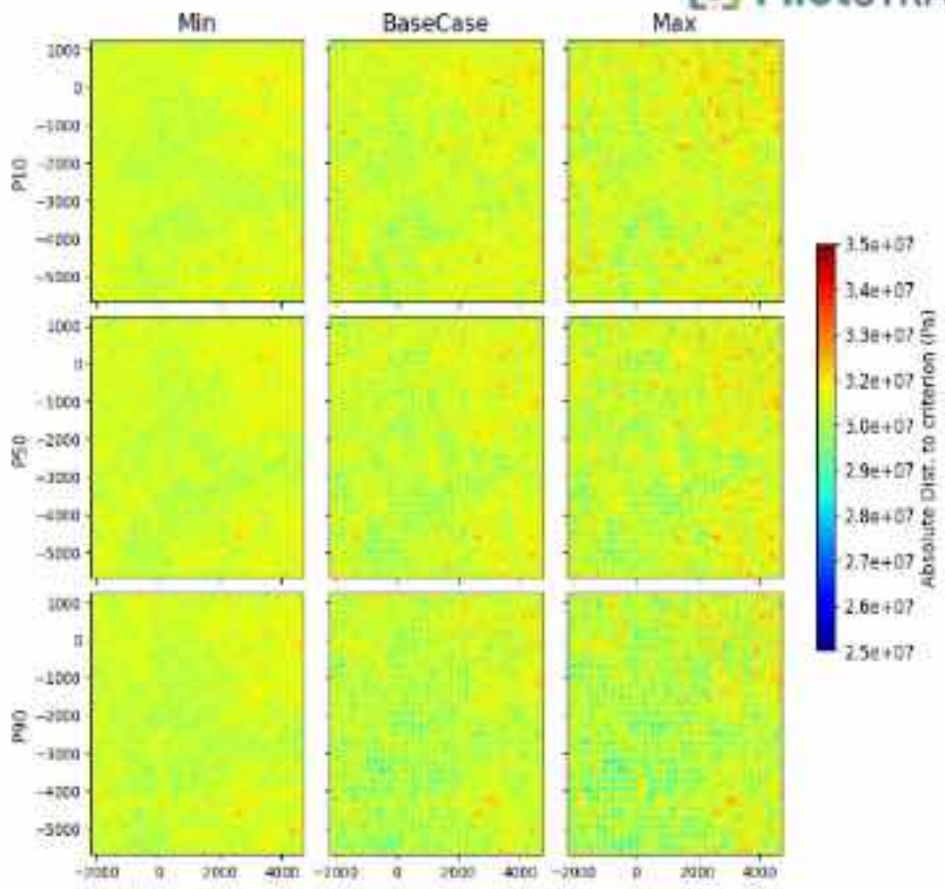


*Figure 4-43: Minimum vertical ortho-distances from the failure criterion evaluated in the reservoir, at initial state (prior to injection) and for all 9 models*

The same kind of representation is quite difficult to obtain for the caprock, due to the grid refinement that adds complexity to the structure and arrangement of the cells. They are no longer all aligned in simple columns from the top to the bottom of the caprock formation, unlike in the reservoir. This is why, another representation of the stress state of the cells over the reservoir and caprock was used in Figure 4-44.

In Figure 4-44, all cells of the grid are represented, for all models, in their stress state at the end of injection, in a normalised (P, Q) plane. Points from caprock and reservoir are in red and blue respectively. Usually, the stress state of an element is represented in the (p', q) plane, where p' is the mean stress and q is the deviatoric stress of the element. Here, as each stress state is to be compared with a different failure criterion, since it varies with cell data (porosity, rock type), it was found more relevant to normalise the representation following the description of Figure 4-45. This normalisation allows all elements to be represented with respect to a single criterion in the same plane.

From Figure 4-44, even at the end of injection, all cells from reservoir and caprock are still far from the failure criterion, so no matter what type of distance is used as a parameter here, the risk of damaging the caprock or reservoir is really low in these simulations. The P90 models are the ones in which stress states of some elements are closer to the criterion, but when looking at Figure 4-46, the variations of mean stress p' and deviatoric stress q during injection in these models are lower than in P10 and P50 corresponding cases.

The PilotSTRATEGY project has received funding from the European Union's Horizon 2020 research and innovation programme under grant agreement No. 101022664

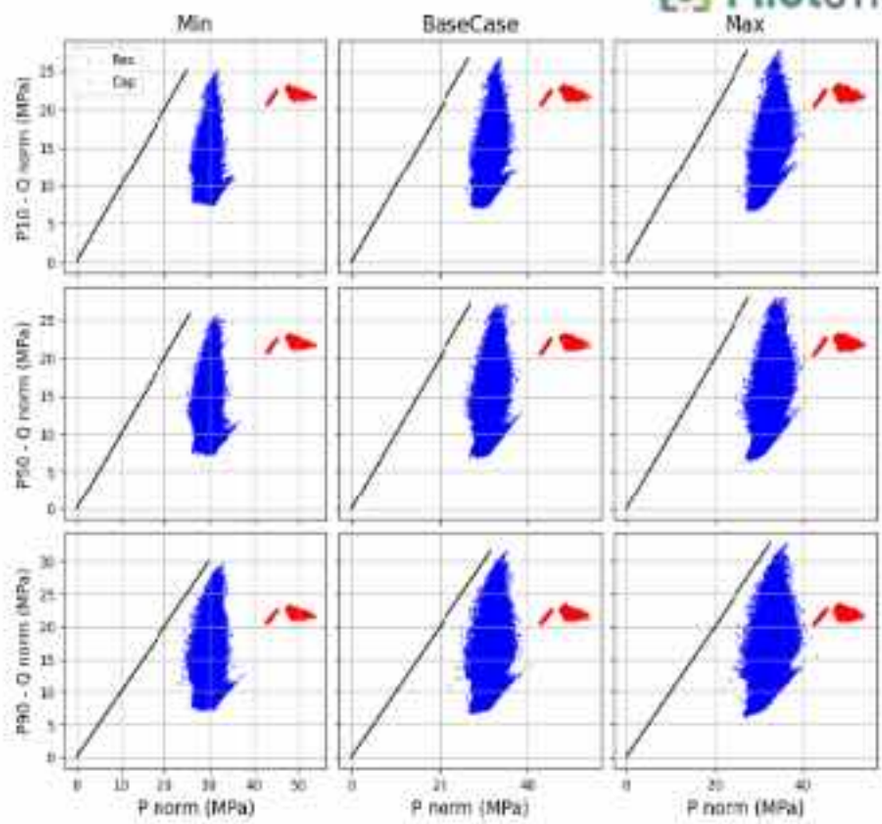


*Figure 4-44: Normalised stress state in (P,Q) plane of cells in caprock (red) and reservoir (blue) with normalised failure criterion (cells from refined LGR only)*

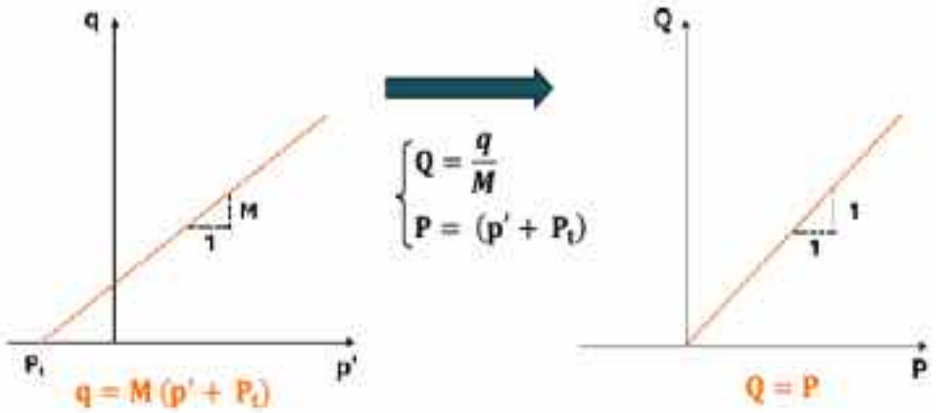


*Figure 4-45: Inner Drücker-Prager criterion in (p',q) plane and in normalised (P,Q) plane*

Figure 4-46 shows the variations of p' and q for all cells in reservoir and caprock at the end of injection for all models. Variations are calculated with respect to the initial state. It appears that, at the end of injection, these variations are limited to values in the range [-0.45;0.45] MPa for p' and to [-5;0] MPa for q, in the reservoir. The maximum changes in stresses occur in the Min cases of the models, while almost no stress changes are seen in the Max cases., this can be related to the magnitude of overpressure in each case. The stress changes of the elements in the caprock are even lower, with less than 1 MPa variation for the deviatoric stress q, and less than 0.1 MPa absolute variation for p'. Compared with the initial distances to the criterion of around 25 to 35 MPa in the reservoir, these

The PilotSTRATEGY project has received funding from the European Union's Horizon 2020 research and innovation programme under grant agreement No. 101022664

variations confirm that the storage integrity (incl. caprock) is well preserved and far from being at risk in this context.

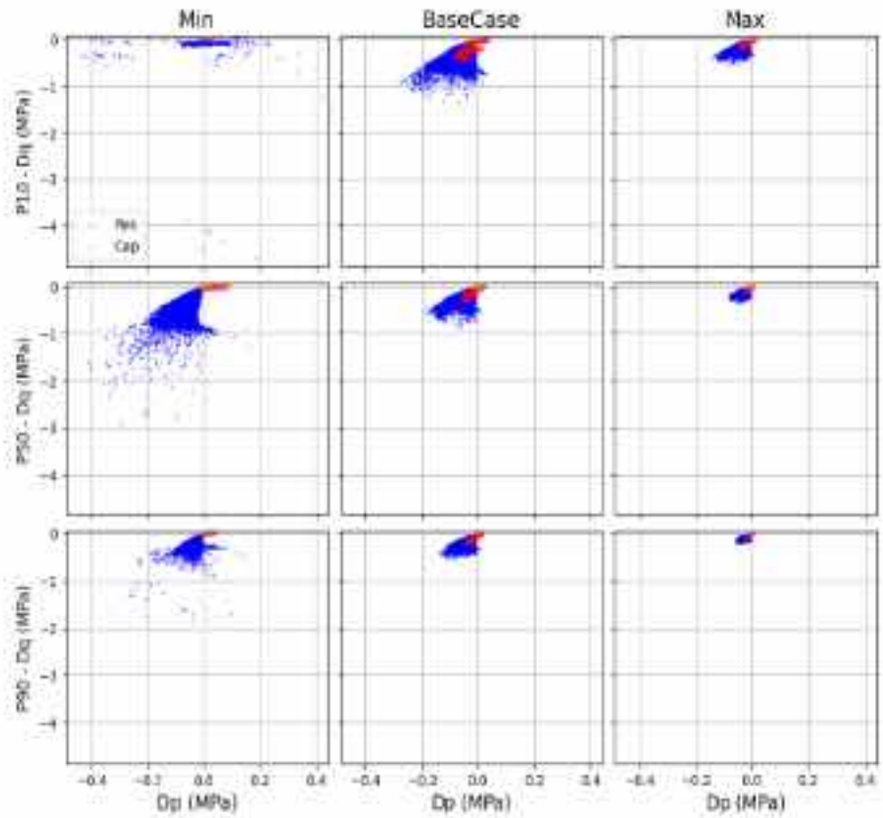


*Figure 4-46: Variations (from initial state) of stresses (p' and q) of cells in caprock (red) and reservoir (blue) at 131 days, the end of injection (cells from refined LGR only)*

*Conclusion*

The geomechanical study of the P10, P50, and P90 models indicates that $CO_2$ injection up to 100 kt over four months is achievable in most scenarios without exceeding critical Bottom-Hole Pressure (BHP) limits, except in the P10-Min and P90-Min cases, where low permeability restricts injectivity. Overpressure levels are highest near the injection point (7 MPa in P10-Min) but significantly dissipate at the caprock level (≤ 0.6 MPa), ensuring caprock integrity. Vertical surface displacements remain minor, peaking at 0.8 mm, and caprock-reservoir interface displacements do not exceed 1.75 mm. Stress states in both caprock and reservoir remain far from failure criteria, with minimal stress variations during injection. These results confirm that $CO_2$ injection under the studied conditions is mechanically safe and does not threaten storage integrity.

### 4.4.3 Enlarged uncertainties analysis on P50 model

For this analysis, the uncertainties have been extended to additional geomechanical parameters compared to previous one (see deliverable D3.3 (Alavoine et al., 2024)) and some uncertainties ranges have been shifted (e.g. K/Phi relationship) in regards with new information coming from SEIF-1 data analyses (BRGM, personal communication, see also D3.4, Ben Rhouma et al., 2026). We consider 12 uncertain parameters which may specifically affect gas migration and/or pressure and displacement results (Table 4-12). We performed a Latin Hypercube Sampling (LHS) of those uncertain parameters to build a Design Of numerical Experiments (DOE) of 175 simulations (Figure 7-2).

The PilotSTRATEGY project has received funding from the European Union's Horizon 2020 research and innovation programme under grant agreement No. 101022664

*Table 4-12: Range of values for uncertain parameters in the DOE*

| Variables | Minimum | Maximum |
|---|---|---|
| K/Phi exponent factor in high porosity facies of the Oolithe Blanche (log10 scale) [-] | 0. | 0.6 |
| Comblanchien anisotropy (log10 scale) [-] | -0.52 | 0.48 |
| Callov-Oxfordian permeability multiplier factor (log10 scale) [-] | -2.3 | 0. |
| Residual gas saturation in high porosity facies of the Oolithe Blanche [-] | 0.05 | 0.3 |
| Kr model exponent in high porosity facies of the Oolithe Blanche [-] | 0.4 | 0.7 |
| Bulk modulus parameter for carbonates [GPa] | 3.8 | 7.5 |
| Shear modulus parameter for carbonates [GPa] | 2.9 | 5. |
| Vp (compressional wave velocity) in shale [m/s] | 3000 | 4500 |
| nu (poisson coefficient) in shale [-] | 0.15 | 0.3 |
| Stress ratio SH/Sv [-] | 0.9 | 1.1 |
| Stress ratio Sh/Sv in shale [-] | 0.75 | 0.85 |
| Stress ratio Sh/Sv in carbonates [-] | 0.55 | 0.65 |

After assessing a low difference between iterative and one-way results, for this case, with a proper estimation of pore compressibility for the flow simulation (see Figure 7-1 in appendix 7.1), only a one-way hydromechanical calculation is performed for this uncertainties study. This leads to a possible negligible pressure overestimation (conservative choice) but allows to save a significant computational time for the 175 hydromechanical models of the design of experiments. For computational cost's reasons and because this DOE covers a large range of possibilities, the following analysis is performed solely on the P50 model.

For the uncertainty and sensitivity analyses, the same methodology as presented in D3.3 is used (calculation of Sobol indices and use of Gaussian Process as metamodel for large sampling). Distances to failure criterion are calculated using the same methodology as previously.

In the following results, the timeline was shifted to start at the injection beginning (e.g. 10 days now means 10 days of injection).

#### 4.4.3.1 *Statistics and sensitivity to uncertain parameters for the well pressure results for the 175 simulations*

With the shift in the range of the porosity/permeability relationship factor to higher values for permeability, the trend in the increase in pressure at the well is even lower than in previous results in D3.3 (uncertainty analysis, section 3.3) and pressure results remain far below the maximum allowed bottom-hole pressure (24.7 MPa). This allows to inject the targeted amount of $CO_2$ (100 kt) in 4 months for all simulations of the P50 model (Figure 4-47). The main parameters influencing the well pressure results are still porosity/permeability relationship factor and parameters related to relative permeability curves (residual gas saturation and factor exponent for the curves) (Figure 4-48).

The PilotSTRATEGY project has received funding from the European Union's Horizon 2020 research and innovation programme under grant agreement No. 101022664

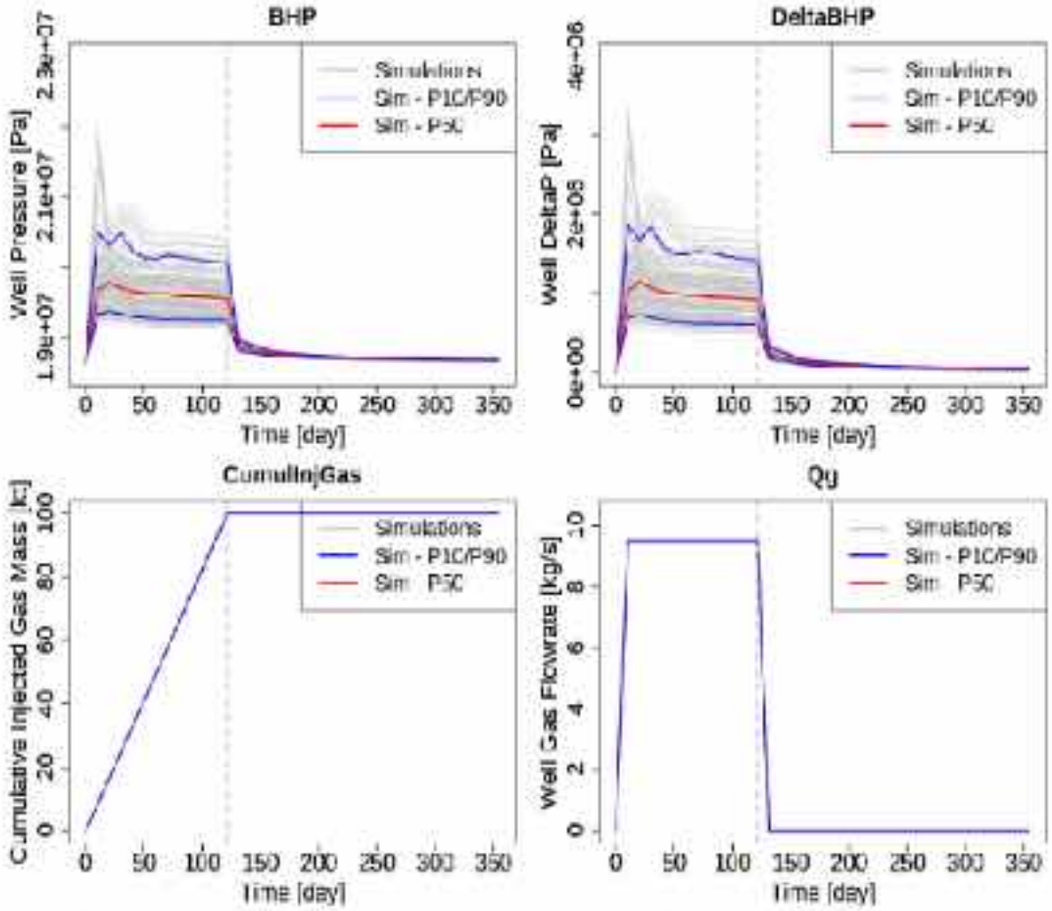


*Figure 4-47: Well results for the 175 realizations with Bottom-Hole Pressure (BHP) (top, left); increase in pressure (relative to the initial state) for the BHP (top, right), cumulative injected gas mass (bottom, left), gas flowrate (bottom, right) function of time, with in grey all the realizations, in red the median results and in blue p10 and p90 percentiles for all realizations.*

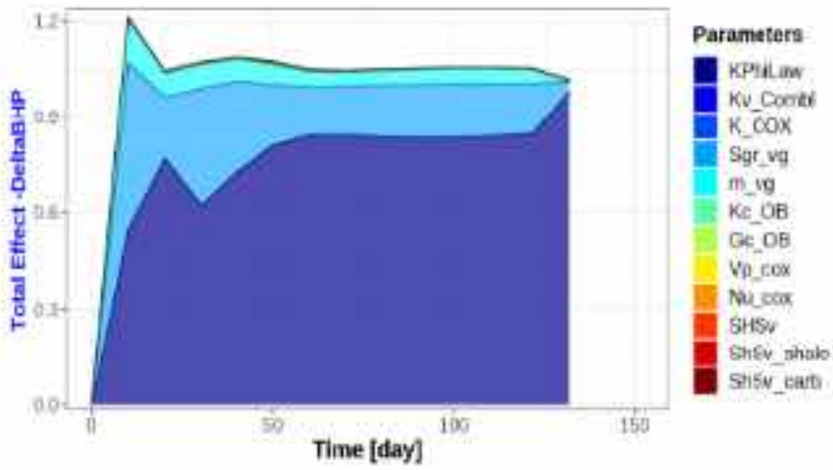


*Figure 4-48: Total effect – Sobol indices for the variation in BHP with time until the end of injection*

### 4.4.3.2 *Statistics and sensitivity to uncertain parameters for the gas saturation migration for the 175 simulations*

According to the first analysis of the flow simulation results (see previous sections and D3.3), $CO_2$ gas (supercritical) remains in the Oolithe Blanche formation, where it is injected, during the injection and up to 8 months after the injection. Therefore, the gas saturation analysis, and its extent will focus on

The PilotSTRATEGY project has received funding from the European Union's Horizon 2020 research and innovation programme under grant agreement No. 101022664

the Oolithe Blanche formation. To study the lateral extent of the gas saturation, we will select per time step the maximum extent of $CO_2$ over the vertical.

Based on maximum results from the ensemble of realizations (Figure 4-49) representing the maximum area that could be impacted considering all uncertainties (i.e. at least one realization reached one element of the area), the extent of the $CO_2$ plume remains below 500 m from the well at the end of injection and 8 months post-injection. According to the Figure 4-50, one should expect at maximum a $CO_2$ plume extent of 350 m from the injection well for the considered uncertainties.

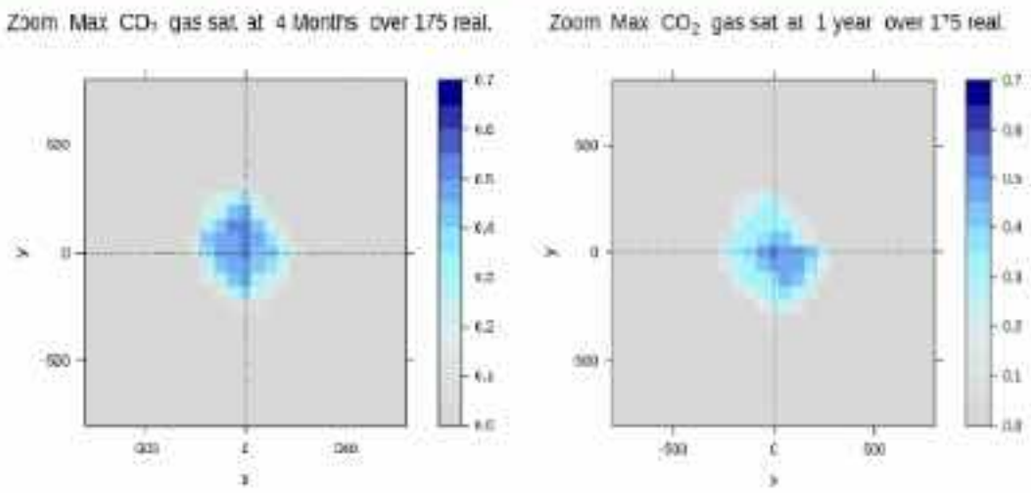


*Figure 4-49: Zoom in the studied area around the injection well. Gas saturation maps at 4 months and 8 months post-injection for the maximum results at each cell from the ensemble of 175 realizations. Coordinates [meters] are relative to the injection well position (0,0).*

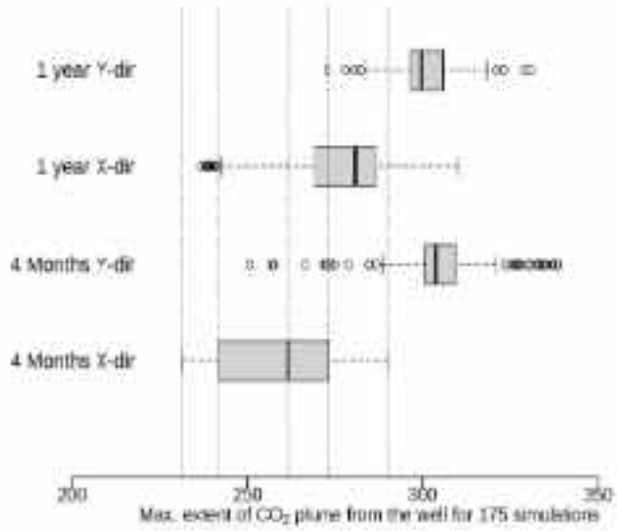


*Figure 4-50: Boxplots of the maximum extent of $CO_2$ plume (in meter) from the well for the ensemble of 175 realizations in X- and Y-directions at the end of injection (4 months) and 8 months post-injection (1 year). The boxplots represent the values distribution with the grey box for p25 to p75, the black line for the p50 value, extremities to dot-lines represent the min-max values except if some values are more than 1.5 times distant to p50 than the p25-to-p75 distance.*

To compute average, variance and percentiles results for the gas saturation maps, we used a random sampling of 20000 on metamodels built on the basis of the 175 realizations (Q2 above 0.9 for 4 months, and above 0.85 for 1 year, except for one value around 0.75). For these metamodels, parameters related to initial stress state are excluded since they are not considered for the flow part

The PilotSTRATEGY project has received funding from the European Union's Horizon 2020 research and innovation programme under grant agreement No. 101022664

of the simulations. Metamodels are thus built with 9 variables (the nine remaining uncertain parameters).

According to Figure 4-51, Figure 4-52 and Figure 4-53 one can notice a gas trend migration slightly toward the NW during the injection, and slightly toward the SE after the injection stopped. Both locations are also the ones with the highest uncertainties, with the highest variance values.

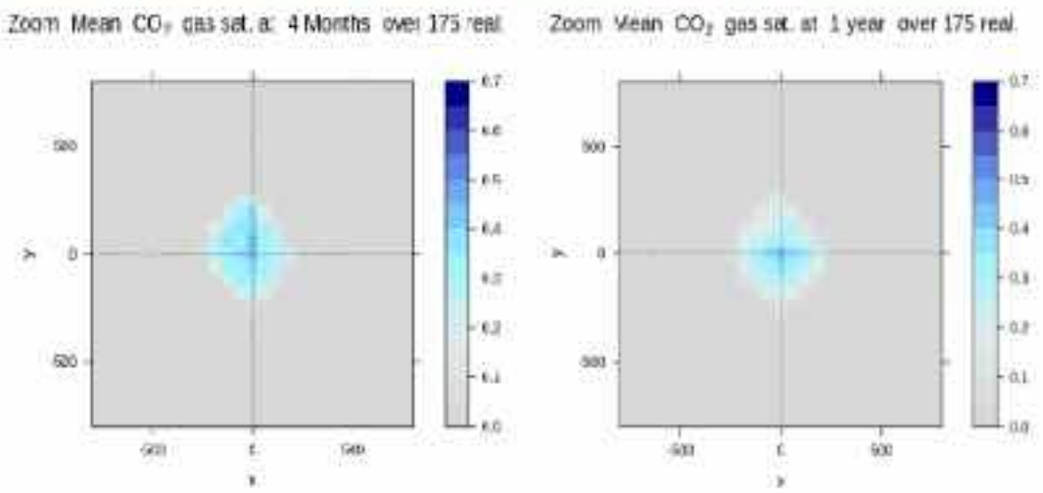


*Figure 4-51: Zoom in the studied area around the injection well. Mean estimates of gas saturation maps at 4 months and 8 months post-injection (based on metamodeling). Coordinates (meters) are relative to the injection well position (0,0).*

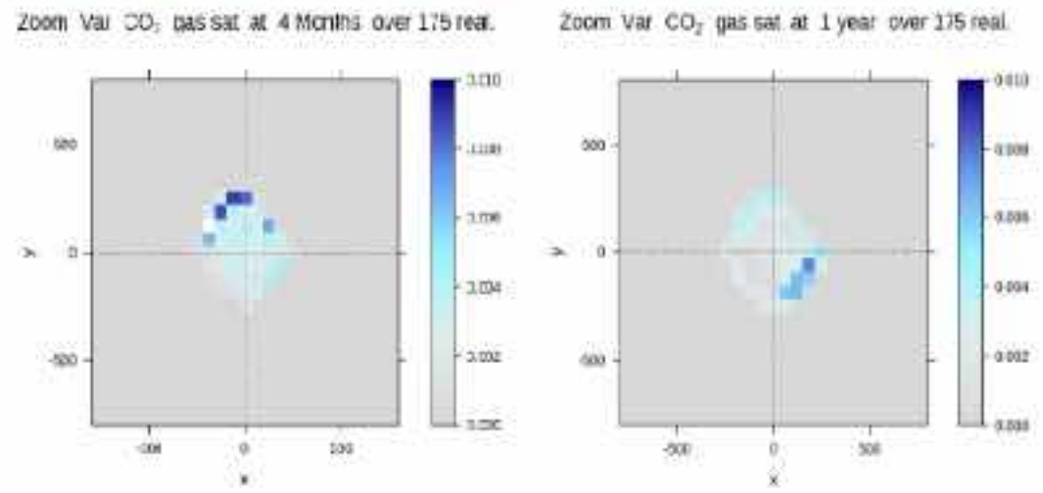


*Figure 4-52: Zoom in the studied area around the injection well. Variance estimates of gas saturation maps at 4 months and 8 months post-injection (based on metamodeling). Coordinates (meters) are relative to the injection well position (0,0).*

The PilotSTRATEGY project has received funding from the European Union's Horizon 2020 research and innovation programme under grant agreement No. 101022664

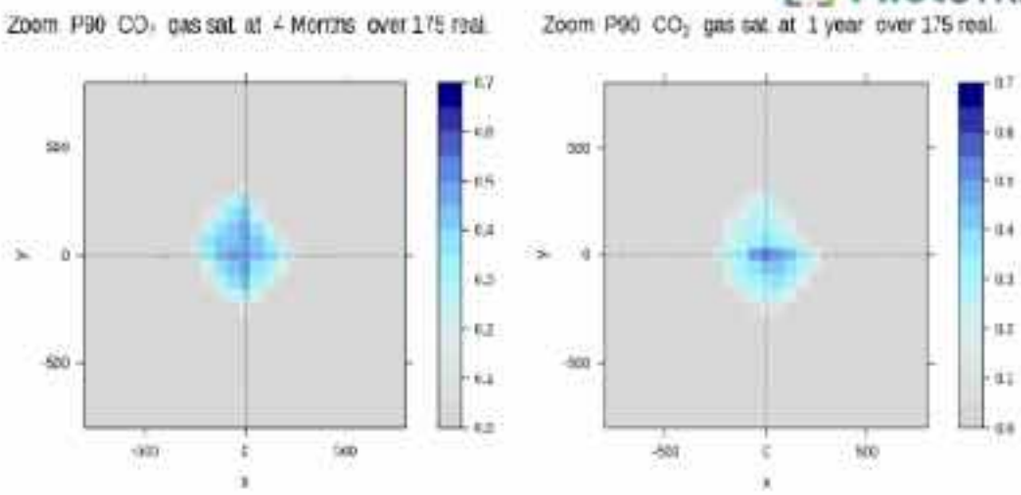


*Figure 4-53: Zoom in the studied area around the injection well. Percentile 90 estimates of gas saturation maps at 4 months and 8 months post-injection (based on metamodeling). Coordinates (meters) are relative to the injection well position (0,0).*

The most influencing parameters of the gas migration are the permeability and permeability curves parameters (Figure 4-54). Interactions between parameters increase post-injection. The cumulative influence of both relative permeability parameters tends to be predominant over the field permeability.

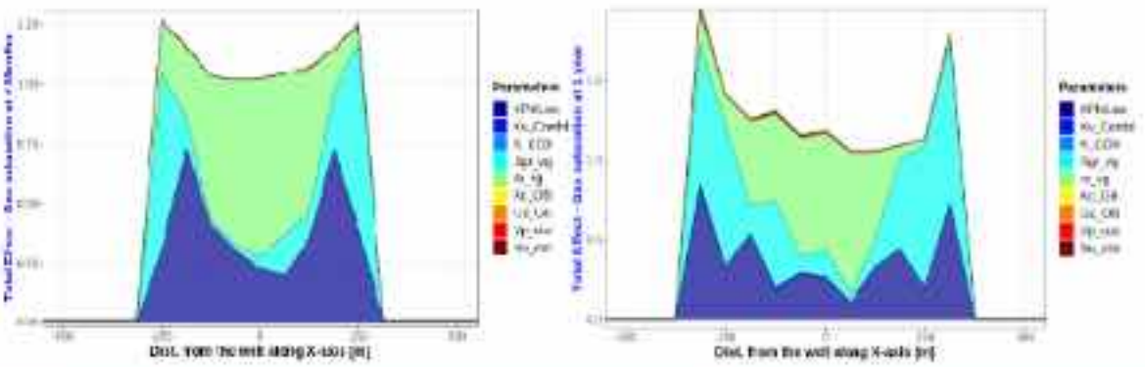

*Figure 4-54: Total effect – Sobol indices for the gas saturation along the X axis (y=0, at the well position) at the end of injection (left) and 8 months post-injection (right).*

Note: For the $CO_2$ dissolution, the uncertainty and sensitivity analyses gave the same trend as in D3.3. The average amount of dissolved $CO_2$ is slightly lower because of the change in permeability ranges (pressure effect).

#### *4.4.3.3 Statistics and sensitivity to uncertain parameters for the overpressure for the 175 simulations*

The maximum overpressure results obtained for the 175 simulations in the storage formations are relevant with results in previous sections, with the significant values of maximum overpressure concentrated around the injection well (Figure 4-55). To recall, the maximum overpressure for each simulation is calculated by the maximum overpressure value over the vertical axis, reducing dimensions from 3 to 2, in the studied formations. After 10 days of injection, some cases exceeded 3 MPa of max. overpressure in the vicinity of the well, and most of overpressure is at max. 1 km from the well (i.e. above 0.1 MPa). At the end of injection, the peak of overpressure has been accommodated and is around 1.6 MPa at maximum. The overpressure has propagated with the injection and is at max. 3 km from the well (for values above 0.1 MPa). Eight months after the well

The PilotSTRATEGY project has received funding from the European Union's Horizon 2020 research and innovation programme under grant agreement No. 101022664

shutting, the overpressure is negligible for all simulations: below 0.1 MPa everywhere.

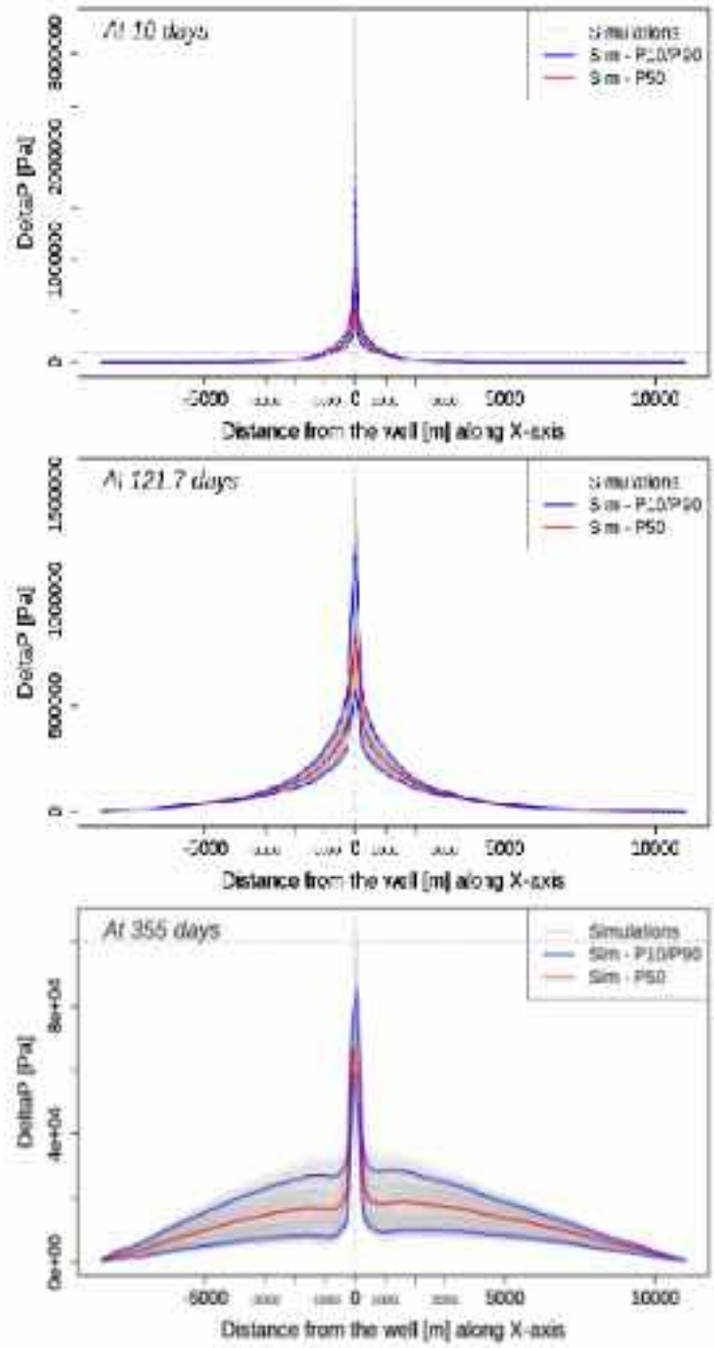


*Figure 4-55: Maximum overpressure in the storage formations, at different time periods, along a X-axis cross-section (y=0, at the well position) with in grey all the 175 simulations, in red the median results and in blue p10 and p90 percentiles for all simulations.*

The sensitivity analysis on the maximum overpressure (Figure 4-56) indicates that permeability and relative permeability parameters are the ones that contribute the most to the overpressure's results variability (i.e. contribution is defined as significant in the area where the overpressure is superior to 0.1 MPa).

The PilotSTRATEGY project has received funding from the European Union's Horizon 2020 research and innovation programme under grant agreement No. 101022664

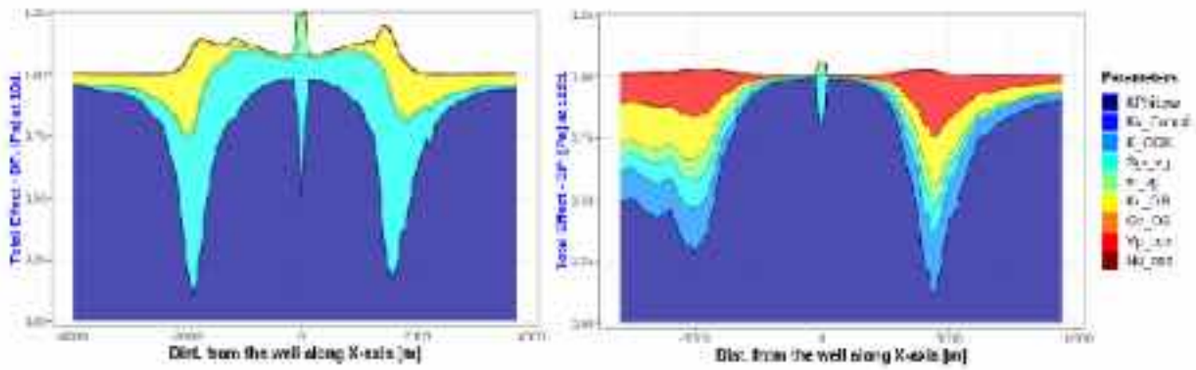


*Figure 4-56: Total effect – Sobol indices for the maximum overpressure in storage formations along the X-axis (y=0, at the well position), 10 days after the injection started (left), and at the end of injection (right).*

As previously, the level of overpressure in the caprock remains low, with a maximum of overpressure around 0.4 MPa in the bottom caprock at the end of injection (Figure 4-57). The discontinuous aspect of the caprock's overpressure is related to the caprock heterogeneities which drive the pressure propagation from the storage formations to the caprock as described previously in Figure 4-37. After the injection ceases, the pressure releases follow the same trend as in the storage formations with an overpressure below 0.07 MPa after 8 months of injection.

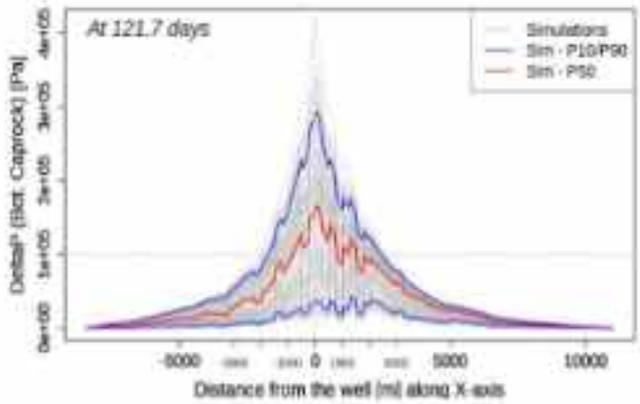


*Figure 4-57: Maximum overpressure in the caprock at the end of injection, along a X-axis cross-section (y=0, at the well position) with in grey all the 175 simulations, in red the median results and in blue p10 and p90 percentiles for all simulations.*

The PilotSTRATEGY project has received funding from the European Union's Horizon 2020 research and innovation programme under grant agreement No. 101022664

#### 4.4.3.4 *Statistics and sensitivity to uncertain parameters for the surface Z-displacement for the 175 simulations*

Both surface velocity of displacement and cumulative displacements are treated here. The velocity gives a hint about the expected velocity of displacement and thus the ability to measure the displacement with the surface monitoring tool while the cumulative displacement gives the order of magnitude of the total surface movement.

Velocity results depend on the studied period size (average value over the considered period). For a periods of 10 days, at the very beginning of the injection, the velocity above the injection well ranges between 2 mm/yr and 5 mm/yr (Figure 4-58) in function of uncertain parameters values. This is above the detection threshold for most monitoring tools (e.g. 1 mm/yr for InSAR). High velocities (negative values) are also recorded, between 2 mm/yr and 4 mm/yr, while shutting the well (again period of 10 days) when subsidence occurs when stopping the injection. These results are consistent with periods of the largest change in pressure regime. Notice that, at the end of the post-injection period, surface displacements are below the InSAR threshold value.

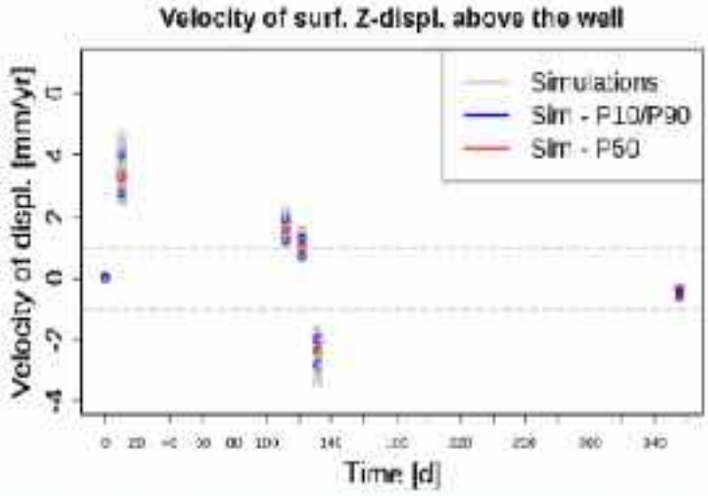


*Figure 4-58: Velocity of surface, Z-displ. [mm/yr] at the well position from the DOE, function of time, with in grey all the 175 realizations, in red the median results and in blue p10 and p90 percentiles for all realizations. The vertical dotted line figures the end of injection (time is relative to the start of injection).*

In Figure 4-59, cumulative displacement results above the well reach a maximum at the end of the injection, with an uncertainty range between 0.4 mm to 0.7 mm. At the end of the post-injection period, with the pressure release inducing subsidence, the surface uplift decreased to a value of 0.3 to 0.1 mm, depending on the subsurface properties.

The PilotSTRATEGY project has received funding from the European Union's Horizon 2020 research and innovation programme under grant agreement No. 101022664

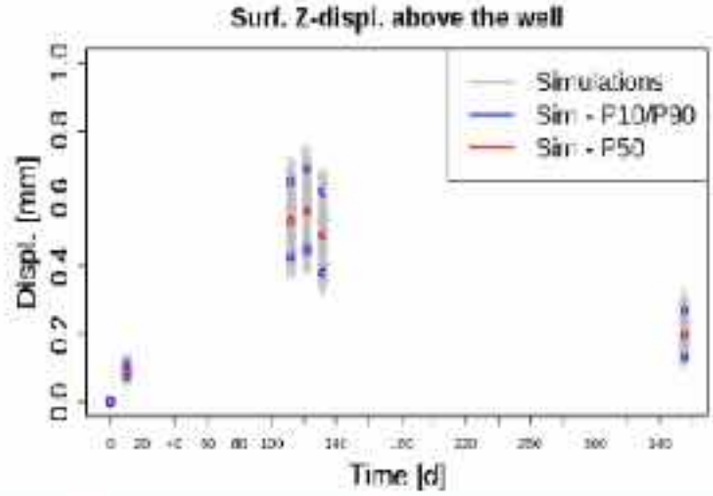


*Figure 4-59: Cumulative surface. Z-displacement. [mm] at the well position from the DOE, function of time, with in grey all the 175 realizations, in red the median results and in blue p10 and p90 percentiles for all realizations. The vertical dotted line figures the end of injection (time is relative to the start of injection).*

In the following analysis, we will treat cumulative displacement at the end of the injection period (122 days, i.e. 4 months of injection) and the end of the post-injection period (355 days after the injection begins), while the velocity will be studied at the beginning of the injection (10 days of injection) and just after stopping the injection (10 days after the injection stops, i.e. 132 days after the injection begins).

The maximum velocity and related maximum cumulative displacements are above the well as shown in Figure 4-60, Figure 4-61, Figure 4-62 and Figure 4-63. For the considered injection period (4 months), the cumulative displacements remain low (<1 mm) and will not impact the surface installation (Figure 4-62). Nevertheless, the velocity is sufficient for measuring and monitoring the displacement in the injection well area (Figure 4-60, Figure 4-61).

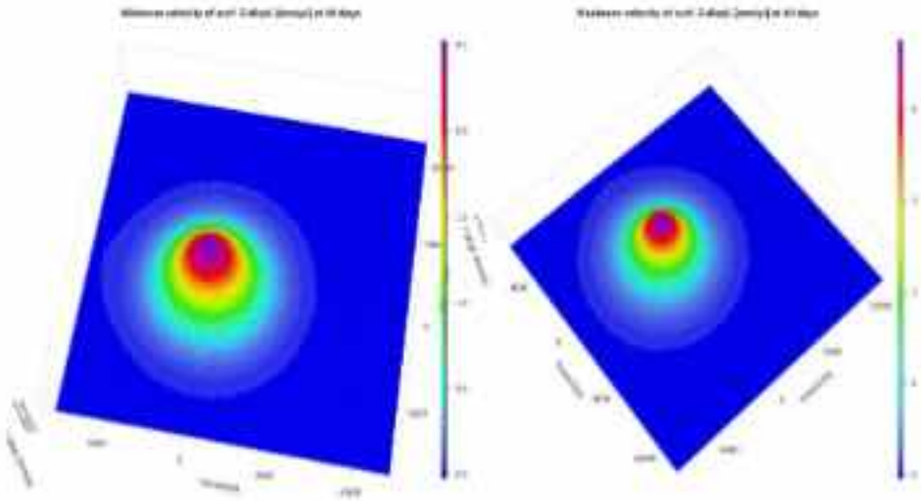

*Figure 4-60: Minimum and maximum velocity of surface displacement [mm/yr] at the beginning of the injection period (10 days after injection started) based on 175 simulations results. Coordinates [meters] are relative to the injection well position (0,0).*

The PilotSTRATEGY project has received funding from the European Union's Horizon 2020 research and innovation programme under grant agreement No. 101022664

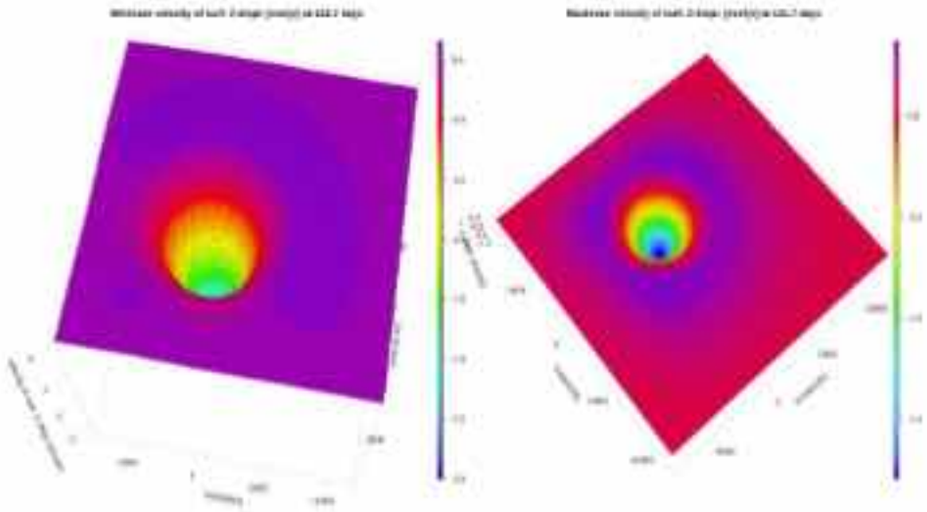

*Figure 4-61: Minimum and maximum velocity of surface displacement [mm/yr] 10 days after stopping the injection based on 175 simulations results. Notice that for this period, velocity has negative values due to the subsidence while relaxing the pressure. Coordinates [meters] are relative to the injection well position (0,0).*

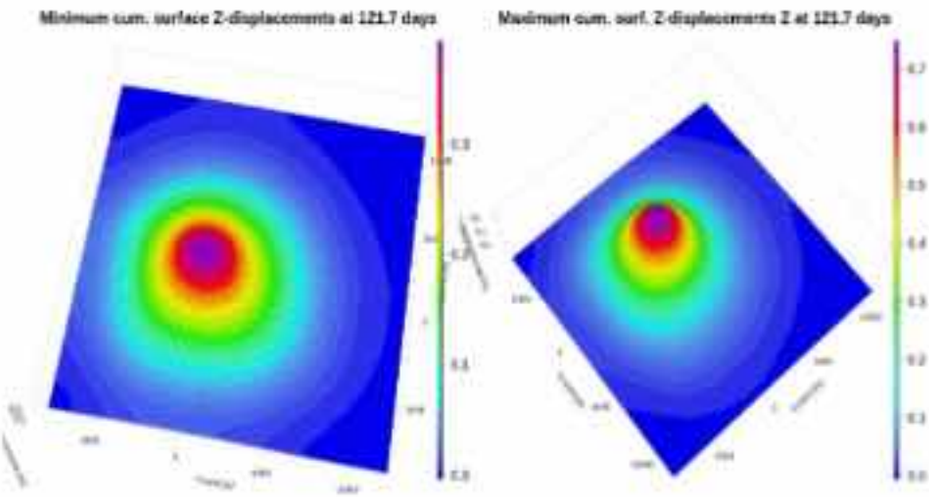


*Figure 4-62: Minimum and maximum cumulative surface displacement [mm] at the end of the injection period based on 175 simulations results. Coordinates [meters] are relative to the injection well position (0,0).*

The PilotSTRATEGY project has received funding from the European Union's Horizon 2020 research and innovation programme under grant agreement No. 101022664

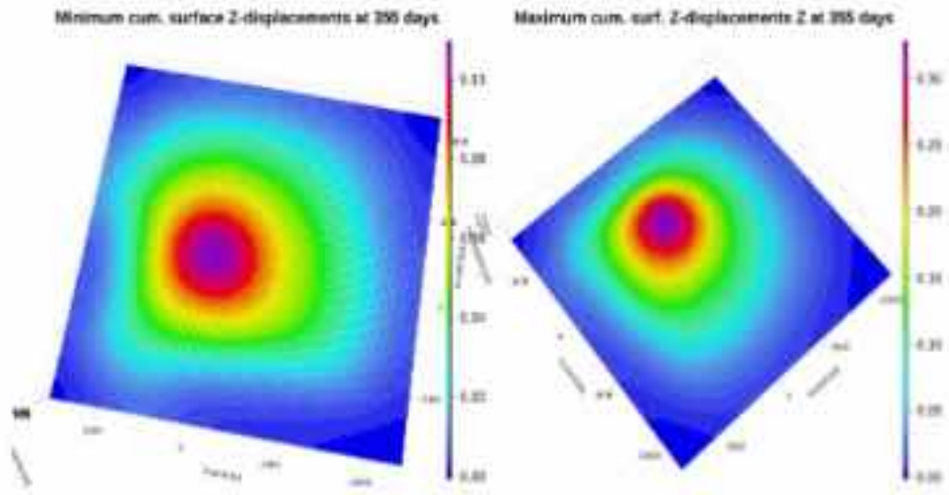


*Figure 4-63: Minimum and maximum cumulative surface displacement (mm) at the end of the simulations (8 months post-injection) based on 175 simulations results. Coordinates (meters) are relative to the injection well position (0,0).*

Indeed, according to Figure 4-64, velocity of displacement will be measurable at maximum about 2.7 km from the well. Differences between P10 and P90 results are measurable in the vicinity of the injection well (differences larger than 1 mm/yr), but standard deviation results remain below the measurable threshold. This is probably limiting for model calibration based on surface monitoring. As for gas saturation, we used a random sampling of 20000 on metamodels built on the basis of the 175 realizations (Q2 above 0.9 for both periods) to obtain these statistical results.

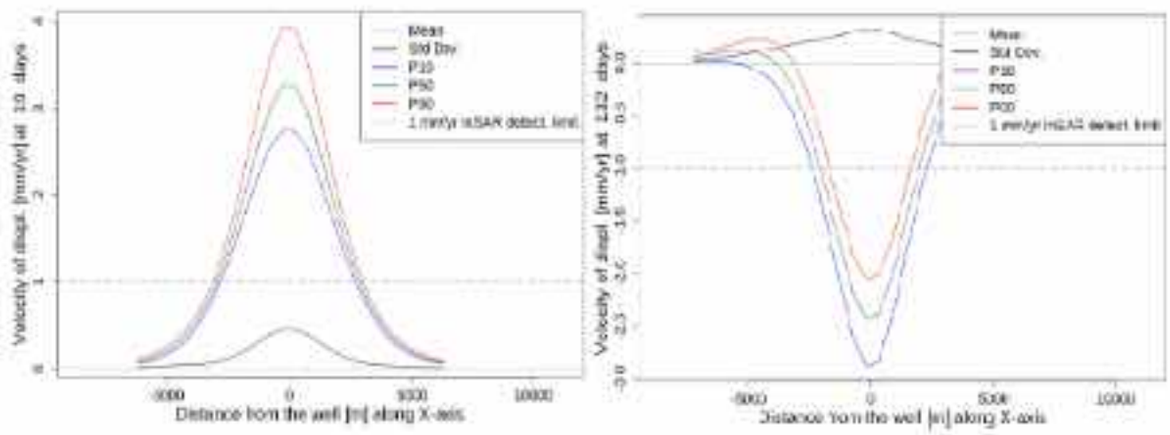


*Figure 4-64: Estimates of surface velocity displacements (mm/yr) (Mean, standard deviation, p10 & p90 percentiles) along a X-axis cross-section (y=0, at the well position), according to the uncertainties in DOE's variables at the beginning of injection (10 days, left) and 10 days after the well shutting (right) (based on metamodeling).*

According to the sensitivity study, the most contributing parameters of the results variability at the well are the permeability (K/Phi relationship parameter) and the elastic parameters of Oolithe Blanche (Figure 4-65). The permeability is predominant when injecting $CO_2$ while the elastic parameters become predominant further away from the well while injecting and in the vicinity of the well after the injection stops (Figure 4-65 and Figure 4-66). The permeability's impact is directly related to its impact on pressure response (dominant parameter on the injection well pressure while injecting, see Figure 4-48) and by consequences on porous media deformation, until impacting the surface displacement. Elastic parameters

The PilotSTRATEGY project has received funding from the European Union's Horizon 2020 research and innovation programme under grant agreement No. 101022664

define the ability of porous media to elastically deform with the stress change and to accommodate this one. Thus, for example, with low values for elastic parameters and a given increase in pressure, we expect higher porous media deformation and consequently a higher surface uplift. The change in pressure being mainly in the Oolithe Blanche formation, it leads to its elastic parameters being predominant here, compared to the caprock ones (low overpressure in the caprock). Further away from the well, the influence of some caprock properties is noticed (permeability and elastic properties) on surface displacement after the injection stops, but in an area with low displacements and at that time, far away from the well, boundaries effect may disturb those results.

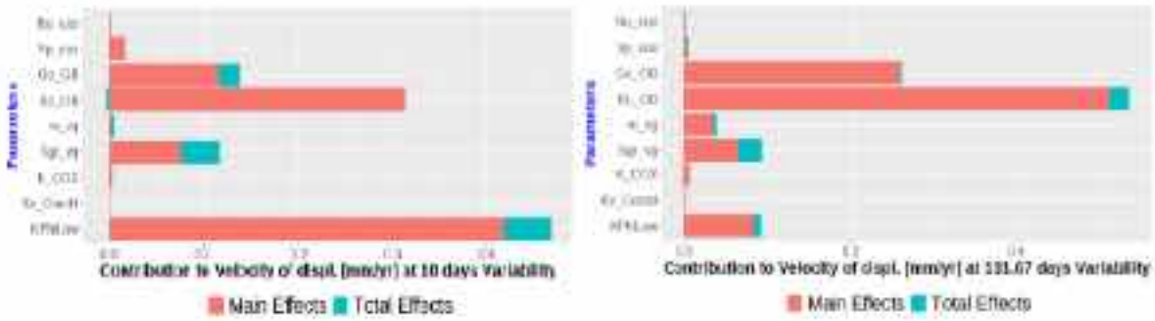


*Figure 4-65: Contribution to surface velocity displacement (above the well) variability from the uncertain parameters at the beginning of injection (10 days, left) and 10 days after the well shutting (right) (based on metamodeling).*

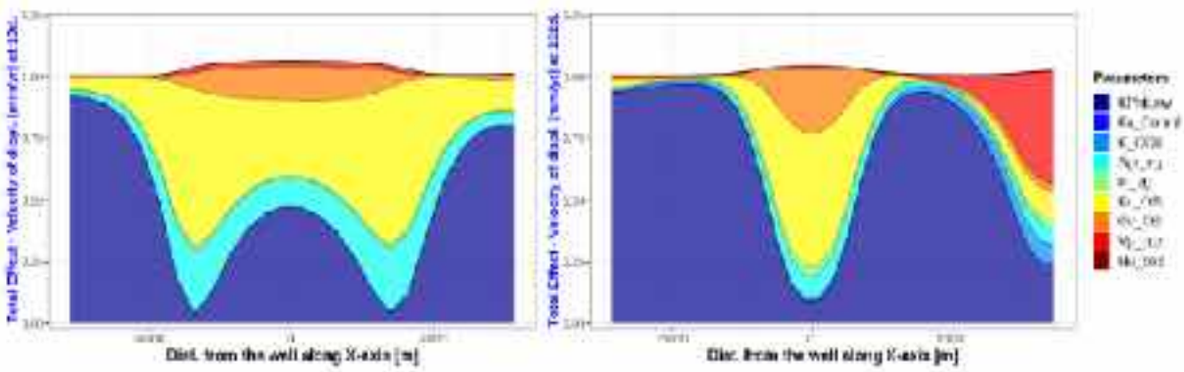


*Figure 4-66 : Total effect – Sobol indices for velocity displacement along the X axis (y=0, at the well position) at the beginning of injection (10 days, left) and 10 days after the well shutting (right) (based on metamodeling).*

### 4.4.3.5 Statistics and sensitivity to uncertain parameters for the distance to failure criterion for the 175 simulations

While previously none of the nine models reaches the failure criterion, either in the Dogger aquifer or in the Callovo-Oxfordian formation (caprock) (see section 4.4.2), here one simulation obtains negative values in terms of distance to the failure criterion in the Dogger aquifer during the injection period (Figure 4-67, right). This means that the considered failure criterion is reached and that the risk of failure must be considered for this parameter configuration. The main reason for this difference is due to different values of initial stress ratio. Indeed, in the initial state, there are already some elements for some specific simulations with stress invariant values close to the failure criterion (Figure 4-68). As previously (Figure 4-46), the distance variations are quite limited but sufficient for one of these simulations to reach the criterion at some points, since they are very close to it at the very beginning.

The PilotSTRATEGY project has received funding from the European Union's Horizon 2020 research and innovation programme under grant agreement No. 101022664

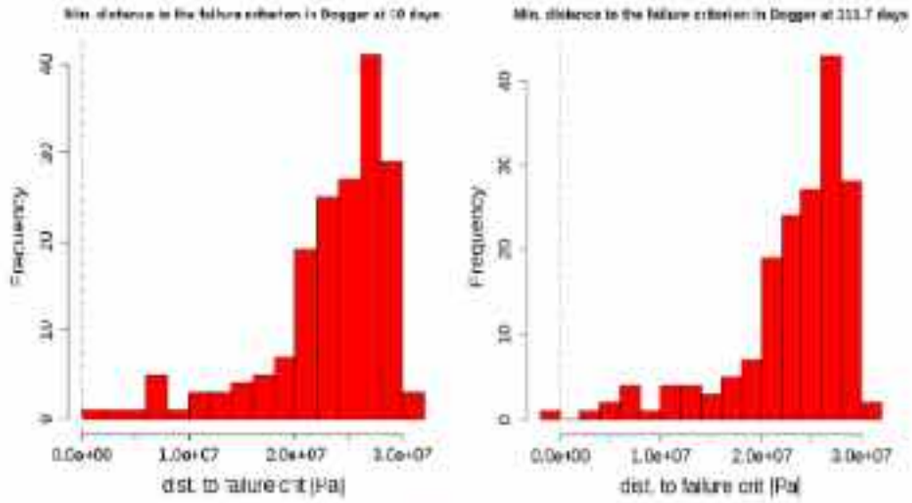


*Figure 4-67: Histogram of the minimum distance to the failure criterion for each simulation in the Dogger aquifer, at the beginning of injection (10 days, left) and 10 days before the well shutting (right).*

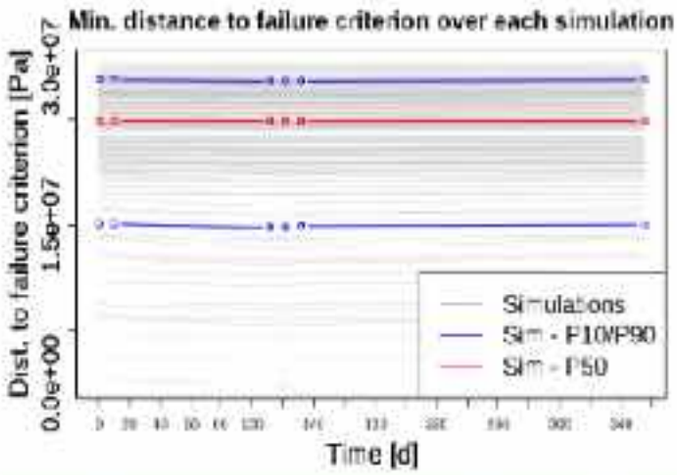


*Figure 4-68: Evolution of the minimum distance to the failure criterion for each simulation, function of time.*

Addressing the specific case of the simulation reaching the failure criterion in Figure 4-69, we observe that the area at risk is less than 2 km south of the injection point (blue colour). During the injection, there is a slight change toward colder colours, meaning a slight decrease in the distance to the failure criterion. This is still sufficient to reach the failure criterion in the blue-coloured area. The area close to the well remains safe. This is also to be related to the heterogeneity of rock properties (porosity will both impact cohesion and friction coefficients, impacting the initial distance and the elastic parameters values, impacting the dynamic behaviour).

The PilotSTRATEGY project has received funding from the European Union's Horizon 2020 research and innovation programme under grant agreement No. 101022664

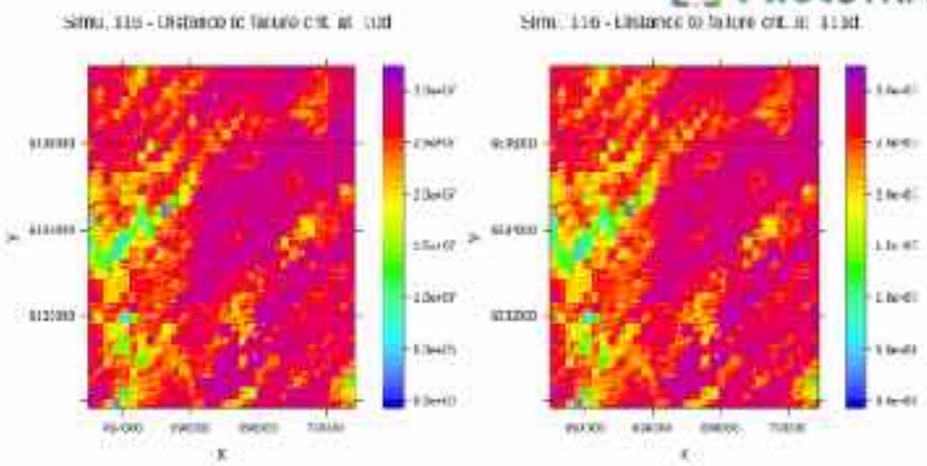

*Figure 4-69: 2D maps of the distance to the failure criterion for the simulation #116, minimum over the vertical in the Dogger aquifer (fine LGR area), at the beginning of injection (10 days, left) and 10 days before the well shutting (right). The injection point is figured at the crossing point of both dark dashed lines (coordinates in meters).*

*Table 4-13: Uncertain parameters values for the simulation #116*

| #Sim | KPhiLaw | Kv_Combl | K_COX | Sgr_vg | m_vg | Kc_OB | Gc_OB | Vp_cox | Nu_cox |
|---|---|---|---|---|---|---|---|---|---|
| 116 | 0.0015 | -0.1925 | -1.822 | 0.210 | 0.695 | 4.70E+09 | 3.97E+09 | 3.13E+03 | 0.259 |

| SHSv | ShSv_shale | ShSv_carb |
|---|---|---|
| **1.089** | 0.8056 | **0.5559** |

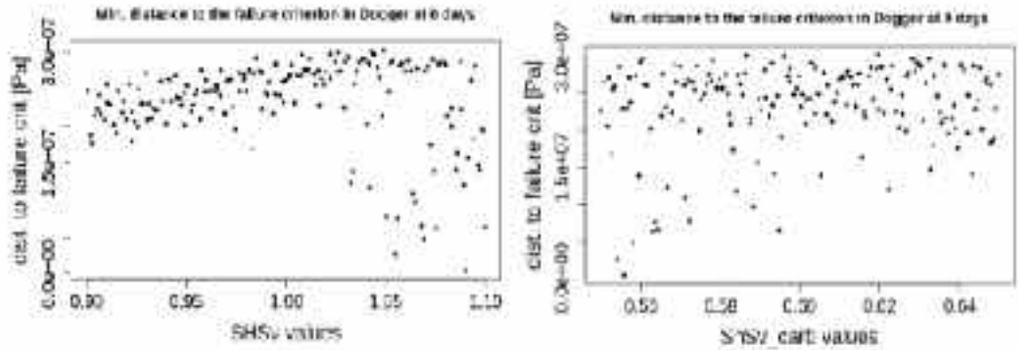


*Figure 4-70: Minimum distance to failure criterion for each simulation in the Dogger aquifer, function of SH/Sv values (left) and Sh/Sv values in carbonates (right) for the 175 simulations (initial state).*

Even if interactions between parameters and non-linear effects make difficult the analysis of simulations results vs. parameters values in a scatter plot, a trend is emerging between initial stress ratio and distance to failure criterion, with clearly the lowest values of distance with a ratio SH/Sv above 1.02 and in a lesser extent with decreasing value of Sh/Sv (in Dogger aquifer). Even with quite low uncertainty range, the value of the initial stress ratio between the principal horizontal stress (SH) and the vertical component stress (Sv) is critical for the estimation of the risk of failure.

Nevertheless, one should remember that the considered failure criterion is the most conservative one (inner criterion). While analysing results for the outer Drucker-Prager failure criterion, even for this simulation, this last failure criterion is not reached. This means that this case is at risk but does not necessarily reach the failure.

The PilotSTRATEGY project has received funding from the European Union's Horizon 2020 research and innovation programme under grant agreement No. 101022664

Regarding the general results of the entire set of simulations, minimum distance for all simulations (Figure 4-71) and standard deviation in distance to the failure criterion (Figure 4-72), it appears that areas with the lowest distance are also the ones with the highest variations (thus highest uncertainties). This is to be related with the heterogeneity of rock properties again, and more specifically to the porosity field. Porosity values control the elastic and plastic parameters values, impacting the initial distance and the dynamic behavior. These low distance values and high variation areas correspond to higher porosity values in the 2D trend of porosity values in Oolithe Blanche (see D3.2).

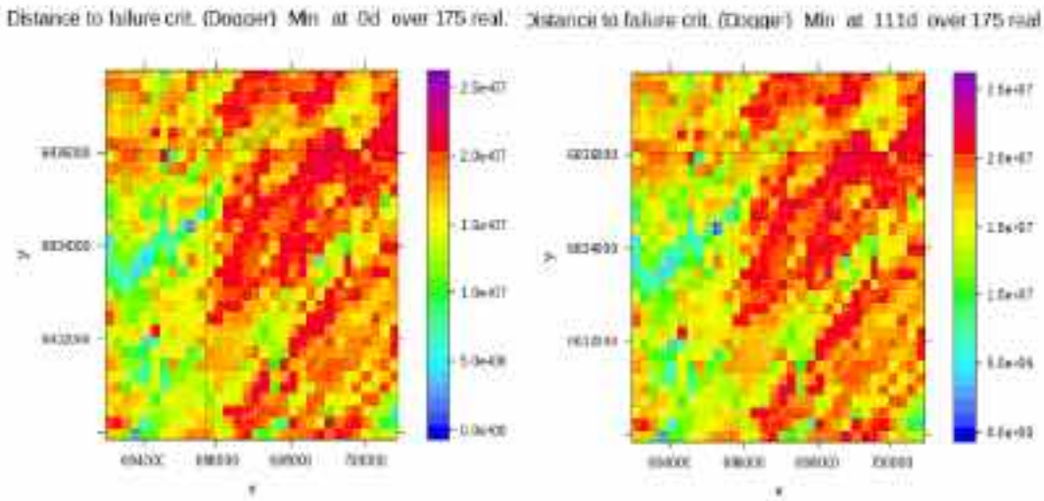


*Figure 4-71: 2D maps of the minimum distance to the failure criterion for the ensemble of 175 simulations (based on their minima over the vertical in the Dogger aquifer, fine LGR area), at the initial state (left) and 10 days before the well shutting (right). The injection point is figured at the crossing point of both dark dashed lines (coordinates in meters).*

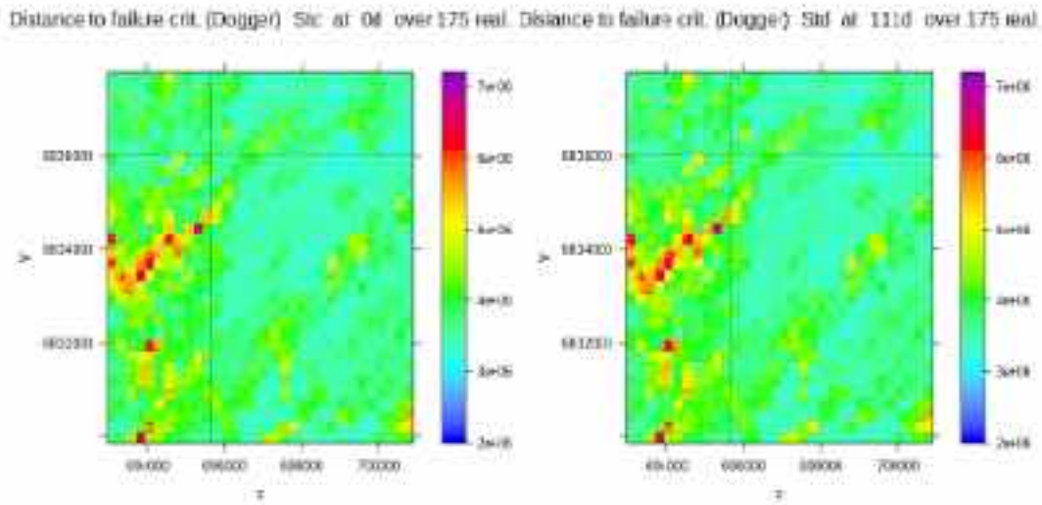


*Figure 4-72: 2D maps of the standard deviation of distance to the failure criterion for the ensemble of 175 simulations (based on their minima over the vertical in the Dogger aquifer, fine LGR area), at the initial state (left) and 10 days before the well shutting (right). The injection point is figured at the crossing point of both dark dashed lines (coordinates in meters).*

Using metamodeling, when resampling over 20,000 samples of uncertain parameters, we obtain around 1% of samples (203 realizations) reaching the failure criterion (Figure 4-73). All negative results are obtained for SH/Sv above 1. and Sh/Sv below 0.59 in carbonates.

The PilotSTRATEGY project has received funding from the European Union's Horizon 2020 research and innovation programme under grant agreement No. 101022664

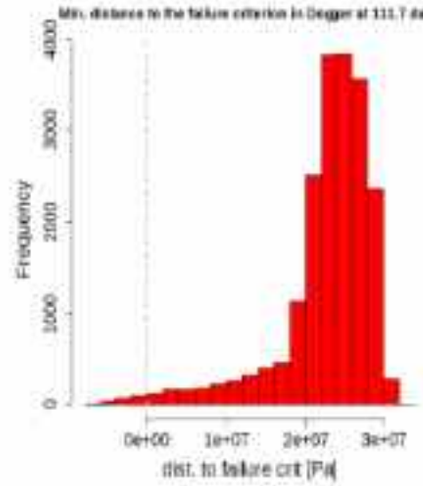


*Figure 4-73: Histogram of the minimum distance to the failure criterion for 20,000 samples of uncertain parameters, based on metamodeling of distance to the failure criterion in the Dogger aquifer, 10 days before the well shutting).*

Because the areas with the highest risk are also the ones with the potential highest variations, it is recommended to constrain these uncertainties by (1) Additional characterization over initial stress state (2) Additional characterization over rock properties (porosity, elastic and plastic properties) (3) avoid these areas for future injection well location (already considered in the suggested well location in D3.3).

On the contrary, for the distance into the Callovo-Oxfordian formation to the failure criterion, we keep the same order of magnitude as for the nine models previously studied, even though SH/Sv and Sh/Sv in marls have been varied. Minimum distances range between 12 and 19 MPa and remain far away from the criterion even during the injection period.

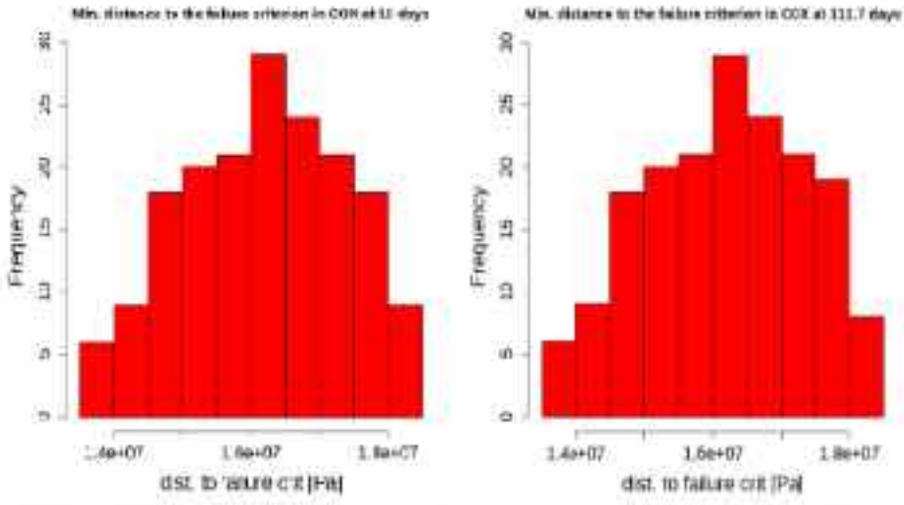


*Figure 4-74: Histogram of the minimum distance to the failure criterion for each simulation in the Callovo-Oxfordian formation (caprock), at the beginning of injection (10 days, left) and 10 days after the well shutting (right).*

## 4.5 Summary and conclusions

To evaluate the integrity of the storage complex, comprehensive numerical geochemical and geomechanical studies were implemented with short- and long-term analyses, coupling flow with

The PilotSTRATEGY project has received funding from the European Union's Horizon 2020 research and innovation programme under grant agreement No. 101022664

geomechanical and geochemical processes. Those studies were achieved for a pilot-scale $CO_2$ injection in the Oolithe Blanche formation (Dogger, deep saline aquifer), Grandpuits area, Paris basin, France.

1. The near wellbore integrity has been quantified in terms of risk of injectivity loss due to salt precipitation and fluid-rock interactions. This numerical study is based on radial wellbore models within a short-term framework. Considering uncertainties in the static model, injection temperature, capillary pressure, injection rate variability, fluid flow parameters, and salinity, the simplified geochemical model (no rock reactivity but salt precipitation) has estimated an injectivity loss of the well perforations ranging between 0% and 4%. Additional losses arise from the uncertainties in capillary pressure (+0.6%) and salinity (+0.7%). However, a 4-month injection stop could significantly reduce the well injectivity (up to 23% for the P90 Max case) in contexts of high permeability (100 – 1000 mD). In this case, the injectivity remains still sufficient to continue to allow the targeted injection rate (300kt/yr) but this higher risk must be considered in cases of long stops for maintenance or for pilot upscaling for commercial exploitation. The complex geochemical model with fluid-rock interactions (but no modelling of dry-out effect and related salt precipitation) simulates a minor 0.09% increase in permeability due to calcite dissolution. This allows to conclude that no significant increase in injectivity loss is anticipated related to rock reactivity.

2. The caprock integrity has been assessed with a comprehensive 2D radial reactive transport simulation, that incorporates complex geochemistry and a realistic system configuration. In a long-term framework, the spatial and temporal evolution of the $CO_2$ plume, as well as the chemical interactions between the injected $CO_2$, water, and the minerals. After 500 years of simulation, (dissolved and gas) $CO_2$ only reaches the first layer of Massingy marls without further penetration, demonstrating a degree of geochemical and structural stability in the studied system. The dissolution of minerals such as calcite and chlorite occurred, accompanied by the precipitation of dolomite, indicating pH buffering mechanisms and a slight reduction in porosity. Overall, this demonstrates a very limited geochemical impact on the caprock of the $CO_2$ injection at pilot-scale in the Dogger aquifer. Therefore, geochemical impact on the caprock is not a major concern for the caprock in the studied case.

3. The risk of failure of storage formation and caprock has been quantified in terms of distance to failure criterion. This risk is related to geomechanical effects of the $CO_2$ injection on the storage complex, in particular in the injection phase. A coupled 3D hydromechanical model was used to evaluate the potential damage induced by $CO_2$ injection, analysing the evolution with time of the overpressure and of the distance to the Drucker-Prager failure criterion. A first analysis was performed considering uncertainties in static models and relevant subsurface properties with nine models covering the uncertainties ranges. Within a prior hypothesis on the initial stress state, all results from these models remain far away from the failure criterion in the storage formation and the caprock, with the prescribed limit of bottom-hole pressure. Except for few cases that were discarded accounting from new information on dynamic behaviour of the area (see Ben Rhouma et al., 2026, D3.4), the pilot capacity is verified without jeopardizing the system integrity in the studied context.
   Another comforting result of these simulations is that the overpressure dissipates in all cases, in a short-term after the injection and no more significant impact on pressure system is expected 8 months after the end of injection.
   Further uncertainty study, with a systematic exploration of uncertain parameters space, leads to similar results in term of overpressure with a maximum expected overpressure around 3 MPa close to the injection well.

The PilotSTRATEGY project has received funding from the European Union's Horizon 2020 research and innovation programme under grant agreement No. 101022664

Regarding the risk of failure, caprock integrity is also safe in all configurations. However, in some specific cases (1% over a resampling of 20,000) regarding the initial stress state, risk of failure may occur in storage formations in a critical area. This was obtained with the most conservative failure criterion (inner Drucker-Prager failure criterion) while the less conservative one (outer Drucker-Prager failure criterion) is never reached for any simulations from the considered design of experiments. This means that those cases are at risk but may not necessarily reach the failure.

Additional analyses were performed on the deformation of the storage complex up to the surface. These analyses indicate that the dynamic of surface displacement would be sufficient to be monitored in the injection well area during the injection phase and shortly after the injection ceases. The total surface displacement due to the pilot-injection remains low (< 1 mm) and will not impact the surface installation.

As no faults were characterized in the studied area, the study of fault stability was out-of-scope for this case.

Overall, those studies are positive regarding the storage complex integrity in a pilot-scale context for the studied area. No major concerns were raised either for the geochemical or geomechanical part. Only some cautions need to be addressed in case of long-term injection stops (> 3 month, even when scaling-up from pilot to industrial) and regarding the initial stress state combined with rock properties characterization that may lead to integrity issues in some specific and minor cases.

## 4.6 References

Ahusborde, E., Amaziane, B., de Hoop, S., Ossmani, M., Flauraud, E., Hamon, F., Kern, M., Socié, A., Su, D. Mayer, K., Tóth, M., Voskov, D. (2024). A benchmark study on reactive two-phase flow in porous media: Part II - results and discussion. Computational Geosciences. 28. 1-18. 10.1007/s10596-024-10269-y.

Alavoine A., Bouquet S., Estublier A., Frey J., Fornel A., Meiller C. (2024) Paris Basin (France); In: Chassagne, R. (Ed.) Report on optimization – Injection strategy and storage capacity. *Deliverable WP3/3.3, EU H2020 PilotSTRATEGY project 101022664 report.*

André L., Audigane P., Azaroual M., Menjoz A. (2007), Numerical modeling of fluid–rock chemical interactions at the supercritical CO2–liquid interface during CO2 injection into a carbonate reservoir, the Dogger aquifer (Paris Basin, France), Energy Conversion and Management 48 (2007) 1782–1797

Bemer, E., Vincké, O., & Longuemare, P. (2004). Geomechanical Log Deduced from Porosity and Mineralogical. In Content. Oil & Gas Science and Technology - Revue de l'IFP 59 (4), pp. 405–426.

Ben Rhouma S. (Ed.), et al. (2026), Report on $CO_2$ fate on the long-term. *Deliverable WP3/3.4, EU H2020 PilotSTRATEGY project 101022664 report.*

Bonte D. (2014), Thermal characterisation of sedimentary basins: implications for geothermal and hydrocarbon exploration in The Netherlands and France, PhD thesis, Utrecht University, ISBN: 978-90-6266-367-5

Bordenave, A., Issautier, B. (2023). Paris Basin (France). In Wilkinson, M. (Ed.), Report on Conceptual Geological Models. *Deliverable WP2/D2.7, EU H2020 PilotSTRATEGY project 101022664 report.* https://pilotstrategy.eu/about-the-project/work-packages/geo-characterisation.

The PilotSTRATEGY project has received funding from the European Union's Horizon 2020 research and innovation programme under grant agreement No. 101022664

Le Brun M., Hamm V., Lopez S., Antics M., Ausseur J.Y., Cordier E., Giuglaris E., Goblet P., Lalos P., Ungemach P., Goyénèche O. (2011), Pratiques de modélisation hydraulique et thermique pour des exploitations géothermiques au Dogger dans la région parisienne, BRGM report RP-59591-FR

Chourdakis, G., David, K. , Rodenberg, B. et al. (2021) preCICE v2: A sustainable and user-friendly coupling library. https://doi.org/10.48550/arXiv.2109.14470

Christ, A.B., Mattioni, L. (2024). Paris Basin (France). In Bouquet, S. (Ed.), Report on static modelling with uncertainties. *Deliverable WP3/D3.2, EU H2020 PilotSTRATEGY project 101022664 report.*

Coussy, O., 2004. Poromechanics. Chichester: John Wiley & Sons Ltd

Drucker, D.-C., Prager, W. (1952). Soil mechanics and plastic analysis or limit design. In Quart. Appl. Math. 10, pp. 157–175.

EDF – Electricité de France (1989-2024), Open source finite element code_aster, Analysis of Structures and Thermomechanics for Studies and Research (Version 16), www.code-aster.org

Gassara O., Estublier A., Garcia B., Noirez S., Cerepi A., Loisy C., Le Roux O., Petit A., Rossi L., Kennedy S., Brichart T., Chiquet P., Luu Van Lang L., André Duboin F., Gance J., Texier B., Lavielle B., Thomas B., The Aquifer-CO2Leak project: Numerical modeling for the design of a CO2 injection experiment in the saturated zone of the Saint-Emilion (France) site, International Journal of Greenhouse Gas Control 104 (2021) 103196, ISSN 1750-5836, https://doi.org/10.1016/j.ijggc.2020.103196.

Gunzburger Y., Magnenet V., (2014): Stress inversion and basement-cover stress transmission across weak layers in the Paris basin, France, Tectonophysics, Volume 617, Pages 44-57, ISSN 0040-1951.

Kilpatrick A., Stephant S., Abad S., Mathurin F., Afonso P., Carneiro J., Martin M.R., Mediato J., Moita P. (2025) In Wilkinson, M. (Ed), Report of geochemical results for 3 areas. *Deliverable WP2/D2.9, EU H2020 PilotSTRATEGY project 101022664 report.* https://pilotstrategy.eu/sites/default/files/2025-04/PilotSTRATEGY%20D2.9.pdf

Kim, J., Tchelepi, H.A., Juanes, R. (2011) Stability and convergence of sequential methods for coupled flow and geomechanics: Fixed-stress and fixed-strain splits. Computer Methods in Applied Mechanics and Engineering, 200.13, 1591-1606. https://doi.org/10.1016/j.cma.2010.12.022

Mathurin F., Carneiro, J., López-Gutiérrez, J., Matos, C., Moreno, I. and Wilkinson, M., 2023. Deliverable WP2/D2.11 – Report on the regional hydrogeology of the three study areas: Paris Basin (France), Lusitanian Basin (Portugal) and Ebro Basin (Spain). EU H2020 PilotSTRATEGY project 101022664, 147 pp.

Menaceur H, Delage P, Tang A-M, Conil N (2015) The thermo-mechanical behaviour of the Callovo–Oxfordian claystone. Int J Rock Mech Min Sci 78:290–303

Mori, T., Tanaka, K., (1973). Average stress in a matrix and average elastic energy of materials with misfitting inclusions. Acta Metall. Mater. 42 (7), 597–629.

Sobol, I.M, (1993). Sensitivity analysis for non-linear mathematical models, Mathematical modelling and computational experiment (translated from Russian: I.M. Sobol', sensitivity estimates for nonlinear mathematical models. Matematicheskoe Modelirovanie 2 (1990), 112–118 407–414).

The PilotSTRATEGY project has received funding from the European Union's Horizon 2020 research and innovation programme under grant agreement No. 101022664

Soreide I., Whitson C.H. (1992) Peng-Robinson predictions for hydrocarbons, CO2, N2, and H2S with pure water and NaCl brine, Fluid Phase Equilib. 77, 217-240.

Vidal-Gilbert, S.; Nauroy, J.-F.; Brosse, É. (2009): 3D geomechanical modelling for CO2 geological storage in the Dogger carbonates of the Paris Basin,. In Int. J. Greenhouse Gas Control 3, pp. 288–299.

The PilotSTRATEGY project has received funding from the European Union's Horizon 2020 research and innovation programme under grant agreement No. 101022664

# 5. Lusitanian Basin (Portugal)

This study focuses on a comprehensive fluid flow, geochemical and geomechanical assessments with short-, mid- and long-term analyses, coupling dynamic simulations with thermal-hydraulic-mechanical-chemical (THMC) processes. It is based on data and numerical models resulting from previous characterization and modelling studies conducted in "WP2 – Geo-characterization" and "WP3 – Simulation", respectively, of the PilotSTRATEGY project (Marques da Silva et al., 2023; Pereira et al., 2024; Khudhur et al., 2024).

The target area for a commercial-scale $CO_2$ injection and storage site in the Portuguese region – specifically the Q4-TV1 prospect – is located in the offshore setting of the northern sector of the Lusitanian Basin (Portugal), approximately 20 km from the Figueira da Foz (Pereira et al., 2024; Khudhur et al., 2024), and comprises the siliciclastic reservoir of the Torres Vedras Group (Marques da Silva et al., 2023; Pereira et al., 2024).

The main phenomena and impacts of the $CO_2$ storage are briefly introduced in the next section, followed by the detailed assessments of each phenomenological impacts at the potential $CO_2$ storage and injection site offshore of the Lusitanian Basin.

## 5.1 Introduction

The secure and permanent geological storage of $CO_2$ is dependent upon the performance of the storage complex, which includes the reservoir, the sealing caprock, and any intersecting structural features like faults. The evaluation of the integrity of the storage system requires a multi-faceted assessment of key phenomenological impacts that could potentially compromise short- and long-term containment and performance. Four critical areas of assessment for the storage complex are presented below: reservoir injectivity integrity, caprock geochemical integrity, caprock geomechanical integrity, and potential reactivation of faults.

### 5.1.1 Phenomena and impacts for the $CO_2$ storage complex

Reservoir injectivity integrity is fundamental to the operational feasibility of a $CO_2$ storage project. It refers to the ability of the target formation to accept the planned volumes of $CO_2$ at the intended injection rates without experiencing significant impairment. This can be affected by processes such as mineral precipitation (e.g., halite) due to geochemical reactions between the injected $CO_2$, the formation brine, and the reservoir rock, potentially reducing porosity and permeability near the wellbore (IEA GHG, 2011). Conversely, dissolution phenomena can also enhance injectivity. A comprehensive understanding of these coupled processes is essential for predicting and managing long-term reservoir performance.

Caprock geochemical integrity assesses the potential for the low-permeability seal, typically shale or mudstone, to be altered by geochemical interactions with the $CO_2$-rich brine. Over long timescales (1000 years or more), the acidic environment formed by dissolved $CO_2$ can potentially dissolve caprock minerals (e.g., carbonates, feldspars) or precipitate new minerals, thereby altering its sealing capacity. However, as highlighted in the IEAGHG report on caprock systems, many shale caprocks are rich in clays and resistant minerals, making them geochemically stable over the timescales relevant for storage security, with reactivity often limited to the immediate vicinity of the caprock-reservoir interface (IEAGHG, 2011).

The PilotSTRATEGY project has received funding from the European Union's Horizon 2020 research and innovation programme under grant agreement No. 101022664

Caprock Geomechanical Integrity is concerned with the mechanical response of the seal to the increased pore pressure during $CO_2$ injection. The primary risk is hydraulic fracturing, where the pressure exceeds the minimum in-situ stress and the tensile strength of the caprock, creating new fractures that could provide a migration pathway. This requires a detailed understanding of the in-situ stress field, the mechanical properties of the caprock, and the evolution of the pressure plume during injection (Zoback & Gorelick, 2012). Maintaining injection pressure below the fracture gradient is a fundamental design criterion to preserve geomechanical integrity.

Fault Reactivation Assessment is a critical component of the geomechanical evaluation. The increase in pore pressure from injection can reduce the effective normal stress acting on pre-existing faults, bringing them closer to failure. This can induce seismicity and, more critically, potentially re-open fault zones, creating conduits for fluid leakage out of the storage complex. A thorough fault reactivation assessment involves mapping faults, characterizing their orientation relative to the in-situ stress field, and determining the critical pressure at which slip may occur, thereby defining a safe operating window to prevent significant induced seismicity and ensure containment (Rutqvist, 2012).

## 5.2 Injectivity integrity

This section presents the injectivity integrity analysis conducted on the reservoir to identify chemical and petrophysical impacts on performance during the $CO_2$ injection period.

First, the dynamic model built for this assessment is introduced, along with the initial and boundary conditions and the main parametrization for the dynamic simulations. Then, the modelling approach used for this assessment is presented, followed by the main results and analysis, which include the base case scenario and an uncertainty analysis of key parameters that may impact reservoir injectivity and potential losses.

### 5.2.1 Dynamic Model

#### *5.2.1.1 Thermal-hydraulic-chemical Model*

The injectivity integrity subtask was developed using the CMG GEM compositional software (CMG, 2022), which enables the integration of chemical data and a reactive transport model to conduct a complex coupled thermal-hydraulic-chemical (THC) dynamic simulation. As described in the following paragraph, chemical reactivity, here, will focus on halite mineral reactivity along with water vaporization.

Since the critical phenomenological impacts to assess occur in the near-wellbore area, the static and dynamic models built in previous tasks (Pereira et al., 2024; Khudhur et al., 2024) were used as a basis but were adapted for the specific needs of this task. This involved not only increasing the vertical and horizontal resolution near the $CO_2$ injection well but also changing the model type from a Cartesian grid to a radial grid model (Figure 4-1). Although this model is represented in 3D, the simulation actually uses a 2D grid section (Figure 4-2) with a 360° sweep parameter applied during the building process to mimic the full radial section of the model (Figure 4-1).

The 2D grid of the radial model for the dynamic simulations comprises 10 000 cells (200 cells in the i-direction, 1 cell in the j-direction and 50 cells in the k-direction). The lateral extension (i-direction) uses progressively sized cells extending up to 50 km (Figure 4-1), and a minimum cell size of about 0.076m at the injection well location. In contrast, the vertical thickness of each cell was refined to 1

The PilotSTRATEGY project has received funding from the European Union's Horizon 2020 research and innovation programme under grant agreement No. 101022664

m, with a total of 50 cells in the k-direction to represent the bottom zone of the reservoir, i.e., the total thickness of the reservoir was not represented in the radial model, since previous simulations indicated that the $CO_2$ plume would remain constrained in the lower zone of the reservoir. This vertical refinement was performed to avoid numerical effects due to spatial discretization and better capture the potential salt precipitation near the well. The remaining part of the reservoir was excluded from this assessment, as its inclusion would increase computational complexity and simulation time without providing significant benefit for the phenomenological impacts evaluated in this subtask.

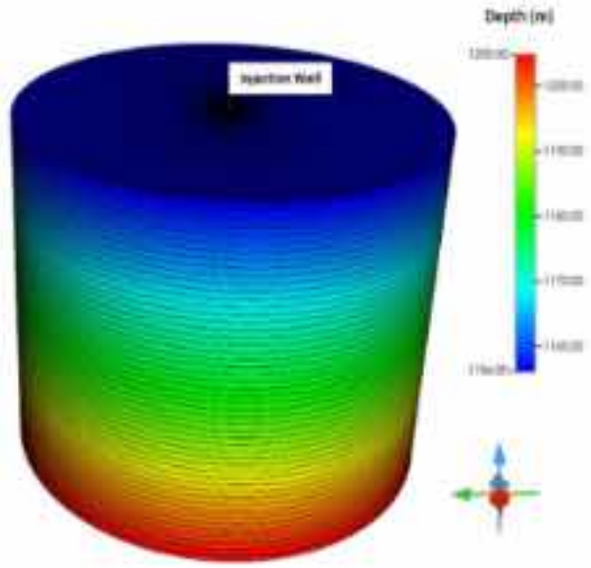


*Figure 4-1: 3D view of the radial model of the reservoir with the injection well in the centre of the model.*

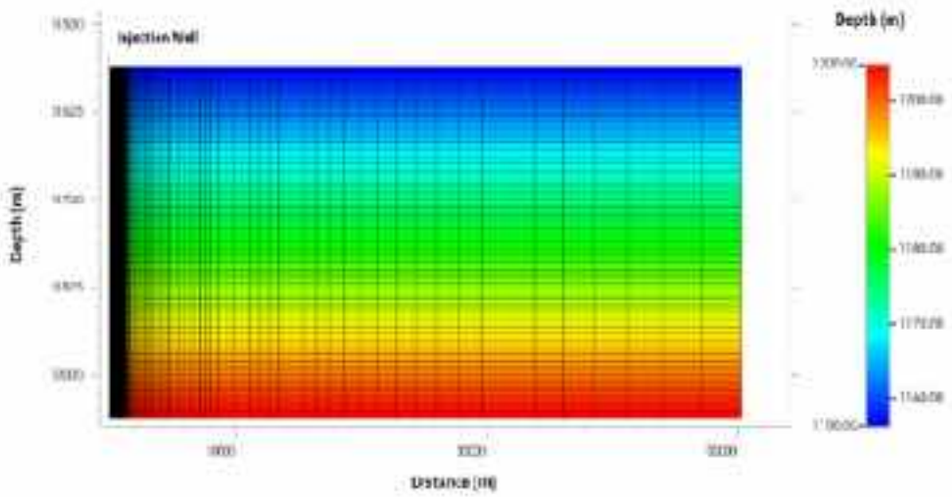


*Figure 4-2: Vertical section of the radial model illustrating the depth of the reservoir and the injection well on the left.*

The petrophysical properties used to build the radial model were based on the porosity and permeability (both horizontal and vertical) models of the P50 case, which were obtained during the task of 3D static modelling with uncertainties (Pereira et al., 2024). Since the vertical thickness of the cells in those models was 5 m, this was translated to the radial model by preserving the vertical heterogeneity from the static models while maintaining a uniform 5-meter thickness in the radial adaptation. Laterally, the reproduction of the petrophysical properties at the well location were homogeneously propagated throughout the radial model. Although this limitation of lateral homogeneity can impact the simulation results, it is not possible to reproduce directly the

The PilotSTRATEGY project has received funding from the European Union's Horizon 2020 research and innovation programme under grant agreement No. 101022664

petrophysical properties from the original Cartesian grid to this radial grid model. The final porosity and horizontal permeability models are illustrated in Figure 4-3 and Figure 4-4, respectively.

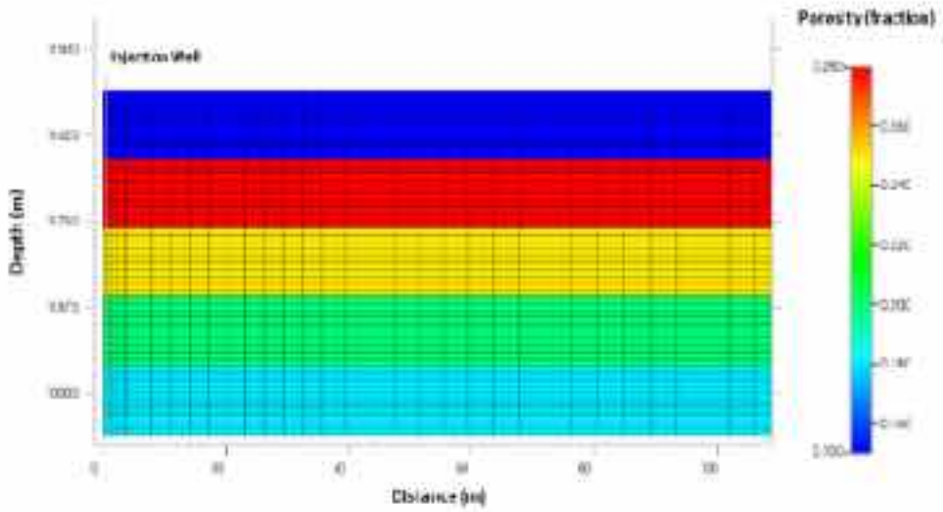


*Figure 4-3: Vertical section illustrating the porosity of the reservoir for the first 120m.*

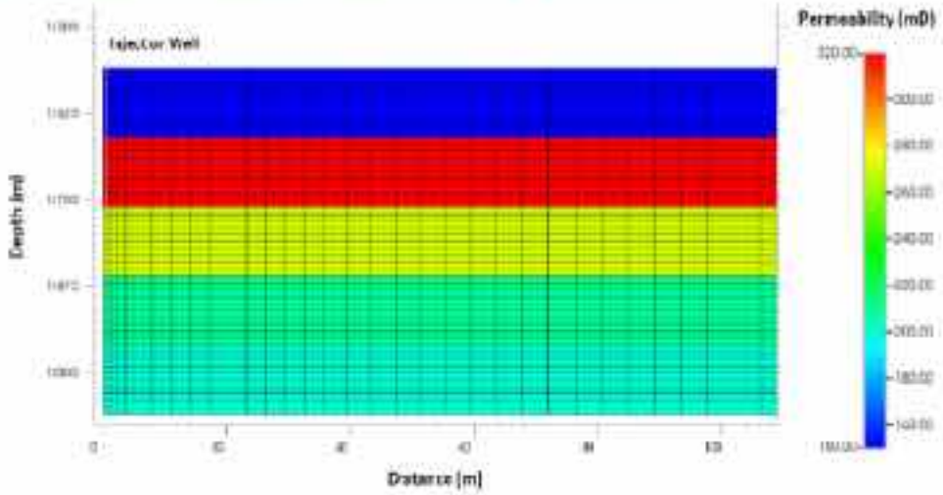


*Figure 4-4: Vertical section illustrating the (horizontal) permeability of the reservoir for the first 120m.*

### 5.2.1.2 Initial state and boundary conditions

The numerical simulations were conducted considering a maximum injection rate of 710 272 $Sm^3$/day over a 30-year injection period, with the objective of achieving a cumulative $CO_2$ mass of approximately 15 Mt (14.5 Mt). This injection strategy was derived from the P50 models for the base case scenario established previously, which assumed no phenomenological impacts such as water vaporization and halite precipitation during injection and their potential consequences for injectivity losses. Therefore, the daily injection flow rate in this assessment remains the same and serves as the benchmark for comparison across the different scenarios in the base case and uncertainty analyses. Additionally, a maximum bottom-hole pressure of 16 500 kPa was imposed as an operational constraint (pressure limit), as previously identified and applied for the reservoir model region (e.g., Khudhur et al., 2024).

The initial pressure distribution of the reservoir is illustrated in Figure 4-5, and the initial temperature distribution is shown in Figure 4-6. These initial conditions represent the reference state for all subsequent simulations, corresponding

The PilotSTRATEGY project has received funding from the European Union's Horizon 2020 research and innovation programme under grant agreement No. 101022664

to approximately 12 MPa and 48°C for the pressure and temperature conditions in the bottom zone of the reservoir.

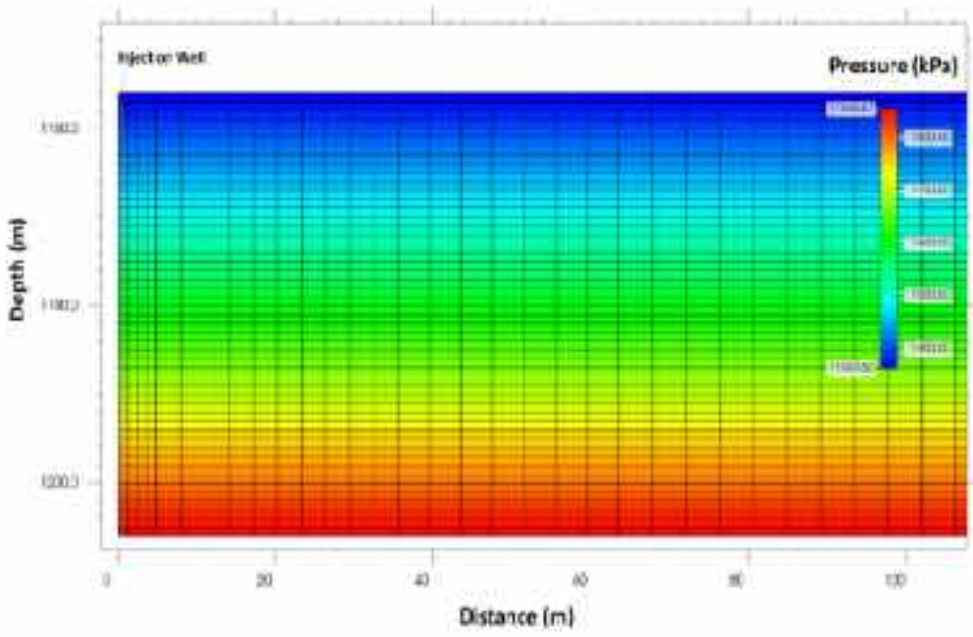


*Figure 4-5: Vertical section of the initial reservoir pressure.*

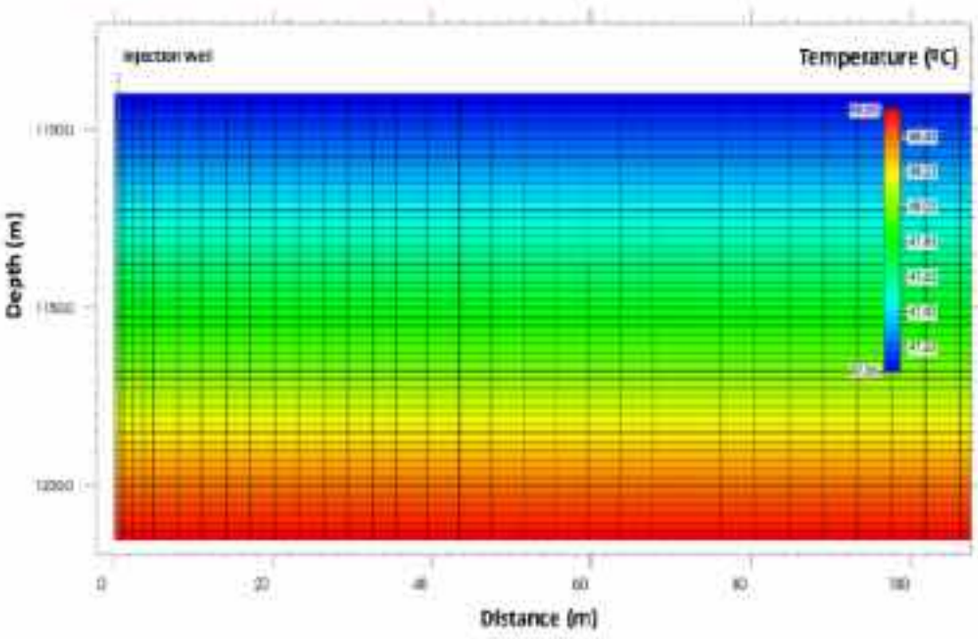


*Figure 4-6: Vertical section of the initial reservoir temperature.*

A reactive transport model was defined for the reservoir area of the model, incorporating thermodynamic data for the chemical interactions. These parameters included the reservoir brine composition and initial aqueous concentrations, the initial volume fraction of reservoir minerals (both primary and secondary), reaction kinetics, and thermal properties.

The pH value of the initial formation water (brine) was 6.90. Due to the lack of real brine composition data from the reservoir, a proxy brine composition was created using laboratory measurements at the University of Edinburgh. This was done using a reservoir rock sample with pure water and NaCl of

The PilotSTRATEGY project has received funding from the European Union's Horizon 2020 research and innovation programme under grant agreement No. 101022664

about 99.5% purity (with a salinity of 55.6 g/L), as reported in the geochemical studies of "WP2 – Geo-characterization" (Afonso et al., 2025). The concentrations of the aqueous elements in the reservoir brine are presented in Table 4-1, and the reservoir mineralogy composition is presented in Table 4-2. Due to the negligible impact of chemical reactions of rock minerals present in the reservoir, verified on the long-term reactive transport modelling conducted in a previous task to quantify the evolution of the trapping mechanisms (Pereira et al., 2026), it is important to note that only water vaporization and salt precipitation phenomenological impacts are addressed here. For this reason, the original reservoir minerals were defined as non-reactive (i.e., in equilibrium), except for the halite mineral. This mineral was included to evaluate potential halite precipitation as a key phenomenon in this injectivity integrity assessment. The initial mineral volume fraction of salt (halite) was set as zero. The reactive transport model uses kinetic parameters for mineral reactions, including reactive surface area, activation energy, and reaction rate constants, governing the rate of $CO_2$-induced mineral dissolution and precipitation. Table 4-3 shows the input data for the reactive transport modelling of halite mineral of this work using the Wolery thermodynamic database (Wolery et al., 2007) for the aqueous and mineral/solid reaction.

*Table 4-1: Brine composition in the reservoir.*

| Aqueous Elements | Concentrations (ppm) |
|---|---|
| $Al^{3+}$ | 0.13 |
| $Ca^{2+}$ | 36.75 |
| $K^{+}$ | 26.51 |
| $Mg^{2+}$ | 13.25 |
| $Na^{+}$ | 22852.20 |
| $SiO_2$ | 7.84 |
| $Cl^{-}$ | 33719.00 |

*Table 4-2: Mineralogy composition (mineral bulk volume fractions) of the reservoir.*

| Minerals | Quartz | Feld-K | Calcite | Dolomite | Kaolinite |
|---|---|---|---|---|---|
| wt% | 73 | 9 | 1 | 5 | 12 |

*Table 4-3: Input data for the reactive transport modelling using the Wolery geochemical database.*

| Minerals | Reactive Surface Area ($m^2/m^3$) | Activation Energy (J/mol) | Log10 of reaction rate (1/sec) |
|---|---|---|---|
| Salt (Halite) | 2163.35 | 7400 | -0.21 |

Thermal properties, critical for THC simulations, are summarized in Table 4-4, with values derived from laboratory measurements conducted in the petrophysical studies of "WP2 – Geo-characterization" (Barradas et al., 2023; Marques da Silva et al., 2023). The thermal properties were considered uniform across the reservoir model, representing a sandstone. Although the reservoir is known to be heterogeneous, most of this heterogeneity is present in the full thickness of the reservoir, which includes interbedded clay layers. These clay layers are not expected in the bottom zone of the reservoir represented in the radial model for this assessment, which is composed essentially of coarse sand and conglomerates.

The PilotSTRATEGY project has received funding from the European Union's Horizon 2020 research and innovation programme under grant agreement No. 101022664

*Table 4-4: Thermal parameters of the reservoir and caprock.*

| Region | Thermal Conductivity (J/m.s.K) | Heat Capacity (J/kg.K) |
|---|---|---|
| Reservoir | 2.6 | 720.8 |
| Caprock | 3.0 | 800.0 |

The solubility tables for the $CO_2$ dissolution in the reservoir brine and the reservoir relative permeability curves used in this work were previously presented in the work from Khudhur et al. (2024).

### 5.2.2 Modelling Approach

The THC dynamic simulations for injectivity integrity allow to assess the phenomenological impact of potential halite precipitation near the wellbore. Consequently, the petrophysical properties of the reservoir may change over time. For this assessment, the halite precipitation and porosity changes were directly evaluated.

After identifying and spatially characterizing the occurrence and extent of these phenomena, the potential injectivity loss of the injected $CO_2$ volume was firstly evaluated based on the evolution of both the instantaneous and cumulative mass of injected $CO_2$.

In addition, the injectivity at the well is commonly evaluated through the injectivity index ($II$), which can be analogously derived from the well productivity formulation (Dake (1978); Ahmed (2019)), and defined by the following relationship (Equation 4-1):

$$II = \frac{Q}{P_{wf} - P_r} \qquad \text{(Equation 4-1)}$$

Where $Q$ is the injection rate (in this case, $Sm^3$/day) and the pressure difference (in this case, kPa) between the well flowing bottom-hole pressure ($P_{wf}$) and the average reservoir pressure around the well ($P_r$). This formulation provides a direct measure of how efficiently a reservoir accepts injected fluid.

This modelling approach was firstly conducted for the reference (base) case. The results from this scenario are then compared with those from other relevant parameters (injection flow rate, reservoir salinity, and $CO_2$ injection temperature) in the uncertainty analysis section. The final assessment evaluated in the uncertainty analysis corresponds to the worst-case scenario, which jointly evaluate the impacts of increasing the injection flow rate and the reservoir salinity. The set of parameters for all these scenarios are presented in the Table 4-5.

*Table 4-5: Parametrization of the reference case and the scenarios for the uncertainty analysis.*

| Scenarios | Reference Case | Higher Case | Lower Case | Worst Case |
|---|---|---|---|---|
| Flow Rate ($Sm^3$/day) | 710 272 | 1 301 440 | - | 1 301 440 |
| $CO_2$ Bottom-hole Injection Temperature (°C) | 26 | 40 | 20 | 26 |
| Salinity (g/L) | 56 | 130 | 10 | 130 |

The PilotSTRATEGY project has received funding from the European Union's Horizon 2020 research and innovation programme under grant agreement No. 101022664

It is important to note that, although the real chemistry of the reservoir brine was not available for this assessment, the information from the conductivity logs from the set of offshore wells in the Lusitanian Basin (at varying reservoir depths) indicate that the reservoir salinity may range from approximately 10 g/L and 130 g/L. This interval of values corresponds, respectively, to lower and higher extreme cases defined for the uncertainty analysis of this parameter, and the value of approximately 56 g/L (coming from the fabricated brine as previously mentioned) corresponds to the average (expected) estimate of reservoir salinity value and used as the reference case in this assessment.

### 5.2.3 Results

This section presents and analyses the results of the injectivity integrity assessment. First, the main results and phenomenological impacts of the base case are presented and discussed. Subsequently, the results from this scenario are compared with those from the uncertainty analysis.

#### *5.2.3.1 Reference Case*

The base case scenario aims to achieve a cumulative mass of $CO_2$ injected of approximately 15 Mt (14.5 Mt), i.e., a $CO_2$ injection flow rate of 710 272 $Sm^3$/day during the 30-years of the injection period. The injection bottom-hole temperature of the $CO_2$ is 26°C and the reservoir salinity was set as 56 g/L.

The results of the halite precipitation, porosity changes, gas resistance factor and, finally the impacts on the injectivity integrity are presented in the next subsections.

##### *5.2.3.1.1 Halite precipitation*

After continuously injecting the $CO_2$ volumes over 30 years, the precipitation of halite occurs and is strongly localized in the near wellbore zone (Figure 4-7), within roughly the first 20-30m from the injection well. Peak halite concentrations (up to approximately 400 mole/$m^3$) occur at discrete depth intervals around 1180-1190m, coinciding with zones of strongest $CO_2$-induced brine displacement and vaporization.

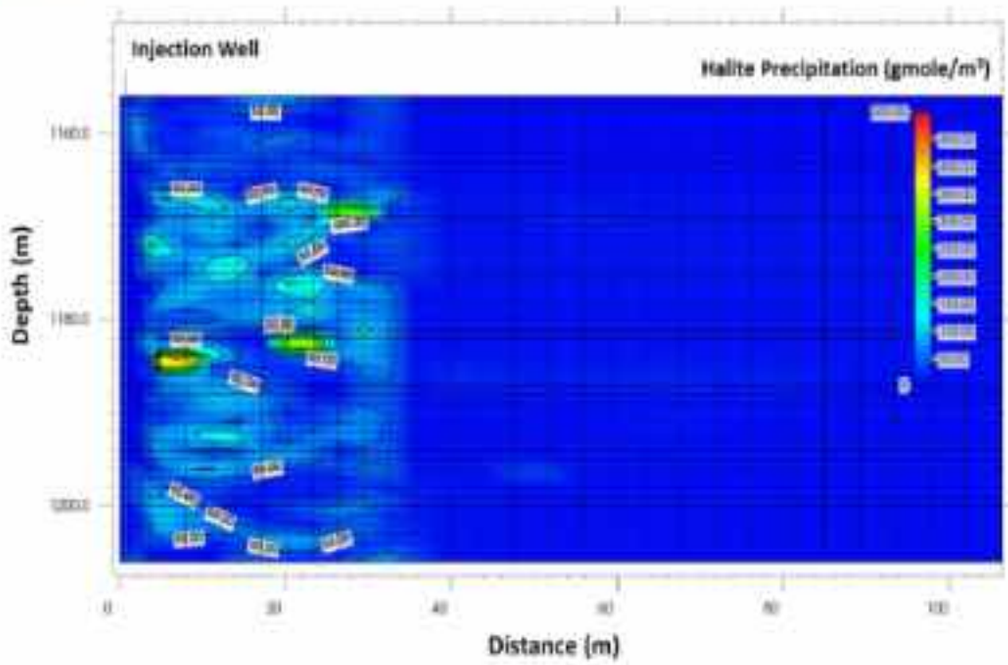


The PilotSTRATEGY project has received funding from the European Union's Horizon 2020 research and innovation programme under grant agreement No. 101022664

*Figure 4-7: Vertical section of the spatial distribution of the halite precipitation near the injection well for the base case scenario and after 30-years of injection.*

Away from the well, halite precipitation rapidly diminishes and becomes negligible beyond approximately 40m, indicating that salt (halite) accumulation is not pervasive at the reservoir scale. This spatial pattern suggests that, under the base case injection and reservoir conditions, injectivity impairment is primarily a near-well phenomenon, potentially leading to localized permeability reduction rather than widespread flow restriction.

#### 5.2.3.1.2 *Reservoir porosity changes*

The porosity change distribution shows that porosity reduction is concentrated in the near-wellbore zone (Figure 4-8), fairly matching the spatial pattern observed for halite precipitation. This is an expected behaviour since it is the only reactivity modelled in this task. Minor porosity reductions up to 0.8-1% occur only within 20-30 m of the injection well due to salt precipitation and brine drying, while beyond this zone, changes are negligible and the bulk reservoir remains unaffected.

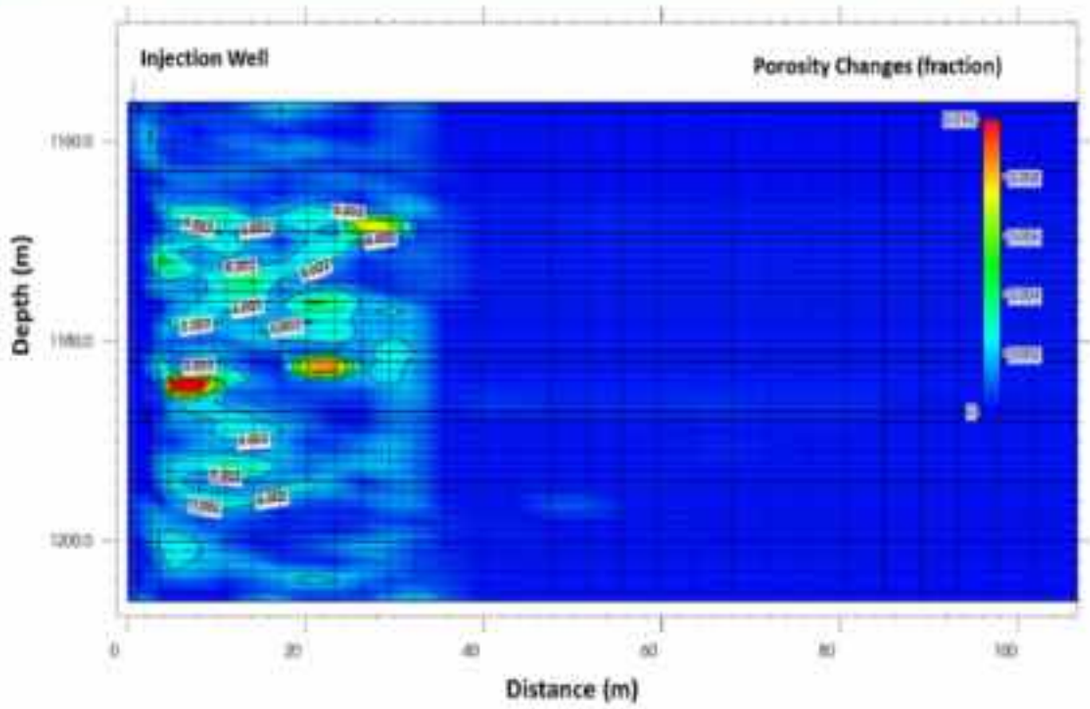


*Figure 4-8: Vertical section of the spatial distribution of the porosity changes (reduction) near the injection well for the base case scenario and after 30-years of injection.*

Despite the relatively small magnitude of porosity reduction, the associated permeability losses can be significant due to the strong non-linear porosity–permeability relationship (e.g., using Kozeny-Carman equation). For the porosity range observed in the reservoir (between 15-28%, Figure 4-3), a reduction of 0.5-1% may result in permeability decreases on the order of about 20 to 700 mD, corresponding to relative losses of approximately 10-35%. These reductions are expected to locally increase gas flow resistance, as verified in the simulation, and therefore have a more pronounced impact on pressure build-up and injectivity than the porosity change itself, particularly in the near-wellbore region where flow velocities are the highest.

The PilotSTRATEGY project has received funding from the European Union's Horizon 2020 research and innovation programme under grant agreement No. 101022664

#### 5.2.3.1.3 *Injectivity impacts*

This section compares the $CO_2$ injection performance, reservoir pressure and injectivity index evolution for scenarios with and without salt precipitation over a 30-year injection period. As shown in Figure 4-9, both scenarios exhibit identical cumulative injected $CO_2$ mass and injection rate, reaching approximately $1.45x10^7$ tonnes after 30 years at a constant rate of about 1250 tonnes/day. This confirms that both simulations are strictly rate-controlled, ensuring that any differences in pressure or injectivity response are related to reservoir behaviour rather than differences in injection volume or operational constraints.

Figure 4-10 shows that reservoir pressure increases progressively in both scenarios due to continuous injection, with the non-reactive scenario consistently exhibiting slightly higher pressure than the reactive scenario. After 30 years, the pressure difference is approximately 50-100 kPa, corresponding to less than 1% of the absolute pressure level (approximately 12600–12700 kPa). This behaviour is attributed to thermodynamic and fluid partitioning effects associated with salt precipitation and brine drying, which increase salinity and reduce $CO_2$ solubility in the reactive case. As a result, a slightly higher proportion of $CO_2$ remains in the free phase, increasing the effective compressibility of the system and allowing accommodation of the injected volume with marginally lower pressure build-up compared to the non-reactive case.

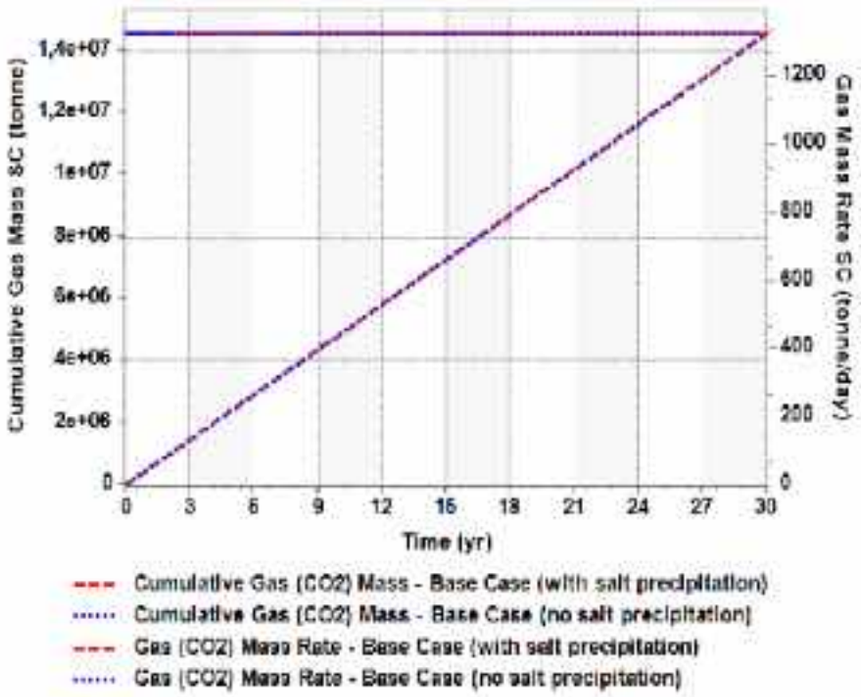


*Figure 4-9: Evolution of the cumulative gas ($CO_2$) mass, and gas ($CO_2$) mass rate for the scenarios with and without salt precipitation over the injection period of 30 years.*

The PilotSTRATEGY project has received funding from the European Union's Horizon 2020 research and innovation programme under grant agreement No. 101022664

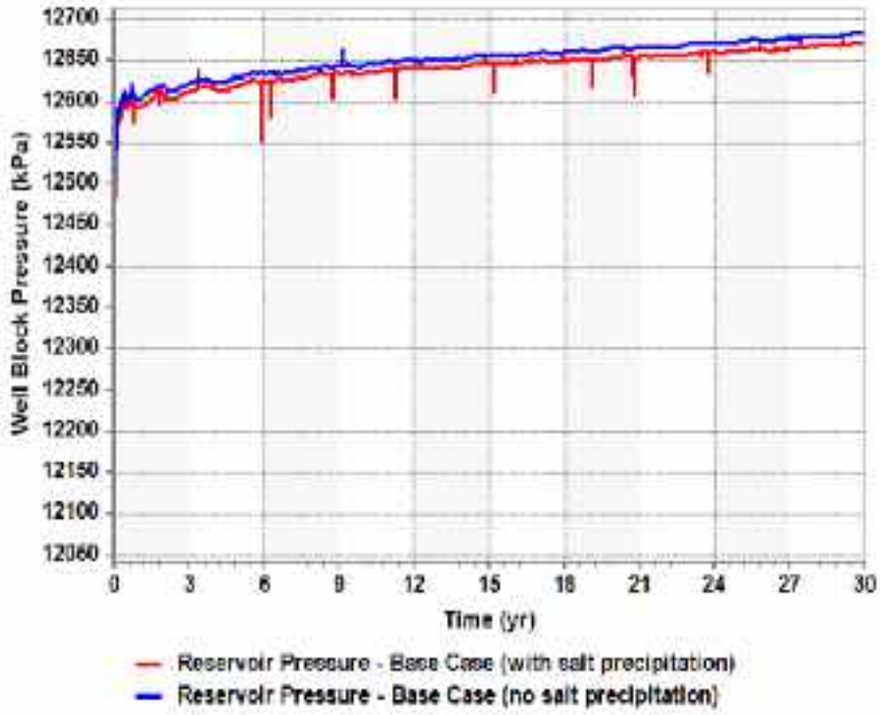


*Figure 4-10: Evolution of the reservoir pressure for the scenarios with and without salt precipitation over the injection period of 30 years.*

Figure 4-11 shows that the injectivity index remains high and stable in both scenarios, with values around 2050-2100 $Sm^3$/day/kPa throughout the injection period. The maximum deviation between the reactive and non-reactive cases is approximately 10-20 $Sm^3$/day/kPa, corresponding to less than about 0.5-1% variation relative to the baseline injectivity. This indicates that no significant injectivity loss occurs due to salt precipitation, and any permeability reduction, although potentially reaching about 10-35% locally (or tens to several hundreds of mD), remains spatially limited to the wellbore region. Overall, the results demonstrate that salt precipitation has negligible impact on long-term injectivity and does not compromise injection performance under the simulated conditions.

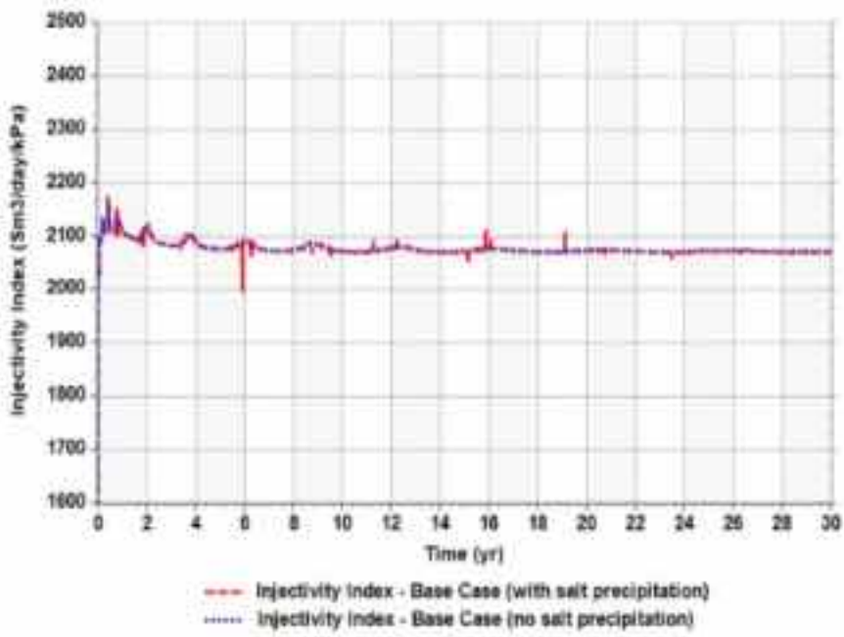


The PilotSTRATEGY project has received funding from the European Union's Horizon 2020 research and innovation programme under grant agreement No. 101022664

*Figure 4-11: Evolution of the reservoir injectivity index for the scenarios with and without salt precipitation over the injection period of 30 years.*

### 5.2.4 Uncertainty Analysis

After presenting the main results from the dynamic simulation of the base (reference) case scenario and the respective quantification of its phenomenological impacts on reservoir injectivity integrity, these results were then compared with those from the uncertainty analysis.

This comparison evaluates the impacts of injection flow rate, reservoir salinity, and $CO_2$ bottom-hole injection temperature. Finally, the last comparison assessment was conducted between the base case scenario with the worst-case scenario. These impacts resulting from the uncertainty analysis are briefly summarised below and explained in more detail in the Appendix (section 6.2.1).

Across all uncertainty scenarios, salt precipitation remains confined to the near-wellbore region and does not propagate into the reservoir far field. In the base case (0.5 Mt/y, 56 g/L, 26°C), precipitation is limited to approximately 20–30 m from the well (Appendix; Figures 6.2-1, 6.2-6, 6.2-11). Increasing injection rate or salinity expands this affected zone moderately to approximately 40–50 m, with salinity exerting the strongest control on precipitation magnitude. In contrast, lower salinity significantly suppresses precipitation, while temperature variations produce only minor differences. The worst-case scenario (1 Mt/y and 130 g/L) produces the greatest precipitation intensity and extent (Appendix, Figure 6.2-16), but even under these conditions, precipitation remains spatially localized and does not affect reservoir-scale flow behaviour.

Porosity reductions follow the same spatial pattern as salt precipitation and remain localized near the injection well. In the base case, porosity reductions reach approximately 0.008–0.010 (<1% absolute reduction) within 20–30 m of the well (Appendix; Figures 6.2-2, 6.2-7, 6.2-12). Variations in injection rate and temperature produce only minor changes in magnitude and extent relative to the base case, while higher salinity increases the affected radius to approximately 40–50 m. The worst-case combined scenario results in the largest porosity reduction, reaching approximately 0.03–0.04 locally (Appendix, Figure 6.2-17), but these reductions remain confined to the near-well region. In all scenarios, porosity beyond approximately 40–50 m remains essentially unchanged, confirming that reservoir-scale storage capacity and connectivity are preserved.

Injection performance remains stable in all uncertainty scenarios, with cumulative injected $CO_2$ mass increasing linearly and target injection rates fully maintained (Appendix; Figures 6.2-3, 6.2-8, 6.2-13, 6.2-18). Reservoir pressure in the base case stabilizes at approximately 12600–12700 kPa, with most uncertainty scenarios producing only minor variations (<150 kPa, or ~1%) relative to this reference (Appendix; Figures 6.2-4, 6.2-9, 6.2-14). Only the worst-case combined scenario shows a more noticeable increase, stabilizing at approximately 13900–14100 kPa, but still well below the operational pressure limit of 16500 kPa (Appendix, Figure 6.2-19). Similarly, the injectivity index in the base case stabilizes at approximately 2050–2100 $Sm^3$/day/kPa, and most uncertainty scenarios produce only minor deviations (<5%) from this reference (Appendix; Figures 6.2-5, 6.2-10, 6.2-15). Higher salinity and the worst-case combined scenario produce the largest reductions, with injectivity stabilizing at approximately 1800–1900 $Sm^3$/day/kPa, corresponding to a maximum injectivity loss of approximately 10–15% relative to the base case (Appendix, Figure 6.2-20). Importantly, injectivity stabilizes after early transient adjustments in all cases, and no progressive or long-term degradation occurs.

The PilotSTRATEGY project has received funding from the European Union's Horizon 2020 research and innovation programme under grant agreement No. 101022664

### 5.2.5 Discussion and Conclusions

This injectivity integrity assessment for the Q4-TV1 prospect in the Lusitanian Basin demonstrates that $CO_2$ injection–induced geochemical and petrophysical alterations are systematically localized to the near-wellbore region and do not compromise long-term reservoir-scale injectivity under the evaluated conditions. Using a high-resolution coupled THC modelling approach, the study shows that halite precipitation driven by $CO_2$-induced brine drying is the dominant mechanism controlling near-wellbore porosity reduction and increased resistance to $CO_2$ flow. In the base case scenario (0.5 Mt/y injection rate, 56 g/L salinity, and 26°C injection bottom-hole temperature), halite precipitation and associated porosity reductions remain limited to approximately the first 20–30 m from the injection well, with maximum porosity decreases of less than approximately 0.008–0.010 (<1% absolute reduction). These localized effects do not result in measurable field-scale injectivity degradation, as evidenced by stable injection rates of approximately 1200–1300 t/day, linear cumulative injection reaching approximately 14.5 Mt over 30 years, reservoir pressures stabilizing at approximately 12600–12700 kPa, and a stable injectivity index of approximately 2050–2100 $Sm^3$/day/kPa.

The uncertainty analysis confirms that injection rate and reservoir salinity are the primary controls on injectivity integrity, while injection temperature exerts only a secondary influence. Increasing injection rate to 1 Mt/y produces only small injectivity reductions of approximately 1–2%, whereas increasing salinity to 130 g/L results in more pronounced reductions to approximately 1850–1900 $Sm^3$/day/kPa, corresponding to injectivity losses of about 8–12%. Injection temperature variations between 20°C and 40°C produce only modest changes of approximately 3–5%. The compounded worst-case scenario (1 Mt/y and 130 g/L) produces the largest injectivity reduction, with injectivity stabilizing at approximately 1800–1850 $Sm^3$/day/kPa, corresponding to a total injectivity loss of approximately 10–15%. Despite this reduction, injection remains stable at approximately 2700 t/day, with cumulative injection reaching approximately 30 Mt over 30 years and reservoir pressures stabilizing at approximately 13900–14100 kPa, well below the operational limit of 16500 kPa.

From a risk and operational perspective, the results indicate that injectivity loss in the Q4-TV1 reservoir is moderate, localized, and self-limiting rather than progressive. Injectivity reductions occur primarily during early injection stages and subsequently stabilize as geochemical and flow conditions reach dynamic equilibrium. No progressive decline in injectivity or reservoir-scale impairment is observed in any uncertainty scenario. Even under adverse combined conditions of high salinity and high injection rate, injectivity loss remains limited to approximately 10–15% and does not compromise the ability of the reservoir to sustain long-term $CO_2$ injection. These risks can be mitigated through appropriate injection management strategies, including gradual ramp-up of injection rates, pressure-controlled injection, and close monitoring of bottom-hole pressure during early operations. Overall, the assessment supports the technical feasibility of $CO_2$ injection and storage in the Q4-TV1 reservoir, provided that near-wellbore injectivity is proactively managed, particularly in scenarios involving high injection rates and elevated formation salinity.

## 5.3 Caprock integrity – Geochemical aspects

This section presents the geochemical aspects for the caprock integrity analysis conducted on the caprock to identify chemical and petrophysical impacts over the long-term (1000-years period).

The PilotSTRATEGY project has received funding from the European Union's Horizon 2020 research and innovation programme under grant agreement No. 101022664

First, the dynamic model built for this assessment is introduced, along with the initial and boundary conditions and the main parametrization for the dynamic simulations. Then, the modelling approach used for this assessment is presented, followed by the main results and analysis, which include the base case scenario and an uncertainty analysis of key parameters that may impact the caprock integrity.

### 5.3.1 Dynamic Model

The dynamic model employed in this study is a fully coupled thermal-hydro-chemical (THC) numerical framework designed to simulate the complex multiphase and reactive processes associated with $CO_2$ injection into a deep saline aquifer overlain by a heterogeneous caprock. This integrated approach captures the interplay between fluid flow, heat transfer, solute transport, and geochemical reactions, providing a comprehensive assessment of $CO_2$ plume migration and its potential impact on caprock integrity over operational and post-injection timescales.

#### *5.3.1.1 Thermal-hydro-chemical Model*

The simulations were performed using the compositional reservoir simulator CMG-GEM (CMG, 2022), which incorporates a coupled thermal-hydraulic-chemical (THC) formulation capable of representing multiphase flow ($CO_2$ gas, aqueous brine, and dissolved species), advective-dispersive transport, and kinetically controlled mineral dissolution/precipitation reactions. The model accounts for the thermodynamic non-ideality of $CO_2$ under reservoir conditions, including fugacity corrections, solubility in brine as a function of pressure, temperature, and salinity, and the consequent formation of carbonic acid leading to pH-dependent geochemical interactions. Thermal effects, such as Joule-Thomson cooling during injection and conductive/convective heat transfer, are explicitly included, although temperature variations in this base case remain minor due to isothermal boundary assumptions. The geochemical module tracks the evolution of aqueous species, mineral assemblages, and rock properties (e.g., porosity and permeability via Kozeny-Carman relations if significant mineral volume changes occur), enabling quantification of buffering capacity, mineral trapping, and potential self-sealing or self-enhancing feedback mechanisms within the aquifer–caprock system.

Due to the intensive computational time required for these complex coupled simulations, a sector model was extracted from the original model domain (Figure 4-12). In addition, the original thickness of the 3D model was reduced, retaining only the first layers of the reservoir and the full caprock.

The PilotSTRATEGY project has received funding from the European Union's Horizon 2020 research and innovation programme under grant agreement No. 101022664

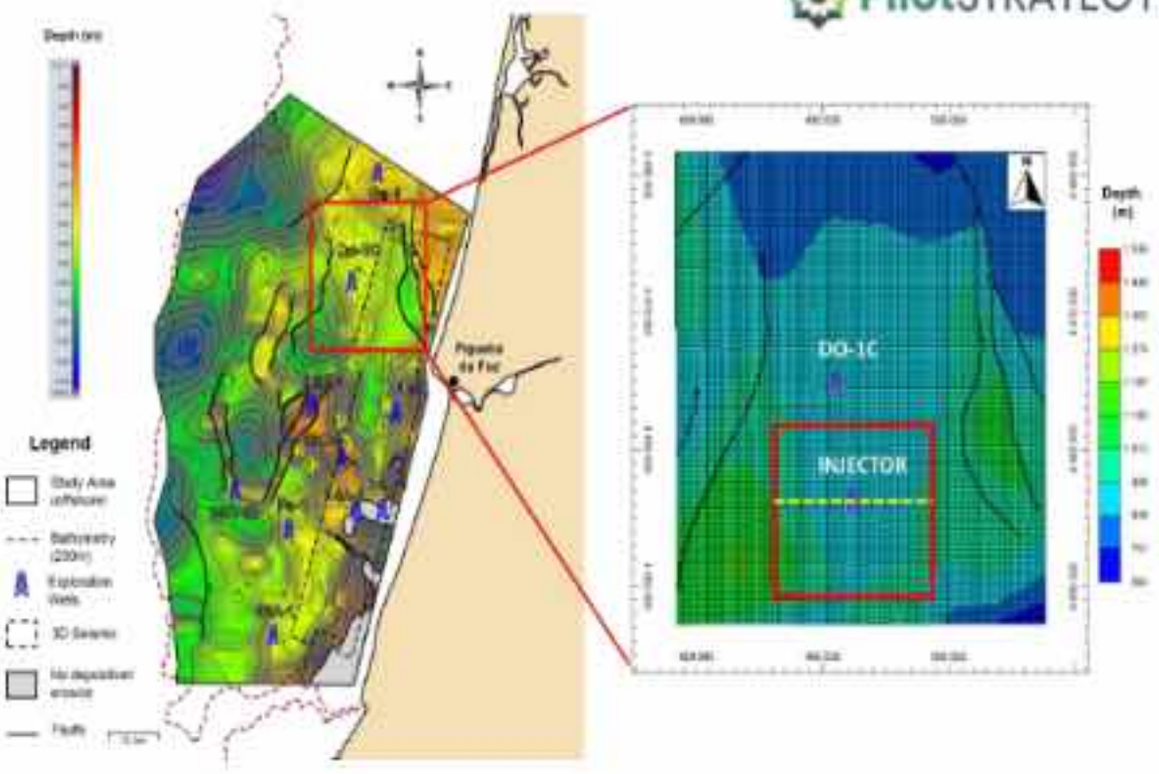


*Figure 4-12: (left) Top view of the reservoir top structure illustrating the area of reservoir model used in the task 3.2 (shown by the red square; and (right) the area of the model reservoir used in current task of this work (task 3.4), as shown by the red square, the $CO_2$ injection well (INJECTOR) and the legacy well Do-1C. The dashed yellow line illustrate the location of the cross-section used later on in this work.*

This modelled domain represents a conservative scenario in which $CO_2$ is injected directly into the topmost layers of the saline aquifer, immediately beneath the caprock, to maximize plume–caprock contact and assess worst-case risks to sealing efficiency. In fact, it tends to represent an "hypothetical" scenario – as the $CO_2$ injection has been originally considered in the bottom zone of the reservoir in Tasks 3.2 and 3.3 (e.g., Khudhur et al., 2024) – in which the $CO_2$ migrates upwards over time and reaches the caprock, although this occurs only after several hundreds of years, as verified from the long-term dynamic simulations for the higher injection flow rate scenario performed in Task 3.3.

From the original caprock model region built in the 3D static modelling (Pereira et al., 2024), which was explicitly discretized into seven vertical layers to reflect its stratigraphic heterogeneity, a much more refined grid was required for this task. Instead of considering the whole caprock as a single model region, two distinct members could be distinguished based on the geological and lithological information from the report of the legacy well Do-1C close to the target storage site. Thus, the lower member comprises three layers, from bottom to top (Figure 4-13):

- shale in direct contact with the aquifer;
- dolomite and marl;
- four limestone-dominated layers.

The PilotSTRATEGY project has received funding from the European Union's Horizon 2020 research and innovation programme under grant agreement No. 101022664

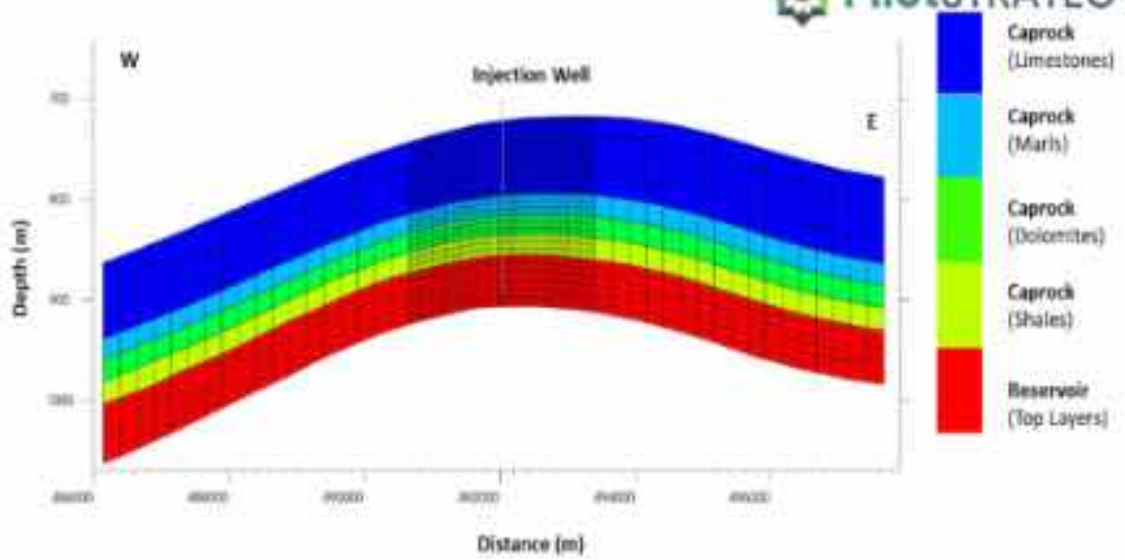


*Figure 4-13: Vertical section illustrating the reservoir model used in this task comprising the five model regions: the top layers of the reservoir, and the four caprock layers discretized based on the distinct lithologies that compose the upper and lower members of the caprock. For the location of this section refer to Figure 4-12.*

The final modelling setup step consisted of applying a local grid refinement in the injection well area (Figure 4-13) to better capture mineralogical contrasts that strongly govern reactivity and transport barriers. From a numerical perspective, particular attention was given to grid resolution in the vicinity of the injection well, where strong gradients in pressure, saturation, and geochemical variables are expected. Accordingly, a locally refined grid zone of 2x2 km was implemented around the injection well, with each grid block subdivided into 5x5x3 cells in the horizontal and vertical directions, respectively, that yields cells of 50x50x6m. This refinement ensures a better representation of near-well $CO_2$ plume development and early-time geochemical processes, while a coarser grid is applied in far-field regions for computational efficiency. This multiscale discretization strategy allows the model to resolve both short-term, localized effects near the injection point and the long-term, basin-scale evolution of $CO_2$ migration and its interaction with the caprock.

The 3D grid for the dynamic simulations comprises 108 585 cells (46 cells in the i-direction, 45 cell in the j-direction and 13 cells in the k-direction). The vertical thickness of the cells was defined as 15 m for the caprock layers and 10 m for the reservoir layers. As mentioned before, a local grid refinement was then applied in the area of the injection well (Figure 4-14).

The PilotSTRATEGY project has received funding from the European Union's Horizon 2020 research and innovation programme under grant agreement No. 101022664

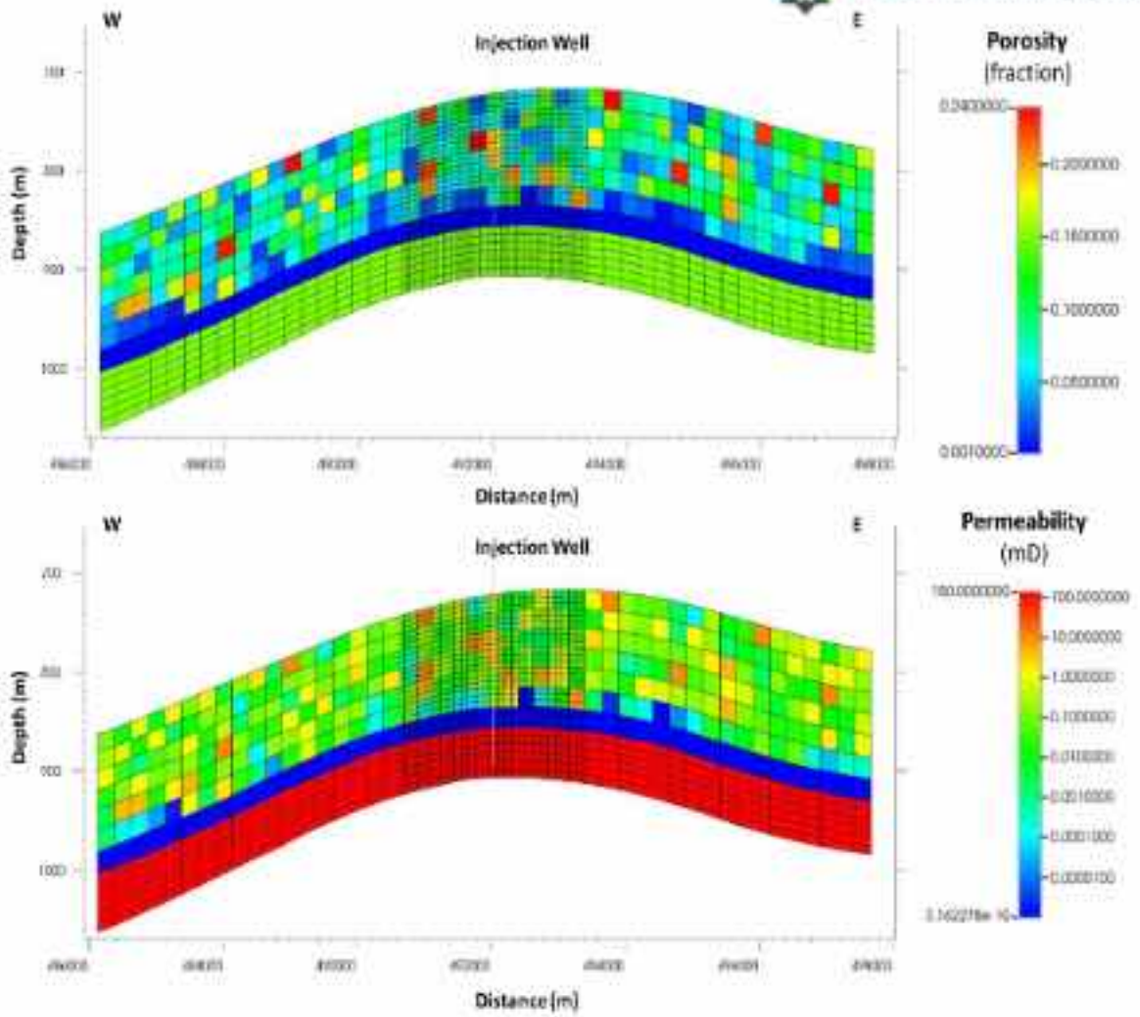


*Figure 4-14: Vertical sections illustrating the porosity and horizontal permeability for the reservoir and caprock, according to each lithofacies present in both upper and lower geological members of the caprock. For the location of this section refer to Figure 4-12.*

The petrophysical properties of the reservoir, both for porosity and permeability, were defined homogeneously based on the median values of the reservoir from the 3D static modelling (Pereira et al., 2024). This was assumed as the most relevant aspect for the development of this task is the interface between the reservoir and the caprock to evaluate the $CO_2$-rock geochemical interactions. For the caprock, and since the lithological discretization was performed, the petrophysical properties were determined by applying stochastic simulation methods in a required pre-processing and characterization task based on the 3D static models (Pereira et al., 2024) and the well log data from the legacy well Do-1C by honouring the main statistics (mean and variance) for each caprock lithofacies. The resulting models for porosity and (horizontal) permeability are illustrated in Figure 4-14.

#### 5.3.1.2 *Initial state and boundary conditions*

Prior to $CO_2$ injection, the model is initialized to a realistic geochemical equilibrium state through a 1000-year steady-state simulation without injection. This initialization phase allows fluid–rock interactions to evolve under constant in situ pressure, temperature, and boundary conditions until aqueous chemistry and mineral volumes reach equilibrium, eliminating artificial transients.

The PilotSTRATEGY project has received funding from the European Union's Horizon 2020 research and innovation programme under grant agreement No. 101022664

Boundary conditions include no-flow lateral boundaries for the caprock to avoid edge effects, a closed top boundary at the upper caprock surface. In contrast, the aquifer was set to have open lateral boundaries.

$CO_2$ is injected at a constant mass rate of 15 kg/s for 10 years, followed by a long-term (1000-years) post-injection simulation period, aiming for the simulated $CO_2$ plume to reach the aquifer–caprock interface and come into direct contact with the lower caprock layers. This setup provides a robust reference for evaluating long-term caprock response under conditions of direct plume contact, enabling a detailed assessment of $CO_2$-induced geochemical alterations within each caprock unit. The long simulation period allows slow geochemical processes to be fully captured.

The initial brine composition is defined with major ions representative of deep formation water, yielding an alkaline pH of 9.5 (Afonso et al., 2025). The chemical composition of the caprock brine is explicitly defined in the model and is reported in (Table 4-6).

*Table 4-6: Brine chemical composition.*

| Aqueous Elements | Concentrations (ppm) |
|---|---|
| $Al^{3+}$ | 2.30 |
| $Ca^{2+}$ | 36.19 |
| $K^{+}$ | 5.77 |
| $Mg^{2+}$ | 8.63 |
| $Na^{+}$ | 20458.80 |
| $SiO_2$ | 8.29 |
| $Cl^{-}$ | 31560.00 |

The mineralogical composition of the heterogeneous caprock units, defined in terms of weight percentages of quartz, K-feldspar, calcite, dolomite, and kaolinite, is summarized in Table 4-7, which represents the reference mineral composition used in the base case scenario. The upper limestone member is characterized by a dominant calcite content, whereas the lower member exhibits pronounced mineralogical heterogeneity, with clay-rich marl, carbonate-rich dolomite, and quartz- and clay-dominated shale.

*Table 4-7: Mineral composition of the caprock geological members and for the specified lithologies.*

| Samples (wt%) | Lithologies | Quartz | Feld-K | Calcite | Dolomite | Kaolinite |
|---|---|---|---|---|---|---|
| **Upper member** | Limestones | 7 | 2 | 79 | 10 | 2 |
| **Lower member** | Marls | 15 | 3 | 32 | 5 | 45 |
| | Dolomites | 5 | 1 | 15 | 75 | 4 |
| | Shales | 25 | 5 | 5 | 2 | 63 |

### 5.3.2 Modelling Approach

Key features of the modelling approach include heterogeneous mineral distributions (Table 4-7), realistic brine chemistry (Table 4-6), equilibrium initialization, and conservative injection placement to facilitate direct plume–caprock contact. The modelling approach aims to capture the coupled effects of multiphase flow, geochemical

The PilotSTRATEGY project has received funding from the European Union's Horizon 2020 research and innovation programme under grant agreement No. 101022664

reactions, and long-term evolution of fluid and rock properties, with particular emphasis on evaluating the integrity of the caprock under $CO_2$ storage conditions. Overall, this base case modelling framework provides a robust reference scenario for evaluating the long-term integrity of the caprock under $CO_2$ sequestration conditions. The results obtained from this reference scenario serve as a benchmark for subsequent uncertainty analyses.

An uncertainty analysis was performed to evaluate the impact of uncertainties in caprock mineralogical composition on the geochemical response to $CO_2$ injection and long-term storage. In addition to the base-case mineralogy, two alternative mineralogical scenarios were considered, representing plausible variations in lithological composition within the caprock. These scenarios were defined to reflect contrasts in carbonate content, clay abundance, and silicate minerals, which are key factors controlling buffering capacity, mineral reactivity, and the long-term evolution of sealing properties.

Compared to the base case, Scenario 1 is characterized by a more heterogeneous mineralogical distribution, with a balanced contribution of carbonate minerals (calcite and dolomite) and a significant presence of clay minerals, particularly kaolinite, in the marl and shale units. This scenario emphasizes clay-rich facies in the lower member and relatively moderate carbonate dominance in the upper limestone unit. In contrast, Scenario 2 exhibits a stronger dominance of carbonate minerals, especially calcite and dolomite, in both the upper and lower members, with reduced clay content in most lithologies except for shale. As a result, Scenario 2 represents a carbonate-dominated end-member compared to the base case, while Scenario 1 reflects a more mixed carbonate–clay system.

The differences between the two scenarios and the base case are summarized in Tables 4-8 and 4-9, highlighting the shift in dominant mineral phases within each lithological unit.

In uncertainty analysis, an additional worst-case scenario was considered to evaluate the potential impact of caprock petrophysical properties on $CO_2$ vertical migration and sealing performance. Unlike the previous scenario of the uncertainty analyses, which focused on mineralogical variability, this scenario specifically targets the petrophysical characteristics of the shale layer located at the base of the caprock.

*Table 4-8: Mineral composition of the caprock for the Scenario 1 for the uncertainty analysis.*

| Scenario 1 for uncertainty analysis | Lithologies/ Minerals (wt%) | Quartz | K-Feldspar | Calcite | Dolomite | Kaolinite |
|---|---|---|---|---|---|---|
| **Upper member** | Limestones | 13 | 1 | 66 | 16 | 5 |
| **Lower member** | Marls | 19 | 2 | 43 | 7 | 30 |
| | Dolomites | 9 | 1 | 12 | 70 | 8 |
| | Shales | 21 | 5 | 9 | 4 | 61 |

The PilotSTRATEGY project has received funding from the European Union's Horizon 2020 research and innovation programme under grant agreement No. 101022664

*Table 4-9: Mineral composition of the caprock for the Scenario 2 for the uncertainty analysis.*

| Scenario 2 for uncertainty analysis | Lithologies/ Minerals (wt%) | Quartz | K-Feldspar | Calcite | Dolomite | Kaolinite |
|---|---|---|---|---|---|---|
| **Upper member** | Limestones | 6 | 2 | 83 | 8 | 2 |
| **Lower member** | Marls | 13 | 3 | 28 | 4 | 52 |
| | Dolomites | 4 | 1 | 12 | 80 | 3 |
| | Shales | 21 | 4 | 4 | 2 | 69 |

In the base case, the shale layer is characterized by a very low mean effective porosity (0.0003) with a variance of 0.002, and a low mean permeability (0.002 mD) with a variance of 50 mD, resulting in an effectively impermeable barrier. In the additional worst-case scenario, the shale layer porosity was intentionally increased to a high mean value of 0.04, with a standard deviation of 0.005, representing a degraded or partially absent shale barrier. The permeability of the shale layer was also adjusted accordingly based on the relationship with the porosity (Pereira et al., 2024).

All other model parameters were kept unchanged. This scenario therefore isolates the effect of petrophysical degradation of the shale layer on $CO_2$ migration, simulating conditions representative of a more marl–carbonate-dominated caprock in which the basal shale layer is either absent or laterally discontinuous.

### 5.3.3 Results

This subsection presents the results obtained for the base case scenario, which serves as the reference configuration for evaluating $CO_2$ injection into the aquifer and its potential impact on the overlying caprock. The analysis focuses on $CO_2$ plume migration, dissolved $CO_2$ distribution, pH evolution, mineral reactions, and porosity changes within both the aquifer and the caprock. These results provide a benchmark against which the scenarios of the uncertainty analysis are later compared and allow for a systematic assessment of caprock integrity under reference conditions.

#### *5.3.3.1 Mineral precipitation and dissolution*

Before the onset of $CO_2$ injection, the model was run for 1000 years without any injection, in order to establish a geochemical steady state. During this period, the simulated mineral mole changes in the caprock remain extremely limited, indicating that the system has reached a quasi-steady state under *in situ* conditions.

Table 4-10 illustrates the temporal evolution of mineral molar changes (in gmoles) within the caprock for the base case scenario, covering three key stages: the steady-state period prior to $CO_2$ injection, the end of the 10-year injection phase, and the long-term monitoring period extending to 1000 years of a post-injection period. The caprock mineralogical composition used in the simulations (Table 4-7), together with the initial brine chemistry (Table 4-6), governs the geochemical response observed throughout the simulation.

The PilotSTRATEGY project has received funding from the European Union's Horizon 2020 research and innovation programme under grant agreement No. 101022664

*Table 4-10: Mineral molar changes within the caprock.*

| Years | Mineral changes (gmoles) | | | | |
|---|---|---|---|---|---|
| | Quartz | K-feldspar | Calcite | Dolomite | Kaolinite |
| 0 | -7.37E+04 | -8.37E+05 | 5.54E+05 | 1.74E+06 | 6.94E+05 |
| 10 | -7.60E+04 | -1.70E+06 | -7.26E+08 | -4.88E+08 | 7.65E+05 |
| 1000 | 2.77E+07 | -1.11E+08 | -1.47E+09 | -9.82E+08 | -4.42E+07 |

These trends indicate a buffered geochemical environment dominated by carbonate stability, in line with the carbonate-rich composition of both the upper limestone member and the lower dolomitic units of the caprock (Table 4-7). Overall, the steady-state results confirm that the caprock system is geochemically stable prior to $CO_2$ injection.

Following 10 years of continuous $CO_2$ injection into the underlying aquifer, a marked shift in mineral reactions is observed as illustrated in Figure 4-15. The most significant changes occur in the carbonate minerals, with substantial dissolution of calcite and dolomite (see Table 4-10. This behaviour is attributed to localized acidification induced by $CO_2$ dissolution at the aquifer–caprock interface, leading to enhanced carbonate reactivity. Despite this dissolution, the reactions remain spatially limited and do not imply structural degradation of the caprock.

Silicate minerals show a contrasting behaviour: K-feldspar dissolution intensifies, while kaolinite continues to precipitate, suggesting secondary clay formation as a result of feldspar alteration. Quartz dissolution remains minor. These coupled reactions indicate an active but controlled geochemical adjustment driven by transient $CO_2$ exposure rather than pervasive alteration of the caprock mineral framework.

The PilotSTRATEGY project has received funding from the European Union's Horizon 2020 research and innovation programme under grant agreement No. 101022664

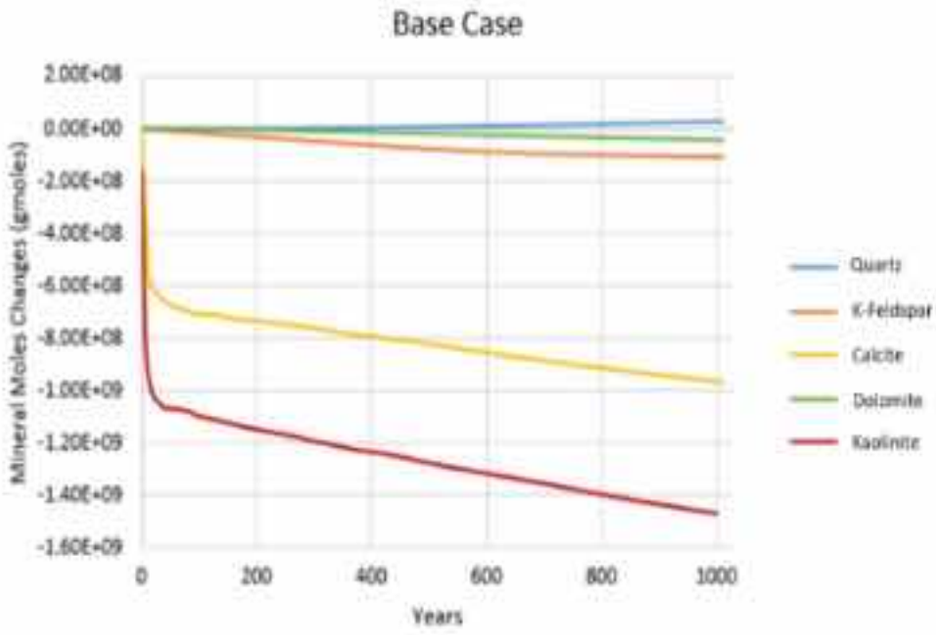


*Figure 4-15: Evolution of the mineral composition of the caprock on the long-term.*

At the end of the 1000-years period, the system evolves toward a new geochemical equilibrium. Carbonate dissolution continues, with cumulative dissolution of calcite and dolomite. However, these changes must be interpreted in the context of the large initial carbonate inventory of the caprock, particularly within the limestone and dolomite units, implying that the relative impact on bulk mineralogy remains limited.

Quartz mineral shows significant net precipitation, reflecting long-term silica redistribution and re-precipitation (amorphous silica or chalcedony) following earlier dissolution stages. In contrast, kaolinite transitions from precipitation to dissolution, indicating clay mineral adjustment under stabilized pH conditions during post-injection equilibration. K-feldspar continues to dissolve, although at a much lower rate compared to carbonate minerals.

#### *5.3.3.2 Evolution of the dissolved $CO_2$ plume*

Figure 4-16 shows the spatial and temporal evolution of gas saturation during 10 years of continuous $CO_2$ injection and 1000 years of post-injection monitoring, providing key insight into plume behaviour and caprock sealing performance.

The PilotSTRATEGY project has received funding from the European Union's Horizon 2020 research and innovation programme under grant agreement No. 101022664

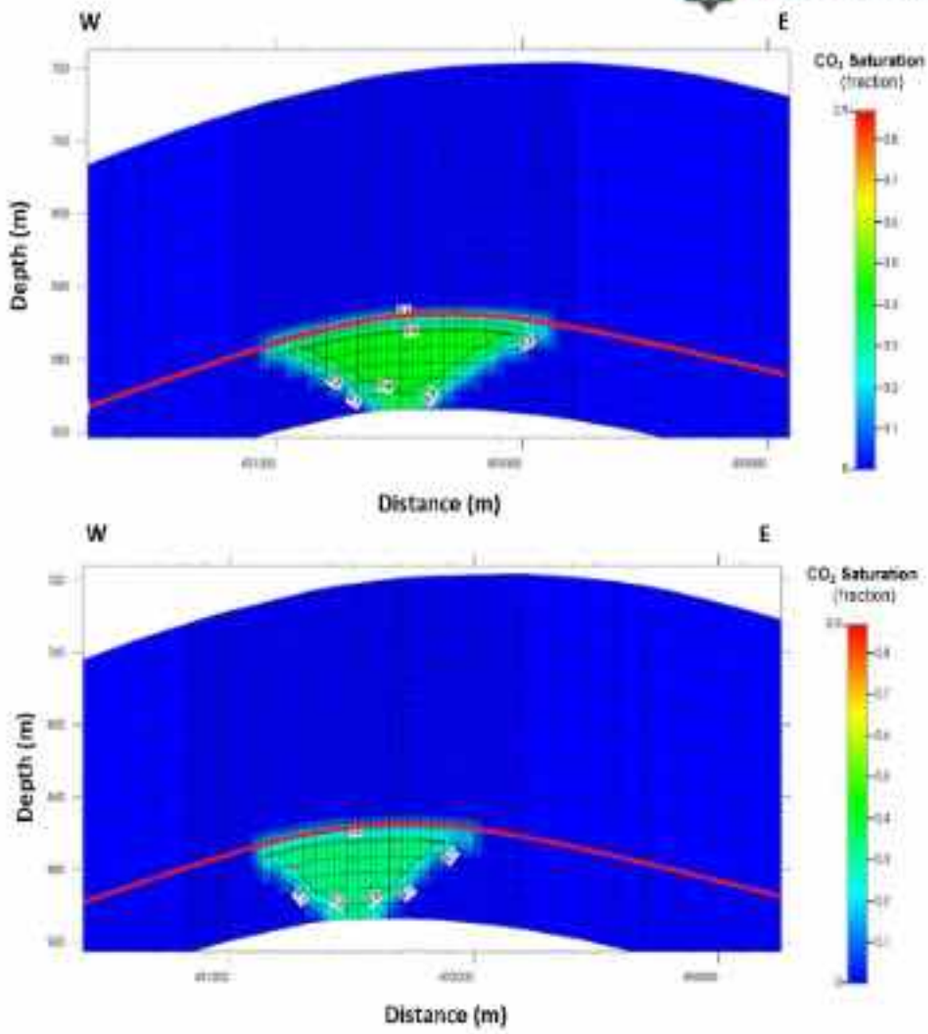


*Figure 4-16. Vertical sections of the spatial distribution of $CO_2$ saturation in the aquifer and caprock after 10 years of $CO_2$ injection (initial state) (top) and 1000 years of post-injection period (bottom). The red line illustrates the interface between the reservoir and the caprock. For the location of this section refer to Figure 4-12.*

During injection, a well-defined buoyant $CO_2$ plume develops within the aquifer. Maximum gas saturation reaches ~0.78 in the injection well block and ~0.43 in the adjacent block beneath the caprock. Importantly, these values occur exclusively within the aquifer. No gas-phase $CO_2$ enters the caprock, indicating that its capillary entry pressure and sealing capacity are not exceeded under sustained injection. After injection ceases, gas saturation progressively decreases due to dissolution and lateral plume spreading. After 1000 years, saturation declines to ~0.49 in the well block and ~0.34 below the caprock. Redistribution is dominated by horizontal migration rather than upward flow, further reducing leakage risk.

The PilotSTRATEGY project has received funding from the European Union's Horizon 2020 research and innovation programme under grant agreement No. 101022664

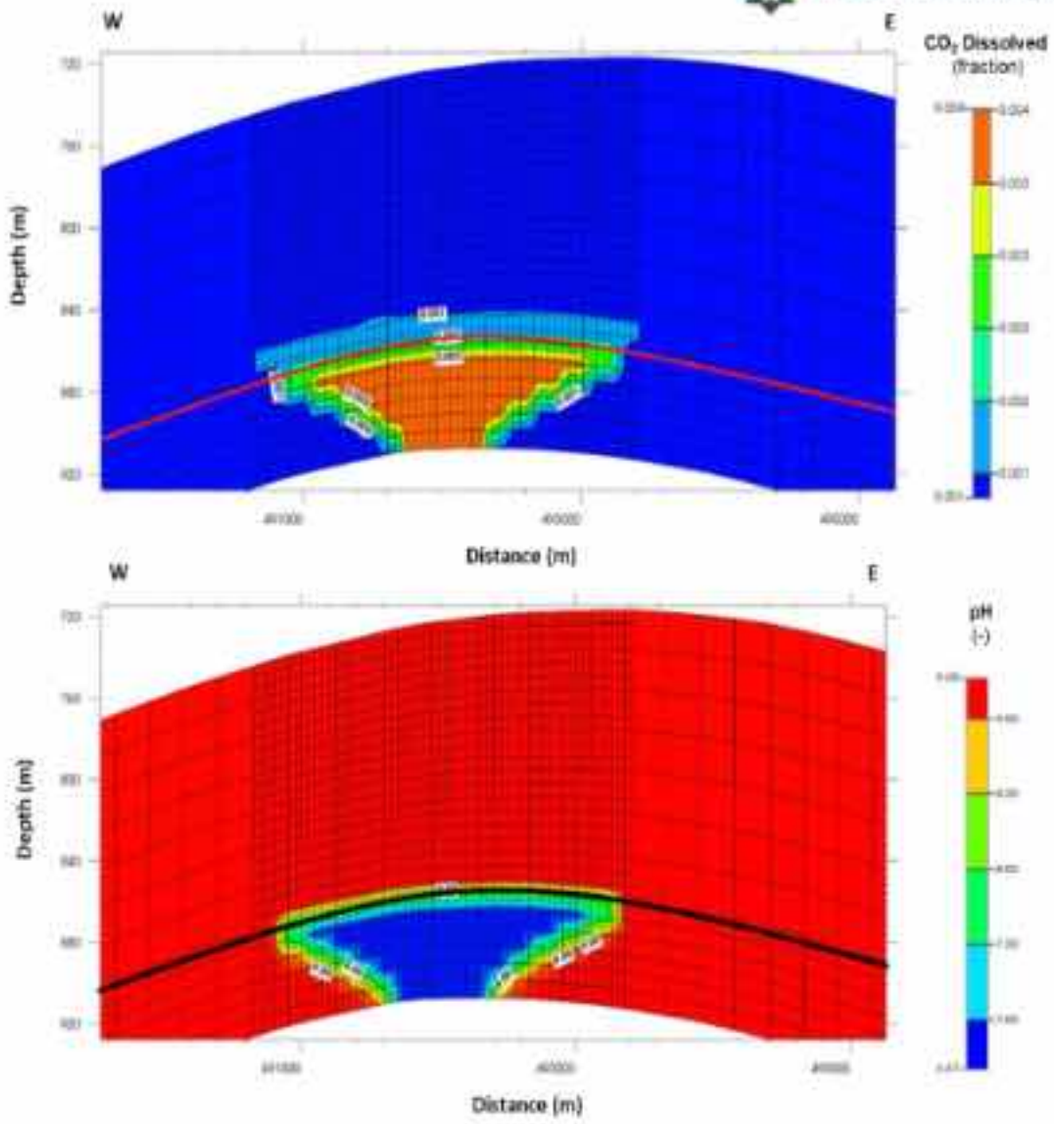


*Figure 4-17. Vertical sections of the spatial distribution of dissolved $CO_2$ mole fraction (top) and pH (bottom) after 10 years of continuous $CO_2$ injection (initial state). The red and black lines illustrate the interface between the reservoir and the caprock. For the location of this section refer to Figure 4-12.*

Critically, gas saturation in all caprock grid blocks remains effectively zero ($\leq 10^{-5}$) throughout both injection and post-injection periods. Even after 1000 years, no gas invasion occurs, confirming the robustness of the caprock seal and the absence of numerical or physical leakage pathways. Combined with limited geochemical alteration, the results demonstrate secure long-term structural and residual trapping within the aquifer.

Figure 4-17 presents the dissolved $CO_2$ mole fraction and pH distribution after 10 years of injection, illustrating the geochemical response of the system. Within the aquifer, dissolved $CO_2$ reaches a maximum mole fraction of ~0.004 near the injection well, reflecting efficient gas–liquid mass transfer and contributing to solubility trapping. Concentrations decrease laterally due to dilution and buffering reactions. In contrast, dissolved $CO_2$ in the caprock remains below 0.001, indicating restricted upward transport and limited chemical exposure.

The PilotSTRATEGY project has received funding from the European Union's Horizon 2020 research and innovation programme under grant agreement No. 101022664

Aquifer pH decreases from 9.5 to ~6.72 near the well due to carbonic acid formation, promoting buffering reactions. However, caprock pH remains close to initial alkaline conditions, demonstrating minimal acidification and strong buffering capacity.

Overall, Figures 4-16 and 4-17 show that $CO_2$ remains confined to the aquifer, where dissolution and lateral spreading dominate plume evolution. Both hydraulic and geochemical sealing mechanisms remain effective, and caprock integrity is preserved over the simulated long-term period.

#### 5.3.3.3 *Porosity changes*

Figure 4-18 presents the porosity evolution in the coupled aquifer–caprock system after 10 years of continuous $CO_2$ injection (base case). Porosity changes within the aquifer are minor and spatially localized, generally ranging between −0.0005 and −0.001 across most of the $CO_2$ plume. These small variations reflect a balance between dissolution and precipitation reactions and are negligible relative to the initial reservoir porosity, indicating no impairment of storage capacity or injectivity.

The largest porosity reduction (up to ~−0.002) occurs at the outer margin of the plume, away from the injection well. This localized effect results from enhanced mineral precipitation at mixing zones between $CO_2$-rich brine and native formation water. However, the impact remains limited in spatial extent and does not extend toward the caprock.

No measurable porosity change is observed within the caprock. As shown in Figure 4-18, geochemical alterations are confined to the aquifer, and the caprock preserves its structural and sealing integrity under base case conditions.

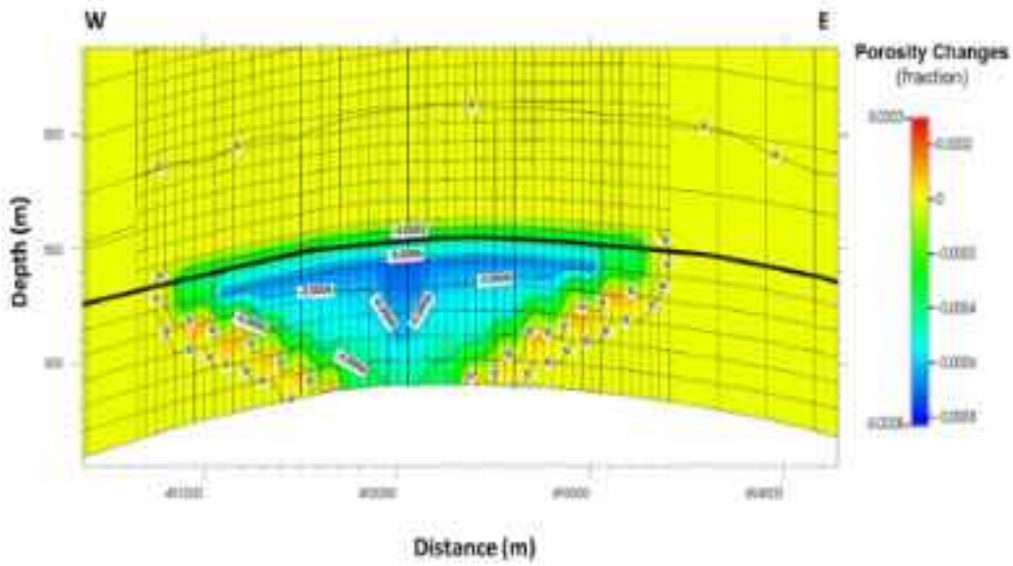


*Figure 4-18: Vertical section of the spatial distribution of porosity change after 10 years of $CO_2$ injection (initial state). The black line illustrates the interface between the reservoir and the caprock. For the location of this section refer to Figure 4-12.*

### 5.3.4 Uncertainty Analysis

#### 5.3.4.1 *Impacts of mineral composition*

Figure 4-19 compares the cumulative mineral mass changes (in gmoles) within the caprock for Scenario 1 and Scenario 2, at the initial state and 1000 years of post-injection evolution, thereby providing a comprehensive assessment of caprock geochemical sensitivity to mineralogical uncertainty.

The PilotSTRATEGY project has received funding from the European Union's Horizon 2020 research and innovation programme under grant agreement No. 101022664

Across both scenarios, the same overall reaction trends are observed. Carbonate minerals, namely calcite and dolomite, exhibit the largest cumulative mass losses, with calcite dissolution reaching approximately $-1.44 \times 10^9$ to $-1.48 \times 10^9$ gmoles and dolomite dissolution ranging between $-9.65 \times 10^8$ and $-9.88 \times 10^8$ gmoles. These values are remarkably consistent between Scenario 1 and Scenario 2 and closely match those obtained for the base case. The similarity in carbonate dissolution magnitudes indicates that the geochemical response of the caprock is primarily governed by $CO_2$-driven acidification and buffering reactions, rather than by moderate variations in initial mineral proportions.

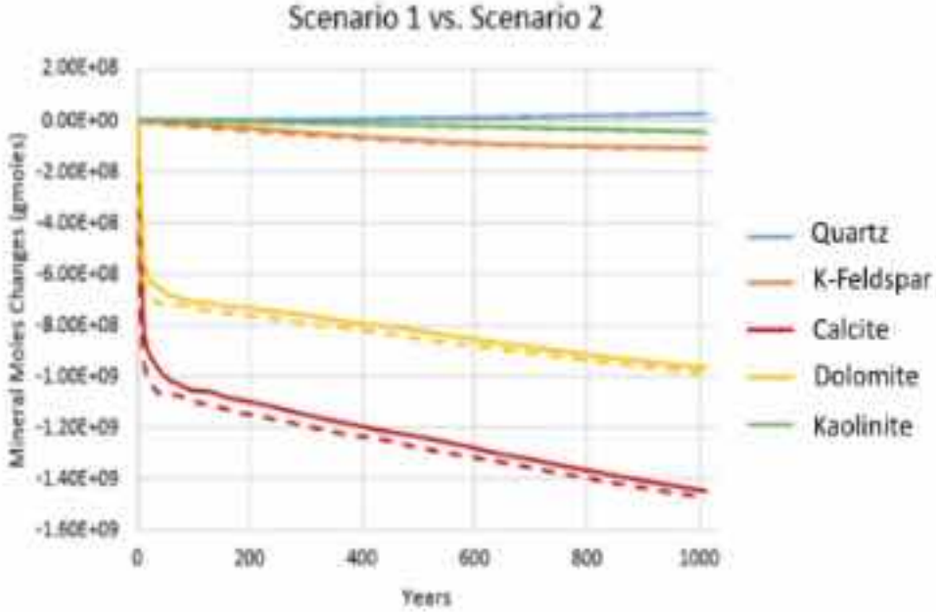


*Figure 4-19: Evolution of the mineral mole changes for the scenarios of uncertainty analysis on the long-term (solid lines: Scenario 1; dashed lines: Scenario 2).*

Silicate and clay minerals display more limited but systematic behaviour. K-feldspar undergoes sustained dissolution in both sensitivity scenarios, with cumulative losses of approximately $-1.08 \times 10^8$ to $-1.10 \times 10^8$ gmoles, again closely aligned with the base case response. This dissolution is accompanied by long-term amorphous silica or chalcedony precipitation (modelled as quartz), with gains of approximately $+2.6 \times 10^7$ to $+2.7 \times 10^7$ gmoles, reflecting silica redistribution and re-equilibration during the post-injection phase. Kaolinite shows moderate net dissolution ($-4.3 \times 10^7$ to $-4.4 \times 10^7$ gmoles), consistent with clay mineral adjustment under stabilized chemical conditions.

Importantly, the differences between Scenario 1, Scenario 2, and the base case are negligible across all minerals, despite the imposed variations in caprock mineralogical composition. This insensitivity demonstrates that the caprock geochemical evolution is robust and not strongly dependent on moderate heterogeneity in mineral content. The dominant reaction pathways and cumulative reaction magnitudes remain effectively unchanged across scenarios.

$CO_2$ injection produces only minor, localized geochemical and petrophysical effects that remain confined to the aquifer, while plume migration is predominantly lateral and vertical containment is fully maintained across all scenarios.

As shown in Figure 4-20, the $CO_2$ plume geometry, lateral extent, and long-term evolution (10 years of injection plus 1000 years of post-injection) are nearly identical for the base case and both

The PilotSTRATEGY project has received funding from the European Union's Horizon 2020 research and innovation programme under grant agreement No. 101022664

mineralogical sensitivity scenarios. Migration is controlled by aquifer properties and buoyancy, with no upward penetration into the caprock and negligible gas saturation within the sealing formation.

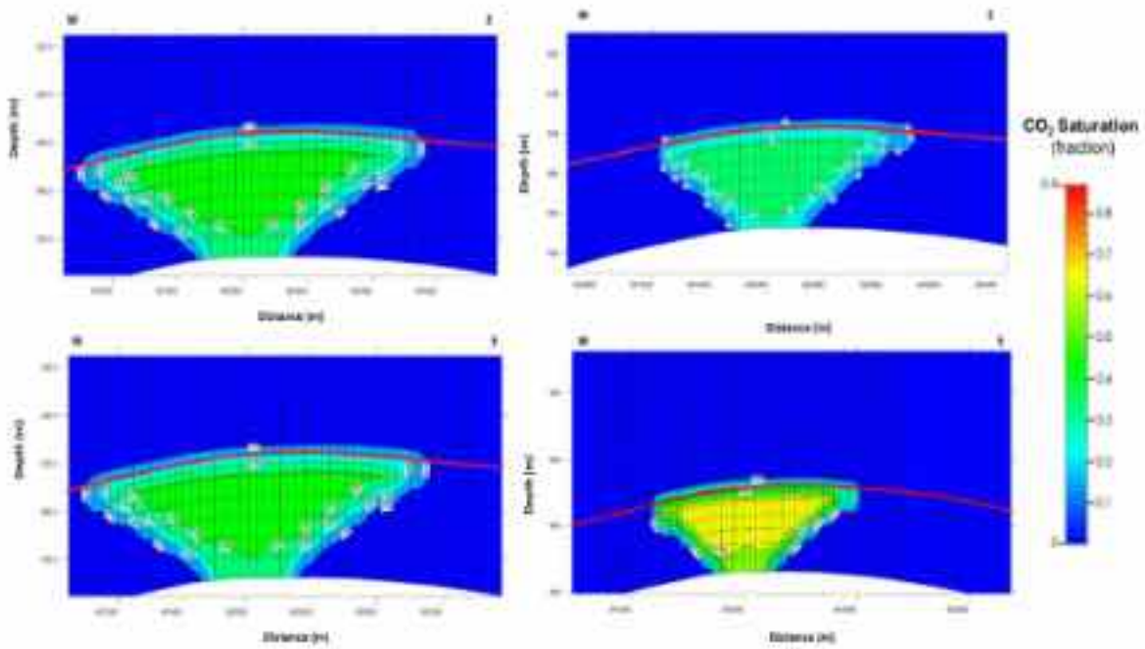


*Figure 4-20: Vertical sections of the spatial distribution of the $CO_2$ saturation in the aquifer for the Scenario 1 (top) and Scenario 2 (bottom) of the uncertainty analysis after injection (initial state) (left) and the long-term period of 1000 years (right). The red lines illustrate the interface between the reservoir and the caprock. For the location of this section refer to Figure 4-12.*

Consistently, Figure 4-21 demonstrates that elevated dissolved $CO_2$ concentrations and localized pH reduction occur only within the aquifer near the injection well. The caprock exhibits negligible dissolved $CO_2$ and no measurable acidification in any scenario, indicating restricted vertical transport and minimal geochemical interaction within the seal.

Porosity evolution follows the same pattern. As illustrated in Figure 4-22, porosity reductions within the plume are minor (−0.0005 to −0.001), with maximum localized decreases of ~−0.002 at plume margins due to precipitation-dominated reactions. No porosity alteration is detected within the caprock. Similarly, Figure 4-19 shows that all scenarios converge toward nearly identical long-term geochemical states, despite differences in initial caprock mineralogy.

The PilotSTRATEGY project has received funding from the European Union's Horizon 2020 research and innovation programme under grant agreement No. 101022664

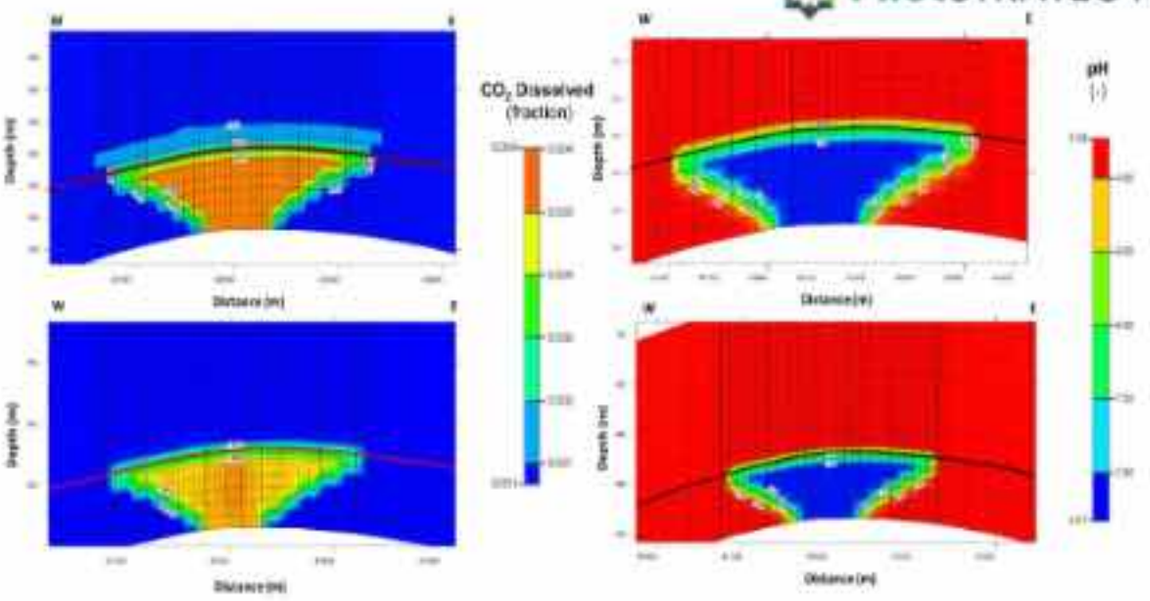


*Figure 4-21: Vertical sections of the spatial distribution of the dissolved $CO_2$ (left) and pH (right) after 10 years of injection (initial state) for the Scenario 1 (top) and Scenario 2 (bottom) of the uncertainty analysis. The red and black lines illustrate the interface between the reservoir and the caprock. For the location of this section refer to Figure 4-12.*

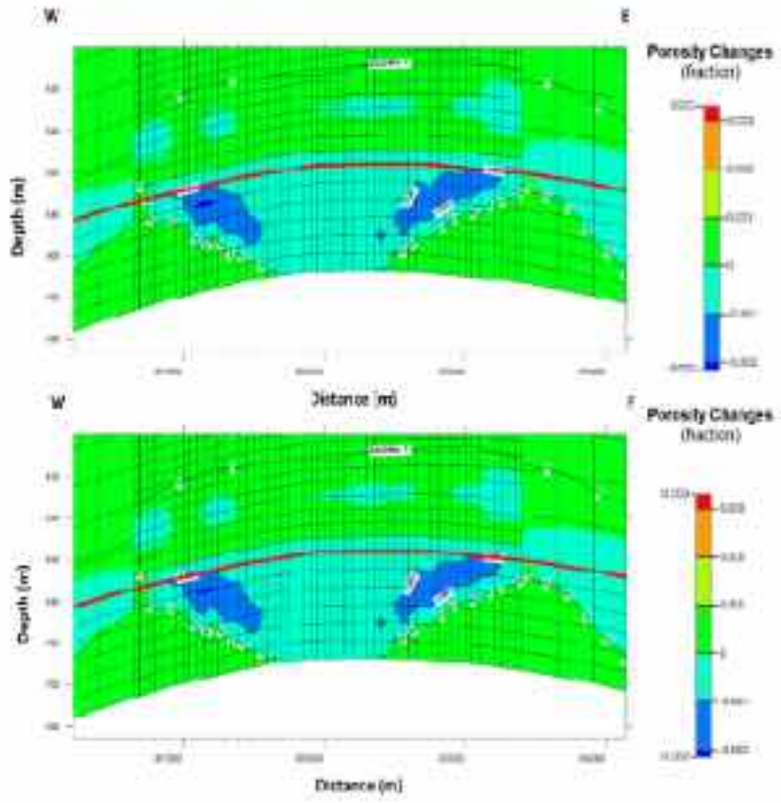


*Figure 4-22: Vertical sections of the spatial distribution of the porosity changes for Scenarios 1 (top) and Scenario 2 (bottom) of the uncertainty analysis. The red lines illustrate the interface between the reservoir and the caprock. For the location of*

Overall, mineral reactions do not generate adverse petrophysical consequences, and caprock sealing capacity is preserved under all investigated conditions. The close agreement between the base case and sensitivity scenarios confirms that plume dynamics, aqueous geochemistry, and porosity evolution are controlled primarily by aquifer processes. Therefore, the storage system demonstrates

The PilotSTRATEGY project has received funding from the European Union's Horizon 2020 research and innovation programme under grant agreement No. 101022664

strong robustness to caprock mineralogical uncertainty and maintains long-term containment integrity.

#### 5.3.4.2 *Impacts of petrophysical properties*

In the worst-case scenario, the shale layer's mean porosity was intentionally increased from 0.0003 to 0.04 to simulate a degraded or partially absent barrier. Consequently, the permeability was adjusted according to the relationship established by Pereira et al. (2024), effectively transitioning the layer from an impermeable seal to a more conductive state for sensitivity analysis.

Figure 4-23 illustrates the spatial evolution of the $CO_2$ plume in the aquifer–caprock system after 10 years of continuous injection and following 1000 years of post-injection period for the petrophysical worst-case scenario in the caprock, in which the shale layer exhibits relatively elevated porosity and permeability compared to the base case scenario.

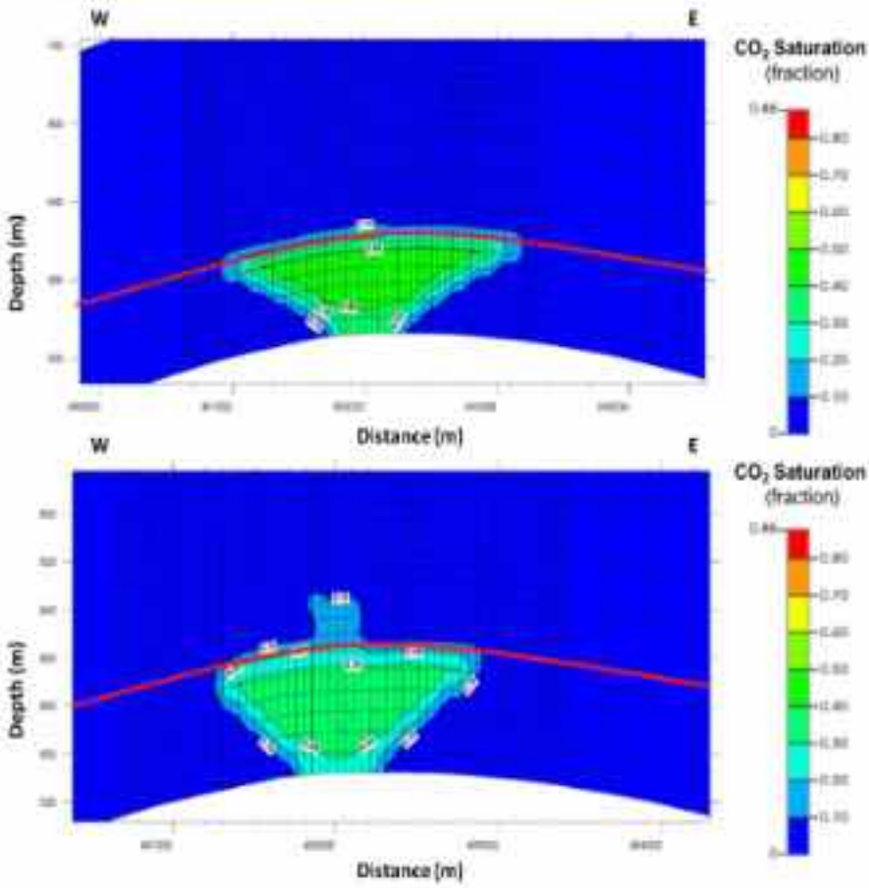


*Figure 4-23: Vertical sections of $CO_2$ saturation after 10 years on continuous injection (initial state) (left) and after 1000 years (right) illustrating the impact of increased shale porosity and permeability on $CO_2$ migration into the caprock. The red lines illustrate the interface between the reservoir and the caprock. For the location of this section refer to Figure 4-12.*

After 10 years of injection, the $CO_2$ plume remains largely confined within the aquifer; however, limited upward penetration into the basal shale layer is observed at the aquifer–caprock interface (Figure 4-23). This localized migration is directly linked to the significantly increased porosity and permeability of the shale layer, which reduces its effectiveness as a hydraulic barrier compared to the base case and mineralogical sensitivity scenarios. During the long-term period of 1000 years, more pronounced $CO_2$ migration into the shale layer occurs. In certain localized areas, $CO_2$ penetrates the

The PilotSTRATEGY project has received funding from the European Union's Horizon 2020 research and innovation programme under grant agreement No. 101022664

full thickness of the shale layer, with gas saturation reaching values of up to 0.2. This behavior reflects the enhanced vertical transmissivity induced by the elevated petrophysical properties and the sustained buoyancy-driven migration of $CO_2$ over long timescales.

Despite this localized penetration, $CO_2$ migration remains confined within the shale layer, and no leakage into the overlying caprock units or higher geological formations is observed. This outcome is primarily attributed to the large overall thickness of the caprock (exceeding 100 m), which provides substantial vertical separation and containment capacity. Consequently, even under deliberately pessimistic assumptions regarding shale petrophysical properties, the caprock system continues to prevent $CO_2$ escape into overlying formations. These results highlight the importance of shale continuity and low permeability for caprock performance, while also confirming the robustness of the storage system under extreme but plausible conditions.

Figure 4-24 presents the spatial distribution of dissolved $CO_2$ concentration and the associated pH field after 10 years of continuous $CO_2$ injection for the worst-case petrophysical scenario.

The dissolved $CO_2$ distribution shows that, in addition to the aquifer, significant amounts of $CO_2$ dissolve within the basal shale layer of the caprock. In localized zones near the aquifer–caprock interface, dissolved gas mole fractions reach values of up to 0.003, which are comparable to those observed in $CO_2$-dominated regions of the aquifer. This behaviour indicates enhanced upward migration of $CO_2$-rich brine into the shale layer, facilitated by the increased petrophysical properties of this unit.

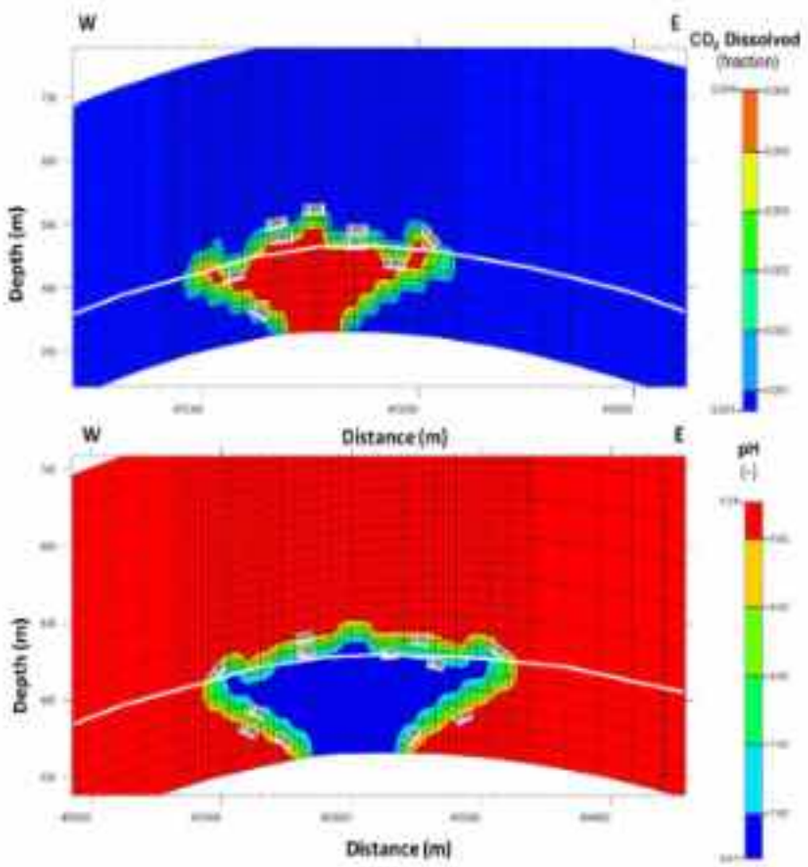


The PilotSTRATEGY project has received funding from the European Union's Horizon 2020 research and innovation programme under grant agreement No. 101022664

*Figure 4-24: Vertical sections of the spatial distribution of the dissolved $CO_2$ (top) and pH (bottom) evolution under degraded shale petrophysical conditions. The white lines illustrate the interface between the reservoir and the caprock. For the location of this section refer to Figure 4-12.*

The pH distribution reflects this enhanced geochemical interaction. Within the aquifer, pH decreases in response to $CO_2$ dissolution, consistent with previous scenarios. Notably, within the shale layer of the caprock, pH locally decreases from initial alkaline values (~9.25) to approximately 6.5, particularly near the injection well and at the aquifer–caprock contact. This localized acidification is directly associated with the presence of dissolved $CO_2$ and carbonic acid formation in zones where vertical migration is permitted.

Despite these localized geochemical perturbations, pH changes remain confined to the basal shale layer and do not propagate into the overlying caprock units. The absence of widespread acidification suggests that buffering reactions and limited vertical transport effectively restrict the extent of chemical alteration. Consequently, although the shale layer experiences increased geochemical reactivity under worst-case petrophysical conditions, the overall caprock system retains its capacity to isolate $CO_2$ from higher geological formations.

Figure 4-25 illustrates the spatial distribution of porosity changes in the aquifer–caprock system for the worst-case petrophysical scenario. The results show that porosity variations are minor and comparable in magnitude and spatial pattern to those observed in the base case and in Scenarios 1 and 2.

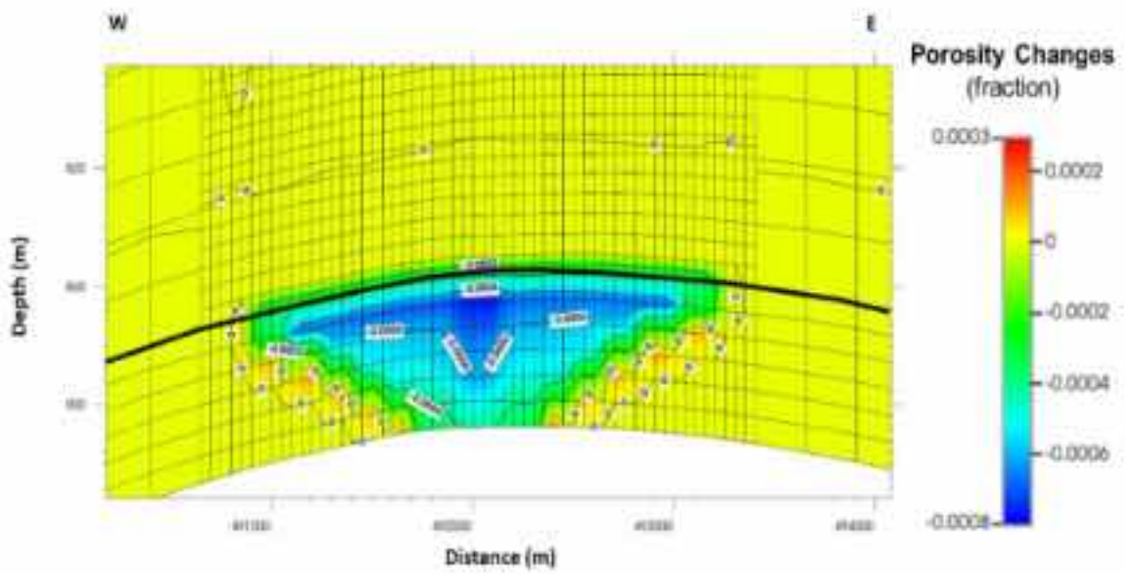


*Figure 4-25: Vertical section of the spatial distribution of porosity changes of the reservoir–caprock system in the scenario under degraded shale petrophysical conditions. The black line illustrates the interface between the reservoir and the caprock. For the location of this section refer to Figure 4-12.*

Within the reservoir, small porosity changes occur as a result of mineral dissolution and precipitation driven by $CO_2$–brine–rock interactions. These variations remain negligible relative to the initial porosity and do not affect reservoir performance. In the caprock, including the shale layer, porosity changes are minimal, indicating that mineralogical activity remains limited despite enhanced $CO_2$ and brine migration.

The similarity of porosity evolution across all scenarios suggests that geochemical reactions are weak and well buffered, and that changes in

The PilotSTRATEGY project has received funding from the European Union's Horizon 2020 research and innovation programme under grant agreement No. 101022664

shale petrophysical properties primarily influence fluid migration rather than mineral reactivity. As a result, porosity alterations do not contribute significantly to caprock weakening or leakage pathways.

### 5.3.5 Discussion and Conclusions

The geochemical assessment of caprock integrity demonstrates that, under reference conditions, $CO_2$ injection into the deep saline aquifer does not compromise the sealing capacity of the overlying formations. In the base case, plume migration remains confined to the aquifer over both injection and long-term monitoring periods, with geochemical reactions dominated by carbonate dissolution and limited silicate redistribution. These reactions induce only minor, spatially localized porosity changes within the aquifer and produce no measurable alterations in gas saturation, dissolved $CO_2$, pH, or porosity within the caprock, confirming its effectiveness as both a hydraulic and geochemical barrier.

The mineralogical sensitivity scenarios further reinforce this conclusion by showing that moderate variations in caprock mineral composition have a negligible influence on plume behaviour and long-term geochemical response. Despite differences in the relative abundances of carbonates, silicates, and clays, the simulated distributions of mineral mass changes, porosity evolution, dissolved $CO_2$, and pH closely mirror those of the base case. This indicates that $CO_2$-driven reactions are controlled primarily by transport processes and buffering capacity, rather than by modest mineralogical heterogeneity within the caprock.

A contrasting behaviour emerges only under the deliberately pessimistic worst-case petrophysical scenario, where the basal shale layer is assigned substantially higher porosity and permeability. In this case, limited upward migration of both free-phase and dissolved $CO_2$ occurs, leading to localized acidification and increased gas saturation within the shale. However, this migration remains confined to the basal unit and does not extend into the overlying caprock formations, demonstrating that even enhanced vertical transmissivity does not trigger large-scale leakage or destabilization of the sealing system.

Importantly, across all scenarios, porosity changes within the caprock remain negligible, indicating that $CO_2$-induced geochemical reactions do not generate significant mineral-driven weakening. These results highlight that caprock integrity is more sensitive to petrophysical degradation than to mineralogical variability, yet even under extreme petrophysical assumptions, the combination of limited vertical connectivity and substantial caprock thickness effectively restricts upward $CO_2$ migration.

Overall, the study provides strong evidence for the long-term robustness of the caprock, with integrity preserved over injection and post-injection timescales of up to 1000 years. The interplay of low vertical permeability, geochemical buffering, and structural thickness ensures effective containment, supporting the suitability of the investigated formation for long-term $CO_2$ sequestration. These findings also underscore the importance of jointly evaluating mineralogical and petrophysical uncertainties when assessing caprock performance and storage security.

The PilotSTRATEGY project has received funding from the European Union's Horizon 2020 research and innovation programme under grant agreement No. 101022664

## 5.4 Caprock integrity – Geomechanical aspects

This section presents the geomechanical integrity assessment of the caprock, focusing on its ability to maintain structural stability and sealing performance under $CO_2$ injection–induced stress and pressure changes.

First, the geomechanical dynamic model used for this analysis is introduced, including the initial stress state, boundary conditions, and key mechanical parameters. Then, the modelling approach and failure criteria applied to evaluate caprock stability are described, followed by the main results and analysis. These include the base case injection scenario and a sensitivity analysis of critical geomechanical parameters that may influence caprock integrity and long-term containment performance.

### 5.4.1 Dynamic Model

#### *5.4.1.1 Thermal-hydraulic-mechanical Model*

The geomechanical integrity of the caprock was assessed using the compositional reservoir simulator CMG-GEM (CMG, 2022), including the geomechanics module, which enables the integration of rock mechanics data along with the fluid-flow data to perform complex two-ways coupled thermal-hydraulic-mechanical (THM) dynamic simulations. The static and dynamic models developed in previous tasks of WP3 (Pereira et al., 2024; Khudhur et al., 2024) were used as a basis but were adapted to meet the specific requirements of this assessment.

Due to the intensive computational time required for these complexes coupled simulations, a sector model was extracted from the original model domain (Figure 4-26). In addition, a lateral grid-coarsening process was applied, increasing the areal cell dimensions from 250x250 m in the original static/ dynamic model to 500x500 m s for all the cells. This approach was applied to the three geological regions in this assessment: the siliciclastic reservoir of the Torres Vedras Group (Lower Cretaceous), the regional argillaceous-carbonated caprock of the Cacém Formation (Upper Cretaceous) and the overlying siliciclastic deposits of the Aveiro Group (Upper Cretaceous), which act as a potential secondary seal (Figure 4-27).

The PilotSTRATEGY project has received funding from the European Union's Horizon 2020 research and innovation programme under grant agreement No. 101022664

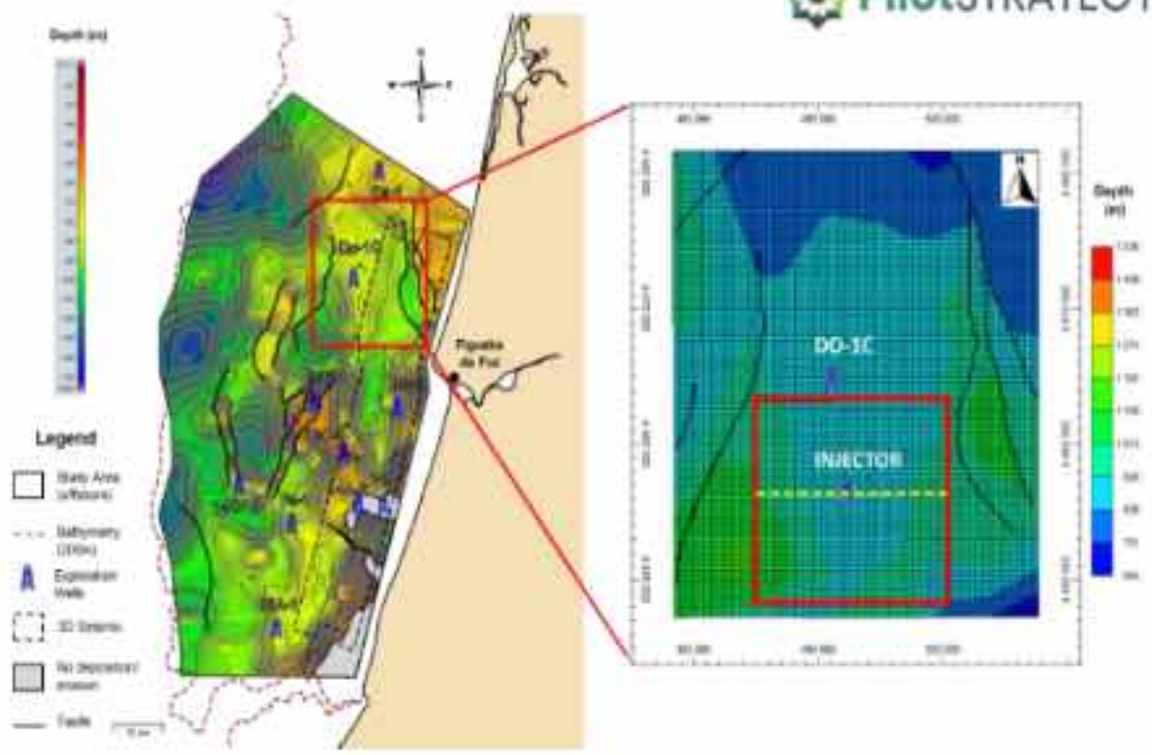


*Figure 4-26: (left) Top view of the reservoir top structure illustrating the area of reservoir model used in the task 3.2 (shown by the red square; and (right) the area of the model reservoir used in current task of this work (task 3.4), as shown by the red square, the $CO_2$ injection well (INJECTOR) and the legacy well Do-1C. The dashed yellow line illustrates the location of the cross-section used later on in this work.*

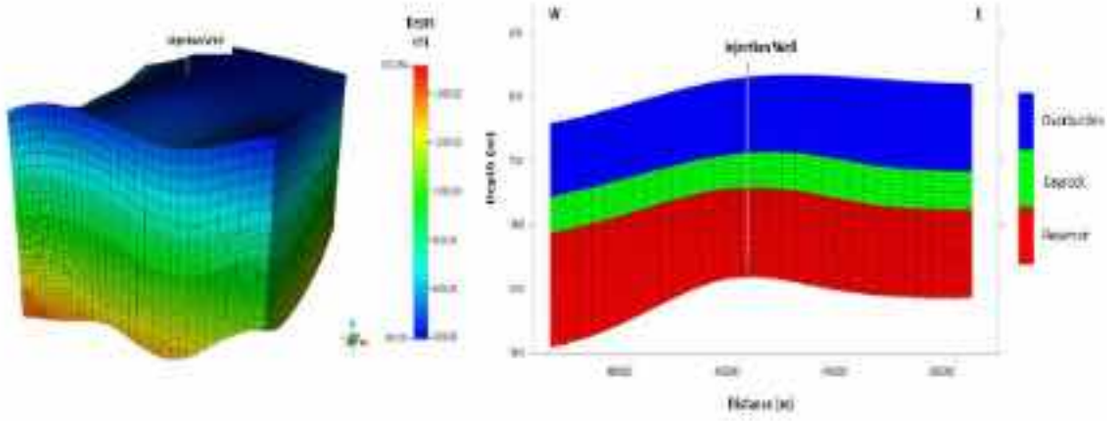


*Figure 4-27: 3D reservoir model (left) and W-E cross-section (right) illustrating the model regions at the injection well, particularly the following succession: reservoir (red), Cacém Formation caprock (green), and Aveiro Group overburden (blue). For the location of this section refer to Figure 4-26.*

The PilotSTRATEGY project has received funding from the European Union's Horizon 2020 research and innovation programme under grant agreement No. 101022664

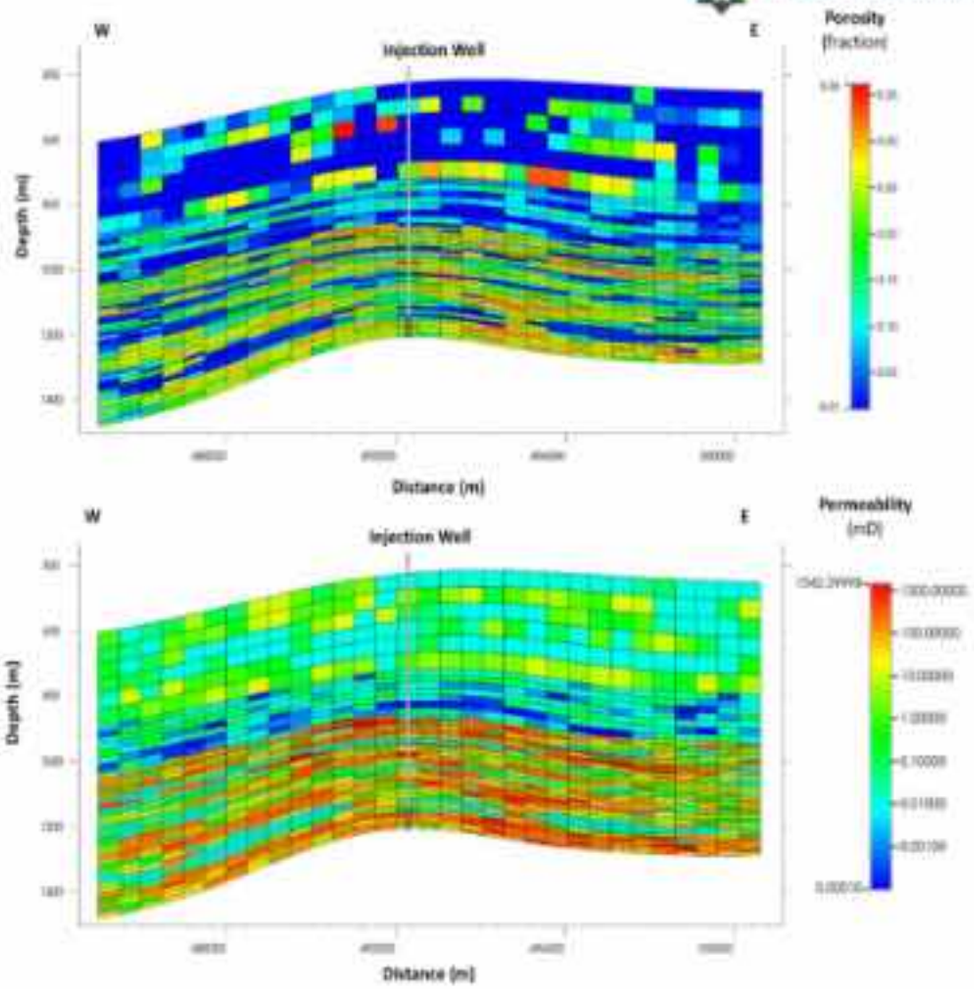


*Figure 4-28: Vertical sections illustrating the porosity (top) and the horizontal permeability (bottom) for the three model regions. For the location of this section refer to Figure 4-26.*

The vertical cell thicknesses of each unit were defined as follows: 10 m for the reservoir, 20 m for the caprock and 50 m for the overlying caprock unit of the Aveiro Group. The final 3D model comprised a total of 46128 cells, with 31 cell blocks in both i- and j-directions and 48 cell blocks for the k-direction.

Despite the application of the grid-coarsening process, the spatial heterogeneity of the petrophysical properties were still reproduced in the models for this assessment, honouring the main statistics, characteristics of the original P50 case for the three model regions from the 3D static modelling task (Pereira et al., 2024). The porosity and the horizontal permeability models are shown in Figure 4-28.

#### *5.4.1.2 Initial state and boundary conditions*

The numerical simulations were conducted considering a maximum injection rate of 710 272 $Sm^3$/day over a 30-year injection period, achieving a cumulative $CO_2$ mass of approximately 15 Mt (14.5 Mt).

Following the injection phase, an additional 70-year post-injection period was simulated, resulting in a total simulation time of 100 years. A maximum bottom-hole pressure of 16 500 kPa was imposed as an operational constraint (pressure limit), as previously identified and applied in earlier WP3 tasks.

The PilotSTRATEGY project has received funding from the European Union's Horizon 2020 research and innovation programme under grant agreement No. 101022664

This operational strategy was derived from the P50 scenario resulting from the Task 3.2 (Khudhur et al., 2024).

The initial pressure and temperature distributions are shown in Figure 4-29. Due to the extraction of a sector model for this assessment, volume modifiers of 50 were applied to the boundary cells to represent the regional extent of the formations and allow for pressure dissipation, while preserving the pressure distribution behaviour in the 3D model observed in previous tasks using the original reservoir model (Figure 4-26).

Geomechanical calculations were performed over all active grid blocks of the model. The mechanical model includes prescribed displacement boundary conditions explicitly defined in the geomechanical module on the external boundaries: lateral boundaries are constrained in their normal direction (i.e., no displacement perpendicular to the boundary), and the bottom boundary is constrained vertically ($u_z = 0$). In contrast, the top boundary is left unconstrained and is free to deform in response to stress changes.

As the injection cells are located at the base of the model, this lower displacement constraint may influence the local stress path and deformation close to the reservoir–caprock interface. In particular, the fixed vertical displacement at the base prevents downward movement, which may contribute to the development of stress redistribution and residual deformation in the overlying formations.

From a flow perspective, no volume modifiers were applied at the top and bottom boundaries (volume modifier = 1), while enlarged volume modifiers were assigned laterally to represent regional pressure dissipation, as previously mentioned. This combination of lateral pressure dissipation and constrained vertical displacement at the base plays a key role in controlling the simulated deformation response.

The PilotSTRATEGY project has received funding from the European Union's Horizon 2020 research and innovation programme under grant agreement No. 101022664

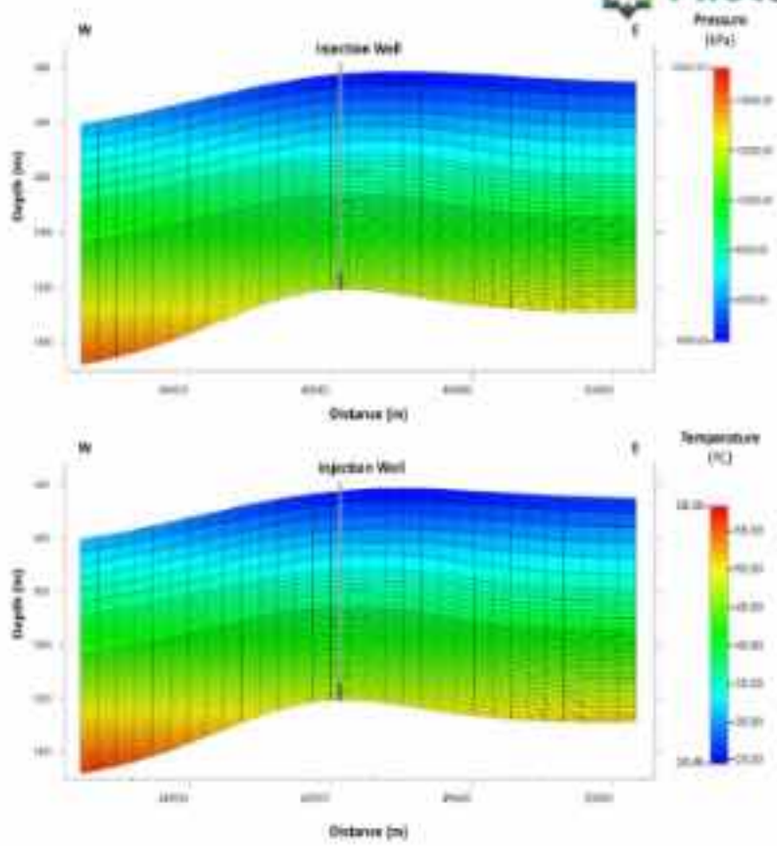


*Figure 4-29: Vertical sections illustrating the initial pressure (top) and temperature (bottom) for the three model regions. For the location of this section refer to Figure 4-28.*

The solubility tables for the $CO_2$ dissolution in the reservoir brine and the reservoir relative permeability curves used in this work were previously presented in the works from Khudhur et al. (2024) and Pereira et al. (2026).

The model was initialized under in-situ stress and hydrostatic pressure conditions representative of local geostatic equilibrium. The initial stress state is presented in Table 4-11, including the normal and shear stress gradients used in this assessment. For more information, refer to the information of the "Fault reactivation assessment" of section 4.5.

The rock mechanical parameters used in this assessment are presented in Table 4-12. The Poisson's ratio and Young's modulus (elastic modulus) values were derived from well-log data, specifically from the P-wave velocity computed from sonic logs and the S-wave velocity predicted using the Greenberg-Castagna equation (Greenberg & Castagna, 1992), with regression coefficients based on Castagna et al. (1993).

*Table 4-11: Initial stress state (in kPa) and normal and shear stress gradients (in kPa/m).*

| $\sigma_{xx}$ | $\sigma_{yy}$ | $\sigma_{zz}$ | $\sigma_{xy}$ | $\sigma_{yz}$ | $\sigma_{xz}$ |
|---|---|---|---|---|---|
| 424.7 | 458.2 | 490.5 | 46.1 | 0.0 | 0.0 |
| $\delta\sigma_{xx}/\delta z$ | $\delta\sigma_{yy}/\delta z$ | $\delta\sigma_{zz}/\delta z$ | $\delta\sigma_{xy}/\delta z$ | $\delta\sigma_{yz}/\delta z$ | $\delta\sigma_{xz}/\delta z$ |
| 22.1 | 23.8 | 25.5 | 2.4 | 0.0 | 0.0 |

The PilotSTRATEGY project has received funding from the European Union's Horizon 2020 research and innovation programme under grant agreement No. 101022664

*Table 4-12: Mechanical parameters for the three model regions.*

| Property/ Model Region | Rock Density (kg/m³) | Poisson's Ratio (-) | Young's Modulus (GPa) | Cohesion (MPa) | Friction Angle (°) |
|---|---|---|---|---|---|
| Upper Cretaceous (Overburden) | 2412 | 0.35 | 10.77 | 5.00 | 35.00 |
| Upper Cretaceous (Caprock) | 2602 | 0.29 | 33.07 | 5.00 | 30.00 |
| Lower Cretaceous (Reservoir) | 2382 | 0.31 | 16.34 | 2.00 | 30.00 |

For the sake of simplicity, only average (homogeneous) values of the rock mechanical parameters were used in this assessment, although parameter distributions (heterogeneous values) were also obtained, particularly from the log data of the legacy well Do-1C. These distributions were used to define the ranges of the key mechanical parameters for the sensitivity analysis conducted and presented later in this work.

Due to the lack of direct mechanical information for the friction angle and cohesion, these values were defined based on the available information on the lithofacies and cementation conditions of each geological unit in the model. The spatial distribution of these mechanical parameters within the model is illustrated in Figure 4-30.

Thermal properties were also considered in this assessment. The thermal conductivity and heat capacity values for the reservoir and the caprock were previously presented in the "Injectivity Integrity" section (Section 4.2). For the overlying Aveiro Group unit (Upper Cretaceous), due to the lack of available data from the studies conducted in "WP2 – Geo-characterization," the thermal parameters were assumed to be the same as those of the caprock. This assumption is justified by the high proportion of argillaceous-carbonated lithofacies in this unit (Pereira et al., 2024) and by its role within the storage complex as a potential secondary seal.

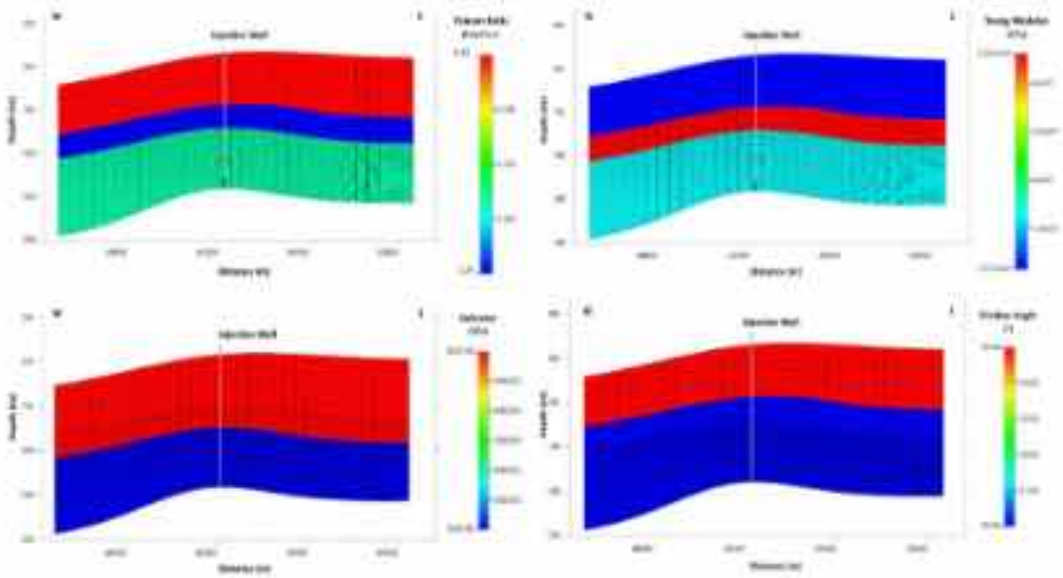

The PilotSTRATEGY project has received funding from the European Union's Horizon 2020 research and innovation programme under grant agreement No. 101022664

*Figure 4-30: Vertical sections illustrating the mechanical properties for the three model regions: Poisson ratio (top left), Young Modulus (top right), cohesion (bottom left) and friction angle (bottom right). For the location of this section refer to Figure 4-26.*

### 5.4.2 Modelling Approach

The THM dynamic simulations carried out to evaluate caprock geomechanical integrity accounted for coupled variations in hydraulic properties (pore pressure and porosity) and kinematic responses (volumetric deformation and vertical displacement). Structural stability and sealing performance were assessed using the Mohr–Coulomb failure criterion, complemented by the calculation of a Safety Factor (SF) to quantify the margin to mechanical failure.

#### *5.4.2.1 Integrity assessment*

The geomechanical integrity assessment focused on evaluating the load-bearing capacity of the caprock under evolving stress conditions induced by $CO_2$ injection. In this framework, rock strength is defined as the maximum shear stress that the material can sustain before failure occurs (Atkinson, 2007). The analysis therefore aimed not only to identify potential failure conditions but also to quantify how close the system approaches these limits during injection and post-injection phases.

#### *5.4.2.2 Mohr-Coulomb failure criterion*

Caprock stability was evaluated using the Mohr–Coulomb failure criterion (Figure 4-31), one of the most commonly applied analytical models in geomechanics for assessing rock strength and failure. This criterion relates shear strength (τf) to the intrinsic mechanical properties of the rock, namely cohesion (c) and internal friction angle (ϕ). Failure is predicted to occur when the applied shear stress exceeds the shear strength, which, in graphical terms, corresponds to the Mohr stress circle intersecting the Mohr–Coulomb failure envelope (Figure 4-32).

Under critical pressure conditions, the critical pore pressure was determined using the analytical formulation of the Mohr–Coulomb criterion, in which the parameter Nϕ depends solely on the internal friction angle ϕ. This approach enables the evaluation of whether injection-induced pressure increases could drive the stress state of the caprock towards failure.

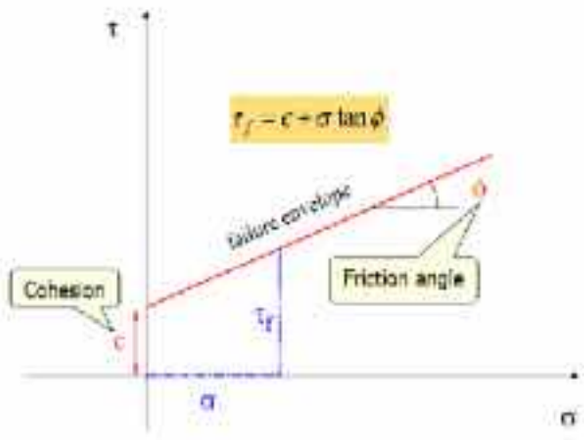


*Figure 4-31: Geometric and analytical definition of Mohr-Coulomb strength criterion and respective governing geomechanical parameters (from Hetty, 2001).*

The PilotSTRATEGY project has received funding from the European Union's Horizon 2020 research and innovation programme under grant agreement No. 101022664

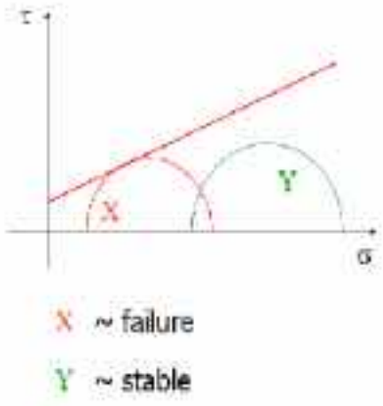


*Figure 4-32: Schematic representation of the Mohr-Coulomb failure criterion: comparison between a critical or failure stress state (semi-circle X) and a stable stress state (semi-circle Y) (from Hetty, 2001).*

Under critical pressure conditions, the overpressure can be determined using the equation below (Equation 4-2):

$$\Delta P_{crit} = \frac{\sigma'_1 - \sigma'_3 N_\phi - 2c_0\sqrt{N_\phi}}{1 - N\phi} \qquad \textit{(Equation 4-2)}$$

Where Nϕ depends solely on the friction angle (Equation 4-3):

$$N_\phi = \frac{1 + \sin(\phi)}{1 - \sin(\phi)} \qquad \textit{(Equation 4-3)}$$

#### 5.4.2.2.1 *Safety Factor*

Rock materials may undergo significant deformation while remaining mechanically competent (Atkinson, 2007). Consequently, geomechanical integrity assessment should not be limited to identifying failure onset but should also quantify the proximity of the stress state to the failure envelope. For this purpose, a Safety Factor was employed.

Following the CMG GEM formulation, the Safety Factor represents the relative distance between the current stress state and the Mohr-Coulomb failure criterion (Figure 4-33).

For a given stress configuration, the Safety Factor is defined as the ratio CB/CA, where ϕ is the internal friction angle, CB' is derived from the constitutive failure envelope, and point C corresponds to the intersection of the stress path with the failure criterion. The Safety Factor is expressed as:

The PilotSTRATEGY project has received funding from the European Union's Horizon 2020 research and innovation programme under grant agreement No. 101022664

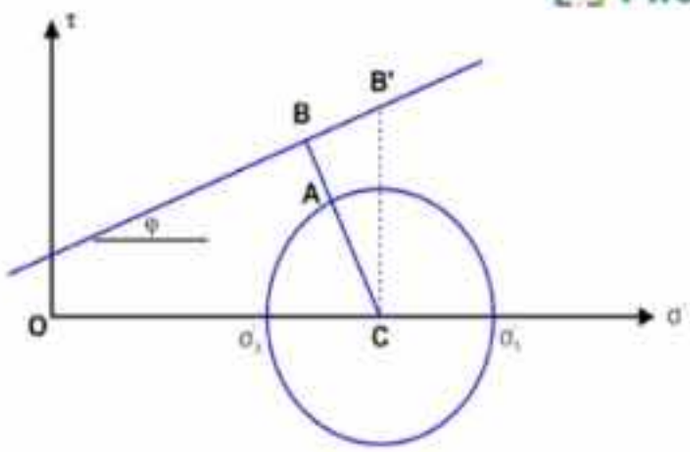


*Figure 4-33: Schematic representation of the Mohr-Coulomb failure criterion and geometric definition of the overall safety factor.*

For this set of voltages, the safety factor is CB/CA, where (Equations 4-4 and 4-5):

$$CA = \frac{(\sigma'_1 - \sigma'_3)}{2} \qquad \textit{(Equation 4-4)}$$

$$CB = \cos(\varphi) \cdot CB' \qquad \textit{(Equation 4-5)}$$

Here ϕ is the friction angle, and the estimated value of CB' is based on the failure of the construction model. The location of C is given by Equation 4-6:

$$OC = \frac{\sigma'_3 - \sigma'_3}{2} \qquad \textit{(Equation 4-6)}$$

The safety factor is defined as (Equation 4-7):

$$SF = 1 - \left(min\left(1, \frac{CA}{CB}\right)\right) \qquad \textit{(Equation 4-7)}$$

If the ratio CA/CB exceeds unity, the Safety Factor is zero, indicating that failure has occurred. Positive values of the Safety Factor (up to one) indicate stable conditions, with stresses remaining below the failure threshold, whereas values approaching zero indicate imminent failure.

### 5.4.2.3 Scenarios for the Uncertainty Analysis

The numerical modelling strategy encompassed a range of $CO_2$ injection scenarios designed to test the robustness of the caprock system under progressively more demanding operational conditions. A reference scenario with an injection rate of 0.5 Mt/y was first simulated, focused on the geomechanical response and integrity of the sealing units, namely the Cacém Formation, which acts as the primary caprock directly overlying the reservoir, and the Aveiro Group, which constitutes a potential stratigraphically higher secondary seal.

As part of the uncertainty analysis, additional simulations were conducted to specifically evaluate the integrity of the primary seal (Cacém Formation), given its direct contact with the reservoir. These simulations adopted an injection rate of 1 Mt/y, corresponding to the P90 injection scenario defined in Task 3.2 (Khudhur et al., 2024), and

The PilotSTRATEGY project has received funding from the European Union's Horizon 2020 research and innovation programme under grant agreement No. 101022664

investigated the impact of different completion strategies. In particular, the response of the caprock was compared between a single perforation interval at the injection well and a dual-perforation configuration, comprising one interval at the base of the reservoir and a second, shallower interval within the wellbore (Figure 4-34).

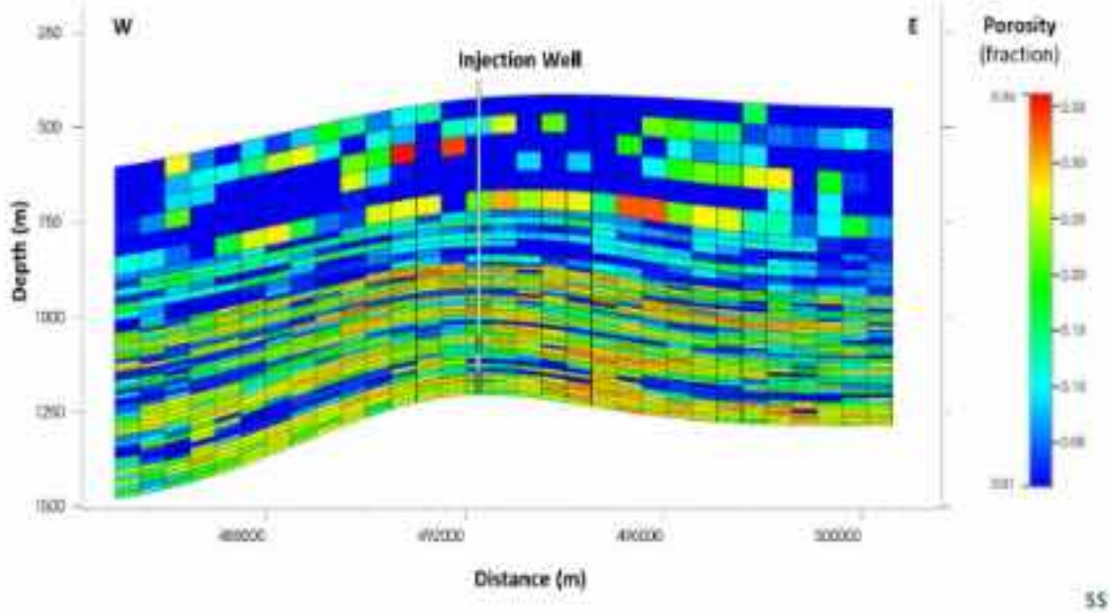


*Figure 4-34: Vertical sections illustrating the porosity for the three model regions, and also the dual-perforation configuration in the $CO_2$ injection well. For the location of this section refer to Figure 4-26.*

Finally, sensitivity analyses were performed for the most critical operational configuration, identified as a 1 Mt/y injection rate using the dual-perforation configuration of the injection well. In these simulations, key geomechanical parameters were systematically varied to identify the principal controls on system stability and to assess the robustness of the caprock integrity under parameter uncertainty, as summarised in Table 4-13.

It is important to note that the high- and low-case values adopted for Young's modulus and Poisson's ratio were derived from the probability distribution functions (PDFs) estimated for both parameters using log data from the legacy well Do-1C, located close to the storage site. These values represent the minimum and maximum bounds of the corresponding PDFs.

*Table 4-13: Geomechanical parameters for the caprock defined for uncertainty analysis: reference, higher and lower case scenarios.*

| Geomechanical Parameters | Symbol | Unit | Reference Case Scenarios | Higher Case Scenarios | Lower Case Scenarios |
|---|---|---|---|---|---|
| **Cohesion** | c' | [MPa] | 5.00 | - | 0.10 and 1.00 |
| **Friction angle** | ϕ' | [°] | 30.00 | - | 10.00 and 20.00 |
| **Young's modulus** | E | [GPa] | 33.07 | 60.00 | 5.00 |
| **Poisson's ratio** | v | [-] | 0.29 | 0.40 | 0.20 |

The PilotSTRATEGY project has received funding from the European Union's Horizon 2020 research and innovation programme under grant agreement No. 101022664

In contrast, the ranges defined for cohesion and internal friction angle were assumed for the purposes of this assessment in order to evaluate the effects of higher and lower values on caprock integrity. Exceptions were made for the cohesion and the friction angle, for which only low-case scenarios were considered, to test a worst-case condition characterised by very weak caprock strength. In particular, minimum cohesion and friction angle values of 0.10 MPa and 10º, respectively, were assumed to represent extreme lower-bound scenarios for these parameters.

### 5.4.3 Results

The results are presented following the established sequence of scenarios, beginning with the reference case scenario, which was defined by a $CO_2$ injection rate of 0.5 Mt/y, evaluates the geomechanical performance of the sealing system, encompassing both the Cacém Formation (primary seal) and the overlying Aveiro Group (secondary seal/ caprock). The geomechanical impacts were evaluated by the evolution of the pore pressure, porosity changes, volumetric strain, vertical displacement (uplift), safety factor, and the estimate of the Mohr-Coulomb failure envelope for the caprock.

Subsequently, the uncertainty analyses examine the effects of different operational variables by simulating more demanding conditions. These included an increased injection rate of 1 Mt/y and a change in the well completion strategy from a single to dual perforation intervals in the injection well, in order to verify the structural integrity of the caprock under elevated pressure regimes.

Finally, the results of the uncertainty analyses also focused on geomechanical properties, assessing the impact of parameter variability on the stability and structural competence of the caprock.

It is important to note that all results were analysed throughout the sealing system (both primary and secondary caprocks). However, the results and figures presented in this section refer to a specific location in the model grid – the deeper cells of both sealing layers at the location of the $CO_2$ injection well – as the mechanical effects are representative of the response in the near-wellbore region and show consistent behaviour across the injection area.

#### *5.4.3.1 Reference Case*

##### *5.4.3.1.1 Evolution of pore pressure*

Throughout the injection phase (30 years), the Aveiro Group (secondary caprock) displays only minor pore pressure variations (Figure 4-35). The pressure curve remains relatively flat at approximately 7200 kPa, with a very gradual and smooth increase over time rather than a strictly isobaric response. This limited pressure perturbation indicates that the secondary seal is largely decoupled from the reservoir–primary seal pressure evolution, consistent with effective hydraulic isolation provided by the Cacém Formation.

In contrast, the Cacém Formation (primary caprock) exhibits a clear pressurisation trend following the onset of injection. After a short initial adjustment period, pore pressure rises progressively from around 9000 kPa to a peak close to 9400 kPa at approximately 35–40 years. This behaviour reflects

The PilotSTRATEGY project has received funding from the European Union's Horizon 2020 research and innovation programme under grant agreement No. 101022664

the poroelastic response of the storage complex to $CO_2$ injection and associated fluid pressurisation within the reservoir–seal system.

During the post-injection (shut-in) phase (30–100 years), the Cacém Formation shows a gradual pressure decline from its maximum value, stabilising at around 9300 kPa by the end of the simulation (Figure 4-35). The smooth, asymptotic relaxation pattern suggests progressive pressure dissipation and redistribution toward a new quasi-equilibrium state rather than an abrupt return to initial conditions.

These pressure profiles support the integrity of the storage complex. The primary seal accommodates the induced pore pressure changes while remaining within a stable geomechanical regime (i.e. below the fracture gradient), and the secondary caprock (Aveiro Group) experiences only minimal pressure perturbation, reinforcing its role as an effective redundant hydraulic barrier.

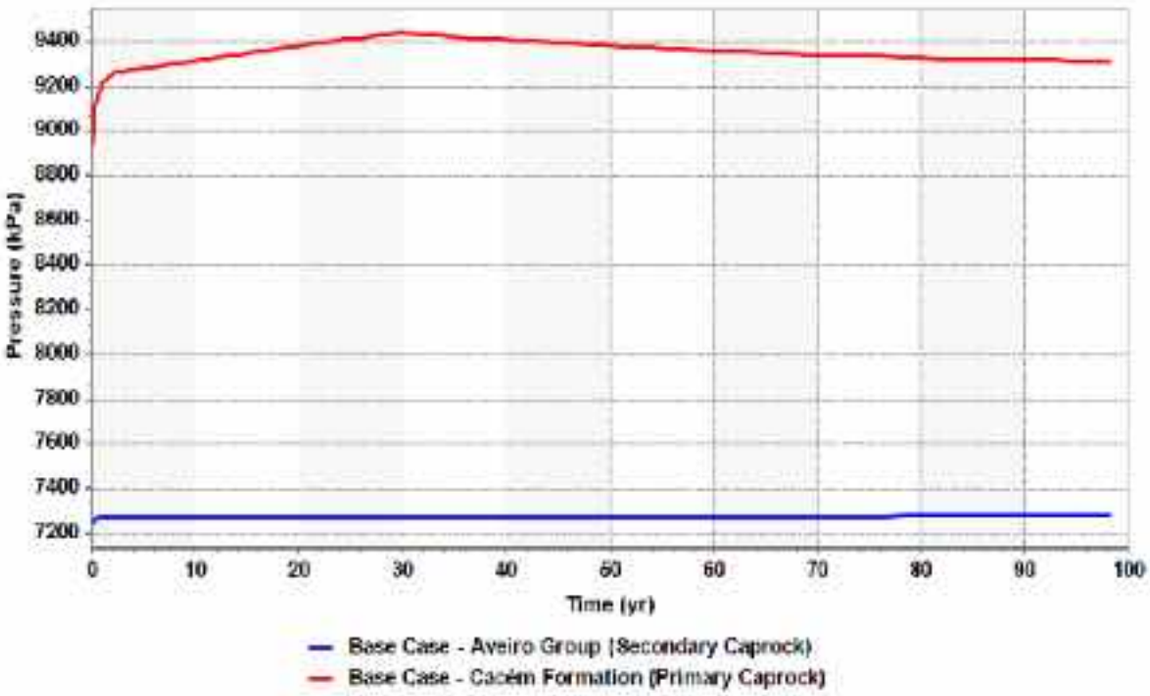


*Figure 4-35: Pressure evolution (kPa) over time in representative model cells at the base of the sealing units (Cacém Formation and Aveiro Group), close to the injection well, during injection (0-30 years) and post-injection simulation (30-100 years).*

#### 5.4.3.1.2 Evolution of porosity changes

During the injection phase (0–30 years), the sealing units exhibit very small but distinct porosity changes (Figure 4-36), reflecting the local poroelastic response to reservoir pressurisation and stress redistribution within the storage complex.

The Cacém Formation (primary caprock) shows a slight increase in porosity during injection. An initial rapid increase is observed in the first few years, followed by a more gradual rise until approximately 30 years. This behaviour is consistent with a locally dilative elastic response at the reservoir–caprock interface, likely associated with stress redistribution and uplift induced by reservoir pressurisation. In contrast, the Aveiro Group (secondary caprock) exhibits a small decrease in porosity throughout the injection period. This indicates a mild compaction response, suggesting that stress perturbations

The PilotSTRATEGY project has received funding from the European Union's Horizon 2020 research and innovation programme under grant agreement No. 101022664

induced by reservoir pressurisation are transmitted upward but are attenuated by the primary seal. The Cacém Formation therefore acts as a mechanical buffer, limiting deformation in the overlying secondary caprock.

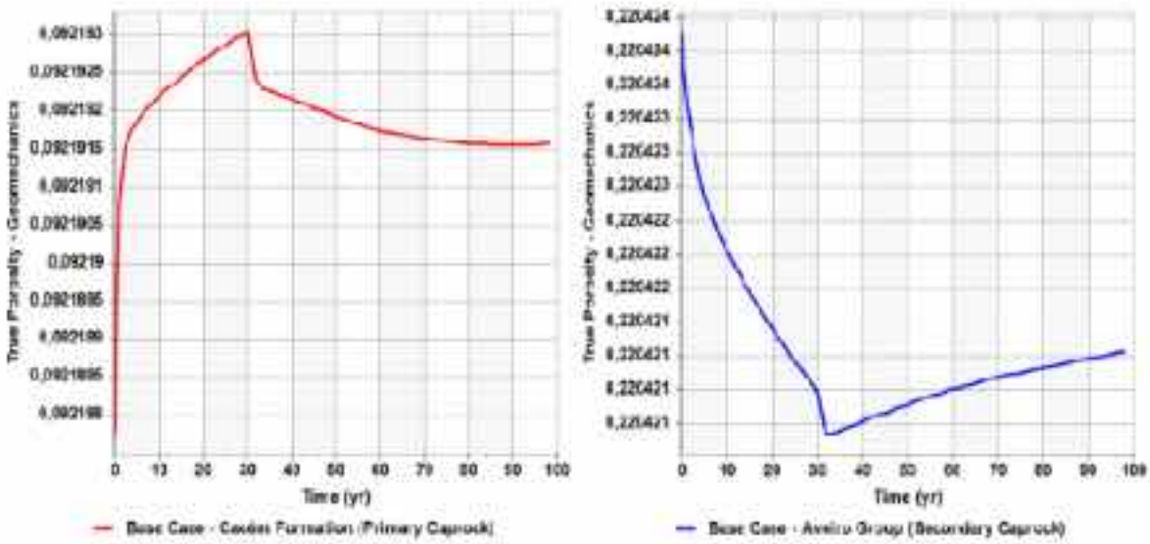


*Figure 4-36: Porosity variation over time in representative model cells at the base of the sealing units (Cacém Formation (left) and Aveiro Group (right)), close to the injection well, during injection (0-30 years) and post-injection simulation (30-100 years).*

During the post-injection (shut-in) phase (30–100 years), both formations display a partial recovery towards their initial porosity values. In the Cacém Formation, porosity decreases slightly after injection stops, while in the Aveiro Group, porosity gradually increases. This behaviour reflects elastic stress relaxation as pore pressure dissipates and the stress field re-equilibrates within the system. The absence of full recovery within the simulated period is consistent with incomplete pressure dissipation and boundary condition effects. Nevertheless, it is important to note that the magnitude of porosity variations in both sealing formations is extremely small (order of $10^{-6}$), indicating a negligible impact on storage properties and sealing capacity.

#### *5.4.3.1.3 Evolution of volumetric strain*

The numerical simulations indicate that both sealing units undergo progressive volumetric deformation throughout the injection and post-injection periods (Figure 4-37). The recorded strain magnitudes remain on the order of $10^{-6}$, well below levels that could compromise mechanical integrity or induced failure of the caprock units.

The PilotSTRATEGY project has received funding from the European Union's Horizon 2020 research and innovation programme under grant agreement No. 101022664

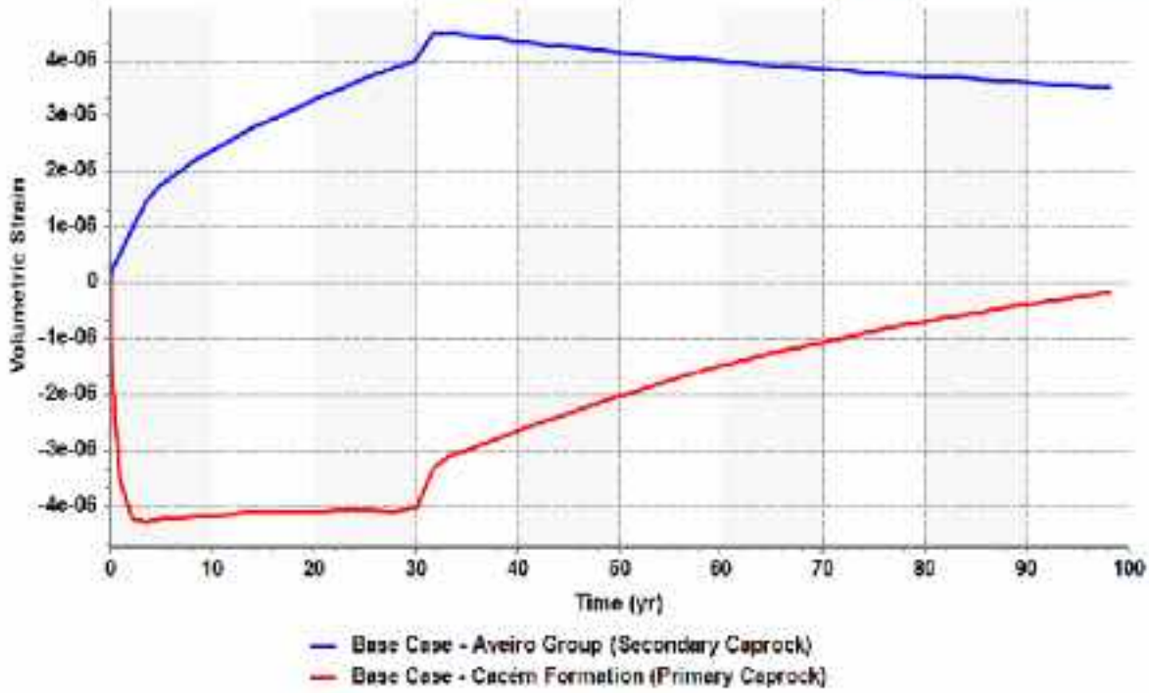


*Figure 4-37: Volumetric strain evolution over time in representative model cells at the base of the sealing formations (Cacém Formation and Aveiro Group), close to the injection well, during the injection (0-30 years) and post-injection simulation (30-100 years).*

The Aveiro Group (secondary caprock) displays a positive volumetric strain (net compaction) during the injection phase. Strain increases rapidly in the early years of injection, then continues to rise more gradually until reaching a peak of approximately $4.5 \times 10^{-6}$ around 30–35 years. This response reflects the poroelastic reaction of the overburden to reservoir pressurisation and associated stress redistribution. During the post-injection (shut-in) phase (30–100 years), the volumetric strain in the Aveiro Group decreases slowly and asymptotically, indicating progressive relaxation of injection-induced stresses. However, strain does not fully return to zero, suggesting a small residual deformation related to the incomplete stress recovery and boundary condition effects.

In contrast, the Cacém Formation (primary caprock) exhibits negative volumetric strain (net dilation) throughout most of the simulation. A rapid initial dilative response occurs in the first few years of injection, followed by a relatively stable period up to about 30 years. Immediately after shut-in, the formation undergoes a transient change in deformation behaviour, after which strain progressively returns toward zero during the post-injection period. This behaviour reflects local stress redistribution at the reservoir-caprock interface, including slight uplift associated with reservoir expansion and subsequent elastic stress relaxation as pore pressure dissipates.

Overall, the contrasting deformation responses – compaction in the Aveiro Group and slight dilation in the Cacém Formation – highlight the different mechanical roles of the two sealing units within the storage complex. The smooth temporal evolution and very small magnitude of volumetric strain in both formations indicate that deformation remains within the elastic–poroelastic regime, with no evidence of mechanical instability or impact on sealing integrity.

#### *5.4.3.1.4 Evolution of safety factor*

The computed Safety Factor values confirm that the storage complex remains geomechanically stable throughout both the injection and post-

The PilotSTRATEGY project has received funding from the European Union's Horizon 2020 research and innovation programme under grant agreement No. 101022664

injection periods (Figure 4-39). For both sealing units, the Safety Factor remains consistently well above zero, indicating that the stress state stays comfortably within the elastic domain and remains far from the Mohr–Coulomb failure envelope (Figure 4-40), indicating that the stress state remains stable and no failure conditions are approached. The pressure and deformation changes induced by $CO_2$ injection are therefore insufficient to compromise rock integrity or materially reduce the mechanical safety margin.

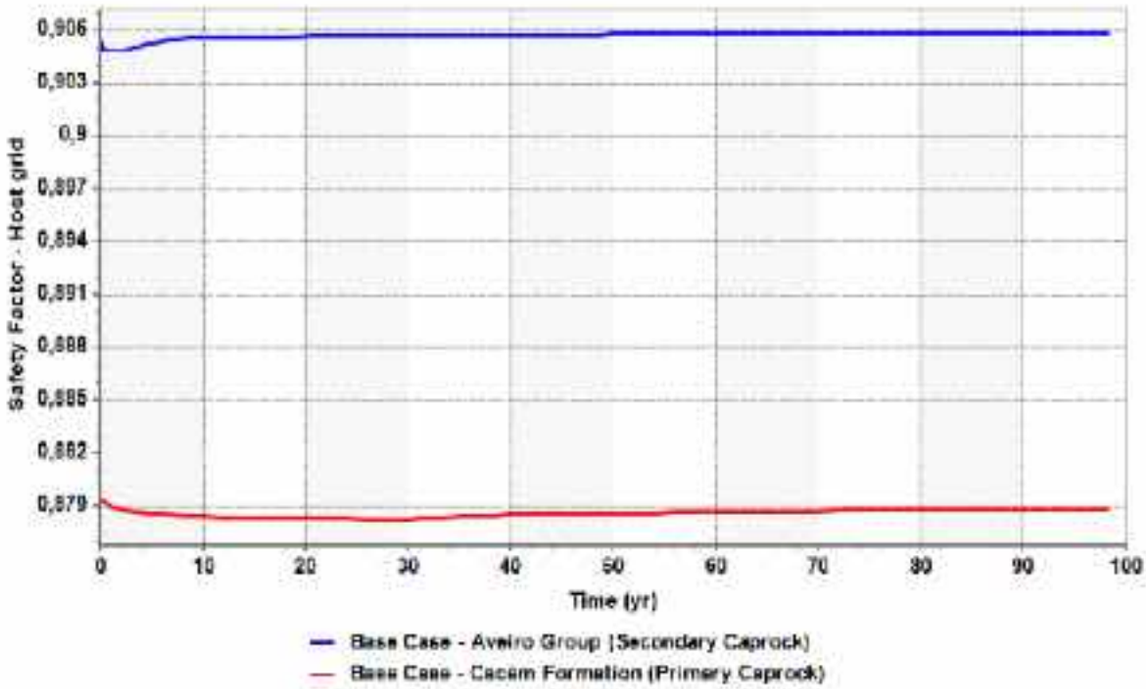


*Figure 4-39: Structural integrity monitoring via the Safety Factor index in representative model cells at the base of the sealing formations (Cacém Formation and Aveiro Group), close to the injection well, during the injection (0-30 years) and post-injection simulation (30-100 years).*

The Aveiro Group (secondary caprock) exhibits a high and nearly constant Safety Factor of approximately 0.905 throughout the entire simulation. A very small, short-lived increase occurs during the early years of injection, after which the value stabilises with negligible temporal variation. This near-invariant behaviour demonstrates that the secondary seal is only minimally affected by reservoir pressurisation and subsequent pressure dissipation, reinforcing its role as a mechanically robust and redundant barrier within the storage system.

The Cacém Formation (primary caprock) displays a slightly lower Safety Factor, stabilising around 0.878–0.879 over most of the simulation. A modest initial decrease is observed during the early injection phase, consistent with rapid pore-pressure build-up and the associated reduction in effective stress. Thereafter, the Safety Factor remains essentially constant, with only very minor fluctuations during both the injection and post-injection periods. This indicates that, despite accommodating most of the pressure and deformation changes, the primary seal maintains a stable stress state and preserves an adequate margin of mechanical safety.

#### *5.4.3.1.5 Estimate of Mohr failure envelope*

The Mohr diagram analysis supports the overall geomechanical interpretation of the storage system. The initial effective stress state (blue dashed circle) lies well within the Mohr–Coulomb failure

The PilotSTRATEGY project has received funding from the European Union's Horizon 2020 research and innovation programme under grant agreement No. 101022664

envelope, indicating a stable pre-injection stress regime (Figure 4-40). At the end of the injection period (30 years), the final effective stress state (blue solid circle) remains clearly inside the failure envelope, demonstrating that the stress changes induced by $CO_2$ injection do not drive the system toward shear failure during active operations.

The stress path between the initial state and the end of injection shows a modest shift toward lower effective normal stress and slightly reduced shear stress, consistent with effective stress reduction associated with reservoir pressurisation and poroelastic coupling. Importantly, the distance between the stress circles and the Mohr–Coulomb envelope remains substantial at the end of injection, confirming that an adequate safety margin is preserved during the critical operational phase.

From a geomechanical perspective, the tendency toward dilative behaviour (poroelastic expansion reflected by porosity increase and negative volumetric strain) observed by the end of injection does not compromise caprock integrity. Rather than promoting mechanical instability, this response reflects reversible elastic-poroelastic deformation under increased pore pressure. The primary seal (Cacém Formation) remains far from failure, and no conditions favourable to shear or tensile fracturing are reached.

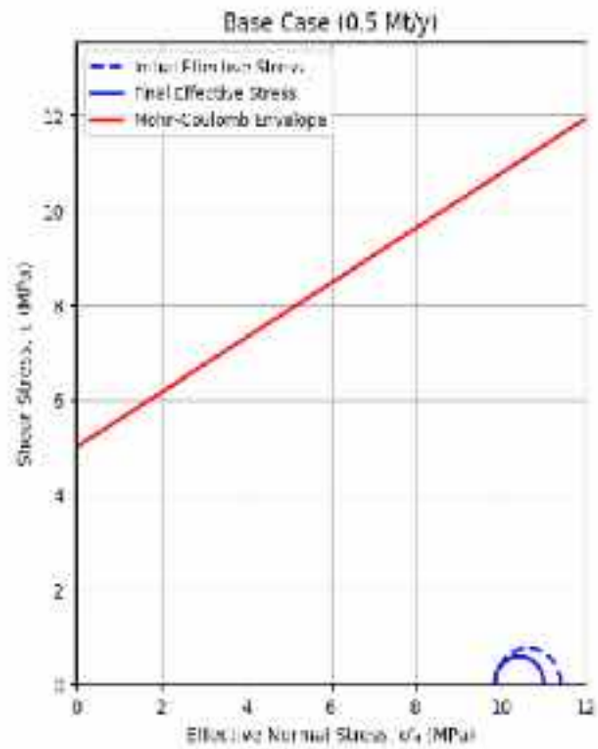


*Figure 4-40: Mohr diagram for caprock stability analysis. The plot depicts the Mohr-Coulomb failure envelope (red line) relative to the initial (dashed line) and final (solid line) effective stress states.*

In addition, and after applying the Equations 4-2 and 4-3, the critical overpressure ($\Delta P_{crit}$) of for the reference (base) case is approximately 0.61 MPa (about 610 kPa). This value indicates the pore pressure increase required to bring the stress state of caprock to the Mohr–Coulomb shear failure limit. Pore pressure increases below this threshold suggest mechanical stability against shear reactivation, whereas exceedance of this value could potentially allow slip or failure. The simulated

The PilotSTRATEGY project has received funding from the European Union's Horizon 2020 research and innovation programme under grant agreement No. 101022664

pressure increase remains well below the critical threshold, confirming a substantial safety margin under the analysed conditions. Because this estimate depends on assumptions regarding rock strength, stress regime, and mechanical homogeneity, it should be regarded as a conservative indicator of caprock stability rather than an absolute integrity limit.

### 5.4.4 Uncertainty Analysis

As highlighted in the previous analyses, the Cacém Formation plays a pivotal role in ensuring system confinement, exhibiting a dynamic response to the interplay between the pressure build-up (pressurisation) due to the $CO_2$ plume and the lithostatic stress imposed by the overburden.

To further test the robustness of the sealing system, additional simulations were conducted to evaluate the geomechanical response under more demanding operational conditions. These scenarios include an increased injection rate and, subsequently, alternative well-completion strategies. The uncertainty analysis focuses on the integrity of the caprock (Cacém Formation), tracking the evolution of the pore pressure, porosity changes, volumetric strain, and vertical displacement, while validating structural stability using the Safety Factor and the Mohr–Coulomb failure criterion.

The impacts of injection flow rate, perforation intervals and mechanical properties resulting from the uncertainty analysis is briefly summarised below and explained in more detail in the Appendix (section 6.2.2).

#### *5.4.4.1 Impacts of injection flow rate*

Increasing the injection rate from 0.5 to 1 Mt/y raises peak pore pressure in the Cacém Formation from about 9.45 MPa to ~9.7 MPa ($\Delta P \approx 250$ kPa) at the end of injection, while remaining well below fracture limits (Appendix, Figure 6.2-21). Post-injection pressure decline trends remain nearly parallel, indicating unchanged hydraulic behaviour.

The higher rate leads to slightly greater porosity increase, reaching a deeper minimum at 30 years and slower recovery during shut-in (Appendix, Figure 6.2-22). Volumetric strain is more negative for 1 Mt/y, indicating stronger dilative response, but remains on the order of $10^{-6}$, within the elastic–poroelastic regime (Appendix, Figure 6.2-23). Early uplift increases to about 2 mm for 1 Mt/y compared with ~1 mm for 0.5 Mt/y, followed by progressive subsidence (Appendix, Figure 6.2-24).

This behaviour reflects a poroelastic response controlled by pressure magnitude, where higher injection rates increase pore-pressure build-up, leading to stronger effective stress reduction and thus greater dilation (porosity increase and negative volumetric strain) and larger early uplift. The overall response pattern remains unchanged because the system stays within the elastic–poroelastic regime, with only the amplitude scaling with pressure.

The Safety Factor shows a small decline during injection, reaching a minimum near 30 years, then partially recovering while staying comfortably within the stable domain (Appendix, Figure 6.2-25).

The PilotSTRATEGY project has received funding from the European Union's Horizon 2020 research and innovation programme under grant agreement No. 101022664

Mohr–Coulomb stress states for both rates nearly overlap and remain far from failure, confirming that the pressure increase is small relative to in-situ stresses of 10–11 MPa (Appendix, Figure 6.2-26).

#### 5.4.4.2 *Impacts of perforation intervals*

At a constant rate of 1 Mt/y, both single- and dual-perforation configurations preserve storage stability and caprock integrity. The dual-perforation case shows a slightly higher peak pore pressure at the end of injection because the extra interval is closer to the caprock, but the difference is small and within safe limits (Appendix, Figure 6.2-27).

Porosity increases steadily during injection in both cases, reaching a minimum around 30 years, with marginally greater porosity increase and slower recovery for the dual-perforation case (Appendix, Figure 6.2-28). Volumetric strain shows the same trend for both cases, with negative values (dilation), yet remains on the order of $10^{-6}$ (Appendix, Figure 6.2-29). Both configurations experience brief early uplift of approximately 2 mm, followed by progressive subsidence, which is slightly greater for the dual-perforation case (Appendix, Figure 6.2-30). The similar behaviour across well perforation configurations indicate that the response is governed by the same pressure-driven poroelastic mechanism, while differences in perforation intervals only slightly modify the local pressure distribution and stress perturbation, affecting the magnitude but not the trend. As a result, porosity, strain and displacement evolve consistently, with only minor variations in amplitude over time.

The Safety Factor reaches a minimum near 30 years then partially recovers and stabilises while staying well within the stable domain for both cases (Appendix, Figure 6.2-31). Mohr–Coulomb stress states nearly overlap and remain far from failure, indicating no added geomechanical risk from two perforations (Appendix, Figure 6.2-32).

#### 5.4.4.3 *Impacts of mechanical properties*

In the adopted geomechanical formulation, cohesion and friction angle are plastic parameters used to define the Mohr–Coulomb failure criterion and evaluate the Safety Factor, but they do not influence the elastic–poroelastic response of the system unless yielding is activated. Since no plastic yielding occurs under the simulated stress conditions, variations in cohesion and friction angle do not affect pore pressure, porosity, volumetric strain, or vertical displacement. Consequently, the hydromechanical response is controlled primarily by elastic parameters, namely Young's modulus and Poisson's ratio.

Safety Factor scales with cohesion but remains comfortably stable even for cohesion equal to 0.1 MPa (Appendix, Figure 6.2-37). Mohr–Coulomb analysis shows that although cohesion shifts the failure envelope, stress states stay far from failure in all cases (Appendix, Figure 6.2-38).

Friction angle only affects the Safety Factor: higher friction angle increases Safety Factor and lower friction angle decreases it, but even for a friction angle equal to 10° remains well above failure (Appendix, Figure 6.2-43). Mohr-Coulomb circles stay far from the failure envelope for all friction angle scenarios (Appendix, Figure 6.2-44).

The PilotSTRATEGY project has received funding from the European Union's Horizon 2020 research and innovation programme under grant agreement No. 101022664

Variations in Young's modulus (5, 33 and 60 GPa) do not compromise operational safety, with pressure evolution nearly identical for all scenarios, showing overlapping peaks and decay trends (Appendix, Figure 6.2-45). Stiffer rock (60 GPa) shows the greatest porosity increase and most negative volumetric strain (dilative response) during injection (minimum at about 30 years), with slower recovery during shut-in, whereas lower stiffness cases exhibit smaller deformation amplitudes (Appendix, Figures 6.2-46 and 6.2-47). Strain remains on the order of $10^{-6}$-10. Safety Factor reaches a minimum near 30 years then stabilises, remaining safely above failure for all cases (Appendix, Figure 6.2-49). Mohr circles nearly overlap and stay far from the failure envelope (Appendix, Figure 6.2-50).

Variations in Poisson's ratio (0.20, 0.29 and 0.40) show minimal influence on pore pressure evolution under the modelling conditions, resulting in almost identical pressure responses, with only negligible late-time differences (Appendix, Figure 6.2-51). Porosity and volumetric strain show dilative behaviour during injection (porosity increase and negative volumetric strain) followed by slow recovery during shut-in; higher Poisson's ratios produce slightly smaller deformation amplitudes, but differences are minor (Appendix, Figures 6.2-52 and 6.2-53). Strain remains approximately $10^{-6}$. Safety Factor dips slightly during injection, reaches a minimum near 30 years, then recovers and stabilises; higher Poisson's ratio yields marginally higher Safety Factor, but all remain safe (Appendix, Figure 6.2-55). Mohr circles are almost superimposed and far from failure for all scenarios (Appendix, Figure 6.2-56).

### 5.4.5 Discussion and Conclusions

The geomechanical assessment of the Q4-TV1 storage complex provides a comprehensive evaluation of the mechanical response of the sealing system (primary and secondary caprocks) to injection-induced pressure perturbations over both operational and early post-injection timescales. By employing a coupled thermal–hydraulic–mechanical modelling framework and a three-dimensional representation of the storage complex, the analysis captures the evolution of stress, deformation and stability within the reservoir–sealing system under realistic injection scenarios and conservative uncertainty bounds. The results consistently demonstrate that the Cacém Formation behaves as a mechanically competent and resilient primary caprock, capable of accommodating the pressure increases associated with commercial-scale $CO_2$ injection without approaching failure conditions.

Across all simulated scenarios, including intensified injection rates, alternative perforation configurations and wide variations in key mechanical parameters, the system remains within the poroelastic domain and well separated from the Mohr–Coulomb failure envelope. Although the Safety Factor exhibits a gradual decline during the injection phase, reaching a minimum around 30 years due to pore-pressure build-up and effective stress reduction, this response is limited in magnitude and partially reversible during shut-in. The favourable initial stress state, moderate burial depth and placement of the injection interval several tens of metres below the caprock collectively contribute to maintaining a high margin of mechanical stability throughout the injection and post-injection periods.

The uncertainty analysis further reinforces the robustness of these conclusions. Systematic variation of cohesion, friction angle, Young's modulus and Poisson's ratio over wide ranges does not lead to instability, even under the most conservative mechanical assumptions. While friction angle primarily controls the theoretical failure envelope and Safety Factor magnitude, and Young's modulus modulates deformation amplitudes, none of these parameters materially affect pore-pressure evolution or bring the system closer to failure. Likewise, higher injection rates and dual-perforation

The PilotSTRATEGY project has received funding from the European Union's Horizon 2020 research and innovation programme under grant agreement No. 101022664

configurations lead to only marginally higher pressures and slightly stronger dilative responses (porosity increase and negative volumetric strain), without altering the overall stress state or compromising seal performance. The thick secondary seal of the Aveiro Group provides an additional mechanical and hydraulic buffer, ensuring that any localized perturbation in the primary caprock would not jeopardize overall containment.

In conclusion, the integrated geomechanical analysis confirms that the Q4-TV1 prospect exhibits a high degree of mechanical robustness and is well suited for long-term $CO_2$ storage from a structural integrity perspective. The Cacém Formation maintains its sealing function under all investigated operational and uncertainty scenarios, with substantial safety margins relative to Mohr-Coulomb failure criteria. These results provide strong evidence that the mechanical integrity of the storage complex does not represent a limiting factor for safe and secure $CO_2$ storage in the offshore Lusitanian Basin, provided that injection operations remain within the defined pressure-controlled operational envelope.

## 5.5 Fault reactivation assessment

### 5.5.1 Objectives

The reactivation of existing tectonic structures such as faults is one of the most impacting geological hazards because of the potential seismic risk. The role of fluids in the triggering of fault reactivation has been studied since few decades especially for seismic events in the shallow part of the earth's crust. Indeed, fluids flow variations, whether they are due to natural meteoric fluctuations or anthropic activities, induce hydromechanical impact affecting stresses in the geological media. In anthropic activities linked to the geological reservoir exploitation of heat, hydrocarbons, water resources or $CO_2$ storage (Elsworth, 2013; Lee, 2019; Rutqvist, 2013; VanWees, 2014; Jeanne, 2017; Pang, 2020), the fluid injection/pumping affect the *in situ* mechanical equilibrium. The hydromechanical perturbation of ambient stresses acting on faults can be due to pore pressure changes within the faults and/or by changes of their loading conditions (Figure 4-41). Of course, the triggering of shearing processes in faults depends on its state of equilibrium before the perturbation and on the level of the solicitation. In some cases, faults can be reactivated because their ambient stress states were closed to mechanical stability equilibrium point, so a little change is enough to trigger displacements of the walls. In other cases, if the faults are in a very stable ambient state, the unlocking of the fault would require a high intensity perturbation due to fluid injection. The assessment of the potential fault reactivation depends on the **most accurate estimation of ambient stress state on faults** before any perturbation and on the **fine description of the solicitation.** In this study, numerical mechanical simulations have been performed to describe the mechanical stresses on faults at the boundary of the reservoir from the initial state to different increasing times of $CO_2$ injection. The perturbation induced by the $CO_2$ injection on the mechanical stress state on faults is simulated by imposing pore pressure fields calculated by dynamic flow simulations at the different injection times.

The PilotSTRATEGY project has received funding from the European Union's Horizon 2020 research and innovation programme under grant agreement No. 101022664

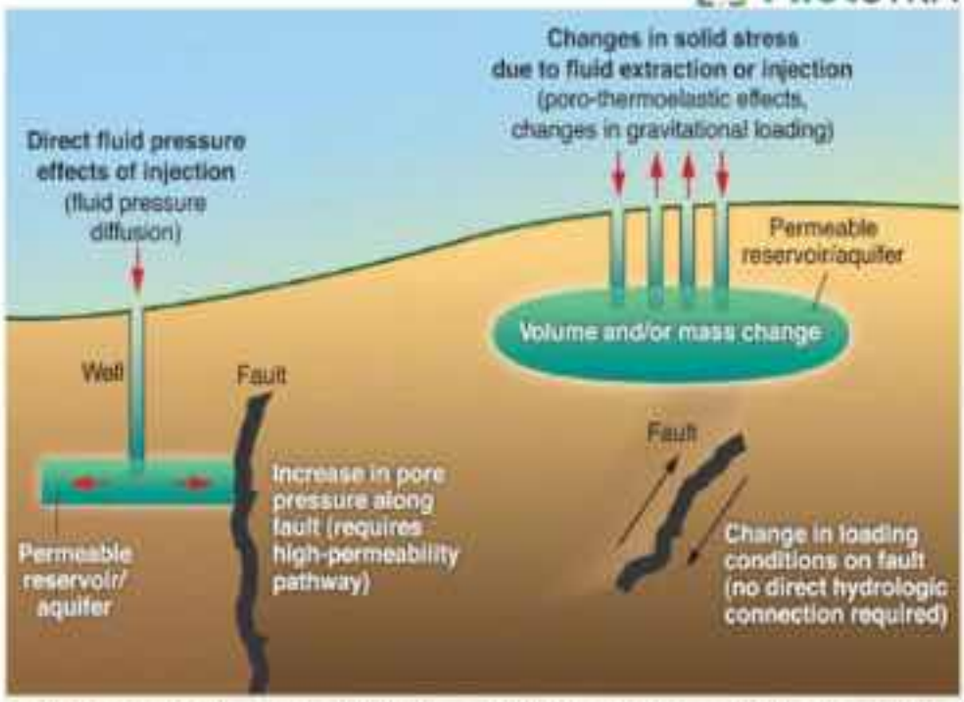


*Figure 4-41: Schematic stress perturbation on faults because of fluids recharge/discharge (issued from Elsworth, 2013).*

### 5.5.2 Context of the study and methodology

To get an efficient workflow for the integration of calculated pore pressure fields at different $CO_2$ injection times, from hydrodynamic simulations previously performed (Khudhur et al., 2024), the mechanical model was directly built based on the hydrodynamic reservoir model geometry (extension, mesh, faults). This has driven the choice of a continuum media approach also for the mechanical numerical code.

### 5.5.3 Description of the model

#### *5.5.3.1 Geology and geometry*

The construction of the model combines both geometrical constraints given by the model used for hydrodynamics simulations and geological aspects to integrate for the mechanical simulations. The extension of the mechanical model was built on the reservoir model area for the hydrodynamic simulations (Figure 4-42). Due to the lack of information about the transmissibility properties of the existing faults, the hydrodynamic behaviour of the faults was assumed to be transmissible, except for the two major faults laterally bounding the Q4-TV1 prospect, designated as faults F2 and F5, which were assumed to be slightly non-transmissible (Khudhur et al., 2024). The boundary conditions of the hydrodynamic simulations were defined as open boundaries. For more details about the hydrodynamic model and the key input data, refer to deliverable D3.3 (Khudhur et al., 2024). The hydrodynamic model focused on the reservoir and integrated only the rock reservoir lithology to estimate the flow of $CO_2$ (considering the cap rock and under burden formations impermeable). For the mechanical simulations, the integration of over- and under-burden with their rock types heterogeneity and characteristics are taken into account to better estimate the stress state. For the mechanical model, a simplification of the geological layers (Figure 4-43) has been made considering the reservoir layer bounded at the bottom by under burden formation and at its top by cap rock and over burden layer (Figure 4-44a). The description of the geology in the mechanical model is completed by the integration of faults localisation (Figure 4-44b).

The PilotSTRATEGY project has received funding from the European Union's Horizon 2020 research and innovation programme under grant agreement No. 101022664

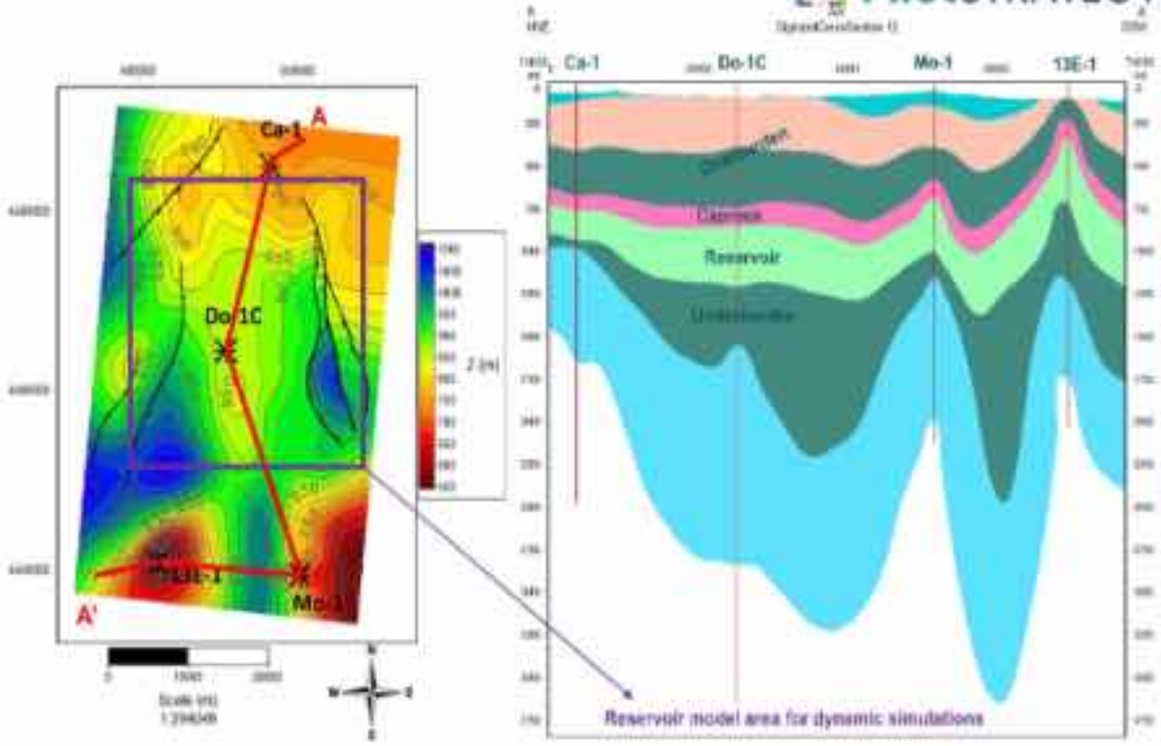


*Figure 4-42: Extension and topography of the hydrodynamics reservoir model (from Pereira et al., 2024).*

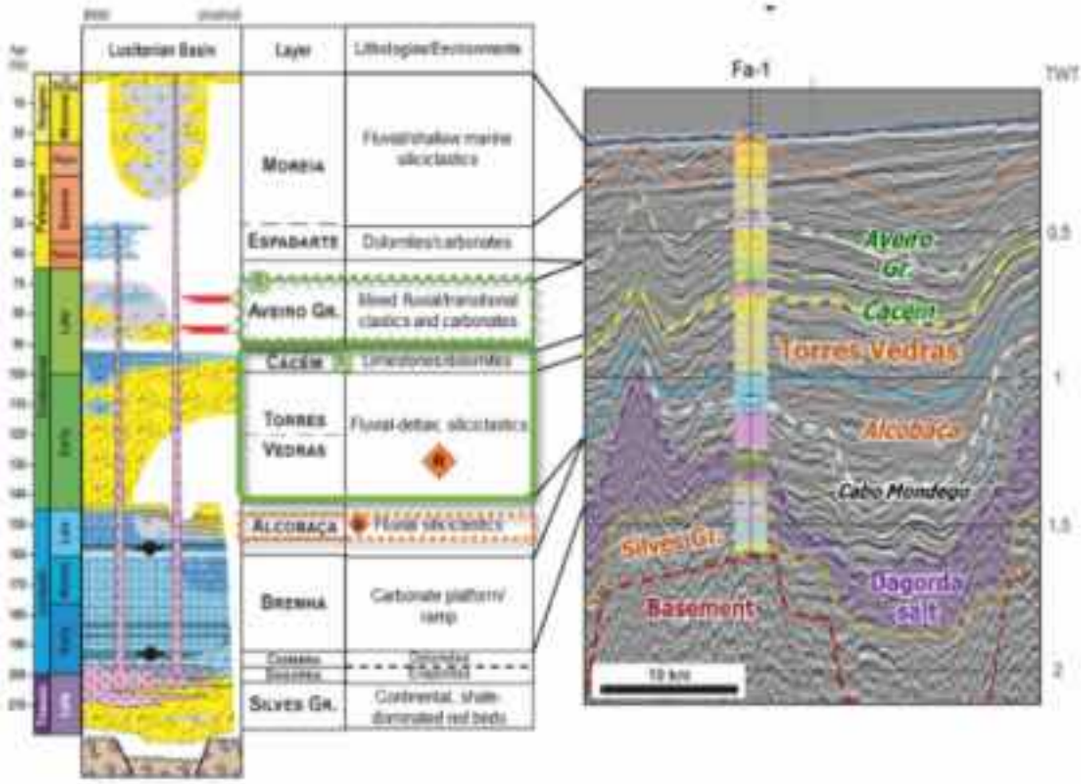


*Figure 4-43: Lithological description of the Lusitanian pilot area (from Marques da Silva et al., 2023).*

The PilotSTRATEGY project has received funding from the European Union's Horizon 2020 research and innovation programme under grant agreement No. 101022664

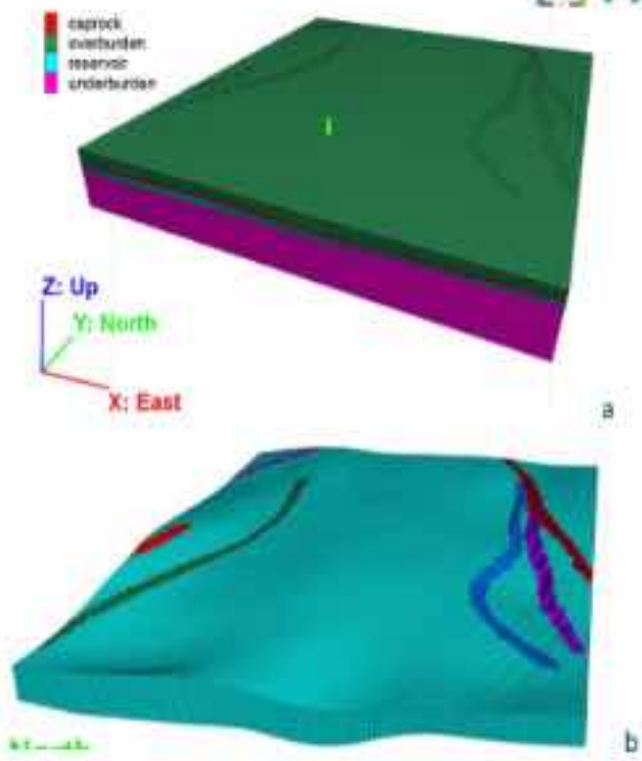


*Figure 4-44: Geological considerations of the mechanical model: rock layers integrated (a) and faults localisation (view in the reservoir layer (b).*

### 5.5.3.2 Mechanical equations

Two entities are to be taken into account in the mechanical simulations: the lithological units and the faults. The later are discontinuous units and should in theory be numerically represented as such instead of continuous elements. However, considering faults as thick damaged regions, using continuous numerical elements has proven relevant in numerous studies (Jeanne et al., 2017; Reiter et al., 2024).

FLAC3D is a widely used mechanical calculation software for engineering applications. It is a finite volume code that solves, for each mesh, the mechanical equilibrium equation (Equation 4-8):

$$\underline{div}\left(\underline{\underline{\sigma}}\right) + \rho \underline{g} = \underline{0} \qquad \textit{(Equation 4-8)}$$

where σ [Pa] is the total stress tensor, ρ [kg·m$^{-3}$] is the bulk density of the medium, and g [m·s$^{-2}$] is the acceleration due to gravity.

The total stress represents the interaction forces between the grains of the porous medium. The pore pressure within the pores tends to push the grains apart and thus opposes the effect of the total stress. Terzaghi's law expresses this relationship in a saturated medium with incompressible grains (Equation 4-9):

$$\underline{\underline{\sigma'}} = \underline{\underline{\sigma}} + p\underline{\underline{\delta}} \qquad \textit{(Equation 4-9)}$$

where σ' [Pa] is the effective stress tensor and p [Pa] is the pore pressure. Note that the negative compression convention is adopted: if the pressure p increases, the stress σ' also increases and thus becomes less compressive.

The PilotSTRATEGY project has received funding from the European Union's Horizon 2020 research and innovation programme under grant agreement No. 101022664

The relationship between effective stress and strain is governed by constitutive laws. In the elastic regime and for a homogeneous, isotropic medium, the constitutive law can be written as (Equation 4-10):

$$\underline{\underline{\sigma'}} = 2\mu\underline{\underline{\varepsilon}} + \lambda Tr\left(\underline{\underline{\varepsilon}}\right)\underline{\underline{\delta}} \qquad \textit{(Equation 4-10)}$$

where ε [–] is the strain tensor, μ [Pa] and λ [Pa] are the Lamé parameters. μ is the same parameter as the shear modulus, denoted G. The Lamé parameters are related to the more commonly used parameters: Young's modulus E [Pa] and Poisson's ratio ν [–], according to Equation 4-11:

$$\mu = \frac{E}{2(1+\nu)} \qquad \textit{(Equation 4-11)}$$
$$\lambda = \frac{E\nu}{(1+\nu)(1-2\nu)}$$

To account for irreversible deformation effects (grain rearrangement, microfracturing, etc.), plasticity laws extend the above equations. FLAC3D offers several plastic laws. In this study, the Mohr-Coulomb law was chosen, as it has proven to be representative in many applications and most notably when applied to fractures. This law involves only two parameters that describe how grains resist forces due to, on the one hand, their irregularities and induced friction, and on the other hand, the cementation between them. These parameters are the internal friction angle ϕ [°] and cohesion c [Pa].

Mathematically, these parameters are introduced in a plasticity limit (Equation 4-12):

$$\sigma_3' = \frac{\sigma_1' + 2c\sqrt{N_\phi}}{N_\phi} \qquad \textit{(Equation 4-12)}$$

where $\sigma_1'$ [Pa] and $\sigma_3'$ [Pa] are the major and minor principal stresses, respectively (in negative compression, $\sigma_1' \leq \sigma_3'$), and $N\phi = (1 + \sin(\phi))/(1 - \sin(\phi))$.

For a given stress $\sigma_1'$, the material remains in an elastic state as long as $\sigma_3'$ is less than the limit given above. When $\sigma_3'$ reaches the limit, the material enters plasticity, and irreversible deformations occur. Plasticity theory implies that $\sigma_3'$ cannot exceed the limit but must remain less than or equal to it: either $\sigma_3'$ < limit (elasticity) or $\sigma_3'$ = limit (plasticity).

#### 5.5.3.3 *Initial state and boundary conditions*

The initial state and boundary conditions are chosen in accordance with local tectonic knowledge of the Lusitanian Basin, where the stress state is estimated to be in slight extensive regime with a major horizontal stress direction of N145° (Heidbach *et al.*, 2025).

The initial state is obtained by applying gravity and stresses on all four lateral sides of the model (Dirichlet conditions). Besides, bottom boundary has fixed normal displacements, and top boundary is free. The applied stresses are obtained using horizontal to vertical stress ratios in accordance with the local tectonic regime: $\sigma_{Hmax} = \sigma_V$ and $\sigma_{hmin} = 0.8 \times \sigma_V$, hence leading to a slightly extensive regime ($\sigma_V$, $\sigma_{Hmax}$, and $\sigma_{hmin}$ are the vertical, maximum horizontal and minimum horizontal stresses, respectively).

Notice that some testing simulations where the model was extended laterally (not shown here) were run to ensure that having the faults close to the boundaries does not introduce bias in the results. We

The PilotSTRATEGY project has received funding from the European Union's Horizon 2020 research and innovation programme under grant agreement No. 101022664

observed that the outermost fault zones were very slightly impacted and the innermost ones, not at all.

The initial pore pressure is hydrostatic, and in accordance with the hydrodynamical computations previously conducted (Khudhur et al., 2024) as can be seen on Figure 4-45.

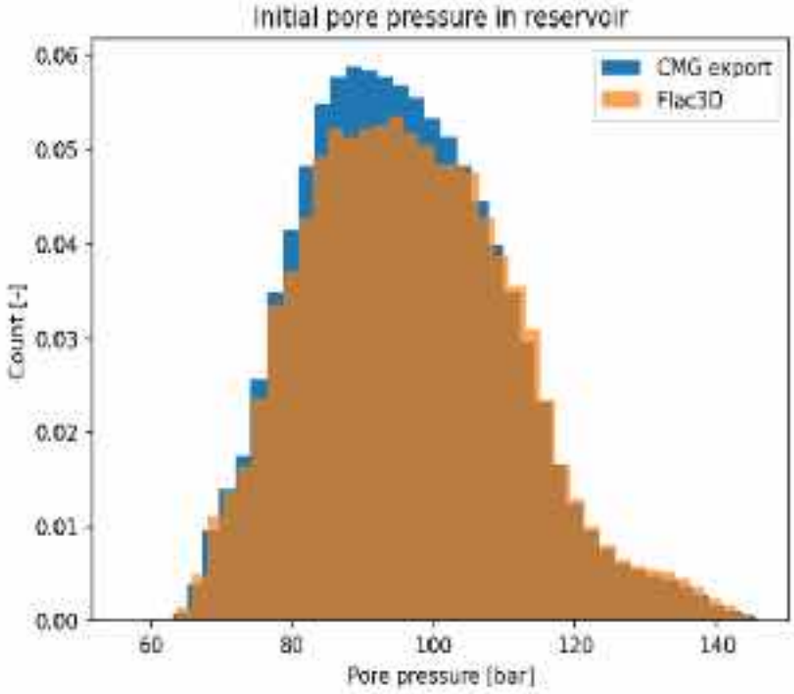


*Figure 4-45: Initial pore pressure distribution in reservoir both in University of Évora simulations (blue) and in BRGM simulations (orange). Note the slight difference of pore pressure distribution results from interpolating aspects.*

The PilotSTRATEGY project has received funding from the European Union's Horizon 2020 research and innovation programme under grant agreement No. 101022664

### 5.5.4 Parameters

The elastic parameters are based on *in situ* data and are plotted in Figure 4-46.

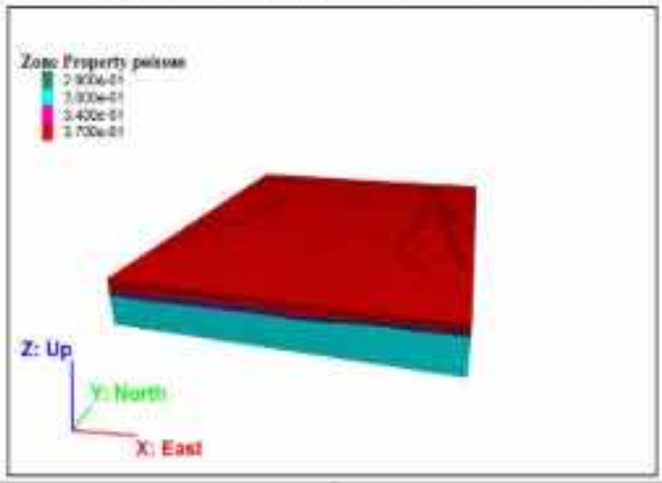


*a*

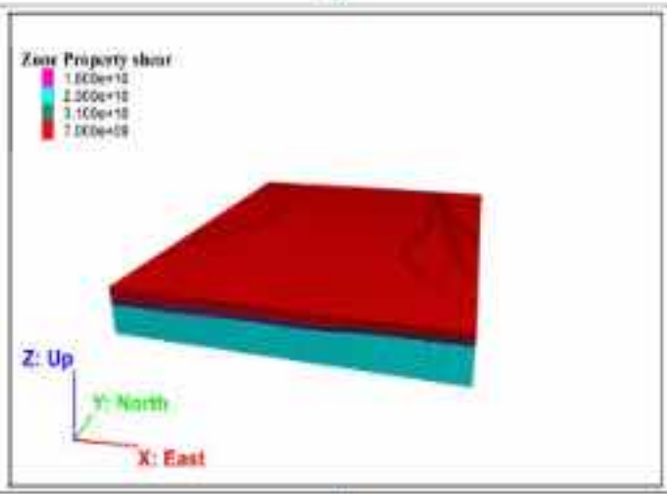


*b*

*Figure 4-46: Model elastic properties: a. Poisson ratio [-], and b. shear modulus [Pa].*

As for the plastic parameters within the faults, no data is available. Standard parameters were used: cohesion c=10 MPa and friction angle $\phi$=30° (Bemer et al., 2004) and are homogeneous throughout all the faults.

### 5.5.5 Results

#### *5.5.5.1 Reference case*

Figure 4-47 to Figure 4-53 show the overpressure evolution in the reservoir layer, where overpressure=0 corresponds to a pore pressure equals to that at the initial state.

Each figure reads as such:

- Top left: reservoir overpressure from top view, and rupture state in faults reservoir traces. Cyan cells indicate no rupture.
- Top right: reservoir overpressure east-west cross-section around modelled injection, and rupture state in faults through whole model (vertical scale is magnified by 5). Cyan cells indicate no rupture.
- Bottom left: overpressure distribution within faults reservoir traces only.

The PilotSTRATEGY project has received funding from the European Union's Horizon 2020 research and innovation programme under grant agreement No. 101022664

- Bottom right: faults stability. The axes depict the minimum and maximum effective stresses (red and black points) and the continuous line shows the Mohr-Coulomb yield as detailed in Equation 4-12. Points located above this line are stable.

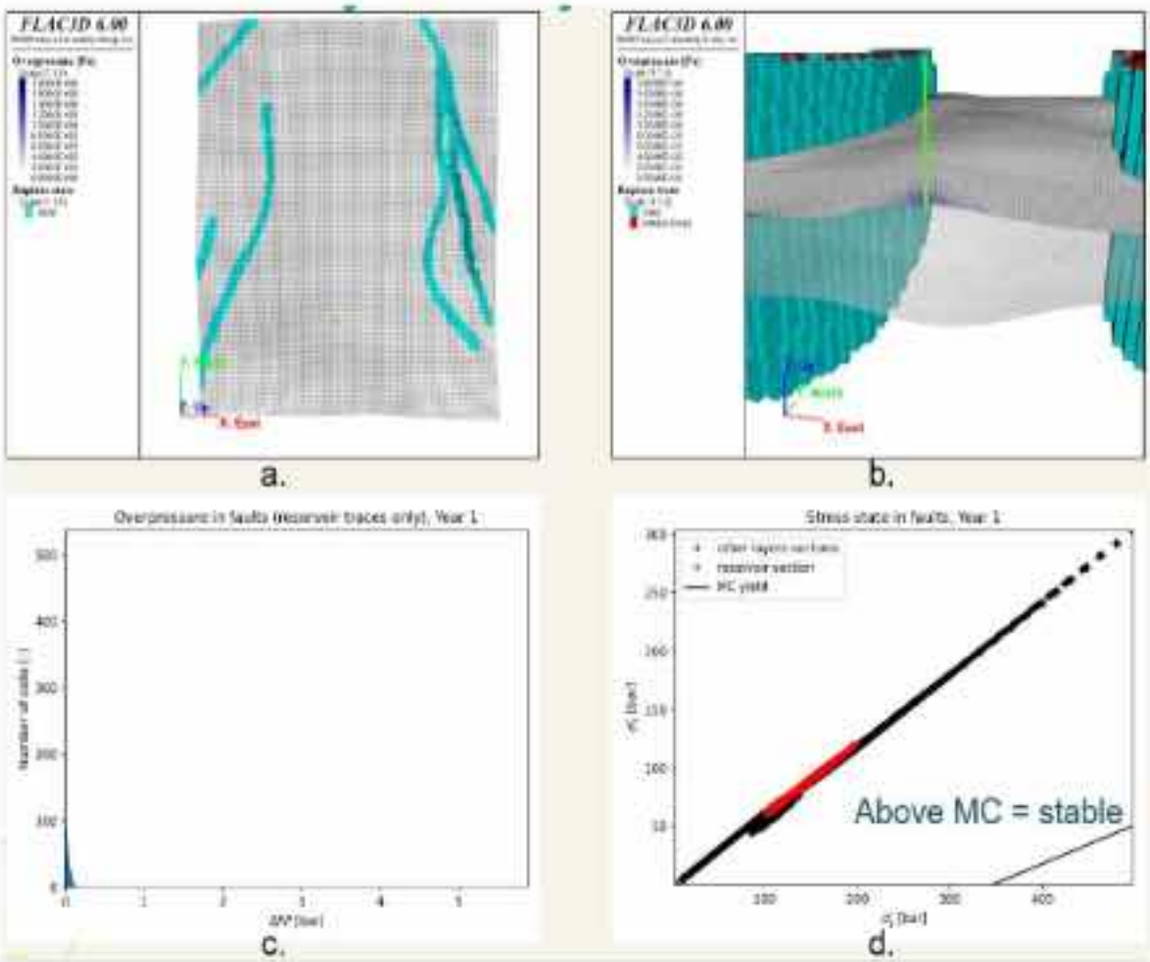


*Figure 4-47: state after 1 year of injection: a. overpressure (top view), b. overpressure (EW cross-section around modelled injection well), c. overpressure distribution in fault cells and d. stress state.*

The PilotSTRATEGY project has received funding from the European Union's Horizon 2020 research and innovation programme under grant agreement No. 101022664

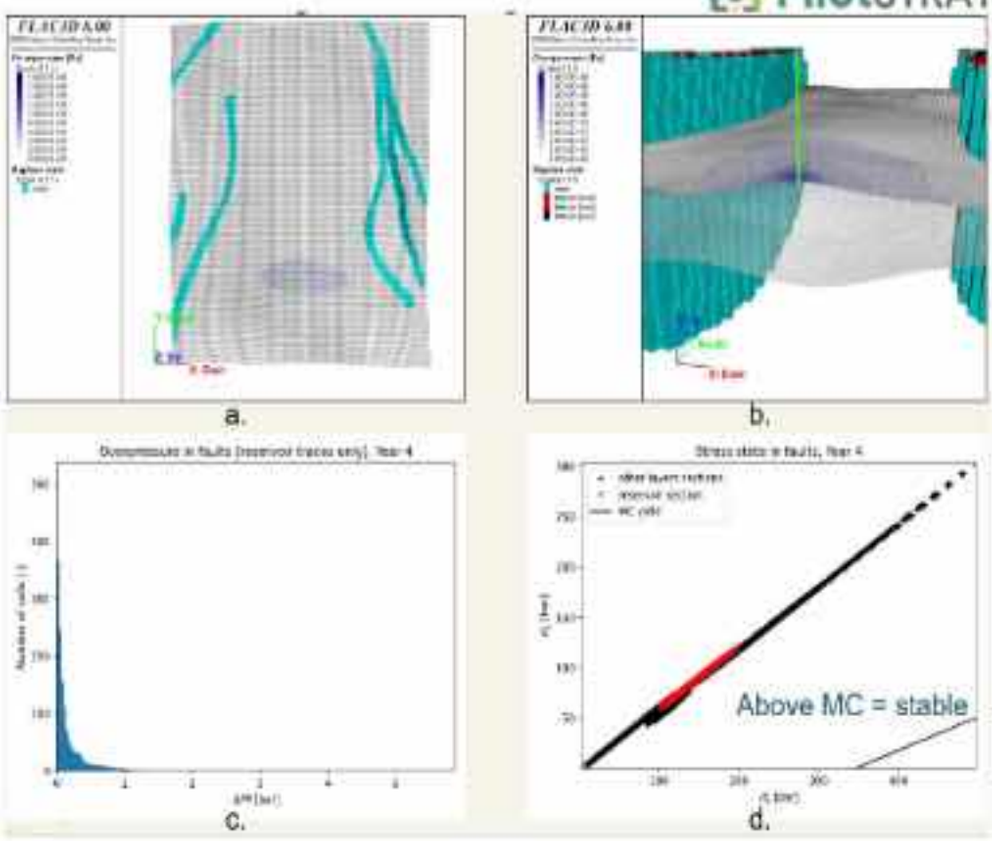


*Figure 4-48: state after 4 years of injection: a. overpressure (top view), b. overpressure (EW cross-section around modelled injection well), c. overpressure distribution in fault cells and d. stress state.*

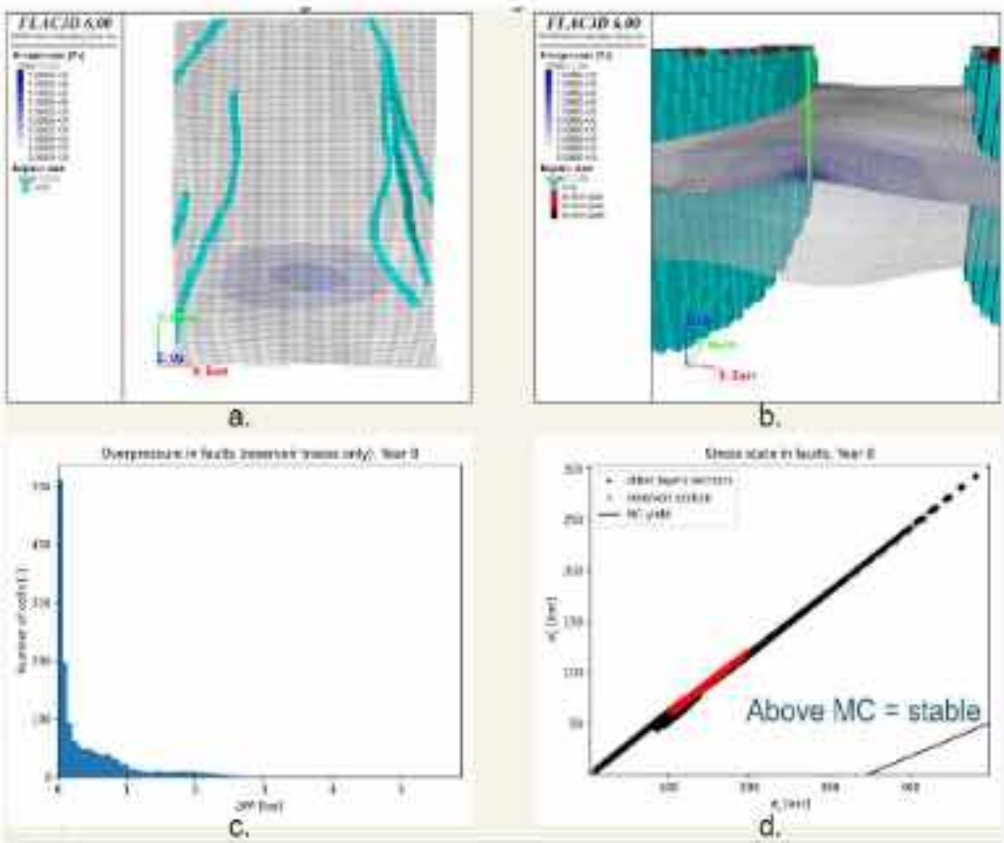


*Figure 4-49: state after 8 years of injection: a. overpressure (top view), b. overpressure (EW cross-section around modelled injection well), c. overpressure distribution in fault cells and d. stress state.*

The PilotSTRATEGY project has received funding from the European Union's Horizon 2020 research and innovation programme under grant agreement No. 101022664

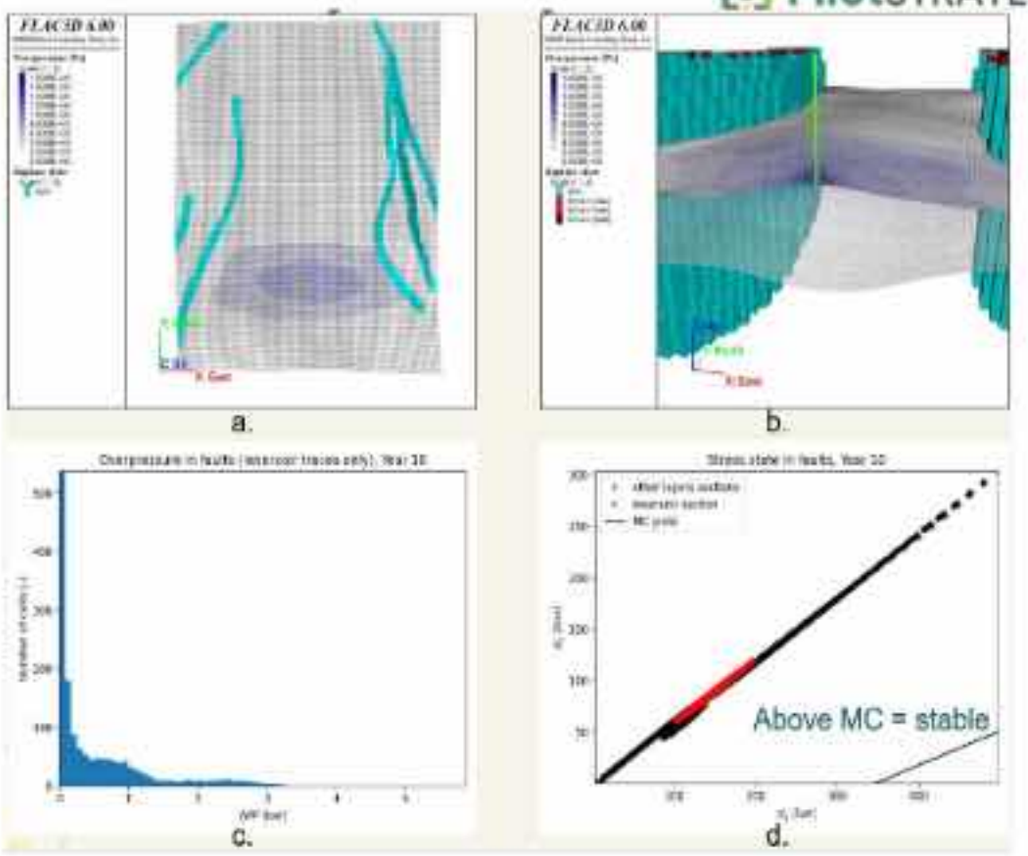


*Figure 4-50: state after 10 years of injection: a. overpressure (top view), b. overpressure (EW cross-section around modelled injection well), c. overpressure distribution in fault cells and d. stress state.*

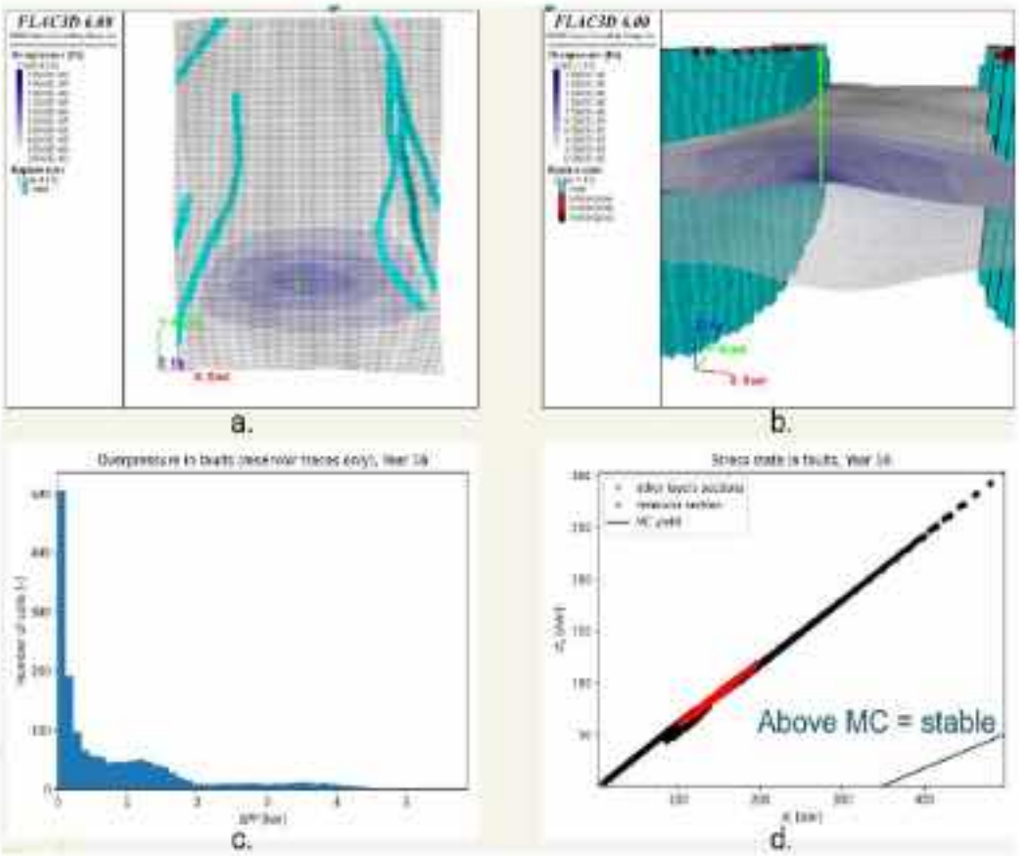


The PilotSTRATEGY project has received funding from the European Union's Horizon 2020 research and innovation programme under grant agreement No. 101022664

*Figure 4-51: state after 16 years of injection: a. overpressure (top view), b. overpressure (EW cross-section around modelled injection well), c. overpressure distribution in fault cells and d. stress state.*

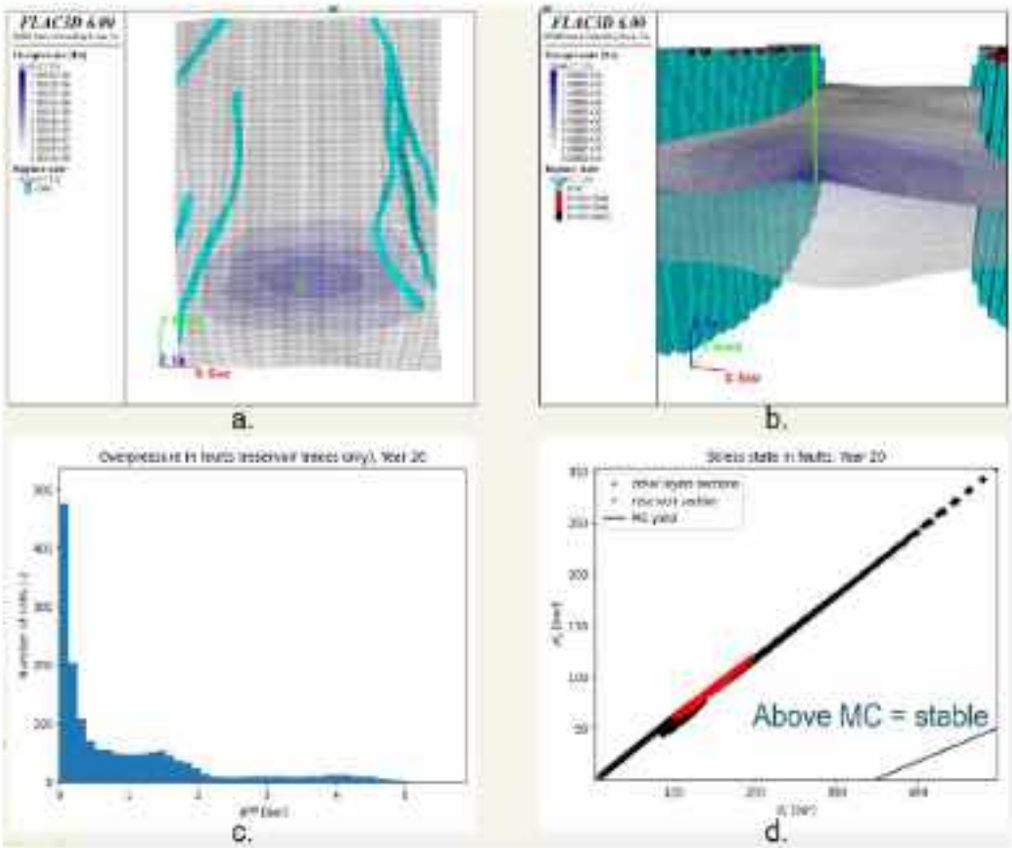


*Figure 4-52: state after 20 years of injection: a. overpressure (top view), b. overpressure (EW cross-section around modelled injection well), c. overpressure distribution in fault cells and d. stress state.*

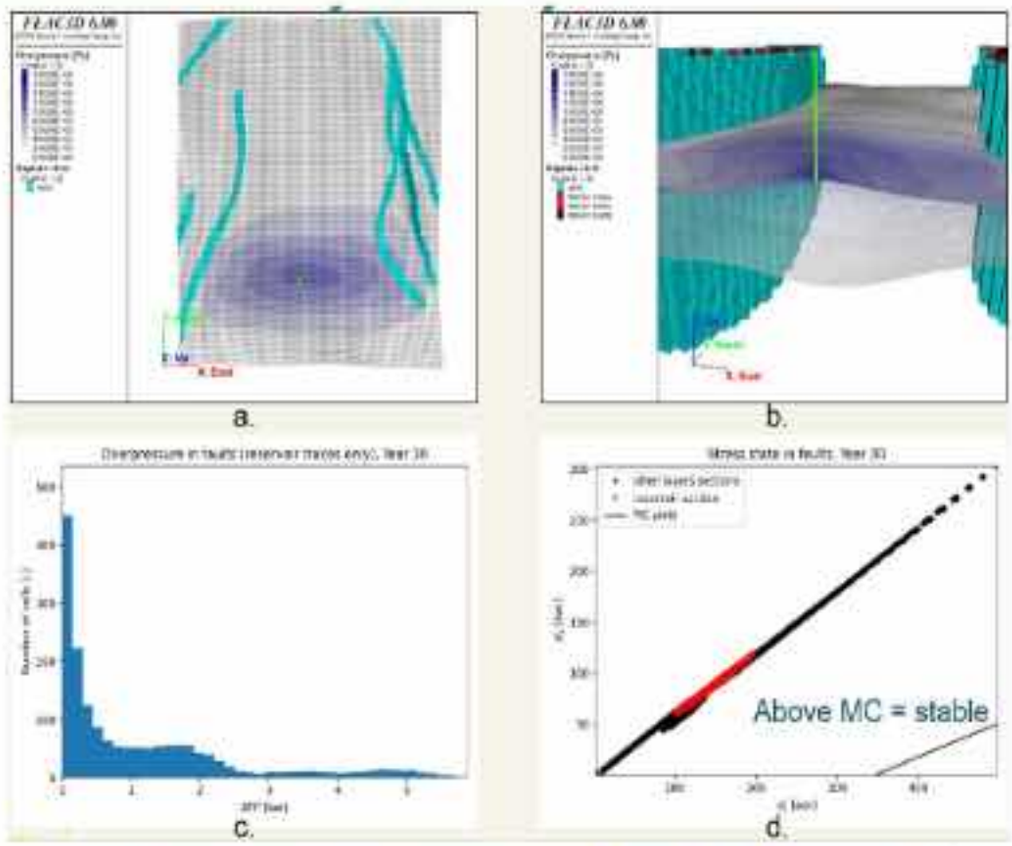


The PilotSTRATEGY project has received funding from the European Union's Horizon 2020 research and innovation programme under grant agreement No. 101022664

*Figure 4-53: state after 30 years of injection: a. overpressure (top view), b. overpressure (EW cross-section around modelled injection well), c. overpressure distribution in fault cells and d. stress state.*

Based on the simulations, faults are far from a potential reactivation even after 30 years of injection. The precise necessary injection pressure to reach rupture cannot be estimated from separate hydrodynamic and mechanic simulations. However, we can give an estimate on the additional overpressure that would be needed in the faults to have rupture. The estimation is derived from Equation 4-11: starting from a local stress state $(\sigma_1', \sigma_3')$ that is stable (i.e., where Equation 4-11 is NOT verified), the necessary additional overpressure $\Delta p_{rupt}$ to reach rupture would be yielded by Equation 4-13:

$$(\sigma_3' + \Delta p_{rupt}) = \frac{(\sigma_1' + \Delta p_{rupt}) + 2c\sqrt{N_\phi}}{N_\phi} \qquad \textit{(Equation 4-13)}$$

Straightforward manipulation leads to (Equation 4-14):

$$\Delta p_{rupt} = \frac{\sigma_1' - \sigma_3' N_\phi + 2c\sqrt{N_\phi}}{N_\phi - 1} \qquad \textit{(Equation 4-14)}$$

Taking the local stress states of the faults cells given by the points in Figure 4-53d, the $\Delta p_{rupt}$ distribution obtained is plotted in Figure 4-54.

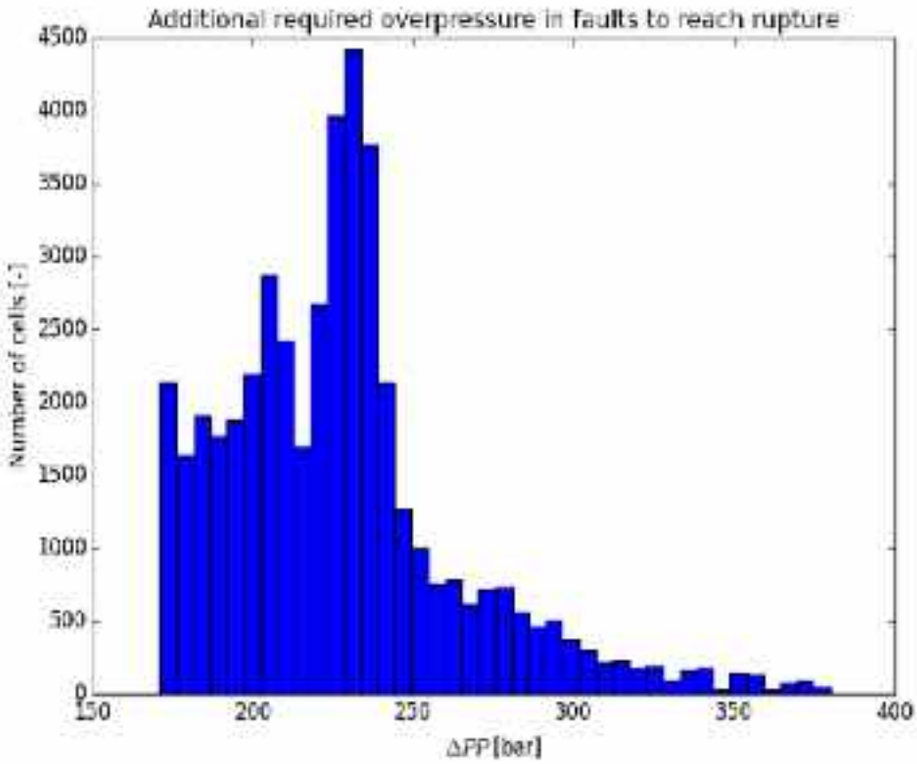


*Figure 4-54: additional pore pressure needed in faults to reach rupture (taking stress state after 30 years as reference state). This result is an approximation not accounting for stress distributions and hydrodynamical effects, actual overpressures might be lower.*

Those results estimate that an additional overpressure of at least 180 bars is required in the faults to reach rupture. The required injection overpressure at well should be estimated by running additional

The PilotSTRATEGY project has received funding from the European Union's Horizon 2020 research and innovation programme under grant agreement No. 101022664

hydrodynamical simulations and finding the critical injection pressure that would bring such values in the vicinity of the faults.

Our results most certainly overestimate the actual required additional overpressure (optimistic hypotheses about fault material properties; hydrodynamical effects and stress redistributions not accounted for). Still, these results illustrate that our model is quite far from rupture, and that tension rupture would occur before shear one.

#### 5.5.5.2 *Worst case scenario*

The faults elastoplastic properties are generic and derive from no measurements. Although based on well accepted ranges of values, they might overestimate the actual values and possibly the faults resistance to rupture. To explore how these parameters could impact the model results, we tried a "worst case "scenario where parameters depict poorly resistant faults due to highly subfractured and poorly cemented fault cores:

- Faults more prone to deformation: Young modulus fault = 80% of intact rock and Poisson ratio = 110%
- Poorer resistance to slip: 20° angle of friction (30° in ref.) and 2 MPa cohesion (10 MPa in ref.)

The simulation results still show results far from rupture. The final stress state is plotted in Figure .

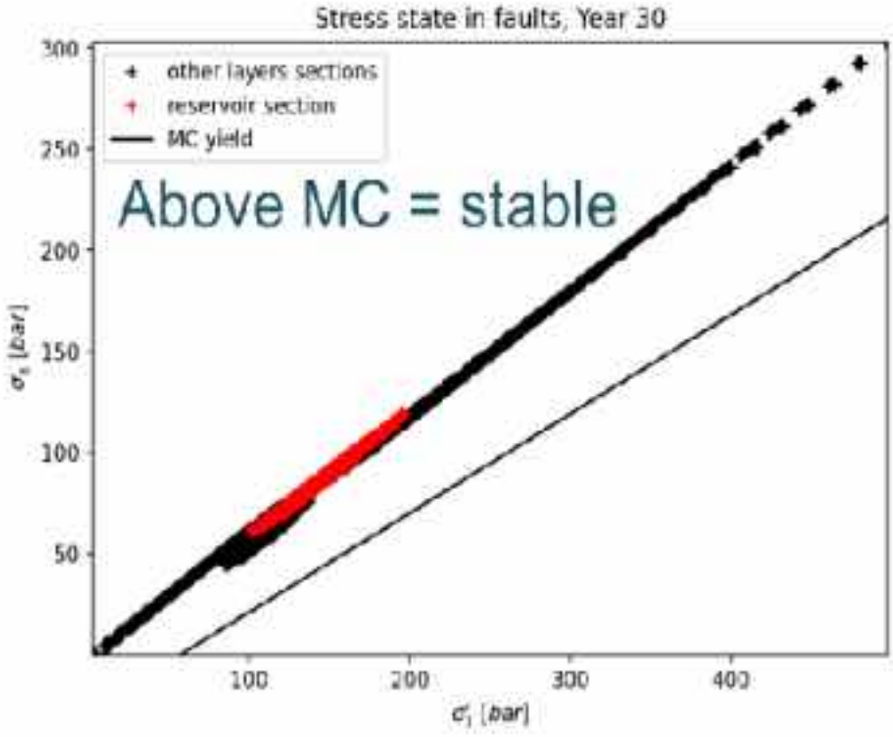


*Figure 4-55: faults stress state after 30 years of injection. The red points correspond to the fault cells located in the reservoir, and the black ones correspond to the fault cells in all other layers. The black line is the Mohr-Coulomb yield, and the space above this line represents stable conditions.*

Using Equation 4-13, an overall estimation of the additional required overpressure is plotted in Figure 4-56 and, according to model assumptions, still estimate high necessary overpressure values (>50 bars).

The PilotSTRATEGY project has received funding from the European Union's Horizon 2020 research and innovation programme under grant agreement No. 101022664

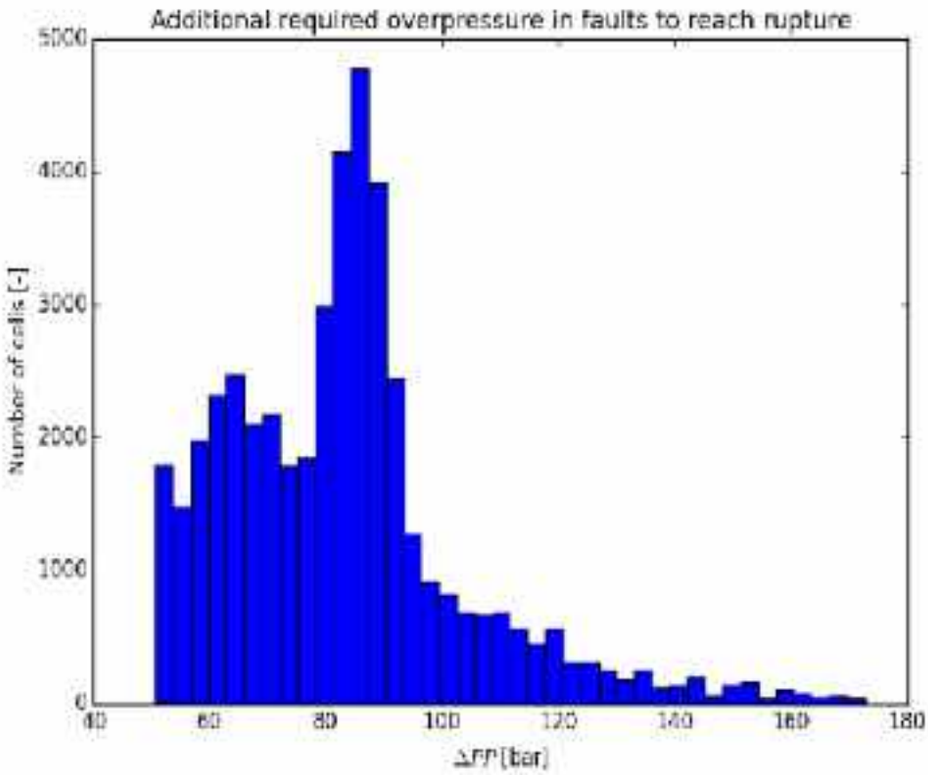


*Figure 4-56: additional pore pressure needed in faults to reach rupture for the worst case scenario (taking stress state after 30 years as reference state). This result is an approximation not accounting for stress distributions and hydrodynamical effects, actual overpressures might be lower.*

### 5.5.6 Discussion and Conclusions

The simulations result tends to highlight that, under the simulations assumptions, the model is quite far from reactivation. However, the model comes with some limitations, most notably on the physical laws used: the poroelastic effects were not accounted for (i.e., pore volume deformation under pressure), elastoplastic state equation (Mohr-Coulomb only) and parameters uncertainty.

When considering poroelasticity, the deformation due to pore pressure variation can be expressed as (Equation 4-15):

$$\varepsilon_V = \frac{1-2\nu}{E}\Delta p \qquad \textit{(Equation 4-15)}$$

With $\varepsilon_V$ is the volumetric strain and $\Delta p$ the overpressure in the medium.

With the simulation parameters and overpressures considered here, a maximum of $\varepsilon_V \approx 10^{-5}$ is expected letting us conclude that poroelastic effects should be negligible and poorly affect model stability. Note that for rocks with rigid properties (as is the case here), the volumetric strain is only affecting the pore volumes and will result in a variation of porosity $\Delta\phi = \varepsilon_V$. With $\varepsilon_V \approx 10^{-5}$, the porosity variation is well below 1% of the initial porosity illustrating how small poroelastic effects can be expected.

Our simulations come of course with limitations and could still be improved. Here is a non-exhaustive list of hints for future improvements: broader parameter value ranges, various mechanical laws of behaviour, different boundary conditions (displacements, stress ratios, etc.), different initial states

The PilotSTRATEGY project has received funding from the European Union's Horizon 2020 research and innovation programme under grant agreement No. 101022664

(e.g., multistage tectonics), even worse case situations (i.e., lower friction/cohesion) and, ideally, a complete poroelastic model.

One of the main feedback from this work, relying on two different softwares (Aspen Tempest/SKUA and Flac3D), is the importance of putting efforts in the inter-softwares compatibility. Among all the combined efforts from the partners involved, the most time-impacting actions were:

- Meshes consistencies;
- Representative interpolation;
- Multi-format conversion;
- Flac3D mesh trial and errors (poor meshing capacities, plus estimating the optimal ratio between precision and computation times).

## 5.6 Final Remarks

The phenomenological assessment of the Q4-TV1 offshore prospect integrates coupled hydrodynamic, thermal, geochemical and geomechanical analyses to evaluate storage integrity over operational and post-injection timescales. By combining high-resolution near-well modelling with long-term basin-scale simulations, the assessment addresses reservoir injectivity, caprock geochemical and geomechanical integrity, and fault stability. The results indicate a robust storage system in which perturbations remain spatially limited, and no mechanisms are identified that would compromise long-term containment. From a risk perspective, the main challenges are operational and localized, rather than structural or systemic, and can be addressed through appropriate injection management and monitoring.

Injectivity integrity represents the dominant short-term operational control, primarily influenced by salt precipitation in the near-wellbore zone during $CO_2$ injection. Under reference conditions, these effects remain confined close to the well and do not affect reservoir-scale performance. Sensitivity analyses confirm that injection rate and reservoir salinity are the main amplifiers of near-well impairment, while injection temperature plays a secondary role. Only under compounded unfavourable conditions do transient injectivity limitations appear, restricted to the early injection phase. Accordingly, the overall risk of injectivity loss is low, increasing to low-to-moderate only under extreme operational scenarios. Mitigation relies on careful control of injection rates, continuous bottom-hole pressure monitoring, gradual ramp-up of injection, and accurate pre-injection characterization of formation salinity.

Caprock geochemical integrity is governed by buffered reactions at the aquifer–caprock interface and represents a long-term containment consideration rather than an operational constraint. Reactive transport simulations show that mineral alterations remain localized and do not induce significant changes in caprock petrophysical properties. Variations in mineralogical composition do not significantly modify sealing performance, confirming the robustness of the geochemical barrier. Only under deliberately pessimistic assumptions, involving degraded basal sealing units, does limited upward $CO_2$ migration occur, without propagation into overlying formations due to the large caprock thickness. The risk of geochemically induced leakage is therefore assessed as low to low-moderate, mainly reflecting geological uncertainty. Mitigation focuses on improving caprock characterization, refining geological models, and implementing targeted monitoring at the reservoir–caprock interface.

The PilotSTRATEGY project has received funding from the European Union's Horizon 2020 research and innovation programme under grant agreement No. 101022664

From a geomechanical perspective, both caprock fracturing risk and fault reactivation potential remain consistently low across all investigated scenarios. Injection-induced pressure changes do not approach failure conditions, and mechanical responses remain elastic and reversible. Uncertainty analyses confirm a high margin of stability even under intensified injection rates and unfavourable mechanical parameter assumptions. Faults remain stable and no permeability enhancement or leakage pathways are generated. However, it is important to mention that these results are obtained under the specific modelling assumptions, parameter ranges, and boundary conditions adopted in this study, and should therefore be interpreted within this context. A broader exploration of parameter variability and alternative boundary conditions would further strengthen the robustness of these conclusions.

The geomechanical risk is therefore assessed as low. Mitigation is essentially preventive, consisting of pressure-controlled injection, avoidance of abrupt rate increases, and periodic updating of geomechanical models as additional field data become available.

This integrated assessment demonstrates that the Q4-TV1 prospect exhibits a high degree of resilience to coupled hydraulic, thermal, geochemical and mechanical perturbations. The dominant risks are localized near-well effects affecting early-time injectivity under unfavourable operational and geochemical conditions, while caprock sealing capacity and fault stability remain robust over long timescales. The storage complex benefits from strong structural, capillary and geochemical trapping, with no evidence of progressive degradation or leakage risk. Although the results support the technical feasibility and long-term security of $CO_2$ storage in the offshore Lusitanian Basin, safe deployment requires disciplined injection management, continuous pressure surveillance, early-time injectivity monitoring, and ongoing refinement of geological and geomechanical models to further reduce residual uncertainties and ensure sustained containment performance.

## 5.7 References

Afonso, P., Carneiro, J. & Moita, P. (2025) Lusitanian Basin (Portugal). In Wilkinson, M. (Ed.), Report on geochemical results for 3 areas. Deliverable WP2/D2.9, EU H2020 PilotSTRATEGY project 101022664 report.

Ahmed, T. (2019). Reservoir Engineering Handbook (5th ed.). Gulf Professional Publishing.

Atkinson, J. (2007). The mechanics of soils and foundations (2.ª ed.). Taylor & Francis.

Barradas, J., Carneiro, J., Correia, A., Moita, P. & Ribeiro, C. (2023). Lusitanian Basin (Portugal). In Wilkinson, M. (Ed.), Report on petrophysics of all regions. Deliverable WP2/D2.6, EU H2020 PilotSTRATEGY project 101022664 report.

Berner, E., Vincké, O. & Longuemare, P. (2004). Geomechanical Log Deduced from Porosity and Mineralogical Content. Oil & Gas Science and Technology - Rev. IFP 59, 405–426. https://doi.org/10.2516/ogst:2004028.

Castagna, J. P., Batzle, M. L., & Kan, T. K. (1993). Rock physics – The link between rock properties and AVO response. In J. P. Castagna & M. Backus (Eds.), Offset-dependent reflectivity: Theory and practice of AVO analysis (Investigations in Geophysics, Vol. 8, pp. 135–171). Society of Exploration Geophysicists. https://doi.org/10.1190/1.9781560802624.

The PilotSTRATEGY project has received funding from the European Union's Horizon 2020 research and innovation programme under grant agreement No. 101022664

Computer Modelling Group Ltd. (2022). GEM User Guide: Advanced Compositional & Reactive Transport Reservoir Simulator. CMG, Calgary, Alberta, Canada.

Dake, L. P. (1978). Fundamentals of Reservoir Engineering. Elsevier.

Ellsworth W. L. (2013). Injection-Induced Earthquakes. Science, 341 (6142), 1225942, DOI: 10.1126/science.1225942.

Greenberg, M. L., & Castagna, J. P. (1992). Shear-wave velocity estimation in porous rocks: Theoretical formulation, preliminary verification, and applications. Geophysical Prospecting, 40, 195–209. https://doi.org/10.1111/j.1365-2478.1992.tb00371.x.

Heidbach O., Rajabi M., Di Giacomo D., Harris J., Lammers S., Morawietz S., Pierdominici S., Reiter K., von Specht S., Storchak D. & Ziegler M. O. (2025). World Stress Map 2025. GFZ Data Services. https://doi.org/10.5880/WSM.2025.002.

Hetty. (2001). Theory of shear strength [PowerPoint slides]. SIVA.

IEAGHG (2011). CAPROCK SYSTEMS FOR $CO_2$ GEOLOGICAL STORAGE. IEA Greenhouse Gas R&D Programme (IEAGHG), Report 2011/03, May 2011.

Jeanne P., Rutqvist J., Foxall W., Rinaldi A. P., Wainwright H. M., Zhou Q., Birkholzer J. & Layland-Bachmann C. (2017). Effects of the distribution and evolution of the coefficient of friction along a fault on the assessment of the seismic activity associated with a hypothetical industrial-scale geologic CO2 sequestration operation. International Journal of Greenhouse Gas Control. n° 66 pp. 254–263. https://doi.org/10.1016/j.ijggc.2017.09.018.

Khudhur, K., Pereira, P., Carneiro, J., Hardwick, J., Santos, M. & Casacão, J. (2024). Lusitanian Basin (Portugal). In Chassagne, R. (Ed.), Report on optimization – injection strategy and storage capacity. Deliverable WP3/D3.3, EU H2020 PilotSTRATEGY project 101022664 report, 73-98.

Lee K. L., Ellsworth W. L., Giardini D., Townend J., Ge S., Shimamoto T., Yeo I.-W., Kang T.-S., Rhie J., Sheen D.-H., Chang C., Woo J.U., Langenbruch C. (2019). Managing injection-induced seismic risks. Science. 364 (6442), 730-732. DOI: 10.1126/science.aax1878.

Marques da Silva, D., Caeiro, M. H., Pereira, P., Ribeiro, C., Carneiro, J., Casacão, J. & Pina, B. (2023). Lusitanian Basin (Portugal). In Wilkinson, M. (Ed.), Report on Conceptual Geological Models. Deliverable WP2/D2.7, EU H2020 PilotSTRATEGY project 101022664 report.

Pang Y., Zhang H., Cheng H., Shi Y., Fang C., Luan X., Chen S., Li Y. & Hao M. (2020). The modulation of groundwater exploitation on crustal stress in the North China Plain, and its implications on seismicity. Journal of Asian Earth Sciences. n° 189, 104141, https://doi.org/10.1016/j.jseaes.2019.104141.

Pereira, P., Caeiro, M.H., Carneiro, J., Khudhur, K., Ribeiro, C., Lopes, A.M., Santos, M. & Marques da Silva, D. (2024). Lusitanian Basin (Portugal). In Bouquet, S. (Ed.), Report on static modelling with uncertainties. Deliverable WP3/D3.2, EU H2020 PilotSTRATEGY project 101022664 report, 105-139.

Pereira, P., Behnous, D., Khudhur, K., Carneiro, J., Caeiro, M. H. & Santos, M. (2026). Lusitanian Basin (Portugal). In Ben Rhouma, S. (Ed.), Report on $CO_2$ fate on the long-term. Deliverable WP3/D3.4, EU H2020 PilotSTRATEGY project 101022664 report.

The PilotSTRATEGY project has received funding from the European Union's Horizon 2020 research and innovation programme under grant agreement No. 101022664

Reiter, K., Heidbach, O. & Ziegler, M.O. (2024). Impact of faults on the remote stress state. Solid Earth 15, 305–327. https://doi.org/10.5194/se-15-305-2024.

Rutqvist, J., (2012). The geomechanics of $CO_2$ storage in deep sedimentary formations. Geotechnical and Geological Engineering, 30(3), pp.525-551.

Rutqvist J., Rinaldi A. P., Cappa F. & Moridis G. J. (2013). Modeling of fault reactivation and induced seismicity during hydraulic fracturing of shale-gas reservoirs. Journal of Petroleum Science and Engineering, n°107, pp.31–44.

VanWees J.D., Buijze L., VanThienen-Visser K., Nepveu M., Wassing B.B.T., Orlic B. & Fokker P.A. (2014). Geomechanics response and induced seismicity during gas field depletion in the Netherlands. Geothermics. n° 52, pp. 206–219.

Wolery T. J., Jove-Colon C. F. & Jareck, R. L. (2007). Qualification of Thermodynamic Data for Geochemical Modeling of Mineral-Water Interactions in Dilute Systems. ANL-WIS-GS-000003 Rev 01. Sandia National Laboratories: Las Vegas, Nevada, ACC: DOC.20070619.0007.

Zoback, M.D. & Gorelick, S.M., (2012). Earthquake triggering and large-scale geologic storage of carbon dioxide. Proceedings of the National Academy of Sciences, 109(26), pp.10164-10168.

The PilotSTRATEGY project has received funding from the European Union's Horizon 2020 research and innovation programme under grant agreement No. 101022664

# 6. Ebro region (Spain)

## 6.1 Introduction and problem definition

The work discussed in the present deliverable is based upon the reservoir simulation work that was presented and discussed in previous Deliverables D3.3 (Blanco Pericana et al., 2024) and D3.4 (Ben Rhouma, 2026).

An initial dynamic model was developed using SLB's Intersect reservoir simulator (version 2023.4) and presented in Deliverable 3.3. In this model, both the maximum storage capacities and the achievable injection rates were found to be relatively low. This behaviour is primarily linked to the poor reservoir properties and the fact that the reservoir is initially overpressured. The low permeabilities assigned in the model were largely derived from laboratory measurements on outcrop samples from the Torre de las Arcas section, as documented in Deliverable D3.2 (Garcia et al., 2024). Under these conditions, the simulated system yielded a total storage capacity of approximately 3.15 Mt for a single injection well operating over a 30-year period. Beyond constraining storage capacity, the combination of low permeability and natural overpressure also has important geomechanical implications, affecting both the fracture pressure and the potential for fault reactivation during injection operations.

Subsequent analysis of the Chiprana-1 well, located near the Lopin site (see location in Fig. 6-2 of Deliverable D3.3; Blanco Pericana et al., 2024), revealed a porosity–permeability relationship that differed significantly from earlier assumptions. Laboratory core measurements confirmed reservoir properties that were markedly more favourable than those inferred from outcrop samples. Based on these new insights, a revised porosity–permeability relationship was established and incorporated into an updated dynamic reservoir model. The updated reservoir simulation, performed using SLB's Intersect (version 2025.1), indicates a maximum storage capacity of 14.62 Mt and a peak injection rate of 0.496 Mtpa for the scenario involving two injection wells. This revised dynamic model is fully documented in Deliverable 3.4 (Ben Rhouma, 2026), and the present deliverable has been prepared using this updated model as its reference framework.

The first part of the analysis described here (section 6.2) addresses wellbore integrity, evaluated through the estimation of potential injectivity loss caused by solid deposition. Because the reservoir target interval is predominantly siliceous, it is considered chemically and mineralogically inert. This assessment is supported by mineralogical analyses of the reservoir section, including observations from the Peña Royas and Torre de las Arcas outcrops and the Chiprana-1 well report, as discussed in Deliverable D2.7 (Ayala, 2023) and further detailed in Deliverable D3.4 (Ben Rhouma, 2026). Nevertheless, given the high salinity of the formation water (160,000 ppm in the base-case scenario), it is necessary to assess the potential impact of NaCl precipitation around the injection well and its influence on achievable injection rates.

Section 6.4, titled "*Storage complex integrity – studies on its mechanical stability*", constitutes the core of this deliverable. This emphasis arises from the reasons outlined previously —namely, the poor reservoir properties and the presence of natural overpressure, which together result in a narrow operational pressure window before reaching the fracture gradient and/or potentially triggering induced seismicity. The chapter is structured into two subsections. The first subsection (Section 6.4.2) focuses on the preparation of a multi-well 1D geomechanical study, using four wells with the most

The PilotSTRATEGY project has received funding from the European Union's Horizon 2020 research and innovation programme under grant agreement No. 101022664

complete dataset available in the study area (well log data). Mechanical properties obtained from laboratory analyses (Deliverable 2.8; Baroni *et al.* 2023) were also incorporated for limited comparative purposes, acknowledging that these measurements were performed on outcrop samples rather than core material. The effective stress ratio (ESR) method was applied to derive in-situ stress conditions, including the magnitudes and gradients of vertical stress, minimum horizontal stress, maximum horizontal stress, pore pressure, and fracture gradient for each well considered. The second subsection (Section 6.4.5) extends the results of the multi-well 1D geomechanical study to a regional scale. These geomechanical parameters were integrated with key reservoir simulation outputs (*i.e.* the initial reservoir pressure and the maximum reservoir pressure reached during injection). By applying the Mohr–Coulomb failure criterion to each mapped fault, and by accounting for the stress state and pressure acting on each structure, the susceptibility of individual faults to reactivation was assessed. As expected, faults situated closest to the planned injection wells show the highest likelihood of reactivation.

## 6.2 Integrity of the wellbore.

Salt precipitation may occur around a $CO_2$ injection well due to evaporative drying, whereby injected $CO_2$ absorbs water from the formation brine, increasing its salinity beyond saturation. This process leads to the formation of solid salt deposits in the near-wellbore pore space, reducing effective permeability and causing injectivity loss. The resulting permeability impairment elevates near-wellbore pressures, potentially bringing operational pressures closer to closure limits—an effect that is particularly critical in low-permeability and overpressured reservoirs. Although some precipitated salt may dissolve if brine later re-enters the affected zone, injectivity impairment during active $CO_2$ injection can be significant and therefore warrants careful consideration in dynamic modelling.

A dedicated study was undertaken to assess the potential injectivity impairment at the Lopin site resulting from salt precipitation during continuous $CO_2$ injection. This analysis focused on simulating halite (NaCl) deposition around the $CO_2$ injection well CCS-1. The primary objective was to evaluate the geochemical interactions between the injected $CO_2$ and the formation brine under conditions favourable for salt precipitation. The model incorporated the reservoir's temperature, pressure, and salinity characteristics to predict the spatial and temporal development of NaCl accumulation in the near-wellbore region.

### 6.2.1 Methodology

Representation of water vaporization and near-wellbore drying must be considered when predicting solid deposition, particularly NaCl precipitation, during $CO_2$ injection into saline formations. In this study, SLB's Eclipse 300 reservoir simulator (version 2025.1) was employed to evaluate these phenomena using the isothermal `CO2STORE` option. The `CO2STORE` option considers three phases: a $CO_2$-rich phase, a $H_2O$-rich phase and a solid phase. The $CO_2$-rich phase is labelled the gas phase while the $H_2O$-rich phase is labelled the aqueous phase (liquid phase). `CO2STORE` provides a compositional treatment of $CO_2$–$H_2O$ interactions and evaluates salt precipitation and dissolution through equilibrium-based reactions, allowing the prediction of solid build-up, pore-throat blockage, and permeability reduction.

The PilotSTRATEGY project has received funding from the European Union's Horizon 2020 research and innovation programme under grant agreement No. 101022664

The partitioning of $CO_2$ and $H_2O$ between the aqueous and gas phases follows the correlations of Spycher and Pruess (2005, 2009), which are applicable for temperature and pressure conditions relevant for geological $CO_2$ storage (12–100 °C and up to 600 bar). Within this framework, salts remain entirely in the aqueous phase unless the `SOLID` keyword is activated; both configurations (*i.e.* with and without the `SOLID` keyword) were assessed in the present study. When the `SOLID` option is enabled, the components NaCl, $CaCl_2$, and $CaCO_3$ may exist in both aqueous and solid phases according to the following equilibrium reactions:

$$H_2O \rightleftharpoons H^+ + OH^-$$

$$CO_2 + H_2O \rightleftharpoons HCO_3^- + H^+$$

$$HCO_3^- \rightleftharpoons CO_3^- + H^+$$

$$NaCl_{(s)} \rightleftharpoons Na^+ + Cl^-$$

$$CaCl_{2(s)} \rightleftharpoons CaCl^+ + Cl^-$$

$$CaCl^+ \rightleftharpoons Ca^{2+} + Cl^-$$

$$CaCO_{3(s)} \rightleftharpoons Ca^{2+} + CO_3^-$$

In the present study, only $CO_2$ and NaCl were included to allow the use of a simplified geochemical system within the simulator. The NaCl solubility model is based upon the work by Potter II *et al.* (1977). The maximum NaCl solubility in the aqueous phase is calculated using the following empirical correlation:

$$w_{NaCl} = 26.218 + 0.0072 \times T + 0.000106 \times T^2, \quad [1]$$

where $w_{NaCl}$ is the maximum solubility of NaCl at the vapour pressure in weight percent and $T$ is the temperature in degrees Celsius. The gas and aqueous saturations are normalised to be between zero and unity, so the two-phase water and gas relative permeability curves can be used. However, the presence of solids reduces the effective fluid volume, $FV$, which is defined as:

$$FV = (1 - S) \times PV, \quad [2]$$

where $PV$ is the pore volume and $S$ is the solid saturation.

The pre-existing reservoir simulation model used in this study (Deliverable D3.3) was converted from Intersect to Eclipse 300 (`CO2STORE`). The conversion was carefully validated, and the results confirm that the Eclipse 300 model correctly reproduces water vaporization in the near-wellbore region during $CO_2$ injection (see Appendix 7.3.1).

In the present study, Eclipse 300's `SOLID` option is used to calculate the permeability reduction caused by solid plugging through a mobility multiplier function. When a solid phase is present, the mobility for component $c$ in phase $p$, $M_p^c$, is given by:

$$M_p^c = x_p^c \cdot k_s \cdot k_{rp}(S_p) \cdot \frac{b_p}{\mu_p}, \quad [3]$$

where $x_p^c$ is the mole fraction of component $c$ in phase $p$, $k_s$ is the mobility multiplier accounting for the presence of solids, $k_{rp}$ is the relative permeability of phase $p$, $S_p$ is the normalized saturation of phase $p$, $b_p$ is the molar density of phase $p$, and $\mu_p$ is the viscosity of phase $p$.

The PilotSTRATEGY project has received funding from the European Union's Horizon 2020 research and innovation programme under grant agreement No. 101022664

The term $k_s$ in Equation [3] represents the mobility reduction resulting from plugging of the pores by adsorbed solids. This mobility multiplier can be specified either as a function of the adsorbed concentration or alternatively as a function of the adsorbed saturation, $S_a$. The latter option, which is adopted in this work, is implemented through the SOLIDMMS keyword in Eclipse 300. With SOLIDMMS, the mobility multiplier is defined as

$$k_s = k_{ss}(S_a) \quad [4]$$

with the adsorbed saturation given by

$$S_a = (1 - f_s)\cdot\bar{S}_s \quad [5]$$

Here, $f_s$ is the (dimensionless) fraction of solid present in the flowing phase and $\bar{S}_s$ is the normalised solid saturation, defined as the solid volume expressed as a fraction of the pore volume. In the present model, the SOLIDMMS mobility multiplier, $k_s$, is applied uniformly to all fluid phases, implying that permeability reduction caused by solid deposition affects the flow of all phases equally. The factor $(1 - f_s)$ ensures that only the adsorbed (*i.e.* immobile) fraction of solids contributes to permeability degradation, while solids remaining in suspension do not directly reduce mobility.

The SOLIDMMS function $k_{ss}(S_a)$ is provided as a tabulated input and represents the mobility multiplier associated with pore plugging and surface coverage by deposited solids. As $S_a$ increases, $k_s$ decreases, reflecting the progressive permeability impairment due to solid deposition within the pore network. This formulation enables the simulator to capture the coupled effects of solid transport, adsorption, and permeability reduction in a fully compositional framework, while maintaining flexibility through user-defined mobility reduction curves.

Due to the absence of field data, laboratory measurements, or literature-based calibration datasets applicable to the specific solid phase and flow conditions considered in this study, the SOLIDMMS permeability multiplier remains poorly constrained. As a result, the functional form of the solid mobility–saturation relationship is subject to significant uncertainty.

To address this limitation, we adopted a bracketing approach, commonly used in reservoir simulation and reactive transport modelling. Two end-member cases were evaluated, representing high- and low-solid-mobility conditions. Each case is defined by a distinct $k_s = k_{ss}(S_a)$ relationship (Figure 3). These relationships are not intended to represent a specific constitutive law, but rather to bound the plausible range of system behaviour given current uncertainties. This approach enables an assessment of the sensitivity of injectivity impairment to solid deposition processes, with particular emphasis on near-wellbore regions, where permeability reduction, flow convergence, and associated injectivity losses are expected to be most pronounced.

The PilotSTRATEGY project has received funding from the European Union's Horizon 2020 research and innovation programme under grant agreement No. 101022664

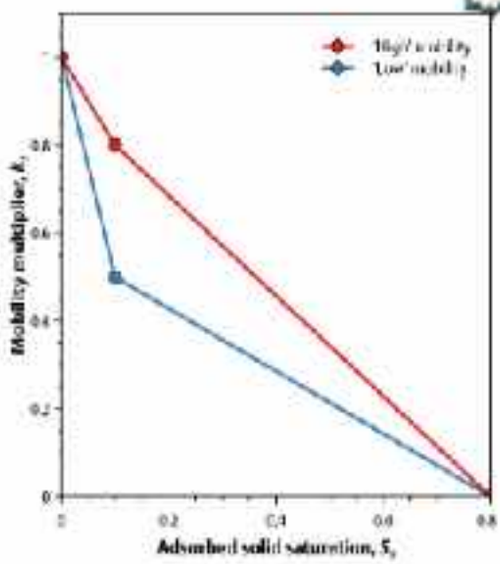


*Figure 6-1: Mobility multiplier, $k_s$, as function of solid saturation, $S_a$, for the high and low solid mobility cases assessed in this study.*

### 6.2.2 Results

The salt-precipitation assessment was performed for the single-injector configurations defined in Deliverable 3.4. These comprise scenario 1, in which $CO_2$ is injected through the CCS-1 well, and scenario 2, where $CO_2$ injection is undertaken from the LOC-D location. Numerical simulation results show that NaCl precipitation consistently develops within the first tens of meters of the near-wellbore region for both scenarios, with the highest solid saturations occurring along intervals of maximum $CO_2$ flux (Figure 6-3 Spatial distribution of solid phase saturation along a representative cross section through CCS-1 for the P10, P50, and P90 realizations, illustrating the sensitivity to different mobility multiplier parameterizations. and Figure 6-5 ). The resulting halite accumulation generates a measurable injectivity decline, reflected by the reduction in well deliverability curves presented in Figure 6-2 Cumulative Gas injection for P10, P50 and P90 cases for CCS-1 at different mobility multipliers versus solid saturation and Figure 6-4 Cumulative Gas injection for P10, P50 and P90 cases for LOC-D at different mobility multipliers vs. solid saturation. The severity of injectivity impairment is sensitive to the selected mobility multiplier function relating relative permeability to solid saturation (implemented via the `SOLIDMMS` keyword). Two end-member parameterizations were evaluated (the 'low' and 'high' mobility cases represented in Figure 6-1: Mobility multiplier, ks, as function of solid saturation, Sa, for the high and low solid mobility cases assessed in this study.), yielding markedly different injectivity responses.

Modeling water vaporization is critical for quantifying salt deposition during $CO_2$ injection, as injected supercritical $CO_2$ evaporates near-wellbore brine driving salinity to halite supersaturation and triggering NaCl precipitation. The resulting porosity and permeability reductions impair injectivity; models that omit vaporization systematically underestimate solid saturation and injectivity loss. Figure 6-3 Spatial distribution of solid phase saturation along a representative cross section through CCS-1 for the P10, P50, and P90 realizations, illustrating the sensitivity to different mobility multiplier parameterizations. and Figure 6-5 show that halite deposition is spatially heterogeneous, producing permeability contrasts that can generate localized flow barriers or preferential pathways, with implications for plume migration and pressure evolution.

The PilotSTRATEGY project has received funding from the European Union's Horizon 2020 research and innovation programme under grant agreement No. 101022664

Accordingly, reliable performance predictions require a coupled modeling framework that accounts for water vaporization, halite-precipitation kinetics, and the associated porosity- and permeability-reduction functions, enabling appropriate design of mitigation measures such as well stimulation, brine co-injection, or operational adjustments.

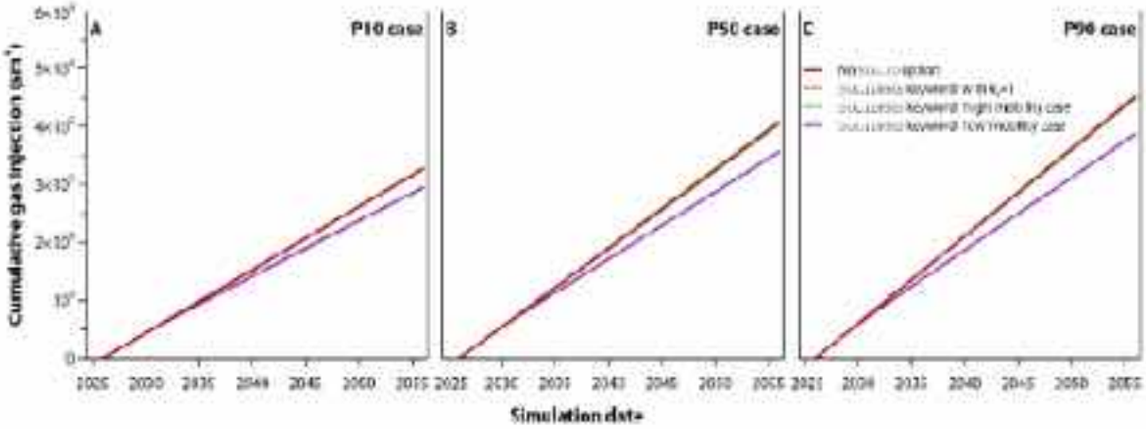


*Figure 6-2 Cumulative Gas injection for P10, P50 and P90 cases for CCS-1 at different mobility multipliers versus solid saturation*

| Solid deposition scenario | | Total $CO_2$ storage ($MtCO_2$) | | |
|---|---|---|---|---|
| SOLID activated? | SOLIDMMS keyword | P10 | P50 | P90 |
| No | *n/a* | 6.08 | 7.58 | 8.41 |
| Yes | $k_i = 1$ | 6.08 | 7.58 | 8.41 |
| Yes | 'High' mobility case | 6.08 | 7.53 | 8.36 |
| Yes | 'Low' mobility case | 5.48 | 6.63 | 7.19 |

*Table 6-1 Storage capacity for P10, P50 and P90 cases for CCS-1 at different mobility multipliers versus solid saturation*

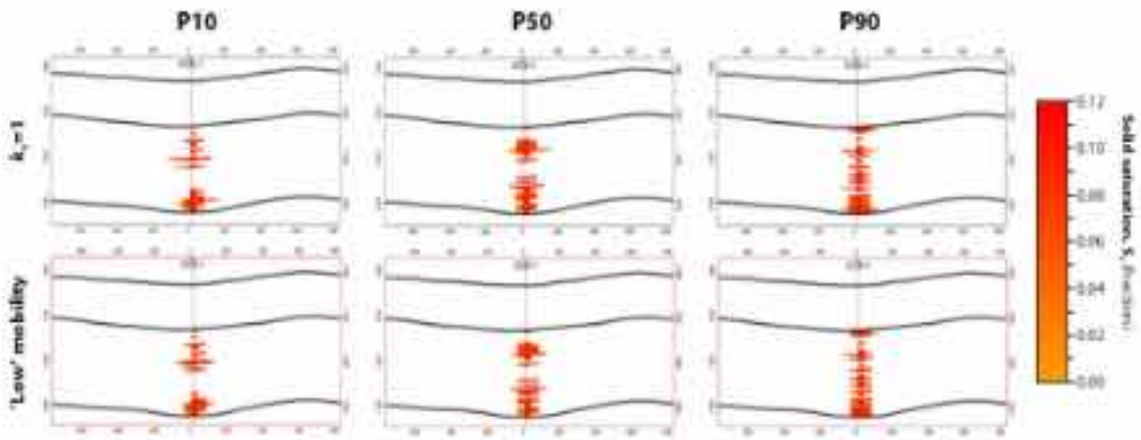


*Figure 6-3 Spatial distribution of solid phase saturation along a representative cross section through CCS-1 for the P10, P50, and P90 realizations, illustrating the sensitivity to different mobility multiplier parameterizations.*

The PilotSTRATEGY project has received funding from the European Union's Horizon 2020 research and innovation programme under grant agreement No. 101022664

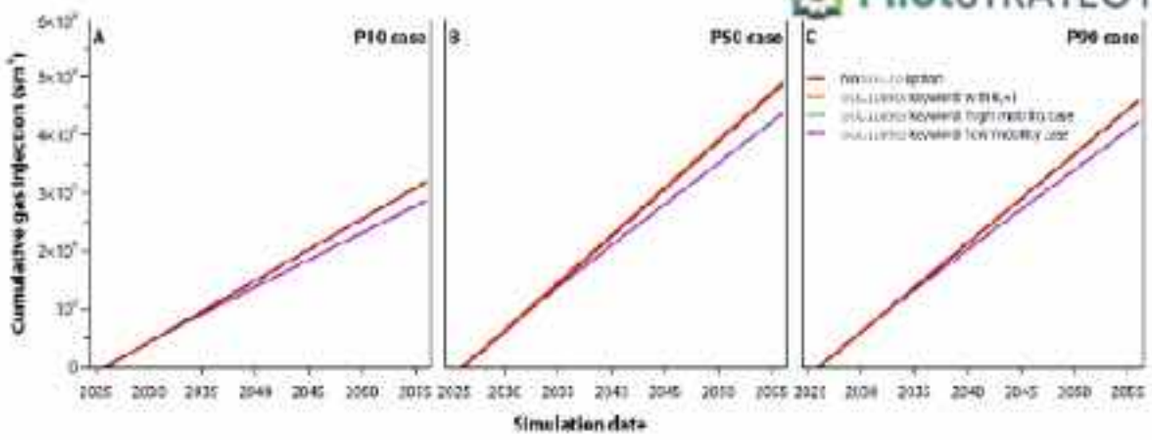


*Figure 6-4 Cumulative Gas injection for P10, P50 and P90 cases for LOC-D at different mobility multipliers vs. solid saturation*

| Solid deposition scenario | | Total $CO_2$ storage ($MtCO_2$) | | |
|---|---|---|---|---|
| SOLID activated? | SOLIDMMS keyword | P10 | P50 | P90 |
| No | *n/a* | 5.93 | 9.04 | 8.52 |
| Yes | $k_s = 1$ | 5.93 | 9.12 | 8.55 |
| Yes | 'High' mobility case | 5.93 | 9.07 | 8.55 |
| Yes | 'Low' mobility case | 5.33 | 8.1 | 7.84 |

*Table 6-2 Total $CO_2$ storage capacity for the P10, P50 and P90 cases in the single-injector LOC-D scenario and for different mobility multipliers versus solid saturation cases*

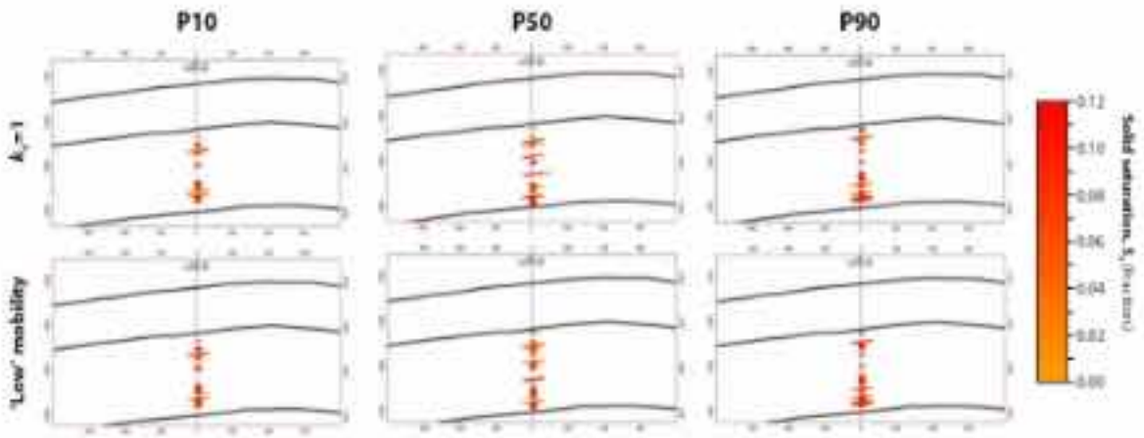


*Figure 6-5 Spatial distribution of solid phase saturation along a representative cross section through LOC-D for the P10, P50, and P90 realizations, illustrating the sensitivity to different mobility multiplier parameterizations.*

The impact of solid deposition on total $CO_2$ storage capacity is summarized in Table 6-1 Storage capacity for P10, P50 and P90 cases for CCS-1 at different mobility multipliers versus and Table 6-2 Total CO2 storage capacity for the P10, P50 and P90 cases in the single-injector LOC-D scenario and for different mobility multipliers versus solid saturation for the single-injector scenarios CCS-1 and LOC-D, respectively. Storage capacities are reported for the P10, P50, and P90 realizations. A consistent decline in injectivity and storage capacity is observed as $k_s$ decreases from the 'high' to 'low' mobility cases. In the CCS-1 scenario, the maximum reduction in storage capacity reaches approximately 10–15% under the 'low' mobility condition.

In contrast, for the LOC-D scenario, P10 storage capacities remain essentially unchanged across all solid-deposition realizations (Table 6-2 Total CO2 storage capacity for the P10, P50 and P90 cases in

The PilotSTRATEGY project has received funding from the European Union's Horizon 2020 research and innovation programme under grant agreement No. 101022664

the single-injector LOC-D scenario and for different mobility multipliers versus solid saturation cases), indicating stable injectivity under these conditions. However, injectivity decreases markedly (by 8–10%) in the 'low' mobility case, reflecting a measurable reduction in effective permeability or flow capacity. The P50 and P90 values show slight increases in injectivity for the $k_s = 1$ and 'high' mobility cases compared to the "No SOLID" case, suggesting that moderate halite deposition may marginally enhance injectivity.

These modest increases in injectivity do not indicate *per se* any beneficial effect of halite deposition. Rather, they arise from early-time increases in $CO_2$ saturation, which temporarily enhance $CO_2$ mobility before salt accumulation becomes significant; this short-lived effect has been documented in simulation studies reporting an initial injectivity rise prior to halite-induced impairment (Ogundipe & Mackay 2025). A concurrent reduction in capillary resistance as water saturation decreases during early dry-out may further facilitate $CO_2$ flow. Once halite precipitation progresses, however, pore-throat blockage dominates and injectivity declines, consistent with established near-wellbore impairment mechanisms.

A grid sensitivity analysis was conducted to assess the influence of cell size in the immediate vicinity of the $CO_2$ injector and its potential effect on solid deposition estimates. Three local grid refinement (LGR) configurations[6] were tested: the base 5×5×1 grid with 40 m spacing, a 7×7×1 grid with 28.6 m spacing, and a 9×9×1 grid with 22.2 m spacing. Table 6-3 . Storage capacity for P10, P50 and P90 cases for CCS-1 at different LGRs resolution with solid deposition summarizes the effects on cumulative mass injected for the 'low' mobility case and the relative change in injectivity (RR) with respect to the $k_s = 1$ case. Total stored mass remains constant at ~7.58 $MtCO_2$ for $k_s = 1$ across all grid configurations, whereas it decreases when the $k_s$ is reduced in the 'low' mobility case. The relative injectivity reduction consistently falls within −13% to −14%, demonstrating that injectivity is largely insensitive to this increased grid resolution. Figure 8 presents the cumulative gas-injection profiles for the CCS-1 P50 scenario for each LGR case. The results confirm that the considered grid refinements do not significantly change injection behaviour over time. Overall, this analysis indicates that the original LGR configuration (5×5×1) provides sufficient accuracy and robustness for modelling salt precipitation processes in the near-wellbore region relatively to the others considered grid refinements.

[6] A $N_x \times N_y \times N_z$ local grid refinement denotes a discretized region around the wellbore in which each coarse grid cell is subdivided into $N_x$ cells in the $x$ direction, $N_y$ in the $y$ direction, and $N_z$ vertical sublayers. This refinement increases spatial resolution in the near-wellbore domain and improves the representation of flow and transport processes.

The PilotSTRATEGY project has received funding from the European Union's Horizon 2020 research and innovation programme under grant agreement No. 101022664

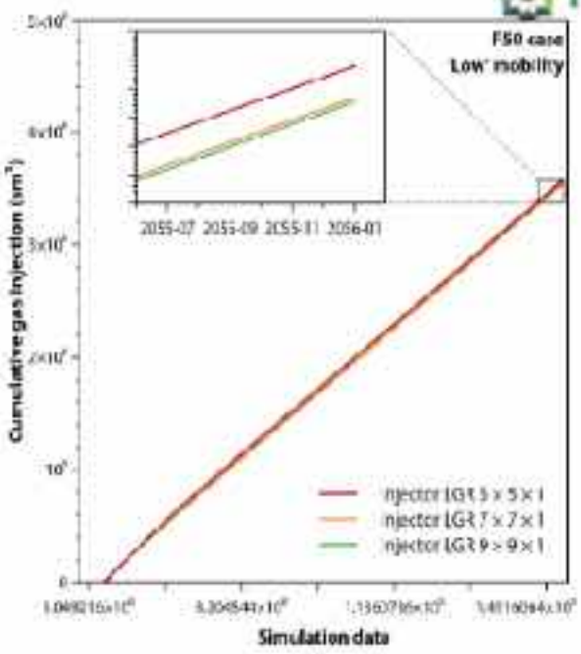


*Figure 6-6 Modelled cumulative gas injection for scenarios with different levels of local grid refinement surrounding the $CO_2$ injector. Results are shown for the CCS -1 single-injector P50 case under the "low" mobility multiplier configuration.*

| | LGR 5x5x1 | LGR 7x7x1 | LGR 9x9x1 |
|---|---|---|---|
| **Storage capacity (Mton) for** Halite MS = 0.5 | 6.49 | 6.58 | 6.57 |
| RR (%) | -14.4 | -13.2 | -13.3 |

*Table 6-3 . Storage capacity for P10, P50 and P90 cases for CCS-1 at different LGRs resolution with solid deposition (RR = relative injectivity reduction factor)*

### 6.2.3 Conclusions

Salt precipitation during $CO_2$ injection can significantly impair injectivity by reducing near-wellbore permeability. In this study, the phenomenon is represented through mobility multiplier functions of solid saturation, $k_{ss}(S_s)$, which prescribe how fluid mobility decreases as the fraction of pore volume occupied by precipitated solids increases. At low solid saturation, mobility reduction is minor, but as saturation grows the multiplier decreases (often non-linearly) resulting in a pronounced decline in injectivity. The functional form of this curve (*e.g.*, exponential, sigmoidal) is therefore critical for predicting the severity and onset of impairment.

Calibrating this relationship ideally requires core-flooding experiments in which $CO_2$ is injected into brine-saturated rock under reservoir conditions. Measurements of pressure drop and flow rate, combined with core imaging (*e.g.*, CT scanning), enable estimation of salt-saturation profiles and their associated permeability reduction. Reactive transport simulations and field-scale injectivity index analyses further refine the multiplier curve to ensure it reflects reservoir behavior. This parameterization is essential for evaluating mitigation strategies and optimizing injection design in $CO_2$ storage operations.

Simulation results indicate that NaCl precipitation is likely under specific thermodynamic and flow conditions, causing localized injectivity decline. However, the impairment remains spatially limited and may be mitigated through operational measures such as periodic water flushing or $CO_2$

The PilotSTRATEGY project has received funding from the European Union's Horizon 2020 research and innovation programme under grant agreement No. 101022664

humidification. Overall, this study provides a basis for assessing salt-related injectivity risks and supports the broader CCS deployment strategy in Lopin. Further work should include field-scale validation and extension of the analysis to multi-component salt systems.

## 6.3 Caprock integrity – Geochemical aspects

To evaluate the inherent geochemical resilience of the caprock, we performed batch reaction modelling using PHREEQC Interactive v3 (Parkhurst and Appelo, 2013). This tier deliberately uses a conservative approach to establish an upper bound on reactivity, avoiding the need for complex reactive transport or high-salinity simulations at the screening stage.

- **Mineralogical Input:** Based on detailed site characterisation (Wilkinson, 2023) and X-ray diffraction analysis, the primary seal (B2) was represented as a mixture of Quartz (34%), Mica (18%), Ca-Montmorillonite (15%), Calcite (13%), K-feldspar (10%), and Chlorite (10%).
- **Modelling Strategy:** The system was first equilibrated with meteoric water at reservoir temperature (69°C) to establish a well-constrained chemical baseline. Meteoric water was chosen deliberately over the high-salinity native brine (>160,000 ppm NaCl) to maximize chemical potential and establish an upper-bound reactivity scenario. It was then perturbed by injecting $CO_2$ to a partial pressure of 143.5 bar. For the seal, a sensitivity analysis was conducted by exposing it to a range of $CO_2$ partial pressures (25% to 100% of the reservoir $pCO_2$) to simulate varying degrees of leakage or diffusion.

High ionic strengths suppress mineral reactivity through common-ion effects and activity coefficient reductions. By using a dilute baseline, we maximize the chemical potential for fluid-rock interaction, thereby establishing an upper-bound on reactivity. This approach maximizes reaction affinity but does not artificially suppress dissolution pathways; therefore, failure to observe destabilizing reactions under these conditions provides a robust upper bound. It does not capture kinetic effects or spatial heterogeneity but is sufficient for bounding thermodynamic behavior at the screening stage. The objective is not to predict reaction rates or spatial evolution, but to test whether any thermodynamically favourable destabilizing pathway exists under maximized reactivity. The absence of such pathways under bounding conditions is sufficient to exclude geochemistry as a first-order risk driver. If even this upper-bound scenario shows negligible risk within the assumptions of the bounding approach, the conclusion is robust. Under realistic in-situ conditions with high-salinity brines, mineral reactivity is expected to be significantly lower. This tier thus allows rapid screening without committing resources to detailed reactive transport.

Geochemical results for the Buntsandstein Primary Seal indicate that key sealing minerals (Ca-montmorillonite, mica, chlorite) remain thermodynamically stable (SI = 0) even under full $CO_2$ exposure. The system exhibits consistent oversaturation of pore-filling minerals like kaolinite (SI = 2.39–2.57) and dolomite (SI = 2.46–2.89) across all $CO_2$ exposure scenarios, indicating a robust thermodynamic drive for pore-filling mineral precipitation. Even under this maximized reactivity scenario, the seal shows a self-sealing tendency.

The PilotSTRATEGY project has received funding from the European Union's Horizon 2020 research and innovation programme under grant agreement No. 101022664

*Table 6-4: Geochemical results for Buntstandstein mineral composition (primary seal)*

| Mineral | 100% $pCO_2$ | 75% $pCO_2$ | 50% $pCO_2$ | 25% $pCO_2$ | Trend |
|---|---|---|---|---|---|
| Ca-Montmorillonite | 0.24 | 0.24 | 0.25 | 0.25 | Stable |
| Kaolinite | 2.57 | 2.56 | 2.55 | 2.52 | Precipitation |
| Dolomite | 2.89 | 2.71 | 2.60 | 2.46 | Precipitation |

In conclusion, geochemical risks for the main seal are negligible for Lopín within the assumptions of the bounding approach. Even under an upper-bound reactivity scenario (dilute baseline), the clay-rich seal shows a consistent thermodynamic tendency for pore-filling mineral precipitation. Under realistic high-salinity conditions, reactivity is expected to be significantly lower.

## 6.4 Storage system integrity – Geomechanical aspects

### 6.4.1 Introduction

The injection of $CO_2$ into deep geological formations induces changes in subsurface pore pressure and stress fields, which may compromise the mechanical stability of the storage system. These pressure- and stress-related perturbations can adversely affect wellbore stability, the sealing capacity of the caprock, and the stability of pre-existing faults. Injection-induced increases in pore pressure leads to a reduction in effective stress within the reservoir and surrounding formations. This reduction may trigger several mechanical responses, including:

- **Wellbore instability**, resulting from shear or tensile failure in the stress-concentrated region surrounding the borehole wall.
- **Caprock damage**, caused either by hydraulic fracturing when injection pressures exceed the local fracture gradient, or by progressive shear weakening that degrades the sealing capacity of the caprock.
- **Fault reactivation**, where critically stressed faults may undergo slip, potentially generating induced seismic events and creating high-permeability pathways that threaten long-term $CO_2$ containment.

To assess and mitigate these risks, a robust geomechanical analysis is essential. These evaluations typically begin with the construction of a 1D geomechanical model at the well location, which provides the foundational data required for further analysis.

The 1D model supports a range of key assessments:

- Wellbore stability simulations, used to define the required mud weight (mud weight window) to prevent collapse or fracturing during drilling.
- Fracture gradient estimation, to establish safe injection pressure thresholds and avoid caprock failure.
- Caprock integrity analysis, to determine the mechanical limits of the sealing unit under changing pressure and thermal conditions.

The PilotSTRATEGY project has received funding from the European Union's Horizon 2020 research and innovation programme under grant agreement No. 101022664

Fault stability assessment, using techniques such as slip tendency or Coulomb failure stress to evaluate the likelihood of fault reactivation.

### 6.4.2 Multi-1D Geomechanical study.

#### *6.4.2.1 Introduction*

Developing a 1D geomechanical model has been a crucial step in obtaining the necessary inputs to evaluate geomechanical risks and establish the conditions for maintaining long-term storage integrity. It is essential for conducting analyses such as wellbore stability simulations, fracture gradient estimation, caprock integrity assessment, and fault stability evaluation.

The main objectives for this 1D geomechanical model are:

- Perform Pore Pressure ($P_p$) & Fracture gradient ($F_g$) profiles.
- Calculate main stresses. Vertical Stress ($S_v$), Maximum Horizontal Stress ($Sh_{max}$) and Minimum Horizontal Stress ($Sh_{min}$)
- Derive a calibrated & integrated model that illustrates well unstable areas.
- Conclude recommendations for future drilling.

Available data come from wells drilled between 1958 and 1981. The average geothermal gradient is 0.0307 °C/m and an assumed mean surface temperature of 15 °C at the surface, which translates into a temperature of approximately 69 °C at 1,760 m TVDSS. Formation water salinity ranges from a minimum of 100,000 ppm to a maximum of 250,000 ppm, with a base case of 160,000 ppm.

Geological history can be summarized in three main steps (Figure 6-7):

- Permo-trias rifting. Outlined the main structural framework.
- Jurassic-Cretaceous rifting. Posterior distensive event that reactivated the previous one, exaggerating previous structural features.
- Alpine inversion. Compressive event. Inverted rift faults and generated some inverted faults in the Upper Section (from Jurassic to Tertiary).

The PilotSTRATEGY project has received funding from the European Union's Horizon 2020 research and innovation programme under grant agreement No. 101022664

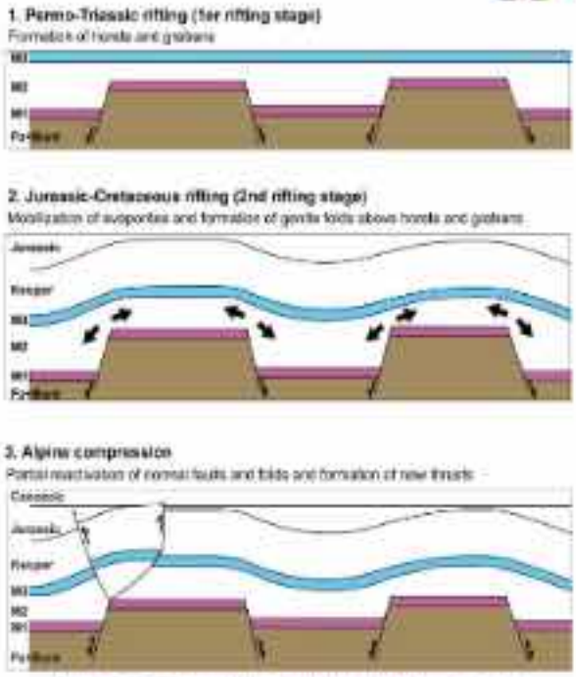


*Figure 6-7 Geological history of Lopin injection site*

### 6.4.2.2 *Available Dataset and Workflow*

Well selection was primarily driven by data availability and proximity to the proposed $CO_2$ injection site. For inclusion in the multi-1D geomechanical analysis, wells were required to contain, at a minimum, the following wireline log datasets: gamma ray (GR), caliper (CALI), bulk density (RHOB), neutron porosity (NPHI), deep resistivity (RD), compressional transit time from sonic logs (DTCO) and drilling mudweight (MW). In addition, wells exhibiting recorded drilling events indicative of pore-pressure or stress-related conditions—such as gas influxes or kicks, mud losses, and tight-hole occurrences—were considered preferable, as these events provide valuable constraints for pore-pressure calibration and wellbore stability assessment. Based on these criteria, only a limited number of wells were deemed suitable for a multi-1D geomechanical study. The selected wells are located at distances ranging from 10 to 60 km from the proposed injection site and include Ebro-1, Ebro-2, Mayals-1 and Lopín-1. The spatial distribution of these wells relative to the injection area is shown in Figure 6-8.

The PilotSTRATEGY project has received funding from the European Union's Horizon 2020 research and innovation programme under grant agreement No. 101022664

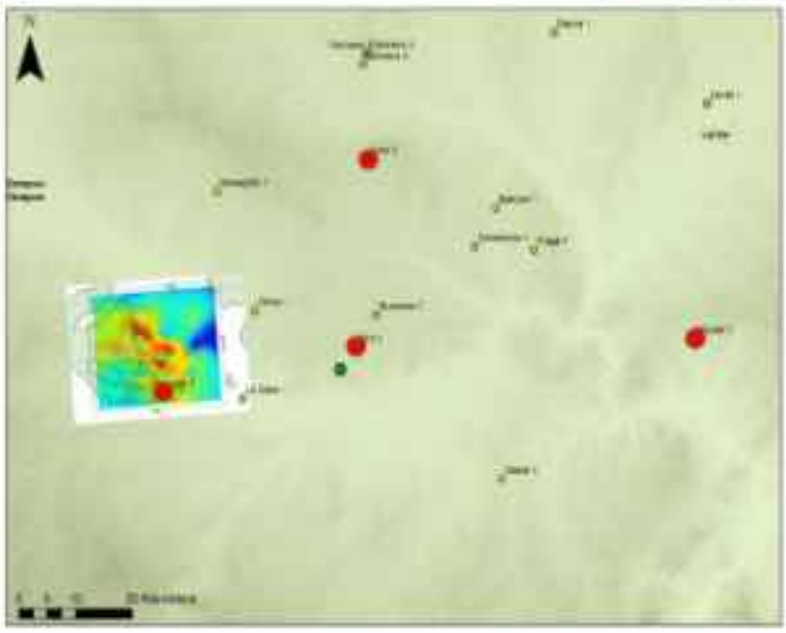

*Figure 6-8. Digital Elevation Model of the study area. Includes Top Buntsandstein structural map & suitable wells for analysis*

Two main approaches are commonly employed in multi-1D geomechanical studies: the **poroelastic method** and the **effective stress ratio (ESR) method**. The poroelastic method is most appropriate when a robust and comprehensive dataset is available, including detailed geomechanical characterization such as elastic properties, Biot's coefficient, and other related parameters. This method provides a more rigorous estimation of in-situ stresses and explicitly accounts for rock deformation induced by pore pressure variations and tectonic strain, resulting in higher accuracy where sufficient data exist. Within the framework of the PilotSTRATEGY project, however, the available laboratory geomechanical characterization is limited and is based on outcrop samples, which significantly reduces the confidence in the representativeness of the results. In addition, available well log data are scarce, as the most recent well in the area was drilled in 1981 (Baroni *et al.* 2023). Given these limitations, the ESR method represents a simpler and more suitable approach for the existing data conditions and has therefore been adopted in this study. This method is particularly appropriate in scenarios where highly detailed and complete datasets are not available. The analysis was carried out using GeoSmart®, a proprietary software tool developed internally by Repsol.

The workflow employed in this analysis can be summarized in the following steps (Figure 6-9):

1. **Data loading**: Selection and importation of the relevant well log curves required for geomechanical analysis, ensuring data integrity and adequate depth coverage.
2. **Well schematic and lithology**: Definition of the lithological profile and well architecture, including identification of drilled formations and construction of a schematic diagram showing wellbore geometry and casing diameters.
3. **Rock mechanical properties**: Estimation of rock mechanical properties using empirical correlations tailored to each rock type. Where available, these estimates are validated against laboratory test data to improve reliability.

The PilotSTRATEGY project has received funding from the European Union's Horizon 2020 research and innovation programme under grant agreement No. 101022664

4. **Vertical stress ($S_v$, overburden) calculation**: Computation of the vertical stress through integration of bulk density logs along the well depth.
5. **Pore pressure ($P_p$) estimation**: Determination of pore pressure, incorporating drilling events and indirect indicators (*e.g.* mud weight changes, kicks, losses) as key constraints in the pressure model.
6. **Calculation of minimum ($Sh_{min}$) and maximum ($SH_{max}$) horizontal stresses**: Estimation of the horizontal stress magnitudes using the selected geomechanical model.
7. **Fracture gradient ($F_g$) calculation**: Derivation of the fracture gradient to assess wellbore stability and mud weight windows.
8. **Wellbore breakout analysis**: Evaluation of borehole breakouts to infer in-situ stress orientations and to further constrain stress magnitudes.
9. **Final analysis and model validation**: Execution of the ESR-based geomechanical model to obtain theoretical predictions of wellbore instability as a function of depth. The stress estimations and overall model performance are considered reliable when the predicted instability zones correspond with observed wellbore enlargements, as verified using calliper log data.

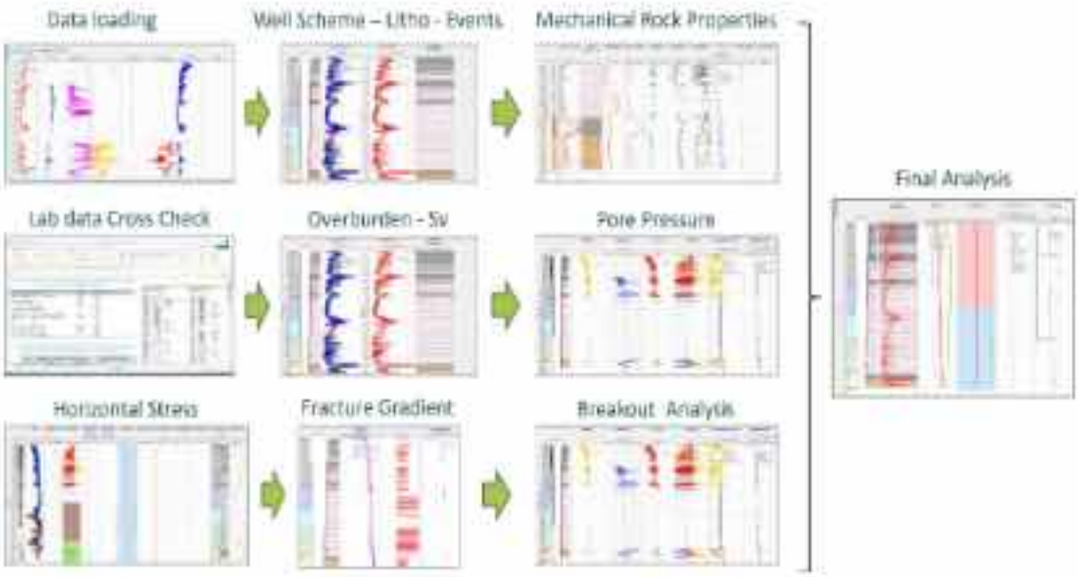


*Figure 6-9. Multi-1D geomechanical workflow used in this study.*

### 6.4.2.3 Drilling events

Drilling events constitute a critical input for 1D geomechanical models, as their occurrence provides constraints on the regional stress field and natural pore pressure conditions. Observations made during drilling can therefore be used to calibrate and validate the geomechanical model.

Although no major safety incidents were reported during drilling operations, several recurrent operational challenges were identified. The most significant issue was lost circulation, particularly while drilling through the Cretaceous–Jurassic and Muschelkalk intervals, primarily associated to karstic lithologies and evaporitic formations. All wells were drilled using water-based mud (WBM) systems, initially employing bentonitic mud and later switching to salt-saturated mud within Keuper. Mud densities are in the 1.1 to 1.6 $kg \cdot L^{-1}$ range. Tight-hole conditions were frequently encountered,

The PilotSTRATEGY project has received funding from the European Union's Horizon 2020 research and innovation programme under grant agreement No. 101022664

mainly related to swelling clays and bit balling, resulting in overpull events and, in some cases, stuck bottom-hole assemblies (BHA) that required fishing operations. Additional drilling issues included cavings in claystone intervals, washouts affecting drill pipes, and restricted wireline logging in certain sections due to reduced borehole diameter. However, no wireline fishing events were reported.

#### 6.4.2.4 *Pressure data*

The most reliable formation pressure measurement available for this study are derived from drill-stem test (DST) data acquired in wells. Wells located farther away from the study area (Ballobar-1, Candasnos-1 and Fraga-1) exhibit pressure regimes consistent with a hydrostatic gradient, with no significant pressure anomalies identified. In contrast, wells situated closer to the injection site display clear pressure deviations from hydrostatic conditions, characterized by overpressure at the level of the injection reservoir (Buntsandstein Formation). These overpressure observations are documented in Chiprana-1, Ebro-1, Ebro-2 and Monegrillo-1. Formation pressure values were extracted from the final DST reports available for each of these wells. Among them, the pressure data from Chiprana-1 are considered the most reliable (Figure 6-10).

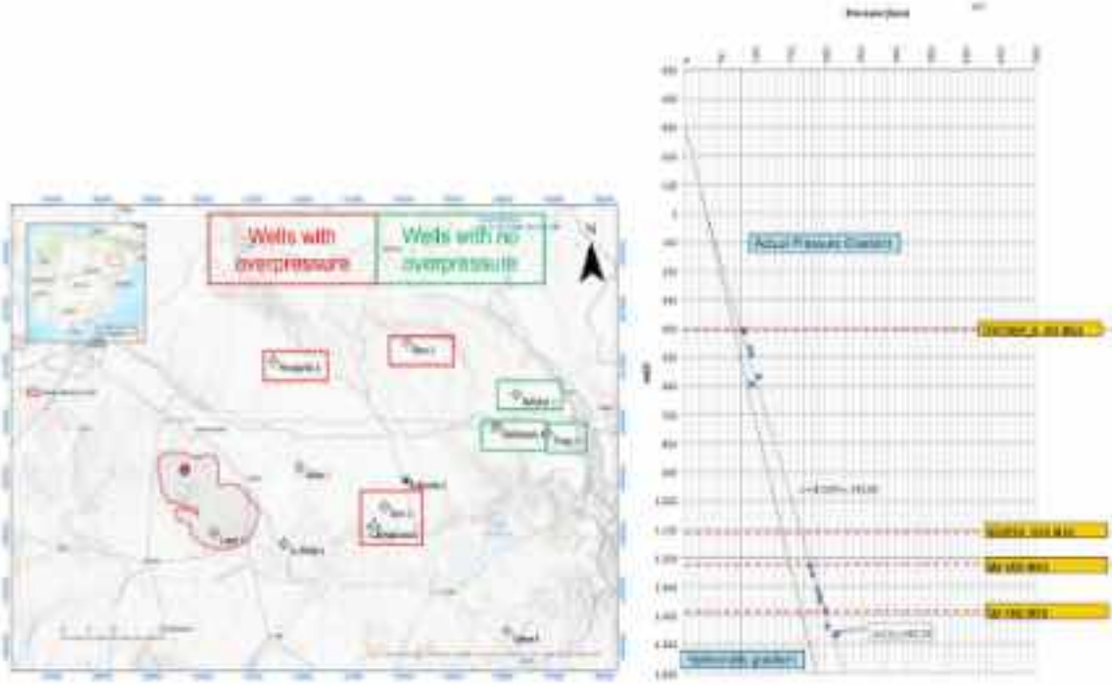


*Figure 6-10 Left. Location map. Wells with reliable pressure data. Right. Depth-Pressure plot for Chiprana -1*

#### 6.4.2.5 *Mechanical Rock Properties*

The mechanical properties of rocks directly control their response to the regional stress field as well as to perturbations induced by $CO_2$ injection. These properties are typically derived either from laboratory measurements or from empirical correlations based on well log data. In the present study, laboratory data are available for the Buntsandstein Formation, providing an important cross-check for the mechanical properties estimated using empirical relationships (Deliverable 2.8). The empirical formulations employed here are primarily based on compressional wave velocity ($V_P$), shear wave velocity ($V_S$), and bulk density (*i.e.* RHOB). Compressional wave velocity is directly obtained from the sonic log (DTCO), while shear wave velocity, unavailable due to the age of the wells, is estimated from $V_P$ using the Gassmann equation. Bulk density is obtained directly from the RHOB log measurements. The resulting rock mechanical properties derived from these inputs are summarized in Table 7-3. All

The PilotSTRATEGY project has received funding from the European Union's Horizon 2020 research and innovation programme under grant agreement No. 101022664

equations and reference values used in the estimation of mechanical parameters are taken from Jaeger *et al.* (2007) and Zoback (2010). Mean values of the measured mechanical properties obtained from Torre de las Arcas outcrop samples (Deliverable 2.8 (Baroni *et al.* 2023)) are shown in Table 7-3 and are used as a qualitative reality check against log-derived properties. Laboratory-derived geomechanical properties from outcrop samples are not directly comparable with in-situ reservoir conditions, as the tests do not reproduce the effective stress, temperature, and compaction state of the reservoir at depths >2500 m. Consequently, laboratory results are used primarily for validation and calibration purposes, while log-derived properties are adopted for the geomechanical model. The rationale for parameter selection is summarized below.

**Sonic log**

Ultrasonic laboratory measurements indicate a P-wave velocity of 2.54 km·s$^{-1}$. However, compressional wave velocity is strongly dependent on compaction, cementation, effective stress, and mineralogy. At reservoir depth, expected $V_P$ values for consolidated sandstones are significantly higher, typically ranging between 3.5 and 4.5 km·s$^{-1}$. Measured sonic log data yield a $V_P$ of approximately 4.5 km·s$^{-1}$, which is considered more representative of in-situ reservoir conditions. Therefore, log-derived sonic velocities were used in the geomechanical analysis.

Shear wave velocity is not available from logs due to the age of the wells. Consequently, $V_S$ was estimated from $V_P$ using elastic relationships derived from the Gassmann framework:

$$V_P = \sqrt{\frac{K + \frac{4}{3}\mu}{\rho}}, V_S = \sqrt{\frac{\mu}{\rho}}$$

where $V_P$ is the compressional wave velocity $V_S$ is the shear wave velocity, $K$ is the bulk modulus, $\mu$ is the shear modulus and $\rho$ is the density.

**Young's modulus**

The static Young's modulus cannot exceed the dynamic Young's modulus. Significant discrepancies were observed between laboratory and log-derived dynamic values: the laboratory measurements indicate ~9 GPa whereas log-derived dynamic modulus at reservoir level point to values around 45 GPa. The dynamic Young's modulus generally ranges between 30 and 50 GPa for consolidated sandstones at depths of 1500–2000 m (Nourifard *et al.* 2021). Given the reservoir depth and rock consolidation, log-derived values were considered more representative and were therefore used in the geomechanical model.

**Uniaxial compressive strength (UCS)**

Laboratory UCS measurements (performed without confinement) on Buntsandstein outcrop samples yielded a mean value of 83.6 MPa, which is consistent with the log-derived UCS estimates as presented in Figure 7-5. As a result, UCS values derived from logs were calibrated using laboratory results, improving confidence in the final UCS profile.

**Poisson's ratio**

The PilotSTRATEGY project has received funding from the European Union's Horizon 2020 research and innovation programme under grant agreement No. 101022664

Static Poisson's ratio derived from laboratory measurements closely matches the values obtained from empirical correlations. Therefore, laboratory values were used as a reality check, confirming the validity of the log-derived Poisson's ratio applied in the model.

#### 6.4.2.6 *Vertical stress calculation (Sv, overburden)*

The vertical stress, or overburden, is calculated using the RHOB log, which is available for all wells analyzed. The RHOB logs exhibit sufficient quality and good vertical coverage across the logged intervals, providing a reliable basis for overburden estimation. As a verification step, a synthetic density log was generated using the Gardner–Bellotti empirical relationships; however, this synthetic log was not used in the final vertical stress calculation, as the measured RHOB data were considered more representative of in-situ conditions. In the shallow portion of the wells, corresponding to the Tertiary section, density measurements are not available for the first few hundred meters. To account for this gap, a polynomial density function was defined to smoothly tie the first measured RHOB values to a representative near-surface density of 1.9 g·cm$^{-3}$ at ground level. sThis approach ensures continuity of the density profile and avoids artificial stress discontinuities in the shallow section. The vertical stress, $S_v$, is computed by integrating the bulk density over depth according to:

$$S_v(z) = \int_0^z \rho(z)\, g\, dz,$$

where $\rho(z)$ is the bulk rock density as a function of depth, $g$ is the acceleration due to gravity (≈9.81 m·s$^{-2}$) and $z$ is the true vertical depth.

#### 6.4.2.7 *Pore Pressure ($P_p$) estimation*

The pore pressure was estimated using the RHOB, DR and DTCO well-log measurements. These logs were used to define normal compaction trend (NCT) lines, which form the basis for pore-pressure estimation. For the definition of the NCT lines, different methodologies were applied depending on the log type:

- Density: NCT derived using the depth equivalent method
- Resistivity and sonic logs: NCT established using Eaton's method (Eaton, 1975)

To improve the robustness of the pore-pressure interpretation, additional constraints were incorporated, including direct formation pressure measurements, drilling events, and drilling mud-weight records.

Once pore pressure profiles were obtained from log-based methods, results were verified using empirical correlations, specifically the Miller–Bower sonic equations (Miller & Bower 1963).

Miller's equation estimates pore pressure, $P_p$, in subsurface formations, primarily in shale, by relating seismic/sonic velocity to effective stress, incorporating matrix and mudline velocities to account for compaction:

$$P_p = S_v - \sigma' = S_v - \frac{1}{\Lambda} \ln\left[\frac{V_m - V_{ml}}{V_m - V_p}\right],$$

where $S_v$ is the vertical stress (from overburden density integration; see previous section), $\Lambda$ is the rate of increase in sonic velocity with effective stress (empirical, typically $3.5 \times 10^{-4}$), $V_m$ is the sonic velocity in shale matrix (≈20,000 ft·s$^{-1}$), $V_{ml}$ is the sonic velocity at the mudline and $V_p$ is the measured sonic velocity.

The PilotSTRATEGY project has received funding from the European Union's Horizon 2020 research and innovation programme under grant agreement No. 101022664

Bower's equation is a velocity-based method to estimate $P_p$:

$$P_p = S_v - \left(\frac{V_p - V_{ml}}{A}\right)^{\frac{1}{B}},$$

where $S_v$ is the vertical stress (from overburden density integration; see previous section), $V_p$ is the measured sonic velocity, $V_{ml}$ is the sonic velocity at the mudline (typically 1,250 m·s$^{-1}$), $A$ is an empirical constant (10–20, commonly 20) and $B$ is an empirical exponent (0.7–0.83, commonly 0.8)

The following drilling observations were assessed for pore pressure calibration:

- Formation pressure measurements: Only DST-derived pressures were considered reliable and used as calibration references (Deliverable 3.2).
- Minor gas influxes: Recorded during drilling but considered insufficient in magnitude to provide reliable pore-pressure constraints.
- Partial to total losses: Observed mainly in carbonate and anhydrite intervals (Muschelkalk–Keuper), likely related to natural fractures or karstification rather than overpressure.
- Pipe-sticking events: Recorded but interpreted as drilling-mechanical issues rather than direct pore-pressure indicators.

Given that drilling events were neither abundant nor highly diagnostic, pore-pressure estimates were primarily calibrated against drilling mud-weight data and subsequently cross-checked using the Miller & Bower equations.

Because the drilled wells did not exhibit significant gas influxes or well-control incidents, it is considered reasonable to assume that the equivalent pore pressure corresponding to the applied mud weight provides a reliable estimate of formation pressure. The resulting pore-pressure profiles and validation comparisons are presented in Figure 6-11, Figure 6-12, Figure 6-13 and Figure 6-14.

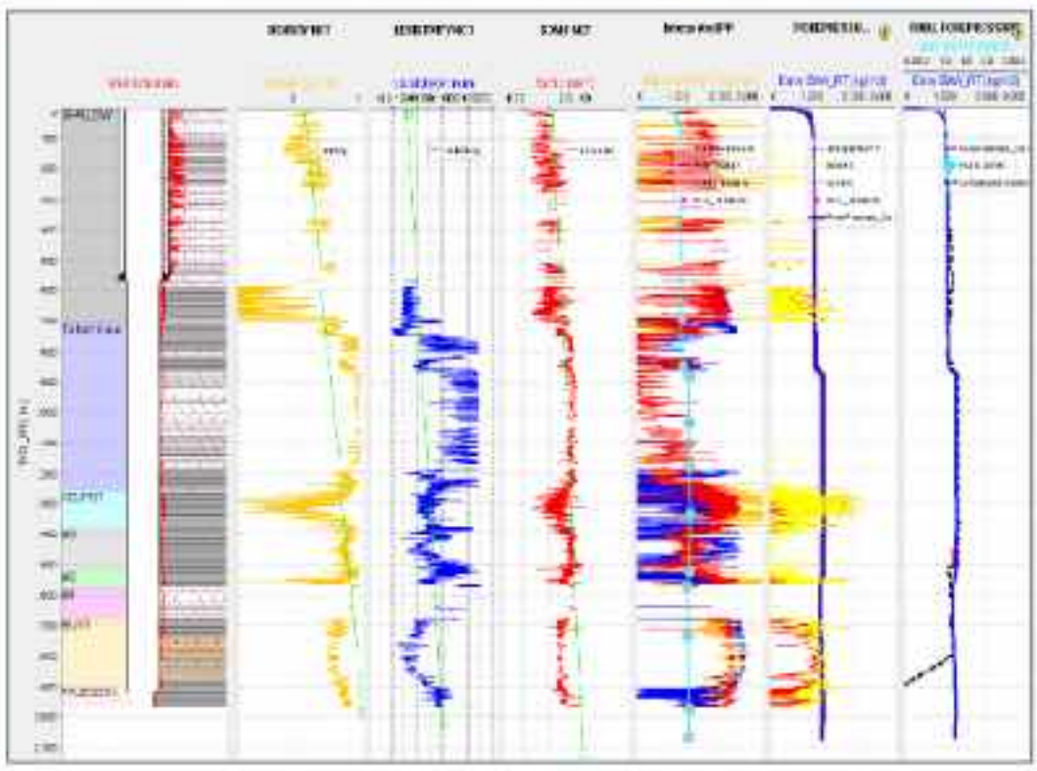

*Figure 6-11. Normal compaction trend and pore pressure derivation for the Ebro-1 well.*

The PilotSTRATEGY project has received funding from the European Union's Horizon 2020 research and innovation programme under grant agreement No. 101022664

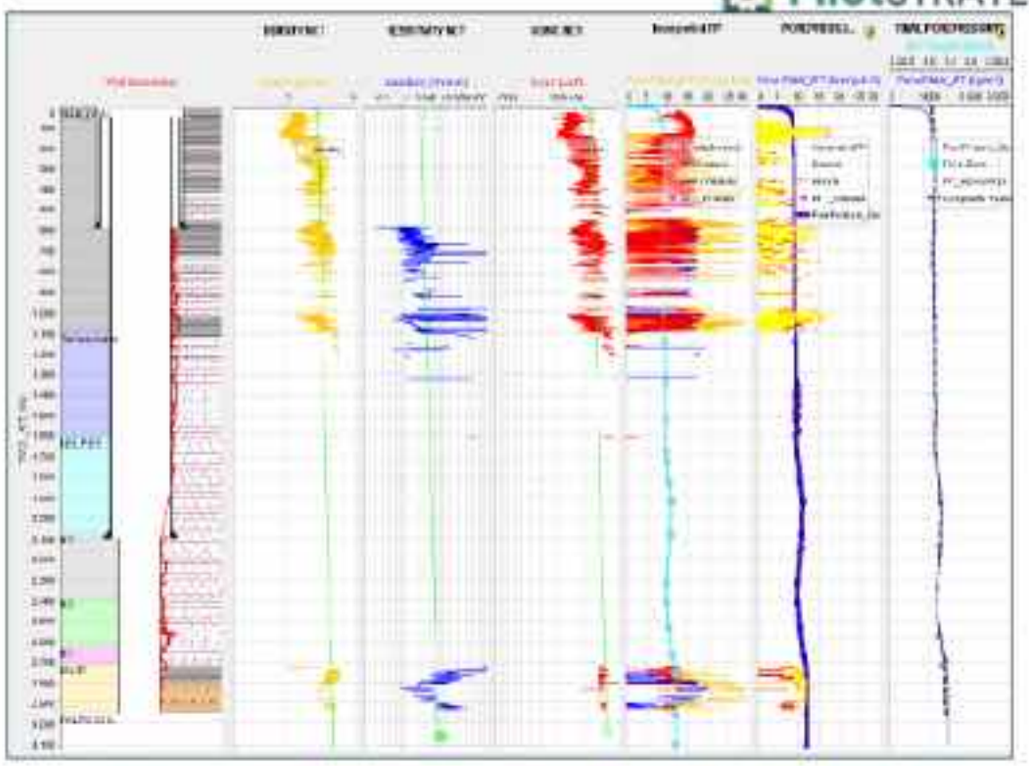

*Figure 6-12. Normal compaction trend and pore pressure derivation for the Ebro-2 well.*

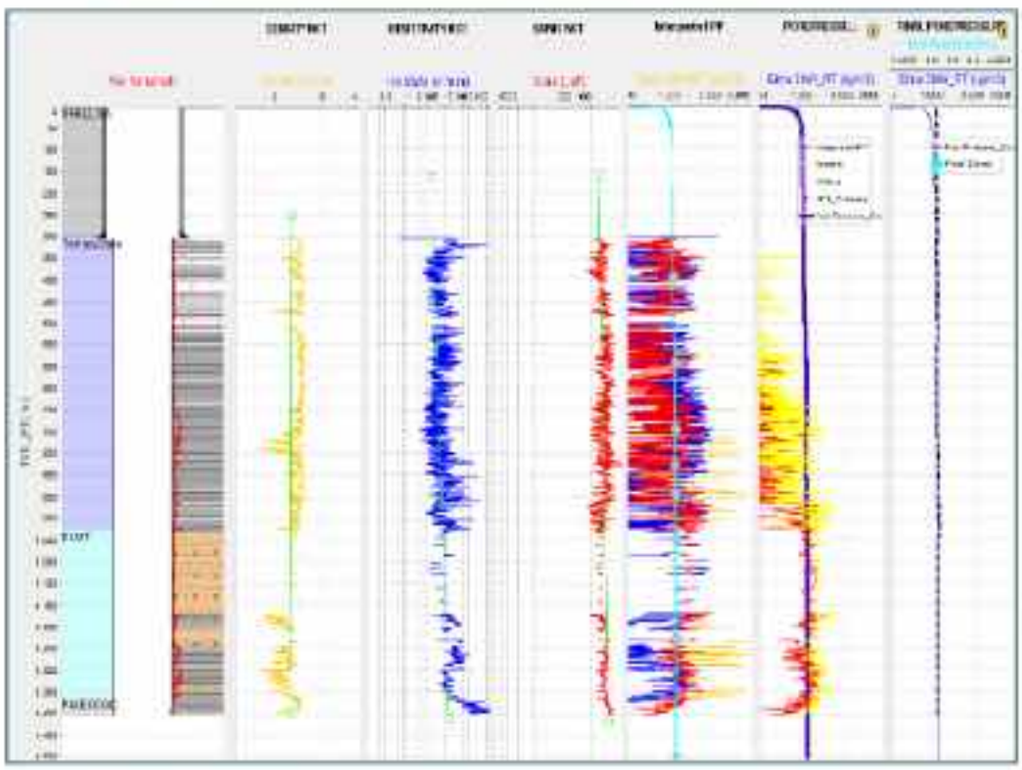

*Figure 6-13. Normal compaction trend and pore pressure derivation for the Mayals-1 well.*

The PilotSTRATEGY project has received funding from the European Union's Horizon 2020 research and innovation programme under grant agreement No. 101022664

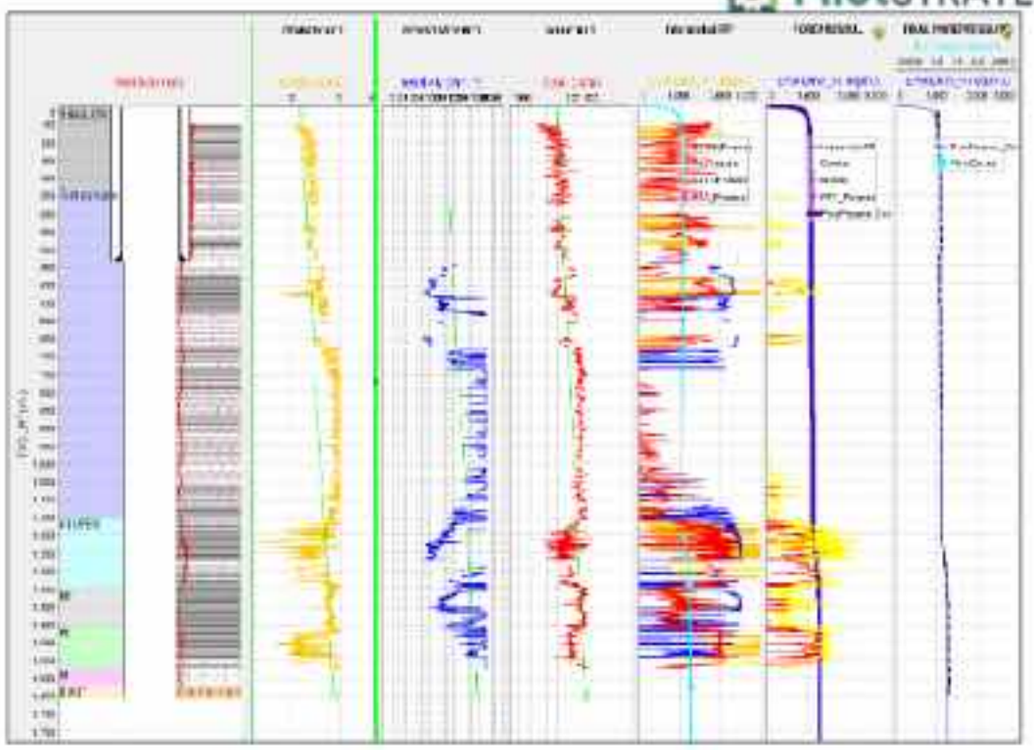

*Figure 6-14. Normal compaction trend and pore pressure derivation for the Lapin-1 well.*

### 6.4.2.8 Horizontal stress estimation

The ESR method involves calculating the ratio of horizontal to vertical effective stress, as illustrated in Figure 6-15. The minimum ($S_{hmin}$) and maximum ($S_{Hmax}$) horizontal stresses are estimated as:

$$S_{hmin} = ESR_{S_{hmin}} \cdot (S_v - \alpha \cdot P_p) + \alpha \cdot P_p, \text{ and}$$

$$S_{Hmax} = ESR_{S_{Hmax}} \cdot (S_v - \alpha \cdot P_p) + \alpha \cdot P_p,$$

where $ESR_{S_{hmin}}$ and $ESR_{S_{Hmax}}$ are the effective stress ratios for $S_{hmin}$ and $S_{Hmax}$ horizontal stresses, respectively, $S_v$ is the vertical stress, $P_p$ is the pore pressure and $\alpha$ is Biot's coefficient (assumed equal to 1).

The PilotSTRATEGY project has received funding from the European Union's Horizon 2020 research and innovation programme under grant agreement No. 101022664

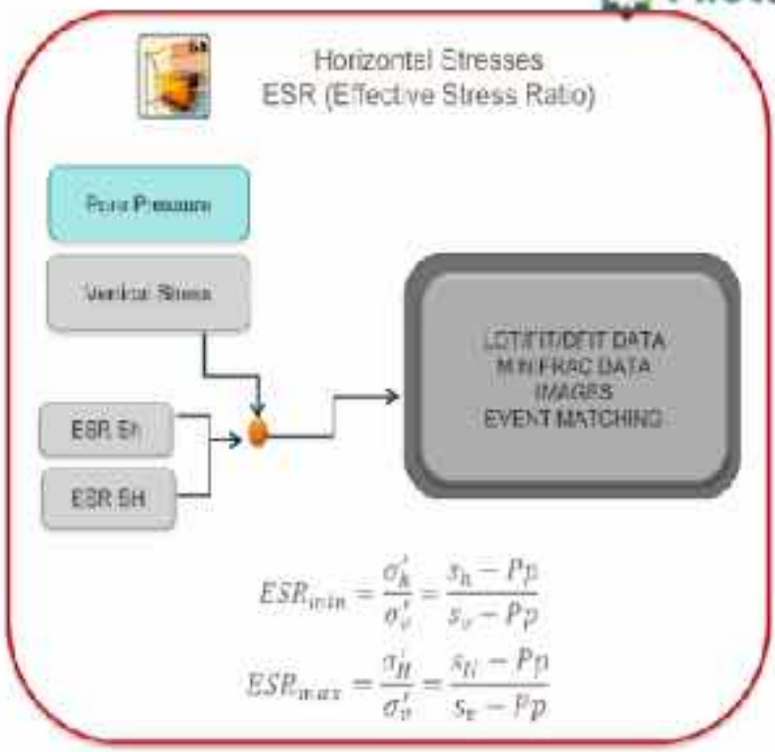


*Figure 6-15 Effective Stress Ratio methodology procedure & formula*

All parameters in the formulations for $S_{hmin}$ and $S_{Hmax}$ can be expressed as depth-dependent gradients. However, the ESRs for $S_{hmin}$ and $S_{Hmax}$ are scalar values that are modeled based on the prevailing tectonic regime rather than directly derived from depth-variant logs. The ESR approach is routinely used to estimate horizontal stress magnitudes and to validate stress models through comparison with observed wellbore failure features, particularly borehole breakout zones with CALI log data. Breakouts form because of stress anisotropy between $S_{hmin}$ and $S_{Hmax}$ and occur where the circumferential compressive stress around the wellbore exceeds the rock's compressive strength. An adequate ESR model should predict breakout locations that align with CALI log anomalies, ensuring consistency between theoretical stress modeling and observed wellbore behavior. The relative magnitudes of the three principal stresses define the tectonic stress regime. These regimes impose first-order constraints on plausible ESR values for $S_{hmin}$ and $S_{Hmax}$ (Table 6-5).

| Effective stress ratio | Tectonic regime | | | | | |
|---|---|---|---|---|---|---|
| | Normal | | Strike slip | | Reverse | |
| | Min. | Max. | Min. | Max. | Min. | Max. |
| $ESR_{S_{hmin}}$ | 0.6 | 0.8 | 0.6 | 0.8 | 0.9 | 1.1 |
| $ESR_{S_{Hmax}}$ | 0.9 | 1 | 1.05 | 1.4 | 1.2 | 1.6 |

*Table 6-5 ESR values for both $S_{hmin}$ and $S_{Hmax}$ and their relation to the tectonic regime after Zoback (2007).*

**$S_{hmin}$ calculation.** To estimate the minimum horizontal stress, formation integrity test (FIT) and leak-off test (LOT) measurements are commonly used, with LOT values generally considered more reliable. In the present case, however, neither FIT nor LOT data are available. Additionally, extensive mud losses were observed over a large portion of the drilling interval, predominantly within carbonate and anhydrite lithologies of the Muschelkalk and Keuper formations. Using the ESR methodology, we

The PilotSTRATEGY project has received funding from the European Union's Horizon 2020 research and innovation programme under grant agreement No. 101022664

adopt $ESR_{S_{hmin}} = 0.6$, for an assumed $\alpha = 1$ and consistent with the tectonic regime inferred for the study area.

**Fracture pressure calculation**. In general, the fracture initiation pressure is related to $S_{hmin}$ through the following relationship:

$$P_{frac} \approx S_{hmin} + P_p + T_0$$

where $P_{frac}$ is the fracture initiation pressure (*i.e.* pressure at which tensile failure of the formation occurs) and $T_0$ is the tensile strength of the rock. The tensile strength is typically small compared to the stress terms and is therefore often neglected in practical applications.

Several analytical models and empirical relationships can be used to estimate fracture pressure or fracture gradient:

- The **ESR methodology** is consistent with effective stress scaling used in Zoback (2007) and related geomechanics workflows that parameterize horizontal stress as a fraction of the vertical effective stress. The fracture pressure, $P_f$, calculated with this approach is:

  $$P_f = P_p + ESR_{S_{hmin}} \cdot (S_v - P_p).$$

  The concept of $P_f$ can be used interchangeably with $P_{frac}$ when tensile failure ($T_0 = 0$) is assumed.
- The **Hubbert-Willies model** calculates $P_f$ as:

  $$P_f = \sigma_{hmin} + P_p + \Delta P,$$

  where $\sigma_{hmin}$ is the minimum horizontal effective stress (not to be confused with the minimum horizontal *total* stress, which we denote $S_{hmin}$ here), and $\Delta P$ is a model-specific parameter that represents additional induced pressure increment and accounts for thermal stresses, injection effects, or transient pressure changes. This method was originally presented for hydraulic fracturing and subsurface stress analysis in Hubbert & Willies (1957).
- The **Eaton model** is a widely used poroelastic formulation stemming from Eaton's overpressure/fracture gradient work (Eaton 1969, 1975). In this formulation, $P_f$ is calculated as:

  $$P_f = P_p + (S_v - P_p) \cdot \left(\frac{1 - 2\nu}{1 - \nu}\right),$$

  where is $\nu$ is the (dimensionless) Poisson's ratio, an elastic parameter describing the ratio of lateral to axial strain. In the present work, this parameter is set for each well (average value).
- The **Mathews & Kelly model** is an operationally focused model introduced in Matthews & Kelly (1967) for drilling and casing design. The fracture pressure is calculated as follows:

  $$P_f = \sigma_{hmin} + P_p + C_m \cdot (S_v - P_p)$$

  where $C_m$ is the model-specific matrix stress coefficient (dimensionless), an empirical parameter dependent on Poisson's ratio and rock compressibility.

The fracture pressure values obtained using the different methodologies yield similar results when expressed as pressure gradients. These values are summarized in Table 6-6, while Figure 6-16. Fracture gradient plot (left side) calculated for each methodology illustrates the calculated fracture gradients for each well, plotted in the left-hand diagram (Matthews & Kelly 1967; Eaton 1975; Zoback 2007).

The PilotSTRATEGY project has received funding from the European Union's Horizon 2020 research and innovation programme under grant agreement No. 101022664

| Well | Fracture pressure model | | | |
|---|---|---|---|---|
| | $ESR_{S_{Hmax}}$ | Hubbert & Willis | Eaton | Matthews & Kelly |
| Ebro-1 | 0.83 | 0.83 | 0.77 | 0.77 |
| Ebro-2 | **0.82** | **0.85** | **0.8** | **0.82** |
| Lopin-1 | **0.84** | **0.84** | **0.81** | **0.77** |
| Mayals-1 | **0.77** | **0.77** | **0.74** | **0.71** |

*Table 6-6 Average values for fracture pressure gradients (in psi ft$^{-1}$) determined using different methods for the studied wells.*

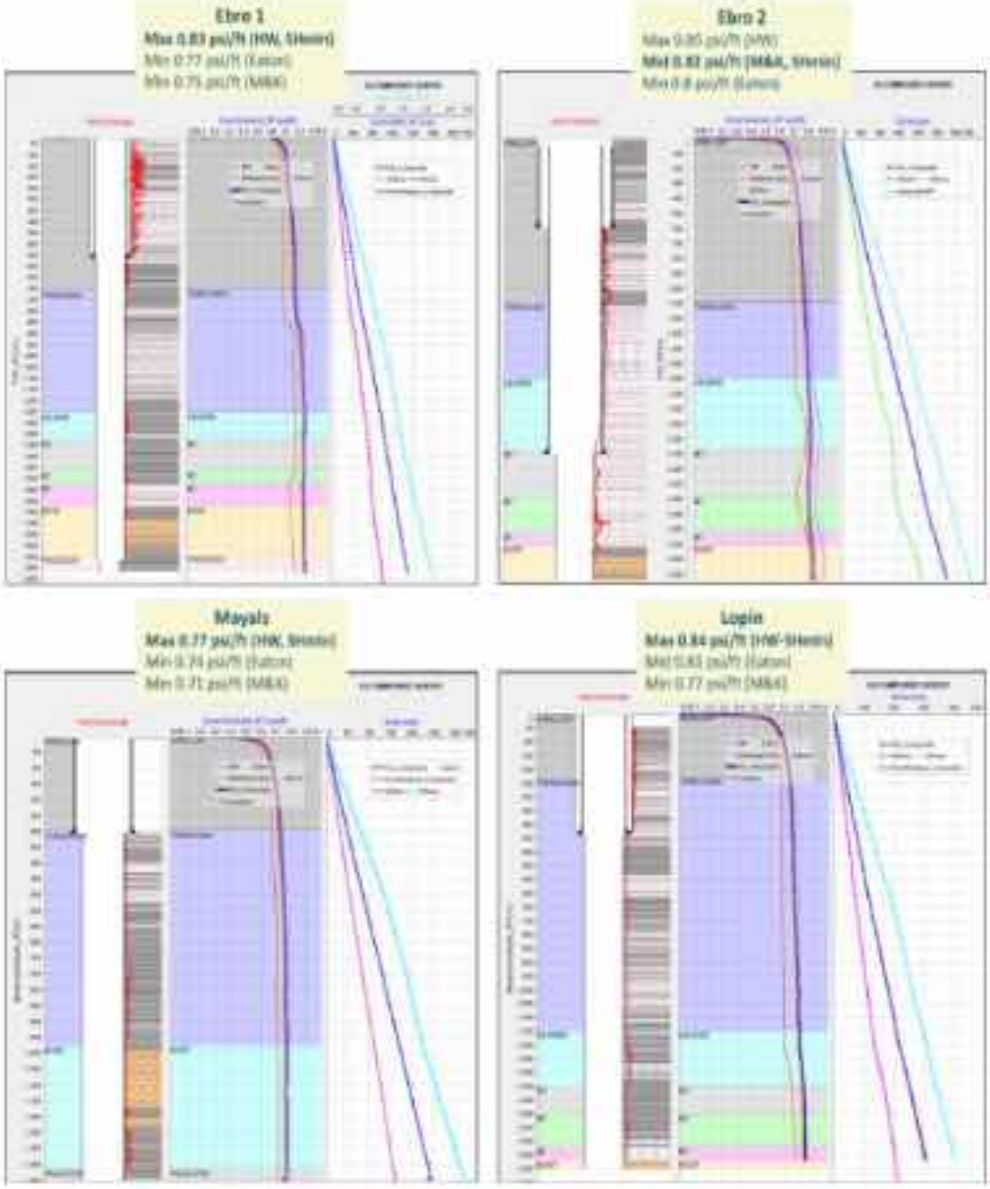


*Figure 6-16. Fracture gradient plot (left side) calculated for each methodology*

**$S_{Hmax}$ calculation**. Estimating $S_{Hmax}$ is typically the most challenging component of regional stress characterization, particularly when high-quality data are limited or lacking. To constrain its orientation in the study area, we used the World Stress Map (Heidbach *et al.* 2016) database. A medium-confidence stress orientation, labeled *wsm05999 JURAMU1997*, is available for this region. This estimate is derived from two borehole breakouts observed at 2225 m MD and 2306 m MD, which indicate an $S_{Hmax}$ azimuth of 76° (Heidbach *et al.* 2016). The locations and breakout signatures are shown in Figure 6-17.

The PilotSTRATEGY project has received funding from the European Union's Horizon 2020 research and innovation programme under grant agreement No. 101022664

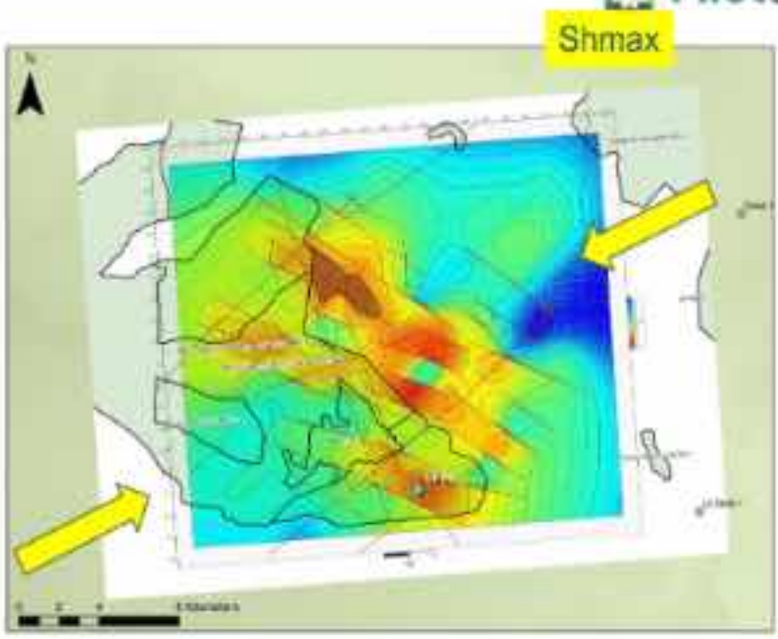


*Figure 6-17 Shmax azimuth extrapolated to Lapin injection area*

After establishing the tectonic regime, the ESR method is applied to ensure that the ranges for $ESR_{S_{hmin}}$ and $ESR_{S_{Hmax}}$ are consistent with the identified regime. These ESR values are not fixed *a priori*; rather, their validity is confirmed only after running the geomechanical model. The model predicts zones of instability along each analyzed well, primarily controlled by horizontal stress anisotropy. These unstable intervals correspond to segments with a high probability of borehole breakout and should coincide with recorded drilling problems such as BHA sticking, stuck pipe, or similar events. Comparing these modeled instability zones with CALI log data provides a key reliability check for model calibration.

A critical factor governing wellbore stability is the magnitude of $S_{Hmax}$ and its relationship to $S_{hmin}$. This stress contrast strongly controls wellbore failure. Because of limited data available for the project, $S_{Hmax}$ is the most challenging parameter to constrain. Its estimation begins with defining a tectonic regime that is compatible with the geological observations for the area. Once this regime is specified, the ESR formulation, dependent on $S_{hmin}$ and $S_{Hmax}$ is applied. Since $S_{hmin}$ has already been estimated and calibrated to fracture pressure, $S_{Hmax}$ must be iteratively adjusted until the resulting ESR values are consistent with the assigned tectonic regime.

The selected $S_{hmin}$ and $S_{EE}$ values are those that (*1*) allow the geomechanical model to reproduce the observed unstable zones identified in the caliper logs, and (*2*) remain consistent with the tectonic regime. It is important to note that the **Ebro Basin** has undergone an extensive geological history since its formation in the Permian through the Tertiary, when the **Alpine orogeny** imposed a compressive pattern, particularly noticeable in the shallow section. For this reason, the obtained effective stress ratio values ($ESR_{Shmin}$ = 0.60 and $ESR_{Shmax}$ = 0.97 for the deeper section, and $ESR_{Shmax}$ = 1.05–1.38 for the shallow section) are compatible with a **normal faulting regime** in the lower section and a **strike-slip regime** in the upper section. Although the Tertiary section exhibits minor reverse faults, the Alpine orogeny had limited influence in this area and did not produce low-angle thrust faults or significant overthrusting. Therefore, this section cannot be classified as compressive according to the **Effective Stress Ratio method**.

The PilotSTRATEGY project has received funding from the European Union's Horizon 2020 research and innovation programme under grant agreement No. 101022664

The final calibrated stress values are as follows:

- $ESR_{Shmin}$: 0.60 (calibrated to fracture pressure)
- $ESR_{Shmax}$:
  - **Upper Interval (Tertiary Section):** 1.05 to 1.38 – Strike-slip regime
  - **Lower Section (Base Tertiary to TD):** 0.97 – Normal faulting regime

This calibration ensures that the geomechanical model accurately predicts breakout-prone zones and provides a robust basis for wellbore stability analysis. In Figure 6-18 an example is shown for Ebro 2 well.

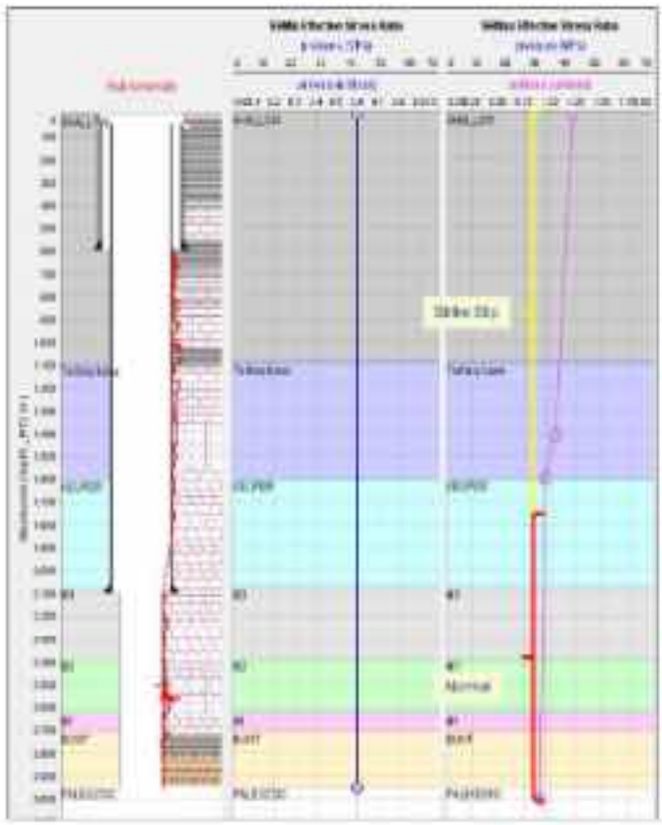

*Figure 6-18 $ESR_{Shmin}$ and $ESR_{Shmax}$ values for Ebro 2 well*

**Results.** As indicated by the model results, breakouts occur when there is significant horizontal stress anisotropy—that is, when $Sh_{min}$ is substantially lower than $Sh_{max}$—a condition more prevalent in the upper section than in the lower section. The following figures illustrate this, showing a comparison between caliper logs and the modeled breakout predictions. Usually, the shallowest sections of the model shows poor calibration. This happens because of (Zoback, 2010):

- **Low Overburden Stress ($S_v$):** In shallow depths, $S_v$ is small, so normalized ratios ($S_h/S_v$) become very sensitive to small changes in $Sh_{min}$ or $Sh_{max}$, leading to instability in ESR interpretation.
- **Influence of Near-Surface Conditions:** Shallow formations often have complex stress perturbations due to topography, faults, and local heterogeneities, which ESR does not fully capture.

The PilotSTRATEGY project has received funding from the European Union's Horizon 2020 research and innovation programme under grant agreement No. 101022664

- **Data Scarcity:** Shallow sections rarely have direct measurements (e.g., leak-off tests, breakouts), making ESR calibration difficult.
- **Non-tectonic Stresses:** Near-surface stresses can be influenced by residual stresses, uplift, or erosion, which ESR assumes negligible.

The following figures show the caliper log for each well, compared with the breakout opening angle predicted by the model based on the input parameters. When the breakout angle exceeds 90°, the well is considered unstable, indicating a higher likelihood that the caliper will reflect borehole wall collapse. It can be observed that the model aligns well with the predictions and, furthermore, that drilling events such as tight hole or stuck pipe occur in areas where instability is predicted.

Ebro 1. Figure 6-19, left. The model results show a poor match in the Upper Section. The rest of the section is very well matched.

Ebro 2. Figure 6-19, right. Slightly better match in the shallow section, and overall, it fits the entire well quite well. Very good match between drilling events and predicted breakouts area (stuck pipe + tight hole).

Lopin 1. Figure 6-20, left. Good match, more obvious in the lower section

Mayals 1. Figure 6-20, right. Good match, more obvious in the lower section

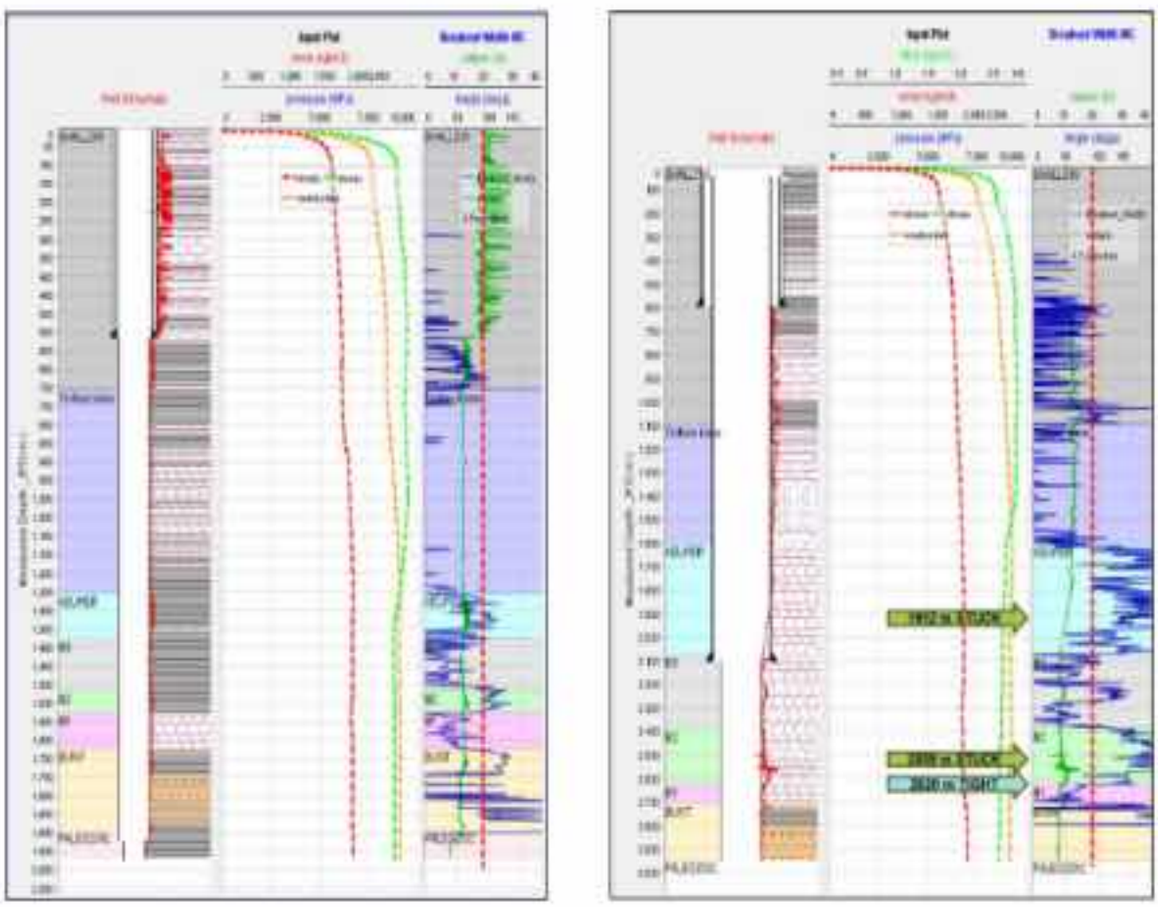

*Figure 6-19. Caliper Log VS Breakout prediction. Left Ebro 1, right Ebro 2.*

The PilotSTRATEGY project has received funding from the European Union's Horizon 2020 research and innovation programme under grant agreement No. 101022664

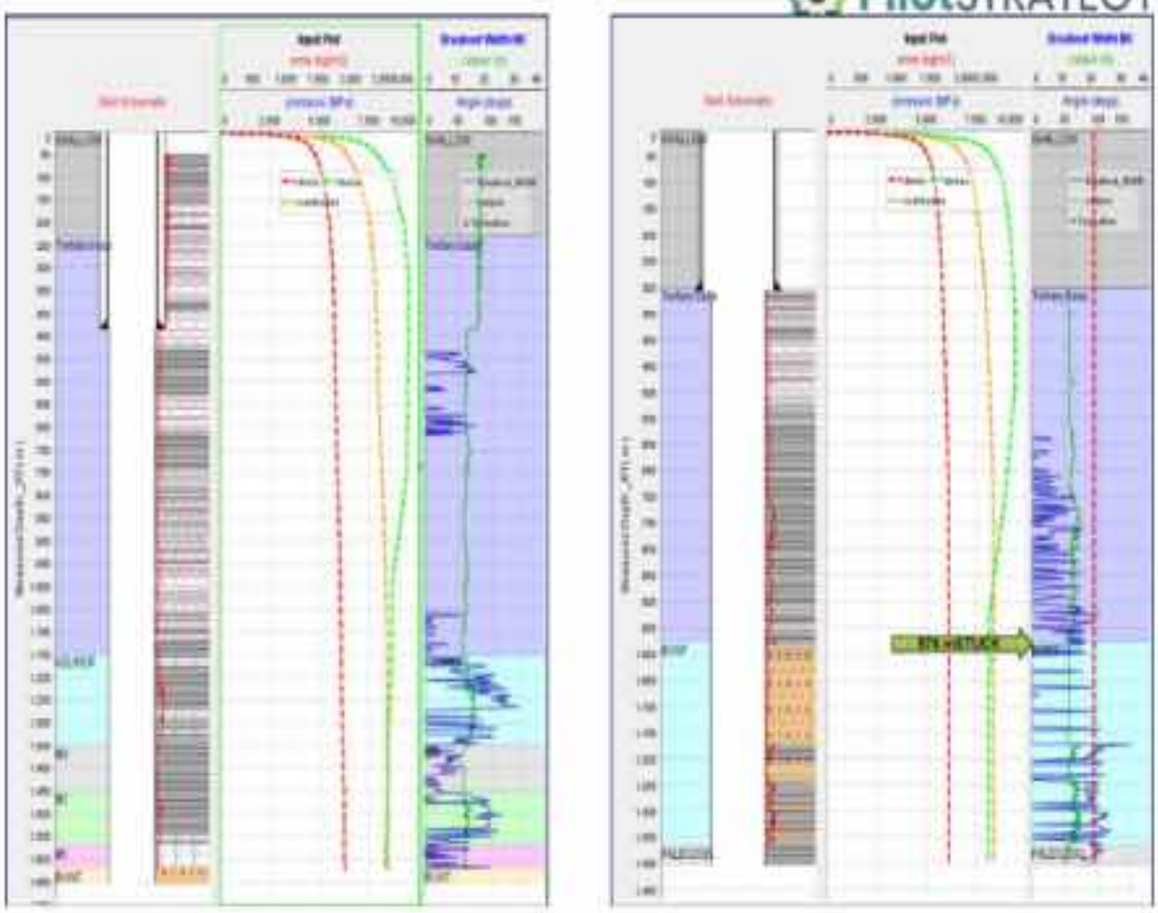

*Figure 6-20. Caliper Log VS Breakout prediction. Left Lopin 1, right Mayola 1*

### 6.4.3 Wellbore stability

Maintaining wellbore stability during the drilling of a $CO_2$ injection well is a critical requirement for safe and efficient operations. Geomechanical instability near the wellbore can lead to severe drilling problems such as borehole collapse, lost circulation, or unintended wellbore fracturing—all of which compromise drilling success and the long-term integrity of the injection well.

Accurate **mud weight prediction** is essential to:

- Maintain near-wellbore mechanical stability,
- Prevent wellbore collapse or fracturing,
- Ensure safe drilling operations and long-term well integrity.

This process begins with the development of a **geomechanical model** that integrates in-situ stress, pore pressure, and rock strength data to define a safe mud weight window tailored to the geological and operational conditions of the $CO_2$ injection site.

Using the parameters calculated from previous analyses, **GeoSmart software** was employed to generate a mud weight window for a hypothetical future injection well (Figure 6-21). This prediction is based on calibrated stress magnitudes, pore pressure, and rock strength, ensuring consistency with the tectonic regime and wellbore stability criteria. The resulting mud weight window provides operational guidance to minimize instability risks during drilling and subsequent $CO_2$ injection.

The PilotSTRATEGY project has received funding from the European Union's Horizon 2020 research and innovation programme under grant agreement No. 101022664

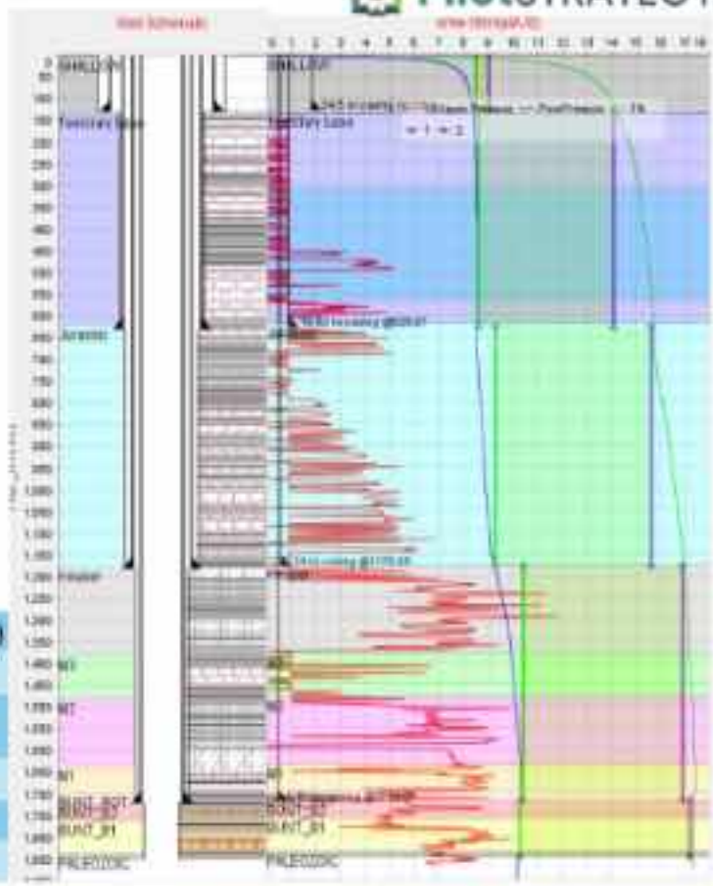

| Formation/Period | Mudweight Range (ppg) |
|---|---|
| Shallow | 8.5 - 9 |
| Tertiary | 8.6 -14.1 |
| Jurassic | 9.3 - 15.6 |
| Keyper & Muschelkalk | 10.4 - 16.9 |
| Buntsandstein | 10.3 - 17.2 |

*Figure 6-21 Mudweight predict for the future injection well based on the results of the model*

### 6.4.4 Seal integrity assessment

This section presents a continuous and integrated evaluation of the mechanical integrity of the caprock at the CCS-1 injector location, considering (a) the initial, pre-injection state, and (b) the End of Injection (EOI) state, defined as the moment of maximum reservoir overpressure after 30 years of continuous $CO_2$ injection (peak injection). The scope is purely geomechanical: the assessment addresses potential seal failure by hydraulic fracture initiation or fracture reactivation; capillary seal capacity (e.g., capillary entry pressure/column height, buoyancy-driven leakage) and other non-mechanical processes are outside the scope of this section. The same geomechanical framework, mechanical thresholds, and fracture criteria are applied in both states to ensure a consistent before/after comparison.

All stress and pressure curves used herein were derived specifically for CCS-1 using a wellbore stability analysis calibrated with the 1D geomechanical models of offset wells Lopin1 and Ebro1. As CCS-1- is undrilled and no LOTs are available to calibrate the fracture gradient (FG), the FG is estimated directly from $S_{hmin}$ following established practice for undrilled locations; for conservatism, we adopt FG_safe = 0.9 × FG as the operational reference in stability checks and pressure limits.

The analysis focuses on the top of the reservoir (~1,722 m TVD)—the base of the seal—where reservoir pressure first interacts with the caprock and where mechanical failure would be expected if thresholds were exceeded. In both states, pore pressure profiles use the $CO_2$ gradient anchored at the reservoir base; the initial profile is anchored to the original reservoir pore pressure, and the EOI profile is anchored to the peak pore pressure at

The PilotSTRATEGY project has received funding from the European Union's Horizon 2020 research and innovation programme under grant agreement No. 101022664

CCS-1- and vertically shifted at CCS-1 to match the depth of maximum mean pore pressure from logs relative to its pre-injection position, keeping the base anchoring.

#### 5.3.7.1. Initial Seal Integrity State (Pre-Injection)

The initial analysis begins with the pore pressure (PP) and minimum horizontal stress ($S_{hmin}$) profiles constructed for CCS-1. These two curves define the effective stress regime in the formation according to:

$$\sigma' = \sigma - \alpha \cdot P_p,$$

where $\sigma'$ is the effective stress, $\sigma$ is the total stress, $P_p$ is the pore pressure, and $\alpha$ is the Biot coefficient (assumed ~1 for shale caprock). This relation governs how increases in pore pressure reduce effective stress and bring the system closer to fracturing. Fracture initiation is theoretically associated with:

$$P_{frac} = S_{hmin} + T_0 - \alpha \cdot P_p$$

but for undrilled wells where tensile strength, $T_0$, and LOT data are unavailable, it is standard to approximate: FG ≈ $S_{hmin}$, providing a conservative fracture threshold.

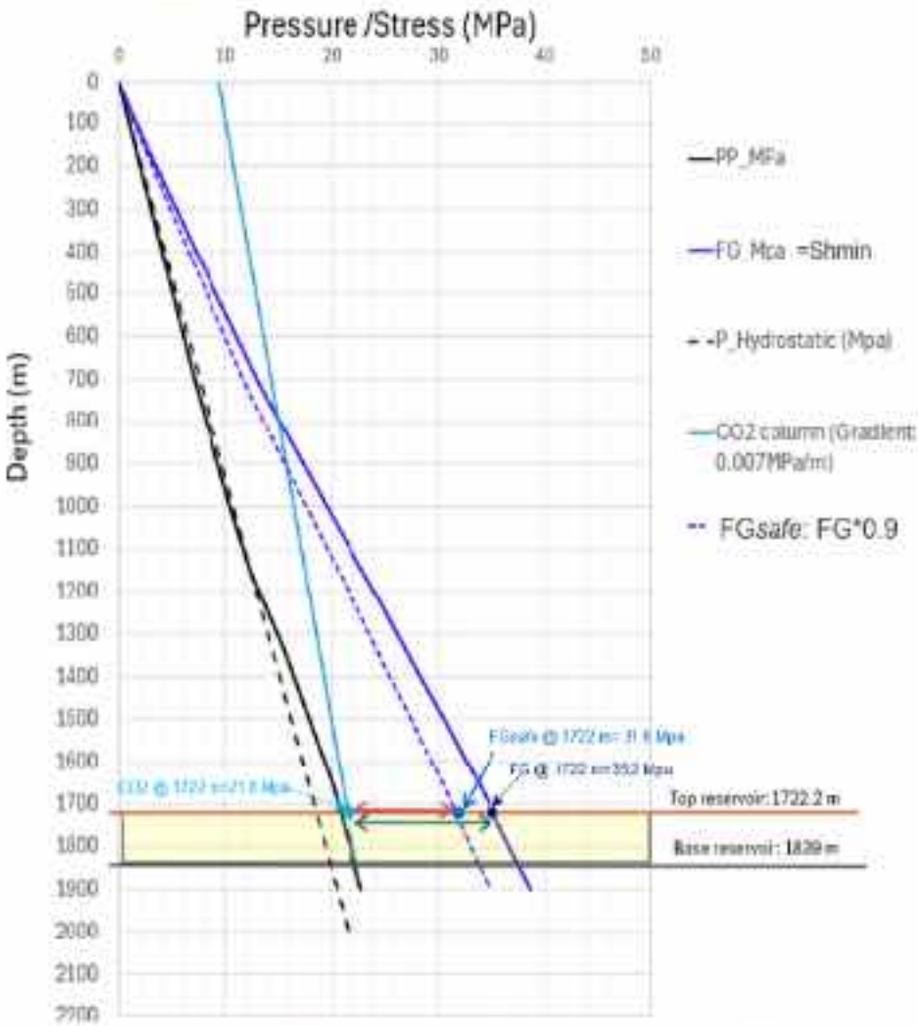


*Figure 6-22: Pre Injection Stress–Pressure Framework at CCS-1.*

The accompanying graphic (Figure 6-22) integrates the principal mechanical and fluid pressure curves required to evaluate caprock containment at the CCS-1 location.

The PilotSTRATEGY project has received funding from the European Union's Horizon 2020 research and innovation programme under grant agreement No. 101022664

- The pore pressure profile (black curve) represents the expected in situ formation pressure at CCS-1, derived from the regional trend and calibrated with the pressure and rock mechanics constraints available from Lopin1 and Ebro1.
- The hydrostatic reference is shown as a dashed black line.
- The $CO_2$ pressure column (cyan line) is computed using a representative dense phase $CO_2$ gradient of 0.007 MPa·m$^{-1}$, consistent with $CO_2$ densities in the range 650–750 kg·m$^{-3}$ (*i.e.* gradient 0.0064–0.0074 MPa·m$^{-1}$). For the initial-state reference, the $CO_2$ static gradient is positioned at the reservoir base (1839 m) and anchored to the initial pore pressure at that depth (PP_base). This choice is conservative for caprock evaluation because it maximizes the effective overpressure at the top of the reservoir relative to fracture thresholds while explicitly accounting for the initial pressure field. At the depth of the reservoir top (≈1,722 m TVD), the resulting static $CO_2$ pressure is ≈21.8 MPa, which is the reference used in this analysis.
- The minimum horizontal stress ($S_{hmin}$) at CCS-1 (blue curve) reaches ≈35.2 MPa at 1,722 m, as determined from the CCS-1 geomechanical model constrained by the mechanical properties from the offset wells. Because CCS-1 is undrilled, no LOT/XLOT/minifrac measurements exist. Accordingly, the fracture gradient (FG) at CCS-1 (blue curve) is obtained directly from the CCS-1 wellbore stability analysis, where FG ≈ $S_{hmin}$ is the conservative and standard assumption under these conditions.
- An operational fracture gradient with a 10% safety factor (FG × 0.9, blue dashed line) is included to represent the maximum allowable operating pressure (MAOP) for injection, ensuring a conservative buffer to induced fracturing.

At CCS-1, the geomechanical model derived from Lopin-1 and Ebro-1 yields:

- $S_{hmin}$ = 35.2 MPa at 1,722 m,
- FG ≈ $S_{hmin}$ = 35.2 MPa,
- FG × 0.9 (10% safety factor) = 31.6 MPa.

**Initial Safety Margins:** Two fracture-related safety margins are computed:

**(a) Operational margin (fracture gradient with safety factor)**

$$\text{Margin}_{oper} = FG_{safe} - P_{CO_2} = 31.6 - 21.8 = \mathbf{9.8\ MPa}.$$

This quantifies the distance to the **operational fracture limit**, i.e., the MAOP used in dynamic injection control.

**(b) Conservative margin (minimum horizontal stress)**

$$\text{Margin}_{cons} = Shmin - P_{CO_2} = 35.2 - 21.8 = \mathbf{13.4\ MPa}.$$

Interpretation of results indicates that, at the initial state, the CCS-1 caprock displays wide mechanical buffers (9.8–13.4 MPa) and lies well below both fracture initiation and reactivation limits, confirming

The PilotSTRATEGY project has received funding from the European Union's Horizon 2020 research and innovation programme under grant agreement No. 101022664

seal integrity and establishing a robust pre-injection mechanical baseline that supports confidence in containment and a conservative operating envelope.

*5.3.7.2 Seal Integrity at End-of-Injection (EOI, Peak Pressure at 30 Years)*

At EOI (End of Injection)—defined as the peak reservoir pressure after ~30 years of modeled $CO_2$ injection at CCS-1—PP_peak denotes the peak simulated pore pressure at the CCS-1 well location from the single-well, P10-permeability dynamic case; it does not represent the absolute field maximum but is expected to be very close, as the highest pressures concentrate near the injector. Using the same mechanical thresholds as in the initial assessment ($S_{hmin}$, FG = $S_{hmin}$, and the safety-factored FG × 0.9), the residual safety margins are evaluated at the reservoir top (~1,722 m TVD) to quantify how the injection-induced $\Delta P$ narrows the operational ($0.9 \times FG - P_{p\_peak}$) and conservative (Shmin – PP_peak_injection) buffers relative to the pre-injection state. For conservatism, the $CO_2$ gradient is kept with unchanged slope, remains anchored at the reservoir base (1,839 m), and is vertically translated to intersect PP_peak_injection; this translated line replaces the initial static column and provides the reference for recomputing the margins, which are assessed at the reservoir top where seal-failure risk is greatest.

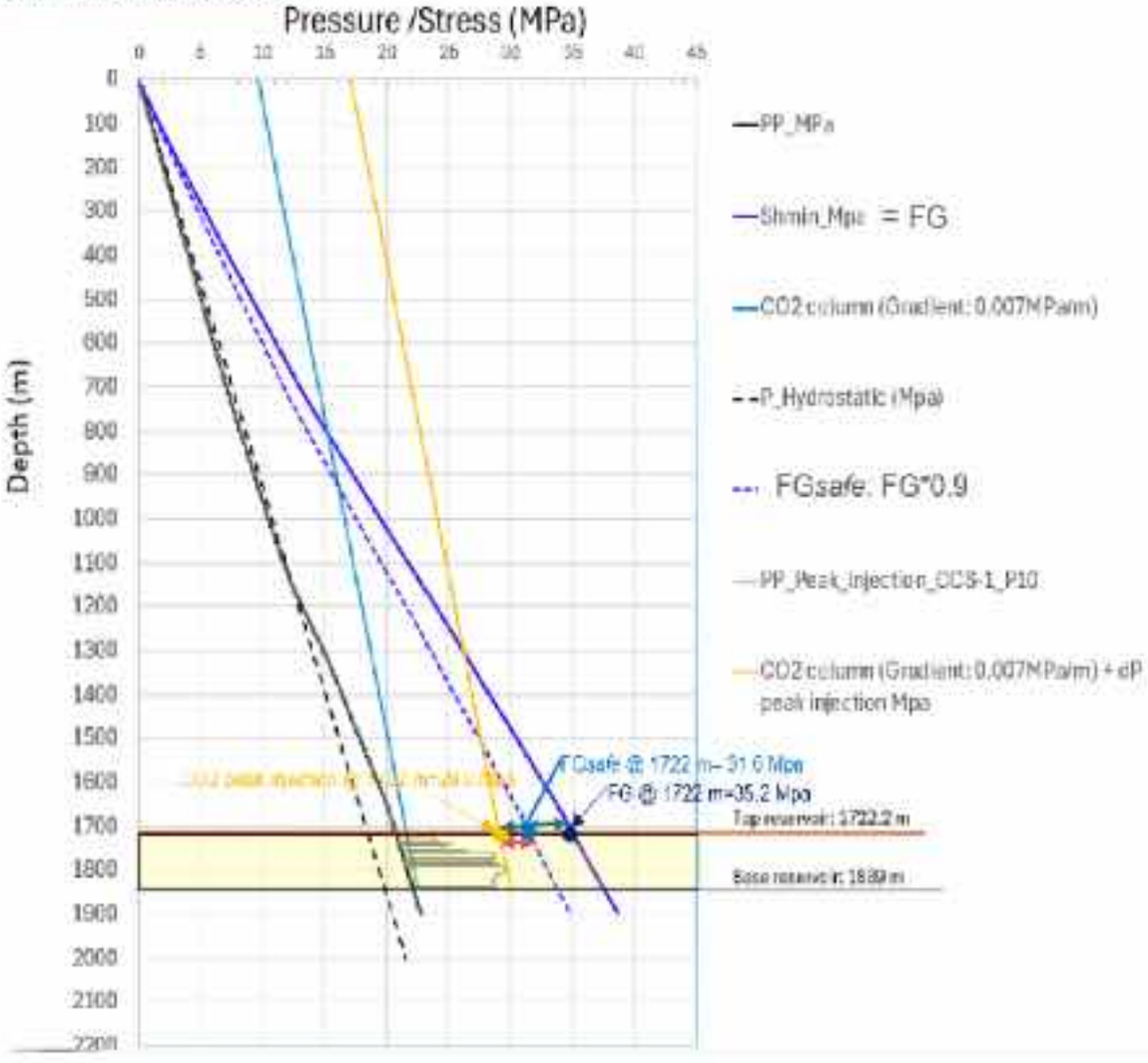


*Figure 6-23 EOI Stress–Pressure Framework at CCS-1, including PP_peak and translated $CO_2$ gradient.*

The PilotSTRATEGY project has received funding from the European Union's Horizon 2020 research and innovation programme under grant agreement No. 101022664

Figure 6-23 shows the peak-state (end-of-injection, EOI) analysis for the CCS-1 caprock, summarizing the reservoir-top pressure and the mechanical thresholds used to evaluate caprock seal integrity under maximum modeled conditions.

At the reservoir top (~1,722 m) the simulation gives $PP_{peak} \approx 29.8$ MPa.This pressure is used in place of the initial $CO_2$ static column for evaluating seal stability under maximum injection conditions.

The mechanical limits remain unchanged from the initial state since they derive from the static stress model:

- $Shmin = 35.2$ MPa
- $FG \approx 35.2$ MPa
- $FG_{safe} = 31.6$ MPa

**EOI Safety Margins**

**(a) Operational margin (FG × 0.9 – PP_peak)**

$$\text{Margin}_{oper,EOI} = 31.6 - 29.8 = \mathbf{1.8\ MPa}.$$

This sharply reduced margin indicates that the pressure at CCS-1 is now close to the safety-factored fracture threshold, reducing operational flexibility.

**(b) Conservative margin (Shmin – PP_peak)**

$$\text{Margin}_{cons,EOI} = 35.2 - 29.8 = \mathbf{5.4\ MPa}.$$

This is the remaining buffer before pre-existing fractures could theoretically reopen.

At the end-of-injection (EOI) state, the analysis indicates that caprock seal integrity is maintained—both the operational margin (vs. safety-factored fracture gradient) and the conservative margin (vs. Shmin) remain positive—but the system now operates much closer to the mechanical failure envelopes. Specifically, the operational margin contracts from 9.8 MPa to 1.8 MPa and the conservative margin from 13.4 MPa to 5.4 MPa, tightly aligning with the ~8 MPa increase in reservoir pressure predicted by the simulation. This means that while new fracture initiation or reactivation is not expected at EOI under the modeled conditions, the available headroom has narrowed, reducing operational flexibility and increasing sensitivity to additional pressure increments or uncertainties (e.g., stress heterogeneity, measurement error). Practically, this supports a conservative operating envelope—careful control of injection rates and vigilant monitoring—to ensure pressures remain comfortably below the relevant thresholds.

*5.3.7.3. Seal integrity assessment Conclusions*

- Before injection, the CCS-1 caprock possessed wide safety margins of 9.8 MPa (operational) and 13.4 MPa (conservative), indicating strong mechanical integrity at the pre-injection state.
- At EOI (peak pressure at 30 years), the margins are reduced but still positive, with 1.8 MPa operational and 5.4 MPa conservative margins remaining at reservoir top depth.
- The reduction in margins is directly attributable to the injection-induced pore pressure increase from 21.8 MPa to 29.8 MPa.

The PilotSTRATEGY project has received funding from the European Union's Horizon 2020 research and innovation programme under grant agreement No. 101022664

- Although the system remains mechanically stable at EOI, it operates close to the fracture gradient with safety factor (FG × 0.9), suggesting a need for careful operational control and monitoring.
- Because both analyses use the same geomechanical stress model for CCS-1, derived from Lopin-1 and Ebro-1, the comparison between the initial and EOI states is rigorous and internally consistent.
- Overall, the CCS-1 seal remains mechanically competent throughout the injection period studied, but with significantly reduced safety buffers at the end of injection, emphasizing the importance of pressure management during late-life injection.

### 6.4.5 Fault stability assessment

Fault stability assessment is a key step in evaluating the risks associated with $CO_2$ injection, as slip along pre-existing faults can lead to induced seismicity, create leakage pathways, and compromise storage integrity. In this case, the 1D geomechanical model was used to support the fault stability analysis by providing vertical profiles of pore pressure, in-situ stresses, and rock mechanical properties.

These data are incorporated into a 2D fault plane model developed using SLB's **Petrel™ subsurface software** and Petroleum Experts Ltd.'s **MOVE™ structural geology modelling software**, which accurately represents the geometry, orientation, and dip of the fault, as well as the mechanical behavior of surrounding formations. The 2D model projects the results directly onto the fault planes, accounting for the dip and dip azimuth of each segment relative to the in-situ stress field. This allows fault orientation to be evaluated with respect to the direction of the maximum horizontal stress ($S_{Hmax}$), which is critical for accurately assessing fault stability. In this context, the stress tensor is decomposed into normal and shear components on each fault segment, with the resulting values directly influenced by the orientation of $S_{Hmax}$. This approach facilitates a high-resolution spatial analysis of fault mechanics under the influence of the current tectonic stress field.

Using a one-way coupling approach, the model integrates pore pressure changes ($\Delta P$) derived from dynamic reservoir simulations, enabling the update of effective stresses over time. This allows for a detailed assessment of fault stability and reactivation potential under evolving operational conditions.

Given that the system starts from a highly stressed and unfavorable initial state, with a limited safety margin for injection, this modeling approach is particularly valuable. It will be essential when repeating the analysis with updated reservoir conditions, as it will help quantify how increasing pore pressure may further reduce stability in an already sensitive system.

When applying this fault stability assessment method, there are certain limitations that need to be considered. The analysis is based on a 2D fault plane model supported by a 1D geomechanical framework, which does not fully capture 3D stress variability or along-strike fault heterogeneity. Mechanical properties and fault friction are assumed to be homogeneous and time-invariant, and the results are strongly dependent on the assumed in-situ stress tensor, particularly $S_{Hmax}$ orientation and magnitude. In addition, the one-way coupling between reservoir pressure and geomechanics neglects stress redistribution, poroelastic effects, and fault-slip feedback, while fault hydraulic behavior is

The PilotSTRATEGY project has received funding from the European Union's Horizon 2020 research and innovation programme under grant agreement No. 101022664

treated implicitly. Under highly stressed initial conditions with a limited safety margin, the results are therefore sensitive to uncertainties in baseline stress and pore pressure.

Despite these limitations, we consider this to be the most appropriate method given the available data density. Only one well is available within the model domain to constrain the geomechanical properties, which is insufficient to reliably populate a 3D geomechanical model without imposing unrealistic lateral continuity. Implementing a 3D approach under these conditions would require extrapolating single-well 1D geomechanical profiles across the entire model volume, providing no additional insight or improvement in result quality, while introducing significant uncertainty. Moreover, the effort and computational cost associated with a full 3D model would be disproportionate to the expected benefits. A 2D fault-plane approach, constrained by the available 1D geomechanical data and the in-situ stress framework, is therefore sufficient and appropriate to support robust conclusions on fault stability and reactivation potential in the present context.

#### *6.4.5.1 Methodology*

This study employs a one-way coupled geomechanical workflow to assess the risk of fault reactivation during $CO_2$ injection. The methodology integrates dynamic reservoir simulation outputs with geomechanical modeling based on the Mohr-Coulomb failure criterion.

Figure 6-24 illustrates the workflow implemented for conducting the fault stability analysis.

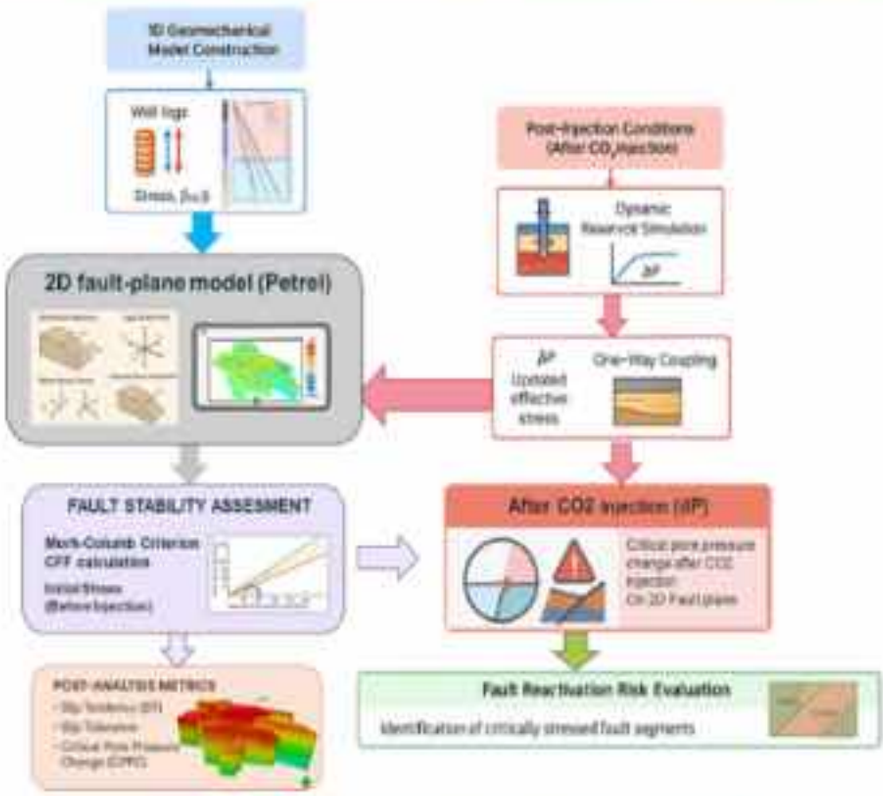


*Figure 6-24 Workflow diagram for a fault stability analysis.*

The key steps are outlined below:

**1. Data Acquisition and 1D Geomechanical Model Construction**

A 1D geomechanical model was developed using well log data and regional stress information to obtain the initial stresses state. Explained in the previous section.

The PilotSTRATEGY project has received funding from the European Union's Horizon 2020 research and innovation programme under grant agreement No. 101022664

## 2. 2D Fault Plane Modeling

To improve both the understanding and representation of the fault stability analysis results, a two-dimensional (2D) geomechanical model was developed along the fault plane. This model integrates one-dimensional (1D) geomechanical data from well locations and interpolates stress and pore pressure conditions across the entire fault surface, both laterally and with depth.

Importantly, the model enhances the analysis by explicitly considering the orientation of the fault relative to the direction of the maximum horizontal stress ($SH_{max}$). This allows for accurate resolution of the stress tensor components—normal and shear—on the fault plane, providing a more realistic depiction of the mechanical interaction between the regional stress field and the fault geometry.

By capturing depth-dependent variations in stress and pore pressure, the 2D model enables a more detailed and reliable assessment of fault reactivation potential. It reveals heterogeneities and critical zones along the fault that are not visible in 1D profiles, thereby strengthening the geomechanical interpretation under dynamic reservoir conditions.

## 3. Fault Stability Assessment Using Mohr–Coulomb's Criterion

Fault stability was evaluated for each fault-plane segment using the Mohr–Coulomb failure criterion (Figure 6-25), implemented through the application of the Coulomb failure function (CFF). The analysis was carried out under both initial (pre-injection) stress conditions and the altered stress state resulting from $CO_2$ injection, thereby allowing the assessment of potential fault reactivation driven by changes in pore pressure and effective stress. The *CFF* is defined as:

$$CFF = \tau - [f_{st} \cdot (\sigma_n - P_p) + C],$$

where $\tau$ is the shear stress acting on the fault plane, $\sigma_n$ is the normal stress, $P_p$ is the pore pressure before injection, $f_{st}$ is the coefficient of friction, related to the friction angle, $\phi$, by $f_{st} = \tan\phi$, and $C$ is the cohesion of the fault material. In accordance with common practice in fault stability analysis, the cohesion term is assumed to be $C = 0$ for pre-existing faults. This assumption reflects the fact that such faults have previously experienced slip or fracturing, resulting in the degradation or loss of intergranular bonding. Consequently, their shear strength is primarily governed by frictional resistance rather than cohesive strength. Moreover, adopting zero cohesion provides a conservative assessment, ensuring that potentially unstable or near-critical faults are not overlooked.

A fault segment is considered critically stressed or prone to reactivation when $CFF \geq 0$, indicating that the applied shear stress equals or exceeds the frictional resistance of the fault; a negative *CFF* suggests mechanical stability under current conditions.

To complement the analytical evaluation, Mohr's circles were constructed at each depth level to visualize the in-situ stress state relative to the failure envelope. This graphical approach enables direct assessment of proximity to shear failure, highlighting fault segments where stress conditions approach or intersect the failure criterion.

The PilotSTRATEGY project has received funding from the European Union's Horizon 2020 research and innovation programme under grant agreement No. 101022664

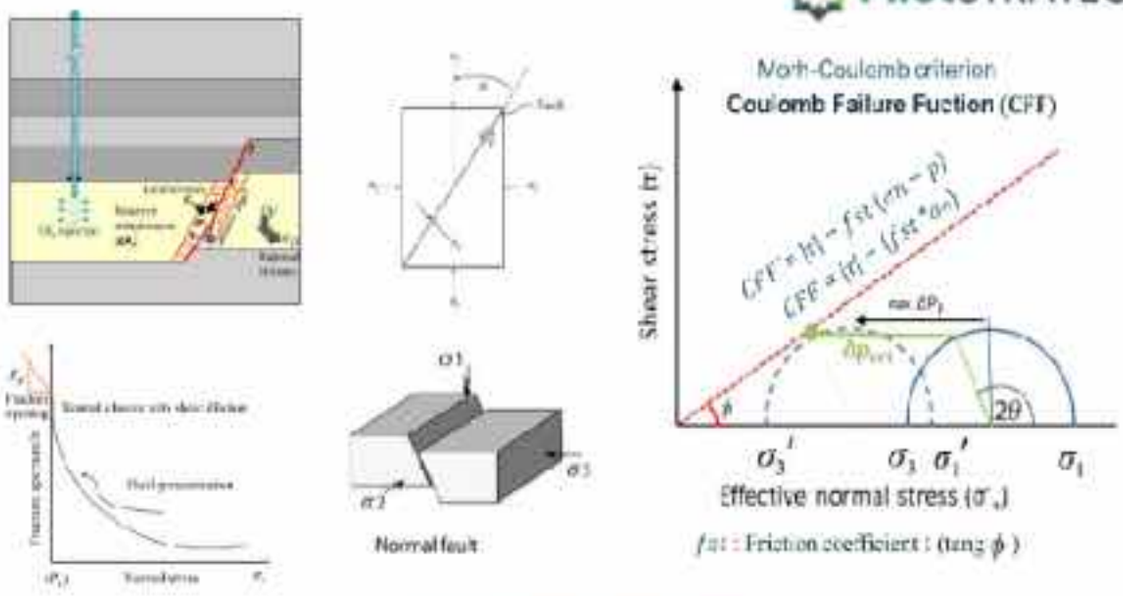


*Figure 6-25 Mohr-Coulomb criterion*

**4. Post-analysis metrics.**

To evaluate the likelihood of fault reactivation and define the initial mechanical state of the system prior to injection, the following metrics are used:

- **Slip tendency**, $f_{mob}$, is defined as the ratio of the shear stress to the resolved normal stress acting on a fault face:

$$f_{mob} = \frac{\tau}{\sigma_n}$$

  It represents the *mobilised* friction on the fault face. A higher $f_{mob}$ indicates that the fault orientation is more favourably aligned for slip under the present stress field. However, slip tendency alone does not determine whether slip will occur, as it does not incorporate frictional strength.
- **Slip tolerance**, *ST*, quantifies how close a fault is to frictional failure by comparing the shear stress acting on the fault to the shear stress required for sliding along the Coulomb failure envelope at the same normal stress.

$$ST = \frac{\tau}{C + \sigma_n \cdot f_{st}}$$

  The fault is critically stressed or likely to reactivate if $ST \geq 1$; the fault face is stable when $ST < 1$. *ST* therefore normalises the shear stress against the frictional strength of the fault and provides a threshold condition for reactivation.
- The **critical pore pressure change** (CPPC or $\Delta p_{cri}$) represents the additional pore pressure required to bring the fault face to failure under the Coulomb criterion It is the pore pressure increase needed to reduce the effective normal stress such that the shear stress equals the shear strength:

$$\Delta p_{cri} = \sigma_n - \frac{\tau - C}{f_{st}}$$

The PilotSTRATEGY project has received funding from the European Union's Horizon 2020 research and innovation programme under grant agreement No. 101022664

Physically, this quantifies how much pore-pressure reduction of effective stress is required for sliding to occur. It is therefore crucial for identifying pressure-sensitive faults, and for defining safe upper bounds for injection pressures to avoid induced seismicity.

To support and validate the fault stability assessment under $CO_2$ injection conditions, a multi-representation workflow was applied, integrating analytical and graphical tools to provide a comprehensive evaluation. The approach included:

- **Mohr's circles**, constructed at multiple depths to characterize the in-situ stress state and evaluate proximity to shear failure.
- **Stereonets**, used to analyze fault orientation relative to the principal stress directions (particularly $S_{Hmax}$) and identify segments optimally oriented for slip.
- **Two-dimensional fault plane projections**, generated from interpolated 1D geomechanical inputs, mapping shear stress, normal stress, pore pressure, and CFF across the fault surface. These projections account for fault geometry and stress orientation to locate zones that are critically stressed.

All metrics are computed and analyzed for the initial (pre-injection) stress state to establish the baseline fault stability conditions and identify unfavorable fault orientations.

For the final fault stability assessment under $CO_2$ injection, only the CPPC metric is applied, as it directly quantifies the additional pore pressure required to induce fault reactivation under injection-altered conditions.

**5. End of Injection (EOI) - Peak injection Condition.**

Fault stability was evaluated under end of injection (EOI) conditions at year 30, which corresponds to the period of maximum pore-pressure buildup ($\Delta P_{max}$) during $CO_2$ storage operations. This time step occurs immediately prior to injection shut-in, after three decades of continuous injection, when cumulative pressure within the reservoir reaches its highest magnitude. At EOI, pore pressure is at its maximum and thus produces the largest reduction in effective normal stress acting on pre-existing faults. This makes EOI the most critical and conservative moment for fault stability assessment, as it represents the peak likelihood of injection-induced reactivation prior to any post-injection pressure dissipation or stress re-equilibration.

When injecting $CO_2$, pore pressure (PP) increases in the reservoir, playing a critical role in fault stability. This elevated PP reduces the effective normal stress acting on the fault plane, which in turn lowers the shear strength of the fault according to the Mohr-Coulomb failure criterion. This effect is visualized through Mohr's circle, which shifts leftward (toward lower effective stress) as pore pressure increases. This shift brings the circle closer to—or even intersecting—the failure envelope, indicating a higher likelihood of fault slip.

Following the initial evaluation of fault stability under pre-injection stress conditions, the analysis was extended to incorporate the effects of pore pressure increases induced by $CO_2$ injection. This was implemented using a one-way coupling approach, in which the pressure data from dynamic reservoir simulations are used as input to the geomechanical model. Specifically, the pore pressure increment was manually applied to the 2D fault plane model, enabling a spatially resolved, cell-by-cell assessment of the pressure reaching each fault segment. This approach provides a more realistic

The PilotSTRATEGY project has received funding from the European Union's Horizon 2020 research and innovation programme under grant agreement No. 101022664

representation of the pressure field and its influence on fault stability, while maintaining computational efficiency.

To assess the potential for fault reactivation, the methodology involves a direct comparison between the pore pressure increase (ΔP) and the Critical Pore Pressure Change (CPPC), which is derived from the initial in-situ stress conditions. Assuming a constant stress tensor, the analysis evaluates whether the pore pressure increase alone is sufficient to bring fault segments to a critical state.

In practical terms, this is achieved by subtracting the simulated pore pressure increase (ΔP) from the CPPC value at each fault cell. The resulting difference (CPPC - ΔP) indicates the remaining pressure margin before failure. If this value is negative or close to zero, it suggests that the fault segment has reached or exceeded the failure threshold. This differential mapping provides a clear and conservative screening tool to identify areas where fault slip is most likely to occur due to $CO_2$ injection, without requiring a full recomputation of the stress field.

The methodology was applied to a range of dynamic reservoir model scenarios, each representing distinct geological and operational conditions. Specifically, the analysis considered permeability realizations corresponding to the P90, P50, and P10 percentiles, as well as injection configurations involving one and two $CO_2$ injection wells. For each scenario, the pore pressure increase was extracted at the peak injection time—corresponding to 30 years of continuous injection—and used to evaluate fault stability through the CPPC comparison framework. This multi-scenario approach enables a robust and comprehensive understanding of fault sensitivity under varying reservoir behaviors.

**6. Fault reactivation risk evaluation.**

Finally, a risk evaluation was conducted by identifying the scenarios in which unstable fault segments emerge. This step enables a systematic assessment of the conditions under which fault reactivation is most likely to occur. By analyzing the spatial distribution and extent of critically stressed or failed segments across all scenarios, the methodology supports the identification of high-risk configurations.

These results provide a basis for drawing conclusions and defining injection strategies. For instance, scenarios showing widespread fault instability may indicate the need to reduce injection rates, modify well placement, or implement pressure management strategies such as brine extraction. Conversely, scenarios with minimal or localized fault reactivation may be considered operationally safe, supporting continued injection under current conditions. This integrated approach ensures that fault stability considerations are embedded into the decision-making process for $CO_2$ storage operations, enhancing both safety and long-term containment integrity.

The PilotSTRATEGY project has received funding from the European Union's Horizon 2020 research and innovation programme under grant agreement No. 101022664

### 6.4.5.2 *Results from initial stress state condition*

The application of an integrated workflow—combining 1D and 2D geomechanical modelling, dynamic reservoir simulation, and multi-representation analysis—resulted in a set of key findings. This section presents the results of the 1D well models, used to define the inputs for the 2D modelling, and the corresponding 2D geomechanical results on the fault planes in their initial configuration.

#### 6.4.5.2.1 Data Acquisition and 1D Geomechanical Model Construction

This section presents an analysis of the 1D geomechanical well data to select the most reliable and representative parameters for this study. Key datasets, including pore pressure profiles and in-situ stress measurements are evaluated based on their quality, consistency, and applicability to fault stability assessment. This selection process ensures that the inputs used in the modeling accurately reflect the subsurface conditions, thereby enhancing the robustness of the fault stability analysis.

The following image Figure 6-26 presents a correlation between the wells located in the area of interest in Lopin, overlaid with the results from the 1D geomechanical models. The display includes key geomechanical curves such as pore pressure, vertical and horizontal stresses. Additionally, the tectonic stress regimes interpreted at each well location are shown, providing insight into the regional stress orientation and faulting style (normal, strike-slip, or reverse).

The well correlation across the Lopin area reveals a notable change in tectonic stress regime starting from the Keuper Formation. Above this formation, the stress regime is interpreted as strike-slip, while below it, the regime transitions to normal faulting. This shift is supported by the 1D geomechanical model outputs, which include stress magnitudes and orientations, and is consistent across multiple wells in the area.

This observation is critical for understanding fault behavior and stress evolution with depth, particularly in the context of $CO_2$ injection, where fault reactivation potential is strongly influenced by the prevailing stress regime.

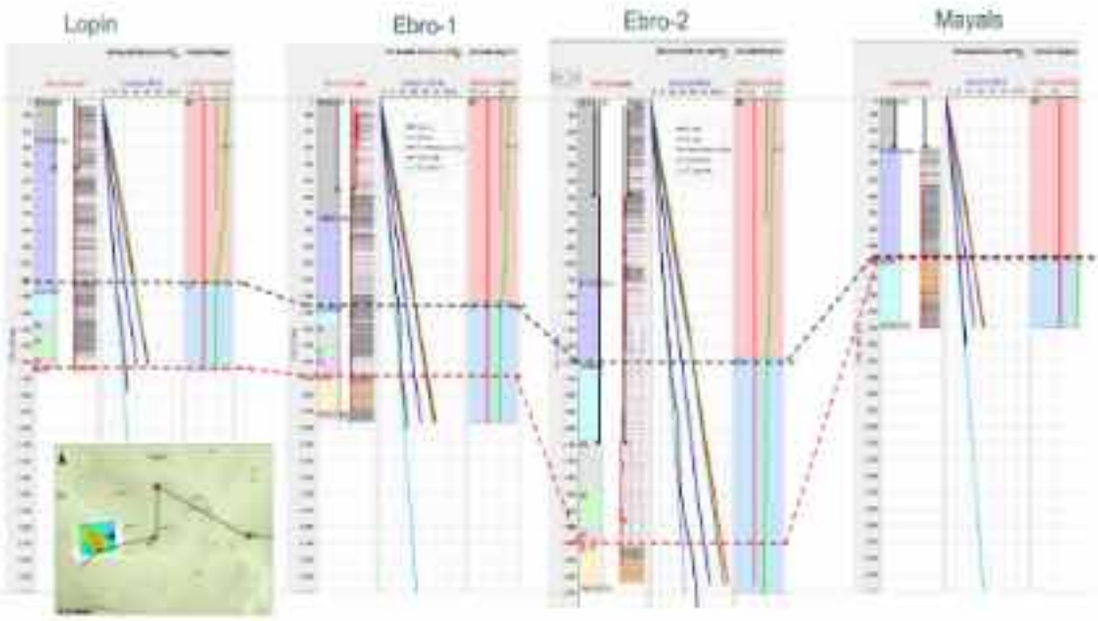


*Figure 6-26 Correlation between wells & tectonic stress regimes interpretation (geomechanical curves: pore pressure, vertical and horizontal stresses) located in the area of interest.*

The PilotSTRATEGY project has received funding from the European Union's Horizon 2020 research and innovation programme under grant agreement No. 101022664

Figure 6-27 focuses specifically on Lopin and Ebro-1, the two wells closest to the fault system under investigation. These wells are considered the most appropriate for the fault stability analysis, as they not only lie within the immediate vicinity of the study area but also clearly capture the transition in tectonic regime—from strike-slip to normal faulting—at the level of the Keuper Formation. In contrast, the other wells, due to their distance, already show substantial differences in stress and pore pressure profiles, making them less reliable for localized fault stability assessment.

Additionally, the data from these wells indicate that the reservoir is initially overpressured, a condition that significantly influences fault stability. Elevated pore pressure reduces the effective normal stress on fault planes, increasing the likelihood of fault reactivation under $CO_2$ injection scenarios.

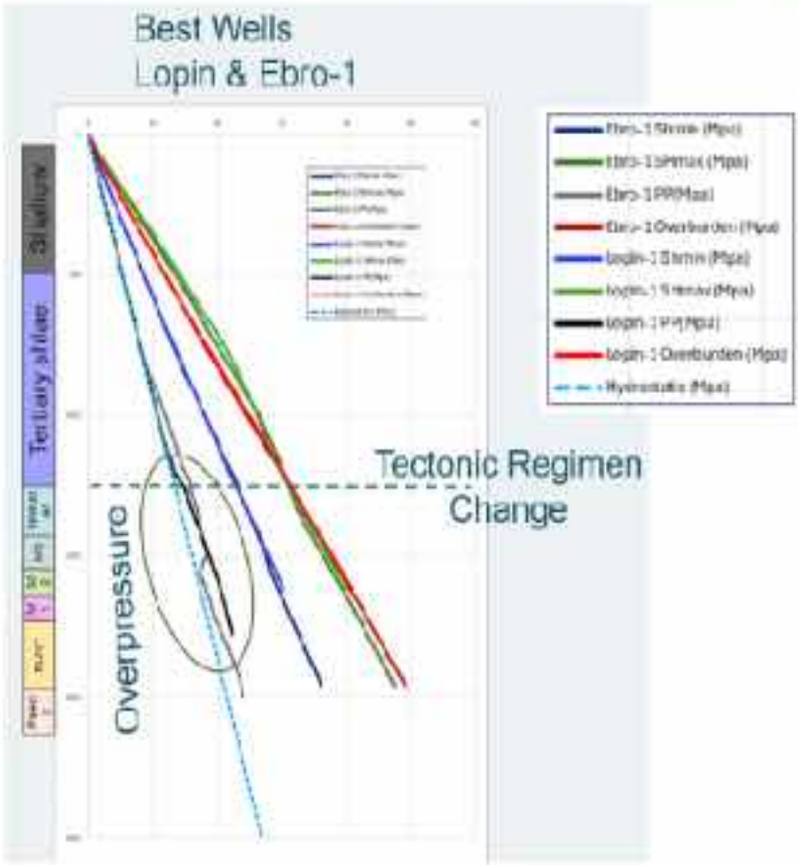


*Figure 6-27 Comparative analysis of all wells in the region.*

This transition into the tectonic regime is particularly important because all identified faults are located below the Keuper Formation, within the normal faulting regime. As a result, the fault stability analysis will be focused exclusively on this regime, which governs the mechanical behavior of the reservoir and surrounding formations at the depths of interest. By considering the normal faulting stress state, the study ensures that the evaluation of fault reactivation risk during $CO_2$ injection is both geologically consistent and technically robust.

Figure 6-28 presents a table summarizing the average values and gradients of pore pressure and stress for each geological formation. These values are calculated at the central depth point of each unit and include both the absolute magnitudes (MPa) and the vertical gradients (MPa/m). This dataset provides a consistent geomechanical framework for evaluating fault stability across the stratigraphic column.

The PilotSTRATEGY project has received funding from the European Union's Horizon 2020 research and innovation programme under grant agreement No. 101022664

All identified faults are located below the M3 Formation, indicating that the fault stability analysis should focus on the deeper stratigraphic intervals. These formations are characterized by a normal stress regime and an initially overpressured state, which significantly influences fault stability. Elevated pore pressure reduces the effective normal stress and lowers fault shear strength in accordance with the Mohr–Coulomb criterion, placing faults closer to failure prior to $CO_2$ injection. This condition increases sensitivity to additional pressure perturbations and must be considered when defining safe injection limits and assessing fault reactivation risk.

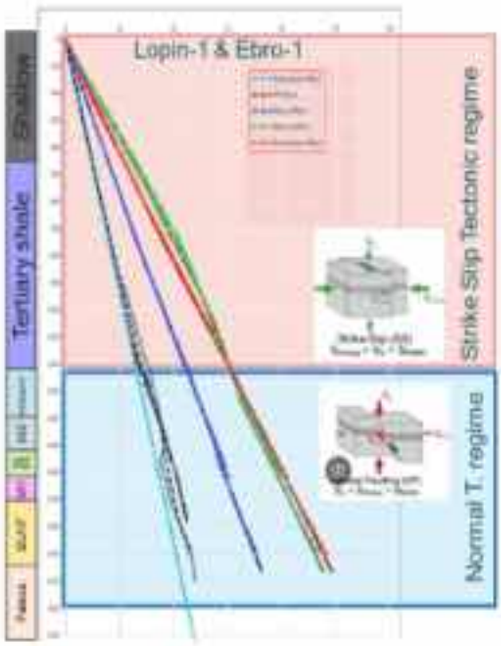


| Formation | Mid point (Average) m | Top (Average) m | PP (Average) kPa | kPa/m | Shmin (Average) kPa | kPa/m | SHmax (Average) kPa | kPa/m | Overburden (Average) kPa | kPa/m |
|---|---|---|---|---|---|---|---|---|---|---|
| Shallow | 0 | 0 | 0.00 | 0.01052 | 0.00 | 0.01017 | 0.00 | 0.02119 | 0.00 | 0.02183 |
| Tertiary Shale | 838.2 | 467 | 9.51 | 0.01137 | 14.62 | 0.01759 | 22.19 | 0.02649 | 20.77 | 0.02448 |
| Keuper | 1283 | 1222 | 15.01 | 0.01207 | 22.58 | 0.01829 | 31.54 | 0.02457 | 32.28 | 0.02540 |
| M3 | 1423 | 1382 | 17.02 | 0.01220 | 26.28 | 0.01886 | 36.89 | 0.02656 | 38.63 | 0.02693 |
| M2 | 1557 | 1483 | 18.52 | 0.01158 | 28.14 | 0.01842 | 37.48 | 0.02543 | 39.39 | 0.02613 |
| M1 | 1609 | 1572 | 19.28 | 0.01183 | 28.88 | 0.01848 | 38.50 | 0.02556 | 40.53 | 0.02578 |
| Buntsandstein | 1779 | 1647 | 20.84 | 0.01177 | 32.80 | 0.01992 | 43.29 | 0.02455 | 44.54 | 0.02533 |
| Paleozoic | 1900 | 1863 | 23.02 | 0.01236 | 30.39 | 0.01631 | 40.75 | 0.02186 | 46.44 | 0.02490 |

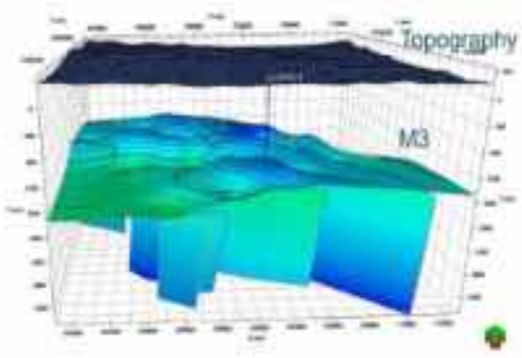


*Figure 6-28 Pp and stresses gradients versus depth and table summarizing the average values and gradients.*

### 6.4.5.2.2 Fault Stability Assessment Using Mohr-Coulomb Criterion

This section details the results of the Mohr's circle analyses depicting the initial in-situ stress state at various depths, derived from the data provided by the 1D geomechanical study.

Figure 6-29 presents a series of Mohr's circles constructed at multiple depths to illustrate the evolution of the stress state with depth, based on the stress and pore pressure data extracted from the geomechanical model. These circles are used to assess the proximity of the stress state to the failure envelope defined by the Mohr-Coulomb criterion.

The image illustrates that as depth increases; the size of the Mohr's circle also increases. However, the distance to the failure envelope line (failure criterion) likewise grows, indicating a greater margin of stability at greater depths.

The PilotSTRATEGY project has received funding from the European Union's Horizon 2020 research and innovation programme under grant agreement No. 101022664

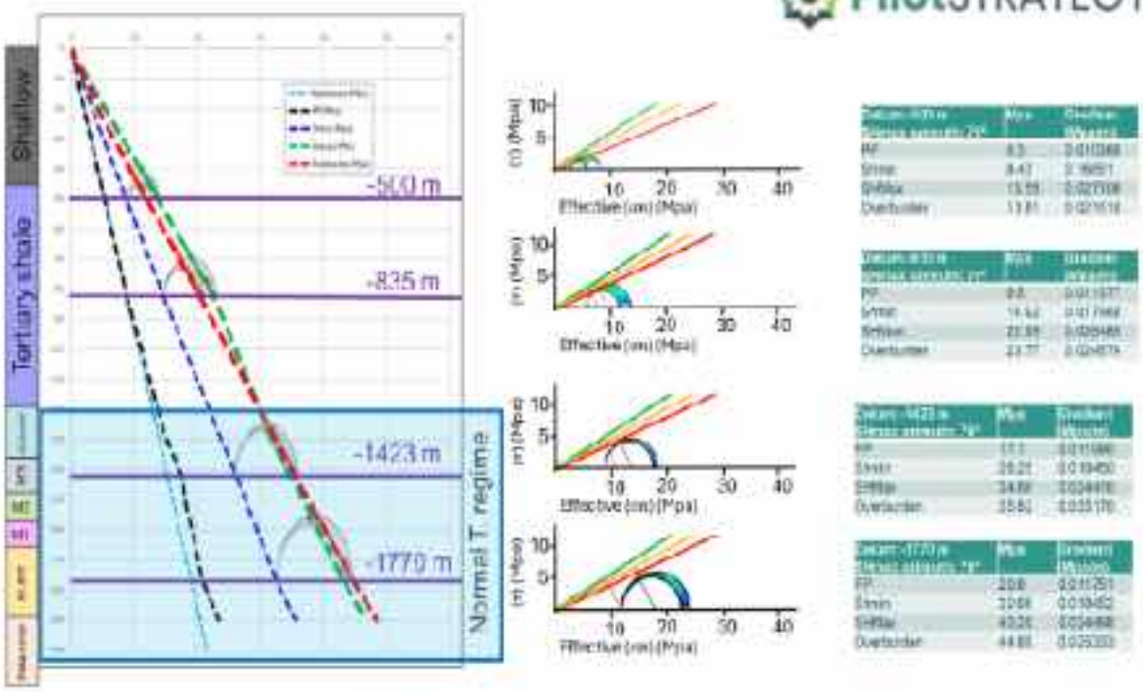


*Figure 6-29 Mohr's circles constructed at multiple depths.*

To evaluate fault stability sensitivity to the internal friction angle, a range of plausible values was considered due to limited direct calibration data. For each depth, the critical pore pressure increase (Δp_cri) required to cause fault failure was calculated for each friction angle, assuming zero cohesion (C=0) to represent cohesionless pre-existing faults.

In normal faulting regimes, typical friction angles range between 25° and 35°, reflecting the fault's shear resistance. Fresh or unaltered fault surfaces usually have friction angles from 30° to 35°, while fault zones with clay-rich gouge or alteration minerals have lower friction angles, often between 20° and 25°, due to reduced shear strength. Understanding these values is essential for applying the Mohr-Coulomb failure criterion to assess slip potential and fault reactivation risk. Therefore, to account for this uncertainty, all analyses will be performed using friction angles of 30°, 25°, and 20°. These values will be used to calculate the Mohr's circles and the Coulomb Failure Function (CFF), enabling a comprehensive evaluation of fault stability and slip potential under varying shear resistance conditions.

Table 6-7 presents the $\Delta P_{cri}$ associated with the previously shown Mohr's circles, calculated at various depths. It demonstrates that $\Delta P_{cri}$ increases with depth, indicating greater fault stability due to higher confining stresses. Lower friction angles substantially reduce $\Delta P_{cri}$, especially near the surface, revealing that faults with weaker shear strength are more susceptible to reactivation. Near-surface faults with low friction angles may be close to failure, while deeper faults require higher pressure increases to slip. This emphasizes the importance of considering friction angle variability and depth in fault stability assessments during $CO_2$ injection.

| Depth (m) | ϕ: 30° | ϕ: 25° | ϕ: 20° |
|---|---|---|---|
| -500 | $\Delta p_{crit}$:0.9 Mpa | $\Delta p_{cri}$:0.1 Mpa | $\Delta p_{cri}$:0 Mpa |
| -835 | $\Delta p_{cri}$:1.7 Mpa | $\Delta p_{cri}$:0.2 Mpa | $\Delta p_{cri}$:0 Mpa |

The PilotSTRATEGY project has received funding from the European Union's Horizon 2020 research and innovation programme under grant agreement No. 101022664

| | | | |
|---|---|---|---|
| -1423 (M3) | $\Delta p_{crit}$:4.4 Mpa | $\Delta p_{crit}$:2.7 Mpa | $\Delta p_{crit}$:0.2 Mpa |
| -1770 (Buntsandstein) | $\Delta p_{crit}$:6.5 Mpa | $\Delta p_{crit}$:4.3 Mpa | $\Delta p_{crit}$:1 Mpa |

*Table 6-7 Critical pore pressure increase associated with the Mohr circles*

For the purposes of this analysis, a depth of -1609 m has been adopted as the reference datum, corresponding to the entry into the Bunt reservoir in the Lopin reference well, which is also the $CO_2$ injection interval. This depth lies approximately midway within the normal stress regime and coincides with the onset of the identified faults. In practice, the specific choice of datum is not critical, as stresses and pore pressure are governed by their gradients and decompose consistently with depth along the fault plane regardless of whether the reference level is placed shallower or deeper. Nevertheless, using the reservoir entry provides a representative snapshot of the Mohr state prior to entering the reservoir, capturing the most critical condition; at greater depths, increasing normal stress would progressively increase the stability margin.

The figure below (Figure 6-30) depicts a Mohr-Coulomb failure analysis conducted at a depth of –1609 meters within the M1 Formation. It includes the Mohr's circle derived from the effective principal stresses at this depth, along with failure envelopes corresponding to internal friction angles of 30°, 25°, and 20 degrees, which represent the initial stress conditions. This reference depth and associated stress gradients will be used for all subsequent calculations to ensure a consistent and rigorous assessment of fault stability within a normal faulting regime during $CO_2$ injection operations.

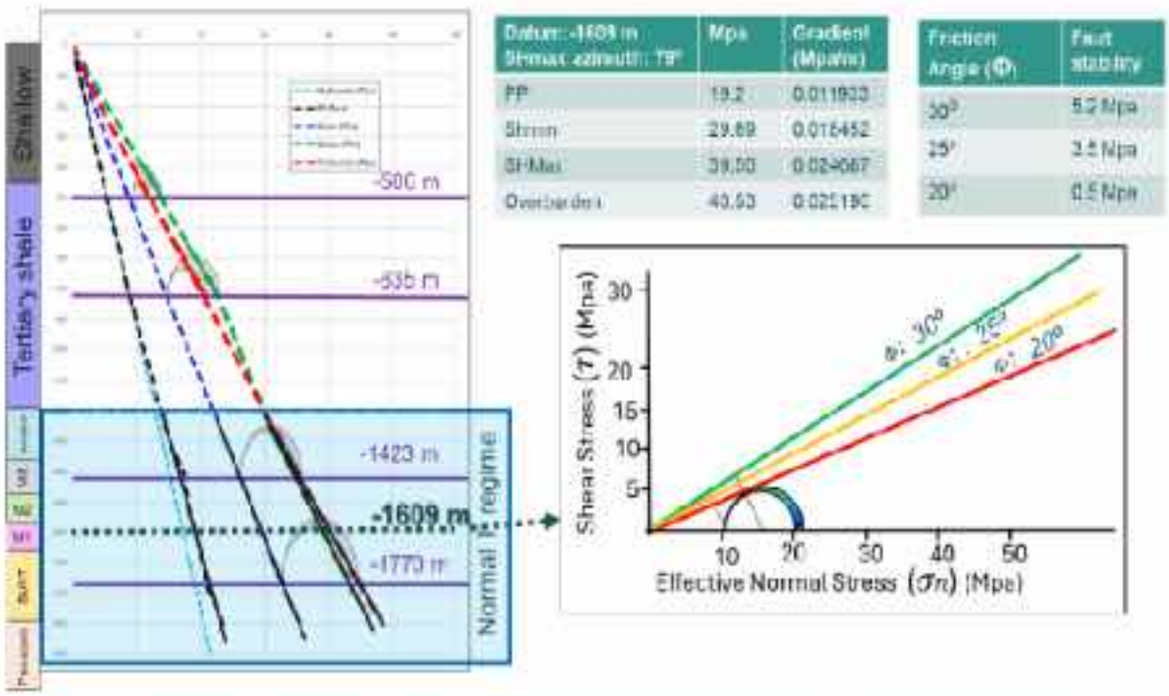


*Figure 6-30 Mohr-Coulomb failure analysis conducted at a depth of –1609 meters within the M1 Formation.*

The following Figure 6-31 presents the results of a 2D fault stability analysis conducted directly on the fault planes using Petrel, illustrating the initial state of stress at a reference depth of –1609 meters, which corresponds to the top of the M1 Formation. This analysis assumes a friction angle of 30° and incorporates vertical gradients of pore pressure, vertical stress, and horizontal stress to estimate the effective stress conditions along the fault surfaces as a function of depth. Additionally, the direction

The PilotSTRATEGY project has received funding from the European Union's Horizon 2020 research and innovation programme under grant agreement No. 101022664

of the maximum horizontal stress, set at 76°, is taken into account to ensure the accurate distribution of both normal and shear stress components across the fault plane, based on its dip and dip direction.

This precise alignment of stress is crucial for the 2D analysis, as it ensures that the fault stability is calculated correctly, facilitating an accurate evaluation of the potential for slip and reactivation under different stress conditions, particularly in overpressured environments. This methodology offers a more spatially resolved and depth-sensitive evaluation of fault stability, enabling the identification of specific fault segments that could be vulnerable to reactivation under current or changing stress states.

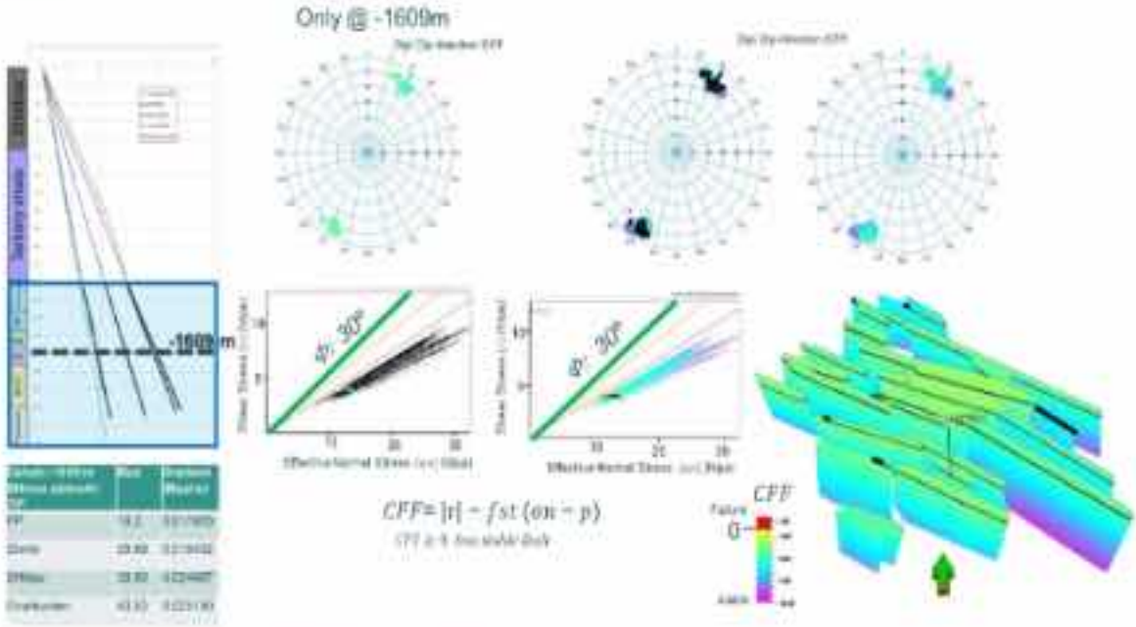


*Figure 6-31 2D Fault stability analysis performed on fault planes using Petrel.*

All computed points were plotted in a crossplot of effective normal stress versus shear stress, with the Mohr-Coulomb failure envelope superimposed to assess the proximity of each point to failure. This crossplot serves as an equivalent to the Mohr-Coulomb circle but is applied across the entire fault plane rather than at a single depth. In the left plot, the colored points represent the Mohr's circle at the specific depth of −1609 m, while the black points correspond to the rest of the fault's stress conditions. This distinction enables a focused assessment of the stress state at the datum compared to the overall fault planes. In the right plot, the entire fault plane is color-coded to visualize the distribution of the Coulomb Failure Function (CFF), with the datum highlighted in black.

In addition to the effective stress analysis, stereonet plots were used to visualize the spatial distribution of fault orientations and their Coulomb Failure Function (CFF) values. Each point, representing a fault plane pole with defined dip and dip direction (no strike), is color-coded by its CFF value. This enables the identification of orientation-dependent trends in fault stability, highlighting fault segments with higher CFF values that are closer to failure, and correlating them with specific dip ranges. By combining this stereonet analysis with the effective stress versus shear stress crossplot, a more comprehensive assessment of fault stability is achieved, considering both mechanical and geometric factors influencing reactivation potential.

On the fault plane, the Coulomb Failure Function (CFF) is represented in color, with the black line indicating the datum at −1609 meters. The analysis reveals that for a friction angle of 30°, no points

The PilotSTRATEGY project has received funding from the European Union's Horizon 2020 research and innovation programme under grant agreement No. 101022664

intersect the failure line, suggesting that under the given conditions, the fault remains stable and does not approach the failure criterion. Additionally, the absence of red regions, which correspond to areas where the CFF is positive and indicate instability according to the color scale, further confirms that there are no unstable areas along the fault at this friction angle.

Furthermore, the margin of safety increases with depth, as the effective normal stress becomes more dominant relative to shear stress. This depth-dependent stabilization is consistent with the increasing confining stress in deeper formations, which enhances fault resistance to slip.

However, the results vary significantly when different friction angles are applied. Figure 6-32 presents a comparative fault stability analysis using crossplots of effective normal stress versus shear stress, evaluated for three different friction angles: 30°, 25°, and 20°. Each point represents a location on the fault plane and is color-coded based on its Coulomb Failure Function (CFF) value.

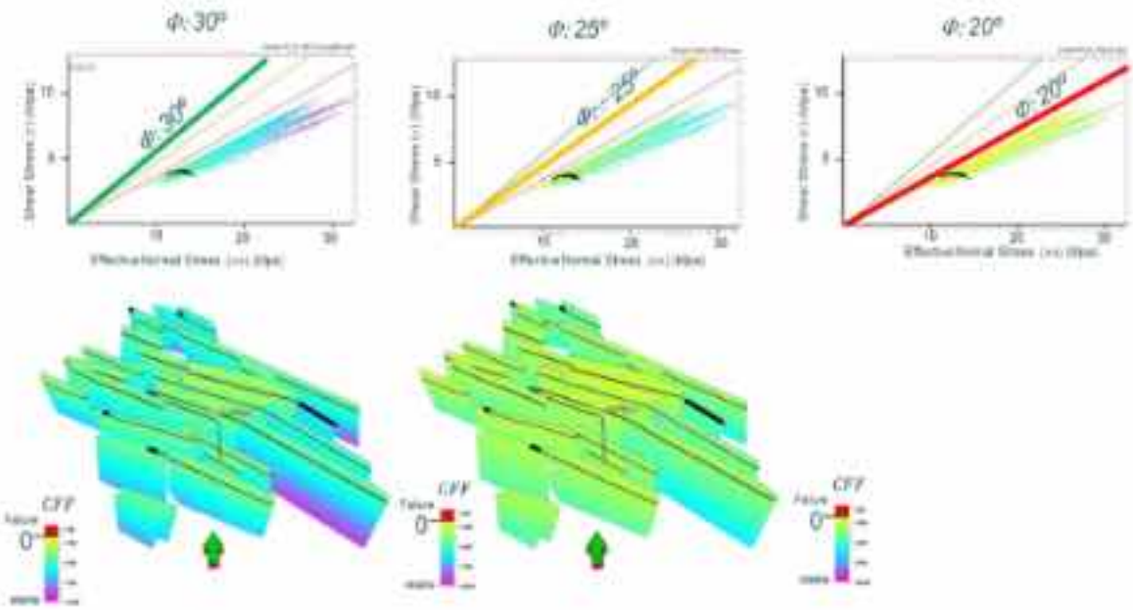


*Figure 6-32 Comparative fault stability analysis results evaluated for three different friction angles: 30°, 25°, and 20°.*

For a friction angle of 30°, all points on the fault plane remain well below the Mohr-Coulomb failure envelope, indicating stable conditions. However, when the friction angle is reduced to 25°, several points begin to move closer to the failure threshold. At a friction angle of 20°, a significant number of points lie very near the failure line, suggesting that the fault is approaching reactivation under the current stress and pore pressure conditions. These findings highlight the critical role of the friction angle in fault stability, with lower angles increasing the likelihood of fault reactivation and potential failure.

#### 6.4.5.2.3 Post-analysis metric

As described in the methodology section, fault stability was evaluated using several metrics, with the primary results coming from the slip tendency analysis. This approach offers an additional layer of insight, complementing the Mohr-Coulomb failure criterion and further confirming the fault's stability under the assumed conditions.

##### 5.3.4.2.3.1 Slip tendency analysis

The PilotSTRATEGY project has received funding from the European Union's Horizon 2020 research and innovation programme under grant agreement No. 101022664

Figure 6-33 presents the results of the **slip tendency analysis**, which evaluates fault plane stability based on initial in-situ stress conditions and a friction angle of 30°. The analysis was performed across all fault planes in the model, considering their orientation and inclination relative to the regional stress field. A fault is deemed unstable when its slip tendency exceeds the critical threshold of approximately 0.577 for a 30° friction angle.

The results show that no regions on the fault plane exceed this threshold, indicating that the fault remains stable under current stress and pore pressure conditions, with no indication of reactivation risk. This analysis provides a spatially resolved evaluation of fault stability, demonstrating the impact of fault geometry and stress orientation on the potential for reactivation.

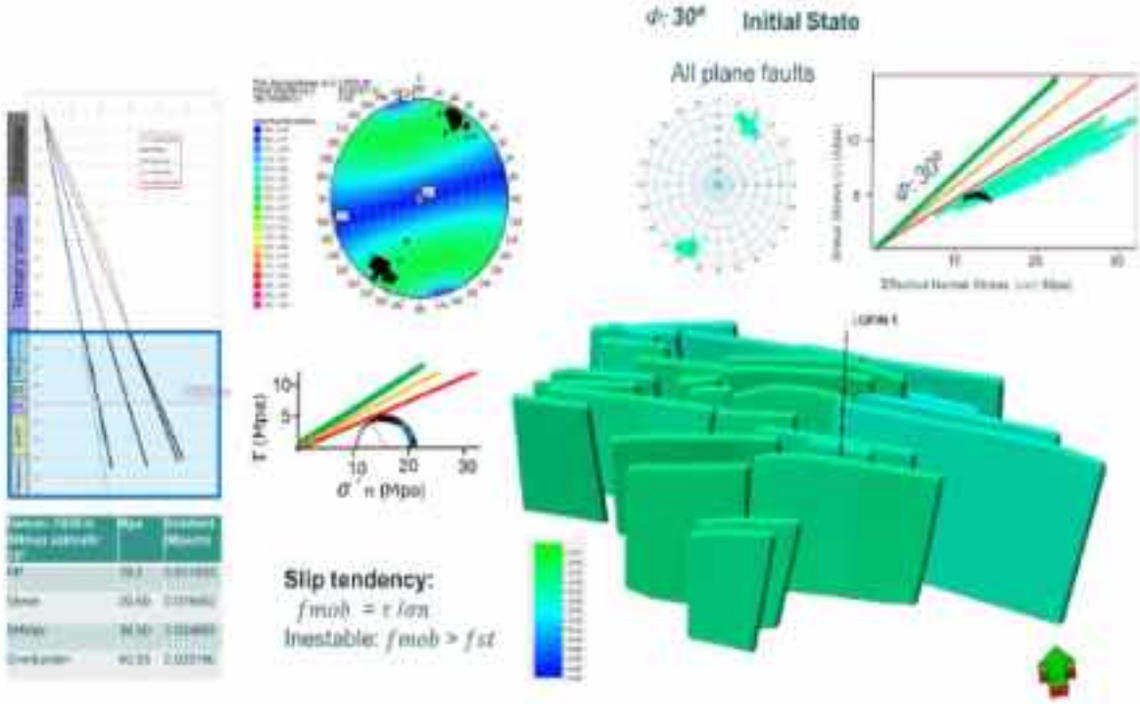


*Figure 6-33 slip tendency analysis on fault plane based on initial in-situ stress conditions and a friction angle of 30°.*

Figure 6-34 presents the results of the Slip Tendency analysis for three friction angles (ϕ = 30°, 25°, and 20°), calculated under the initial in-situ stress conditions, prior to any $CO_2$ injection or pore-pressure changes. The histograms show the distribution of Slip Tendency values for all evaluated points along the fault plane and are compared with their corresponding critical threshold, defined by the tangent of the friction angle.

The PilotSTRATEGY project has received funding from the European Union's Horizon 2020 research and innovation programme under grant agreement No. 101022664

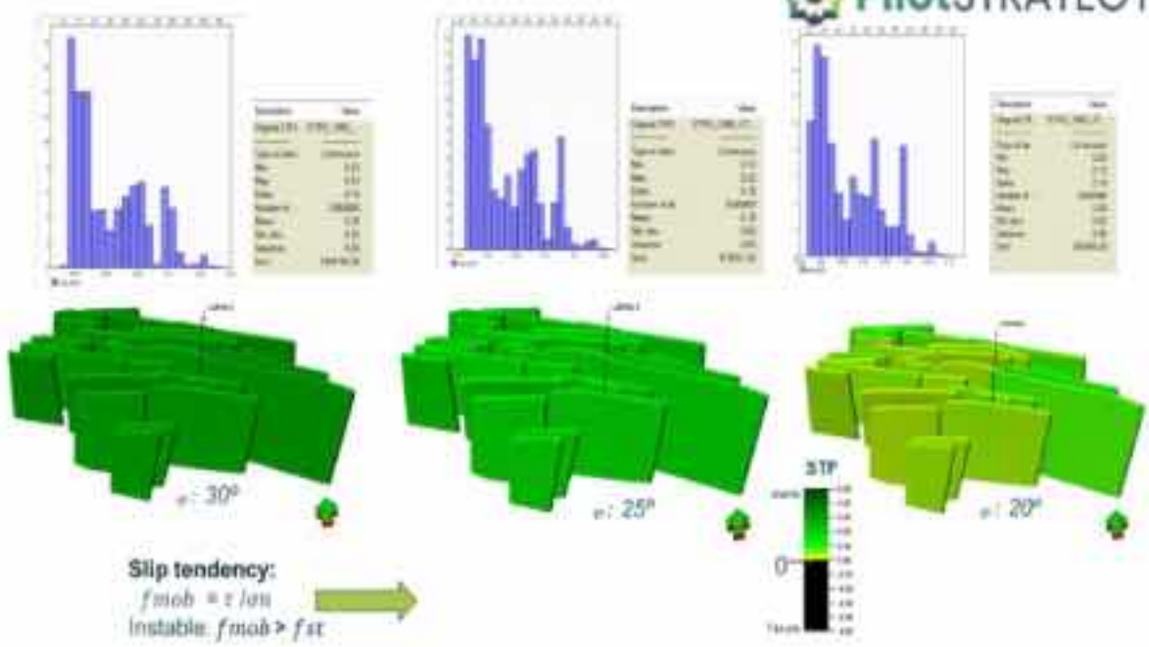


*Figure 6-34 results of the Slip Tendency analysis for three different friction angles: 30°, 25°, and 20°.*

Table 6-8 summarizes the minimum, mean, and maximum Slip Tendency values for each friction angle. In this analysis, Slip Tendency values approaching zero indicate increasingly unstable conditions, while higher values indicate greater stability. For all friction angles, the values remain below the critical threshold, indicating that the fault is stable under the current stress state. Nevertheless, a clear dependence on friction angles is observed. The ϕ = 30° case shows the highest Slip Tendency values and represents the most stable scenario. The ϕ = 25° case indicates intermediate stability, with lower values for some fault segments. The ϕ = 20° case presents the lowest Slip Tendency values, with a minimum of 0.02, highlighting localized segments that are close to a critically stressed state, although failure is not reached.

| Friction angle ϕ (°) | Slip Tendency min | Slip Tendency mean | Slip Tendency max | Stability implication |
|---|---|---|---|---|
| 30 | 0.23 | 0.28 | 0.33 | Most stable case; low slip tendency over the entire fault surface |
| 25 | 0.12 | 0.15 | 0.22 | Intermediate stability; some fault segments closer to instability |
| 20 | 0.02 | 0.12 | 0.05 | Most critical case; very low slip tendency values indicating proximity to failure in localized areas |

*Table 6-8 Summarizes the statistical distribution of slip tendency values in the initial stress state.*

Overall, the combined interpretation confirms that decreasing friction angle progressively reduces fault stability, identifying ϕ = 20° as the most critical configuration under initial conditions.

The PilotSTRATEGY project has received funding from the European Union's Horizon 2020 research and innovation programme under grant agreement No. 101022664

5.3.4.2.3.2 Slip Tolerance analysis

The following analysis applies **Slip Tolerance** as an alternative, friction-dependent metric to evaluate fault instability and reactivation potential under initial in-situ stress conditions, assuming a 30° friction angle.

The results are displayed directly on the fault planes, with each point color-coded according to their Slip Tolerance value. This color scale allows for a clear visual interpretation of stability conditions: black indicates values greater than 1, corresponding to unstable fault segments. In this case, no points exceed this threshold, meaning no black areas are present, and all evaluated fault segments remain within the stable range. A Mohr-Coulomb diagram complements the analysis by plotting effective normal versus shear stress, with the failure envelope overlaid, while stereonet and spatial plots further illustrate fault orientations and highlight areas that, although closer to critical conditions, remain stable under the current stress state. (Figure 6-35)

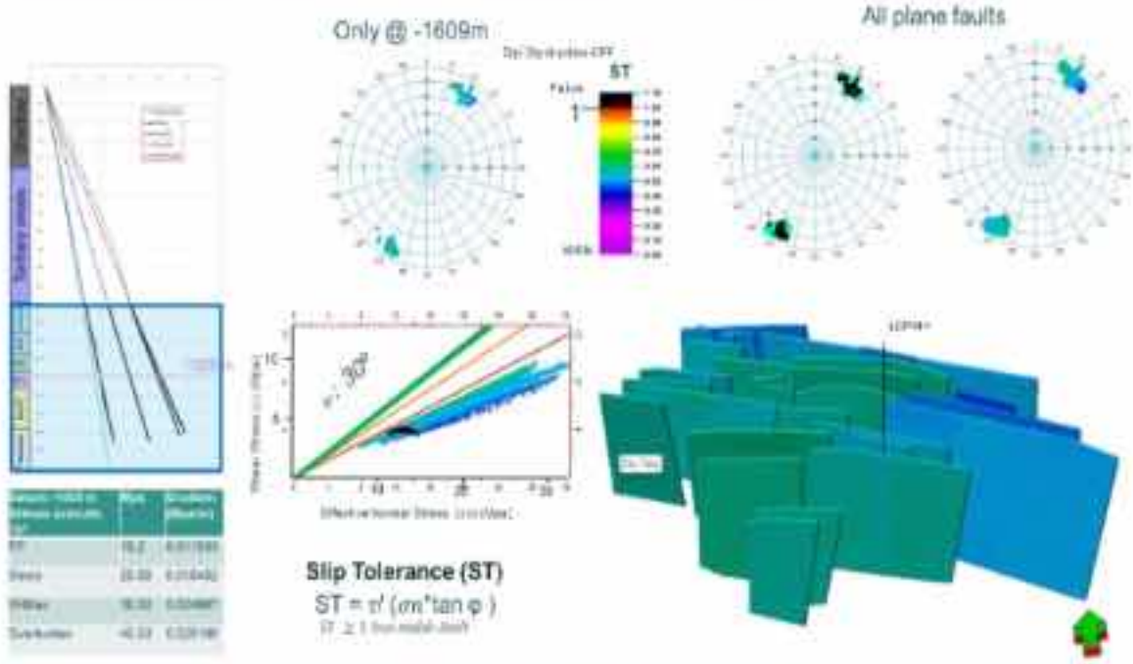


*Figure 6-35 Slip Tolerance analysis results under initial in-situ stress conditions, assuming a 30° friction angle.*

Figure 6-36 shows the results of the Slip Tolerance analysis computed under the initial stress state for three friction angles (ϕ = 30°, 25°, and 20°). Slip Tolerance is used as an indicator of fault reactivation potential, where a value of 1 represents the instability threshold, and values below 1 indicate stable conditions. The 2D results, visualized through stereonet plots, histograms, Mohr–Coulomb diagrams, and fault-plane projections, provide a comprehensive view of the fault mechanical response.

The PilotSTRATEGY project has received funding from the European Union's Horizon 2020 research and innovation programme under grant agreement No. 101022664

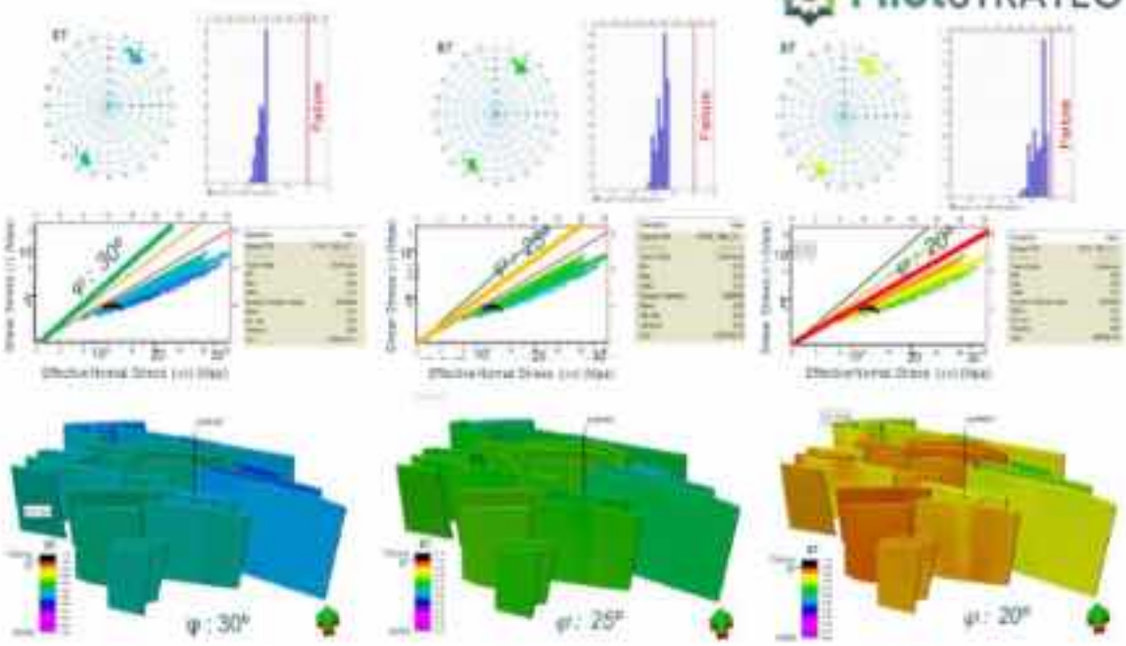


*Figure 6-36 Slip Tolerance analysis Results Comparison, calculated under the initial stress state for three different friction angles: 30°, 25°, and 20°.*

Table 6-9 summarizes the minimum, mean, and maximum Slip Tolerance values calculated over the entire fault surface. The lowest values generally correspond to shallow fault segments, where stability is more critical, whereas the highest values are associated with deeper fault portions, which are more stable. None of the analyzed cases exceed the instability threshold; however, the $\phi = 20°$ scenario shows values approaching Slip Tolerance = 1, particularly at shallow depths, indicating a reduced safety margin and highlighting the sensitivity of fault stability to frictional strength.

| Friction angle ϕ (°) | Slip Tolerance min | Slip Tolerance mean | Slip Tolerance max | Stability implication |
|---|---|---|---|---|
| 30 | 0.42 | 0.55 | 0.59 | Most stable case; large tolerance to slip over most fault segments |
| 25 | 0.52 | 0.68 | 0.74 | Intermediate stability; some shallow segments closer to failure |
| 20 | 0.66 | 0.87 | 0.94 | Most critical case; limited slip tolerance, especially at shallow depths |

*Table 6-9 Summarizes the statistical distribution of slip tolerance values in the initial stress state.*

#### 5.3.4.2.3.3 Critical Pore Pressure Change analysis

The next parameter used to assess fault stability is the **Critical Pore Pressure Change Parameter**, which quantifies the increase in pore pressure required to bring a fault to failure under current stress conditions. This metric complements the Slip Tolerance analysis by providing a direct measure of how much fluid pressure would need to rise to induce fault reactivation.

As in the previous cases, the following Figure 6-37 Critical Pore Pressure Change (CPPC) for initial stress state and friction angle of 30° to 25° and 20°. illustrates the variation of the Critical Pore Pressure Change (CPPC) Parameter as

The PilotSTRATEGY project has received funding from the European Union's Horizon 2020 research and innovation programme under grant agreement No. 101022664

the friction angle is reduced from 30° to 25° and 20°. The results are visualized using a combination of stereonet plots, histograms, Mohr-Coulomb diagrams, and 2D fault plane projections, with CPPC values represented through a color scale.

Table 6-10 reports the minimum, mean, and maximum CPPC values calculated for all fault points. Minimum CPPC values correspond to the shallowest portions of the faults, whereas maximum values occur at greater depths as a result of increasing stresses with depth. This stress increase leads to higher effective normal stress and therefore provides a larger stability margin in deeper fault segments.

| Friction angle ϕ (°) | CPCP min (MPa) | CPCP P50/Mean (MPa) | CPCP max (MPa) | Sensitivity to ΔP | Risk implication |
|---|---|---|---|---|---|
| 30 | 3.23 | 8.68 | 13.10 | Lower | Larger safety margin |
| 25 | 2.17 | 6.21 | 12.97 | Moderate | Transitional; possible reactivation |
| 20 | 0.63 | 2.47 | 8.44 | Higher | Most critical; small ΔP may reactivate |

*Table 6-10 Summarizes the statistical distribution of CPPC values in the initial stress state.*

However, to complement these results, the following Table 6-11 includes the 1D CPPC values, which provide a direct quantitative comparison of the critical pressure increase ($\Delta p_i cri_i$) or CPPC required to induce failure at a reference depth at = −1770 m (Buntsandstein reservoir)

| Depth (m) | φ: 30° | φ: 25° | φ: 20° |
|---|---|---|---|
| -1770 (Buntsandstein) | $\Delta p_{cri}$:6.5 Mpa | $\Delta p_{cri}$:4.3 Mpa | $\Delta p_{cri}$:1 Mpa |

*Table 6-11 1D CPPC ($\Delta p_i cri_i$) values at −1770 m depth for the three friction angle scenarios.*

The analysis shows that as the friction angle decreases, the fault system becomes more critical, requiring smaller pore pressure increases to reach failure. However, this criticality generally decreases with depth, indicating that deeper fault planes tend to be more stable under the same stress regime. At a friction angle of 20°, the system approaches a highly critical state, although this represents a conservative scenario. These results highlight the sensitivity of fault stability to changes in shear strength and underscore the importance of frictional properties in assessing reactivation potential.

The PilotSTRATEGY project has received funding from the European Union's Horizon 2020 research and innovation programme under grant agreement No. 101022664

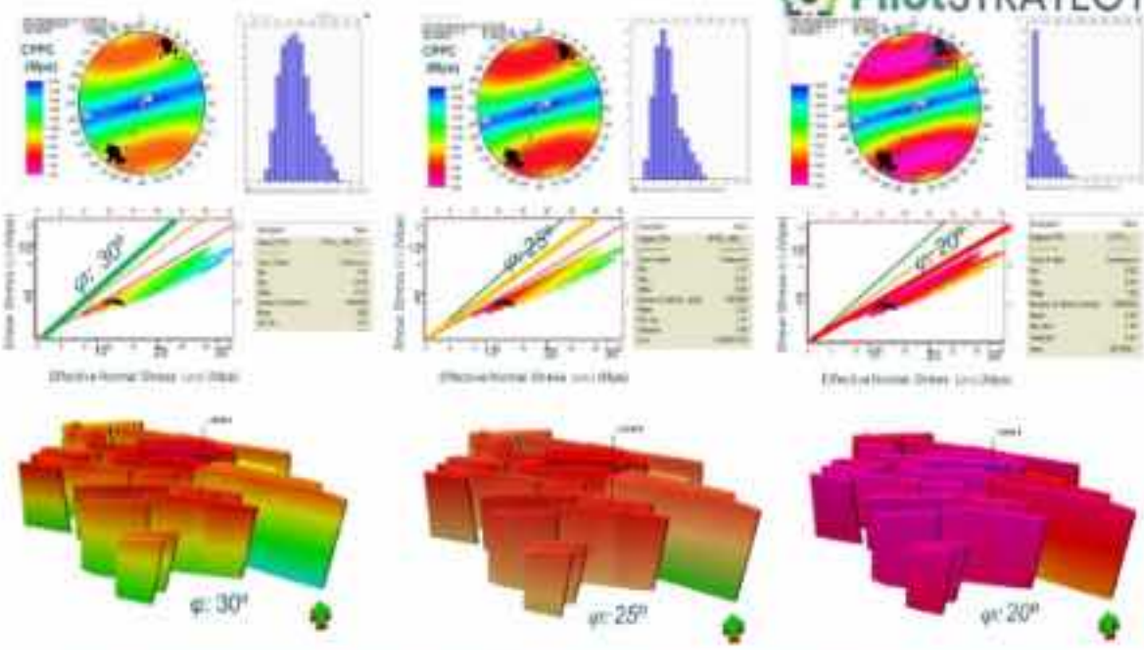





*Figure 6-37 Critical Pore Pressure Change (CPPC) for initial stress state and friction angle of 30° to 25° and 20°.*

#### 6.4.5.2.4 Conclusions initial stress state.

All parameters used to assess fault stability under the current initial stress state—Slip Tendency, Slip Tolerance, and Critical Pore Pressure Change (CPPC)—yield similar results and lead to consistent conclusions. Although each represents a different metric and approach to evaluating fault behavior, they all highlight comparable fault orientations as being closer to failure. This alignment strengthens the robustness and credibility of the geomechanical interpretation, supporting a coherent understanding of fault stability under present stress conditions.

The analysis also underscores the significant influence of the friction angle on fault stability. As the friction angle decreases, the fault system becomes increasingly susceptible to failure. Even under the most favorable condition—a friction angle of 30°—the safety margin is limited to approximately 5.2 MPa. In contrast, under the most conservative scenario—a friction angle of 20°—the system approaches a highly critical state, with a safety margin of only about 0.5 MPa. This narrow margin of stability may be attributed to the reservoir already being overpressured, which reduces the effective normal stress acting on fault planes and increases the likelihood of reactivation.

It is important to emphasize that the reported safety margin values—5.2 MPa for a friction angle of 30° and 0.5 MPa for 20°—are strictly applicable at the reference depth (datum) of –1609 m, corresponding to the top of the LOPIN formation. These figures may not accurately reflect the conditions within the reservoir interval, where stress states and pore pressure levels can vary considerably. Therefore, a dedicated analysis targeting fault segments situated within the reservoir is recommended to obtain a more representative assessment of fault stability.

To refine the fault stability assessment, the analysis was repeated focusing exclusively on the reservoir interval, where pore pressure increase was explicitly estimated through dynamic simulation. This localized evaluation offers a more realistic view of the actual safety margins under injection conditions. The Critical Pore Pressure Change (CPPC) was filtered to include only the fault segments intersecting the M1 and Buntsandstein units, providing a reservoir-specific threshold for fault reactivation. In this case, the results—shown in Figure 6-38—indicate a minimum CPPC of 4.28 MPa,

The PilotSTRATEGY project has received funding from the European Union's Horizon 2020 research and innovation programme under grant agreement No. 101022664

a maximum of 11.25 MPa, and a mean value of 6.7 MPa. This average value can be considered a representative threshold for the reservoir under a friction angle of 30°, which corresponds to the most favorable shear strength scenario.

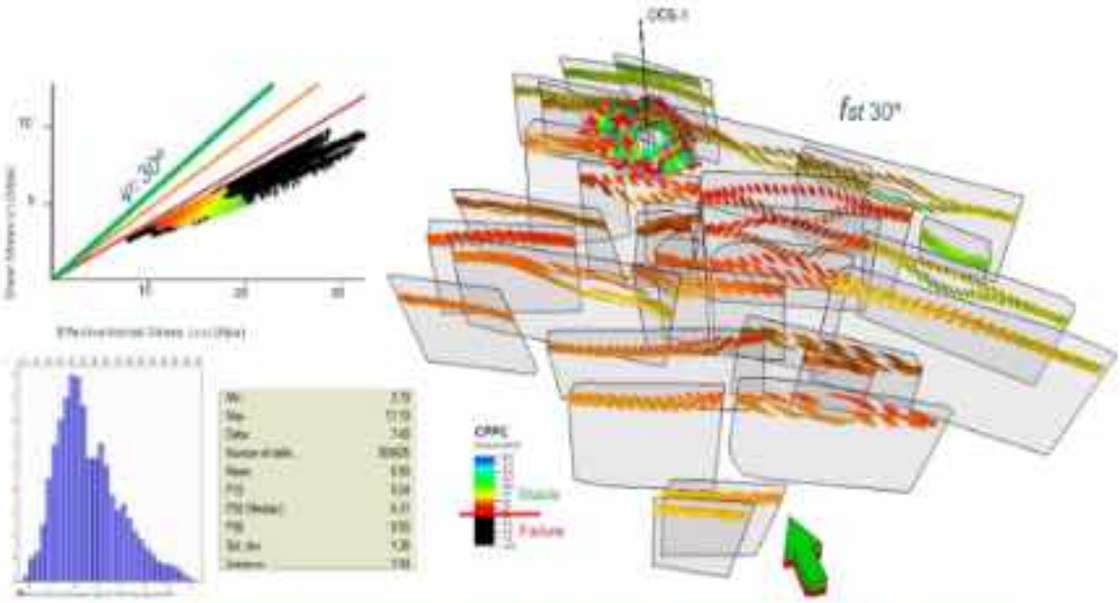


*Figure 6-38 Critical pore pressure changes in the M1 and Buntsandstein for case 30° friction angle.*

To better understand the sensitivity of fault behavior to shear strength, the same analysis was extended to less favorable scenarios. For a friction angle of 25°, the CPPC values decrease, ranging from 2.54 to 9.15 MPa, with a mean of 4.75 MPa. Under the most conservative condition, with a friction angle of 20°, the CPPC drops further, ranging from 0.71 to 6.20 MPa and averaging 3.49 MPa.

The following Figure 6-39 presents a comparative view of the CPPC distributions for the three friction angle scenarios, highlighting how fault stability thresholds evolve with decreasing shear strength.

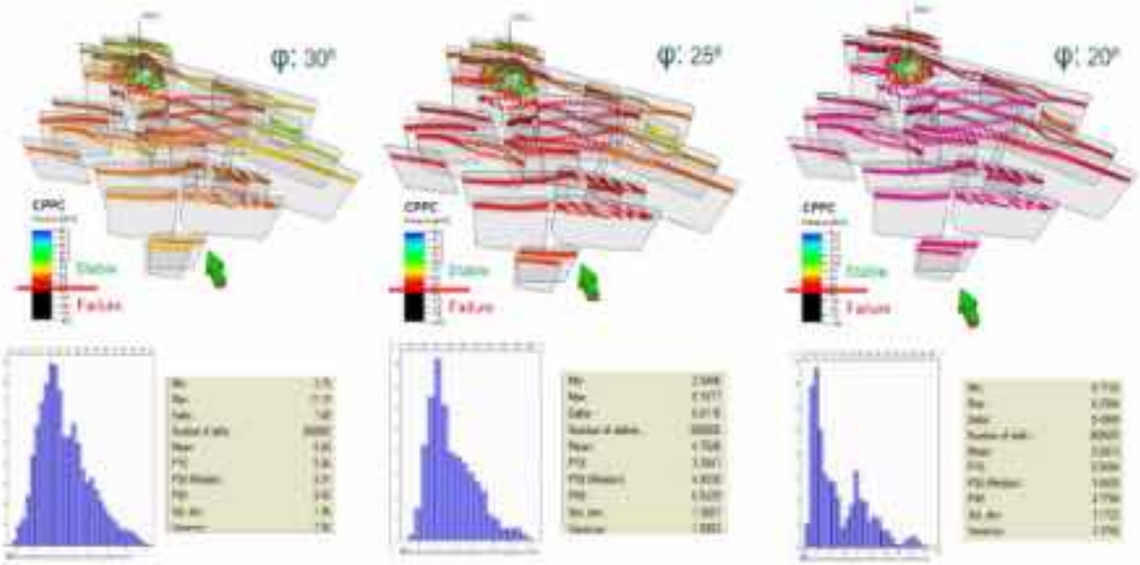


*Figure 6-39 Critical pore pressure change in the M1 and Buntsandstein per friction angle 30°, 25° and 20°.*

Figure 6-40, presented as a comparative histogram, together with Table 6-12, summarizes the reservoir-focused CPPC analysis for the different friction angle scenarios. The histogram compares the

The PilotSTRATEGY project has received funding from the European Union's Horizon 2020 research and innovation programme under grant agreement No. 101022664

CPPC distributions for fault segments intersecting the M1 and Buntsandstein units, where pore-pressure changes were explicitly derived from dynamic simulation. The comparison shows a systematic shift of the CPPC distributions toward lower values as friction angle decreases, reflecting progressively reduced fault stability within the reservoir interval. The statistics reported in Table 6-12 provide the quantitative bounds for this trend, confirming that lower friction angles consistently reduce the pressure increase required to reach fault reactivation. Overall, the combined interpretation highlights the strong sensitivity of reservoir fault stability to frictional variability, especially under conditions close to critical stress.

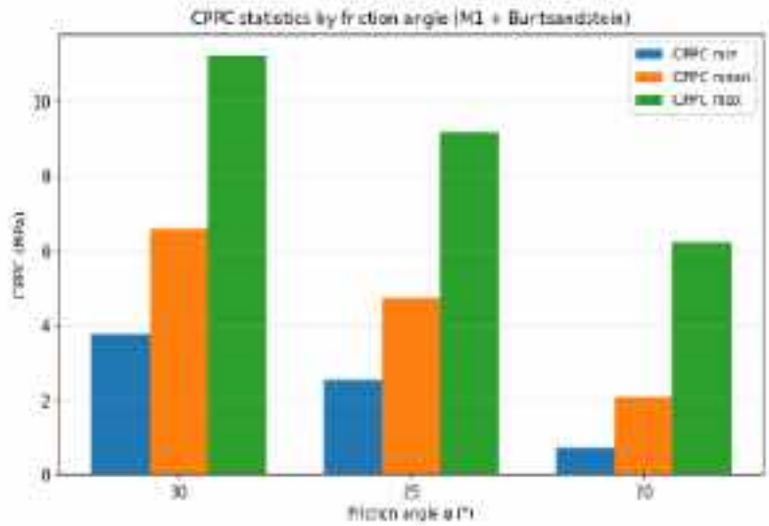


*Figure 6-40 Comparative histogram of the CPPC distributions for friction angles of 30°, 25°, and 20°.*

| Friction angle ϕ (°) | CPPC min (MPa) | CPPC mean (MPa) | CPPC max (MPa) | Stability implication |
|---|---|---|---|---|
| 3.79 | 3.79 | 6.56 | 11.25 | Representative stability threshold for reservoir conditions |
| 25 | 2.54 | 4.75 | 9.15 | Reduced stability under moderate friction decrease |
| 20 | 0.71 | 2.08 | 6.20 | Most critical scenario, high reactivation susceptibility |

*Table 6-12 Summary of CPPC statistics for reservoir fault segments under different friction angle scenarios*

### 6.4.5.3 Peak of Injection Condition or EOI.

After evaluating fault stability under initial stress conditions, the analysis was expanded to account for pore pressure increases resulting from $CO_2$ injection. A one-way coupling approach was used, integrating pressure outputs from dynamic reservoir simulations into a 2D fault plane model. This allowed for a detailed, cell-by-cell assessment of how pressure changes affect each fault segment, offering a more accurate representation of subsurface conditions.

The methodology was applied to multiple reservoir scenarios, covering P90, P50, and P10 permeability cases and different injection setups (CCS-1, LOCD-1, and both). Pressure data at peak injection (30 years) were used to evaluate fault response under varying geological and operational conditions. By comparing pressure buildup across the different permeability realizations and injection

The PilotSTRATEGY project has received funding from the European Union's Horizon 2020 research and innovation programme under grant agreement No. 101022664

configurations, the analysis also addresses the uncertainty associated with fault stability predictions, identifying how variations in pressure increase may affect the likelihood of fault reactivation.

Prior to applying the fault reactivation methodology, it is crucial to thoroughly interpret the results of the dynamic reservoir simulation. This analysis provides insight into the maximum pressure increase and its spatial distribution, allowing us to determine how much of the injected $CO_2$ reaches the fault system. Understanding which faults are most affected by the injection is essential for accurately assessing the potential for reactivation. This step ensures that the evaluation is based on realistic reservoir behaviour and enhances the reliability of the fault stability analysis.

Figure 6-41 illustrates the results for the P50 permeability scenario with a single $CO_2$ injection well (CCS-1) at peak injection time (30 years). The left panel shows the spatial distribution of pore pressure increase across the reservoir, highlighting the injection zone and surrounding buildup. The center panel projects this pressure onto the fault planes, revealing how much is transmitted to the faults. The right panel filters the data to the area used for fault stability assessment, focusing on regions where pressure changes are most critical.

In this case, the reservoir reaches a maximum pressure increase of 8.35 MPa, while the fault plane receives approximately 5.83 MPa (maximum pressure, close to the injection point). This difference underscores the attenuation of pressure during propagation and highlights the importance of evaluating transmission specifically along fault structures.

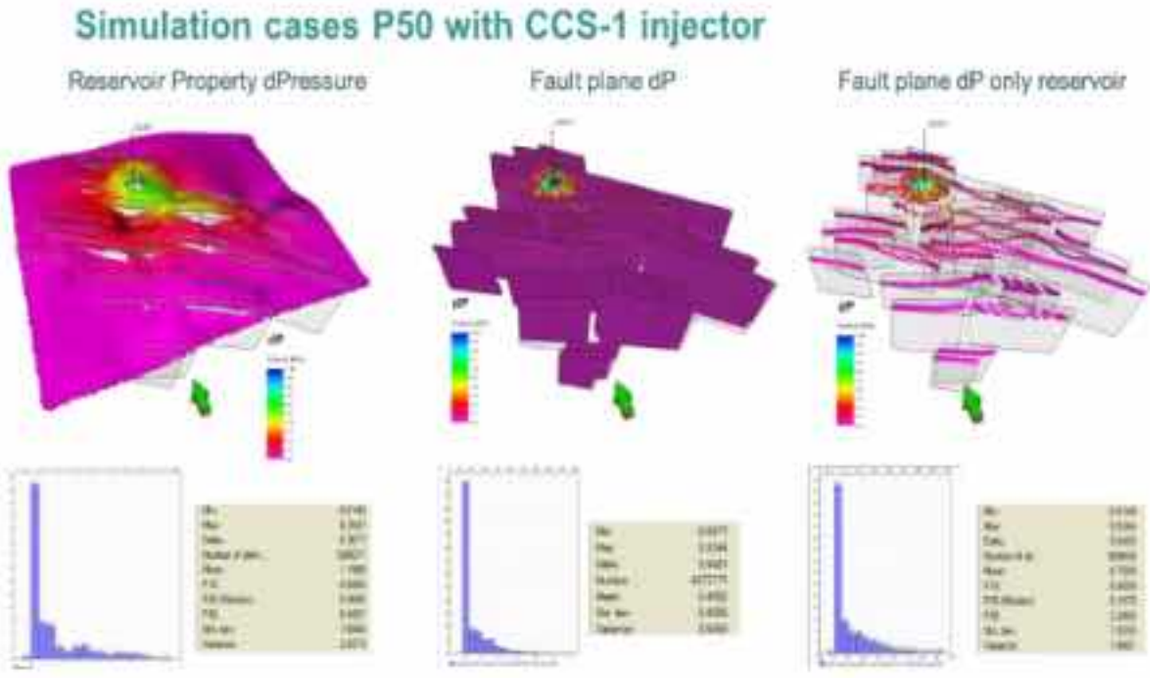


*Figure 6-41 results of the dynamic simulation case P50, illustrating the spatial distribution of pressure increase both across the reservoir and along the fault plane for each scenario.*

The following Figure 6-42 shows the pore pressure increase results for the P10 permeability case, evaluated at the peak of injection after 30 years. It compares three dynamic simulation cases: Case 1 with injector CCS-1, Case 2 with injector LOCD-1, and Case 3 with both injectors operating simultaneously. Although all scenarios exhibit similar pressure ranges (from approximately −0.025 MPa to just above 9 MPa), the spatial distribution of the pressure perturbation differs significantly, as reflected in the corresponding histograms. The mean pressure increase is 1.19 MPa for Case 1, 0.84

The PilotSTRATEGY project has received funding from the European Union's Horizon 2020 research and innovation programme under grant agreement No. 101022664

MPa for Case 2, and 2.14 MPa for Case 3, indicating a substantial increase in reservoir pressure when both injectors are active. In terms of maximum pressure, Case 1 reaches 8.52 MPa, Case 2 reaches 9.04 MPa, and Case 3 reaches 9.11 MPa. While the differences in peak values are not large, the results clearly show that LOCD-1 contributes more significantly to pressure buildup than CCS-1. This suggests that the location or connectivity of LOCD-1 leads to more concentrated pressure accumulation, which may have stronger implications for fault stability in its vicinity—especially under low-permeability conditions.

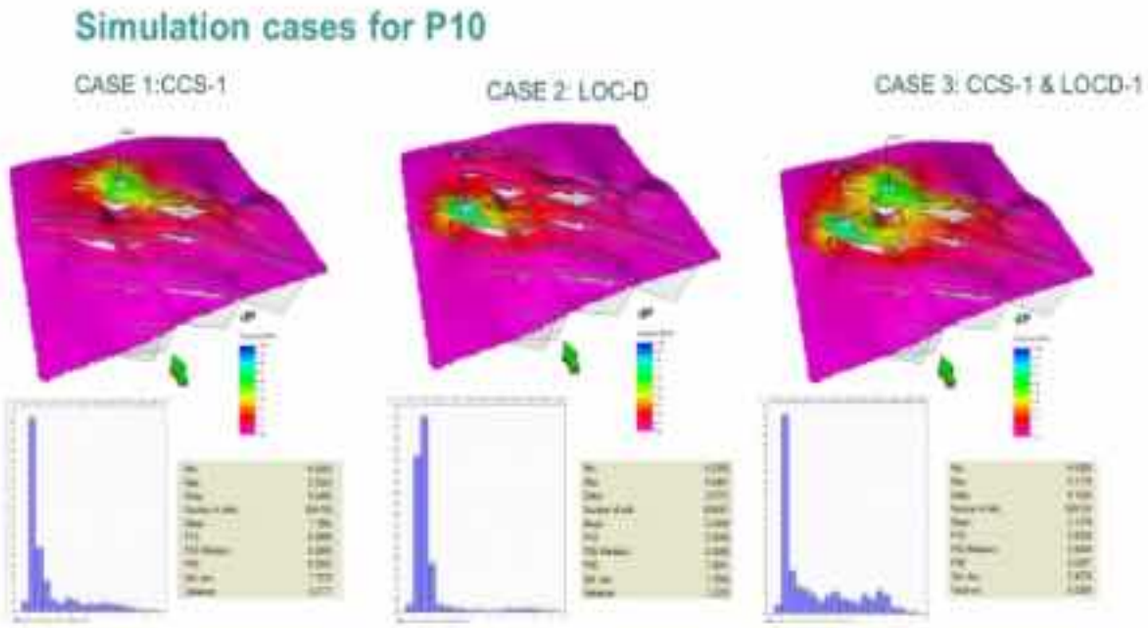


*Figure 6-42 Delta Pressure (top reservoir in 2D and histogram of DP values in the reservoir) comparison for P10 simulation scenario and different wells configuration.*

To better understand how pressure affects fault stability, this analysis focuses on the pressure increase measured directly along fault planes, rather than the general reservoir pressure distribution. Figure 6-43 captures only the pressure that effectively reaches the faults. In the P10 permeability case, the maximum pressure increase on faults is 5.71 MPa for Case 1 (injector CCS-1), 8.04 MPa for Case 2 (injector LOCD-1), and 8.18 MPa for Case 3 (both injectors), (maximum pressure, close to the injection point). Although the differences between Cases 2 and 3 are relatively small, the results clearly show that LOCD-1 generates a stronger pressure impact on faults than CCS-1, and that the maximum value in the dual-injector scenario is primarily driven by LOCD-1. This highlights the importance of injector location and connectivity when assessing fault reactivation risk under low-permeability conditions.

The PilotSTRATEGY project has received funding from the European Union's Horizon 2020 research and innovation programme under grant agreement No. 101022664

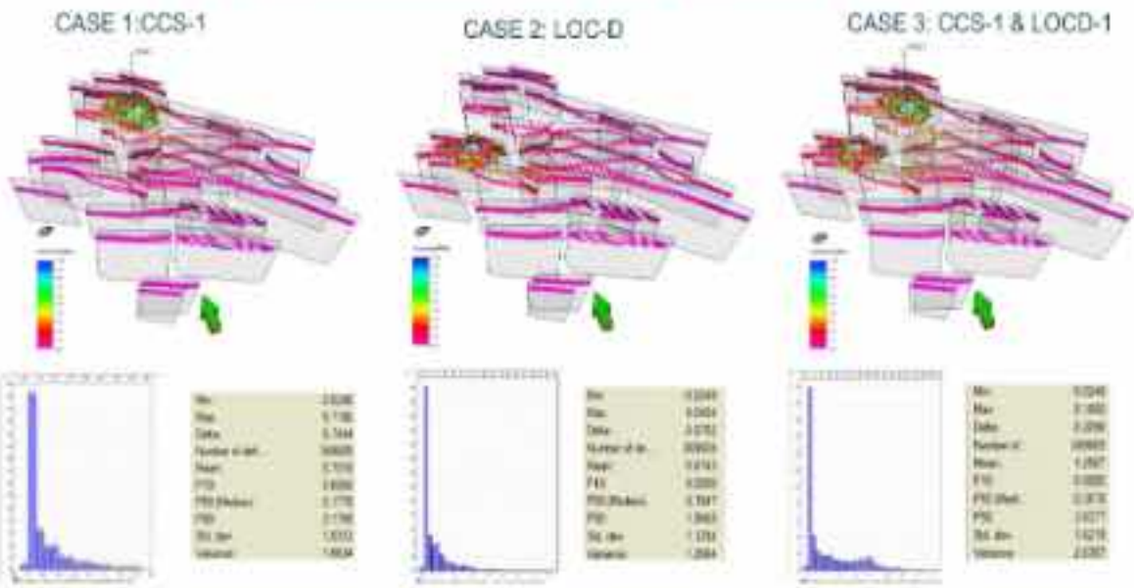


*Figure 6-43 Delta pressures that reach the fault planes for P10 and different injector configuration.*

As with the P10 permeability realization, the P50 case was evaluated under three injection configurations: CCS-1 alone (Case 1), LOC-D alone (Case 2), and both injectors operating simultaneously (Case 3) (Figure 6-44). When considering the full reservoir pressure field, the maximum pressure values are very similar across the three scenarios—ranging from 8.35 MPa to 8.93 MPa—while the spatial distribution of the pressure perturbation varies significantly. These differences are clearly reflected in the corresponding histograms, which show distinct pressure distribution profiles for each case. The mean pressure increase is 1.19 MPa in Case 1, 1.01 MPa in Case 2, and 2.13 MPa in Case 3, confirming that simultaneous injection leads to a broader and more intense pressurization of the reservoir.

However, when focusing specifically on the pressure component projected onto the fault plane, notable differences emerge (Figure 6-45). In particular, Case 1 shows a significantly lower maximum projected pressure (5.83 MPa) compared to the full-field maximum, indicating that the fault is less impacted under this configuration. Similar reductions are observed in the mean projected pressures, which are consistently lower than the reservoir-wide means: 0.72 MPa, 0.72 MPa, and 1.26 MPa for Cases 1, 2, and 3, respectively.

The PilotSTRATEGY project has received funding from the European Union's Horizon 2020 research and innovation programme under grant agreement No. 101022664

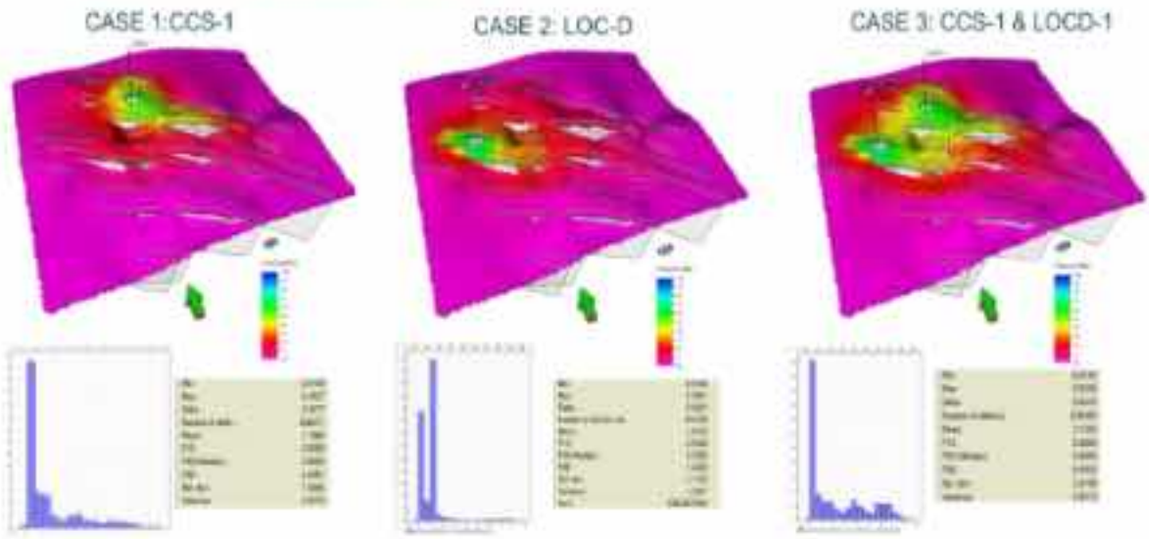


*Figure 6-44 Spatial variability into the reservoir and statistical distribution of delta pressure for P50 and different injector configuration.*

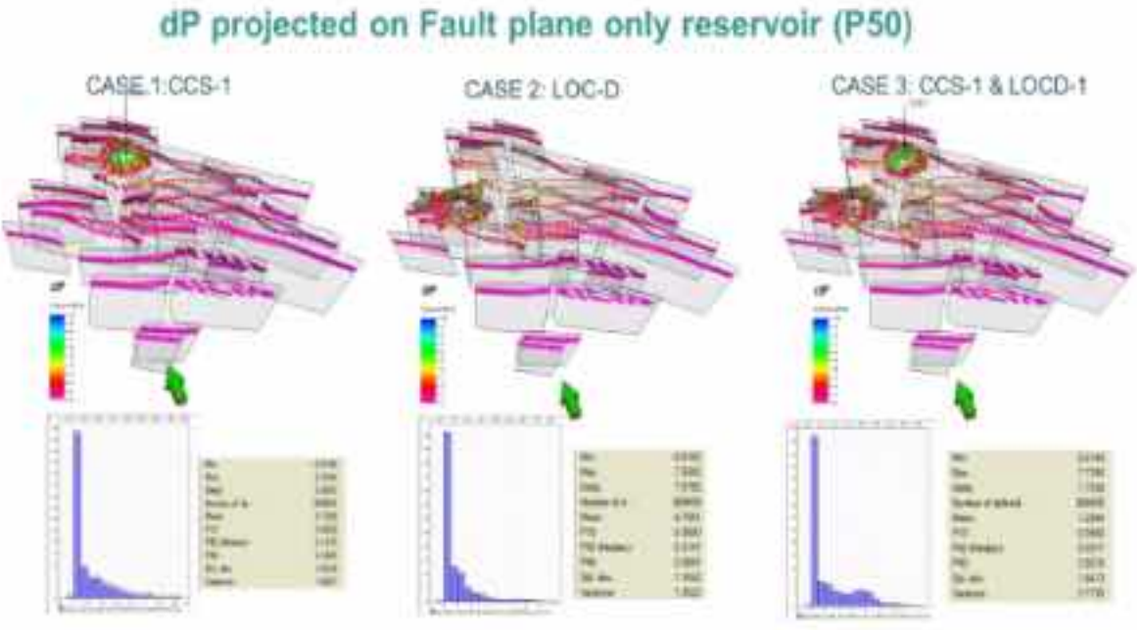


*Figure 6-45 distribution of delta pressure (P50) across the fault plane for each injection configuration.*

In addition, the P90 permeability realization was evaluated under the same three injection scenarios. Maximum pressure increases across the reservoir reached 7.84 MPa, 8.93 MPa, and 9.09 MPa, respectively, reflecting the overall pressure response within the reservoir volume. (Figure 6-46)

When pressure is projected onto the fault plane (maximum pressure, close to the injection point), a noticeable reduction is observed—particularly in Case 1. The maximum fault-related pressure increases were 4.94 MPa, 7.09 MPa, and 7.83 MPa for Cases 1, 2, and 3, respectively (Figure 6-47).

The PilotSTRATEGY project has received funding from the European Union's Horizon 2020 research and innovation programme under grant agreement No. 101022664

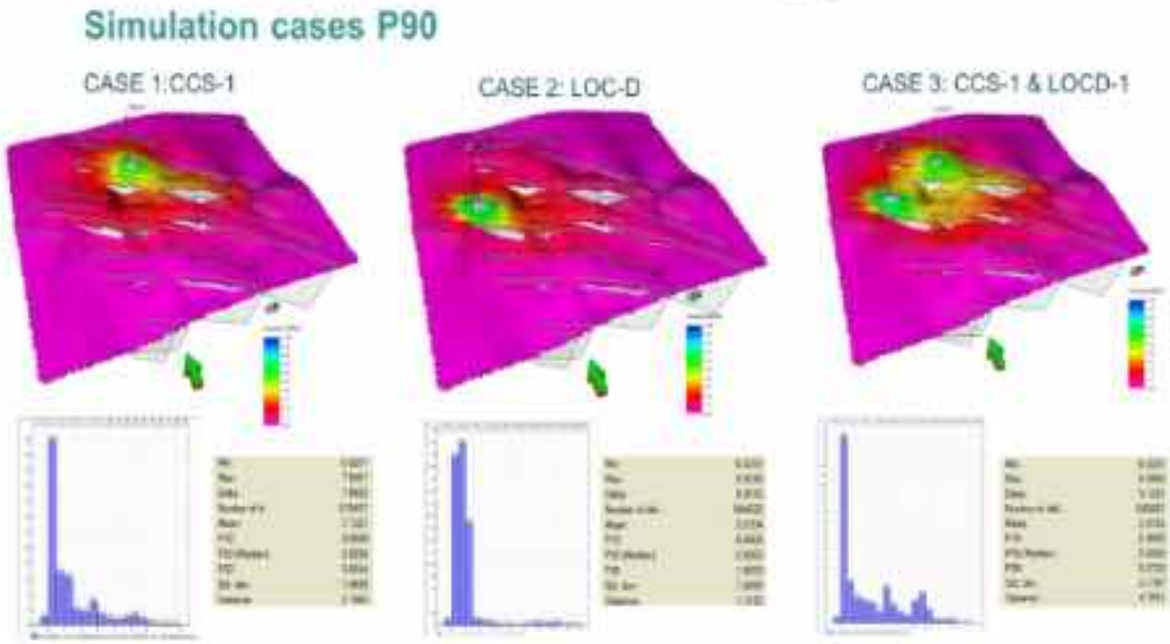


*Figure 6-46 Delta pressure distribution into the reservoir for P90 and different injector configuration.*

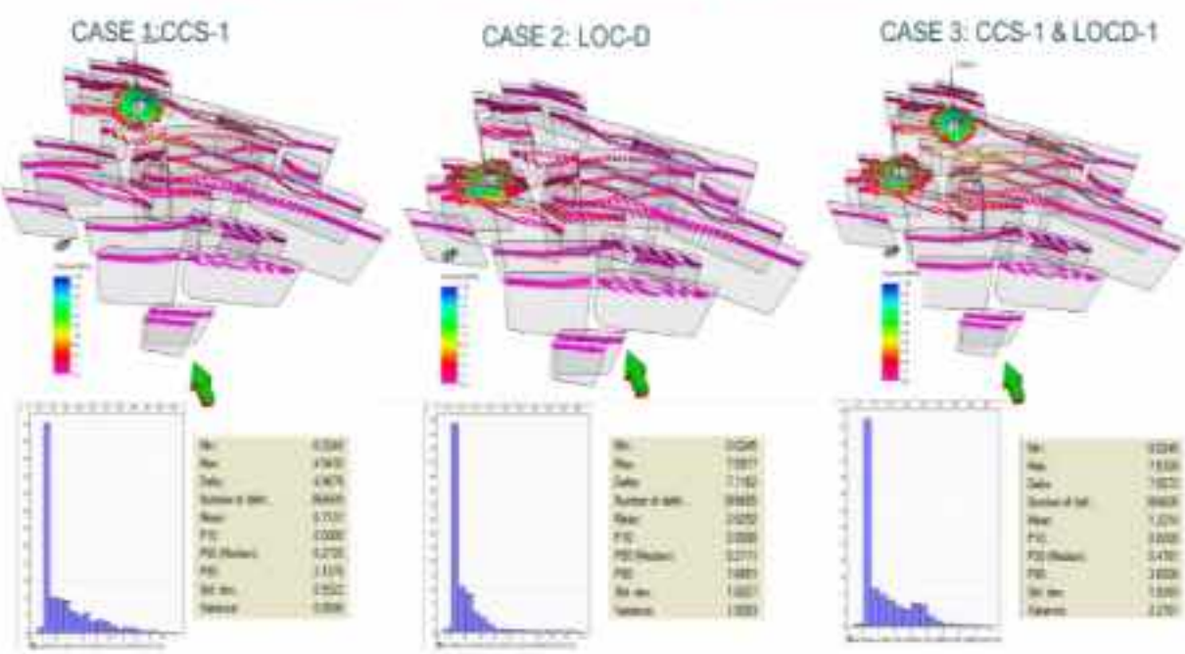


*Figure 6-47 Delta pressure distribution projected on the fault plain for P90 and different injector configuration.*

Table 6-13 integrates all permeability realizations and injection configurations to provide a clear and concise comparison of ΔP values across the full reservoir domain and the pressures transmitted to the fault planes.

The PilotSTRATEGY project has received funding from the European Union's Horizon 2020 research and innovation programme under grant agreement No. 101022664

| Permeability | Case | Injector configuration | ΔP max Reservoir (MPa) | ΔP mean Reservoir (MPa) | ΔP max Fault (MPa) | ΔP mean Fault (MPa) |
|---|---|---|---|---|---|---|
| P10 | Case 1 | CCS-1 | 6.52 | 1.19 | 5.71 | 0.7 |
| | Case 2 | LOCD-1 | 9.04 | 0.84 | 8.04 | 0.67 |
| | Case 3 | CCS-1 + LOCD-1 | 9.11 | 2.14 | 8.18 | 1.25 |
| P50 | Case 1 | CCS-1 | 6.35 | 1.19 | 5.83 | 0.72 |
| | Case 2 | LOCD-1 | 6.85 | 1.01 | 7.56 | 0.72 |
| | Case 3 | CCS-1 + LOCD-1 | 6.93 | 2.13 | 7.73 | 1.28 |
| P90 | Case 1 | CCS-1 | 7.84 | 1.31 | 4.94 | 1.13 |
| | Case 2 | LOCD-1 | 6.93 | 0.83 | 7.09 | 0.83 |
| | Case 3 | CCS-1 + LOCD-1 | 9.09 | 2.01 | 7.83 | 2.13 |

*Table 6-13 Reservoir and Fault ΔP Comparison*

This comparative analysis of $CO_2$ injection scenarios across P10, P50, and P90 permeability cases demonstrates how reservoir properties and injection strategy influence pressure evolution and fault stability. Lower permeability (P10) results in more localized and intense pressure buildup, limiting dissipation and increasing fault pressurization risk. In all cases, dual-well injection (Case 3) leads to the highest mean pressure increases and broader plume spread, while LOCD-1 (Case 2) consistently shows a stronger impact on fault pressurization than CCS-1 (Case 1), likely due to its location or connectivity.

Importantly, the pressure projected onto fault planes is consistently lower than the maximum values observed in the full 3D reservoir field. This difference is most pronounced in Case 1 across all permeability scenarios, indicating that CCS-1 has a more limited impact on fault pressurization. However, in Cases 2 and 3, the pressure reaching the faults is significantly higher, especially in the P10 scenario, where values exceed 8 MPa. These findings underscore the importance of evaluating fault-specific pressure behavior separately from general reservoir dynamics, as the spatial distribution and connectivity of injectors can lead to localized pressure concentrations that are not evident from reservoir-wide averages.

Overall, the analysis confirms that both reservoir permeability and injection configuration play a critical role in determining pressure evolution and fault stability. Under less favorable conditions (low permeability and dual injection), the risk of fault reactivation increases, highlighting the need for careful injector placement and pressure monitoring in $CO_2$ storage operations.

#### 6.4.5.4 *Fault Stability Assessment Based on Critical Pore Pressure Change (CPPC)*

This section investigates the evolution of the Critical Pore Pressure Change (CPPC) resulting from $CO_2$ injection across all evaluated scenarios, with the objective of identifying fault segments susceptible to injection-induced reactivation. The assessment is conducted at the end of the 30-year injection period, immediately prior to injection shut-in, when pore pressure reaches its maximum level, representing the most critical condition for fault stability analysis.

CPPC is first computed under pre-injection stress conditions, defining the pore pressure increase required to bring each fault segment to failure. The injection-induced pore pressure increase (ΔP) is then extracted from flow simulations for each injection configuration. The reduction in stability

The PilotSTRATEGY project has received funding from the European Union's Horizon 2020 research and innovation programme under grant agreement No. 101022664

associated with pressure buildup is quantified by subtracting ΔP from the initial CPPC, yielding an effective CPPC that represents the remaining pressure margin to fault reactivation, assuming a constant regional stress tensor:

$$CPPC_{effective} = CPPC_{initial} - \Delta P$$

Fault reactivation potential is evaluated by directly comparing ΔP along the fault plane with the initial CPPC. Fault segments for which CPPC $_{effective} < 0$ are classified as critically stressed and prone to slip, whereas CPPC $_{effective} \geq 0$ indicates mechanically stable conditions under the evaluated assumptions, with positive values quantifying the remaining stability margin.

This methodology provides an efficient and conservative first-order screening of fault sensitivity across scenarios, enabling the identification of potentially unstable fault segments under peak pore pressure conditions without recalculating the full stress field.

#### 5.3.4.4.1 Results of all evaluated scenarios.

This part of the report presents the results derived from the complete set of evaluated scenarios, encompassing the full range of permeability cases (P10, P50, and P90), injection configurations (CCS-1, LOCD-1, and dual-injector), and fault friction angles (30°, 25°, and 20°). The combination of these parameters results in a total of 27 scenarios analyzed, allowing a systematic assessment of uncertainty associated with reservoir properties, injection strategy, and fault frictional behavior, and providing a robust basis for evaluating variability in pressure evolution and fault reactivation potential. For the sake of clarity, exhaustive results with an intermediate fault friction angle of 25° are presented in Appendix 7.3.3. Results for these cases are summarized together with the other cases in the following sections.

##### 5.3.4.4.1.1 CCS-1 location cases.

This subsection presents all scenarios corresponding to the P10 permeability realization, including the different injector configurations and fault friction angle combinations

In the **P10 permeability case with injector CCS-1**, the maximum pressure increase in the reservoir grid reaches 8.52 MPa, while the pressure transmitted to the fault plane is approximately 5.71 MPa. Based on the final CPPC value, and assuming a friction angle of 30°, the fault remains within the safety margin, although very close to the failure threshold. Only the areas with negative CPPC values—represented in black—indicate mechanical failure. These appear as isolated zones enclosed by a black doted polygon, highlighting localized regions where fault slip is likely to occur.

Figure 6-48 CPPC after injection (P10) for case 1(CCS-1) and friction angle of 30°. presents the results for this specific case, focusing on the reservoir zone within formations B1 and Buntsandstein. The image on the left shows the initial CPPC, calculated under pre-injection stress conditions assuming a friction angle of 30°. The central image displays the pore pressure increase (ΔP) corresponding to the P10 scenario for injector CCS-1, as obtained from the dynamic reservoir simulation. The image on the right shows the change in CPPC after injection, calculated by subtracting the pressure increase from the initial CPPC. This sequence clearly illustrates the evolution of fault stability due to $CO_2$ injection. In this case, only a few points along fault Falla008 exceed the failure threshold, with CPPC values dropping below zero. These localized zones of potential mechanical failure are highlighted in black and enclosed by a contour, indicating areas where fault slip may occur. The minimum CPPC value

The PilotSTRATEGY project has received funding from the European Union's Horizon 2020 research and innovation programme under grant agreement No. 101022664

reaches −0.56 MPa, confirming that while most of the fault remains stable, isolated critical points exist. These are also visible in the histogram as values falling below zero.

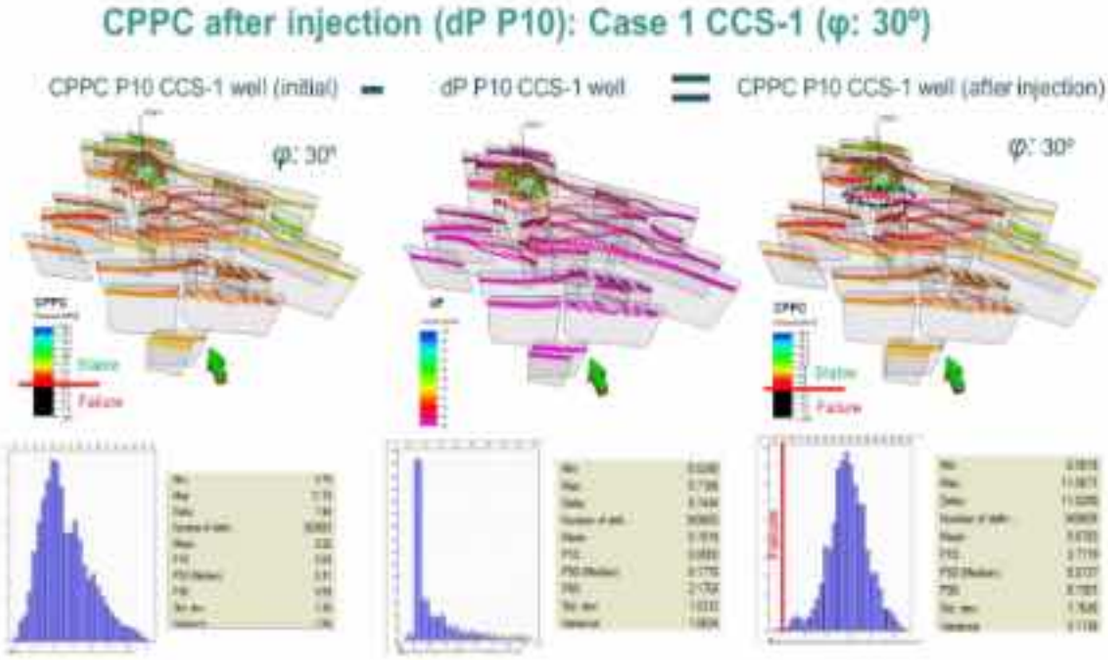


*Figure 6-48 CPPC after injection (P10) for case 1(CCS-1) and friction angle of 30°.*

The next Figure 7-6 shows the same analysis but assuming a friction angle of 25°, while keeping the same P10 scenario and injector CCS-1. As in the previous case, the sequence includes the initial CPPC, the pore pressure increase (ΔP), and the resulting change in CPPC after injection.

In this case, a greater number of faults exhibit points with CPPC values below zero, indicating potential instability. Specifically, faults Falla008, Falla009, and Falla005—the ones closest to the injector—show several points exceeding the failure threshold. These critical areas are also visible in the histogram, where a larger portion of values fall into the negative range. The minimum CPPC value reaches −2.17 MPa, confirming a more widespread reduction in fault stability compared to the case with a 30° friction angle, and highlighting the importance of mechanical parameter selection in fault reactivation assessments.

The PilotSTRATEGY project has received funding from the European Union's Horizon 2020 research and innovation programme under grant agreement No. 101022664

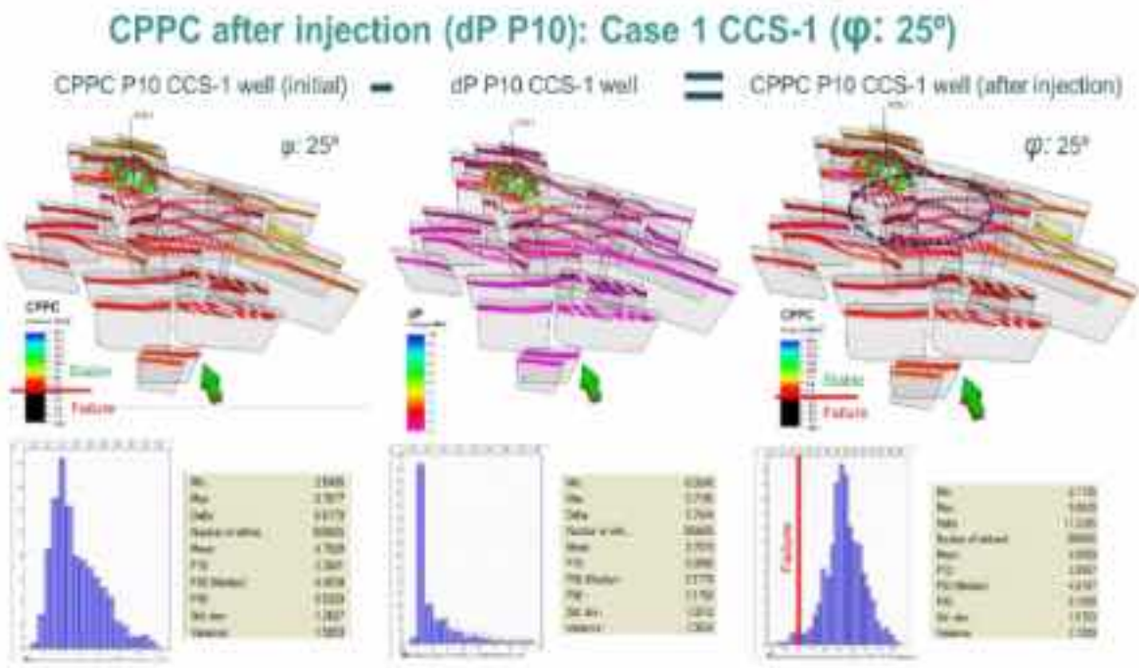


*Figure 6-49 CPPC after injection (P10) for case 1(CCS-1) and friction angle of 25°.*

A reduction in the friction angle to 20°, while maintaining the P10 scenario and injection from CCS-1, reveals a markedly more critical stability condition. The results show a substantial increase in the number of faults with CPPC values below zero, indicating widespread potential for mechanical failure. Faults Falla005, Falla006, Falla008, Falla009, Falla028, Falla029, Falla015, Falla014, Falla018, and Falla027—many of them located near the injector—display multiple unstable points that exceed the failure threshold. These areas are clearly visible in the histogram, which shows a broader and deeper distribution of negative values. The minimum CPPC value reaches –4.53 MPa, confirming that this configuration represents the most unfavorable scenario analyzed, with a significantly increased risk of fault reactivation under lower friction angle conditions. This result is illustrated in Figure 6-50.

The PilotSTRATEGY project has received funding from the European Union's Horizon 2020 research and innovation programme under grant agreement No. 101022664

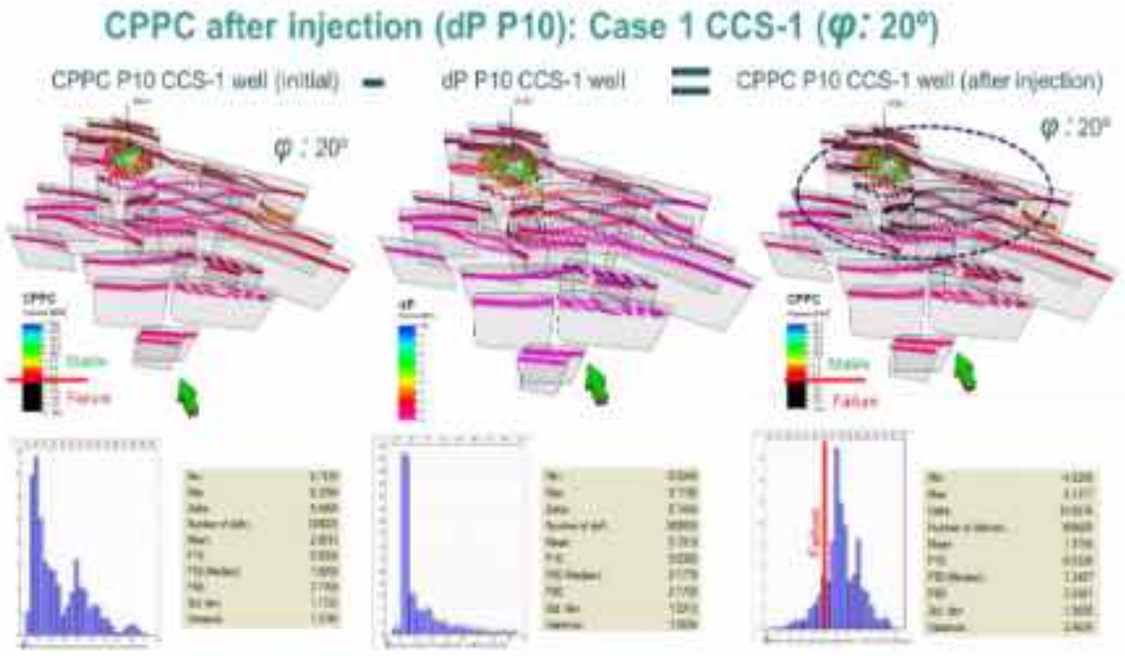


*Figure 6-50 CPPC after injection (P10) for case 1(CCS-1) and friction angle of 20°.*

The results clearly demonstrate the strong sensitivity of fault stability to the assumed friction angle. When a friction angle of 30° is considered, only Falla008 exhibits limited instability. Reducing the angle to 25° leads to a broader impact, with several faults near the injector (Falla005, Falla008, Falla009) reaching critical conditions. The scenario with a 20° friction angle is the most unfavourable, showing widespread instability across multiple faults (including Falla005, Falla006, Falla008, Falla009, Falla028, Falla029, Falla015, Falla014, Falla018, and Falla027). These findings underscore the critical importance of accurately constraining the fault friction angle when assessing the feasibility and safety of subsurface injection operations.

The analysis continues with the results corresponding to the P50 scenario under the CCS-1 injection configuration. In this case, pressure within the reservoir grid reaches up to 8.35 MPa, while the pressure transmitted to the fault plane is approximately 5.83 MPa (maximum pressure, close to the injection point). Assuming a friction angle of 30°, Falla008 remains technically stable, although it approaches the failure threshold. Only a few isolated cells exhibit negative CPPC values—as low as −0.10—indicating localized mechanical failure. These zones, delineated in black on the fault plane, represent areas where fault slip could potentially occur; however, their spatial extent remains limited (Figure 6-51).

The PilotSTRATEGY project has received funding from the European Union's Horizon 2020 research and innovation programme under grant agreement No. 101022664

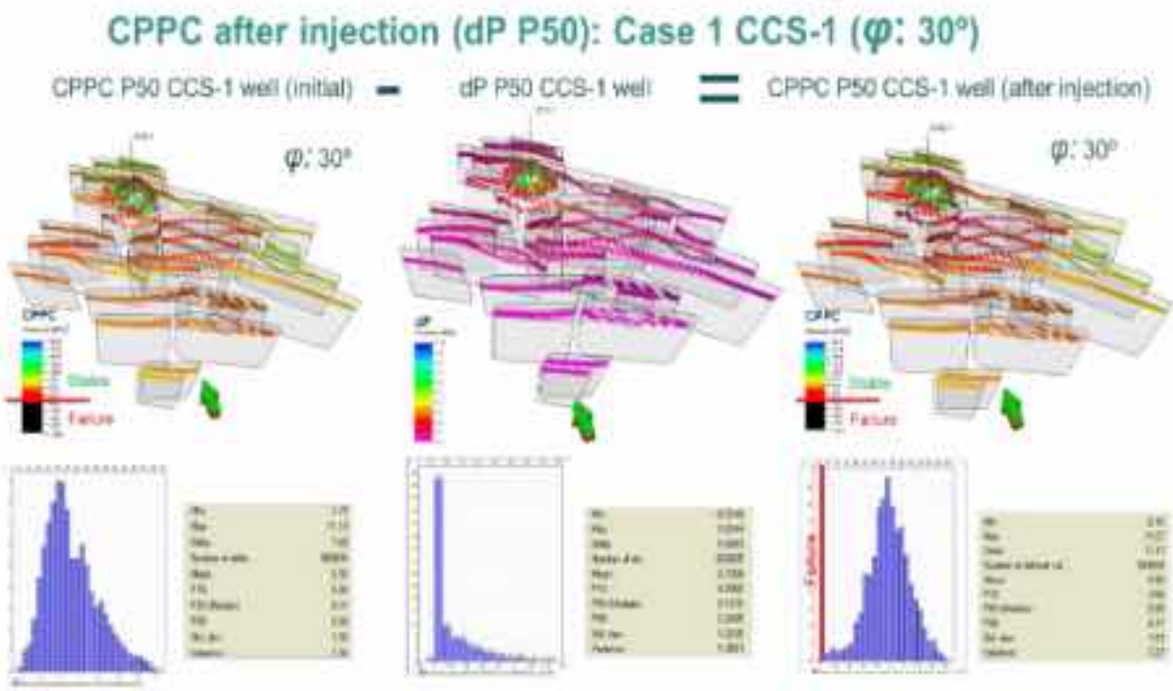


*Figure 6-51 CPPC after injection (P50) for case 1(CCS-1) and friction angle of 30°.*

Under a friction angle of 20°, conditions become significantly less favorable for injection. CPPC values drop to –4.14, and instability becomes widespread. Multiple faults near the injector—including Falla005, Falla006, Falla008, Falla009, Falla014, Falla015, Falla018, Falla027, Falla028, and Falla029—exhibit numerous points below the failure threshold. These areas are clearly highlighted in the maps and histograms, making this the most unfavorable case among those analyzed (Figure 6-52).

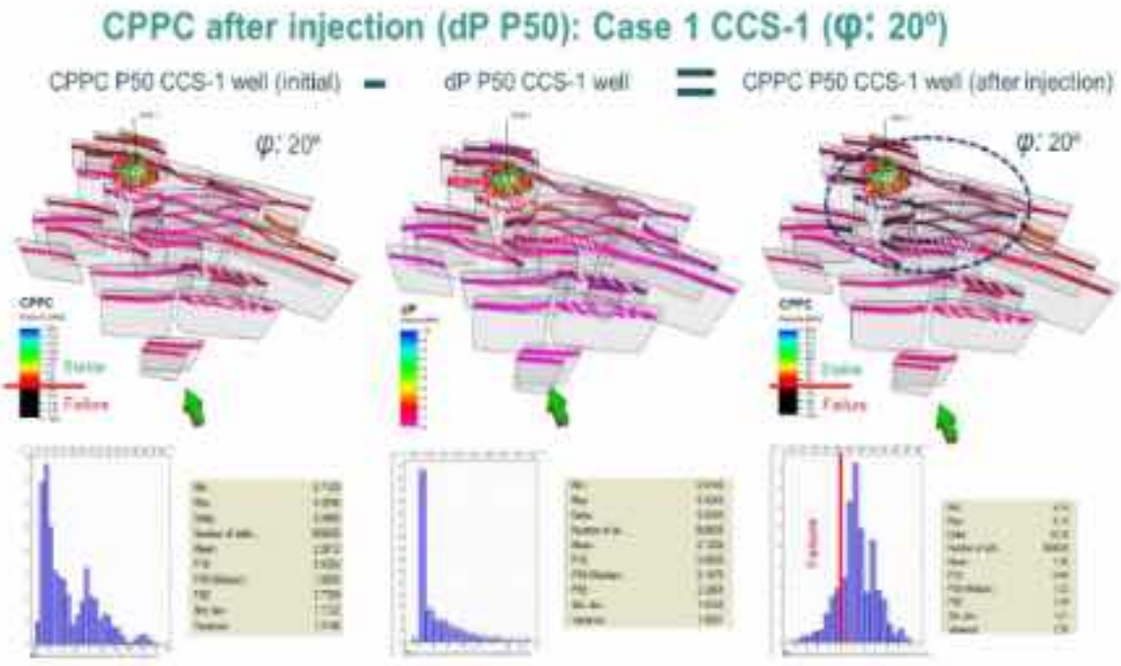


*Figure 6-52 CPPC after injection (P50) for case 1(CCS-1) and friction angle of 20°.*

The PilotSTRATEGY project has received funding from the European Union's Horizon 2020 research and innovation programme under grant agreement No. 101022664

The results are very similar to those observed in the P10 scenario. Although the maximum negative CPPC values are slightly lower in P10, the same faults are affected in both cases. This consistency reinforces the interpretation of fault behavior under varying friction angles and highlights the importance of accurately constraining this parameter when evaluating $CO_2$ injection feasibility and associated risks.

In the P90 scenario with injector CCS-1, the pressure increase in the reservoir grid reaches a maximum of 7.84 MPa, and the pressure projected onto the fault plane is 4.94 MPa (maximum pressure, close to the injection point), both values being the lowest among all well and permeability cases analyzed. With a friction angle of 30°, the CPPC value remains entirely positive, with a minimum of 0.36. No cells on the fault plane are in a critical state, indicating complete mechanical stability across the domain (Figure 6-53).

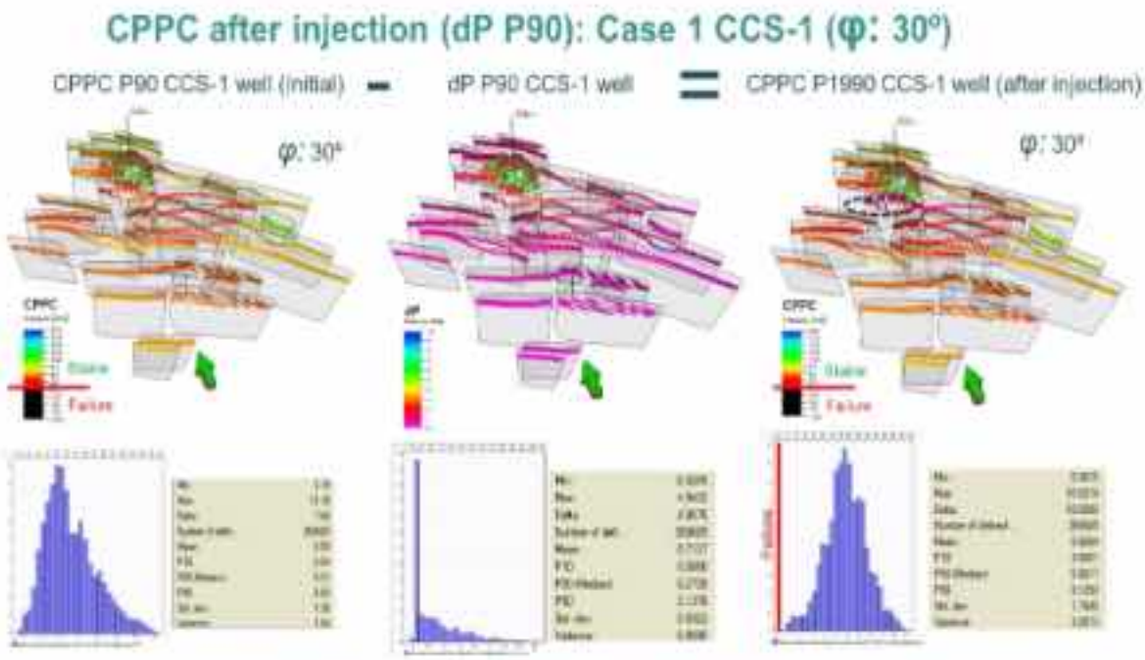


*Figure 6-53 CPPC after injection (P90) for case 1(CCS-1) and friction angle of 30°.*

At 20°, the system becomes more reactive, with CPPC values reaching –3.62. Several faults near the injector—including Falla005, Falla006, Falla008, Falla009, Falla014, Falla015, Falla018, Falla027, Falla028, and Falla029—show points below the failure threshold. However, the number and severity of these critical points are lower than in the P10 and P50 scenarios. (Figure 6-54).

The PilotSTRATEGY project has received funding from the European Union's Horizon 2020 research and innovation programme under grant agreement No. 101022664

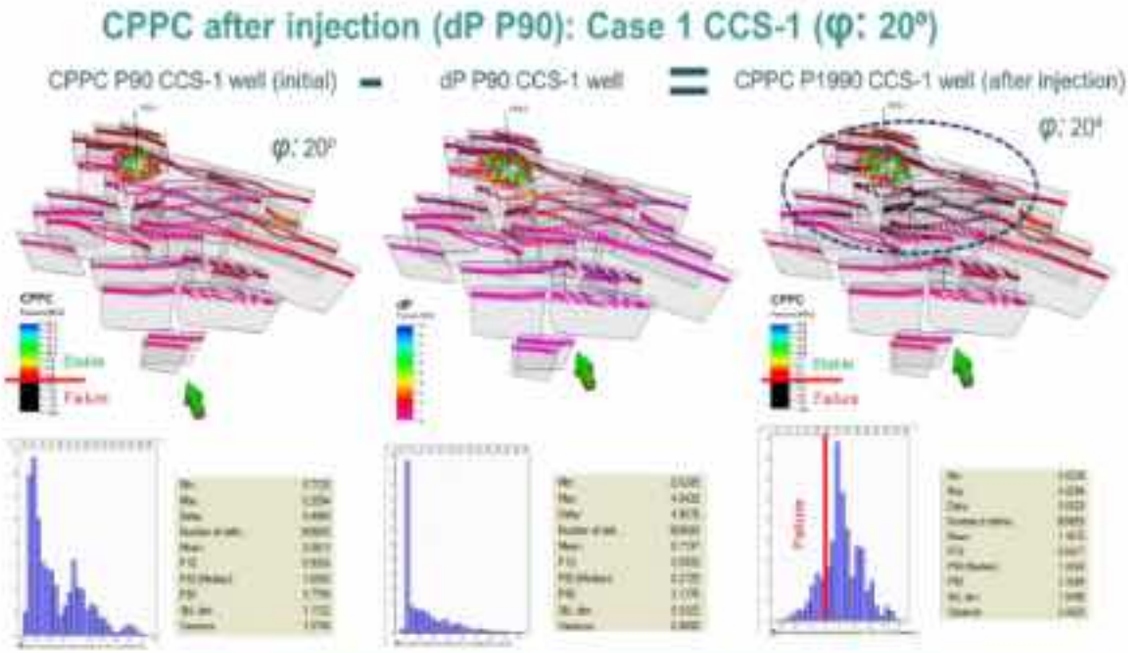


*Figure 6-54 CPPC after injection (P90) for case 1(CCS-1) and friction angle of 20°.*

Overall, the P90 case stands out as the most favorable scenario. It shows the lowest pressure increase and the least fault instability, with no critical cells on the fault plane when assuming a friction angle of 30°. This reinforces the robustness of the system under conservative injection conditions and highlights the importance of friction angle and pressure transmission in controlling fault stability.

The following Table 6-10 Summarizes the statistical distribution of CPPC values in the initial stress state. summarizes the results of all analyzed cases for the CCS-1 injection location, providing a clear and efficient overview that facilitates rapid comparison and understanding of CPPC evolution, pressure increase, and fault stability outcomes.

| Permeability | Friction angle (°) | Min CPPC_initial (MPa) | Max DP_Fault (MPa) | Min CPPC_after injection (MPa) | Unstable faults (CPPC < 0) | Stability summary |
|---|---|---|---|---|---|---|
| P10 | 30° | 5.16 | 5.71 | 0.10 | Fault001 (single point) | Near-critical, very localized instability |
| | 25° | 5.14 | 5.71 | 2.17 | Fault001, Fault006, Fault003 | Localized instability near injector |
| | 20° | 5.16 | 5.71 | -4.59 | Fault001, Fault006, Fault003, Fault038, Fault014, Fault007, Fault016, Fault027, Fault028, Fault019 | Widespread instability (most unstable case) |
| P50 | 30° | 5.28 | 5.82 | 0.10 | Fault001 (new isolated cells) | Mostly stable, marginal instability |
| | 25° | 4.28 | 5.82 | -1.74 | Fault001, Fault006, Fault003 | Increased fault instability |
| | 20° | 4.29 | 5.82 | -4.14 | Fault001, Fault006, Fault003, Fault038, Fault014, Fault007, Fault016, Fault027, Fault028, Fault019 | Widespread instability |
| P90 | 30° | 5.28 | 5.91 | +0.10 | None | Stable |
| | 25° | 5.29 | 5.91 | -1.16 | Fault001, Fault006, Fault003 (same as P50) | Localized instability |
| | 20° | 5.32 | 5.91 | -3.22 | Fault001, Fault006, Fault003, Fault038, Fault014, Fault007, Fault016, Fault027, Fault028, Fault019 | Moderate instability (less severe than P10–P50) |

*Table 6-14 Overview of CPPC Evolution and Fault Stability Outcomes at CCS-1*

The PilotSTRATEGY project has received funding from the European Union's Horizon 2020 research and innovation programme under grant agreement No. 101022664

5.3.4.4.1.2 LOCD-1 location cases.

The analysis continues with Case 2, using injector LOCD-1, across the three permeability scenarios: P10, P50, and P90.

In the P10 scenario with injector LOCD-1, the maximum pressure increase in the reservoir reaches 9.048 MPa, while the pressure transmitted to the fault plane is 8.04 MPa (maximum pressure, close to the injection point), the highest among all cases analyzed. This elevated pressure transmission results in a more critical response in terms of fault stability.

Assuming a friction angle of 30°, the minimum CPPC value drops to −3.34, indicating that some cells on the fault plane have entered the failure domain. This marks a clear contrast with the CCS-1 scenarios, where the system remained stable at this friction angle. The presence of negative CPPC values confirms that fault slip is likely in localized zones, and the system is no longer within the safety margin.

In this case (Figure 6-55), the unstable faults include Falla014, Falla011, and Falla017, representing a broader and more severe impact compared to the P10 scenario with injector CCS-1, where fewer faults were affected. This highlights the increased sensitivity of the system when injecting from LOCD-1 under low-permeability conditions.

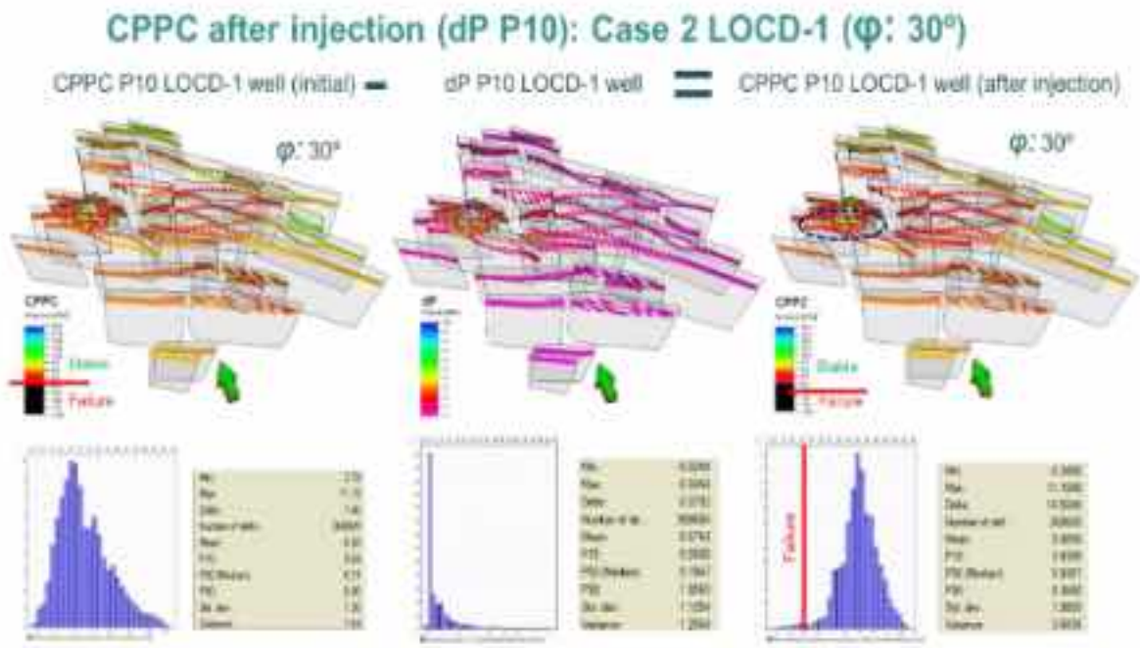


*Figure 6-55 CPPC after injection (P10) for case 2(LOCD-1) and friction angle of 30°*

When the friction angle is further reduced to 20°, the system shows a marked increase in instability. The minimum CPPC value drops to −7.16, the lowest observed across all scenarios, indicating a widespread mechanical response. In addition to the previously affected faults—Falla014, Falla011, and Falla017—several new faults become unstable, including Falla008, Falla009, Falla018, Falla015, Falla029, Falla012, Falla028, and Falla019. The expansion of affected zones and the severity of negative CPPC values suggest a high likelihood of fault slip across multiple structures. This scenario represents the most critical configuration for the P10 permeability case with injector LOCD-1. (Figure 6-56).

The PilotSTRATEGY project has received funding from the European Union's Horizon 2020 research and innovation programme under grant agreement No. 101022664

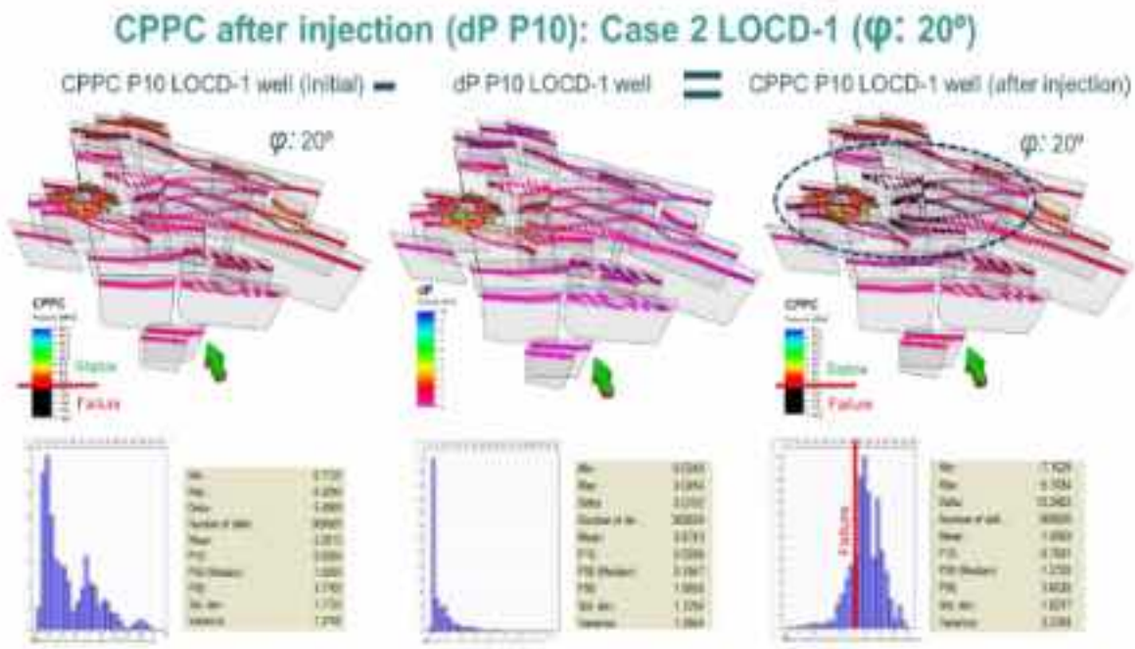


*Figure 6-56 CPPC after injection (P10) for case 2(LOCD-1) and friction angle of 20°.*

In the P50 scenario with injector LOCD-1, the pressure increases in the reservoir and on the fault planes remains high, though slightly lower than in the P10 case. The system shows signs of instability across all friction angles, but with fewer affected cells and less severe CPPC values.

At a friction angle of 30°, the minimum CPPC value reaches –2.696, indicating localized fault slip. The same faults identified in the P10 case—Falla014, Falla011, and Falla017—remain affected, though the extent of instability is reduced. Fewer cells fall below the failure threshold, and the histograms reflect a more moderate distribution of negative values. Figure 6-57.

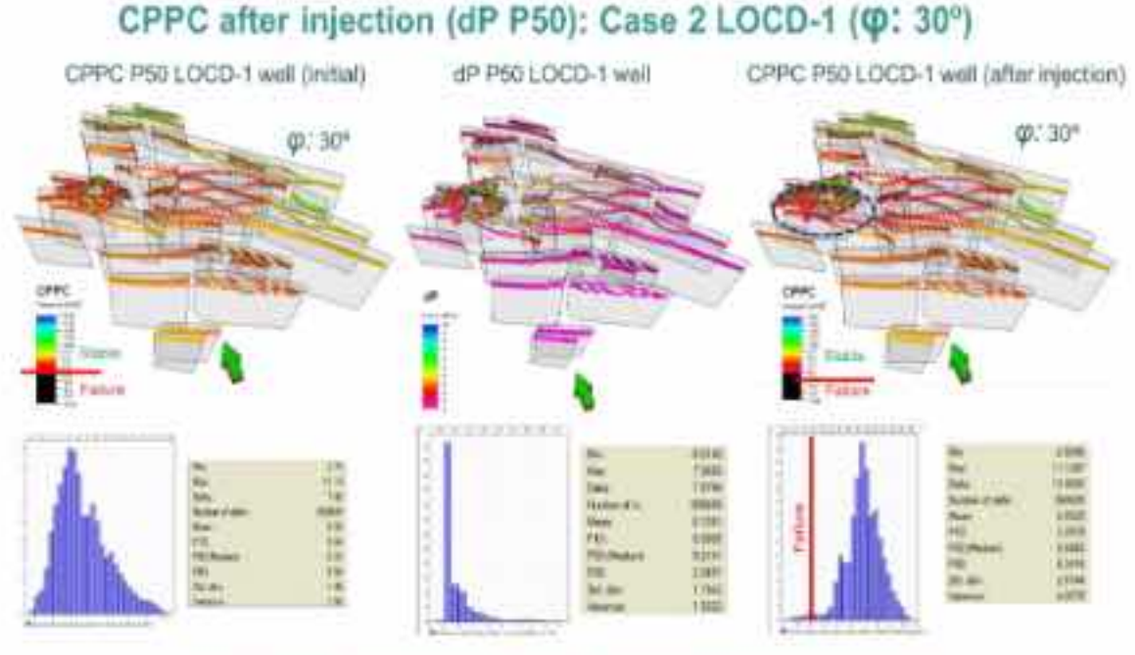


*Figure 6-57 CPPC after injection (P50) for case 2(LOCD-1) and friction angle of 30°.*

The PilotSTRATEGY project has received funding from the European Union's Horizon 2020 research and innovation programme under grant agreement No. 101022664

At 20°, the system becomes more unstable, with the minimum CPPC value reaching –6.49. Although Falla014, Falla011, and Falla017 remain affected, several additional faults also enter the failure domain, including Falla008, Falla009, Falla018, Falla015, Falla029, Falla012, Falla028, and Falla019. Despite the broader distribution of negative CPPC values, the number of affected cells and the severity of the response remain lower than in the P10 scenario. This is consistent with the histograms, which show a more moderate spread of instability. Figure 6-58.

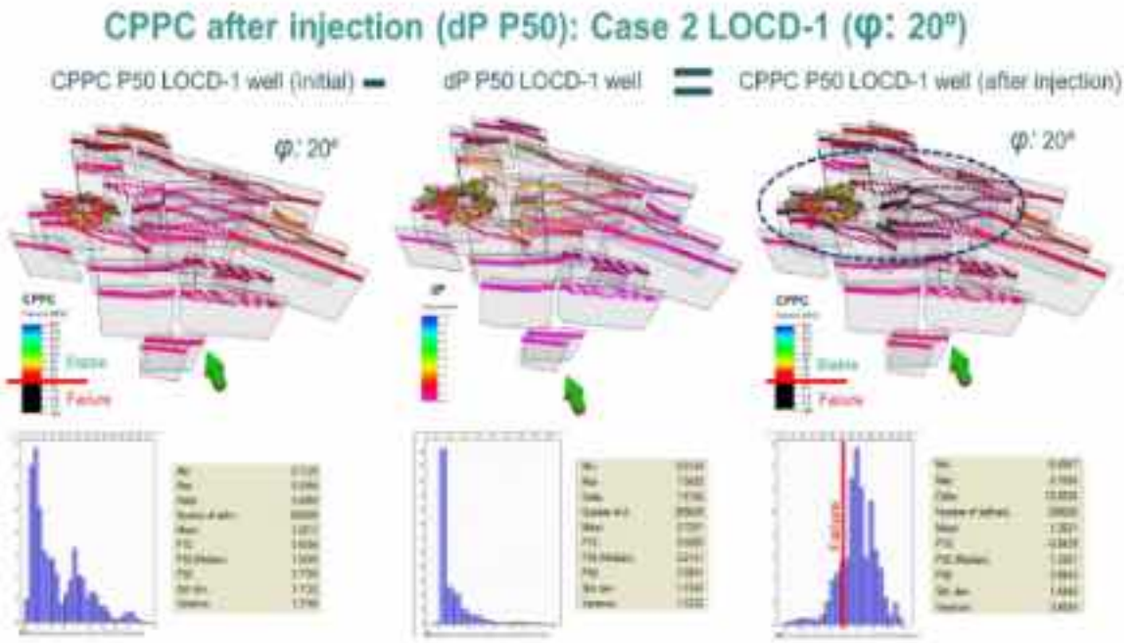


*Figure 6-58 CPPC after injection (P50) for case 2(LOCD-1) and friction angle of 20°.*

Overall, the P50 scenario with injector LOCD-1 shows a consistent pattern of fault activation across the same structures, but with reduced severity and extent compared to P10. This highlights the influence of reservoir permeability on fault response and reinforces the importance of evaluating multiple scenarios when assessing injection safety.

In the P90 scenario with injector LOCD-1, the pressure transmitted to the fault plane reaches 7.09 MPa, the lowest among the three permeability cases. Despite this, fault instability is still observed across all friction angles, though with reduced severity.

At 30°, the minimum CPPC is –2.37, affecting Falla014, Falla011, and Falla017, but with fewer critical cells. At 20°, the system becomes more reactive, reaching –6.17, and additional faults become unstable: Falla008, Falla009, Falla018, Falla015, Falla029, Falla012, Falla028, and Falla019. The result of this case is illustrated in the following three Figure 6-59, Figure 7-11 and Figure 6-60.

The PilotSTRATEGY project has received funding from the European Union's Horizon 2020 research and innovation programme under grant agreement No. 101022664

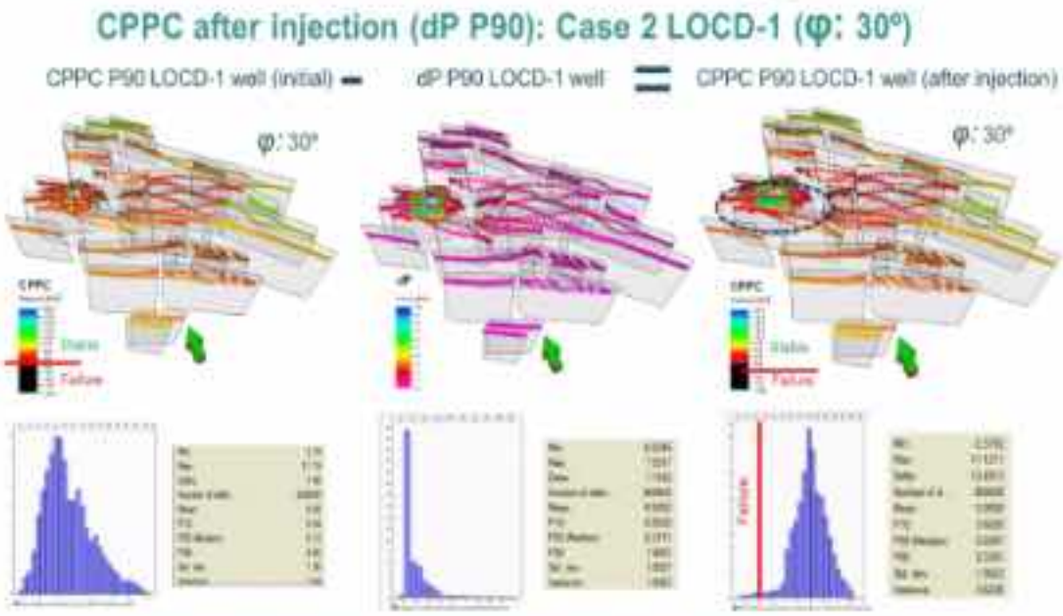


*Figure 6-59 CPPC after injection (P90) for case 2(LOCD-1) and friction angle of 30°*

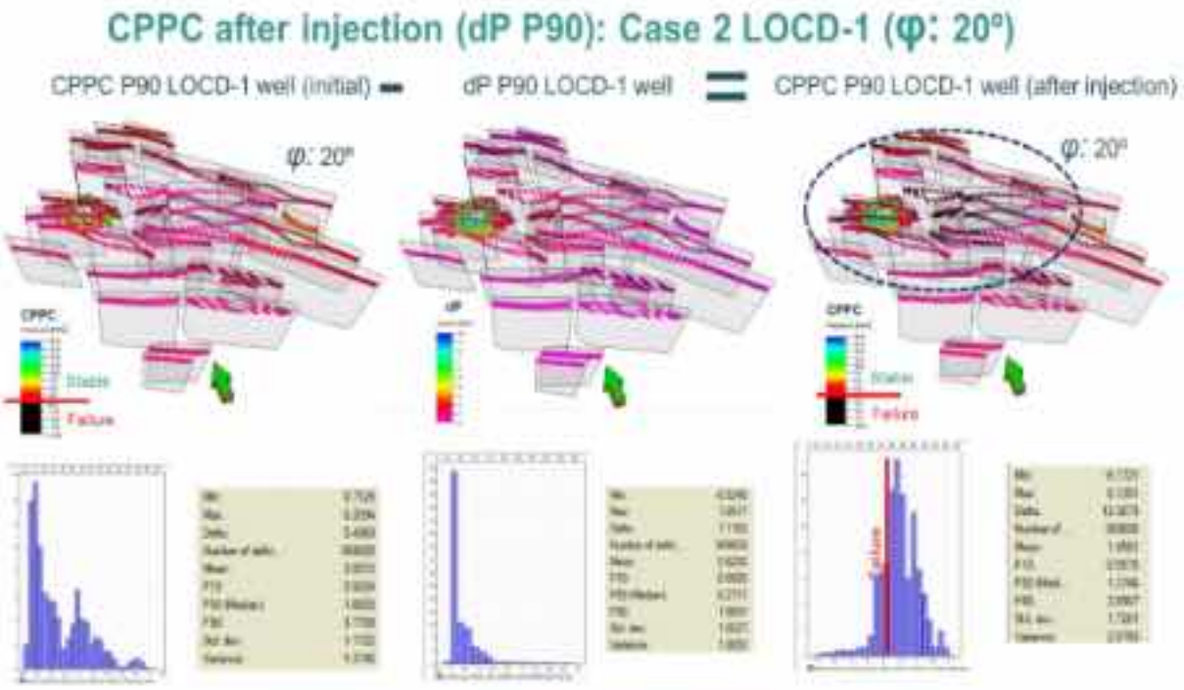


*Figure 6-60 CPPC after injection (P90) for case 2(LOCD-1) and friction angle of 20°.*

The following Table 6-15 summarizes the results of all analyzed scenarios for the LOCD-1 injection location, providing a clear and rapid comparison of CPPC evolution, pressure transmission to the faults, and the resulting fault instability patterns.

The PilotSTRATEGY project has received funding from the European Union's Horizon 2020 research and innovation programme under grant agreement No. 101022664

| Permeability | Friction angle (°) | Min CPPC_initial (MPa) | Max ΔP_fault (MPa) | Min CPPC_after injection (MPa) | Unstable faults (CPPC < 0) | Stability summary |
|---|---|---|---|---|---|---|
| P10 | 30° | 4.70 | 8.04 | −3.34 | Falla014, Falla011, Falla017 | Localized but clear instability |
| | 25° | 3.15 | 8.04 | −4.89 | Falla014, Falla011, Falla017 | Expanded instability in same faults |
| | 20° | 0.80 | 8.04 | −7.10 | Falla014, Falla011, Falla017, Falla009, Falla015, Falla018, Falla019, Falla020, Falla029, Falla012 | Widespread instability – most critical case |
| P50 | 30° | 6.24 | 7.08 | −2.70 | Falla014, Falla011, Falla017 | Localized instability |
| | 25° | 5.34 | 7.08 | −4.22 | Falla014, Falla011, Falla017 | Moderate instability |
| | 20° | 1.87 | 7.08 | −6.49 | Falla014, Falla011, Falla017, Falla009, Falla015, Falla018, Falla019, Falla020, Falla029, Falla012 | Widespread instability (less severe than P10) |
| P90 | 30° | 6.19 | 7.09 | 2.37 | Falla014, Falla011, Falla017 | Localized instability |
| | 25° | 3.80 | 7.09 | −5.91 | Falla014, Falla011, Falla017 | Increased instability |
| | 20° | 1.29 | 7.09 | −6.17 | Falla011, Falla011, Falla017, Falla009, Falla009, Falla015, Falla018, Falla019, Falla020, Falla029, Falla012 | Moderate-widespread instability |

*Table 6-15 Overview of CPPC Evolution and Fault Stability Outcomes at LOCD -1*

#### 5.3.4.4.1.3 CCS-1 & LOCD-1 location cases

The analysis continues with Case 3, which involves simultaneous injection from both wells—CCS-1 and LOCD-1—across the three permeability scenarios: P10, P50, and P90.

In the P10 scenario, the pressure transmitted to the fault plane reaches 8.18 MPa, slightly higher than in the individual injection cases. This elevated pressure results in a more critical mechanical response. At a friction angle of 30°, the minimum CPPC value drops to −3.48 MPa, indicating localized fault slip. The unstable faults at this angle include Falla006, Falla008, Falla009, Falla011, Falla014, and Falla017. When the friction angle is reduced to 25°, the minimum CPPC decreases to −5.034 MPa, and additional faults become unstable, including Falla028, Falla005, and Falla018. At 20°, the system becomes highly reactive, with the minimum CPPC reaching −7.30 MPa. In this configuration, further faults such as Falla003 and Falla027 also enter the failure domain, indicating widespread mechanical instability across multiple structures. The result of this case is illustrated in the following three Figure 6-61, Figure 7-12 and Figure 6-62.

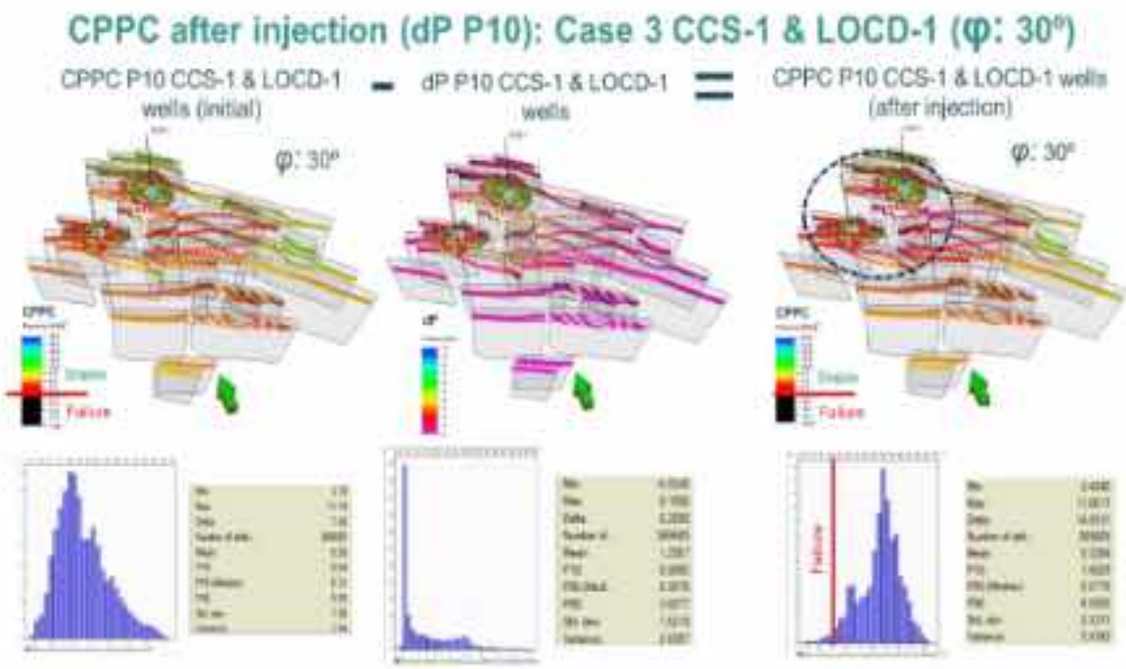


*Figure 6-61 CPPC after injection (P10) for case 3(CCS-1 &LOCD-1) and friction angle of 20°.*

The PilotSTRATEGY project has received funding from the European Union's Horizon 2020 research and innovation programme under grant agreement No. 101022664

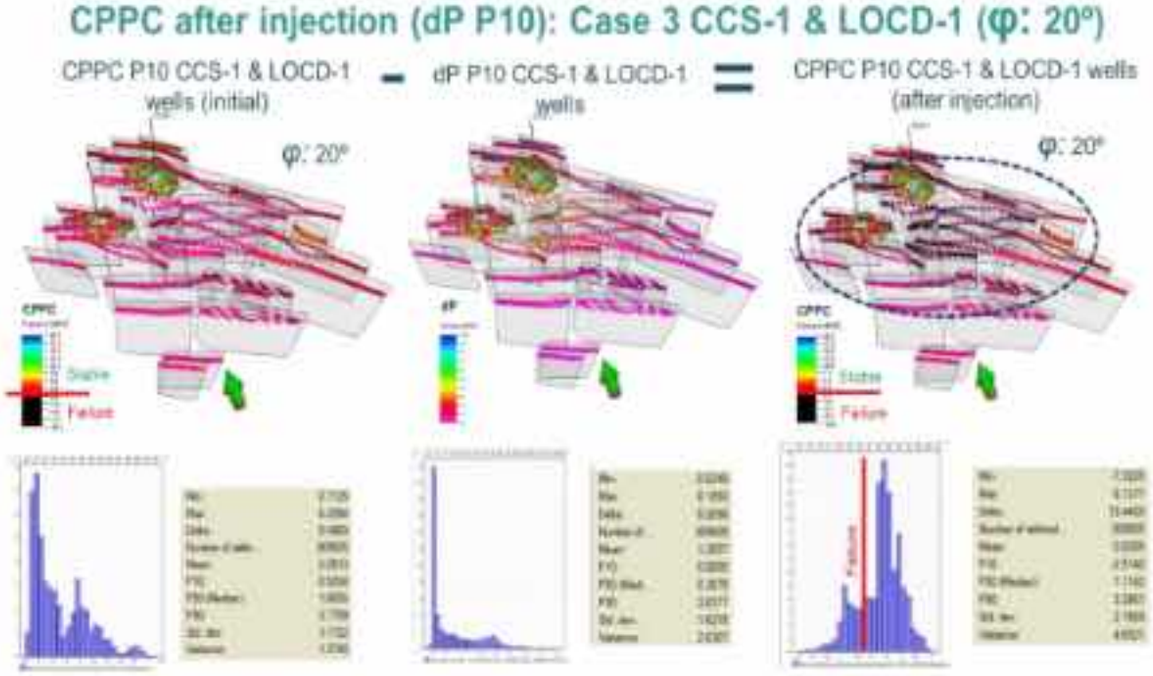


*Figure 6-62 CPPC after injection (P10) for case 3(CCS-1 &LOCD-1) and friction angle of 20°.*

In the P50 scenario, the pressure transmitted to the fault plane is 7.73 MPa, slightly lower than in P10 but still sufficient to trigger instability. At 30°, the minimum CPPC reaches −2.84 MPa, with the same set of faults—Falla006, Falla008, Falla009, Falla011, Falla014, and Falla017—showing signs of localized slip. Reducing the friction angle to 25° leads to a more pronounced response, with a minimum CPPC of −4.40 MPa, and the activation of Falla028, Falla005, and Falla018. At 20°, the system becomes increasingly unstable, reaching a minimum CPPC of −6.67 MPa, and additional faults Falla003 and Falla027 also become unstable, confirming the broader impact of dual injection under moderate permeability conditions. The result of this case is illustrated in the following three Figure 6-63, Figure 7-13, and Figure 6-64.

The PilotSTRATEGY project has received funding from the European Union's Horizon 2020 research and innovation programme under grant agreement No. 101022664

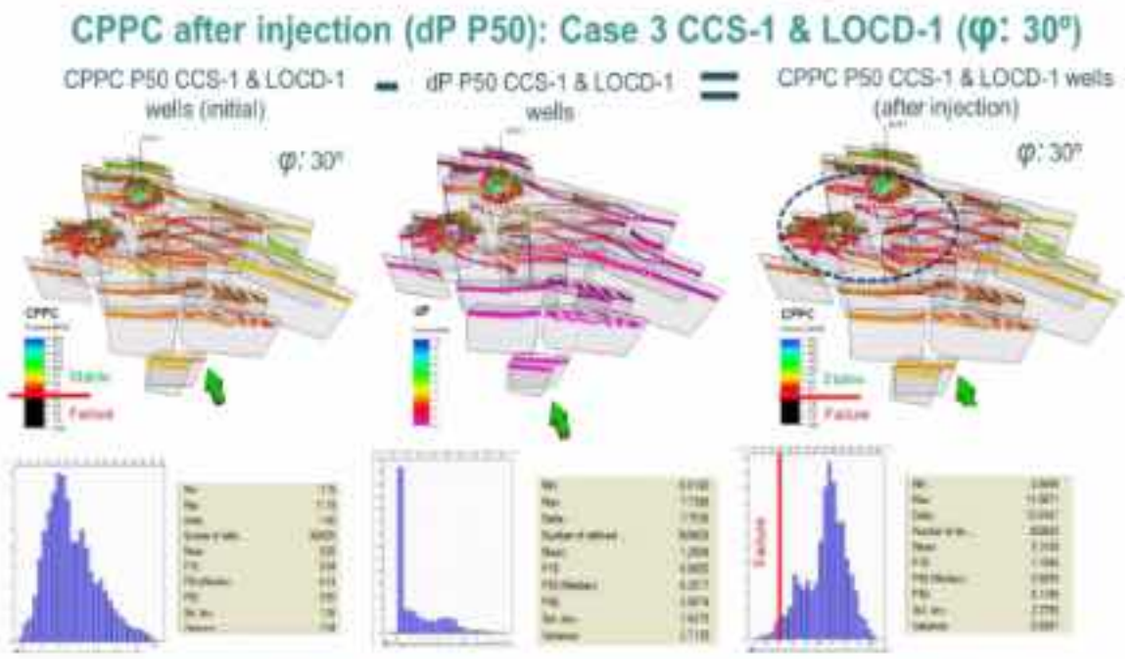


*Figure 6-63 CPPC after injection (P50) for case 3(CCS-1 &LOCD-1) and friction angle of 30°*

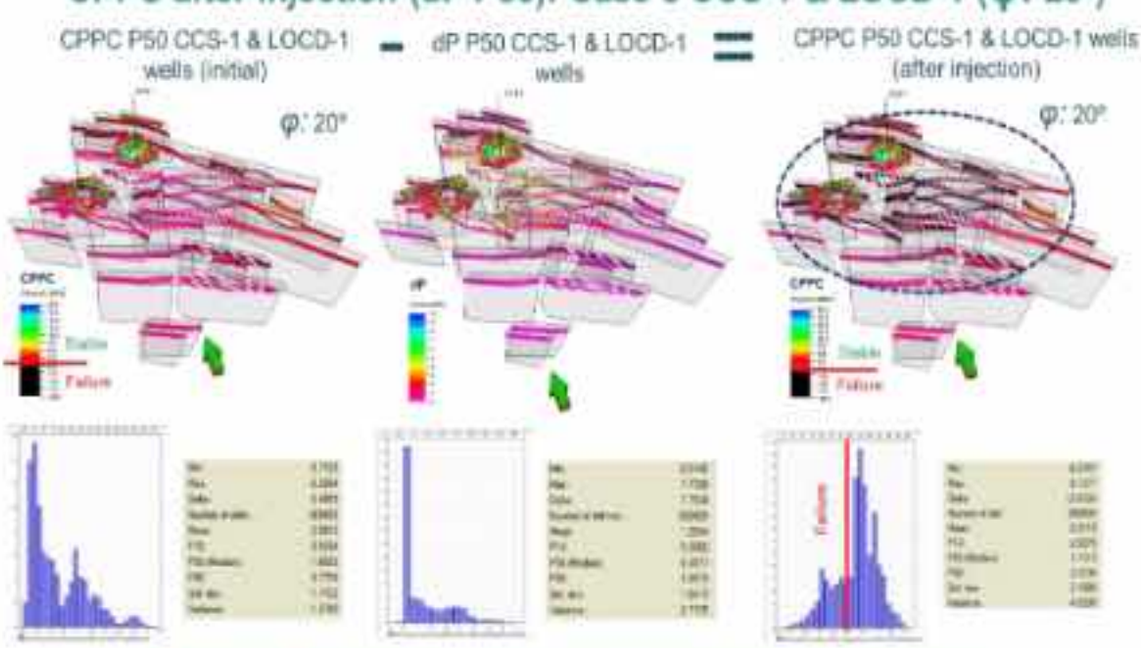


*Figure 6-64 CPPC after injection (P50) for case 3(CCS-1 &LOCD-1) and friction angle of 20°*

In the P90 scenario, the pressure transmitted to the fault plane is 7.83 MPa, slightly higher than in P50 but still lower than in P10. At a friction angle of 30°, the minimum CPPC is –2.94 MPa, with instability observed in Falla006, Falla008, Falla009, Falla011, Falla014, and Falla017. When the friction angle is reduced to 25°, the minimum CPPC drops to –4.48 MPa, and faults Falla028, Falla005, and Falla018 also become unstable. At 20°, the system becomes more reactive, reaching a minimum CPPC of –6.67 MPa, and additional faults Falla003 and Falla027 are affected. Although the number of unstable cells is lower than in P10, the spatial distribution of instability remains significant, highlighting

The PilotSTRATEGY project has received funding from the European Union's Horizon 2020 research and innovation programme under grant agreement No. 101022664

the persistent sensitivity of the system to friction angle even under high-permeability conditions. The result of this case is illustrated in the following three Figure 6-65, Figure 7-14 and Figure 6-66.

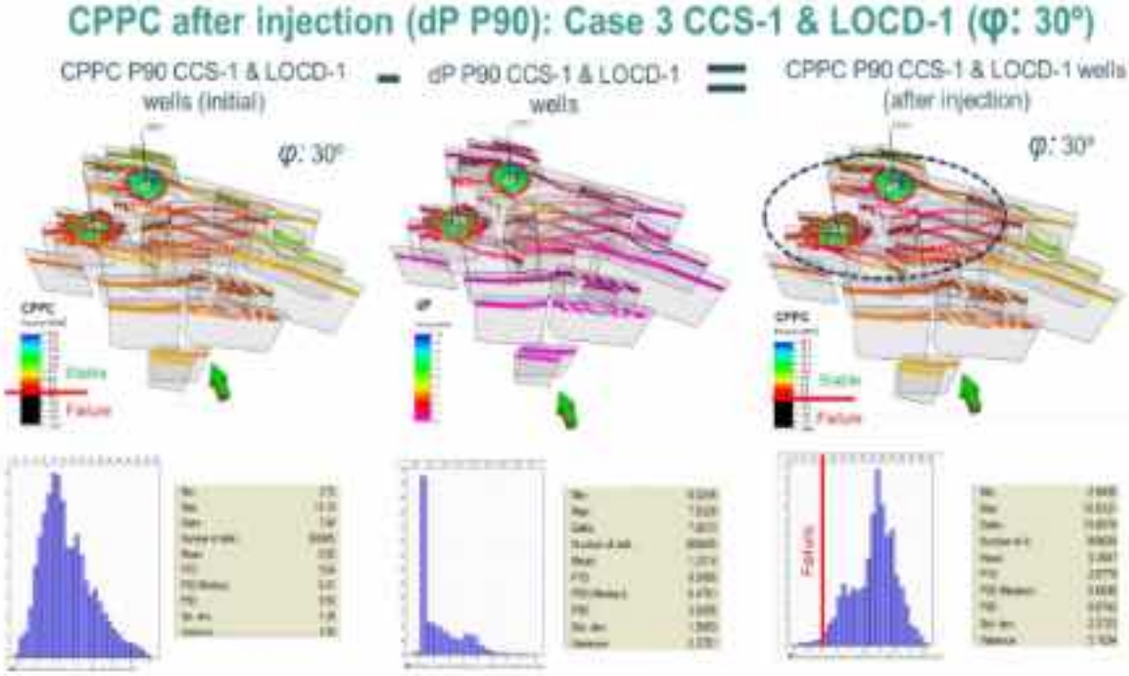


*Figure 6-65 CPPC after injection (P90) for case 3(CCS-1 &LOCD-1) and friction angle of 30°.*

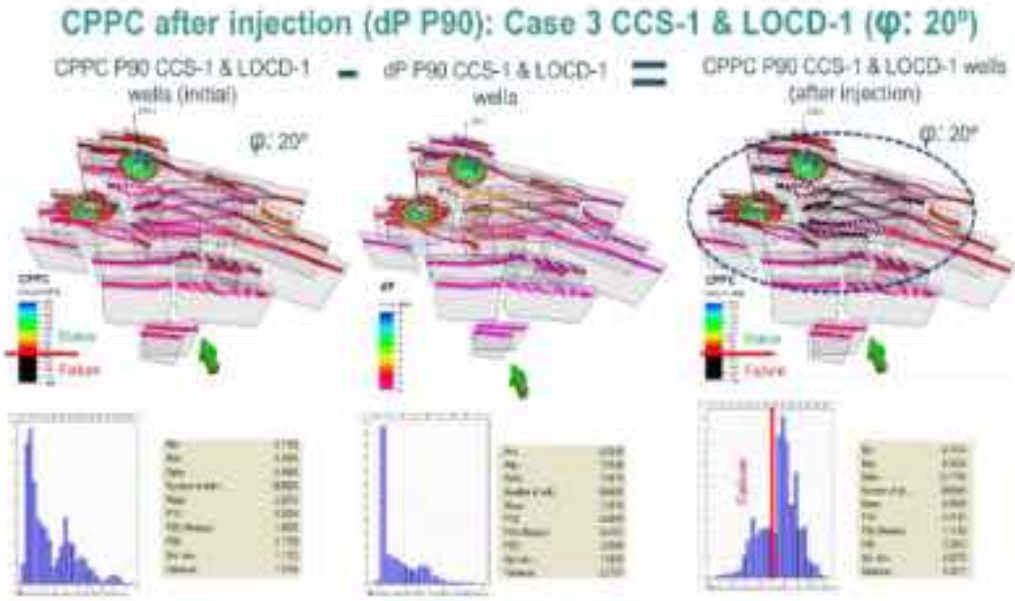


*Figure 6-66 CPPC after injection (P90) for case 3(CCS-1 &LOCD-1) and friction angle of 25°.*

The following Table 6-16 summarizes the results of all analyzed scenarios for the dual-well injection configuration (CCS-1 and LOCD-1), providing a clear and rapid overview of pressure transmission to the fault planes, CPPC reduction, and the resulting patterns of fault instability.

The PilotSTRATEGY project has received funding from the European Union's Horizon 2020 research and innovation programme under grant agreement No. 101022664

| Permeability | Friction angle (°) | Min CPPC_initial (MPa) | Max ΔP_fault (MPa) | Min CPPC_after injection (MPa) | Unstable faults (CPPC < 0) | Stability summary |
|---|---|---|---|---|---|---|
| P10 | 30° | 1.11 | 6.35 | −4.46 | Fclu006, Fclu008, Fclu009, Fclu011, Fclu014, Fclu017 | Limited unstable area |
| | 25° | 1.11 | 6.35 | −5.84 | Fclu006, Fclu008, Fclu009, Fclu011, Fclu014, Fclu017, Fclu019, Fclu020, Fclu021 | Extensive instability |
| | 20° | 1.11 | 6.35 | −7.30 | Fclu006, Fclu008, Fclu009, Fclu011, Fclu014, Fclu017, Fclu019, Fclu020, Fclu021, Fclu022, Fclu027 | Widespread instability, most critical |
| P50 | 30° | −0.35 | 1.39 | −3.84 | Fclu006, Fclu008, Fclu009, Fclu011, Fclu014, Fclu017 | Localized instability |
| | 25° | −0.35 | 1.39 | −4.40 | Fclu006, Fclu008, Fclu009, Fclu011, Fclu014, Fclu017, Fclu019, Fclu020, Fclu021 | Moderate instability |
| | 20° | −0.35 | 1.39 | −7.67 | Fclu006, Fclu008, Fclu009, Fclu011, Fclu014, Fclu017, Fclu019, Fclu020, Fclu021, Fclu022, Fclu027 | Widespread instability |
| P90 | 30° | 1.04 | 1.03 | +0.36 | Fclu006, Fclu008, Fclu009, Fclu011, Fclu014, Fclu017 | Localized instability |
| | 25° | 1.04 | 1.03 | −4.46 | Fclu006, Fclu008, Fclu009, Fclu011, Fclu014, Fclu017, Fclu019, Fclu020, Fclu021 | Extensive instability |
| | 20° | 1.04 | 1.03 | −6.87 | Fclu006, Fclu008, Fclu009, Fclu011, Fclu014, Fclu017, Fclu019, Fclu020, Fclu021, Fclu022, Fclu027 | Broad instability across most faults |

*Table 6-16 Overview of CPPC Evolution and Fault Stability Outcomes at CCS-1 & LOCD-1*

### 6.4.5.5 Fault reactivation risk evaluation.

The results demonstrate that fault stability during $CO_2$ injection is strongly governed by both the fault friction angle and the magnitude of pore pressure transmitted to the fault plane. Across all scenarios, lower friction angles systematically lead to more negative CPPC values and a wider spatial extent of fault reactivation, with 20° representing the most critical condition. For friction angles of 30°, stability is generally maintained or only marginally exceeded, whereas reductions to 25° and 20° result in progressively larger stability losses.

Among the single-well injection strategies, CCS-1 under the P90 permeability scenario is the most stable configuration, with a maximum fault-plane pressure of 4.94 MPa and a minimum CPPC of +0.36 MPa, indicating no fault reactivation at 30°. In contrast, LOCD-1 under the P10 permeability scenario represents the most critical single-well case, where pressure transmitted to the fault reaches 8.04 MPa and CPPC values drop to −7.16 MPa, leading to widespread fault instability.

Dual-well injection (CCS-1 + LOCD-1) further amplifies the mechanical response. Under low-permeability conditions (P10), pressure transmitted to the fault plane reaches 8.18 MPa, and the minimum CPPC falls to −7.30 MPa, the lowest value observed across all analyzed scenarios. This configuration results in instability across multiple fault structures even at a friction angle of 30°, with severity increasing markedly as the friction angle is reduced.

Based on these quantitative results, a risk evaluation was conducted to identify the conditions most prone to fault reactivation. This assessment focuses on scenarios in which CPPC becomes negative, either locally or over large fault segments, and considers the combined effects of permeability, injection strategy, and friction angle. The analysis highlights that low permeability, high pressure transmission to faults, dual-well injection, and low friction angles constitute the most unfavorable combination, providing a clear numerical basis for defining safe and effective $CO_2$ injection strategies and for prioritizing mechanical parameter uncertainty in storage site assessments.

- **Most Unstable Faults**

The PilotSTRATEGY project has received funding from the European Union's Horizon 2020 research and innovation programme under grant agreement No. 101022664

These faults are consistently unstable across all injection strategies (CCS-1, LOCD-1, Dual) and all friction angles (30°, 25°, 20°). They are the most sensitive to pressure changes and mechanical stress.

- **Falla014** – Highly reactive in every scenario. Shows instability even at 30°, especially under LOCD-1 and Dual injection.
- **Falla011** – Frequently unstable in LOCD-1 and Dual injection, across all friction angles.
- **Falla017** – Similar to Falla011, with persistent instability under all conditions.

- **Frequently Unstable Faults**

These faults show instability mainly under low friction angles (25° and 20°) and are affected by multiple injection strategies. They are moderately sensitive but become critical under more aggressive conditions.

- **Falla005** – Affected in CCS-1 and Dual injection, especially at 25° and 20°.
- **Falla006** – Similar behavior to Falla005, with instability increasing at lower friction angles.
- **Falla008** – Unstable in all three strategies (CCS-1, LOCD-1, Dual), particularly at 25° and 20°.
- **Falla009** – Mirrors Falla008's behavior, with widespread instability under low friction.
- **Falla015** – Becomes unstable at 20°, especially in LOCD-1 and Dual injection.
- **Falla018** – Reacts similarly to Falla015, with instability under high-pressure, low-friction conditions.
- **Falla028** – Frequently unstable at 20°, across all strategies.
- **Falla029** – Same pattern as Falla028, indicating structural sensitivity.

- **Critically Unstable Only Under Extreme Conditions**

These faults are only affected at 20° friction angle and under high-pressure scenarios (mainly LOCD-1 and Dual injection). They represent localized but severe risk zones.

- **Falla003** – Only becomes unstable under Dual injection at 20°, indicating deep-seated sensitivity.
- **Falla012** – Affected in LOCD-1 at 20°, not present in other scenarios.
- **Falla019** – Similar to Falla012, with instability limited to the most critical conditions.

The summary of this analysis is visually represented in Figure 6-67, which graphically illustrates the fault instability results across the evaluated scenarios and conditions. The spatial distribution of the most critical faults and their relative instability is further illustrated in the following Figure 6-68 and Figure 6-69.

The PilotSTRATEGY project has received funding from the European Union's Horizon 2020 research and innovation programme under grant agreement No. 101022664

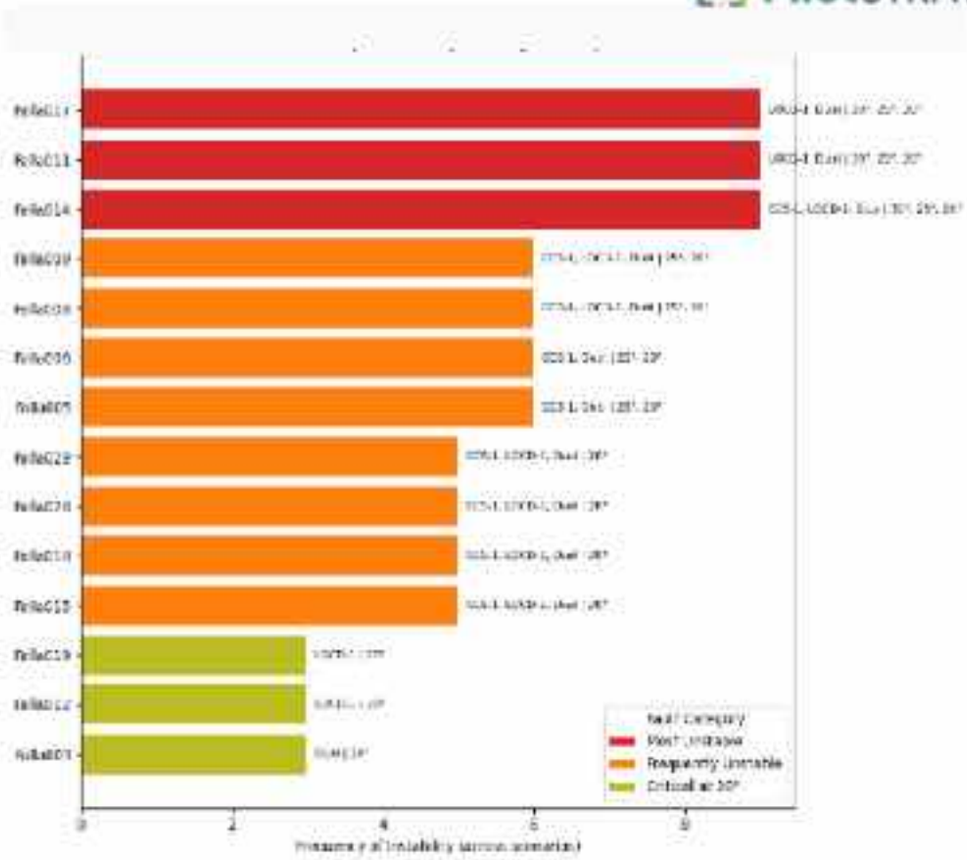


*Figure 6-67 Summary unstable faults for different injection scenarios and friction angles.*

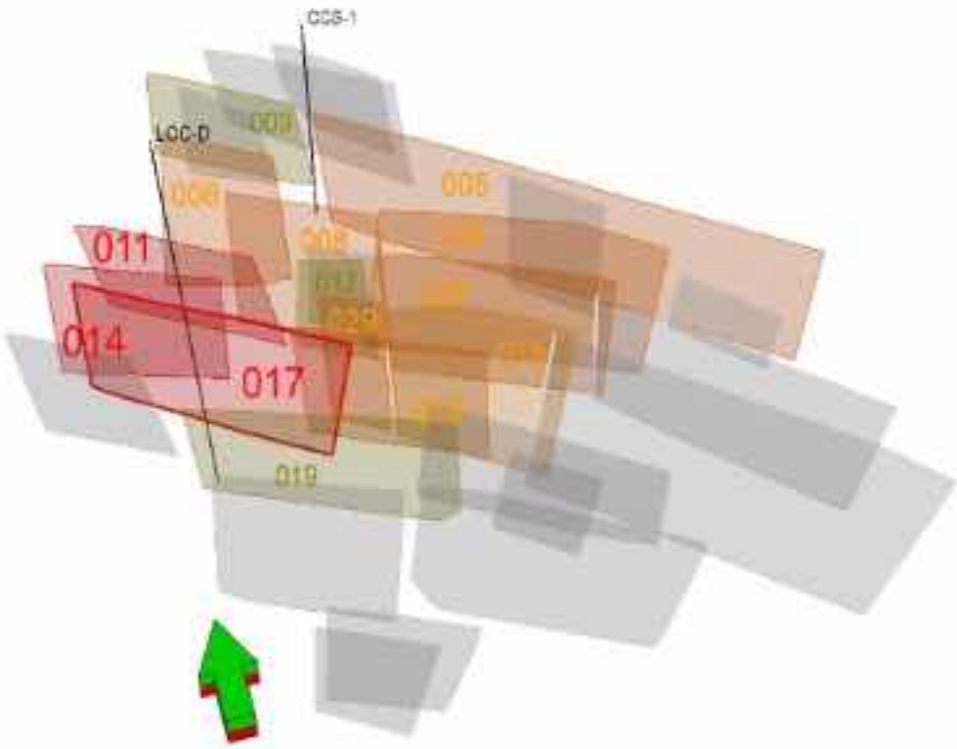


*Figure 6-68 Spatial Distribution of Fault Instability and Dual Injection Well Locations*

The PilotSTRATEGY project has received funding from the European Union's Horizon 2020 research and innovation programme under grant agreement No. 101022664

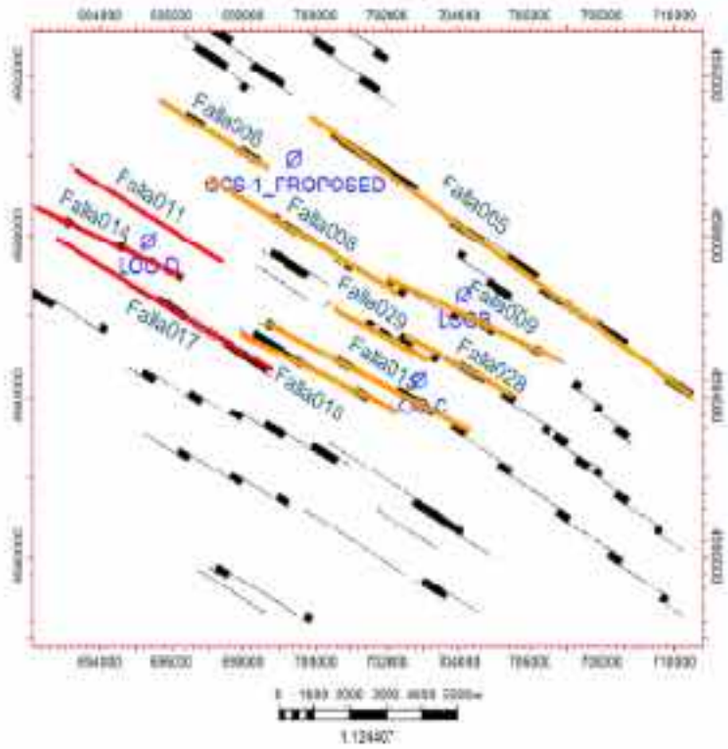


*Figure 6-69 Fault Stability Map Based on CPPC-Derived Instability Intensity*

To support a comprehensive understanding of fault behavior under varying injection conditions, a heatmap analysis (Figure 6-70) was conducted to visualize the spatial and scenario-based distribution of fault instability. This graphical representation captures the presence or absence of mechanical failure (CPPC < 0) for each fault across all combinations of injection strategy, permeability scenario, and friction angle. By highlighting the frequency and conditions under which each fault becomes unstable, the heatmap serves as a diagnostic tool for identifying the most critical faults and for assessing the sensitivity of the system to key operational parameters.

The results indicate that injection strategy and friction angle exert a first-order control on fault stability, whereas geological variability as permeability plays a secondary role. In particular, the dual injection scenario is characterized by a systematically high occurrence of unstable faults across nearly all realizations and friction angles, suggesting that this operational configuration is intrinsically prone to fault reactivation and therefore likely infeasible from a geomechanical perspective. In contrast, the alternative single-injection scenarios exhibit a more differentiated response yet still show a high frequency of instability for low friction angles (20°), largely independent of the permeability scenario considered. This pattern indicates that low fault friction dominates the mechanical response, overriding stabilizing effects introduced by geological heterogeneity.

Overall, Figure 6-71 demonstrates that an increasing number of unstable cases corresponds to a higher degree of fault instability, allowing critical faults and unfavorable operational conditions to be readily identified. The heatmap therefore provides a robust framework for ranking injection

The PilotSTRATEGY project has received funding from the European Union's Horizon 2020 research and innovation programme under grant agreement No. 101022664

strategies according to geomechanical risk and for informing decisions aimed at minimizing fault reactivation potential.

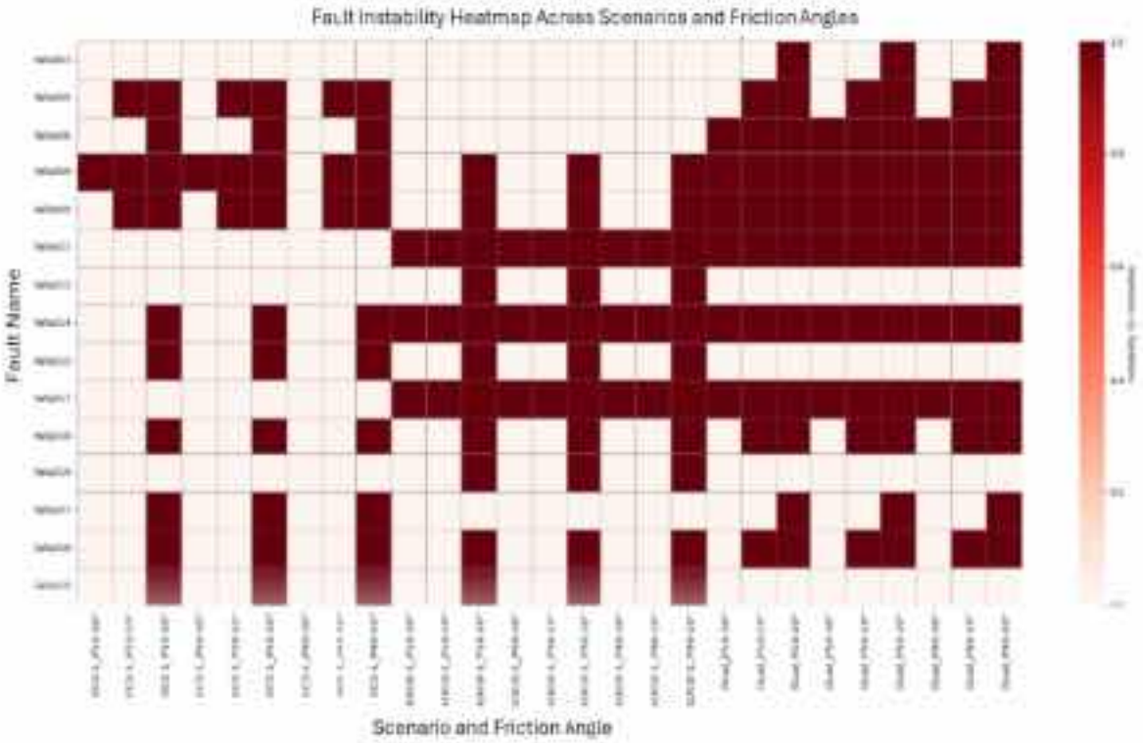


*Figure 6-70 Heatmap analysis was conducted to visualize the spatial and scenario-based distribution of fault instability*

Figure 6-71 summarizes the minimum post-injection CPPC values and their distributions for different friction angles (Φ: 30°, 25°, and 20°), injection wells (CCS-1, LOCD-1, and Both), and permeability scenarios (P10, P50, P90). Each cell in the table contains a histogram showing the distribution of CPPC values. The red vertical line represents the failure threshold, i.e., where CPPC = 0. Values to the left of this line are negative, indicating that the fault has reached or exceeded the failure condition.

The more negative the CPPC value, the greater the degree of instability of the fault. This is because a lower CPPC implies that the pore pressure increase has significantly reduced effective normal stress, bringing the fault closer to reactivation.

The PilotSTRATEGY project has received funding from the European Union's Horizon 2020 research and innovation programme under grant agreement No. 101022664

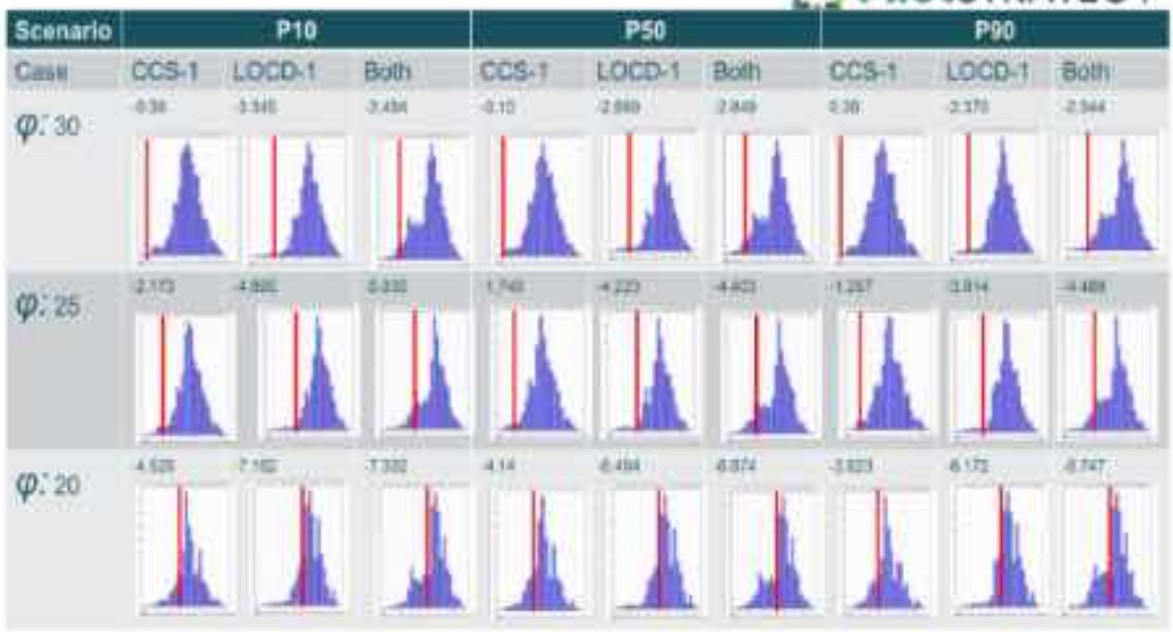


*Figure 6-71 Summary of the minimum post-injection CPPC values and their distributions for different friction angles (φ: 30°, 25°, and 20°), injection wells (CCS-1, LOCD-1, and Both), and permeability scenarios (P10, P50, P90).*

### 6.4.5.6 *Conclusions EOI or Peak injection conditions.*

Fault stability is evaluated using Critical Pore Pressure Change (CPPC) as the primary geomechanical indicator, assessed under peak pore pressure conditions reached at the end of the 30-year $CO_2$ injection period, immediately prior to injection cessation. This timing represents the most conservative condition for fault reactivation analysis.

The methodology focuses on the evaluation of CPPC at peak conditions. Initially, CPPC is computed under pre-injection stress conditions, defining the pore pressure increase required to bring each fault segment to failure. The injection-induced pore pressure increase (ΔP) at peak conditions is then subtracted from this initial CPPC to obtain an effective CPPC, which represents the remaining mechanical stability margin of each fault segment at peak pressure. This effective CPPC is used as the sole metric for stability assessment, providing a conservative, first-order evaluation without recalculating the full stress field and assuming a constant regional stress tensor.

Within this framework, negative effective CPPC values (CPPC < 0) indicate that fault segments become mechanically unstable, implying an increased potential for fault reactivation and the possible occurrence of induced seismicity. Moreover, the more negative the CPPC value and the farther it deviates from zero, the higher the degree of mechanical instability, reflecting a progressively larger exceedance of failure conditions. However, no explicit or deterministic process is assumed to directly correlate the inferred fault instability with the occurrence, magnitude, or spatio-temporal distribution of seismic events.

Conversely, non-negative CPPC values (CPPC ≥ 0) define stable fault conditions under the evaluated geological and operational assumptions. Overall, this approach provides a consistent and decision-oriented screening methodology, directly linking injection-induced pore pressure buildup to fault stability at peak pressure conditions.

The fault stability analysis) reveals the following key findings:

1. **Sensitivity to Friction Angle.**

The PilotSTRATEGY project has received funding from the European Union's Horizon 2020 research and innovation programme under grant agreement No. 101022664

Fault stability is strongly controlled by the assumed fault friction angle, which governs shear resistance along fault planes. Increasing the friction angle from 20° to 30° leads to progressively less negative minimum CPPC values, indicating a systematic reduction in fault instability and a lower susceptibility to pressure-induced reactivation.

For example, in the most critical injection scenario (Both injectors, P10 permeability):

- $\phi$ **20°**: –7.302 MPa
- $\phi$ **25°**: –5.035 MPa
- $\phi$ **30°**: –3.484 MPa

This trend reflects fundamental fault mechanics, whereby higher friction angles increase the available shear strength, requiring larger pore pressure perturbations to reach failure conditions. Consequently, uncertainty in fault friction properties represents a key control on stability outcomes and should be considered a primary sensitivity parameter in risk assessments.

2. **Influence of Permeability (P10, P50 and P90).**

Reservoir permeability exerts a secondary but consistent influence on fault stability. Across all friction angle scenarios, higher permeability cases (P90) tend to yield less negative CPPC values than lower permeability cases (P10). This behavior indicates that increased permeability facilitates more efficient pressure dissipation, limiting pore pressure accumulation near fault planes at peak injection conditions.

Although the magnitude of the permeability effect is smaller than that associated with friction angle variations, the observed trend demonstrates that low-permeability scenarios represent more conservative assumptions for fault stability, particularly when combined with low friction angles and multi-well injection. For instance, in the $\phi$ 20° case with Both injectors:

- **P10**: –7.302 MPa
- **P50**: –6.674 MPa
- **P90**: –6.747 MPa

3. **Impact of Injection Configuration**

The combined injection scenario (CCS-1 + LOCD-1) consistently produces the most negative CPPC values across the tested parameter space. This configuration results in the largest cumulative pressure buildup and therefore represents the most unfavorable condition in terms of fault stability.

The results indicate that pressure contributions from multiple injectors can interact constructively, increasing the likelihood of exceeding failure thresholds at peak conditions. This finding highlights the importance of evaluating multi-well injection strategies not only in terms of reservoir performance but also with respect to their combined geomechanical impact.

4. **Comparison Between Injectors: CCS-1 vs. LOCD-1**

The PilotSTRATEGY project has received funding from the European Union's Horizon 2020 research and innovation programme under grant agreement No. 101022664

A systematic difference is observed between the two individual injectors. For equivalent friction angles and permeability assumptions, LOCD-1 consistently generates more negative CPPC values than CCS-1, indicating a greater destabilizing effect on nearby faults.

For example, at ϕ: 25°, P10:

- **CCS-1**: −2.173 MPa
- **LOCD-1**: −4.895 MPa

This contrast suggests that injector location, connectivity, or proximity to critically oriented faults plays a significant role in controlling local pressure buildup and fault response. As such, injector-specific assessments are essential for discriminating spatial variations in geomechanical risk.

5. **Most Critical and Most Stable Scenarios**

- The **most unstable condition** is observed at ϕ: 20°, P10, Both injectors, with a minimum CPPC of −7.302 MPa.
- The **most stable condition** is found at ϕ: 30°, P90, CCS-1, where the minimum CPPC is +0.36 MPa, remaining above the failure threshold.

#### *6.4.5.7 Overall Implications and Operational Recommendations*

Negative CPPC values indicate mechanical instability in fault segments, with the degree of instability increasing as CPPC becomes more negative and departs further from zero. While this implies a higher potential for fault reactivation and the possible occurrence of induced seismicity, no deterministic or direct correlation is assumed between CPPC-based instability and the timing, magnitude, or spatial distribution of seismic events. Accordingly, CPPC should be interpreted as a screening-level indicator of mechanical susceptibility, rather than a predictor of seismic occurrence.

Within this framework, the CPPC-based assessment provides a conservative basis for discriminating between operational configurations and for identifying scenarios that may require additional risk management measures. Scenarios combining low fault friction angles, low reservoir permeability, and simultaneous injection from multiple wells consistently yield the most negative CPPC values and therefore represent the least favorable operational configurations from a fault-stability perspective. These conditions amplify pore pressure buildup near critically stressed faults and result in reduced mechanical stability margins at peak pressure.

In contrast, single-injector operation, particularly when dominated by CCS-1, and scenarios characterized by higher friction angles or higher permeability realizations, are associated with less negative or locally positive CPPC values and thus provide more robust stability margins. These configurations are therefore preferable as baseline operational strategies under the current assumptions.

From an operational standpoint, configurations identified as potentially unstable should not be implemented without mitigation. Recommended actions include avoiding simultaneous multi-well injection, applying injector-specific operational constraints, and adopting phased or staggered injection strategies to limit peak pore pressure buildup. Particular attention should be given to injector configurations that have a stronger destabilizing influence on nearby faults.

The PilotSTRATEGY project has received funding from the European Union's Horizon 2020 research and innovation programme under grant agreement No. 101022664

Overall, these results highlight the importance of accurately constraining fault mechanical properties (e.g., friction angle) and reservoir flow characteristics (e.g., permeability) using conservative assumptions, in order to avoid underestimating fault reactivation risk. Within these limitations, CPPC evaluated at peak pore pressure provides a practical and decision-oriented tool to guide operational design, prioritize monitoring and model refinement efforts, and support risk-informed decision-making for $CO_2$ injection projects.

## 6.5 Conclusions

1. **Conditional feasibility.** $CO_2$ storage at Lopín is technically feasible under conservative configurations: single-well operation, strict pressure management, and focused control of geomechanical risks linked to low permeability and natural overpressure.
2. **Injectivity & halite.** Compositional runs capture near-wellbore drying; NaCl precipitation degrades injectivity and attainable capacity. For a mobility multiplier ~MS=0.5, capacity reductions of ~10–15% are observed, warranting mitigation ($CO_2$ humidification, water flush) and laboratory calibration of the mobility curve.
3. **Seal integrity.** At the seal base (~1,722 m TVD), safety margins decrease from 9.8 MPa (FG×0.9) and 13.4 MPa initially to 1.8 MPa and 5.4 MPa at end-of-injection (EOI). Margins remain positive but tight, requiring conservative MAOP limits and continuous surveillance; geochemical risks to the seal are secondary to geomechanics.
4. **Wellbore stability.** The 1D-based mud-weight window aligns with local experience; breakouts cluster where $S_{hmax}$–$S_{hmin}$ anisotropy is highest. Use conservative densities/BHAs and salt-saturated muds across evaporites.
5. **Fault stability (CPPC).** Proximity to failure is governed by fault friction ($\phi$) and fault-plane pressure. $\phi$=30° is largely stable or shows limited local failures; $\phi$=25–20° broadens instability, especially for low-k (P10) and near injectors. Dual injection (CCS-1+LOC-D) is least favorable; LOC-D tends to pressurize faults more than CCS-1, while CCS-1 with P90 & $\phi$=30° retains positive CPPC.
6. Operational recommendation. Favor single-well injection (CCS-1) with ramp-up/ramp-down, conservative pressure limits, and strengthened MMV (downhole P/T, microseismic). Avoid co-injection; if a second well is considered, use staggered/alternating schemes.
7. Key uncertainties & next steps. (i) Constrain fault friction ($\phi$) with targeted tests and LOT/minifracs; (ii) run focused 3D poroelastic coupled cases over high-risk domains; (iii) conduct core-floods to calibrate $k_s(S_s)$ for halite; (iv) further refine near-wellbore gridding for salt-damage and transient BHP studies.

## 6.6 References

Blanco Pericana, A., Ron Martin, M., Mañas Fernandez, M., Ibañez, E., Fernandez-Canteli, P., & Pangaro, F. 2024. Ebro Basin (Spain). In Chassagne, R. (Ed.) *Report on optimization – Injection strategy and storage capacity*. DeliverableWP3/D3.3. EU H2020 PilotSTRATEGY project 101022664, report, 98–121.

The PilotSTRATEGY project has received funding from the European Union's Horizon 2020 research and innovation programme under grant agreement No. 101022664

Ayala, C.; Benjumea, B.; Berrezueta, E. R.; Bordenave, A.; Carneiro, J.; Casacão, J.; Castillo, M.; Clariana, P.; Caeiro, M. H.; del Moral, B.; Fernández de Arévalo, E.; Fernández-Canteli, P.; García, A.; García, D. M.; García, J.; Issautier, B.; Llorente, J. M.; López, J.; Marques da Silva, D.; Martínez, J.; Mediato, J. F.; Moreno; Ordóñez, B.; Pereira, P.; Pina, B.; Pueyo, E.; Rey, C.; Ribeiro, C.; Rubio, F.; Soto, R. (2023) Deliverable 2.7 – Conceptual Geological Models. PilotSTRATEGY project, Grant Agreement: 101022664

Baroni, A.; Barradas, J.; Canteli, P.; Carneiro, J.; Casacão, J.; Faria, P.; Fernandes, J.; Fernandez de Arévalo, E.; Fleury, M.; García Crespo, J.; García Fernández-Valderrama, D.; Koukouzas, N.; Marques da Silva, D.; Martinez, J.; Mediato, J.; Moita, P.; Pangaro Bedoya, F.; Pedro, J.; Pina, B.; Ribeiro, C.; Rousseau, N.; Tyrologou, P.; Wilkinson, M. (2023). Deliverable WP2/D2.8 – Report on Geomechanical results for the 3 areas. PilotSTRATEGY project, Grant Agreement: 101022664

Ben Rhouma S. (Ed.), et al. (2026), Report on $CO_2$ fate on the long-term. *Deliverable WP3/D3.4, EU H2020 PilotSTRATEGY project 101022664 report.*

Eaton, B. A. (1969). Fracture gradient prediction and its application in oilfield operations. *Journal of Petroleum Technology*, 21 (10), 1353–1360 (paper no. SPE-2163-PA). DOI: 10.2118/2163-PA

Eaton, B. A. (1975). The equation for geopressure prediction from well logs. SPE Annual Fall Technical Conference and Exhibition, Dallas. Paper no. SPE-5544-MS. DOI: 10.2118/5544-MS

García, J., Moreno, I., Mediato, J.F., & Fernández-Canteli, P., 2024. Ebro Basin (Spain). In Bouquet, S. (Ed.), Report on static modelling with uncertainties. *Deliverable WP3/D3.2, EU H2020 PilotSTRATEGY project 101022664 report*, 139–159.

Heidbach, O., Rajabi, M., Reiter, K., and Ziegler, M. (2016). World Stress Map 2016, GFZ Data Service. DOI: 10.5880/WSM.2016.002

Horsrud, P. (2001). Estimating mechanical properties of shale from empirical correlations. *SPE Drilling & Completion*, 16 (2), 68–73 (paper no. SPE-56017-PA). DOI: 10.2118/56017-PA

Hubbert, M. K., and Willis, D. G. (1957). Mechanics of hydraulic fracturing. *Transactions of the AIME*, 210, 153–168.

Jaeger, J. C., Cook, N. G. W., and Zimmerman, R. (2007). *Fundamentals of rock mechanics*. Wiley-Blackwell.

Knauss, K.G. & Wolery, T.J. (1987/1988). Dissolution kinetics of quartz as a function of pH and time at 70°C. Geochimica et Cosmochimica Acta, 52(1), 43–53. DOI: 10.1016/0016-7037(88)90055-5. [osti.gov]

Matthews, W. R., and Kelly, J. (1967) How to predict formation pressure and fracture gradient. *Oil and Gas Journal*, 65, 92–1066.

McNally, G.H. (1987). Estimation of coal measures rock strength using sonic and neutron logs. *Geoexploration*, 24 (4–5), 381–395. DOI: 10.1016/0016-7142(87)90008-1

Miller, R. L., and Bower, F. M. (1963). Study of abnormal pressures in deep wells. Journal of Petroleum Technology, 15(9), 1021–1026.

Militzer, H., and Stoll, R. (1973). Einige Beitrageder geophysics zur primadatenerfassung im Bergbau, Neue Bergbautechnik. *Lipzig*, 3 (1), 21–25.

Nourifard, N., Pasternak, E., and Lebedev, M. (2021). Simultaneous experimental study of dynamic and static Young's moduli in sandstones. *Exploration Geophysics*, 52 (6), 601–611. DOI: 10.1080/08123985.2020.1865107

The PilotSTRATEGY project has received funding from the European Union's Horizon 2020 research and innovation programme under grant agreement No. 101022664

Ogundipe, O.M., and Mackay, E.J. (2025) Modelling halite precipitation during $CO_2$ injection in a heterogeneous reservoir: A North Sea field case. SPE International Conference on Oilfield Chemistry, Galveston. Paper no. SPE-224277-MS. DOI: 10.2118/224277-MS

Potter II, R. W., Babcock, R. S., and Brown, D. L. (1977). A new method for determining the solubility of salt in aqueous solutions at elevated temperatures. *Journal of Research of the U.S. Geological Survey*, 5 (3), 389–395.

Rezk, M.G. & Ibrahim, A.F. (2025). Impact of rock mineralogy on reactive transport of $CO_2$ during carbon sequestration in a saline aquifer. Journal of Petroleum Exploration and Production Technology, 15, Article 10. (States that "Quartz exhibits minimal dissolution" under $CO_2$ sequestration reactive-transport simulations.)

Spycher, N., and Pruess, K. (2005). $CO_2$–$H_2O$ mixtures in the geological sequestration of $CO_2$. II. Partitioning in chloride brines at 12–100 °C and up to 600 bar. *Geochimica et Cosmochimica Acta*, 69 (13), 3309–3320. DOI: 10.1016/j.gca.2005.02.027

Spycher, N. and Pruess, K. (2009). A phase-partitioning model for $CO_2$–brine mixtures at elevated temperatures and pressures: Application to $CO_2$-enhanced geothermal systems. *Transport in Porous Media*, 82 (1), 173–196. DOI: 10.1007/s11242-009-9425-y

Zoback, M. D. (2010). *Reservoir geomechanics*. Cambridge University Press.

# 7. Appendix

## 7.1 Appendix – Paris Basin Region (France)

*Table 7-1: Homogenisation models and parameters for elastic properties (Bemer 2004), (Mori 1973)*

| | Law | Parameters (GPa) | | | | Biot's coeff. b |
|---|---|---|---|---|---|---|
| | | Ks | Gs | Kc | Gc | |
| **Overb./ underb.** | Mori-Tanaka | 48.8 | 13.3 | | | **1.0** |
| **COX (Caprock)** | Mori-Tanaka | 43.4 | 13.2 | | | **0.8** |
| **Dalle nacrée** | Bemer (cap) | 72.6 | 31.6 | 5.08 | 3.79 | **equation*** |
| **Comblanchien** | Bemer (cap) | 72.6 | 31.6 | 5.08 | 3.79 | **equation*** |
| **Oolithe blanche** | Bemer (cap) | 72.6 | 31.6 | 5.08 | 3.79 | **equation*** |
| **Lower bathonien** | Bemer (cap) | 72.6 | 31.6 | 5.08 | 3.79 | **equation*** |

***poroelastic (or compatibility) equation**

$$b = 1 - \frac{K}{K_s}$$

*Table 7-2: Empirical correlation and parameters for plastic properties (Bemer 2004)*

| | $f_1$ | $f_2$ | $c_1$ | $c_2$ |
|---|---|---|---|---|
| **COX (caprock)** | -0.268 | 27,3 | 16.2 | 0.060 |

The PilotSTRATEGY project has received funding from the European Union's Horizon 2020 research and innovation programme under grant agreement No. 101022664

| | | | | |
|---|---|---|---|---|
| Dalle nacrée | -0.893 | 42 | 23.7 | 0.054 |
| Comblanchien | -0.893 | 42 | 23.7 | 0.054 |
| Oolithe blanche | -0.893 | 42 | 23.7 | 0.054 |
| Lower bathonien | -0.893 | 42 | 23.7 | 0.054 |

$$c'(\phi) = c_1 e^{-c_2 \phi(\%)}$$

$$\varphi'(\phi) = f_1 \phi(\%) + f_2$$

*Table 7-3: Initial stress ratios (Vidal-Gilbert 2009), (Günzburger 2014).*

| | $S_H/S_v$ | $S_h/S_v$ |
|---|---|---|
| Overb./ underb. | 1.0 | 0.8 |
| COX (Caprock) | 1.0 | 0.74 |
| Dalle nacrée | 1.0 | 0.6 |
| Comblanchien | 1.0 | 0.6 |
| Oolithe blanche | 1.0 | 0.6 |
| Lower bathonien | 1.0 | 0.68 |

a)

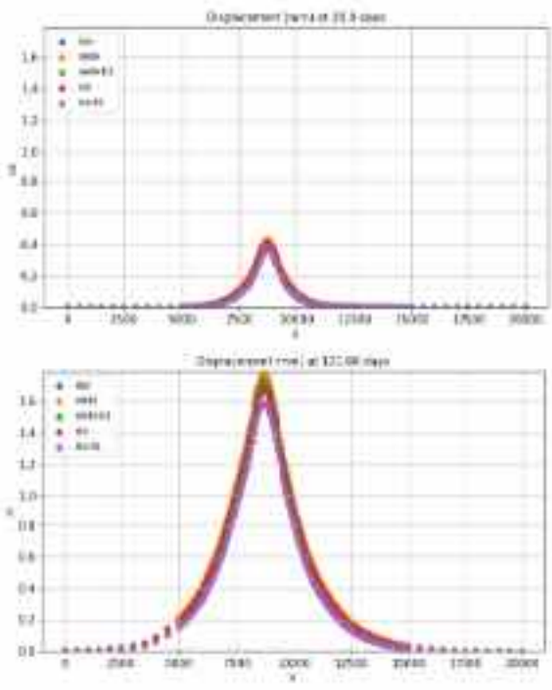

b)

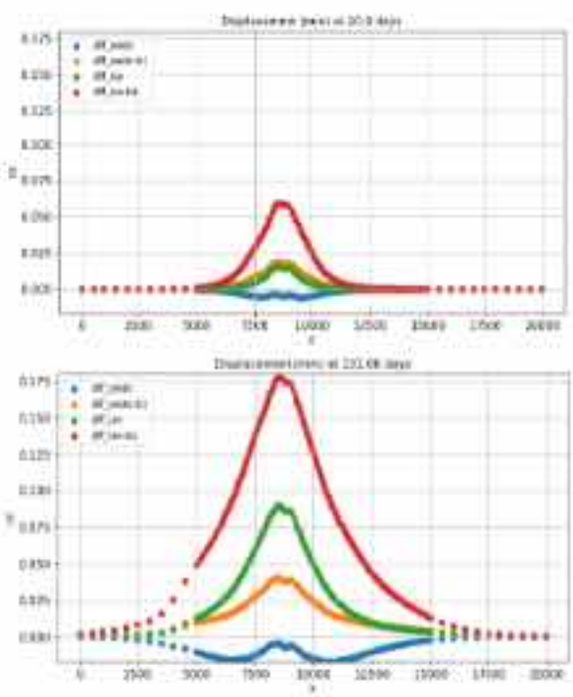

The PilotSTRATEGY project has received funding from the European Union's Horizon 2020 research and innovation programme under grant agreement No. 101022664

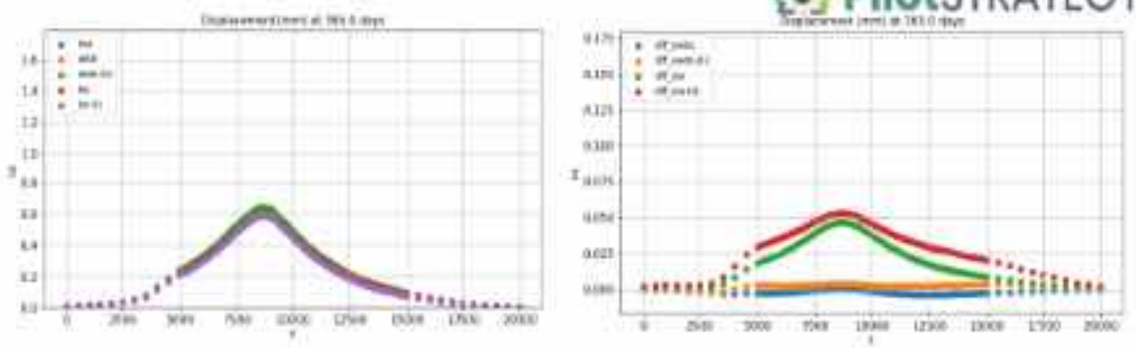

*Figure 7-1: a) Surface displacement on cross-section for the P50 Min case at 20 days, 131.6 days (end of injection) and 1 year. Comparison of the iterative model (iter) with 4 one-way models based on different assumptions for compressibility calculation. b) difference in displacement between iterative model and one-way models.*

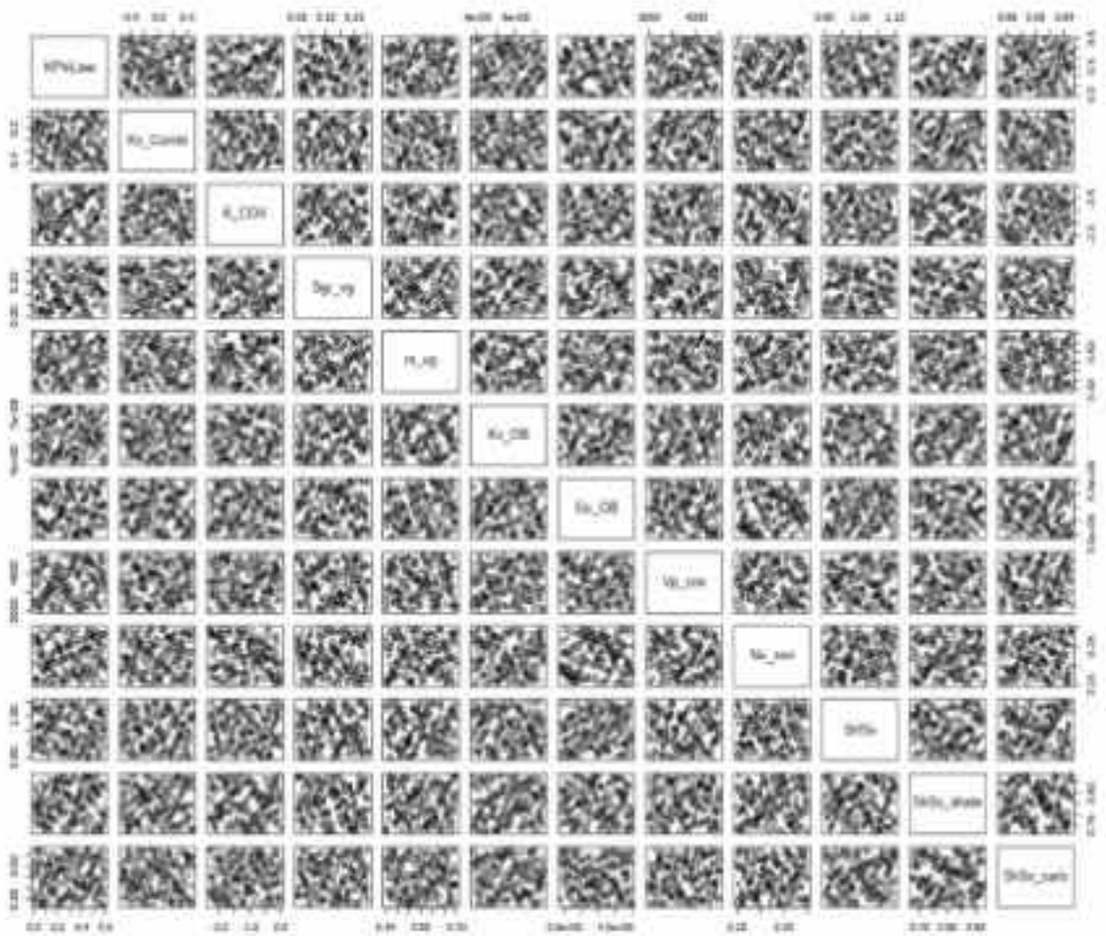

*Figure 7-2: Design of Experiments for the enlarged uncertainties study with 12 uncertain parameters (175 numerical experiments)*

The PilotSTRATEGY project has received funding from the European Union's Horizon 2020 research and innovation programme under grant agreement No. 101022664

## 7.2 Appendix – Lusitanian Basin (Portugal)

### 7.2.1 Injectivity Integrity (Uncertainty Analysis)

#### *7.2.1.1 Impacts of injection flow rate*

The impact of increasing the $CO_2$ injection rate from the base case value of 0.5 Mt/y to a higher rate of approximately 1 Mt/y (1 301 440 $Sm^3$/day) was evaluated to assess the sensitivity of near-wellbore processes and injectivity integrity to operational conditions.

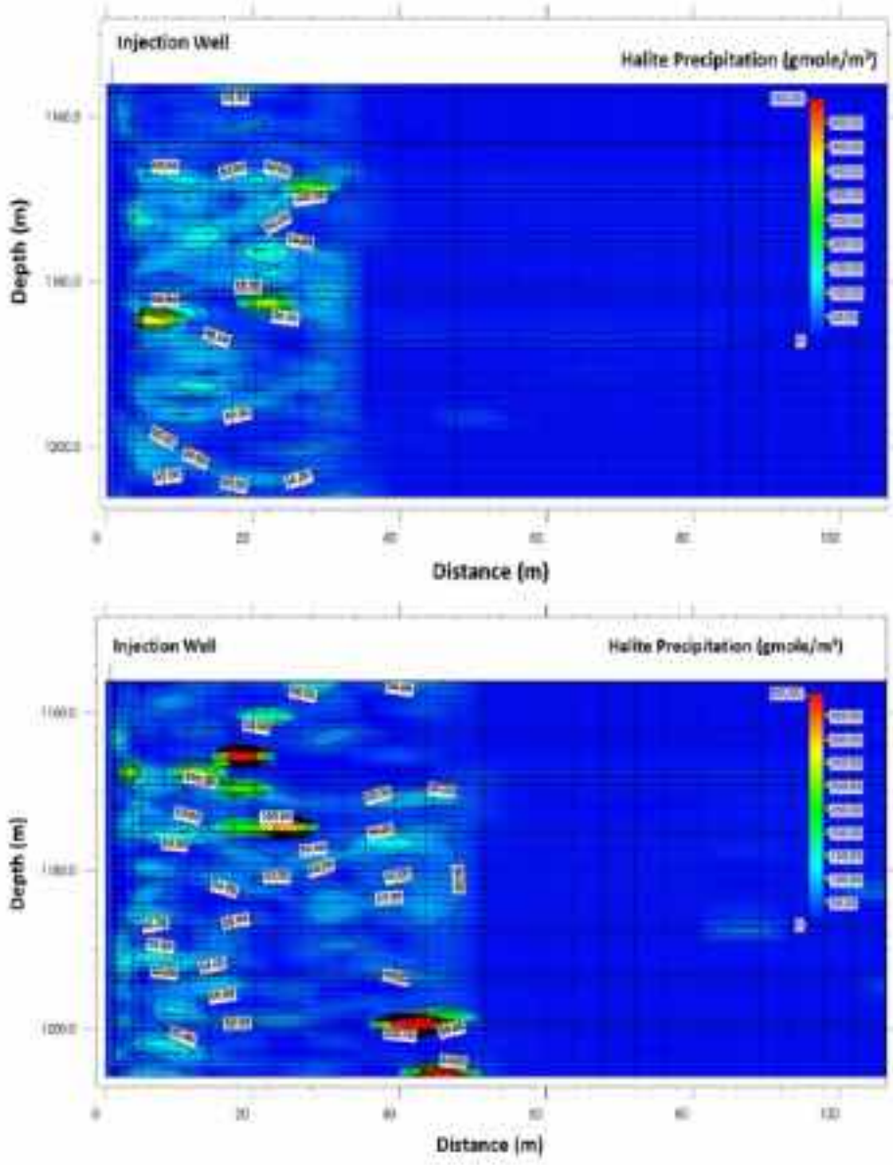


*Figure 7.2-1: Vertical section of the spatial distribution of the halite precipitation near the injection well for the base case scenario of 0.5 Mt/y (top) and the higher case scenario of 1Mt/y (bottom), after 30 years of injection.*

Under base case conditions, halite precipitation remains confined to the immediate near-wellbore region, with moderate peak values and limited lateral extent, consistent with previously discussed localized injectivity effects. Increasing the injection rate leads to both higher precipitation magnitudes and a broader spatial distribution of halite, with peak concentrations exceeding those of the base case and extending laterally to distances of up to approximately 50 m from the well (Figure 6.2-1). This intensification and vertical spreading of halite accumulation reflect enhanced brine displacement and stronger drying effects associated with

The PilotSTRATEGY project has received funding from the European Union's Horizon 2020 research and innovation programme under grant agreement No. 101022664

higher $CO_2$ fluxes. Despite this amplification, halite precipitation remains predominantly localized around the injection well, indicating that even under increased injection rates, salt-related impacts are controlled and do not propagate extensively into the reservoir.

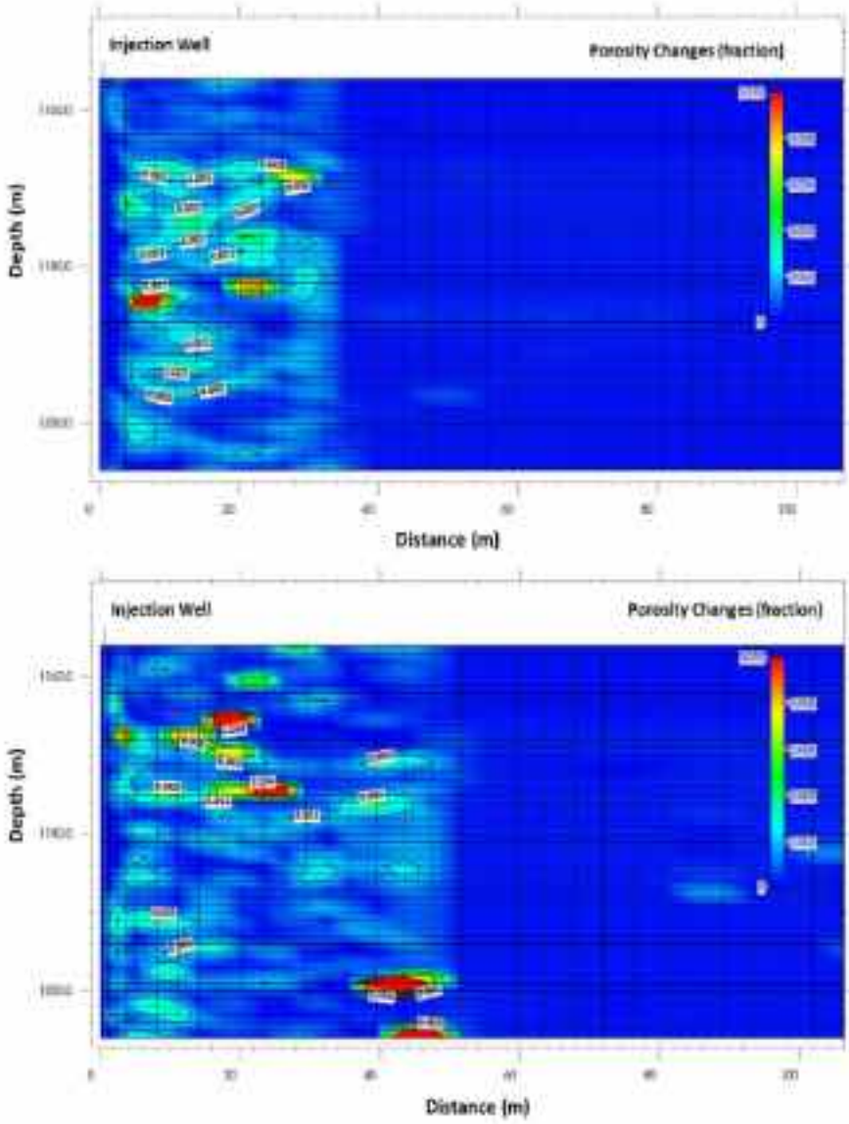


*Figure 6.2-2: Vertical section of the spatial distribution of the porosity changes near the injection well for the base case scenario of 0.5 Mt/y (top) and the higher case scenario of 1Mt/y (bottom), after 30 years of injection.*

In the base case, porosity reductions are modest and strongly localized within the first approximately 20–30 m from the well, with maximum decreases on the order of approximately 0.008–0.010 (Figure 6.2-2). At the higher injection rate, porosity reduction becomes both more intense and more spatially extensive, with peak values of similar or slightly higher magnitude but extending laterally to approximately 40–50 m and affecting a broader vertical interval. These enhanced porosity losses reflect the greater degree of salt precipitation driven by higher injection rates, leading to more pronounced pore clogging in the near-wellbore zone. Nevertheless, porosity changes remain negligible in the far field, indicating that even under the higher injection rate scenario, reservoir-scale porosity is largely preserved and that the main impacts remain confined to the vicinity of the injection well.

The PilotSTRATEGY project has received funding from the European Union's Horizon 2020 research and innovation programme under grant agreement No. 101022664

The temporal response of injectivity highlights the operational implications of increasing the injection rate from 0.5 Mt/y (base case) to 1 Mt/y (higher case). An early-time injectivity adjustment is observed during the initial days to months of injection, as indicated by the star (or half-star) symbols in Figures 6.2-3 and 6.2-4. These markers reflect transient behaviour associated with well start-up conditions, including rapid pressure build-up and near-well saturation redistribution. However, unlike what might be expected under severe injectivity impairment, the higher-rate scenario does not exhibit sustained rate limitation. Instead, the target injection rate of approximately 2700 t/day is achieved and maintained throughout the injection period, resulting in a cumulative injected mass of about $3.0 \times 10^7$ tonnes after 30 years, compared to approximately $1.5 \times 10^7$ tonnes for the base case (Figure 6.2-3).

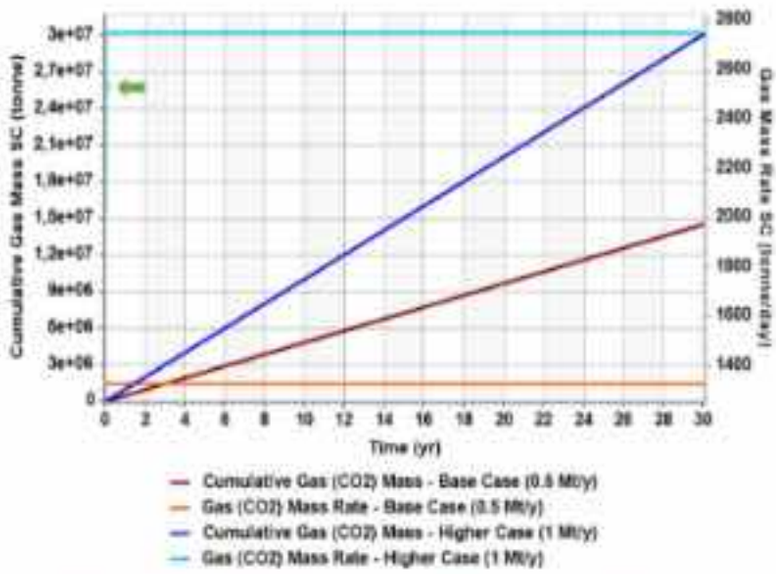


*Figure 6.2-3: Evolution of the cumulative gas ($CO_2$) mass, and gas ($CO_2$) mass rate for the base case scenario 0.5 Mt/y and the higher case scenario of 1Mt/y over the injection period of 30 years. The green arrow point to the star (or half-star) symbol to indicate some injectivity issues at the beginning of the injection period (during the first days/months).*

The reservoir pressure response reflects the imposed injection rates. As shown in Figure 6.2-4, the higher injection rate scenario leads to a slightly higher reservoir pressure compared to the base case, stabilizing around approximately 12650–12700 kPa after 30 years, compared to about 13800–13900 kPa for the base case. These pressures remain well below the imposed bottom-hole pressure constraint of 16500 kPa and below expected fracture pressure limits, confirming that the reservoir can accommodate the increased injection rate without exceeding operational pressure thresholds. The initial transient pressure adjustment observed in both cases corresponds to early-time near-well flow establishment and saturation equilibration rather than sustained injectivity impairment.

The injectivity index evolution (Figure 6.2-5) confirms that injectivity remains high and stable in both scenarios over the full injection period. The injectivity index stabilizes at approximately 2050–2100 $Sm^3$/day/kPa for the base case and slightly lower values of approximately 2030–2060 $Sm^3$/day/kPa for the higher injection case. This corresponds to a marginal injectivity reduction of approximately 1–2% in the higher-rate scenario. The small early-time fluctuations correspond to transient flow and pressure equilibration rather than permanent formation damage. Importantly, no progressive decline in injectivity is observed over time, indicating that near-well effects such as salt precipitation and localized porosity reduction do not significantly impair long-term injection performance.

The PilotSTRATEGY project has received funding from the European Union's Horizon 2020 research and innovation programme under grant agreement No. 101022664

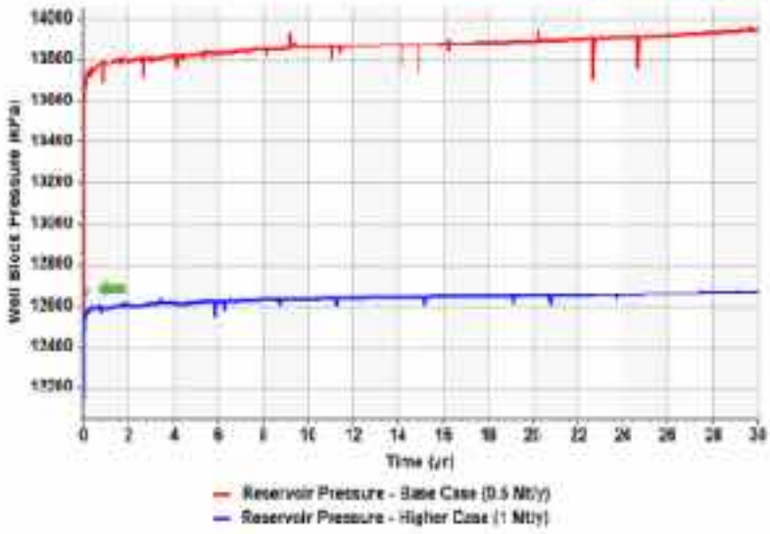


*Figure 6.2-4: Evolution of the reservoir pressure for the base case scenario 0.5 Mt/y and the higher case scenario of 1Mt/y over the injection period of 30 years. The green arrow point to the star (or half-star) symbol to indicate some injectivity issues at the beginning of the injection period (during the first days/months).*

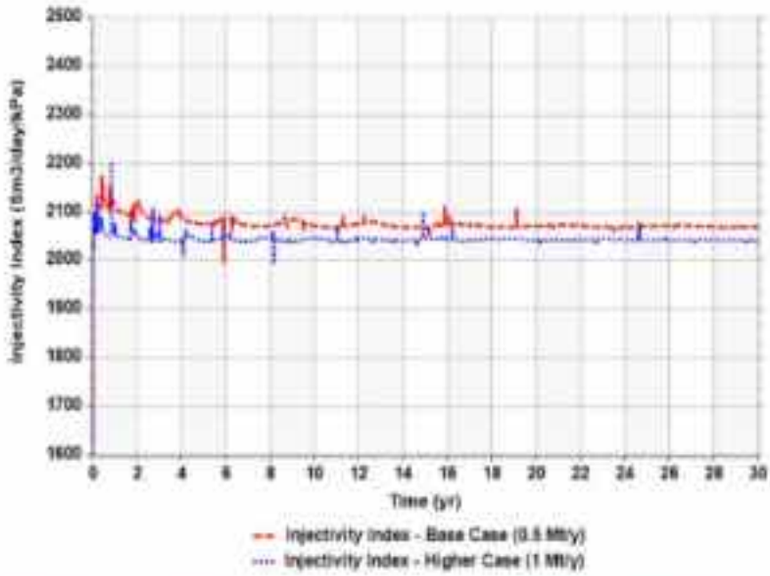


*Figure 6.2-5: Evolution of the reservoir injectivity for the base case scenario 0.5 Mt/y and the higher case scenario of 1Mt/y over the injection period of 30 years.*

Overall, increasing the injection rate from 0.5 Mt/y to 1 Mt/y does not result in significant or sustained injectivity loss. Any early-time injectivity adjustments are transient and operationally manageable, and long-term injectivity remains essentially stable. The minor injectivity reduction observed in the higher-rate scenario (<2%) confirms that salt precipitation and associated petrophysical changes remain localized and do not compromise the capacity of the reservoir to sustain higher injection rates over the 30-year injection period.

#### *7.2.1.2 Impacts of reservoir salinity*

The impact of reservoir salinity on near-wellbore processes and injectivity integrity was evaluated by comparing the base case salinity of 56 g/L with a lower-salinity scenario of 10 g/L and a higher-salinity scenario of 130 g/L.

The PilotSTRATEGY project has received funding from the European Union's Horizon 2020 research and innovation programme under grant agreement No. 101022664

Under low-salinity conditions (10 g/L), halite precipitation is effectively suppressed, with only negligible amounts forming in the near-wellbore region (Figure 6.2-6). This reflects the reduced availability of dissolved NaCl and the lower likelihood of reaching halite saturation during $CO_2$-induced brine drying. In contrast, increasing reservoir salinity to 130 g/L leads to a marked intensification of halite precipitation, with substantially higher peak concentrations and a much broader near-wellbore footprint. In the high-salinity scenario, halite accumulation extends laterally to approximately 40-50 m from the injection well and affects a thicker vertical interval compared with both the base and low-salinity cases. Despite this amplification, salt precipitation remains predominantly localized around the wellbore, indicating that even under highly saline conditions, halite-related impacts do not propagate extensively into the far field.

For the low-salinity case, porosity reductions are minimal and remain close to zero throughout most of the domain, confirming that the suppression of halite precipitation effectively preserves pore space in the near-wellbore region. In the base case, porosity losses are modest and localized, with maximum reductions on the order of approximately 0.008-0.010 within the first 20-30 m from the well (Figure 6.2-7). In contrast, the high-salinity scenario exhibits substantially larger and more spatially extensive porosity reductions, with localized decreases approaching the upper bound of the colour scale and extending laterally to approximately 40-50 m while also affecting a broader vertical interval. These enhanced porosity losses are a direct consequence of the intensified halite precipitation under high-salinity conditions, leading to stronger pore clogging and reduced effective flow capacity near the wellbore.

Despite differences in reservoir salinity, long-term injection performance remains stable across all scenarios. As shown in Figure 6.2-8, the cumulative injected $CO_2$ mass increases linearly over the 30-year injection period in all cases, reaching approximately $1.45 \times 10^7$ tonnes, and the imposed injection rate is consistently maintained. This confirms that injectivity remains sufficient to sustain the target injection rate regardless of salinity conditions, and no sustained injection interruptions or rate reductions occur.

The PilotSTRATEGY project has received funding from the European Union's Horizon 2020 research and innovation programme under grant agreement No. 101022664

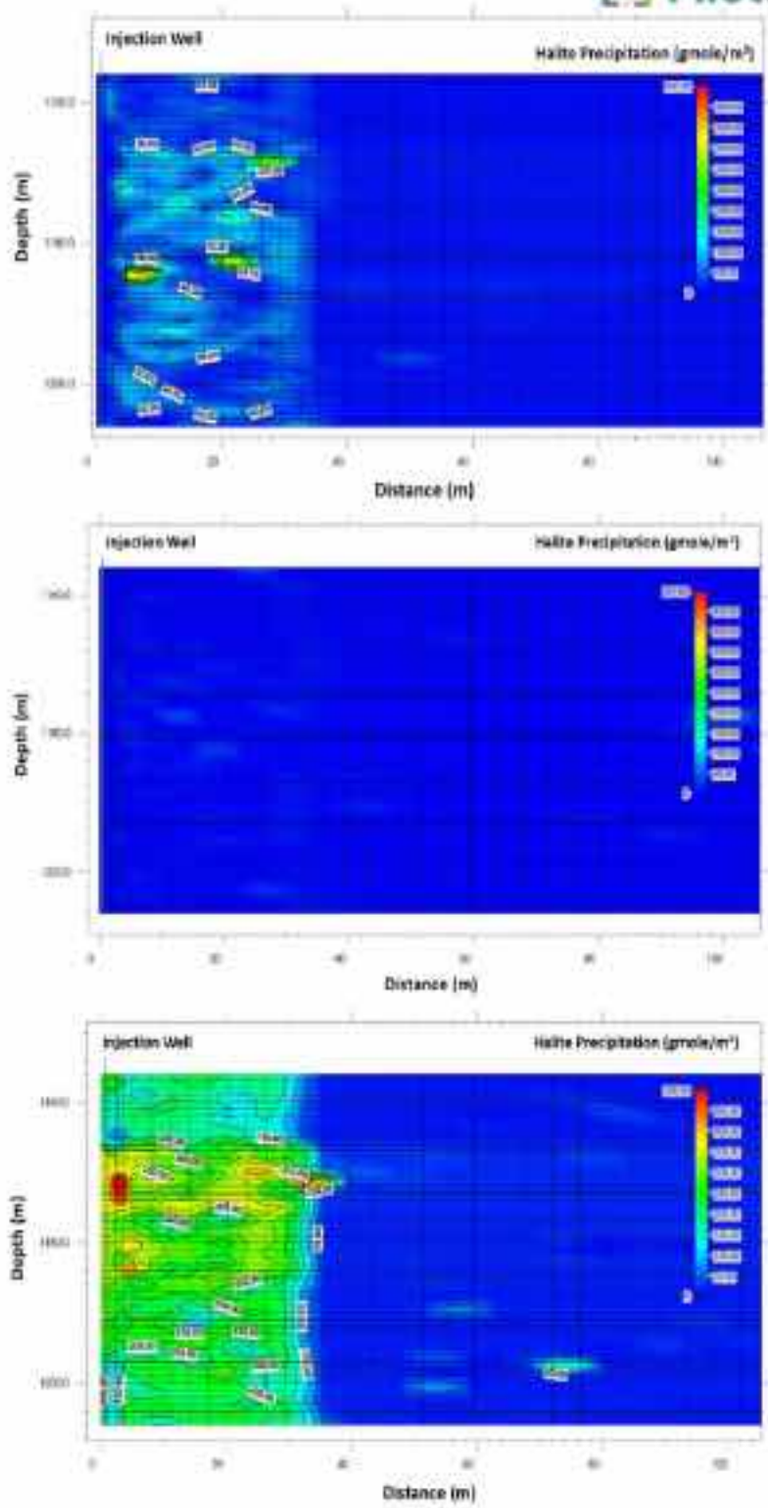


*Figure 6.2-6: Vertical section of the spatial distribution of the halite precipitation for the base (top), lower (middle) and higher (bottom) case scenarios of reservoir salinity of 56 g/L 10 g/L and 130 g/L, respectively, after 30 years of injection.*

The PilotSTRATEGY project has received funding from the European Union's Horizon 2020 research and innovation programme under grant agreement No. 101022664

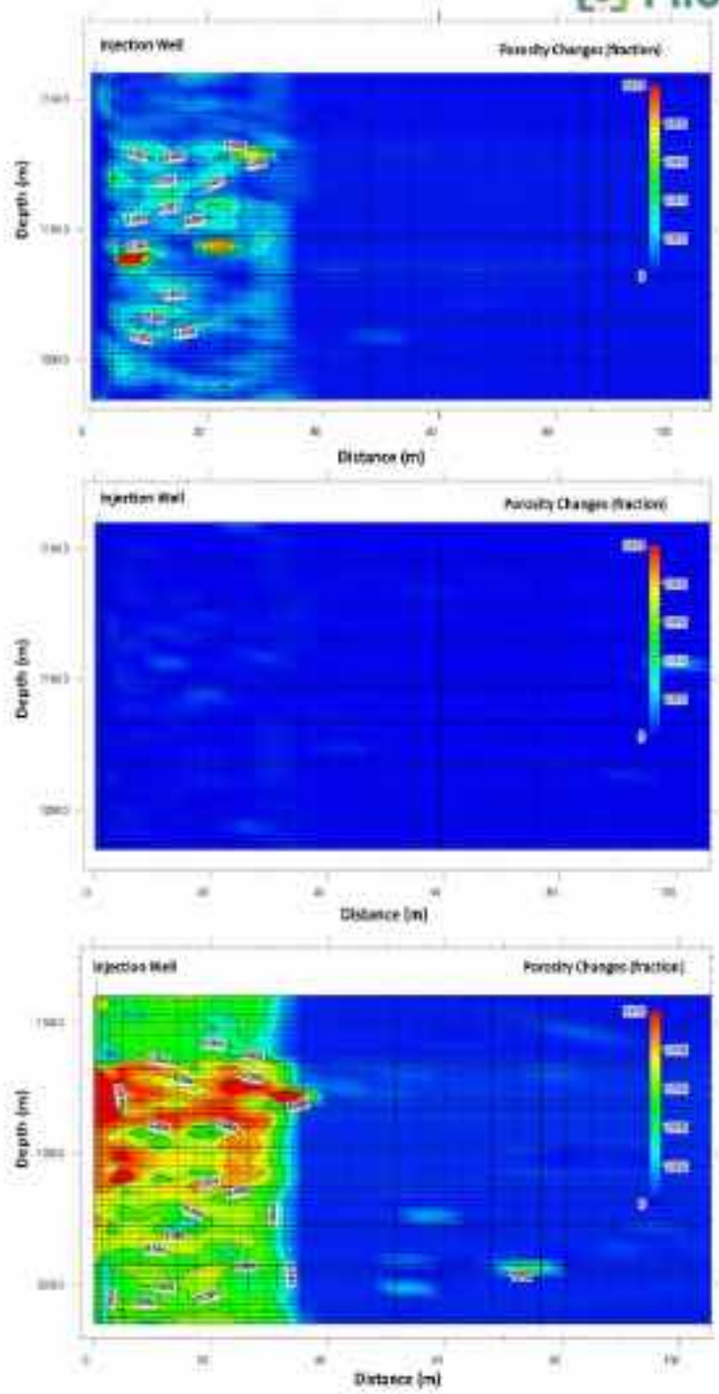


*Figure 6.2-7: Vertical section of the spatial distribution of the porosity changes for the base (top), lower (middle) and higher (bottom) case scenarios of reservoir salinity of 56 g/L 10 g/L and 130 g/L, respectively, after 30-years of injection.*

The PilotSTRATEGY project has received funding from the European Union's Horizon 2020 research and innovation programme under grant agreement No. 101022664

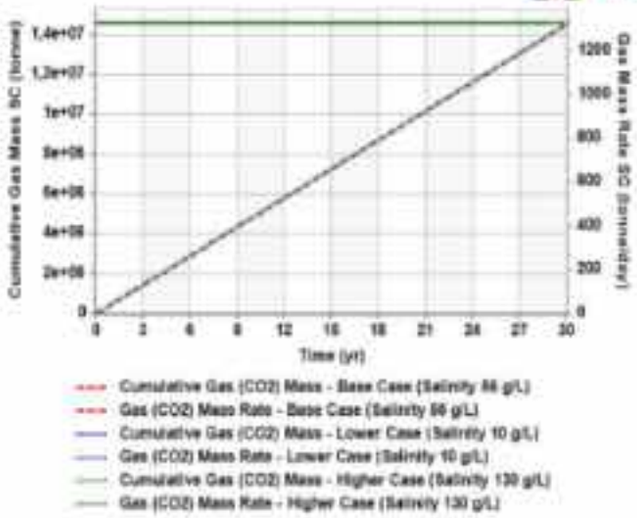


*Figure 6.2-8: Evolution of the cumulative gas ($CO_2$) mass, and gas ($CO_2$) mass rate for the base, lower and higher case scenarios of reservoir salinity of 56 g/l, 10 g/l, and 130 g/l, respectively, after 30-years of injection.*

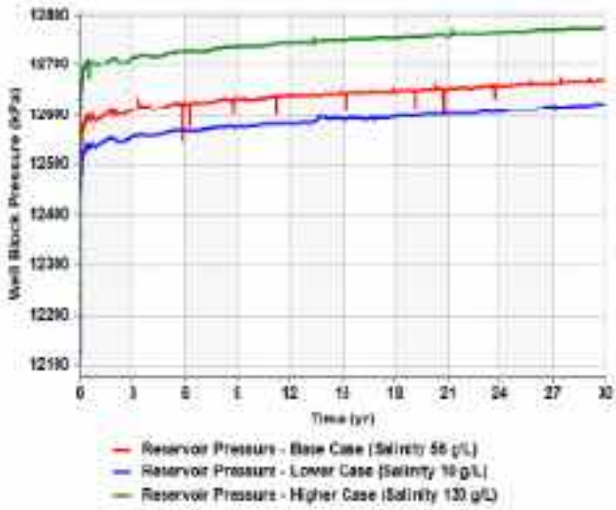


*Figure 6.2-9: Evolution of the reservoir for the base, lower and higher case scenarios of reservoir salinity of 56 g/l, 10 g/l, and 130 g/l, respectively, after 30-years of injection.*

Reservoir pressure responses vary systematically with salinity, as shown in Figure 6.2-9. The high-salinity case (130 g/L) exhibits the highest reservoir pressure, stabilizing around approximately 12750–12780 kPa after 30 years, followed by the base case (56 g/L) at approximately 12650–12680 kPa, and the low-salinity case (10 g/L) at approximately 12600–12630 kPa. The pressure difference between the low- and high-salinity scenarios is approximately 120–150 kPa, corresponding to about 1% of the absolute pressure level. This behaviour reflects the salinity-dependent reduction in $CO_2$ solubility and increased halite precipitation potential at higher salinity, which reduces effective pore space and increases flow resistance, resulting in slightly higher reservoir pressure. However, reservoir pressure remains well below operational and fracture pressure limits in all scenarios, indicating safe and sustainable injection conditions.

The injectivity index evolution (Figure 6.2-10) provides clear evidence of salinity-dependent injectivity behaviour. The low-salinity and base case scenario show very similar injectivity values, stabilizing around approximately 2050–2100 $Sm^3$/day/kPa. In contrast, the high-salinity case exhibits a

The PilotSTRATEGY project has received funding from the European Union's Horizon 2020 research and innovation programme under grant agreement No. 101022664

consistently lower injectivity index of approximately 1850–1900 Sm³/day/kPa. This represents an injectivity reduction of approximately 8–12% relative to the base and low-salinity cases. The reduction occurs primarily during the early injection period and stabilizes thereafter, with no progressive decline over time. This indicates that salt precipitation and associated porosity reduction are localized near the wellbore and reach a dynamic equilibrium, after which injectivity remains stable.

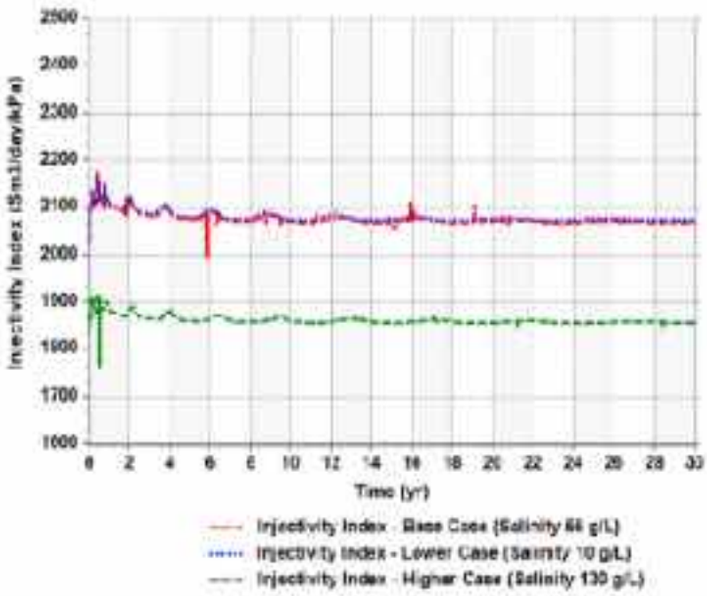


*Figure 6.2-10: Evolution of the injectivity index for the base, lower and higher case scenarios of reservoir salinity of 56 g/L 10 g/L and 130 g/L, respectively, after 30-years of injection.*

Overall, reservoir salinity has a measurable but moderate impact on injectivity. Higher salinity increases the extent of salt precipitation and near-wellbore flow resistance, resulting in a limited injectivity loss of approximately 8–12%. However, this reduction does not impair the ability to sustain the target injection rate over the long term. Injectivity remains stable after the initial adjustment period, and no progressive degradation occurs. These results demonstrate that while reservoir salinity influences the magnitude of near-wellbore impairment, its overall impact on long-term injectivity and storage performance remains limited under the simulated conditions.

#### *7.2.1.3 Impacts of injection temperature*

The impact of $CO_2$ bottom-hole injection temperature on near-wellbore processes and injectivity integrity was evaluated by comparing the base case injection bottom-hole temperature of 26°C with a lower-temperature scenario of 20°C and a higher-temperature scenario of 40°C. The results indicate that injection temperature exerts a secondary control on halite precipitation, porosity reduction, and gas flow resistance when compared with injection rate and reservoir salinity, primarily affecting the intensity of near-wellbore processes rather than their spatial extent.

The PilotSTRATEGY project has received funding from the European Union's Horizon 2020 research and innovation programme under grant agreement No. 101022664

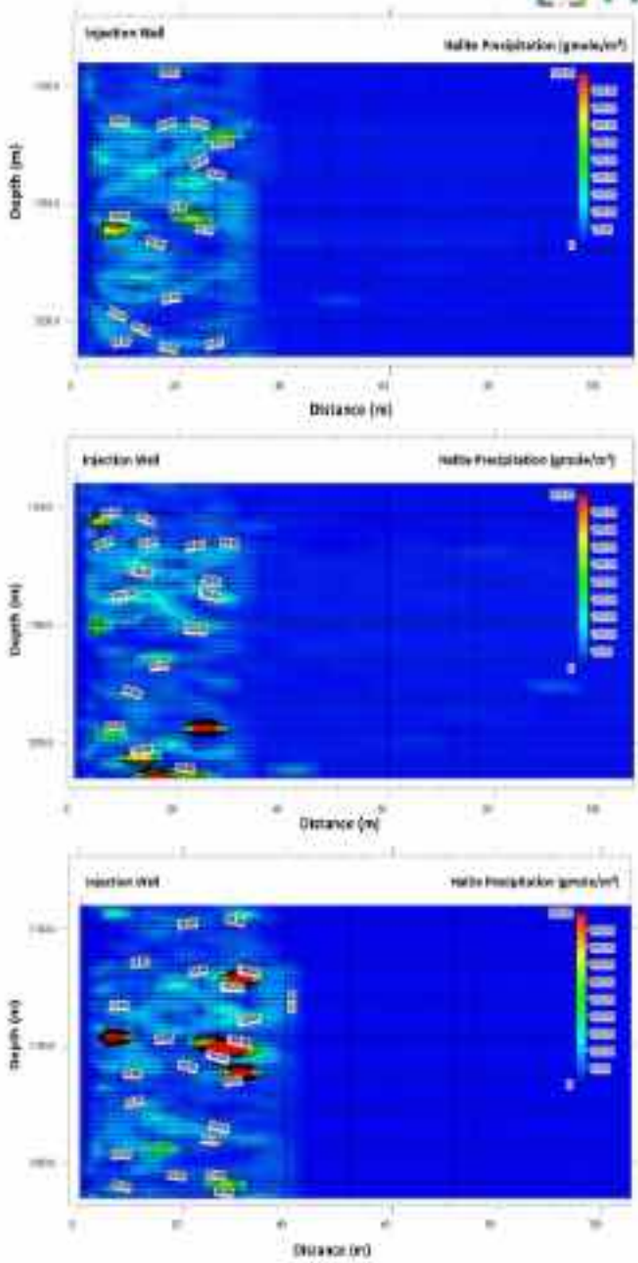


*Figure 6.2-11: Vertical section of the spatial distribution of the halite precipitation for the base (top), lower (middle) and higher (bottom) case scenarios of CO2 injection temperature of 26°C, 20°C and 40°C, respectively, after 30-years of injection.*

Under lower injection temperature conditions (20°C), halite precipitation is slightly intensified relative to the base case, reflecting enhanced brine cooling and increased water vaporization potential during $CO_2$ injection. Peak halite concentrations are modestly higher than those of the base case and remain confined to the near-wellbore region, with the affected zone extending laterally to approximately 20-30 m from the injection well (Figure 6.2-11). In contrast, increasing the injection temperature to 40°C results in a slight reduction in halite precipitation intensity, with lower peak concentrations and a more restricted spatial footprint. In all temperature scenarios, halite precipitation remains strongly localized around the injection well and rapidly diminishes beyond approximately 30-40 m, indicating that temperature variations do not fundamentally alter the spatial confinement of salt-related impacts.

The PilotSTRATEGY project has received funding from the European Union's Horizon 2020 research and innovation programme under grant agreement No. 101022664

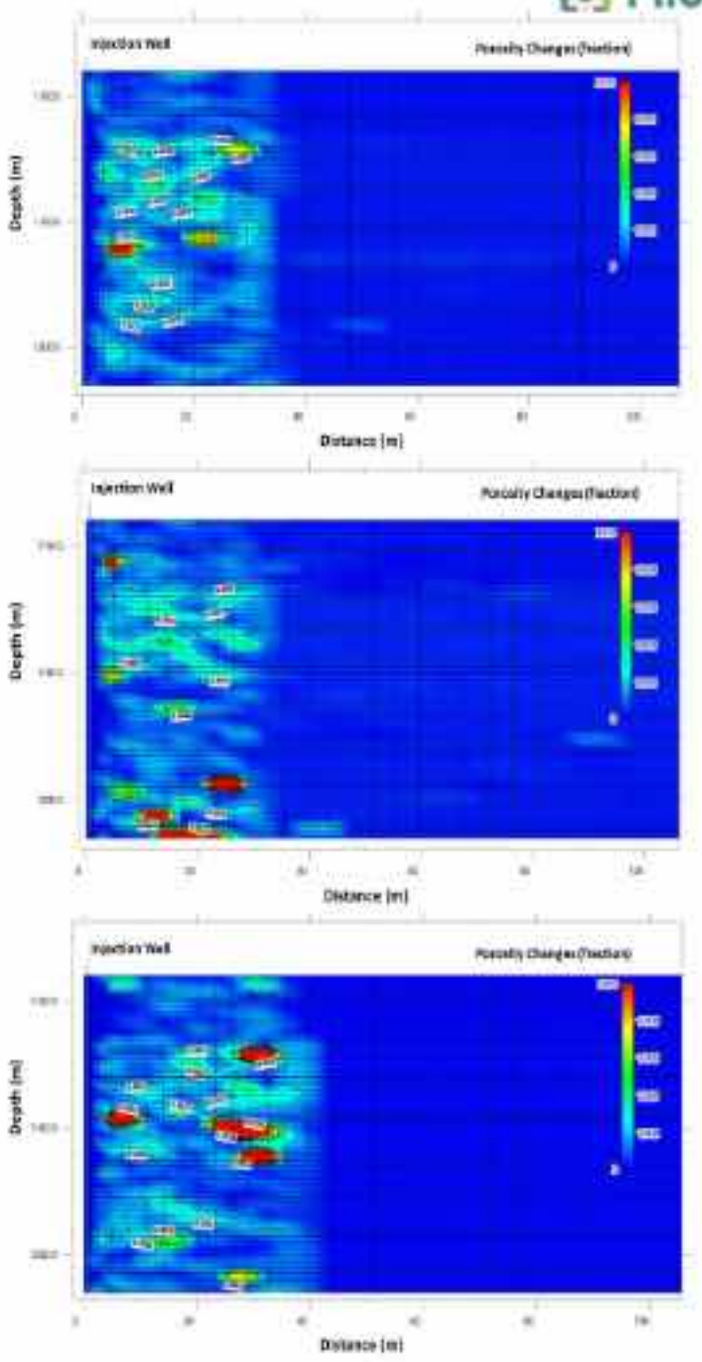


*Figure 6.2-12: Vertical section of the spatial distribution of the porosity changes for the base (top), lower (middle) and higher (bottom) case scenarios of $CO_2$ injection temperature of 26ºC, 20ºC and 40ºC, respectively, after 30-years of injection.*

In the lower-temperature case, porosity reductions are slightly enhanced relative to the base case, with localized decreases approaching approximately 0.008-0.010 in the near-wellbore region (Figure 6.2-12). The base case exhibits similar but marginally smaller porosity losses, while the higher-temperature scenario displays the weakest porosity reduction, generally below approximately 0.006-0.008. In all cases, porosity changes remain confined to the first 20–30 m from the well and are negligible in the far field, confirming that injection temperature primarily modulates the magnitude of near-wellbore pore-space degradation without inducing broader reservoir-scale impacts.

Despite variations in injection temperature, long-term injection performance remains stable across all scenarios (Figure 6.2-13). In all three cases (20°C, 26°C, and 40°C), the cumulative injected $CO_2$ mass

The PilotSTRATEGY project has received funding from the European Union's Horizon 2020 research and innovation programme under grant agreement No. 101022664

increases linearly over the 30-year injection period, reaching approximately 1.45x10⁷ tonnes, and the imposed injection rate of approximately 1200–1300 t/day is consistently maintained. This confirms that injection temperature does not impose operational limitations on the ability to sustain the target injection rate, and no sustained injectivity decline is observed.

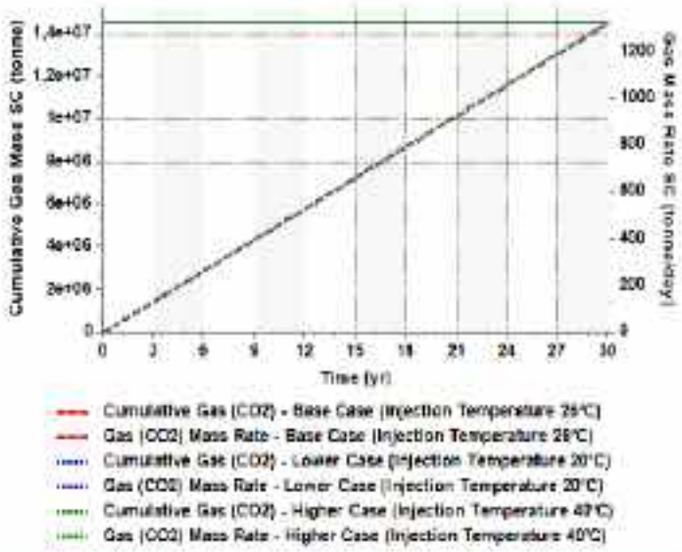


*Figure 6.2-13: Evolution of the cumulative gas ($CO_2$) mass, and gas ($CO_2$) mass rate for the base, lower and higher case scenarios of $CO_2$ injection temperature of 26ºC, 20ºC and 40ºC, respectively, after 30-years of injection.*

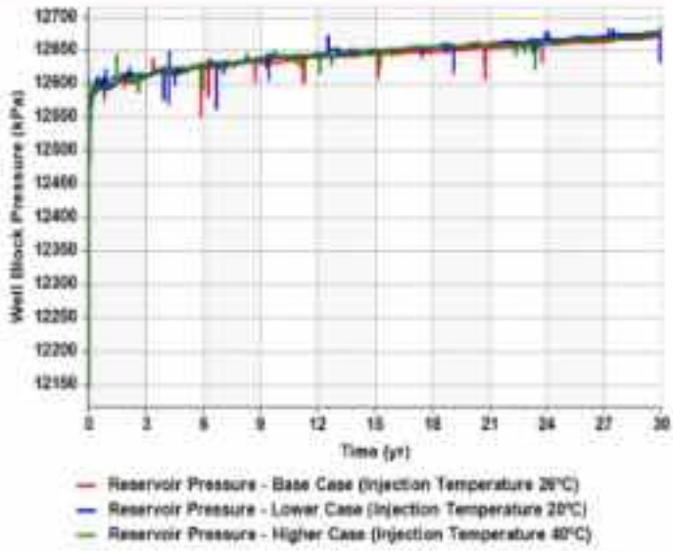


*Figure 6.2-14: Evolution of the reservoir for the base, lower and higher case scenarios of $CO_2$ injection temperature of 26ºC, 20ºC and 40ºC, respectively, after 30-years of injection.*

Reservoir pressure evolution shows only minor differences between temperature scenarios (Figure 6.2-14). All cases stabilize within a narrow range of approximately 12600–12670 kPa after 30 years. The lower temperature case (20°C) exhibits slightly higher reservoir pressure, while the higher temperature case (40°C) shows marginally lower pressure compared to the base case (26°C). The maximum difference between scenarios is approximately 30–50 kPa, corresponding to less than 0.5% of the absolute pressure level. These small differences reflect temperature-dependent fluid properties and salt precipitation behaviour but remain operationally insignificant, with reservoir pressures well below fracture and operational limits.

The PilotSTRATEGY project has received funding from the European Union's Horizon 2020 research and innovation programme under grant agreement No. 101022664

The injectivity index evolution (Figure 6.2-15) shows a clear but moderate temperature dependence. The higher temperature case (40°C) exhibits the highest injectivity, stabilizing at approximately 2150–2180 Sm³/day/kPa, followed by the base case (26°C) at approximately 2070–2100 Sm³/day/kPa, and the lower temperature case (20°C), which shows the lowest injectivity at approximately 1980–2000 Sm³/day/kPa. This corresponds to an injectivity reduction of approximately 3–5% in the lower temperature case relative to the base case, and an improvement of approximately 3–4% in the higher temperature case. The early-time fluctuations correspond to transient flow and thermal equilibration effects, after which injectivity stabilizes with no progressive decline over time.

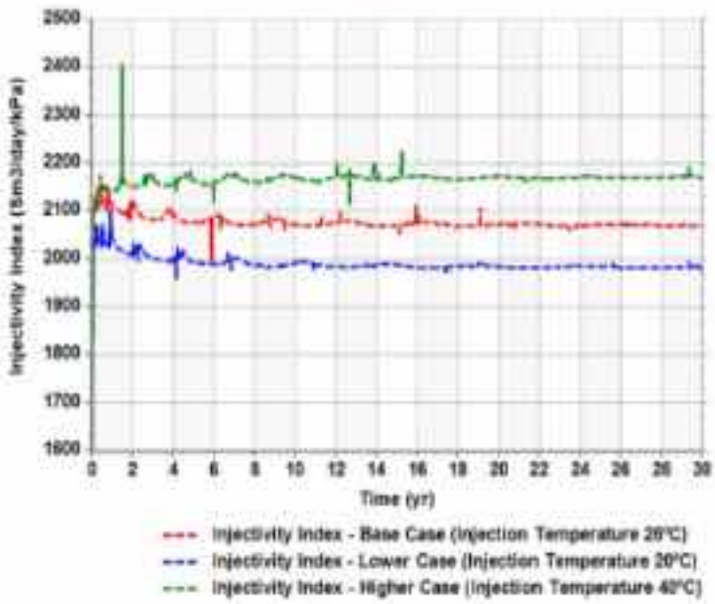


*Figure 6.2-15: Evolution of the injectivity index for the base, lower and higher case scenarios of $CO_2$ injection temperature of 26°C, 20°C and 40°C, respectively, after 30-years of injection.*

Overall, these results demonstrate that injection temperature has a measurable but limited impact on injectivity. Lower injection temperatures slightly reduce injectivity due to increase near-well flow resistance and enhanced salt precipitation potential, while higher temperatures improve injectivity. However, the magnitude of injectivity loss remains small (less than approximately 5%), and no progressive injectivity degradation occurs over the injection period. These findings confirm that injection temperature is a secondary control on injectivity performance compared to parameters such as reservoir salinity and injection rate, and does not compromise long-term injection feasibility under the simulated conditions.

#### *7.2.1.4 Impacts of joint increase of injection flow rate and reservoir salinity*

The combined impact of increasing both the $CO_2$ injection flow rate and reservoir salinity was evaluated by comparing the base case scenario (0.5 Mt/y and 56 g/L) with a compounded worst-case scenario (1 Mt/y and 130 g/L). This joint perturbation represents the most unfavourable operational and geochemical conditions considered in the uncertainty analysis and provides an upper-bound estimate of near-wellbore injectivity loss.

The compounded worst-case scenario exhibits a pronounced intensification of halite precipitation relative to the base case, reflecting the effect of higher $CO_2$ flux and elevated dissolved salt content. Peak halite concentrations are substantially higher and extend over a much broader near-wellbore

The PilotSTRATEGY project has received funding from the European Union's Horizon 2020 research and innovation programme under grant agreement No. 101022664

footprint, with salt accumulation laterally propagating to approximately 40-50 m from the injection well and affecting a thicker vertical interval (Figure 6.2-16). In contrast, the base case remains characterized by moderate halite precipitation confined to the first approximately 20-30 m. Despite the strong amplification in the worst-case scenario, halite precipitation remains spatially localized around the injection well, indicating that even under the most adverse conditions considered, salt-related impacts do not propagate into the far-field reservoir.

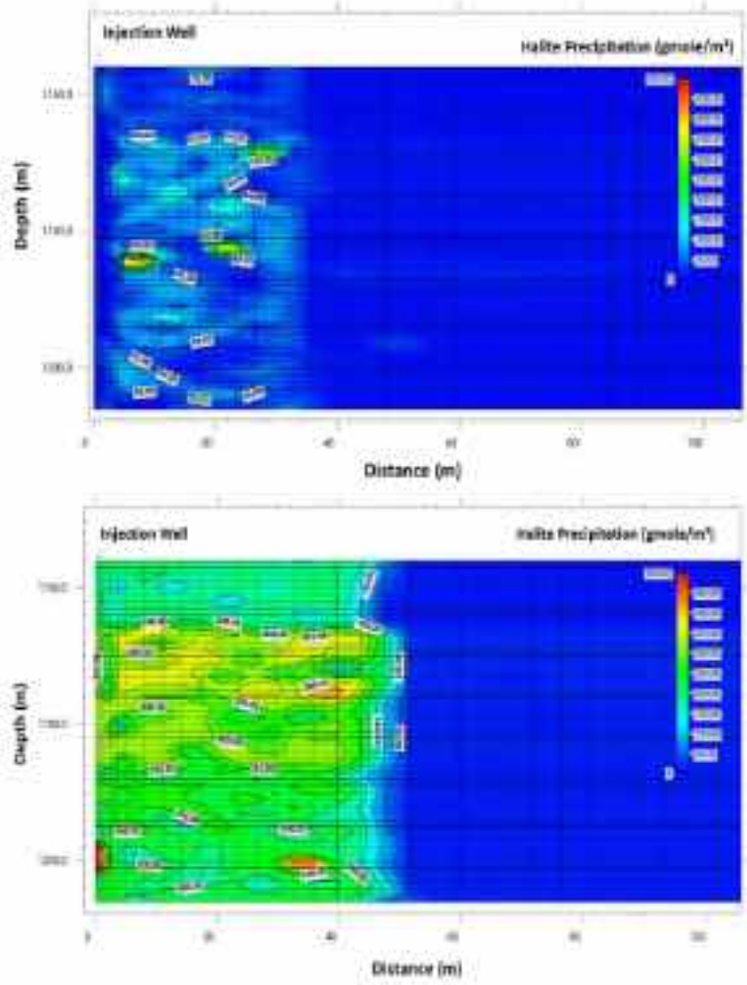


*Figure 6.2-16: Vertical section of the spatial distribution of the halite precipitation for the base case scenario (top) and the worst case scenario of 1Mt/y and 180 g/l (bottom), after 30-years of injection.*

In the base case, porosity reductions are modest and localized, with maximum decreases on the order of approximately 0.008-0.010 within the near-wellbore region (Figure 6.2-17). In the worst-case scenario, porosity losses are significantly intensified and more spatially extensive, with localized reductions approaching approximately 0.03-0.04 and extending laterally to approximately 40-50 m. These enhanced porosity losses reflect the combined effect of intensified halite precipitation and increased brine drying associated with the higher injection rate and salinity. Nevertheless, porosity changes remain negligible in the far field, confirming that even under compounded adverse conditions, pore-space degradation remains confined to the vicinity of the injection well.

The PilotSTRATEGY project has received funding from the European Union's Horizon 2020 research and innovation programme under grant agreement No. 101022664

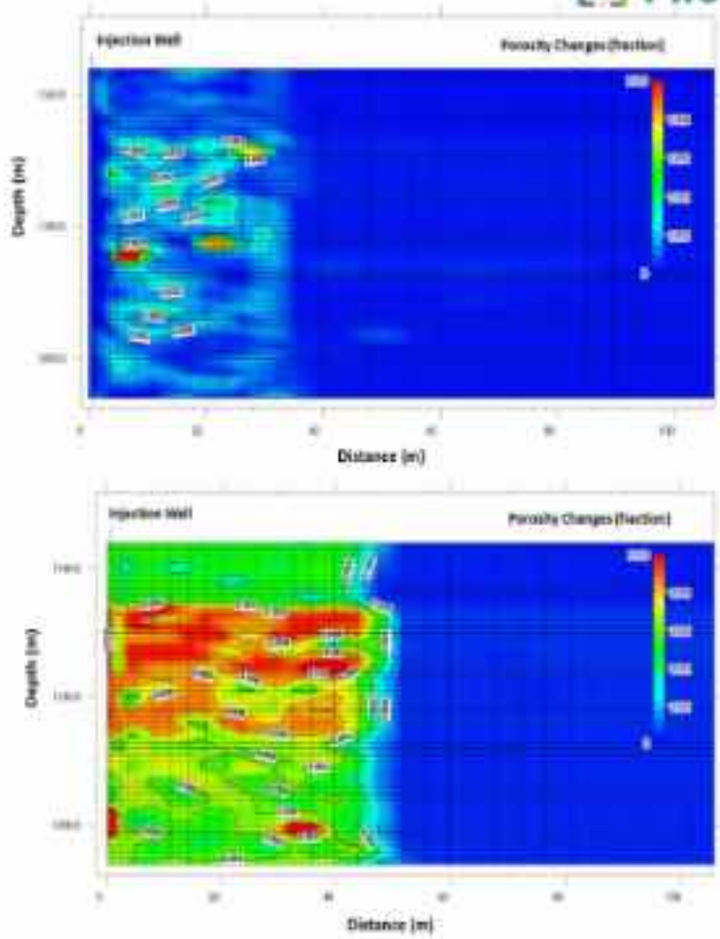


*Figure 6.2-17: Vertical section of the spatial distribution of the porosity changes for the base case scenario (top) and the worst case scenario of 1Mt/y and 130 g/L (bottom), after 30-years of injection.*

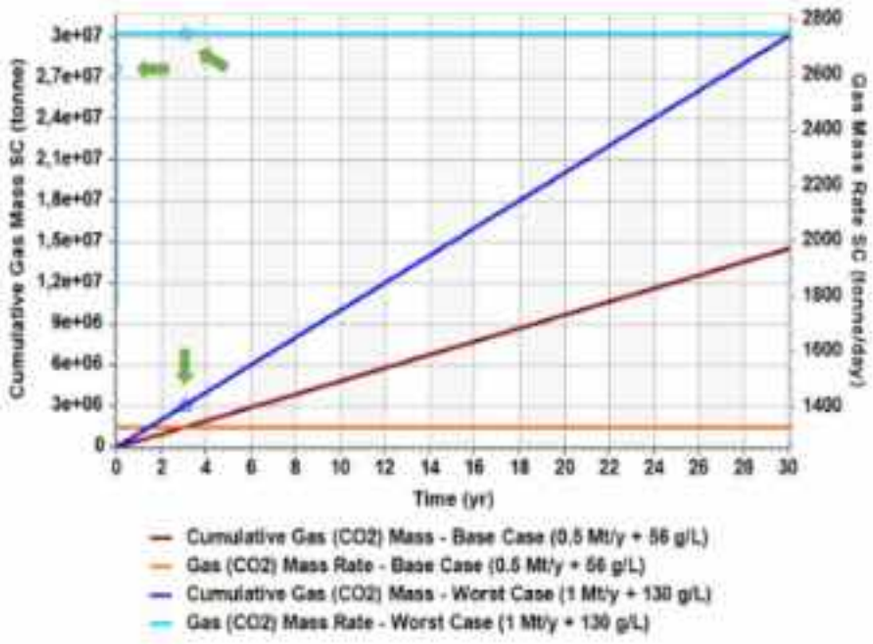


*Figure 6.2-18: Evolution of the cumulative gas ($CO_2$) mass, and gas ($CO_2$) mass rate for the base case scenario and the worst case scenario of 1Mt/y and 130 g/L, after 30-years of injection. The green arrows point to the stars (or half-stars) symbols to indicate some injectivity issues at the beginning of the injection period (during the first days/months).*

The PilotSTRATEGY project has received funding from the European Union's Horizon 2020 research and innovation programme under grant agreement No. 101022664

Despite the compounded near-wellbore effects associated with higher injection rate and elevated salinity, long-term injection performance remains stable in both scenarios. As shown in Figure 6.2-18, the worst-case scenario (1 Mt/y + 130 g/L) achieves and maintains the target injection rate of approximately 2700 t/day throughout the injection period, resulting in a cumulative injected mass of approximately $3.0 \times 10^7$ tonnes after 30 years, compared to approximately $1.45 \times 10^7$ tonnes for the base case (0.5 Mt/y + 56 g/L). The green arrows indicate early-time transient behaviour during the first days to months of injection, corresponding to initial pressure build-up and near-well flow adjustment. However, no sustained rate limitation or prolonged well shut-in is observed, and the injection rate remains stable thereafter.

The reservoir pressure response reflects the increased injection rate and salinity in the worst-case scenario (Figure 6.2-19). Reservoir pressure stabilizes at approximately 13900–14100 kPa in the worst-case scenario, compared to approximately 12600–12700 kPa in the base case. This represents an increase of approximately 1200–1400 kPa (about 9–11%), which remains well below the imposed bottom-hole pressure constraint of 16,500 kPa and below expected fracture pressure limits. The higher pressure in the worst-case scenario is consistent with increased flow resistance associated with intensified salt precipitation, higher salinity, and the elevated injection rate, but does not compromise operational safety or injection continuity.

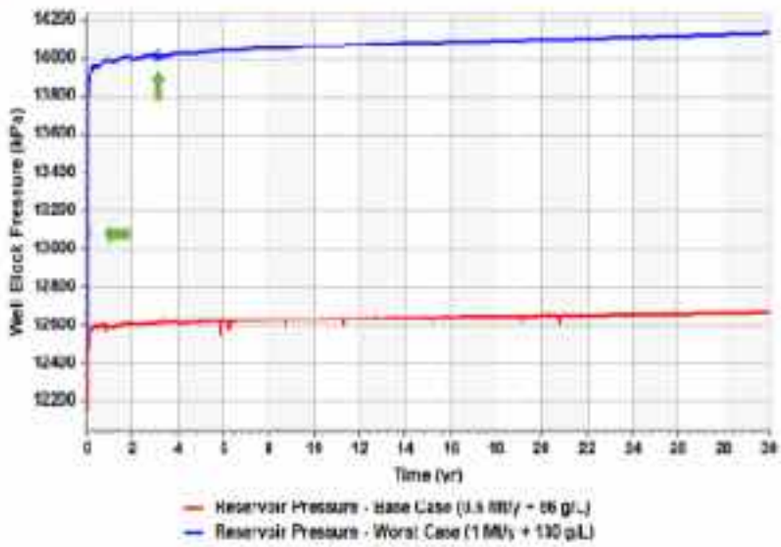


*Figure 6.2-19: Evolution of the reservoir pressure for the base case scenario and the worst case scenario of 1Mt/y and 130 g/L, after 30-years of injection. The green arrows point to the stars (or half-stars) symbols to indicate some injectivity issues at the beginning of the injection period (during the first days/months).*

The injectivity index evolution (Figure 6.2-20) confirms a measurable but stable injectivity reduction under worst-case conditions. The base case exhibits a stable injectivity index of approximately 2050–2100 $Sm^3$/day/kPa, whereas the worst-case scenario stabilizes at approximately 1800–1850 $Sm^3$/day/kPa. This corresponds to an injectivity reduction of approximately 10–15% relative to the base case. The reduction occurs early during the injection period and stabilizes thereafter, with no progressive decline over time. The early transient fluctuations indicated by the green arrows correspond to near-well saturation redistribution and initial salt precipitation effects, after which a dynamic equilibrium is established.

Overall, the worst-case scenario represents the upper bound of injectivity impairment under the combined influence of elevated injection rate and reservoir salinity. While injectivity is reduced by

The PilotSTRATEGY project has received funding from the European Union's Horizon 2020 research and innovation programme under grant agreement No. 101022664

approximately 10–15%, the system remains fully capable of sustaining the target injection rate over the full 30-year period. Importantly, no progressive or runaway injectivity loss occurs, indicating that salt precipitation and associated porosity reduction remain spatially localized near the wellbore. These results confirm that even under adverse conditions, injectivity loss in the Q4-TV1 reservoir remains moderate, stable, and operationally manageable, and does not represent a reservoir-scale limitation to long-term $CO_2$ storage.

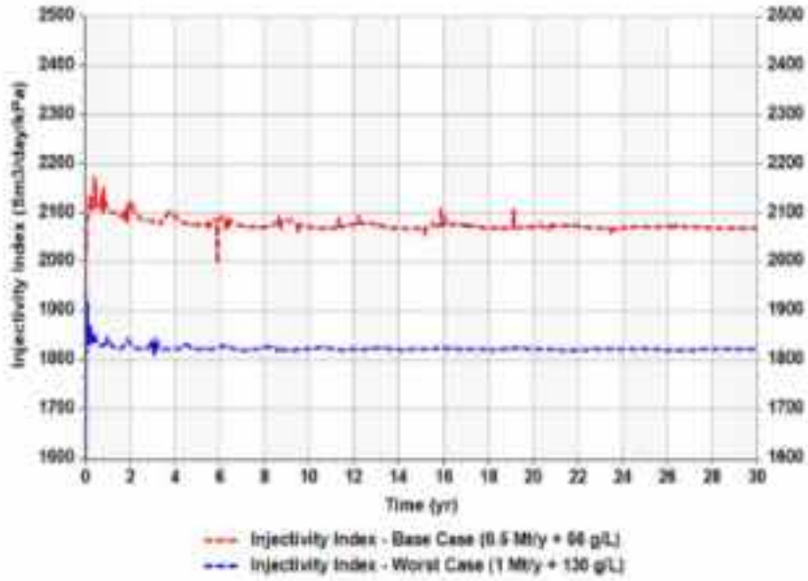


*Figure 6.2-20: Evolution of the injectivity index for the base case scenario and the worst case scenario of 1Mt/y and 130 g/L, after 30-years of injection. The green arrows point to the stars (or half-stars) symbols to indicate some injectivity issues at the beginning of the injection period (during the first days/months).*

## 7.2.2 Caprock integrity – Geomechanical aspects (Uncertainty Analysis)

### *7.2.2.1 Evolution of vertical displacement*

The storage system is characterised by a predominantly decreasing response over the full simulation period, following a very short initial phase of minor uplift during the first few years of injection (Figure 6-38). The recorded vertical displacements remain on the millimetre scale, ranging from a peak uplift of approximately 1 mm to cumulative subsidence of about 6–7 mm by the end of the simulation, measured relative to the initial geomechanical state.

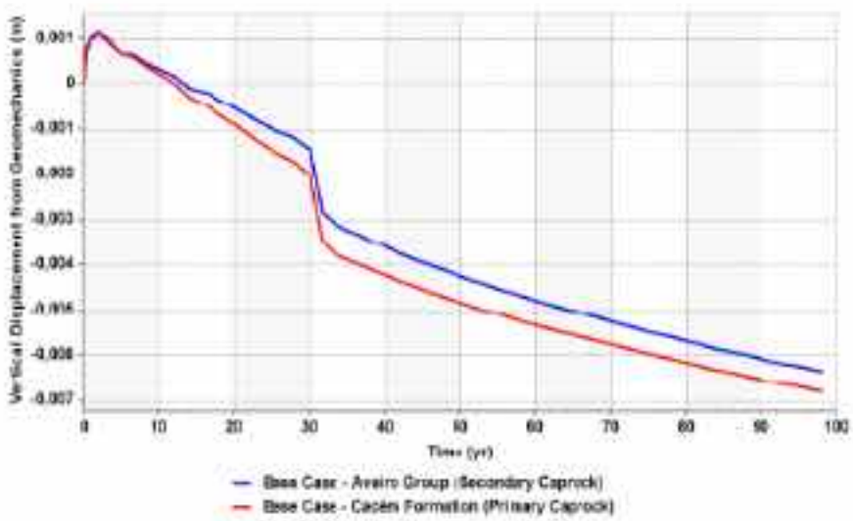


The PilotSTRATEGY project has received funding from the European Union's Horizon 2020 research and innovation programme under grant agreement No. 101022664

*Figure 4-38: Vertical displacement over time in representative model cells at the base of the sealing formations (Cacém Formation and Aveiro Group), close to the injection well, during the injection (0-30 years) and post-injection simulation (30-100 years).*

During the early injection phase, both the Cacém Formation and the overlying Aveiro Group exhibit a small, transient uplift, which correlates with rapid reservoir pressurisation and the initial poroelastic expansion of the reservoir–caprock system. This upward movement is short-lived and quickly transitions to downward displacement as the mechanical response becomes increasingly controlled by stress redistribution within the storage complex. As injection continues toward 30 years, a progressive and nearly linear increase in subsidence is observed in both sealing units. The Cacém Formation shows slightly larger downward displacement than the Aveiro Group, indicating that deformation is more pronounced near the reservoir-caprock interface, where stress changes are strongest and influenced by the imposed boundary conditions at the base of the model. During the post-injection (shut-in) phase (30–100 years), subsidence continues in both formations but at a gradually decreasing rate. This behaviour reflects the slow dissipation of pore pressure, progressive stress redistribution, and poroelastic relaxation of the rock matrix. The absence of full recovery towards zero displacement is consistent with the fact that the system does not return to its initial stress state within the simulated timeframe, as well as the influence of mechanical boundary conditions, particularly the vertical constraint at the base of the model. Overall, the limited magnitude of vertical displacements indicates that deformation remains within the elastic–poroelastic regime, with no evidence of mechanical instability or compromise of caprock integrity.

### *7.2.2.2 Impacts of injection flow rate*

Increasing the injection rate from 0.5 to 1 Mt/y leads to a clear amplification of pore pressure build-up within the Cacém Formation. Under the higher injection scenario, pore pressure rises more rapidly and reaches a peak close to 9700 kPa around 30 years, compared with a peak of approximately 9450 kPa in the base case (Figure 6.2-21). This corresponds to an additional pressurisation of roughly $\Delta P \approx 250$ kPa at the end of the injection period. Although this represents a noticeable increase, the resulting pressures remain well below levels associated with caprock fracturing or mechanical failure, indicating that the integrity of the sealing unit is preserved.

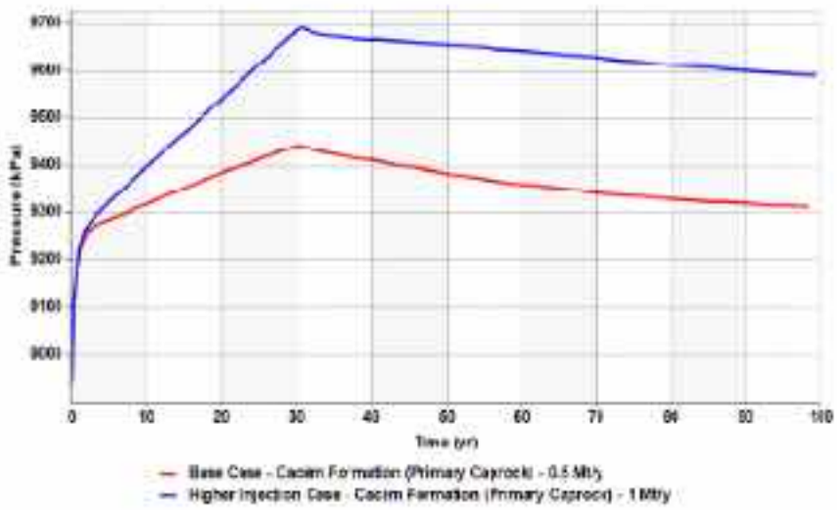


The PilotSTRATEGY project has received funding from the European Union's Horizon 2020 research and innovation programme under grant agreement No. 101022664

*Figure 6.2-21. Temporal evolution of pore pressure at the base of the Cacém Formation (Primary Caprock) for different injection scenarios: 'Base Case' (0.5 Mt/y rate) and the 'High Injection Case' (1 Mt/y rate).*

During the post-injection (shut-in) phase, both scenarios exhibit very similar pressure relaxation patterns, with nearly parallel decline trends over time. This suggests that the higher injection rate does not alter the intrinsic hydraulic behaviour of the system, such as permeability or diffusivity, and that the stress response remains within the elastic–poroelastic regime. Consequently, the primary difference between the two cases lies in the magnitude of the pressure perturbation at shut-in rather than in the rate or character of pressure dissipation.

The higher injection rate produces a more pronounced dilative response in the Cacém Formation throughout the injection period. From the onset of injection, both scenarios show a slight increase in true porosity (geomechanics-derived), but the magnitude of compaction is consistently greater under the 1 Mt/y case. During the first 10–15 years, porosity decreases more rapidly in the higher-rate scenario, reflecting stronger effective-stress perturbations associated with faster pressure build-up. Between approximately 15 and 30 years, porosity continues to increase in both cases, with the 1 Mt/y scenario reaching a deeper porosity minimum of around $-1.0 \times 10^{-5}$ at the end of injection, compared with roughly $-8 \times 10^{-6}$ in the base case (Figure 6.2-22). This difference is consistent with the larger pore-pressure gradients and stress redistribution induced by the elevated injection rate.

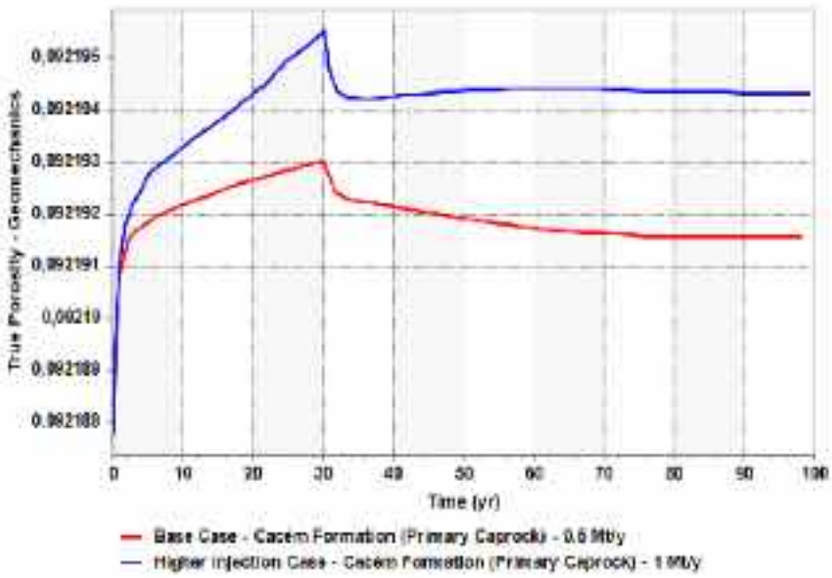


*Figure 6.2-22. Temporal evolution of porosity changes at the base of the Cacém Formation (Primary Caprock) for different injection scenarios: 'Base Case' (0.5 Mt/y rate) and the 'High Injection Case' (1 Mt/y rate).*

During the post-injection (shut-in) phase, a slow partial porosity recovery is observed in both scenarios as pore pressure dissipates and effective stresses relax. In this context, recovery corresponds to a slight decrease in porosity towards initial values, which is more limited and slower for the 1 Mt/y case, reflecting the greater stress perturbation experienced during injection.

Volumetric strain responses highlight a distinctly more dilative behaviour under the higher injection rate (Figure 6.2-23). In both scenarios, the Cacém Formation experiences negative volumetric strain

The PilotSTRATEGY project has received funding from the European Union's Horizon 2020 research and innovation programme under grant agreement No. 101022664

(net dilation) from the onset of injection, but the magnitude of compaction is consistently greater for the 1 Mt/y case. During the early injection period, strain becomes more negative more rapidly in the higher-rate scenario, reflecting stronger effective-stress perturbations associated with faster pressure build-up. By the end of injection at 30 years, the 1 Mt/y case reaches a deeper compaction minimum of approximately $-7 \times 10^{-4}$, compared with about $-4 \times 10^{-4}$ in the base case. This contrast is consistent with the larger stress changes induced by the elevated injection rate.

During the post-injection phase, both scenarios show a gradual recovery toward less negative strain as pore pressure dissipates and effective stresses relax. Recovery is more pronounced in the base case, whereas the 1 Mt/y scenario retains a larger residual compaction over the long term, reflecting its greater cumulative deformation during injection.

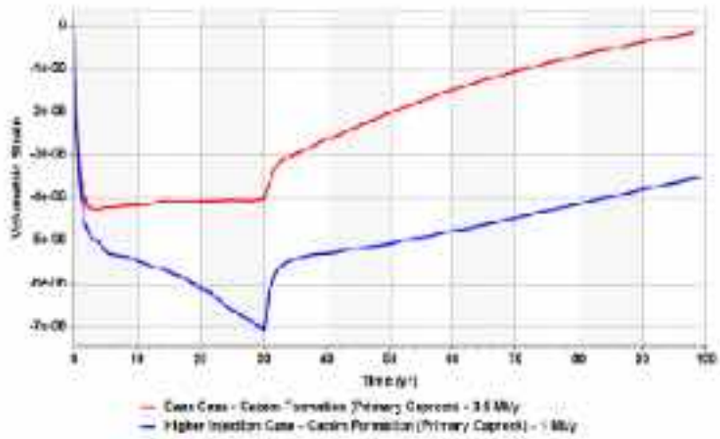

*Figure 6.2-23. Temporal evolution of volumetric strain at the base of the Cacém Formation (Primary Caprock) for different injection scenarios: 'Base Case' (0.5 Mt/y rate) and the 'High Injection Case' (1 Mt/y rate).*

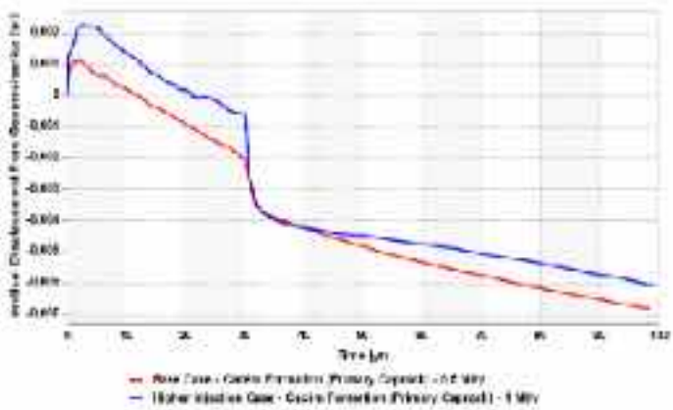

*Figure 6.2-24. Temporal evolution of vertical displacement at the base of the Cacém Formation (Primary Caprock) for different injection scenarios: 'Base Case' (0.5 Mt/y rate) and the 'High Injection Case' (1 Mt/y rate).*

The early hydromechanical response in terms of vertical displacement is similarly amplified. During the first 2–3 years, uplift effects (Figure 6.2-24) reach approximately 1.3 mm for the base case (0.5 Mt/y) and about 3 mm for the high-injection scenario (1 Mt/y). This uplift reflects the poroelastic expansion of the reservoir–caprock system in response to pressurisation. Over longer timescales, the system transitions to a settlement

The PilotSTRATEGY project has received funding from the European Union's Horizon 2020 research and innovation programme under grant agreement No. 101022664

regime driven by pore-pressure dissipation and stress redistribution within the storage complex. The long-term displacement behaviour is also influenced by the imposed mechanical boundary conditions (notably the fixed base), which limit full recovery and contribute to the residual subsidence observed. Counterintuitively, final subsidence is slightly mitigated and delayed under the higher injection rate. This behaviour is attributed to the sustained residual overpressure in the reservoir, which provides prolonged hydrostatic support, retarding the increase in vertical effective stress and reducing rock-matrix compaction relative to the base case, where pressure dissipation occurs more rapidly.

The higher injection rate amplifies the early vertical displacement response of the Cacém Formation (Figure 6.2-24). During the first few years of injection, both scenarios exhibit transient uplift, reaching about 1 mm for the 0.5 Mt/y case and approximately 2 mm for the 1 Mt/y case, reflecting poroelastic expansion associated with rapid pressurisation. As injection continues, uplift reverses to progressive subsidence in both scenarios. By the end of injection, downward displacement becomes similar for both cases, followed by continued but gradually decelerating settlement during the post-injection phase as pore pressure dissipates and effective stresses are restored. Overall, doubling the injection rate increases the magnitude of early elastic uplift but does not significantly alter the long-term subsidence trend. Absolute displacements remain within the millimetre scale, indicating that deformation stays within the elastic–poroelastic regime and does not threaten caprock integrity.

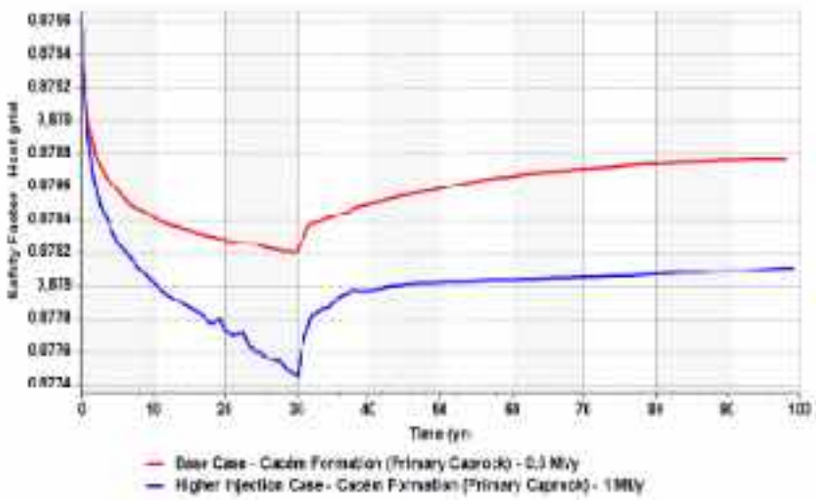


*Figure 6.2-25. Temporal evolution of safety factor at the base of the Cacém Formation (Primary Caprock) for different injection scenarios: 'Base Case' (0.5 Mt/y rate) and the 'High Injection Case' (1 Mt/y rate).*

The temporal evolution of the Safety Factor (Figure 6.2-25) indicates a small but systematic reduction during the injection phase, particularly under the higher injection rate. In both scenarios, the Safety Factor decreases most rapidly during the early years of injection as pore pressure builds up and effective stresses are reduced. This decline is more pronounced for the 1 Mt/y case, reflecting the faster pressurisation of the Cacém Formation. By the end of injection (around 30 years), the Safety Factor reaches a minimum in both cases, with the higher-rate scenario displaying the lowest value. Immediately after shut-in, a partial recovery occurs as pore pressure dissipates and effective stresses are progressively restored. Thereafter, the Safety Factor increases slowly and stabilises over the long term. Despite these variations, the Safety Factor remains consistently high and well within the stable

The PilotSTRATEGY project has received funding from the European Union's Horizon 2020 research and innovation programme under grant agreement No. 101022664

domain throughout the simulation for both injection rates.

The Mohr–Coulomb stress states for the 0.5 and 1 Mt/y scenarios lie very close to each other and remain far from the failure envelope (Figure 6.2-26). The slight shift associated with the higher injection rate is minor compared with the magnitude of the in-situ effective stresses (≈10–11 MPa). This indicates that doubling the injection rate has little influence on the overall stress state and does not reduce the mechanical safety margin of the Cacém Formation.

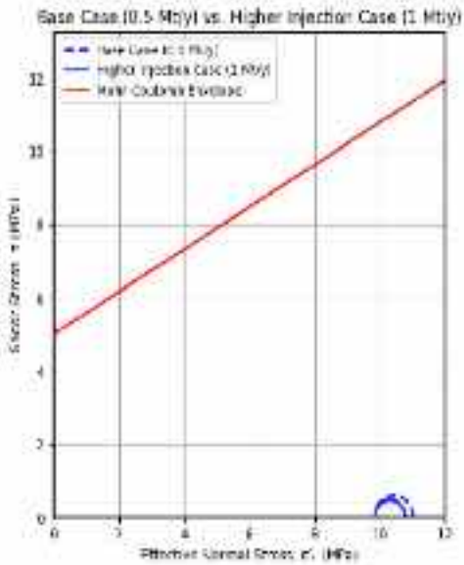


*Figure 6.2-26: Mohr diagram for caprock stability analysis under injection flow rate variations. The plot depicts the Mohr-Coulomb failure envelope (red line) relative to the initial (dashed line) and final (solid line) effective stress states.*

### 7.2.2.3 Impacts of perforation intervals

To assess the influence of well design on pressure transmission to the caprock, a dual-perforation configuration was compared with the reference single-perforation case, while maintaining the same total injection rate of 1 Mt/y.

The pore-pressure evolution shows very similar trends for both configurations, indicating that overall storage stability is preserved (Figure 6.2-27). However, peak pressures at the end of injection are slightly higher for the two-perforation case. This modest increase is attributed to the vertical position of the additional perforation, which is closer to the Cacém Formation and thus shortens the pressure transmission pathway to the caprock. This effect slightly outweighs any pressure-relief benefit from distributing the injection flow.

The PilotSTRATEGY project has received funding from the European Union's Horizon 2020 research and innovation programme under grant agreement No. 101022664

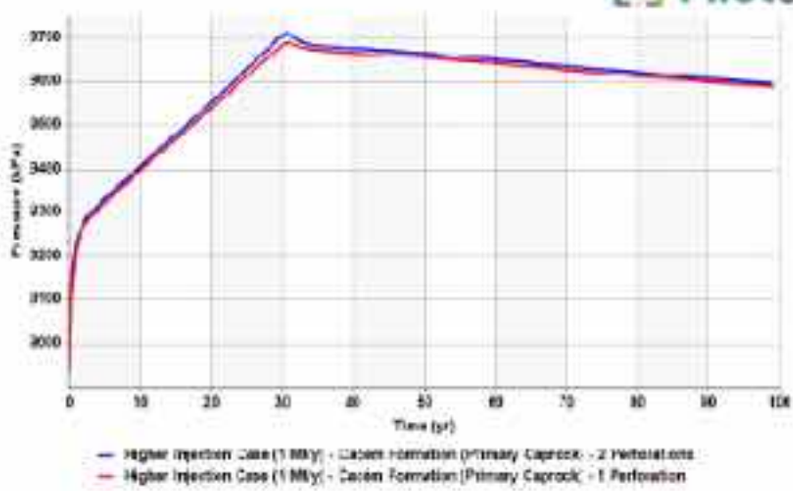


*Figure 6.2-27. Temporal evolution of pore pressure at the base of the Cacém Formation (Primary Caprock) for different perforation intervals scenarios and with an injection rate of 1Mt/y: 1 Perforation and the 2 Perforations.*

Porosity in the Cacém Formation increases steadily throughout the injection period for both perforation configurations, indicating a predominantly dilative response (Figure 6.2-28). The dual-perforation case shows a slightly greater porosity increase, consistent with the marginally higher pore pressures transmitted to the caprock. During the post-injection phase, both cases exhibit a slow partial porosity recovery as pore pressure dissipates, with porosity gradually decreasing towards initial values, though recovery remains somewhat more limited for the dual-perforation scenario.

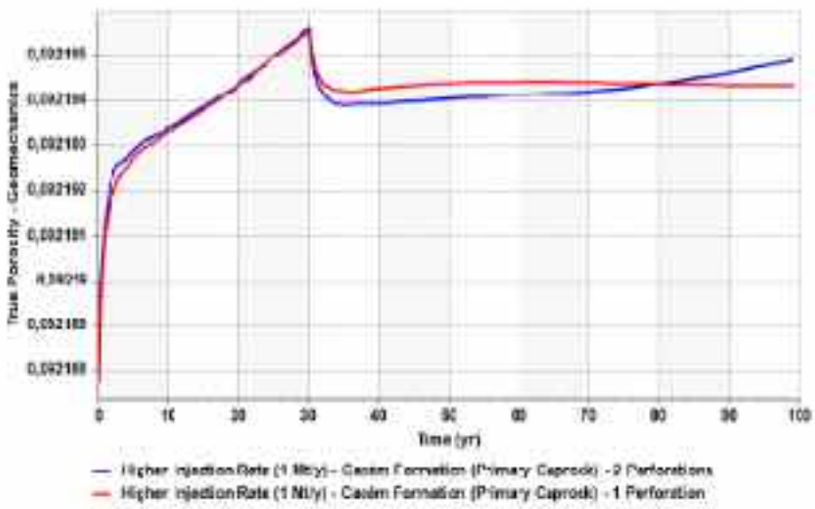


*Figure 6.2-28. Temporal evolution of porosity changes at the base of the Cacém Formation (Primary Caprock) for different perforation intervals scenarios and with an injection rate of 1Mt/y: 1 Perforation and the 2 Perforations.*

The volumetric strain response indicates a predominantly dilative behaviour for both perforation configurations (Figure 6.2-29). From the onset of injection, the Cacém Formation exhibits negative volumetric strain (net dilation), which becomes more pronounced until the end of the injection period at around 30 years. Immediately after shut-in, both cases show a transient change in deformation rate, followed by a gradual recovery toward less negative strain as pore pressure dissipates and effective stresses relax. Over the post-injection period, the dual-perforation case retains slightly more

The PilotSTRATEGY project has received funding from the European Union's Horizon 2020 research and innovation programme under grant agreement No. 101022664

negative strain than the single-perforation case, indicating marginally greater cumulative dilative deformation.

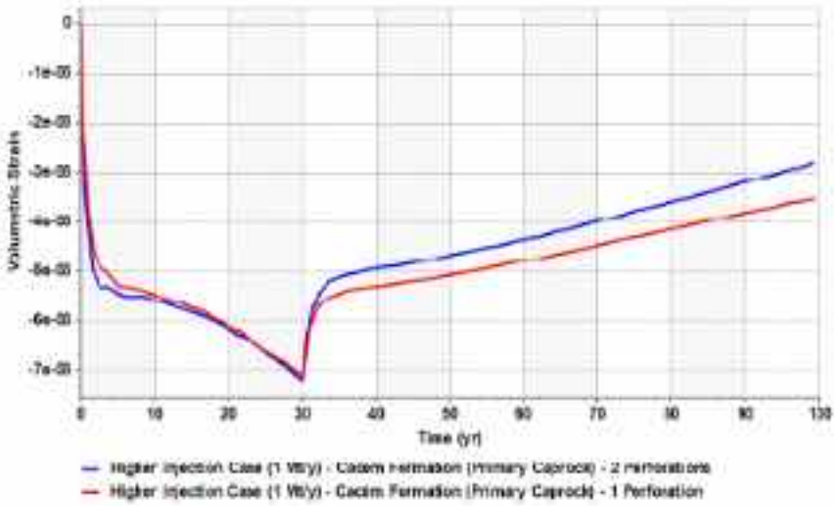


*Figure 6.2-29. Temporal evolution of volumetric strain at the base of the Cacém Formation (Primary Caprock) for different perforation intervals scenarios and with an injection rate of 1Mt/y: 1 Perforation and the 2 Perforations.*

The vertical displacement response shows a short-lived uplift phase during the early years of injection for both configurations, reaching about 2 mm in the dual-perforation case and slightly less in the single-perforation case (Figure 6.2-30). This transient uplift reflects the initial poroelastic expansion of the reservoir–caprock system in response to rapid pressurisation. As injection proceeds, uplift reverses to progressive subsidence in both scenarios. By the end of injection (30 years), downward displacement becomes more pronounced, followed by continued settlement during the post-injection phase as pore pressure dissipates and effective stresses are redistributed.

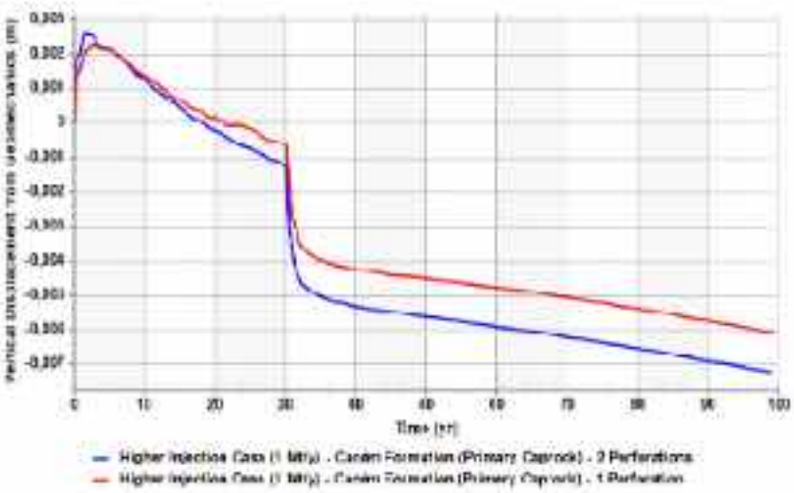


*Figure 6.2-30. Temporal evolution of vertical displacement at the base of the Cacém Formation (Primary Caprock) for different perforation intervals scenarios and with an injection rate of 1Mt/y: 1 Perforation and the 2 Perforations.*

The Safety Factor decreases gradually during injection for both perforation configurations, reaching a minimum at around 30 years, with a slightly lower value for the dual-perforation case (Figure 6.2-31). After shut-in, the Safety Factor partially recovers and then stabilises over the long term as pore

The PilotSTRATEGY project has received funding from the European Union's Horizon 2020 research and innovation programme under grant agreement No. 101022664

pressure dissipates. Throughout the simulation, the Safety Factor remains comfortably within the stable domain for both cases, indicating that introducing a second perforation interval does not compromise caprock integrity.

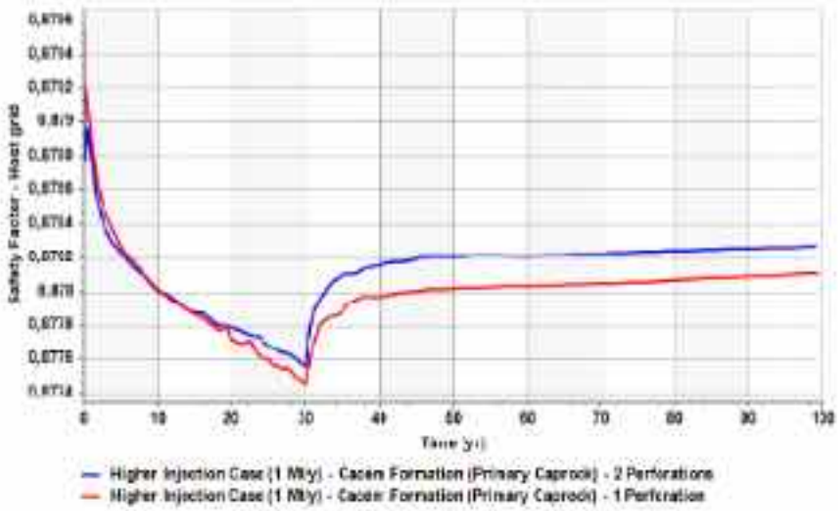


*Figure 6.2-31. Temporal evolution of safety factor at the base of the Cacém Formation (Primary Caprock) for different perforation intervals scenarios and with an injection rate of 1Mt/y: 1 Perforation and the 2 Perforations.*

The Mohr–Coulomb stress states for the single- and dual-perforation configurations are nearly identical and remain well within the elastic domain, far from the failure envelope (Figure 6.2-32). This indicates that adding a second perforation interval does not materially affect the stress state of the Cacém Formation and does not introduce any additional geomechanical risk to caprock integrity.

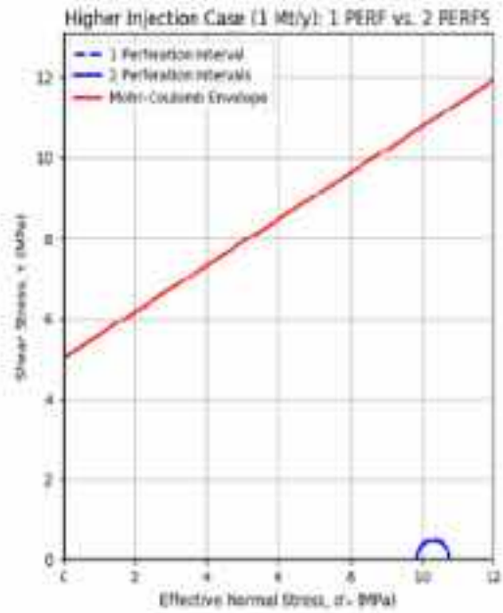


*Figure 6.2-32: Mohr diagram for caprock stability analysis under perforation intervals variations. The plot depicts the Mohr-Coulomb failure envelope (red line) relative to the initial (dashed line) and final (solid line) effective stress states.*

The PilotSTRATEGY project has received funding from the European Union's Horizon 2020 research and innovation programme under grant agreement No. 101022664

#### 7.2.2.4 *Impacts of mechanical properties*

Geological formations are naturally heterogeneous, with variability in petrophysical and geomechanical properties that can influence storage performance. To assess this, additional simulations were conducted by systematically varying key geomechanical parameters following the previously established methodology. Where only one curve appears in the plots, the tested scenarios produced identical results and therefore overlap completely, indicating that the system response is governed by elastic-poroelastic processes and is insensitive to the parameter variation within the investigated range.

#### 7.2.2.5 *Cohesion*

The uncertainty analysis indicates that variations in caprock cohesion (c) have no discernible effect on pore-pressure evolution (Figure 6.2-33). The complete overlap of the pressure curves for all tested cohesion values (0.1, 1, and 5 MPa) demonstrates that changes in cohesive strength do not influence hydraulic diffusivity or pressure transmission under elastic conditions. In all cases, pore pressure remains well below lithostatic limits, confirming that caprock integrity is preserved across the range of cohesion values considered.

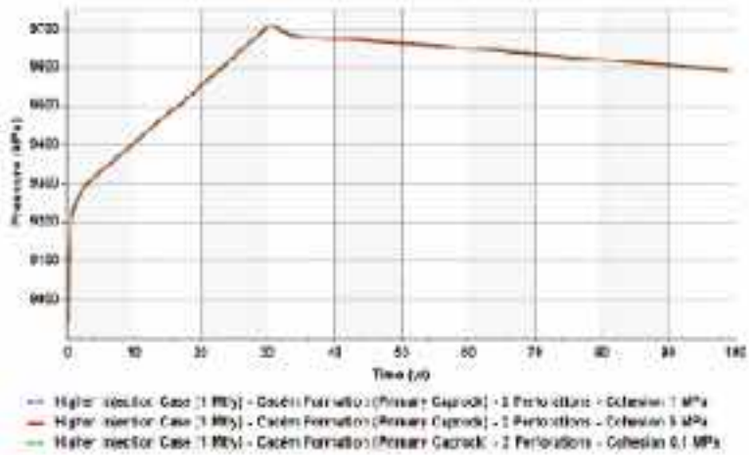


*Figure 6.2-33. Temporal evolution of pore pressure at the base of the Cacém Formation (Primary Caprock) for different cohesions, and 2 perforation intervals with an injection rate of 1Mt/y: 5 MPa (base case), 1 MPa (lower case 1) and 0.1 MPa (lower case 2).*

Porosity evolution is identical (overlap) for all cohesion values (Figure 6.2-34). The Cacém Formation shows steady increase in true porosity (from geomechanics) during injection, reaching a minimum at about 30 years, followed by a slow partial recovery during shut-in as pore pressure dissipates.

The PilotSTRATEGY project has received funding from the European Union's Horizon 2020 research and innovation programme under grant agreement No. 101022664

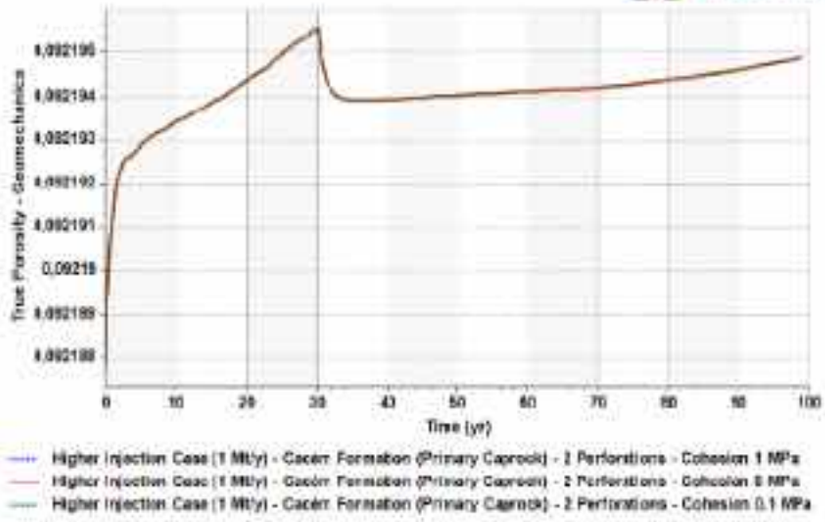


*Figure 6.2-34. Temporal evolution of porosity changes at the base of the Cacém Formation (Primary Caprock) for different cohesions, and 2 perforation intervals with an injection rate of 1Mt/y: 5 MPa (base case), 1 MPa (lower case 1) and 0.1 MPa (lower case 2).*

Volumetric strain evolution is identical (overlap) for all cohesion values (Figure 6.2-35). The magnitudes remain on the order of $10^{-6}$. The Cacém Formation shows progressive dilative deformation during injection, reaching a maximum at about 30 years, followed by slow partial recovery during shut-in as pore pressure dissipates. This is reflected by negative volumetric strain (net dilation) becoming less negative over time.

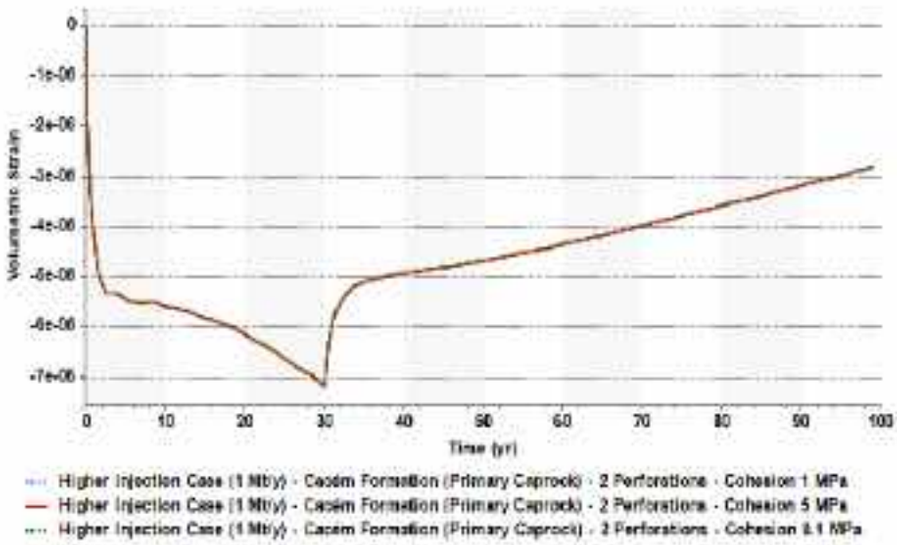


*Figure 6.2-35. Temporal evolution of volumetric strain at the base of the Cacém Formation (Primary Caprock) for different cohesions, and 2 perforation intervals with an injection rate of 1Mt/y: 5 MPa (base case), 1 MPa (lower case 1) and 0.1 MPa (lower case 2).*

Vertical displacement histories are identical for all cohesion values (Figure 6.2-36). All scenarios show a brief early uplift (approximately 2.5–3 mm) during injection, followed by progressive subsidence that continues into the post-injection phase as pore pressure dissipates and effective stresses are redistributed. The complete overlap of the curves indicates that cohesion does not influence the

The PilotSTRATEGY project has received funding from the European Union's Horizon 2020 research and innovation programme under grant agreement No. 101022664

overall deformation response of the caprock.

This overlapping behaviour observed in Figure 6.2-34, Figure 6.2-35 and Figure 6.2-36 for the three scenarios is physically consistent, as cohesion only controls the onset of plastic yielding in the Mohr-Coulomb model. Since no yielding is activated under the simulated stress conditions, the response remains purely elastic-poroelastic, and therefore independent of cohesion varying values.

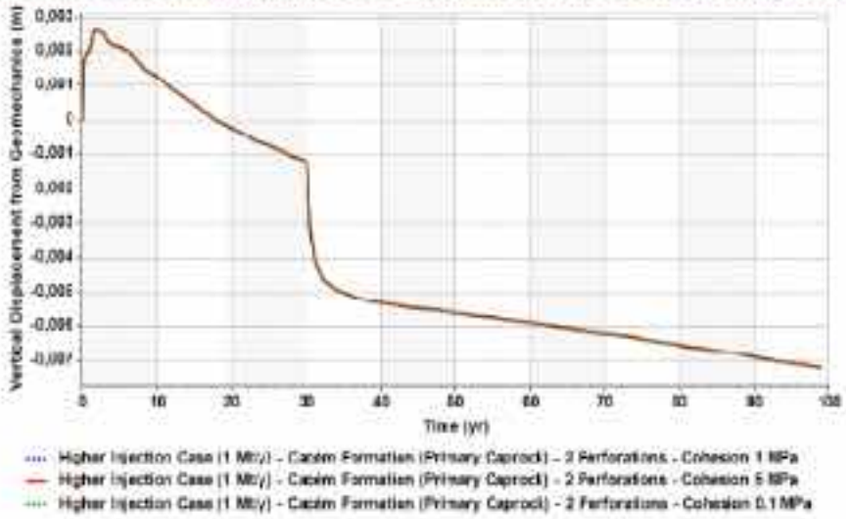


*Figure 6.2-36. Temporal evolution of vertical displacement at the base of the Cacém Formation (Primary Caprock) for different cohesions, and 2 perforation intervals with an injection rate of 1Mt/y: 5 MPa (base case), 1 MPa (lower case 1) and 0.1 MPa (lower case 2).*

Safety Factor values remain nearly constant over time for all cohesion scenarios (Figure 6.2-37). As expected, lower cohesion yields lower Safety Factors, but even in the worst case (c = 0.1 MPa) values stay comfortably above the failure threshold, confirming that caprock stability is maintained throughout the simulation.

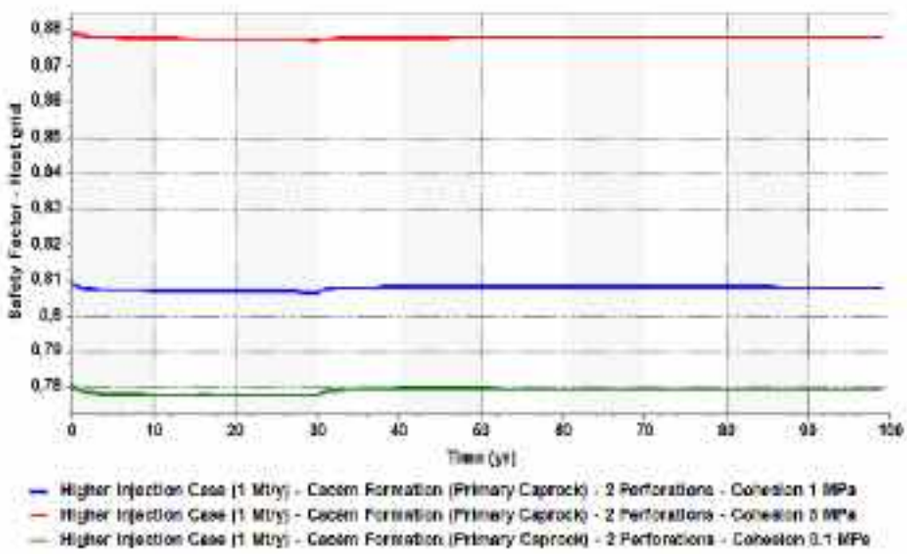


*Figure 6.2-37. Temporal evolution of safety factor at the base of the Cacém Formation (Primary Caprock) for different cohesions, and 2 perforation intervals with an injection rate of 1Mt/y: 5 MPa (base case), 1 MPa (lower case 1) and 0.1 MPa (lower case 2).*

The PilotSTRATEGY project has received funding from the European Union's Horizon 2020 research and innovation programme under grant agreement No. 101022664

The Mohr–Coulomb analysis shows that reducing cohesion shifts the failure envelope downward, as expected, but the stress states remain well inside the elastic domain and far from failure for all cases (Figure 6.2-38).

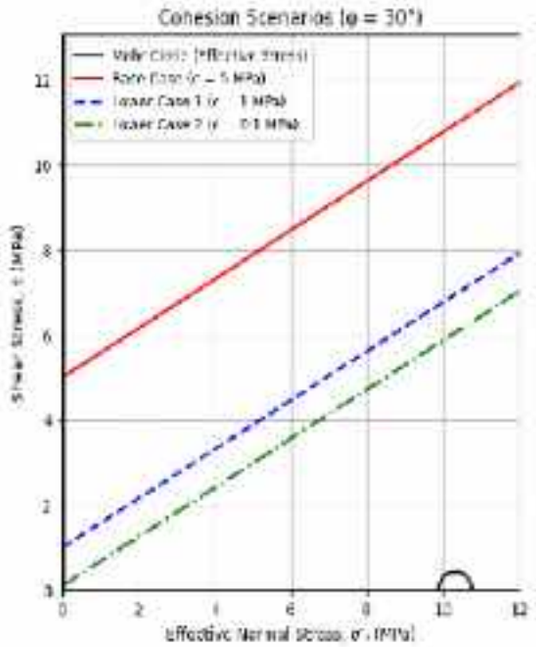


*Figure 6.2-38: Mohr diagram for caprock stability analysis under cohesion variations. The plot depicts the Mohr-Coulomb failure envelopes relative to the base case (red line), lower case 1 (blue line) and lower case 2 (green line).*

Overall, although cohesion controls the theoretical failure boundary, it has little influence on pressure, deformation, or strain responses within the investigated stress range. The system remains within the elastic-poroelastic regime, with no plastic yielding activated, and caprock integrity is maintained even under low-cohesion assumptions.

#### 7.2.2.6 *Friction angle*

Variations in internal friction angle (10°, 20°, and 30°) do not affect pore-pressure evolution in the Cacém Formation (Figure 6.2-39). The complete overlap of the pressure curves shows that shear-strength parameters are decoupled from hydraulic behaviour under the tested conditions. Even for the intensive injection case (1 Mt/y with two perforations), pressures remain within the design envelope and within the elastic regime.

The PilotSTRATEGY project has received funding from the European Union's Horizon 2020 research and innovation programme under grant agreement No. 101022664

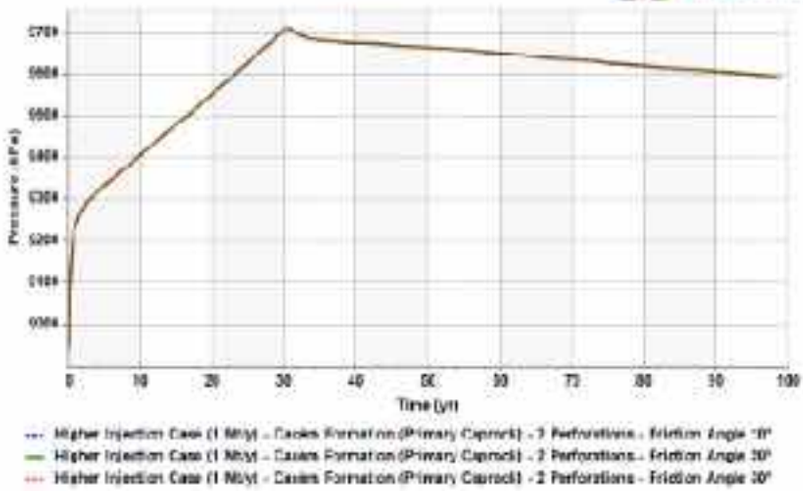


*Figure 6.2-39. Temporal evolution of pore pressure at the base of the Cacém Formation (Primary Caprock) for different cohesions, and 2 perforation intervals with an injection rate of 1Mt/y: 30º MPa (base case), 20º (lower case 1) and 10º (lower case 2).*

Porosity evolution is identical for all friction angle scenarios (Figure 6.2-40). The Cacém Formation shows a steady increase in true porosity (from geomechanics) during injection, reaching a minimum at about 30 years, followed by a slow partial recovery during shut-in as pore pressure dissipates.

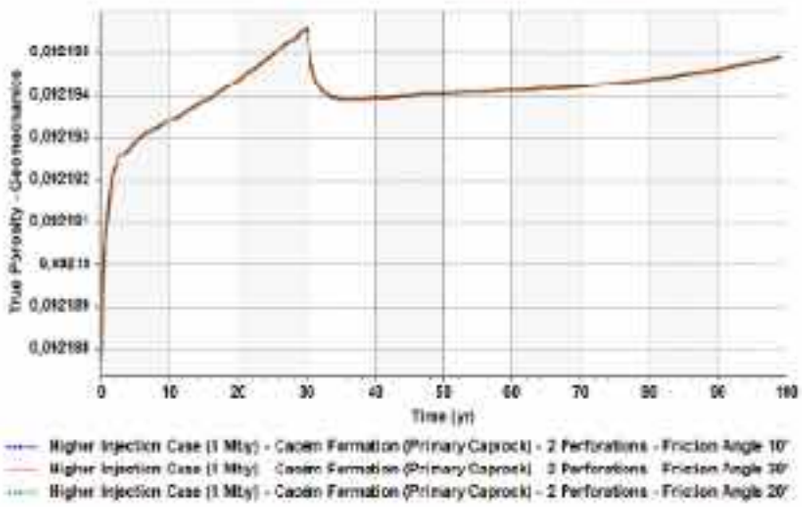


*Figure 6.2-40. Temporal evolution of porosity changes at the base of the Cacém Formation (Primary Caprock) for different cohesions, and 2 perforation intervals with an injection rate of 1Mt/y: 30º MPa (base case), 20º (lower case 1) and 10º (lower case 2).*

Volumetric strain behaviour is identical (overlap) for all friction angle scenarios (Figure 6.2-41). The Cacém Formation shows progressive dilative deformation during injection, reaching a maximum at about 30 years, followed by slow partial recovery during shut-in as pore pressure dissipates. This is reflected by negative volumetric strain (net dilation) becoming less negative over time.

The PilotSTRATEGY project has received funding from the European Union's Horizon 2020 research and innovation programme under grant agreement No. 101022664

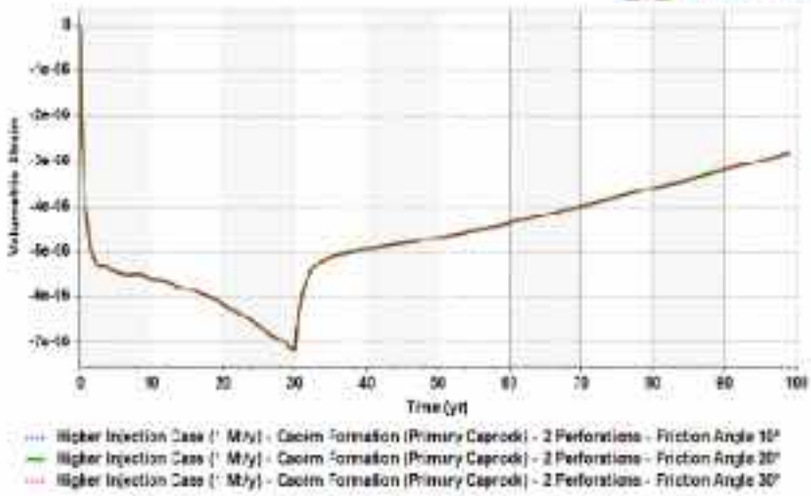


*Figure 6.2-41. Temporal evolution of volumetric strain at the base of the Cacém Formation (Primary Caprock) for different cohesions, and 2 perforation intervals with an injection rate of 1Mt/y: 30º MPa (base case), 20º (lower case 1) and 10º (lower case 2).*

The vertical displacement response is essentially identical for all friction angle scenarios (Figure 6.2-42). Each case exhibits a brief early uplift during the initial years of injection, followed by a clear transition to progressive subsidence that continues through the post-injection period as pore pressure dissipates and effective stresses are redistributed. The complete overlap of the displacement curves demonstrates that variations in internal friction angle do not influence the global deformation behavior of the caprock, confirming that the observed displacements are governed primarily by poroelastic processes rather than shear-strength parameters.

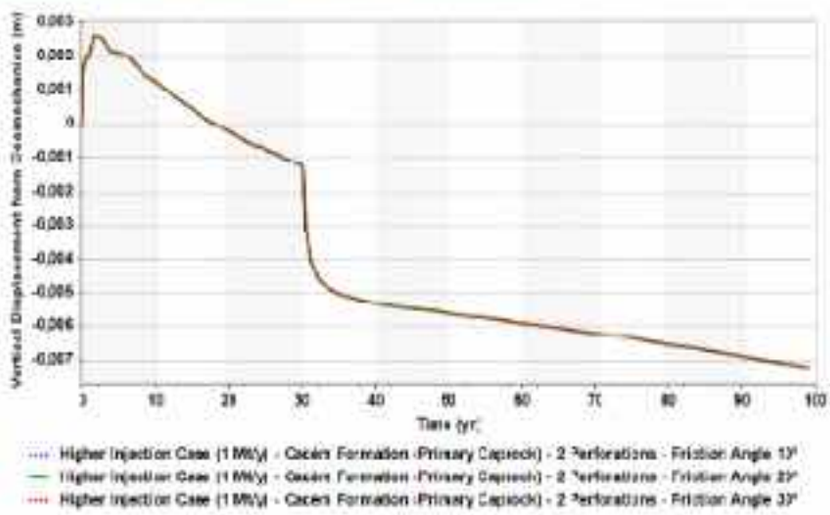


*Figure 6.2-42. Temporal evolution of vertical displacement at the base of the Cacém Formation (Primary Caprock) for different cohesions, and 2 perforation intervals with an injection rate of 1Mt/y: 30º MPa (base case), 20º (lower case 1) and 10º (lower case 2).*

This behavior is physically consistent, as the friction angle only affects shear failure conditions in the Mohr–Coulomb model. Since no plastic yielding is activated under the simulated stress conditions, the response remains purely elastic–poroelastic and therefore independent of friction angle.

The PilotSTRATEGY project has received funding from the European Union's Horizon 2020 research and innovation programme under grant agreement No. 101022664

The influence of friction angle is clearly reflected in the Safety Factor evolution (Figure 6.2-43). The Safety Factor curves remain nearly constant over time but are systematically separated according to the assigned friction-angle value, consistent with the direct role of $\phi$ in controlling shear strength. Higher friction angles correspond to higher Safety Factor values and a larger safety margin, whereas lower friction angles yield slightly reduced values.

Nevertheless, for all tested friction angles, the Safety Factor remains comfortably above the failure threshold throughout both injection and post-injection periods. The magnitude of variation is therefore not sufficient to affect the overall risk profile, and the system maintains a robust and stable mechanical performance across the full range of friction angles considered.

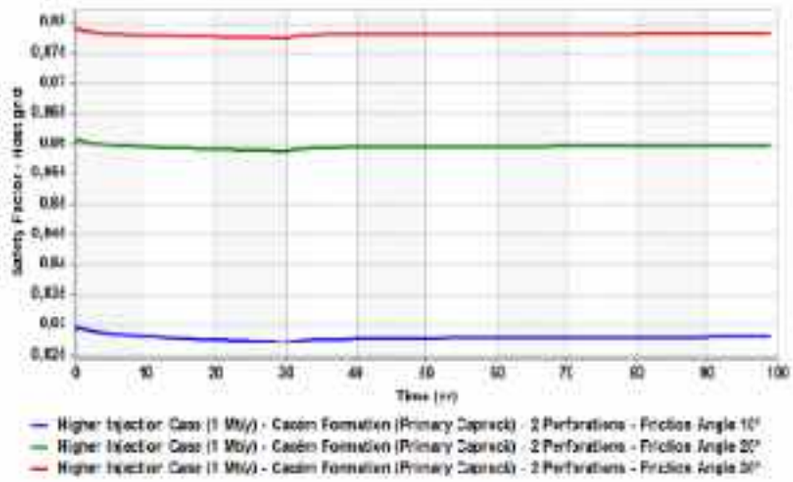


*Figure 6.2-43. Temporal evolution of safety factor at the base of the Cacém Formation (Primary Caprock) for different cohesions, and 2 perforation intervals with an injection rate of 1Mt/y: 30º MPa (base case), 20º (lower case 1) and 10º (lower case 2).*

Variations in friction angle change the slope of the Mohr–Coulomb failure envelope, but the stress states remain well inside the elastic domain for all cases (Figure 6.2-44).

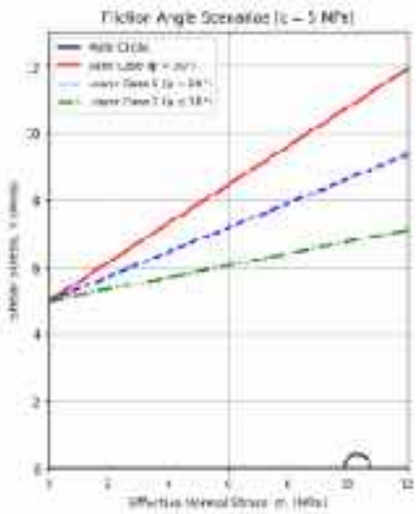


*Figure 6.2-44: Mohr diagram for caprock stability analysis under friction angle variations. The plot depicts the Mohr-Coulomb failure envelopes relative to the base case (red line), lower case (blue line) and higher case (green line).*

The PilotSTRATEGY project has received funding from the European Union's Horizon 2020 research and innovation programme under grant agreement No. 101022664

Although friction angle controls the theoretical failure boundary and Safety Factor magnitude, it does not affect pressure, porosity, strain, or displacement under the tested conditions. The system remains safely within the elastic-poroelastic regime, with no plastic yielding activated, and caprock integrity is preserved across all friction-angle scenarios.

#### *7.2.2.7 Elastic modulus*

Pore-pressure evolution is essentially insensitive to variations in Young's modulus (Figure 6.2-45). All tested elastic stiffness values (33, 55, and 60 GPa) produce almost identical pressure trajectories during both the injection and post-injection phases, with fully overlapping peak pressures at the end of injection and very similar pressure decay trends thereafter. This indicates that changes in elastic stiffness do not materially affect pressure build-up or dissipation within the Cacém Formation under the tested conditions. In all cases, pore pressures remain well within safe operational limits, confirming that uncertainties in elastic modulus do not compromise caprock integrity or storage performance.

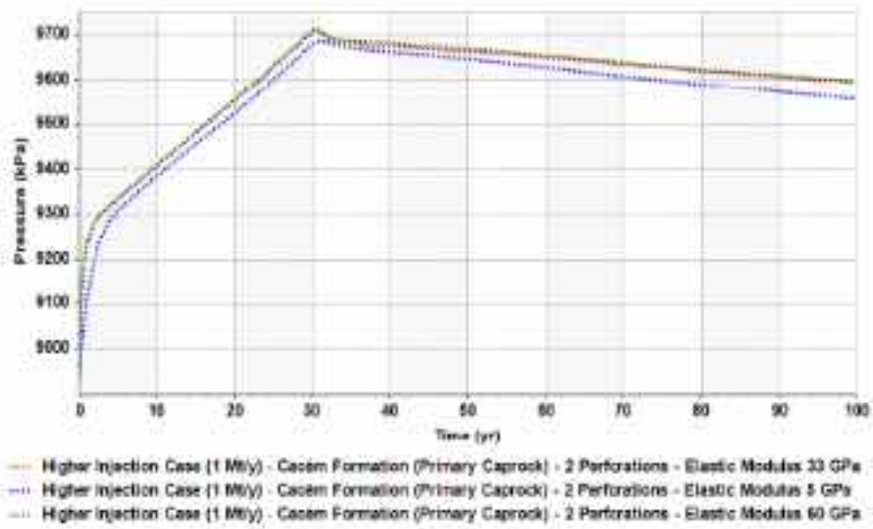


*Figure 6.2-45. Temporal evolution of pore pressure at the base of the Cacém Formation (Primary Caprock) for different Young's modulus, and 2 perforation intervals with an injection rate of 1Mt/y: 33 GPa (base case), 60 GPa (higher case) and 5 GPa (lower case).*

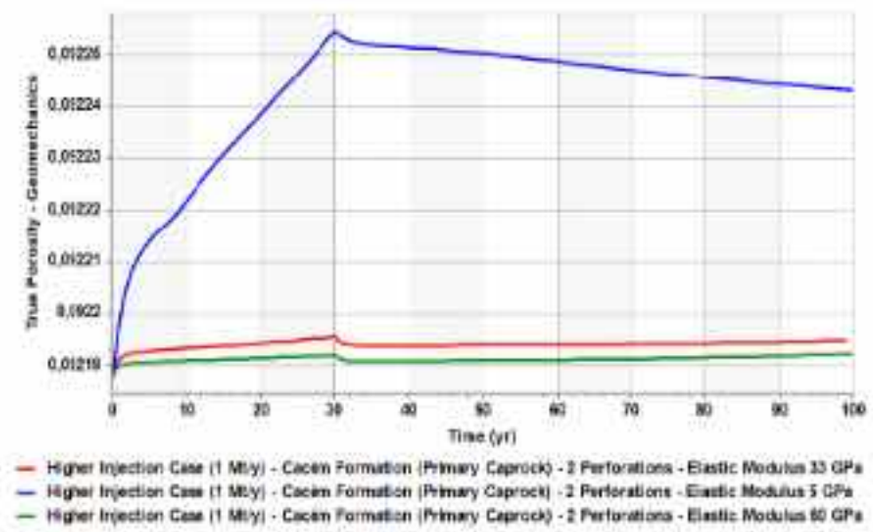


The PilotSTRATEGY project has received funding from the European Union's Horizon 2020 research and innovation programme under grant agreement No. 101022664

*Figure 6.2-46. Temporal evolution of porosity changes at the base of the Cacém Formation (Primary Caprock) for different Young's modulus, and 2 perforation intervals with an injection rate of 1Mt/y: 33 GPa (base case), 60 GPa (higher case) and 5 GPa (lower case).*

The response of porosity changes exhibits a clearer sensitivity to Young's modulus. Softer rock (E equal to 5 GPa) shows a larger transient porosity increase during early pressurization, followed by a more pronounced reduction towards initial values after shut-in. In contrast, stiffer lithologies (33–60 GPa) display attenuated porosity variations and a more gradual recovery trend. Despite these contrasts in amplitude, the overall evolution pattern is consistent across all cases (Figure 6.2-46), indicating that stiffness mainly controls the magnitude of elastic pore volume changes without inducing any irreversible porosity loss.

Volumetric strain shows a clear dependence on Young's modulus (Figure 6.2-47). The stiffest case (60 GPa) develops the largest dilative response during injection, reaching the most negative strain (net-dilation) at about 30 years, whereas lower stiffness cases show much smaller strain amplitudes. During shut-in, all scenarios display a slow partial recovery toward less negative strain as pore pressure dissipates, with the stiffest case retaining the greatest residual deformation.

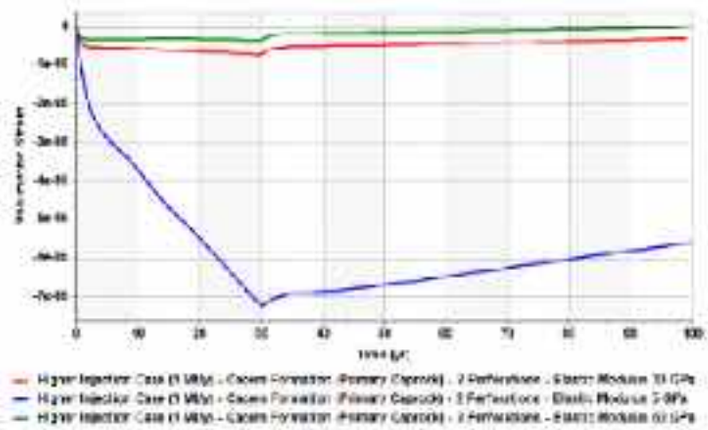

*Figure 6.2-47. Temporal evolution of volumetric strain at the base of the Cacém Formation (Primary Caprock) for different Young's modulus, and 2 perforation intervals with an injection rate of 1Mt/y: 33 GPa (base case), 60 GPa (higher case) and 5 GPa (lower case).*

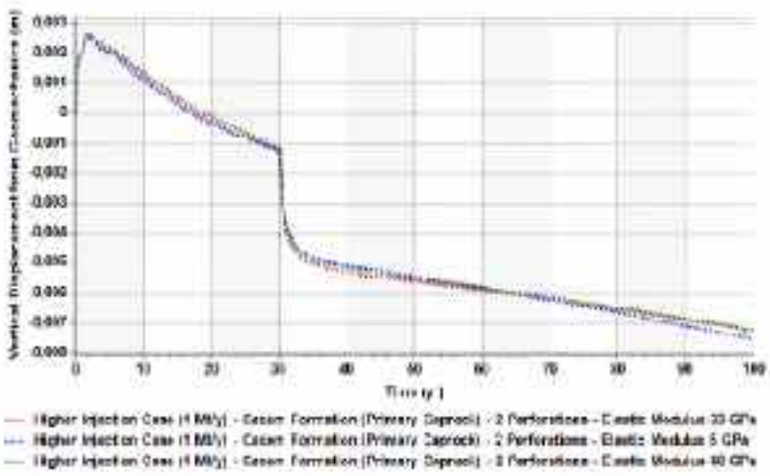

The PilotSTRATEGY project has received funding from the European Union's Horizon 2020 research and innovation programme under grant agreement No. 101022664

*Figure 6.2-48. Temporal evolution of vertical displacement at the base of the Cacém Formation (Primary Caprock) for different Young's modulus, and 2 perforation intervals with an injection rate of 1Mt/y: 33 GPa (base case), 60 GPa (higher case) and 5 GPa (lower case).*

Vertical displacement shows the same general pattern for all elastic moduli: brief early uplift during injection followed by progressive long-term subsidence (Figure 6.2-48). Differences between stiffness scenarios are minimal and remain within the millimetre range, indicating that variations in Young's modulus do not significantly affect the global deformation response or caprock integrity.

The Safety Factor decreases gradually during injection for all stiffness scenarios, with the largest drop occurring in the stiffest case (60 GPa), reaching a minimum around 30 years (Figure 6.2-49). After shut-in, the Safety Factor partially recovers and then stabilises over the long term. Despite these variations, Safety Factor values remain consistently high and well within the stable domain for all elastic moduli, indicating that changes in Young's modulus do not compromise caprock integrity.

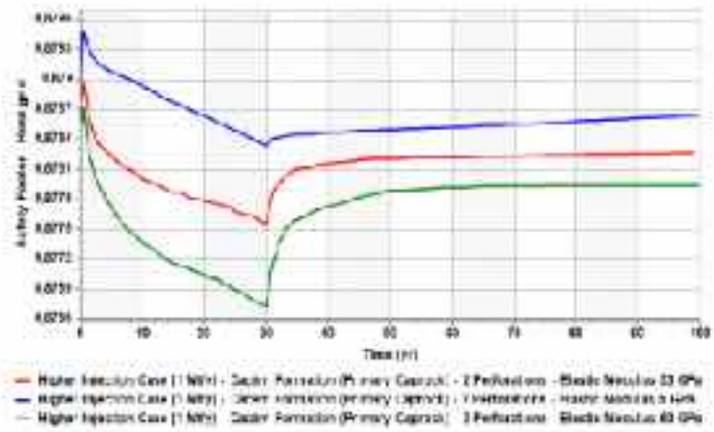

*Figure 6.2-49. Temporal evolution of safety factor at the base of the Cacém Formation (Primary Caprock) for different Young's modulus, and 2 perforation intervals with an injection rate of 1Mt/y: 33 GPa (base case), 60 GPa (higher case) and 5 GPa (lower case).*

The Mohr–Coulomb analysis shows that the stress states for all stiffness scenarios are nearly identical and remain far from the failure envelope (Figure 6.2-50).

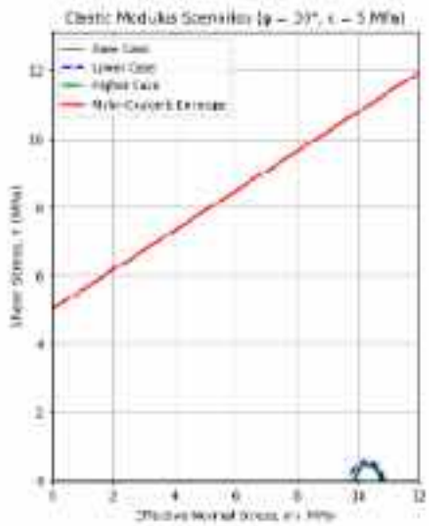

The PilotSTRATEGY project has received funding from the European Union's Horizon 2020 research and innovation programme under grant agreement No. 101022664

*Figure 6.2-50: Mohr diagram for caprock stability analysis under Young's modulus variations. The plot depicts the Mohr-Coulomb failure envelope (red line) relative to the base case (black line), lower case (blue line) and higher case (green line) effective stress states.*

Overall, variations in Young's modulus mainly affect deformation amplitudes but do not alter the stress state or threaten caprock integrity. The system remains within the elastic-poroelastic domain, with deformation controlled by reversible poroelastic processes, confirming robust long-term stability.

### *7.2.2.8 Poisson's ratio*

The uncertainty analysis for Poisson's ratio (v) indicates that variations in lateral deformability have little influence on pore-pressure evolution within the Cacém Formation. Pressure trajectories for v = 0.20, 0.29, and 0.40 are almost fully superimposed during both the injection and post-injection phases (Figure 6.2-51), demonstrating that changes in Poisson's ratio do not materially affect pressure build-up or transmission. Only marginal differences are discernible in the late post-injection period, where the highest Poisson's ratio (v = 0.40) exhibits a slightly higher residual pressure compared with the lower values. However, this effect is minimal and does not alter the overall behaviour of the system. In all cases, pore pressures remain comfortably within operational limits, confirming that uncertainties in Poisson's ratio do not compromise hydraulic or geomechanical safety.

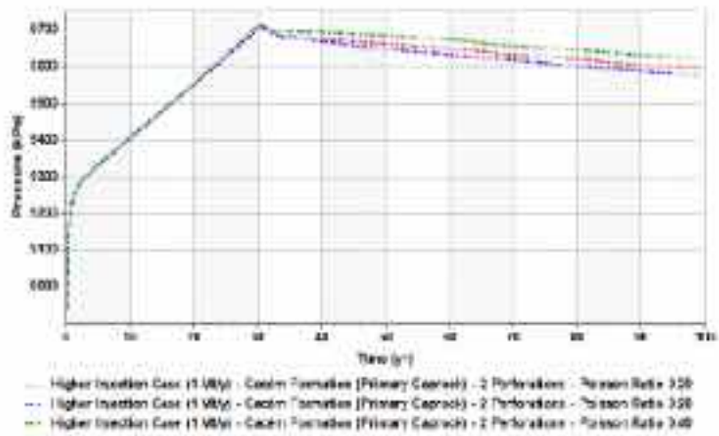

*Figure 6.2-51. Temporal evolution of pore pressure at the base of the Cacém Formation (Primary Caprock) for different Poisson's ratios, and 2 perforation intervals with an injection rate of 1Mt/y: 0.29 (base case), 0.40 (higher case) and 0.20 (lower case).*

The PilotSTRATEGY project has received funding from the European Union's Horizon 2020 research and innovation programme under grant agreement No. 101022664

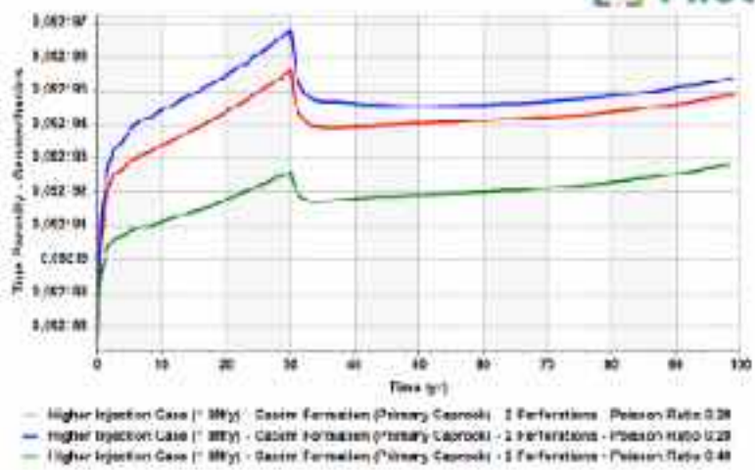

*Figure 6.2-52. Temporal evolution of porosity changes at the base of the Cacém Formation (Primary Caprock) for different Poisson's ratios, and 2 perforation intervals with an injection rate of 1Mt/y: 0.29 (base case), 0.40 (higher case) and 0.20 (lower case).*

Porosity increases during injection for all Poisson's ratio values, reaching a minimum at about 30 years (Figure 6.2-52). Higher Poisson's ratio (ν = 0.40) results in slightly lower porosity increase (smaller dilative response), while lower values produce larger porosity increases. During shut-in, all cases show a slow partial recovery as pore pressure dissipates, with porosity decreasing towards initial values, indicating that Poisson's ratio has a secondary control on porosity evolution.

Volumetric strain shows net dilative behaviour during injection for all Poisson's ratio values, reaching a maximum (most negative values, i.e., dilation) around 30 years (Figure 6.2-53). Higher Poisson's ratio (ν = 0.40) results in less dilation (strain closer to zero), whereas lower values produce more negative strain (greater dilation). During shut-in, all cases exhibit a slow partial recovery as pore pressure dissipates. Overall, differences are minor, indicating that Poisson's ratio has only a secondary influence on the deformational response of the caprock.

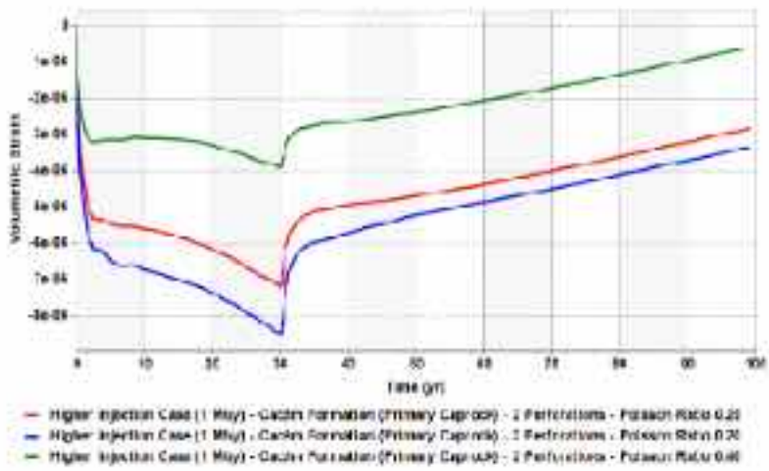

*Figure 6.2-53. Temporal evolution of volumetric strain at the base of the Cacém Formation (Primary Caprock) for different Poisson's ratios, and 2 perforation intervals with an injection rate of 1Mt/y: 0.29 (base case), 0.40 (higher case) and 0.20 (lower case).*

The PilotSTRATEGY project has received funding from the European Union's Horizon 2020 research and innovation programme under grant agreement No. 101022664

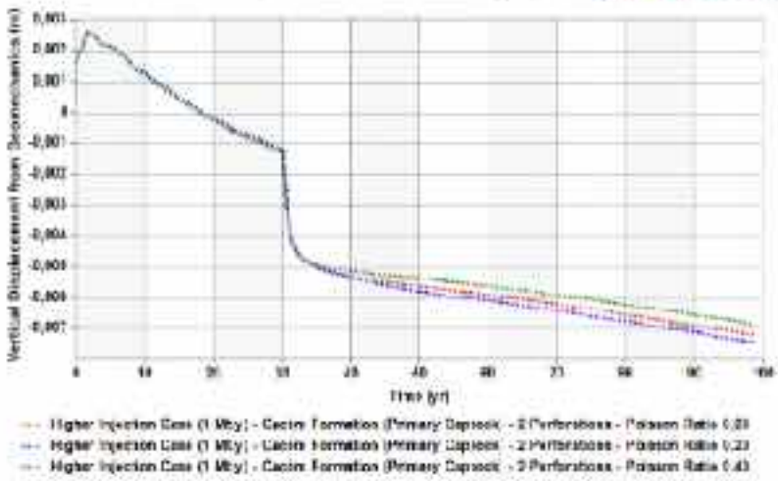


*Figure 6.2-54. Temporal evolution of vertical displacement strain at the base of the Cacém Formation (Primary Caprock) for different Poisson's ratios, and 2 perforation intervals with an injection rate of 1Mt/y: 0.29 (base case), 0.40 (higher case) and 0.20 (lower case).*

The Safety Factor decreases gradually during injection for all Poisson's ratio values, reaching a minimum around 30 years, then partially recovers and stabilises during shut-in (Figure 6.2-55). Higher Poisson's ratio (ν = 0.40) yields slightly higher Safety Factor values than lower ratios, but differences are small. In all cases, the Safety Factor remains comfortably within the stable domain, indicating that uncertainty in Poisson's ratio does not compromise caprock integrity.

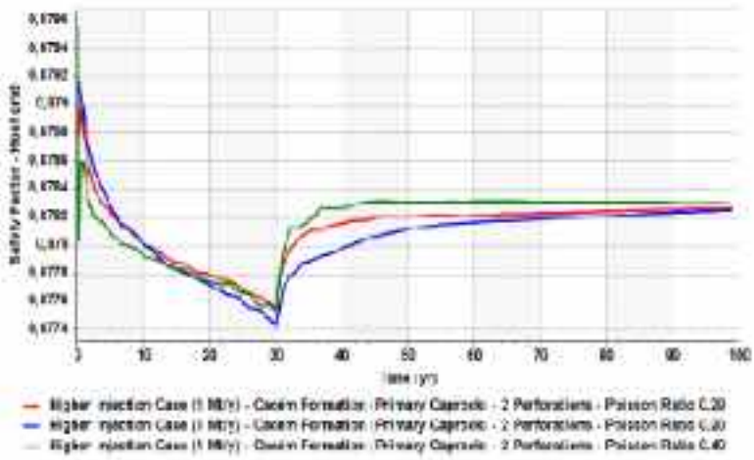


*Figure 6.2-55. Temporal evolution of safety factor at the base of the Cacém Formation (Primary Caprock) for different Poisson's ratios, and 2 perforation intervals with an injection rate of 1Mt/y: 0.29 (base case), 0.40 (higher case) and 0.20 (lower case).*

The Mohr–Coulomb analysis shows that variations in Poisson's ratio have a negligible effect on the stress state relative to the failure criterion. The Mohr circles corresponding to all scenarios are almost perfectly superimposed and remain far from the Mohr–Coulomb envelope (Figure 6.2-56), demonstrating that changes in lateral deformability do not bring the system closer to shear failure under the tested operational conditions.

The PilotSTRATEGY project has received funding from the European Union's Horizon 2020 research and innovation programme under grant agreement No. 101022664

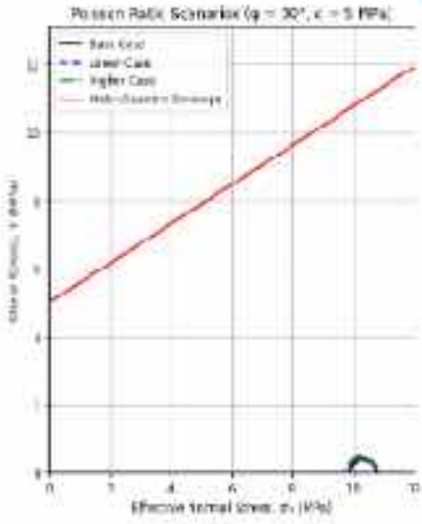

*Figure 6.2-56: Mohr diagram for caprock stability analysis under Poisson's ratio variations. The plot depicts the Mohr-Coulomb failure envelope (red line) relative to the base case (black line), lower case (blue line) and higher case (green line) effective stress states.*

Overall, the uncertainty analysis confirms that Poisson's ratio has little influence on pore pressure evolution, porosity changes, volumetric strain, vertical displacement, or structural stability. The system consistently remains within the elastic–poroelastic regime, with deformation dominated by reversible poroelastic processes, and robust safety margins preserved across the full range of Poisson's ratio values considered. Consequently, uncertainty in lateral deformation behaviour does not compromise the mechanical integrity of the Cacém Formation or the long-term safety of $CO_2$ storage operations.

## 7.3 Appendix – Ebro region (Spain)

### 7.3.1 Well Integrity – Software Validation

Accurately representing this drying-out process is essential for predicting salt precipitation near the wellbore. The conversion from Intersect to Eclipse 300 (CO2STORE) was validated, with the Eclipse 300 model correctly reproducing water vaporization in the near-wellbore region during $CO_2$ injection (Figure 7-3). A slight decrease in injectivity is nevertheless observed in the Eclipse 300 (CO2STORE) results (Figure 7-4). This difference leads to a modest 1.1% variation in total storage capacity between the two simulators, *i.e.* 7.50 Mt for Intersect versus 7.58 Mt for Eclipse 300 (CO2STORE) for the single-injector CCS-1 scenario under the P50 case. This small discrepancy is attributed to the different

The PilotSTRATEGY project has received funding from the European Union's Horizon 2020 research and innovation programme under grant agreement No. 101022664

solubility models implemented in each simulator: Intersect uses tabulated solubility data, whereas Eclipse 300 (CO2STORE) employs the Spycher and Pruess correlations.

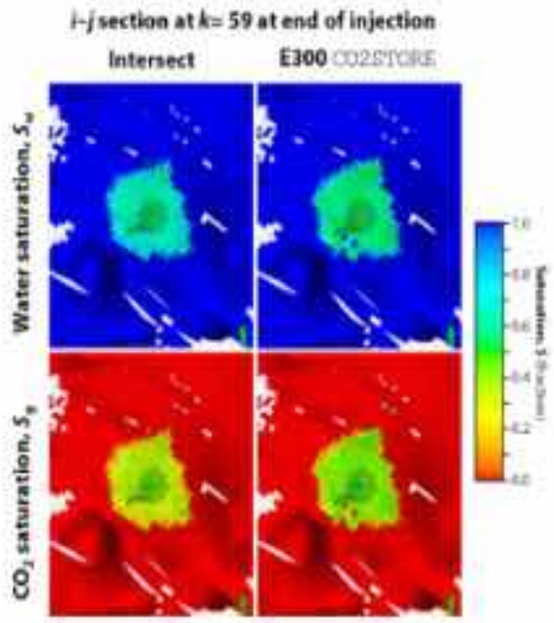


*Figure 7-3. Comparison of water saturation (Sw, upper row) and CO2 saturation (Sg, lower row) in the near-wellbore region between the Intersect and Eclipse 300 (CO2STORE) simulations. Water vaporization and the associated dry-out effect are evident in the Eclipse*

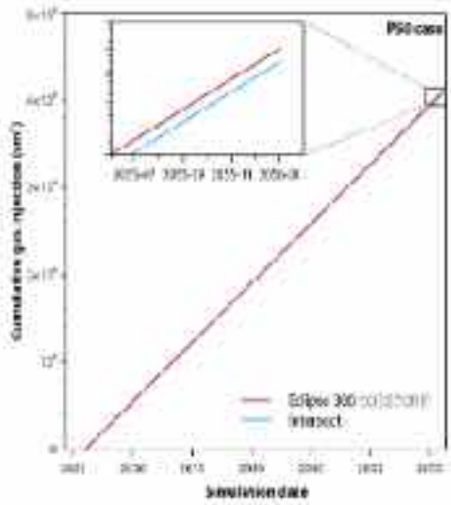


*Figure 7-4 Comparison of cumulative $CO_2$ injected for the CCS-1 single injector scenario (P50 case) obtained from the Intersect and Eclipse 300 (CO2STORE) simulations. The results show a relatively very small variation in total injected mass at the end of the injection period.*

The PilotSTRATEGY project has received funding from the European Union's Horizon 2020 research and innovation programme under grant agreement No. 101022664

### 7.3.2 Mechanical rock properties for Ebro basin

| DYNAMIC PROPERTIES | | | |
|---|---|---|---|
| **Dynamic Young's modulus, $E_{dyn}$** | **Dynamic Poisson's ratio, $\nu_{dyn}$** | **Dynamic shear modulus, $G_{dyn}$** | **Bulk modulus, $K_{dyn}$** |
| $\rho_b V_S^2 \frac{3V_P^2 - 4V_S^2}{V_P^2 - V_S^2}$ | $\frac{V_P^2 - 2V_S^2}{2(V_P^2 - V_S^2)}$ | $\rho_b V_S^2$ | $\rho_b \left(V_P^2 - \frac{4}{3} V_S^2\right)$ |
| **STATIC PROPERTIES** | | | |
| **Static Young's modulus, $E_{stat}$** | **Static Poisson's ratio, $\nu_{stat}$** | **Static shear modulus, $G_{stat}$** | **Static bulk modulus, $K_{stat}$** |
| $E_{stat} = 0.032 \times E_{dyn}^{1.632}$ (Fuller) | **Anhydrite**: 0.49<br>**Dolomite, limestone, sandstone**: 0.2<br>**Shale**: 0.35 | $G_{stat} = \frac{E_{stat}}{2(1+\nu_{stat})}$ | $K_{stat} = \frac{E_{stat}}{3(1+2\nu_{stat})}$ |
| **STRENGTH PROPERTIES** | | | |
| **Uniaxial, or unconfined, compressive strength, *UCS*** | **Tensile strength, $\sigma_t$** | **Internal friction coefficient, $\mu$** | |
| $UCS = (13.8/2) \times E_{dyn}^{0.51}$ (anhydrite; Chang-E) | $\sigma_t \approx 0.1 \times UCS$ | $\mu = \tan\left(\sin\frac{V_P - 1}{V_P + 1}\right)$ | |
| $UCS = \frac{\left(\frac{7682}{\Delta t}\right)^{1.82}}{145}$ (carbonates; Militzer & Stoll 1973) | | | |
| $UCS = 1200 \times e^{-0.036 \times \Delta t}$ (sandstone; McNally 1987) | | | |
| $UCS = 1.46 \times 10^7 \times \Delta t^{-2.03}$ (shale; Horsrud 2001) | | | |

*Table 7-1: Table 7-2 Definition of rock mechanical properties and empirical equations employed in the present study. Young's modulus (E) and shear modulus (G) are reported in gigapascals (GPa), whereas the bulk modulus, unconfined compressive strength (UCS), and tensile strength.*

The PilotSTRATEGY project has received funding from the European Union's Horizon 2020 research and innovation programme under grant agreement No. 101022664

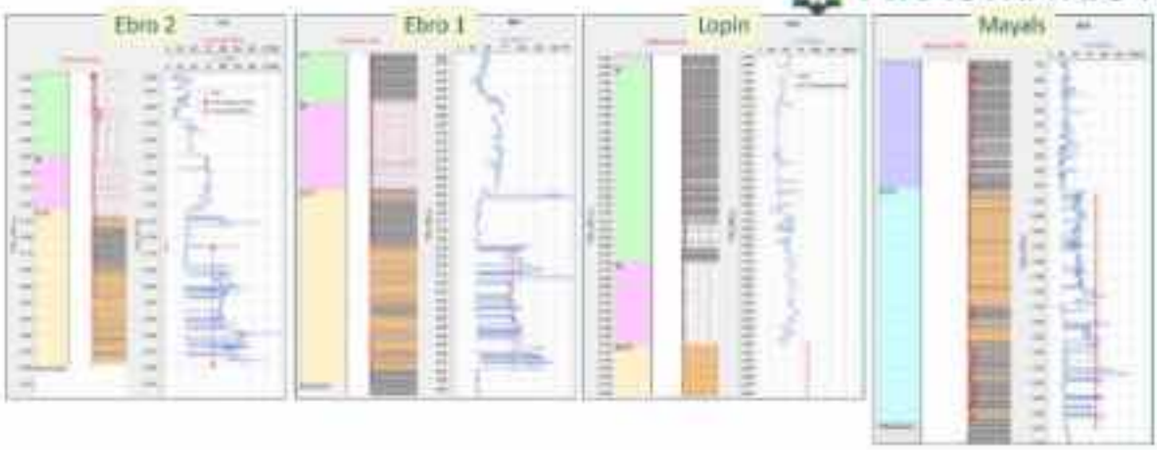


*Figure 7-5 Uniaxial compressive strength (UCS) derived from log data (blue log curve; values in MPa) versus UCS derived from laboratory measurements performed on a Buntsandstein outcrop sample (red vertical line).*

| Rock mechanics property | Average value | Units |
|---|---|---|
| Unconfined compressive strength, *UCS* | 83.16 | MPa |
| Tensile strength, $\sigma_t$ | 7.22 | MPa |
| Static Young's modulus, $E_{stat}$ | 19.41 | GPa |
| Static Poisson's ratio, $\nu_{stat}$ | 0.33 | — |
| Ultrasonic P-wave propagation velocity, $V_p$ | 2.54 | km·s$^{-1}$ |
| Ultrasonic S-wave propagation velocity, $V_S$ | 1.22 | km·s$^{-1}$ |
| $V_p/V_S$ | 1.99 | — |
| Spatial wave attenuation, $\alpha_L$ | 7.08 | dB·cm$^{-1}$ |
| Dynamic Young's modulus, $E_{dyn}$ | 9.26 | GPa |
| Static Poisson's ratio, $\nu_{dyn}$ | 0.33 | — |

*Table 7-3 Rock mechanical properties obtained from laboratory measurements of outcrop samples from the Torre de las Arcas section. Values reported are mean values for each parameter. Source: Baroni et al. (2023), deliverable 2.8.*

### 7.3.3 Fault Stability Assessment Based on Critical Pore Pressure Change (CPPC) – Results for a friction angle of 25°

#### *7.3.3.1 CCS-1 location cases*

The Figure 7-6 shows the fault stability analysis assuming a friction angle of 25°, with the P10 scenario and injector CCS-1. The sequence includes the initial CPPC, the pore pressure increase (ΔP), and the resulting change in CPPC after injection.

In this case, a greater number of faults exhibit points with CPPC values below zero, indicating potential instability. Specifically, faults Falla008, Falla009, and Falla005—the ones closest to the injector—show several points exceeding the failure threshold. These critical areas are also visible in the histogram, where a larger portion of values fall into the negative range. The minimum CPPC value reaches –2.17 MPa, confirming a more widespread reduction in fault stability compared to the case with a 30° friction angle, and highlighting the importance of mechanical parameter selection in fault reactivation assessments.

The PilotSTRATEGY project has received funding from the European Union's Horizon 2020 research and innovation programme under grant agreement No. 101022664

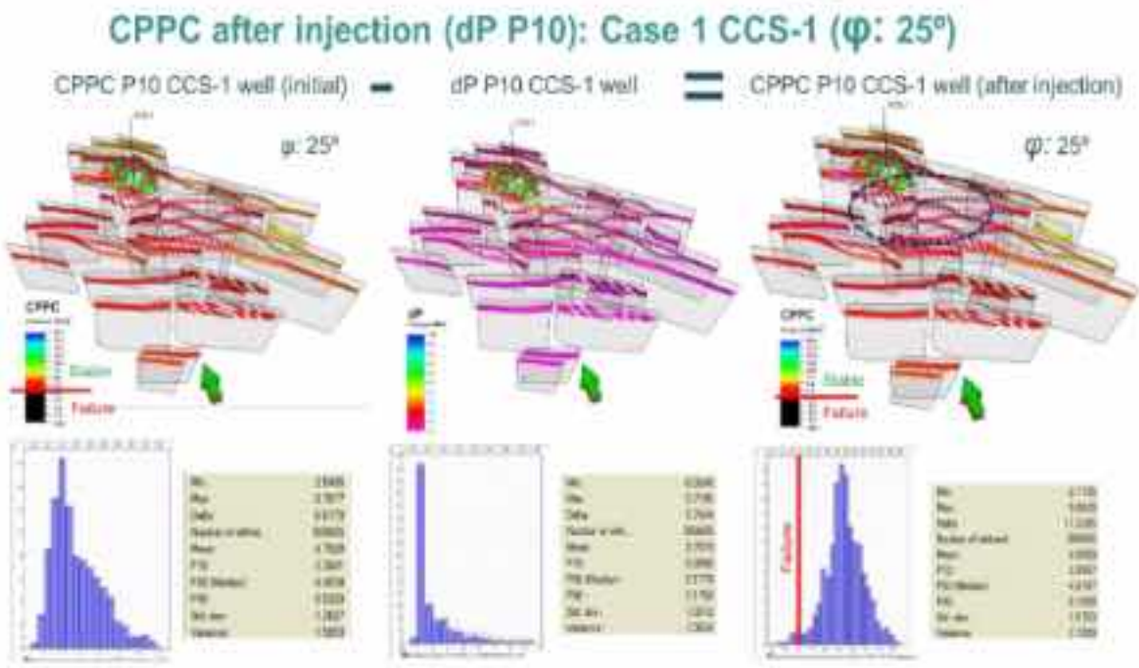


*Figure 7-6 CPPC after injection (P10) for case 1(CCS-1) and friction angle of 25°.*

For the P50 scenario, with a friction angle of 25°, a great number of points fall below the failure threshold, with CPPC values reaching –1.74. Falla008, Falla009, and Falla005—the faults closest to the injector—display several critical points, clearly visible in both the spatial maps and the histogram (Figure 7-7).

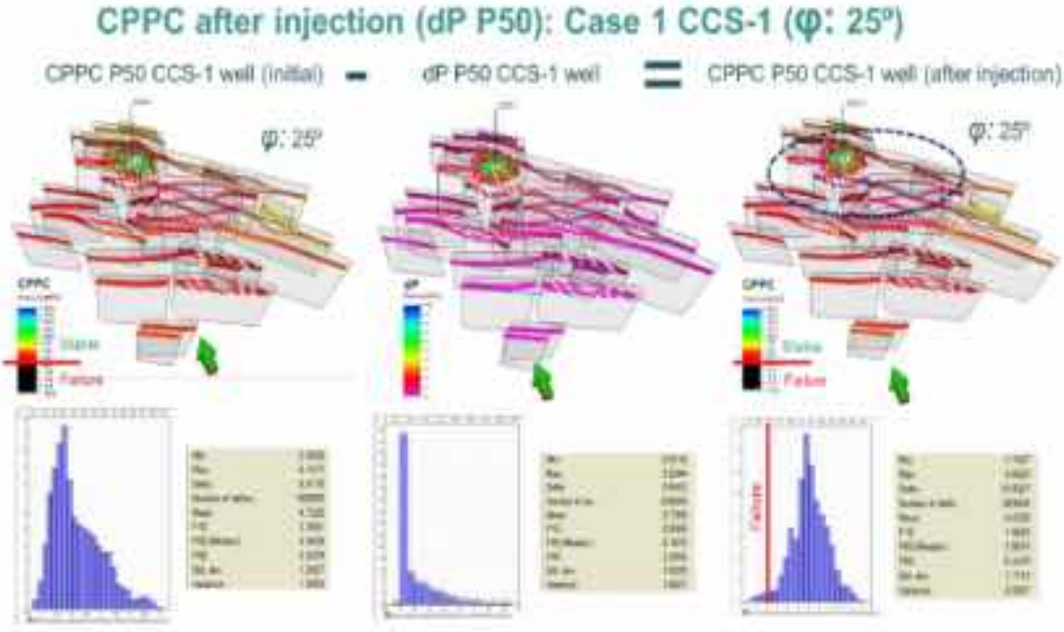


*Figure 7-7 CPPC after injection (P50) for case 1(CCS-1) and friction angle of 25°.*

For the P90 scenario, with friction angle of 25°, the system shows some sensitivity, with CPPC values dropping to –1.25. A few points approach the failure threshold, mainly affecting faults Falla008, Falla009, and Falla005, but the extent of instability remains limited (Figure 7-8).

The PilotSTRATEGY project has received funding from the European Union's Horizon 2020 research and innovation programme under grant agreement No. 101022664

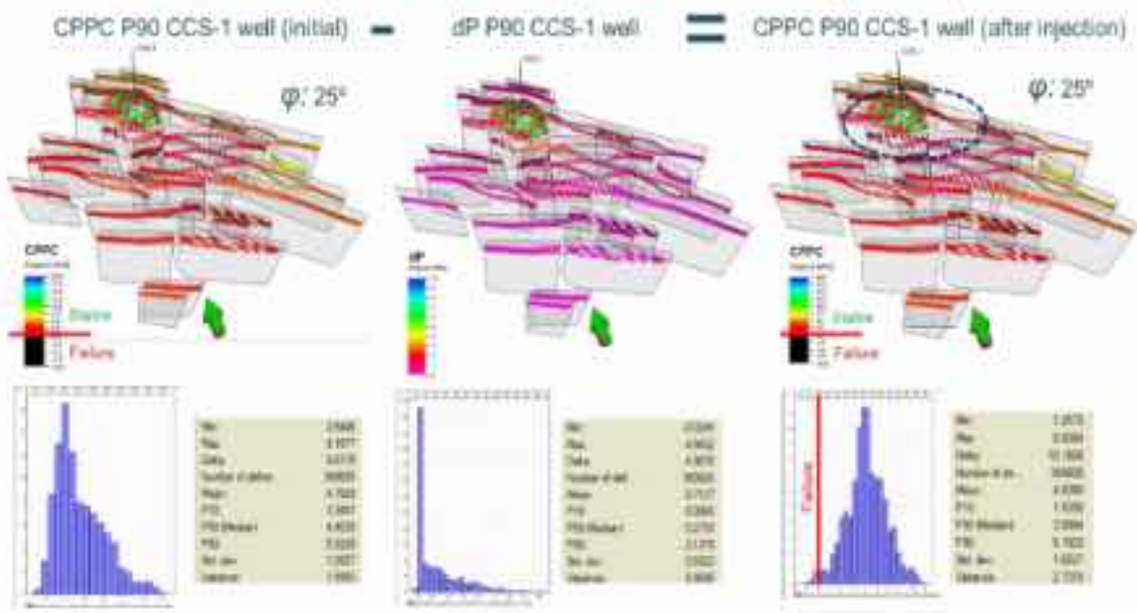


*Figure 7-8 CPPC after injection (P90) for case 1(CCS-1) and friction angle of 25°.*

### 7.3.3.2 LOCD-1 location cases

With the injection location at LOCD-1, for the P10 scenario, with a friction angle of 25°s, the system becomes significantly sensitive. The minimum CPPC value drops to –4.89, indicating a broader and more severe mechanical response than for an angle of 30°. The same faults identified at 30°—Falla014, Falla011, and Falla017—remain affected, but the extent of instability increases notably, with a much larger number of cells on the fault plane showing negative CPPC values. This expansion of unstable zones suggests a higher likelihood of fault slip and highlights the critical role of friction angle in controlling fault behaviour under high-pressure conditions (Figure 7-9).

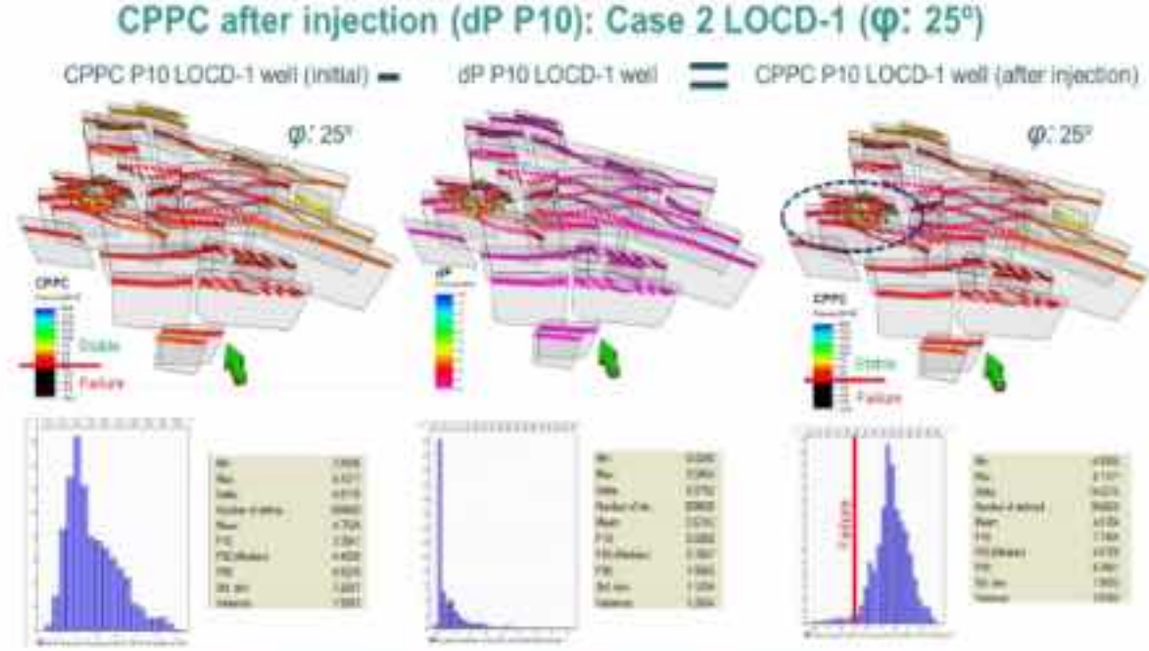


*Figure 7-9 CPPC after injection (P10) for case 2(LOCD-1) and friction angle of 25°.*

The PilotSTRATEGY project has received funding from the European Union's Horizon 2020 research and innovation programme under grant agreement No. 101022664

For the P50 scenario, with a friction angle of 25°, the minimum CPPC reaches –4.22. The same faults continue to show instability, but again with fewer affected zones compared to the P10 scenario. The histogram shows a broad spread of negative values, though less intense than in the more critical cases. Figure 7-10.

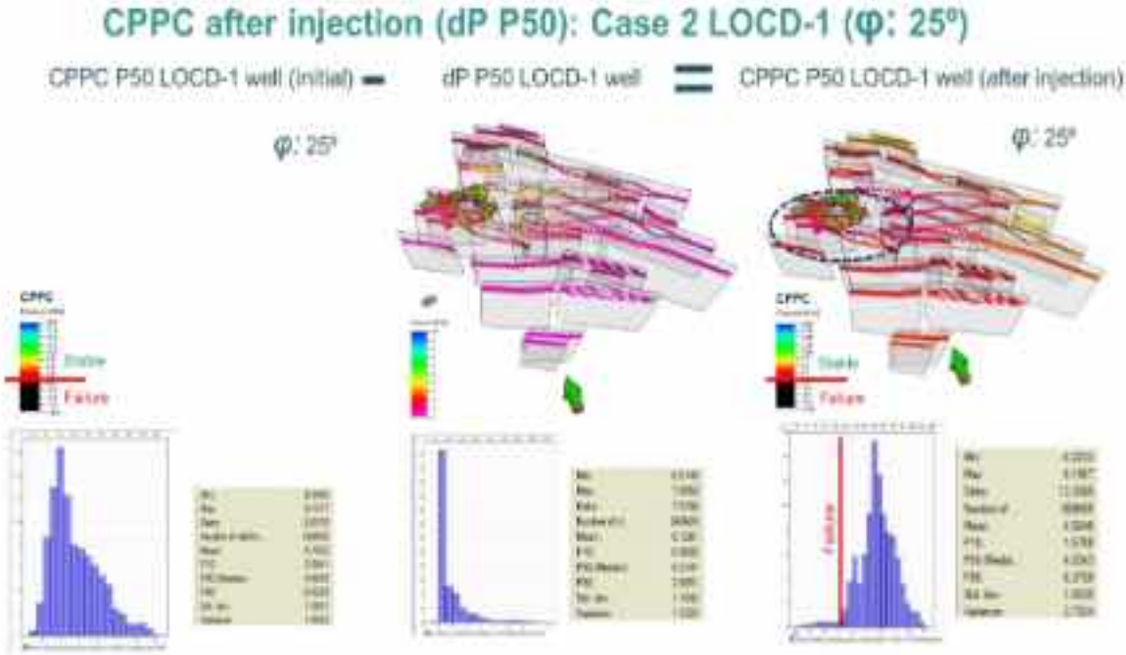


*Figure 7-10 CPPC after injection (P50) for case 2(LOCD-1) and friction angle of 25°.*

For the P90 scenario, with a friction angle of 25°, the minimum CPPC reaches –3.91, with the same faults, as for a friction angle of 30°, showing broader instability.

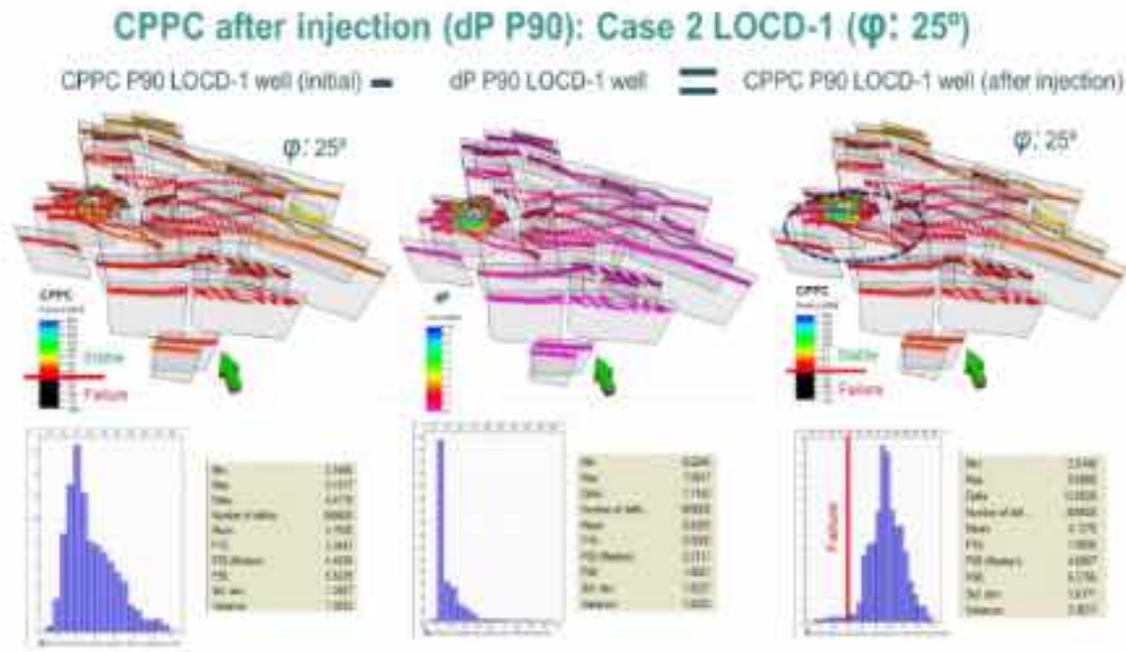


*Figure 7-11 CPPC after injection (P90) for case 2(LOCD-1) and friction angle of 25°.*

The PilotSTRATEGY project has received funding from the European Union's Horizon 2020 research and innovation programme under grant agreement No. 101022664

### 7.3.3.3 CCS-1 & LOCD-1 location cases

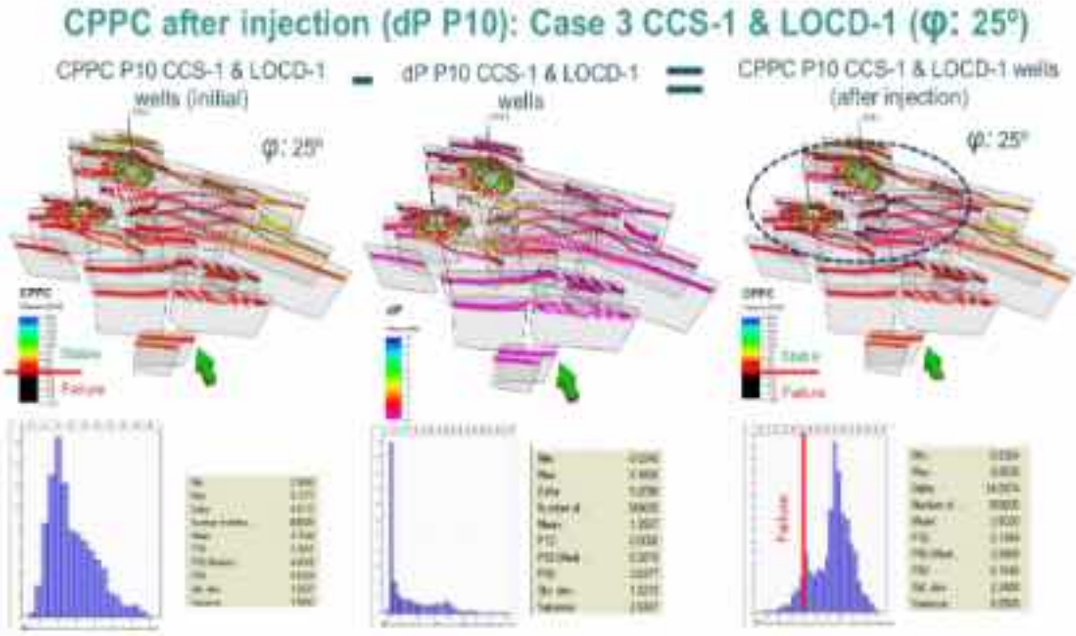


*Figure 7-12 CPPC after injection (P10) for case 3(CCS-1 &LOCD-1) and friction angle of 25°.*

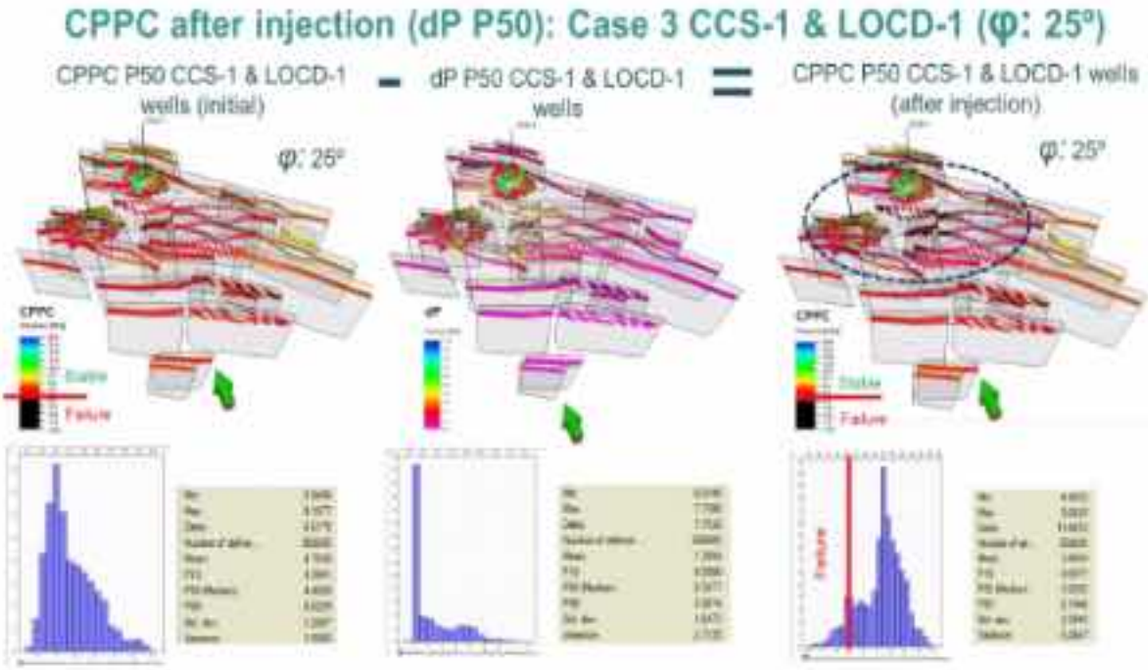


*Figure 7-13 CPPC after injection (P50) for case 3(CCS-1 &LOCD-1) and friction angle of 25°.*

The PilotSTRATEGY project has received funding from the European Union's Horizon 2020 research and innovation programme under grant agreement No. 101022664

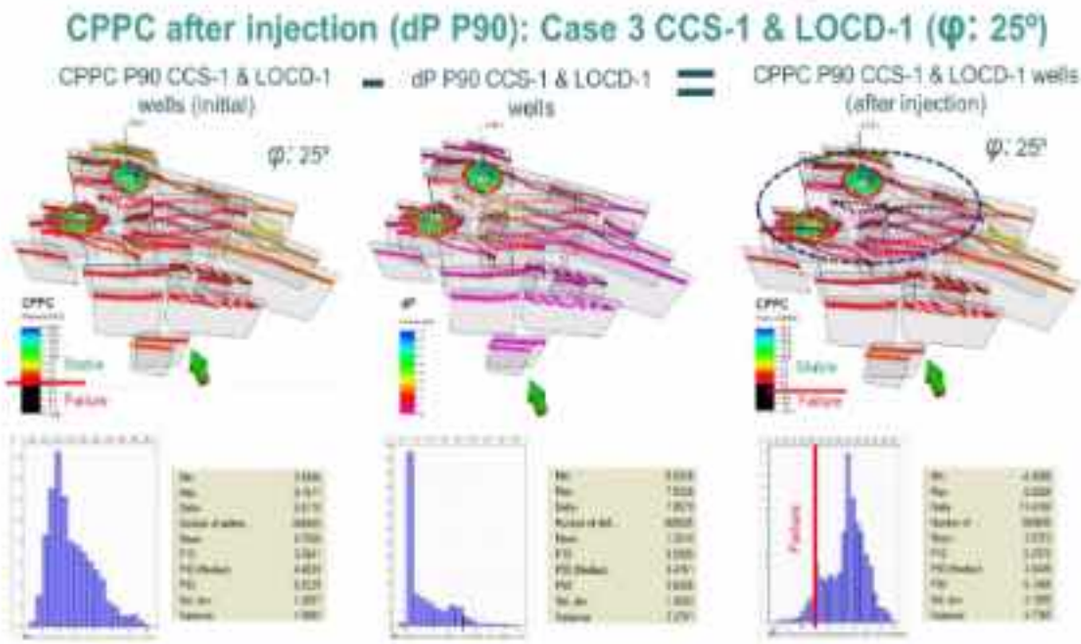


*Figure 7-14 CPPC after injection (P90) for case 3(CCS-1 &LOCD-1) and friction angle of 25°.*

The PilotSTRATEGY project has received funding from the European Union's Horizon 2020 research and innovation programme under grant agreement No. 101022664